Institut d'Astrophysique

Faculté des Sciences

A multiwavelength observational study of the non-thermal emission from O-type stars

by

Michaël De Becker

– December 2005 –

Dissertation présentée en vue
de l'obtention du grade de
Docteur en Sciences

Acknowledgements

First of all, it is a pleasure to thank Gregor Rauw for the supervision of this thesis and for the many things I have learned by working with him. Either as a teacher or as a thesis supervisor, he is the main contributor to my introduction to the job of researcher in astrophysics. It was also very stimulating to work in the 'Groupe d'AstroPhysique des Hautes Energies (GAPHE)', that is mainly driven by Gregor's dynamism. It is not common to meet people that give the impression that they benefit from more than 24 hours in a day, and Gregor belongs to this scarce category. In addition, most of the data analysed and discussed in this thesis were made available thanks to the numerous time proposals submitted mainly at OHP and at ESA by Gregor. I think that this point deserves to be mentioned here.

I am greatful to Jean-Pierre Swings, Jean-Marie Vreux and Gregor Rauw or the financial support I benefitted for this thesis. They always managed the things in order to warrant the financing of my thesis, of my participation to conferences, and of the many observing runs executed at the Observatoire de Haute-Provence.

I would also like to thank my two fellows of the GAPHE, namely Hugues Sana and Yaël Nazé. I have also learned a lot of things through all the discussions we had during the four years we spent together in the group, and it was a pleasure to work with them.

Many people deserve my gratitute for their help and useful discussions. First, I am very grateful to Eric Gosset for discussions on statistics and other subjects. I sincerely appreciated his availability to answer my questions. Christophe Jean, Chirstophe Libbrechts and Joël Poels are thanked for their useful advice that allowed me to be introduced to C programming. I am grateful to Alain Detal for the installation of the softwares I used for the processing of the data discussed in this work. Many thanks also to the two youngest members of the GAPHE, namely Natacha Linder and Jean-Christophe Leyder, respectively for observations at OHP and for helpful information concerning INTEGRAL data processing. I wish both of them good luck for the next few years, they are the next ones to present a thesis in our group.

There is also one person who deserves many thanks, because a crucial aspect of the life of the Institute depends on her. I am speaking about Denise Caro. She is always there to help us to find solutions to administrative issues whose list would be too long to be enumerated here. On an ashtray she was offered a few years ago, one can read "Kéne pufkène, châle!", but she would certainly deserve a notice on which one could read "C'èst une binameye, Denise! Si èl n'esteu nin là, on s'rait to pierdou!".

It is a pleasure to thank colleagues who have contributed to the obtaining of some of the data used in this work: Gregor Rauw, Jean Manfroid, Hugues Sana, Philippe Eenens. In the past four years, many collaborators contributed to improve my knowledge concerning many topics addressed in this thesis: Ronny Blomme, Julian Pittard, Ian Stevens, Andy Pollock, Mark Runacres, Sven Van Loo, Igor Antokhin. May they be thanked for their contributions to the studies included in this work. I am also grateful to other colleagues for stimulating discussions and for their interest in some parts of my work, namely Sean Dougherty, Gustavo Romero, Paula Benaglia and others...

This page is also the opportunity to thank all my colleagues here in Liege for making of our Institute a very nice place, and not only for work. Lunch times, outreach activities, 'pops', the many discussions not necessarily related to astronomy, coffee breaks... contributed to the nice moments I spent in this Institute.

Of course, I would like to thank my family to be always there. If I have been able to prepare this thesis, it is mainly thanks to them.

Finally, I would like to thank Ronny Blomme, Eric Gosset, Gregor Rauw, Julian Pittard, Jean Surdej, Jean-Pierre Swings, Jean-Marie Vreux, and Peredur Williams to have accepted to devote some part of their time to participate to the Jury of my thesis.

Michaël De Becker

The beginning of knowledge is the discovery
of something we do not understand.
Frank Herbert

If knowledge can create problems,
it is not through ignorance
that we can solve them.
Isaac Asimov

A significant fraction of the content of this thesis is presented in the form of papers already published in refereed journals, or that will be submitted in the near future. A lot of details concerning the studies compiled hereafter can be found in these articles. However, all these results have been summarized and are presented just before the insertion of the original articles. A complete overview of this thesis can therefore be achieved by reading all the chapters, from the introduction to the final conclusions and prospects for future works, without the need to read through all the detailed contributions included in the form of articles. However, the reading of these papers is of course necessary if the reader wishes to get a more detailed insight in the studies compiled in this work.

Abstract

The present work is devoted to an observational multiwavelength study of the non-thermal emission of O-type stars. The non-thermal radio emission is believed to be synchrotron radiation, therefore requiring the existence of a magnetic field as well as of a population of relativistic electrons. The physical circumstances responsible for the acceleration of electrons up to relativistic velocities are not yet completely elucidated, but such an acceleration most probably occurs through the first order Fermi mechanism in the presence of hydrodynamic shocks, also called the Diffusive Shock Acceleration (DSA) mechanism. In the context of massive stars, the shocks responsible for this acceleration process may be intrinsic to their stellar winds, or arise from the collision between stellar winds in binary systems. In addition, the existence of non-thermal emission processes such as inverse Compton scattering suggests the possibility to detect a high-energy counterpart to the non-thermal emission observed in the radio domain. The objectives of this work are to (1) study the impact of the multiplicity on the non-thermal emission, (2) investigate the issue of the non-thermal emission of massive stars in the high-energy domain, and (3) discuss the possibility to constrain physical quantities such as the magnetic field strength through the study of these non-thermal emission processes.

We investigate in detail several non-thermal emitting O-type stars, namely HD 168112, HD 167971, Cyg OB2 #8A, Cyg OB2 #9, and HD 15558. For most of these targets, high quality *XMM-Newton* data are used in order to study their X-ray properties. In most case, the question of the multiplicity is also addressed through optical studies performed on the basis of data obtained with ground-based telescopes. The most intensive study is carried out on the Cyg OB2 region, for which we also obtained and analysed *INTEGRAL* data, in order to investigate the possible relation between the massive stars in Cyg OB2 and the unidentified EGRET source 3EG J2033+4118. In addition, high quality *XMM-Newton* data of the close massive binary HD 159176 are also studied. Even though this latter target does not belong to the category of non-thermal radio emitters, its study unexpectedly turns out to be crucial in the context of this campaign as it might be the first O + O system likely to be classified as an non-thermal X-ray emitter.

Considering our observational results, along with results from radio observations mainly coordinated by colleagues from the Royal Observatory of Belgium, we propose a general qualitative schematic view of the non-thermal emission from massive stars. First, it seems that the multiplicity plays a crucial role in the non-thermal emission processes. Second, we have found that the simultaneous detection of non-thermal radiation in the radio and X-ray (below 10.0 keV) domains is unlikely. Non-thermal radio emitters are indeed most probably binaries with periods longer than a few weeks, whilst only close binaries with periods of at most a few days may be non-thermal emitters in the soft X-ray domain. However, such a simultaneous detection is possible if the very hard X-rays or soft γ-rays are considered, i.e. in a domain where the thermal emission from the colliding winds does not overwhelm the non-thermal emission. Moreover, it appears that the existence of non-thermal X-ray emitters without a non-thermal radio counterpart should be envisaged. Finally, the simultaneous detection of radio and high-energy non-thermal emissions is likely to lead to an indirect method to estimate the local magnetic field strength in the colliding-wind region of massive binaries.

Résumé

Ce travail est dédié à l'étude observationnelle et multifréquentielle de l'émission non-thermique des étoiles de type O. L'émission radio non-thermique est très probablement due à du rayonnement synchrotron, nécessitant dès lors la présence d'un champ magnétique et l'existence d'une population d'électrons relativistes. Les circonstances physiques responsables de l'accélération des électrons jusqu'à des vitesses relativistes ne sont pas encore totalement élucidées, mais cette accélération est supposée se produire via le mécanisme de Fermi de premier order en présence de chocs hydrodynamiques. Dans le contexte des étoiles massives, les chocs responsables de ce processus d'accélération peuvent être intrinsèques aux vents stellaires, ou être produits par la collision des vents stellaires dans un système binaire. De plus, l'existence de processus d'émission non-thermique tels que la diffusion Compton inverse suggère la possibilité de détecter une contrepartie de haute énergie à cette émission non-thermique observée dans le domaine radio. Les objectifs de ce travail sont (1) d'étudier l'impact de la multiplicité sur l'émission non-thermique, (2) d'investiguer la question de l'émission non-thermique des étoiles massives dans le domaine des hautes énergies, et (3) de discuter la possibilité de contraindre des quantités physiques telles que l'intensité du champ magnétique au travers de l'étude des processus d'émission non-thermique.

Nous étudions en détails plusieurs étoiles de type O émettrices de rayonnement radio non-thermique, à savoir HD 168112, HD 167971, Cyg OB2 #8A, Cyg OB2 #9, et HD 15558. Pour la plupart de ces cibles, des données *XMM-Newton* de haute qualité sont utilisées en vue d'étudier les propriétés de leur émission X. Dans la plupart des cas, la question de la multiplicité est aussi abordée au travers d'études dans le domaine visible réalisées sur base de données obtenues au moyen de télescopes au sol. L'étude la plus intensive est menée dans la région de Cyg OB2, pour laquelle nous avons aussi obtenu et analysé des données *INTEGRAL* en vue d'étudier la relation possible entre les étoiles massives de Cyg OB2 et la source EGRET non-identifiée 3EG J2033+4118. De plus, des données *XMM-Newton* de haute qualité sur la binaire massive serrée HD 159176 sont aussi étudiées. Quoique cette dernière cible n'appartienne pas à la catégorie des émetteurs radio non-thermiques, son étude s'avère cruciale dans le contexte de cette campagne puisqu'il pourrait s'agir du premier système O + O classé en tant qu'émetteur X non-thermique.

En considérant nos résultats observationnels, ainsi que les résultats d'observations radio principalement coordonnées par nos collègues de l'Observatoire Royal de Belgique, nous sommes en mesure de proposer une vue générale qualitative de l'émission non-thermique des étoiles massives. D'abord, il semble que la multiplicité joue un rôle crucial dans les processus non-thermiques. Ensuite, nous avons découvert que la détection simultanée de rayonnement non-thermique dans les domaines radio et X (en-dessous de 10 keV) est peu vraisemblable. Les émetteurs radio non-thermiques sont en effet très probablement des systèmes binaires de période plus longue que quelques semaines, alors que seules les binaires serrées avec des périodes tout au plus de quelques jours pourraient être des émetteurs non-thermiques dans le domaine des X mous. Toutefois, une telle détection simultanée est possible si les X durs et les rayons γ mous sont considérés, c'est à dire dans un domaine où l'émission thermique en provenance de la collision des vents ne dissimule plus l'émission non-thermique. De plus, il apparaît que l'existence d'émetteurs X non-thermiques sans contrepartie radio non-thermique devrait être envisagée. Enfin, la détection simultanée d'émissions non-thermiques en radio et dans les hautes énergies pourrait conduire à une méthode indirecte en vue d'estimer l'intensité du champ magnétique local dans la région de collision des vents des binaires massives.

Contents

Introduction

As a preamble, we introduce the concept of non-thermal radio emission that will be omnipresent throughout the following chapters. The main observational and theoretical elements that motivated this work will be described. A catalogue of the non-thermal radio emitting massive stars will be presented, with emphasis on the O-type stars to which this work is devoted. Considering some preliminary theoretical ideas along with known properties of the non-thermal radio emitters, the main questions that will guide us throughout this study will be formulated.

Thermal vs. non-thermal radio emission from massive stars

The observational study of massive stars revealed a wealth of crucial information concerning the physical processes at work in their expanding atmospheres. For instance, early-type stars have been detected in the infrared and radio domains. Independently, Wright & Barlow (1975) and Panagia & Felli (1975) developed models to explain the production of the radio and infrared spectra of massive stars by a free-free radiation from their extended envelope. The main characteristic of this *thermal* radiation is a continuum emission that can be described by a power law of the type:

$$S_\nu \propto \nu^\alpha$$

where S_ν is the flux density, ν is the frequency, and α is the spectral index of the free-free emission. For a homogeneous mass loss, at constant or accelerating velocity, α is about equal to 0.6, in agreement with many observations. This thermal emission is intimately related to the mass loss rate of massive stars. A popular method to determine mass loss rates is moreover based on the measurement of the thermal radio flux (Wright & Barlow 1975; Panagia & Felli 1975).

However, some of the massive stars observed in the radio domain present significant deviations from this well-defined thermal behaviour (see e.g. White & Becker 1983; Abbott et al. 1984). The main characteristics of such a radio emission disagreeing with the classical thermal emission discussed hereabove are the following:

- the spectral index (α) is not equal to 0.6, but is significantly lower than the thermal spectral index, and might even be negative.

- the radio emission is not steady, and the flux and/or the spectral index can present strong variations.

- the emission level is generally higher than expected for the purely thermal emission.

This *non-thermal* radiation was proposed to be synchrotron radiation by White (1985). Such a radiation mechanism requires two main ingredients. First, the existence of *a magnetic field* is needed. The direct detection of the magnetic field of massive stars is not an easy task, mostly because of the difficulty to investigate a Zeeman broadening in line profiles already broadened due to the fast rotation of the star. However, some recent observations led to the direct measurement of the magnetic field strength in the case of a few O- and B-type stars (see Chapter 1 for a discussion). Second, *a population of relativistic electrons* is required. The acceleration of particles in astrophysical sources has mainly been proposed to proceed through the Fermi mechanisn, in the presence of hydrodynamic shocks (see Chapter 1 for a discussion).

From this preliminary discussion, it becomes clear that we can discriminate between two main kinds of radio emission, produced by two distinct mechanisms whose physical requirements are very different. To constrain the physical conditions likely to generate a non-thermal emission in the case of massive stars, we need to gather as much observational elements as possible. In this regard, a complete census of the non-thermal emitting massive stars is necessary.

Inventory of the non-thermal radio emitting massive stars

As the number of radio observations of massive stars increased, the number of targets displaying the non-thermal emission increased as well. From these observations, we know that non-thermal radio emitters can be found within both the classes of Wolf-Rayet (WR) and O-type stars (for a review, see e.g. Rauw 2004).

Table 1: List of the non-thermal radio emitting WR stars as of November 2005. The information collected in this table are taken from (a) Dougherty & Williams (2000), (b) Chapman et al. (1999), (c) Benaglia et al. (2005), (d) Cappa et al. (2004) and (e) Monnier et al. (2002).

Star	Sp. Type	Ref.	Comments on the multiplicity
WR 11	WC8 + O8.5	a	Confirmed binary with a period of 78.5 d
WR 14	WC7	b	Suspected binary
WR 21a	WN6 + O3	c	Confirmed binary
WR 39	WC7	b	Possible visual binary
WR 48	WC6 + O9.5	a	Confirmed binary; suspected triple system
WR 79a	WN9ha + ?	d	Visual binary
WR 89	WN8ha + OB	d	Visual binary
WR 90	WC7	b	No evidence for binarity
WR 98a	WR + OB	e	Confirmed binary with a period of about 1 yr
WR 104	WR + OB	e	Confirmed binary with a period of about 1 yr
WR 105	WN9	a	No evidence for binarity
WR 112	WC9	a	No evidence for binarity
WR 125	WC7 + O9	a	Confirmed binary with a period of > 15 yr
WR 137	WC7 + OB	a	Confirmed binary with a period of > 13 yr
WR 140	WC7 + O5	a	Confirmed binary with a period of about 7.9 yr
WR 146	WC5 + O8	a	Visual binary
WR 147	WN8 + B0.5	a	Visual binary

First, let us consider WR stars. At the time of the writing of this work, 17 WR stars have revealed a non-thermal contribution in their radio spectrum (see Table 1). In most cases, the non-thermal nature of the radio emission is revealed by the spectral index that deviates significantly from 0.6. In some cases, the non-thermal emission is strongly suggested by significant variations in the radio flux. A striking feature of the list provided in Table 1 is the large fraction of double or multiple systems among the non-thermally emitting WR stars. Out of 17 non-thermal radio emitters, 14 are at least suspected binaries, with most of them (12) being confirmed binaries.

Table 2: List of the non-thermal radio emitting O-type stars. The information on the non-thermal nature of the radio emission from the targets collected in this table are taken from (a) Contreras et al. (1997), (b) Bieging et al. (1989), (c) Setia Gunawan et al. (2003), (d) Drake (1990), (e) Benaglia & Koribalski (2004), (f) Leitherer et al. (1995) and (g) Benaglia et al. (2001a). For the multiplicity and/or the spectral types, the information are taken from (h) Rauw et al. (1999), (i) De Becker et al. (2004b), included in this thesis, (j) Rauw et al. (2005b), (k) Gies et al. (1993), (l) Harvin et al. (2002), (m) Garmany & Massey (1981), (n) Nelan et al. (2004), (o) Rauw et al. (2003c), (p) Gies (1987), (q) Gosset (2005) (r) Leitherer et al. (1987), and (s) De Becker et al. (2004a), included in this thesis.

Star	Sp. Type	Ref.	Comments on the multiplicity
Cyg OB2 #5	O6-7Ib + Ofpe/WN9	a	Confirmed binary, probably triple^{h,a}
Cyg OB2 #8A	**O6f + O5.5(f)**	**b**	**Confirmed binary with a period of 21.908 d**^{i}
Cyg OB2 #9	**O5If**	**b**	**Multiplicity currently under investigation**
Cyg OB2 - 335	O7V	c	Multiplicity not yet investigated
9 Sgr	O4f^{+} + ?	b	Confirmed binary with a period of a few years^{j}
15 Mon	O7Ve	d	Confirmed binary^{k}
δ Ori A	O9.5II + ?	b	Confirmed multiple system^{l}
σ Ori AB	O9.5V + ?	d	Confirmed multiple system^{d}
HD 15558	**O5III + O7V**	**b**	**Confirmed binary with a period of about 440 d**^{m}
HD 93129A	O2If	e	Visual binary^{n}
HD 93250	O3V((f))	f	Suspected binary^{o}
HD 124314	O6V(n)((f)) + ?	g	Confirmed binary^{p}
HD 150136	O5IIIn(f) + ?	g	Confirmed binary, probably triple^{q}
HD 167971	**O5-8V + O5-8V + O8I**	**b**	**Confirmed binary, probably triple**^{r}
HD 168112	**O5III(f^{+})**	**b**	**Suspected binary**^{s}
CD -47°4551	O5If	g	Multiplicity not yet investigated

In the case of O-type stars, the situation is rather similar. Up to now, 16 non-thermal radio emitters of spectral type O are known (see Table 2). In this category, 11 are confirmed binaries and two more are suspected binaries. The multiplicity of a few of them (Cyg OB2 #8A, Cyg OB #9, HD15558, HD168112) is investigated in this thesis. In Table 2, the non-thermal radio emitters investigated in the context of this thesis are highlighted by bold characters.

Main questions addressed in this work

Considering the various points discussed hereabove, we can formulate a series of questions, related to the physical processes and to the astrophysical circumstances that are responsible for the non-thermal radio emission from massive stars:

- In the sample of non-thermal radio emitters presented in Tables 1 and 2, we see that a significant fraction of sources are confirmed binary systems. *Is binarity a necessary condition to produce a non-thermal emission in the radio domain? As the non-thermal radiation process requires the existence of relativistic electrons, can these electrons be accelerated only in binary systems, or can we expect this to happen also in the case of single stars?*

- Synchrotron radiation is not the only known non-thermal emission process. In the presence of a population of relativistic electrons embedded in the strong UV radiation field of an early-type star, other processes such as inverse Compton scattering are also likely to produce high-energy photons (X-rays, γ-rays). *Is there any possibility to observe a high-energy counterpart to this non-thermal radio emission?*

- As synchrotron radiation and the mechanism responsible for the acceleration of particles are intimately dependent on the existence of a magnetic field (see Chapter 1), *could the observation of these non-thermal processes provide an indirect way to estimate the magnetic field strength of massive stars?*

In order to investigate these questions, we carried out for a sample of O-type stars[1] a multiwavelength campaign including data from several ground-based and space-borne observatories. The spectral domains investigated in this thesis are mostly the visible, the X-rays, and the soft γ-rays. Several results from radio observations (obtained in tight collaboration with the massive star group of the Royal Observatory of Brussels) are also included in the discussions. Our observational material is described with more details in Appendix A.

---

[1] Most of these O-type stars are non-thermal radio emitters presented in Table 2, even though we also included in this thesis some results concerning other targets for reasons that will be described throughout the work.

Chapter 1

Theoretical considerations

In this chapter, we briefly discuss several astrophysical aspects likely to play a role in the production of non-thermal emission in massive stars. The main topics that will be addressed are respectively the physics of individual stellar winds and their interaction in binary systems, the acceleration of relativistic electrons, the magnetic field of massive stars, and finally the non-thermal emission processes relevant to the cases discussed in this study. Though some of these contributions are poorly understood – and therefore may be somewhat speculative – this discussion aims at the elaboration of a consistent schematic view of the theoretical aspects of the non-thermal emission from early-type stars. Several important concepts used throughout the thesis will be introduced in this chapter.

1.1 Generalities

Massive stars are known to produce strong stellar winds. In the case of O-type stars, these stellar winds can reach velocities up to 2000–3000 $\mathrm{km\,s^{-1}}$ with mass loss rates of about 10^{-6}–$10^{-5}\,\mathrm{M_\odot\,yr^{-1}}$. The mass loss from massive stars is driven by their strong radiation field, able to transfer momentum to the ions present in their outer envelope. This line driving mechanism was first proposed by Lucy & Solomon (1970) and developed by Castor, Abbott, & Klein (1975) – the so-called CAK-theory – before being further investigated and refined for instance by Abbott & Lucy (1985), Vink et al. (2000), Pauldrach et al. (1986, 1994) and Kudritzki (1996). A general discussion of this process can be found in De Becker (2001).

In the basic CAK-theory, the stellar wind is considered to be stationary, i.e. the radial flow of matter is smooth. However, Lucy & White (1980) pointed out the fact that radiatively driven stellar winds should be unstable, leading to the appearance of perturbations in the mass outflow. These instabilities, leading to intrinsic hydrodynamic shocks in stellar winds, were investigated in details for instance by Owocki & Rybicki (1985), Owocki et al. (1988) and Feldmeier (1995). The presence of the structures resulting from outflow instabilities is believed to produce several observational phenomena:

- *statistical fluctuations in emission lines in the optical domain*, in the case of O-type (see e.g. Eversberg et al. 1996; 1998) and WR stars (see e.g. Moffat et al. 1994; Brown et al. 1995). Such fluctuations have generally low amplitudes (of order a few percent at most) and individual 'clumps' affect rather narrow velocity intervals.

- *the emission of thermal X-rays*, likely produced by hydrodynamical shocks between plasma shells travelling at different velocities in the wind of isolated stars, and leading to local temperature enhancements of a few 10^6 K (see Feldmeier et al. 1997). The thermal nature of the X-rays produced within stellar winds is clearly revealed in their spectra by emission lines associated to highly ionized elements such as O, N, Si, Mg, Ne or Fe. Such emission line spectra have been observed by the *XMM-Newton* and *Chandra* X-ray observatories.

Beside these intrinsic radiatively driven instabilities, the winds of massive stars can be involved in strong collisions if the star is member of a massive binary system. In this scenario, the two companions produce their own stellar wind, that interact in a wind-wind collision zone somewhere between the two stars. This interaction zone is confined between two hydrodynamic shocks. We may distinguish two main kinds of shocks (Stevens et al. 1992; Pittard & Stevens 1997). On the one hand, the *radiative* case is observed when the cooling time-scale (t_{cool}) of the hot gas is short in comparison to the time-scale for this gas to escape out of the system (t_{esc}). In this case, the entire kinetic energy provided by the shock is almost immediately radiated, mostly in X-rays, and the shocked gas region is very thin. This situation occurs only if the shocked region is dense enough for the cooling to be efficient. Such shock regions may undergo instabilities able to disrupt the collision zone (Stevens et al. 1992). On the other hand, the *adiabatic* limit is reached when the cooling time-scale is larger than the escape time-scale. Here, the cooling is not efficient enough to convert all the kinetic energy into radiation, and the plasma heated by the collision undergoes some adiabatic cooling as it flows ouf of the interaction region. The key parameter that rules the properties of the collision zone is therefore the cooling. A characteristic measure of the relative importance of the cooling is the *cooling parameter* (χ_{cool}):

$$\chi_{cool} = \frac{t_{cool}}{t_{esc}} \approx \frac{v_8^4\, d_{12}}{\dot{M}_{-7}} \tag{1.1}$$

where v_8 is the wind velocity just before the collision in units of $1000\,\mathrm{km\,s^{-1}}$, d_{12} is the distance to the contact in units of 10^7 km, and $\dot{M}_{-7}$ is the mass loss rate in units of $10^{-7}\,\mathrm{M_\odot\,yr^{-1}}$. The wind can be considered to be *adiabatic* for $\chi \geq 1$, and *radiative* if $\chi < 1$ (Stevens et al. 1992).

In this context, when we are dealing with the hydrodynamics of stellar winds (individually, or in binary systems), an important concept worth introducing is that of *strong shocks*. Strong shocks are particular cases of hydrodynamic shocks where the pressure of the *upstream* gas (the gas that has not yet crossed the shock, i.e. *pre-shock* gas) is negligible in comparison to that of the *downstream* gas (the gas that has already travelled through the shock, i.e. *post-shock* gas). Consequently, if the flow is considered to consist of perfect gas, we obtain the following relation for the *compression ratio (χ)*:

$$\chi = \frac{\rho_d}{\rho_u} = \frac{v_u}{v_d} = \frac{\gamma+1}{\gamma-1} \tag{1.2}$$

where ρ_d (resp. v_d) and ρ_u (resp. v_u) are the downstream and upstream gas densities (resp. velocities). For a monoatomic gas, the adiabatic coefficient (γ) is equal to 5/3, and we derive the main property of strong shocks, i.e. $\chi = 4$.

A consequence of the colliding winds is the production of thermal X-rays, in addition to those produced intrinsically in individual stellar winds. The temperature of the plasma heated by this collision can reach a few 10^7 K, while that of individual stellar winds reach at most a few 10^6 K. This additional emission component generally makes binary systems brighter in X-rays than the individual stars constituting them. Empirically, the ratio between the X-ray and bolometric luminosities of a single star[1] is about 10^{-7}, and any excess with respect to this ratio could be considered as an indication of an interaction between stellar winds in a binary system.

In summary, as illustrated in Fig. 1.1, hydrodynamic shocks are common features in stellar wind physics, be they due to intrinsic instabilities or to wind-wind collisions in binary systems. This is a crucial point in the context of the non-thermal emission from massive stars, as it appears to be a mandatory ingredient required to accelerate electrons.

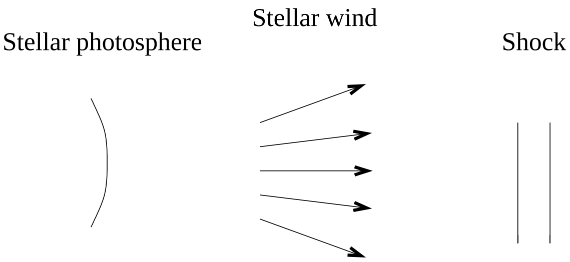

Figure 1.1: Schematic view of the basics of the physics of stellar winds. The wind of a massive star is first produced through radiative driving. The stellar wind gives rise to instabilities that take the form of intrinsic hydrodynamic shocks. In the case of binary systems, the interaction of the stellar winds between the two companions can produce additional shocks in a collision zone.

---

[1] A canonical relation between X-ray and bolometric luminosities based on a large albeit heterogenous sample of O-stars was proposed by Berghoefer et al. (1997). More recently, Sana et al. (2005) established a similar relation on the basis of a more reduced sample of stars harboured by the open cluster NGC 6231. The homogeneity of this latter sample led to a dispersion of the canonical relation of only about 40 %, whilst that of Berghoefer et al. (1997) is about a factor 2.

1.2 Particle acceleration mechanism

A first approach to explain the acceleration of particles was proposed by Fermi (1949). In his scenario, particles reflected between randomly moving "magnetic mirrors" (i.e. irregularities or turbulences in the magnetic field) are accelerated, resulting in a relative increase of their energy (Δ E/E) of the order of $(V/c)^2$, where V is the velocity of the shock in the frame of the ambiant plasma and c is the speed of light.

A variant of this original idea, but in the presence of strong hydrodynamic shocks, was then developed for instance by Blandford & Ostriker (1978) and Bell (1978a,b). In this context, the crucial point is that, from the particles point of view, only head-on collisions occur and the accelerated particles do not undergo the decelerating effect of any following collisions, contrary to what happens in the original scenario proposed by Fermi. In the literature, this acceleration process is also referred to as the Diffusive Shock Acceleration – DSA – mechanism (see e.g. Pittard et al. 2006).

This is illustrated in Fig. 1.2, where four situations are individually presented. In situation **(a)**, the upstream gas is considered to be stationary, and the shock crosses the medium at a supersonic velocity U. If the shock is considered to be stationary (**b**), the upstream gas crosses it with a bulk velocity $v_u = U$. However, as we are dealing with a strong shock (see Eq. 1.2), v_d is equal to $v_u/4 = \frac{U}{4}$. In situation **(c)**, i.e. from the point of view of the upstream gas considered to be stationary, the downstream gas moves with a velocity $v_{d\prime} = U - \frac{U}{4} = \frac{3}{4}U$. And in the reverse situation (**d**), i.e. when the downstrem gas is considered to be stationary, $v_{u\prime\prime} = \frac{3}{4}U$ (see Longair 1992 for details). The main conclusion of this discussion is that the particles crossing the shock encounter gas moving with the same velocity, whatever the direction of the crossing of the shock. Consequently, the particle undergoes exactly the same process of receiving a small amount of energy Δ E when crossing the shock from downstream to upstream as it did in travelling from upstream to downstream. There are no crossings in which the particles lose energy : as a result, the process goes linearly with V/c, and is therefore much more efficient than the original Fermi mechanism.

Another crucial aspect of this mechanism is that it is an iterative process. After travelling through the shock front, the high-energy particles can interact with magneto-hydrodynamic waves and magnetic turbulence. The consequence is an isotropic scattering of the particles which are allowed to cross the shock once again in the other direction. This results in the multiplication of the crossings, and therefore of the increases in energy, that allows the particles to reach very high energies up to very large Lorentz factors. As a result of this iterative process, the energy spectrum of the relativistic particles is a power law:

$$N(E) \propto E^{-n} \tag{1.3}$$

where n is the index of the power law. As we are mostly dealing with electrons, this index will mostly be referred to as the *electron index* of the relativistic electron population. Following the study of Bell (1978a), the compression ratio of the shock and the index of the relativistic electron population can be related:

$$n = \frac{\chi + 2}{\chi - 1} \tag{1.4}$$

This general mechanism is believed to be responsible for the production of cosmic rays, probably at least partly accelerated in supernova remnants. In the context of stellar winds of massive stars, the first order Fermi mechanism in the presence of hydrodynamic shocks

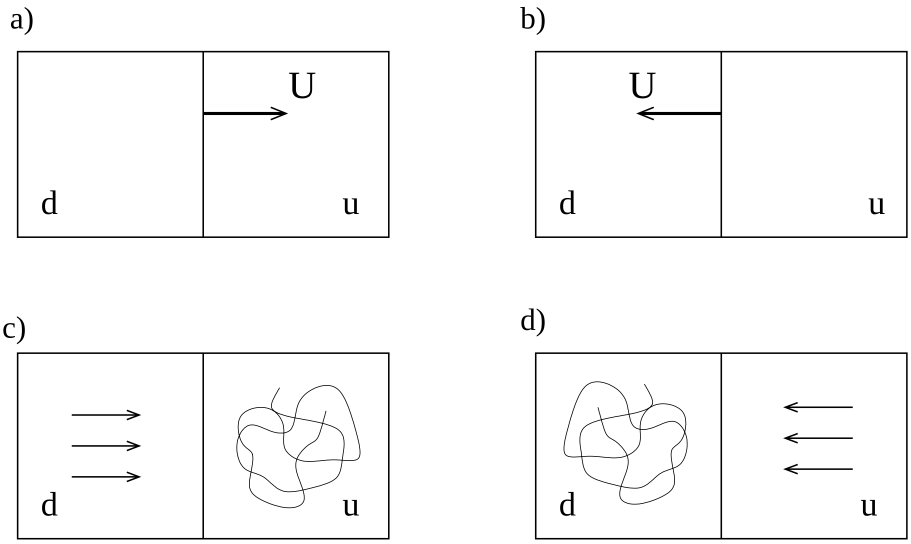

Figure 1.2: Illustration of the dynamics of high-energy particles in the presence of a strong shock where particles are accelerated through the first order Fermi mechanism. The *upstream* and *downstream* parts of the flow are respectively referred to by the letters u and d. The curves in panels (c) and (d) illustrate the scattering due to magneto-hydrodynamic phenomena, and responsible for the isotropic distribution of particles in the frame of reference where the gas is at rest. The four situations are individually described in the text.

(intrinsic or in wind-wind interaction zones) is a good candidate to explain the existence of the population of relativistic electrons needed to produce the observed radio synchrotron emission. Figure 1.3 summarizes the iterative process of acceleration of relativistic electrons in the presence of (i) hydrodynamic shocks and (ii) magneto-hydrodynamic phenomena likely to scatter isotropically the high-energy particles. This last point suggests that the role of the magnetic field of massive stars is not negligible in this acceleration process.

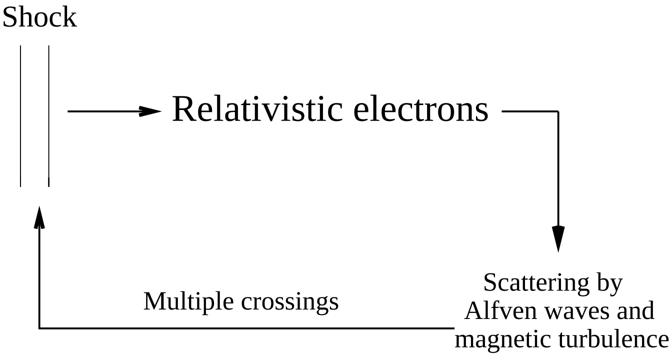

Figure 1.3: Schematic representation of the Fermi acceleration mechanism in the presence of strong shocks. The iterative nature of this process through the interaction of magneto-hydrodynamic phenomena is illustrated.

We mention that, very recently, a model has been developed applying the DSA mechanism to the particular physical conditions of hydrodynamic shocks of colliding-wind binaries (Reimer et al. 2006).

1.3 Magnetic fields of massive stars

The magnetic field of stars is certainly one of the most poorly understood aspects of stellar physics. The observation of the Sun brought a huge amount of relevant information on stellar magnetism, but our general understanding of stellar magnetic fields is still very poor. However, as our knowledge of stellar astrophysics increases, the importance of the role played by magnetic phenomena becomes more and more obvious. In this context, it is worth considering with more details the generation of magnetic fields within stellar interiors.

Section 1.3.1 provides a short discussion of some fundamental hydromagnetic concepts. Sections 1.3.2 and 1.3.3 are devoted to hydrodynamic processes likely to be responsible for the presence of a stellar magnetic field. These discussions are mostly inspired by Tassoul (1976) and Campbell (1997). An alternative approach to produce a magnetic field is briefly described in Sect. 1.3.4. Section 1.3.5 summarizes the various processes possibly at work in the particular case of massive stars. In Sect.1.3.6, we briefly discuss the phenomenon of magneto-hydrodynamic waves, omnipresent in astrophysics. Finally, Sect. 1.3.7 gives some words on observational methods used recently to estimate the strength of surface magnetic fields of a few massive stars.

1.3.1 Hydromagnetic considerations

Let us first consider some general equations of electromagnetism. For an electrically conducting fluid such as a plasma, Maxwell's equation relating the curl of the magnetic field ($\mathbf{B}$) and the current density ($\mathbf{J}$) is the following

$$\nabla \times \mathbf{B} = \mu_\circ \mathbf{J} \tag{1.5}$$

where $\mu_\circ$ is the permeability of free space. An additionnal equation useful for our purpose is Faraday's law

$$\nabla \times \mathbf{E} = -\frac{\partial \mathbf{B}}{\partial t} \tag{1.6}$$

If we include the induction electric field in Ohm's law, we obtain

$$\mathbf{J} = \sigma\,(\mathbf{E} + \mathbf{v} \times \mathbf{B}) \tag{1.7}$$

where σ, $\mathbf{E}$ and $\mathbf{v}$ stand respectively for the electric conductivity of the fluid, the intensity of the electric field, and the velocity of the flow.

By taking the curl of Eq. 1.7, we obtain

$$\nabla \times \mathbf{J} = \sigma \Big[\nabla \times \mathbf{E} + \nabla \times (\mathbf{v} \times \mathbf{B})\Big]$$

Using Eq. 1.5 in the left hand side and Eq. 1.6 for the first term of the right hand side yields

$$\nabla \times \frac{\nabla \times \mathbf{B}}{\mu_\circ} = \sigma \Big[-\frac{\partial \mathbf{B}}{\partial t} + \nabla \times (\mathbf{v} \times \mathbf{B})\Big]$$

$$\frac{1}{\mu_\circ\,\sigma}\nabla \times (\nabla \times \mathbf{B}) = -\frac{\partial \mathbf{B}}{\partial t} + \nabla \times (\mathbf{v} \times \mathbf{B})$$

where we considered the permeability of free space as being constant. If we define the magnetic diffusivity as $\lambda = \frac{1}{\mu_\circ\,\sigma}$, and use the vector identity $\nabla \times (\nabla \times \mathbf{B}) = \nabla \cdot \nabla \cdot \mathbf{B} - \nabla^2 \mathbf{B}$ where the first term of the second hand side is equal to zero because $\mathbf{B}$ is divergenceless, we finally obtain the *induction equation*:

$$\frac{\partial \mathbf{B}}{\partial t} = \nabla \times (\mathbf{v} \times \mathbf{B}) + \lambda \nabla^2 \mathbf{B} \tag{1.8}$$

This equation expresses the temporal variation rate of the magnetic field in a plasma of finite conductivity through two terms: (i) the first one, also called the motion term, corresponding to a gain of intensity, and (ii) the second one standing for the decay of the magnetic field due to the resistivity of the medium (Campbell 1997).

1.3.2 Fossil magnetic field

It has been proposed that the magnetism of some stars could be the relic of a magnetic field that was present in the gas cloud from which the star was formed by gravitational collapse (see e.g. Tassoul 1976 for a discussion). When trapped in a star without any mass motion, such a magnetic field would decay due to the finite conductivity of the stellar material. This can be illustrated by the *diffusion equation*, which expresses the decay of the magnetic field without any source of magnetic energy.

In the development of the *induction equation* (Eq. 1.8), the neglect of any induction in Ohm's law yields

$$\mathbf{J} = \sigma \, \mathbf{E}$$

Using this equation thoughout the same approach as followed in Sect. 1.3.1, we obtain the *diffusion equation*.

$$\frac{\partial \, \mathbf{B}}{\partial \, t} = \lambda \nabla^2 \mathbf{B} \tag{1.9}$$

We note that it corresponds to the *induction equation* where the motion term is ignored. On the basis of this relation, we obtain an estimate of the diffusion time-scale (τ_d) through the following relation

$$\tau_d = \frac{l^2}{\lambda} \tag{1.10}$$

where l is the typical length scale of the plasma. Consequently, if the plasma is turbulent, l will decrease substantially, leading to a rapid decay of the magnetic field.

The Sun

In the case of the Sun, Cowling (1945) showed that the time-scale of electromagnetic decay is about 10^{10} years, i.e. the same order of magnitude as its evolution time-scale on the main-sequence. This suggests that any putative primeval magnetic field could possibly be responsible for its current magnetic activity. Consequently, the fossil magnetism has been considered as a good candidate to explain the magnetism of the Sun, and other stars as well.

However, it is not yet clear whether or not a large-scale primeval magnetic field could survive the pre-main-sequence phases. Moreover, in the particular case of the Sun, it is commonly assumed that the magnetic field is continuously generated, and that all traces of primeval magnetism have long since vanished. The reasons are the following: (i) a turbulent convection in the surface layers would cause the decay of the fossil field on a very short time-scale (typically a decade), and (ii) the polar solar magnetic field shows periodic reversals in contradiction with the existence of a stable primeval magnetism[2].

---

[2] We note that such a periodic reversal of the stellar magnetic field has also been observed in the case of another star, i.e. the K0 dwarf LQ Hydrae (Kitchatinov et al. 2000).

For these reasons, an alternative theory is needed. This theory, i.e. the *hydromagnetic dynamo*, is briefly described in Section 1.3.3.

Chemically peculiar (CP) stars

Chemically peculiar (CP) stars are objects displaying atypical abundances, along with abundance inhomogeneities over their surface that may be due to the diffusion of elements under the influence of the stellar magnetic field. The fact that only about 10 % of the near-main sequence stars in the same stellar mass range as CP stars display strong magnetic fields (the so-called '10 % problem') could possibly be explained by a fossil origin (Moss 2003). The amount of magnetic flux trapped during star formation is tentatively expected to vary substantially, with only the high flux tail of the distribution resulting in stars with a detected magnetic field on the main sequence. Magnetic fields of a few 10^2 to several 10^4 G have been measured for chemically peculiar Ap and Bp stars (Michaud et al. 1981; Hubrig et al. 2004).

White dwarfs and neutron stars

The scenario of the fossil origin of the stellar magnetic field has recently been reconsidered in the context of the study of magnetic fields of compact degenerate stars such as white dwarfs (WD) and neutron stars (NS). More details can be found in Tout et al. (2004) and Ferrario & Wickramasinghe (2005).

In this context, a fossil magnetic field is believed to be trapped in stars during their formation process and the magnetic flux should be conserved. For stellar masses lower than about $2\,M_\odot$, the star becomes fully convective during the Hayashi sequence and the fossil magnetic field has no chance to survive. This is typically the example of the Sun where the magnetism must be explained in another way (see the dynamo mechanism in Section 1.3.3). For masses larger than about $2\,M_\odot$, the star does not travel through a totally convective episode during the Hayashi phase and some fossil magnetic field may survive. For instance, the conservation of the magnetic flux as the stellar radius shrinks from that typical for main-sequence OB stars to that of a NS provides an apparently consistent relation between magnetic field strengths during the main-sequence (i.e. a few G to a few kG) and those observed for NSs ($\sim 10^{11}$–10^{15} G). These numbers seem to lend some support to the conservation of the magnetic flux initially of fossil origin to explain the presence of the magnetic field in massive stars. In this scenario, inhomogeneities in the very weak magnetic field present in extended regions of the Galaxy are likely to produce a large dispersion of stellar magnetic field strengths.

The conservation of the magnetic flux provides a possible interpretation to explain the presence of a magnetic field in WDs as well. In this case, magnetic field strengths of about a few kG (Aznar Cuadrado et al. 2004) to 10^6–10^9 G (Schmidt et al. 2003) have been observed. Such a dispersion in the magnetic field strength is also proposed to derive from heterogeneities of the local Galactic magnetic field.

Massive non-degenerate stars

As indicated above, the conservation of the primordial magnetic flux has been proposed to be responsible for the magnetism of massive stars (see e.g. Ferrario & Wickramasinghe 2005). However, we can subdivide the inner structure of massive stars into two main zones: (i) the convective core where the fossil magnetic field is unlikely to survive, and (ii) the radiative envelope which results partly from accretion, and is likely to harbour some residual fossil magnetic field. Moreover, the part of the massive star that shrinks to produce the NS is the core, and not the envelope. So, how can we explain that surface (main-sequence) magnetic fields fit so well core (NS) values after the supernova explosion? Is it fortuitous, or is there any strong physical relation between the convective core and the radiative envelope from the magnetic point of view? At this stage, this question is not elucidated, and it suggests that more than a simple magnetic flux conservation is needed to understand the processes responsible for the observed magnetism of massive stars, be they degenerate or not. Alternative scenarios are discussed in Sections 1.3.3 and 1.3.4.

1.3.3 The dynamo theory

The classical principle of the dynamo action relies essentially on the fact that the motion of a conducting fluid (i.e. a plasma) is able to produce electromotive forces capable of maintaining an initial magnetic field. The energy is supplied by the forces driving the fluid flow before being converted into magnetic energy. Consequently, as a first approximation, we will consider that the initial energy supply is huge, and mostly unaffected by this energy conversion process.

In order to obtain the dynamo equation, we will use the same formalism as for the induction equation (Eq. 1.8). This dynamo equation will then be discussed in the framework of stellar magnetic fields.

The dynamo equation

For many astrophysical bodies, τ_d is shorter than their age, thus they need internal motions of conducting material to explain the observed magnetic fields that would otherwise have undergone ohmic decay to negligible levels. This issue is investigated in this section aiming at establishing a similar equation as Eq. 1.8, but specific to the case of the dynamo effect.

Let's consider an axisymmetric magnetic field that can be split into poloidal and toroidal components. According to 'Cowling's theorem', *a steady axisymmetric magnetic field cannot be maintained by dynamo action* (Cowling 1945). The problem is that in astrophysical bodies, the symmetry is dominantly axial. A solution to solve this problem was proposed by Parker (1955), who noted that convection can cause rising cells of fluid to rotate and carry lines of force of the toroidal field into loops. Consequently, a large number of such loops could regenerate the poloidal component of the magnetic field. Such a turbulence is expected to arise from the Coriolis force, and is most commonly called the *α-effect*.

The velocity and magnetic fields can be expressed as a sum of large-scale (mean field) and small-scale (fluctuating field) contributions. The α-effect is a small-scale turbulence acting on the mean (large-scale) magnetic field through a mean electromotive force (ϵ) given by the following relation

$$\epsilon = \alpha \mathbf{B} - \beta \nabla \times \mathbf{B} \tag{1.11}$$

where α is a coefficient that vanishes for homogeneous isotropic turbulence, and β can be regarded as an additional contribution to the fluid magnetic diffusivity due to the turbulence (also called eddy diffusivity).

Taking into account this additional electric field in the induction equation, we obtain the following equation for the mean field, i.e. the *dynamo equation*

$$\frac{\partial \mathbf{B}}{\partial t} = \nabla \times (\mathbf{v} \times \mathbf{B}) + \nabla \times (\alpha \, \mathbf{B}) + (\lambda + \beta) \, \nabla^2 \, \mathbf{B}$$

This equation allows axisymmetric solutions to exist for the mean magnetic field. As the magnetic diffusivity is essentially dominated by the eddy diffusivity, it is often neglected in the formulation of the dynamo effect.
We note that in this last relation, the magnetic and eddy diffusivities have been considered to be constant throughout the plasma. However, a more general formulation of the *dynamo equation* would be

$$\frac{\partial \mathbf{B}}{\partial t} = \nabla \times (\mathbf{v} \times \mathbf{B}) + \nabla \times (\alpha \, \mathbf{B}) - \nabla \left[(\lambda + \beta) \, \nabla \times \mathbf{B} \right] \tag{1.12}$$

With appropriate boundary conditions, this dynamo problem turns out to be an eigenvalue problem, aiming at finding eigenvalues (ξ) corresponding to non-decaying solutions of the type $\mathbf{B}(\mathbf{x},\mathbf{t}) = \mathbf{B}(\mathbf{x}) \, \exp(\xi \, t)$, where x stands for the spatial position vector. The study of Charbonneau & MacGregor (2001) shows that the solutions for massive main-sequence stars (convective core + radiative envelope) point to magnetic fields that are concentrated in the immediate vicinity of the core-envelope interface. This is interpreted as a consequence of the fact that the magnetic diffusivity is expected to decrease rapidly as one moves from the turbulent core to the stably stratified radiative envelope.

The expression of the velocity can contain a term accounting for the differential rotation. In that case, the expressions for the poloidal and toroidal components of the magnetic field show that a magnetic field can be produced through two main mechanisms, respectively called the α- and Ω-effect:

> **α-effect.** As stated above, it is the production of a magnetic field from turbulence arising from the Coriolis force. This process is able to produce both toroidal and poloidal fields.
>
> **Ω-effect.** It consists in the production of a toriodal field through the shearing of the poloidal component of the field due to the non-uniform rotation of the star.

The general case where both effects act simultaneously is often called the $\alpha^2\Omega$-dynamo. Particular cases of dynamo can also be considered, like the α^2-dynamo where the Ω-effect can be neglected, or the $\alpha\Omega$-dynamo where the impact of the α-effect can be neglected with respect to that of the Ω-effect in the production of a toroidal field from the poloidal field.

Stars with very low mass ($\mathrm{M} \leq 0.4\,\mathrm{M}_\odot$) are essentially fully convective. The dynamo process can occur within the whole stellar interior. In the case of stars of solar and later type ($\mathrm{M} \leq 1\,\mathrm{M}_\odot$), the hydromagnetic dynamo is believed to occur somewhere within the outer convective zone. For instance, a magnetic field of a few Gauss is observed over most of the surface of the Sun, with strong localized fields of up to 4000 G in sunspots (see e.g. Tassoul 1976). In this case, cyclic variations of the chromospheric activity suggests that the Sun-like dynamo produces a time-dependent field responsible for a cyclic magnetic activity.

For massive stars ($\mathrm{M} \geq$ 8-10 $\mathrm{M}_\odot$), the study of Charbonneau & MacGregor (2001) shows that such a dynamo action is possible in the core. However, the question is to know how a magnetic field generated by a core dynamo could travel up to the surface of the star where it can be detected directly (e.g. using spectropolarimetric methods, see Sect. 1.3.7) or indirectly (e.g. synchrotron radio emission, putative magnetic stellar wind confinement). Two scenarios have currently been proposed to address this issue, and they are briefly discussed below.

How to bring the magnetic field to the surface?

The transport of the magnetic field of massive stars from the convective core to the surface constitutes a challenge for the stellar magnetism theory. Two scenarios have been proposed: (i) the meridional circulation through Eddington-Sweet cells (Charbonneau & MacGregor 2001), and (ii) the buoyant rise of magnetic tubes along the rotation axis (MacGregor & Cassinelli 2003).

Meridional circulation – Eddington-Sweet cells. The rotation of early-type stars can lead to departures from sphericity, responsible for pole-equator temperature differences in the radiative interior (see e.g. Charbonneau & MacGregor 2001). These temperature differences cannot be balanced under the assumption of simultaneous radiative and hydrostatic equilibria. The reaction of the star is to generate a large-scale circulation in the meridional plane, known as the Eddington-Sweet circulation. As some of these flow streamlines come close to the surface of the star, and also close to the boundary between the convective core and the radiative envelope, Eddington-Sweet cells may be able to bring the magnetic field from the core up to the surface.
Allowing to the study of Charbonneau & MacGregor (2001), in the case of models with a strong magnetic diffusivity contrast between the core and the envelope (that are probably the most realistic ones), the dynamo effect is inhibited by the meridional circulation if it reaches a level suitable for a significant magnetic flux transport. Moreover, such meridional circulation regimes are not likely to be attained in the interior of early-type main-sequence stars. Consequently, an alternative scenario is needed to carry magnetic fields from the stellar core to the surface.

Buoyant rise of magnetic tubes. In this model of advection of magnetic flux, MacGregor & Cassinelli (2003) consider the dynamics of a circular ring, symmetric about the stellar rotation axis. This ring is an isolated concentration of magnetic field, which is allowed to begin an outward motion from the convective core thanks to the buoyancy. In this model, the ring, or magnetic tube, is in mechanical equilibrium with the surrounding medium. We note however that the radiation pressure is neglected in this simplified approach, therefore restricting the discussion to stars with masses up to about 10 $M_\odot$. The rotation is considered to be homogeneous, and no meridional circulation is taken into account.
The time-scale of the rise of the magnetic tubes is shorter than the typical evolution time-scale of massive stars on the main-sequence. However, the density deficit of such a ring is expected to decrease as it travels through the radiative envelope, causing the upward buoyant acceleration experienced by the ring to decrease as well. The ring indeed spends considerably more time (about a factor 100) travelling through a thin shell between 0.90 and 0.96 $R_\star$, than in ascending from the core to a radius of 0.90 $R_\star$. The inclusion of the meridional circulation is expected to significantly decrease the time needed to transport the magnetic flux through the layers just below the surface. The joint action of the buoyancy transport and of the meridional circulation could therefore possibly lead to short rise

times, able to transport a significant magnetic flux to the surface at the very first stages of the main-sequence of massive stars.

1.3.4 An alternative dynamo scenario

A completely different possibility worth considering is the production of a magnetic field through a dynamo mechanism just below the surface, without the need of bringing it from the core. Such an approach is described for instance by Spruit (2002) or by MacDonald & Mullan (2004). Such a dynamo can be driven by the differential rotation in a stable stratified zone.

According to the study of Spruit (2002), an instability of an initial toroidal field (even small) creates a vertical field component. Such an instability, called Tayler instability (Spruit 1999), consists of non-axisymmetric horizontal displacements of fluid elements. This vertical component of the field is distorted by differential stellar rotation which converts it into additional toroidal field lines. These horizontal field lines become progressively closer and denser, therefore producing a much stronger horizontal field.

This mechanism is usually refered to as the Tayler-Spruit dynamo (Spruit 2002; Maeder & Meynet 2003, 2004). In the context of massive stars, this scenario could be envisaged within the radiative envelope, therefore producing a magnetic field close to the surface.

1.3.5 Summary

Considering the scenarios discussed in this section, we see that the origin of the magnetic field in massive stars is not yet well established. All that we can do is make a census of the physical processes likely to play a role in this context (see Fig. 1.4).

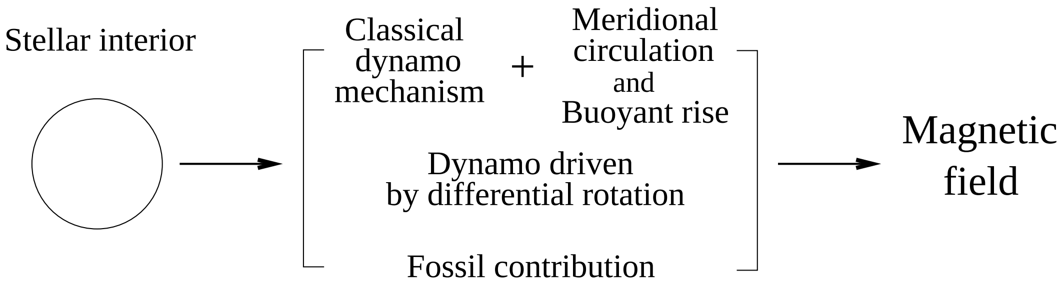

Figure 1.4: Summary of the physical processes likely to play a role in the presence of a magnetic field at the surface of massive stars.

A fossil magnetic field is unlikely to survive in the turbulent regime of the core of the massive star, but a classical dynamo action might produce a magnetic field in that part of the star. Such a classical dynamo cannot be at work in the radiative envelope. However, an alternative dynamo driven by the differential rotation of the star may produce a magnetic field close to the surface. Moreover, the possibility to bring to the surface some magnetic field produced in the core thanks to the combined action of meridional circulation and buoyancy cannot be completely rejected. We also note that a contribution of a fossil magnetic field might be present in the radiative envelope, as it results partly from the accretion of interstellar material that has not experienced a fully turbulent episode.

1.3.6 Basic physics of Alfvén waves

In this section, we propose a simple discussion describing the fundamental physics responsible for the appearance of magneto-hydrodynamic waves in astrophysical plasmas (Alfvén 1950). Such phenomena are believed to occur in various astrophysical environments. For instance, these waves are supposed to be involved in the processes responsible for the acceleration of relativistic electrons (see e.g. Bell 1978a and Longair 1992). Though this topic is rather complex, the following discussion aims at providing a simplified qualitative approach likely to illustrate the basics of Alfvén waves.

Any hydrodynamic motion in an electrically conducting medium harbouring a magnetic field is likely to give rise to induced electric fields, producing electric currents. The combination of electric currents with the presence of the magnetic field will produce forces able to change the state of motion of the plasma. The wave motion produced by this coupling between mechanical and magnetic forces is called a magneto-hydrodynamic wave (Alfvén 1950).

Let us consider the simple case of the motion of a pillar of ionized gas in the z-direction (Fig. 1.5), in a magnetic field pointing in the x-direction with a strength B. The intersection of the moving pillar with the xy-plane is the rectangular box ABCD. Following Eq. 1.13, an electric field is produced within the pillar in the y-direction.

$$\mathbf{E} = \frac{\mu_\circ}{c}\,(\mathbf{v} \times \mathbf{B}) \tag{1.13}$$

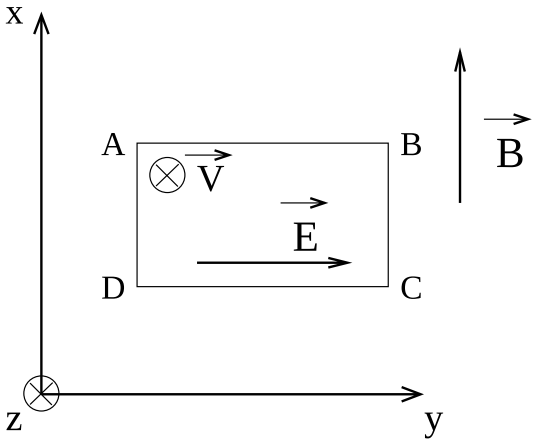

Figure 1.5: Schematic representation of a pillar moving in the z-direction, in the presence of a magnetic field **B** oriented along the x-axis. The rectangular box ABCD is the intersection between the moving pillar and the xy-plane. The vector product of the velocity and magnetic field vectors yields the direction of the induced electric field **E**.

In Fig. 1.6, the curved arrows illustrate the current produced by the induced electric field. The coupling of this current with the magnetic field produces a Lorentz force opposite to the z-direction in the pillar, but the closed currents outside the pillar produce a force in the z-direction. These forces are opposite to the initial motion of the pillar, but induce a motion to the initially static adjacent pillars. Consequently, the parts of the plasma directly beside the initially moving pillar get a state of motion similar to that described in Fig. 1.5. The same process repeats itself and the global effect is the transfer of the initial motion to the surrounding layers, giving rise to an alternate motion in the positive and negative directions of the z-axis. A magneto-hydrodynamic wave, called Alfvén wave, is produced and propagates in the direction of the initial magnetic field.

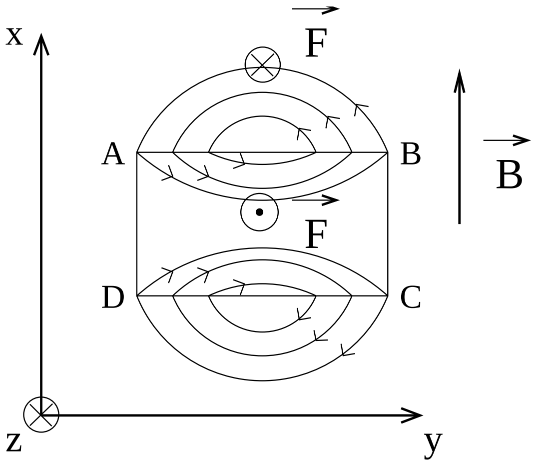

Figure 1.6: The coupling of the electric currents produced by the induced electric field with the magnetic field gives rise to Lorentz forces. These forces are oriented along the z-direction outside the initially moving pillar, and in the opposite direction inside. The induced force is opposed to the initial motion in the rectangular box, and accelerate the adjacent pillars of conducting material.

1.3.7 Direct determination of magnetic field strengths of massive stars

In the presence of a magnetic field, the degeneracy of atomic sublevels can be lifted, splitting a given spectral line into several components (Zeeman effect). This effect has also the particularity of polarizing the light emitted through radiative transitions between sublevels affected by this splitting. The Zeeman effect is mostly efficient in circular polarization. Among the Stokes parameters characterizing the state of polarization of quasi-monochromatic light, this circular component corresponds to the V-Stokes parameter and responds to the line-of-sight component of the magnetic field (longitudinal Zeeman effect). It indicates the intensity difference between right- and left-handed circular polarizations. The other Stokes parameters respectively measure the unpolarized (I) and linearly polarized (Q and U) light.
In the case of massive stars, the strong rotational broadening due to the large projected rotational velocities (V_{rot} sin $i \approx 100$ - 450 km s^{-1}) does not allow to detect directly the line splitting (or broadening) due to the Zeeman effect. Nevertheless, the Zeeman polarization can be observed through spectropolarimetric methods. Recently, on the basis of this principle, the intensity of the magnetic fields of three massive stars have been estimated (the values are given in a subsequent paragraph). These stars are respectively β Cep (B1IV, Donati et al. 2001), θ^1 Ori C (O4-6V, Donati et al. 2002), and ζ Cas (B2IV, Neiner et al. 2003). The method adopted in these cases is described hereafter.

Using high resolution spectropolarimeters, one can obtain a polarized spectrum of a star displaying one of the Stokes components. In order to detect the signature of the Zeeman effect, the V-Stokes (circular polarization) component is prefered. However, the typical relative amplitude of Zeeman signatures is of about 0.1 %, much too low to be measured with high accuracy. To obtain a better detection of the polarized spectrum from a star, Donati et al. (1997) developed the Least Square Deconvolution (LSD) method, allowing to treat the V-Stokes signal of as many lines as possible simultaneously (in one spectrum). This method relies on the assumption that all lines exhibit Zeeman signatures with more or less the same shape. As a result, a line pattern is generated, built from a series of weighted Dirac functions positionned at the spectral locations of the selected lines. One considers then that the Zeeman signature over the whole spectrum consists of the convolution of this line pattern (also called the mask) with a typical V-Stokes profile. In this context, the deconvolution of the observed V polarized spectrum using such a line pattern is expected to give the observed V-Stokes profile.
Once this observed profile is obtained, grids of synthetic V-Stokes profiles can be con-

structured for a given magnetic field model. An example of model is the oblique magnetic rotator. In that case, grids of models covering a two-parameter space are obtained. The two parameters are the intensity of the poloidal magnetic field (B_p), and the inclination of the magnetic axis with respect to the rotation axis (θ). A particular grid is computed for a given value of the inclination (i) of the rotation axis with respect to the line of sight. The computation of the corresponding χ^2 grid allows the determination of the best-fit parameters.

With this method, for a simple dipolar magnetic field model, B_p and θ for β Cep are respectively of 360 ± 60 G and 85° ± 10° (Donati et al. 2001). The same parameters for θ^1 Ori C are of 1100 ± 100 G and 42° ± 6° (Donati et al. 2002), and for ζ Cas, Neiner et al. (2003) obtained 335^{+120}_{-65} G and 18° ± 4°. In the case of these stars, more sophisticated models including higher order field components (quadrupolar,...) donot improve significantly the fit. Finally, we note that as this technique relies on a particular Zeeman component (the longitudinal one), it is sensitive to the phase of the rotational cycle of the star. Consequently, observing exposure times must be significantly shorter than the rotational period. For this reason, and also because of the low amplitude of the Stokes signature, this method is only applicable to bright stars[3].

---

[3] The method was therefore not applicable to the cases of the stars discussed in this study, though a direct determination of their surface magnetic field strength is crucial.

1.4 Non-thermal emission processes

The approach described in our thesis deals with several radiation processes in different wavebands. A crucial point in this context is the distinction between *thermal* and *non-thermal* emission processes. In *thermal* processes, the energy distribution of the electrons involved in the photon production mechanism (e.g. radiative recombination and collisional excitation followed by radiative decay) can be described by a Maxwell-Boltzmann law. In the case of *non-thermal* processes, particles (electrons, and to some extent protons) are relativistic and are distributed according to a power law (see Eq. 1.3).

Among the non-thermal emission processes, we can distinguish *particle-field* interactions (particles interacting with a radiation or a magnetic field) and *particle-matter* interactions. The most common processes are briefly described below.

1.4.1 Particle-field interactions

Synchrotron radiation

A relativistic electron travelling in a magnetic field will be submitted to a Lorentz force orthogonal to the magnetic field direction. Consequently, the electron will adopt a helicoidal path, and will emit photons (*synchrotron radiation*).

The characteristic energy of the photons is given by

$$E_c = \frac{3\,h}{4\,\pi}\,\frac{e\,B\,\sin\,\theta}{m_e\,c}\left[\frac{E}{m_e\,c^2}\right]^2 \tag{1.14}$$

where h is Planck's constant, e the electron charge, B the magnetic field strength, m_e the mass of the electron, c the speed of light, and E the energy of the electron (see e.g. Cheng & Romero 2004). This relation shows clearly that very energetic particles and strong magnetic fields are needed to produce synchrotron radiation in the very high energy domain. However, with rather modest magnetic fields and "moderate" relativistic electrons, synchrotron radiation can easily be produced in the radio domain. In the context of massive stars, the non-thermal radio emission discussed in the introduction of this work is most probably produced following this mechanism (White 1985).

We note that a particular property of the synchrotron emission is that it is characterized by a significant beaming, i.e. the radiation is emitted in preferential directions. This property of the synchrotron emission is important considering the fact that, in a plasma such as that constituting stellar winds, the beaming effect can be substantially reduced, leading therefore to a decrease of the synchrotron emitting power. This effect is called the Razin-Tsytovitch effect (or Razin effect, see e.g. Van Loo 2005).

Inverse Compton scattering

Particles (electrons or protons) can also interact with photons. In the context of this work, only electrons will be considered. If the typical energy of the relativistic electrons is high enough, they can transfer some of their energy to soft photons. This process is known as *inverse Compton (IC) scattering*. In this way, moderately relativistic electrons are able to promote ultra-violet photons to the high-energy domain (X-rays and soft γ-rays). The relation between the average energy of the emerging photons (E_{IC}) and that of the scattered soft photons (E_{soft}) is

$$E_{IC} = \frac{4}{3}\,E_{soft}\,\gamma^2 \tag{1.15}$$

where γ is the Lorentz factor characterizing the relativistic electrons, defined as $\gamma = \sqrt{\frac{1}{1-(v/c)^2}}$ where v is the speed of the particle and c the speed of light.

This process is of particular interest in the framework of massive stars because of the strong supply of UV and visible photons provided by the photosphere. IC scattering is believed to play a significant role in the cooling of relativistic electrons in stellar wind environments, and should be considered in models aiming at the investigation of the non-thermal radio emission from massive stars (see e.g. Dougherty et al. 2003; Pittard et al. 2005, 2006).

1.4.2 Particle-matter interactions

Relativistic Bremsstrahlung

When a relativistic electron is accelerated in the electric field of a nucleus or other charged particles, radiation is produced: *relativistic Bremsstrahlung*. In general, only the emission from the electron has to be considered. It comes from the fact that the intensity of Bremsstrahlung by a nucleus of mass M is $\sim$ $(\mathrm{M}/\mathrm{m}_e)^{-2}$ times the effect by the electron.

We note that such a mechanism requires rather high plasma densities to become significant. For this reason, relativistic Bremsstrahlung is not expected to be responsible for non-thermal emission in the case of O-type stars. However, this scenario was considered by Pollock (1987) in the case of the denser winds of Wolf-Rayet stars.

π^0-decays from proton-proton emission

Even though we are mostly dealing with electrons in the context of this work, we should not neglect the fact that protons are very abundant in astrophysical environments such as stellar winds. Relativistic protons can interact with other 'ordinary' protons to produce neutral pions (π^0), that decay into gamma-rays with a proper lifetime of only 9×10^{-17} s.

The dominant channels producing pions in proton-proton interactions are

$$p + p \rightarrow p + p + a\,\pi^0 + b\,(\pi^+ + \pi^-)$$

$$p + p \rightarrow p + n + \pi^+ + a\,\pi^0 + b\,(\pi^+ + \pi^-)$$

$$p + p \rightarrow n + n + 2\,\pi^+ + a\,\pi^0 + b\,(\pi^+ + \pi^-)$$

where p and n stand respectively for protons and neutrons, a and b are positive integers. For a more detailed discussion of this process we refer to Cheng & Romero (2004).

Manchanda et al. (1996) proposed that the π^0-decay mechanism could be at work in young open clusters. They suggested that the combined winds of massive stars might interact with the gas in the cluster and produce a system of bow shocks. These shocks could then be responsible for the acceleration of protons up to relativistic velocities. Consequently, the relativistic protons may interact to produce a diffuse gamma-ray emission in open clusters and OB associations.

1.5 Overview of the required physics

In this chapter, we have discussed several aspects of the physics of massive stars, or different topics of astrophysics, likely to play a role in the production of non-thermal emission of massive stars. To conclude this chapter, Fig. 1.7 presents an overview of these physical processes. This schematic view in mostly inspired from that given by De Becker et al. (2005c). In this figure, the four boxes individually represent the topics independently discussed in the four previous sections of this chapter in their order of appearance. The intersections between boxes illustrate the noticeable interconnections between these different fields of astrophysics.

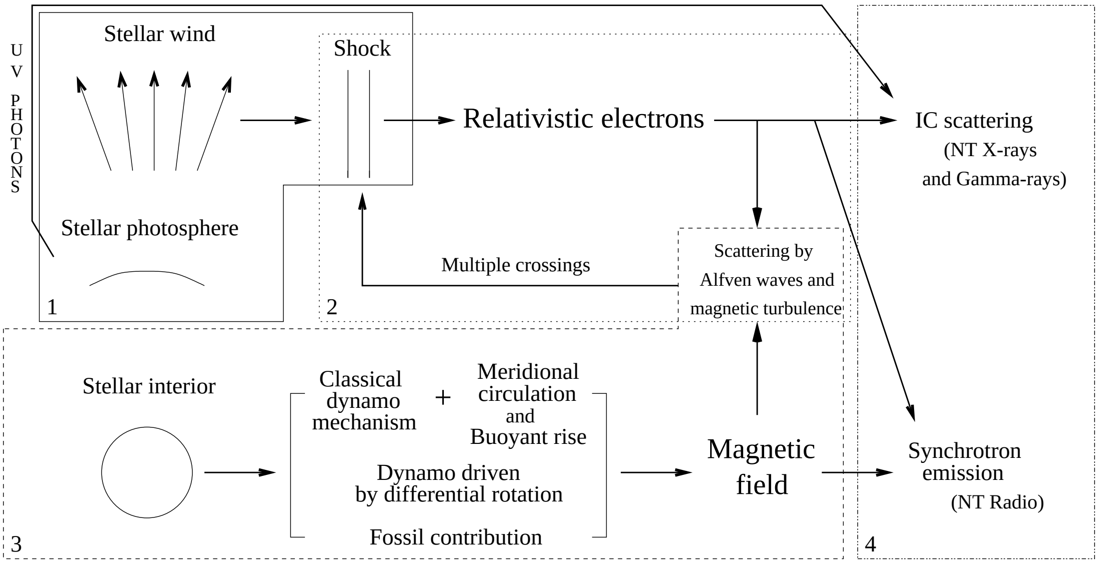

Figure 1.7: Overview of the physical processes likely to contribute to the production of non-thermal emission from massive stars. The main aspects of the problem are subdivided in boxes directly related to the processes discussed with more details in this chapter: (1) stellar wind physics (Sect. 1.1); (2) particle acceleration mechanism (Sect. 1.2); magnetic processes (Sect. 1.3); non-thermal emission processes (Sect. 1.4).

Chapter 2

The non-thermal radio emitter HD 15558 and the open cluster IC 1805

The young open cluster IC 1805 is particularly interesting in the context of the study of the non-thermal emission from massive stars. The first reason is a positional coincidence of the unidentified EGRET source 3EG J0229 +6151 with some of the most massive stars of the cluster. The second reason is the fact that IC 1805 harbours a well-established non-thermal radio emitter, i.e. HD 15558, worth investigating in order to constrain the physical circumstances responsible for its synchrotron radio emission. As IC 1805 appears to be a relevant place to look for the relation between massive stars and non-thermal emission, this chapter will describe an intensive study of the most massive stars of the cluster in order to constrain their multiplicity and their general properties, mainly through observations in the optical domain.

IC 1805 is a young open cluster in the core of the Cas OB6 association, embedded in the molecular cloud W4 which is itself located in the Perseus spiral arm of the Galaxy. The age of the cluster was estimated to be 1-3 Myr by Massey et al. (1995), in reasonable agreement with other previous estimates (Feinstein et al. 1986, and references therein). In their relative proper motion study of 354 stars in the region of IC 1805, Vasilevskis et al. (1965) showed that 143 of them are expected to be members of the cluster. According to the spectroscopic study of Shi & Hu (1999), 80 members of IC 1805 are O or B stars, among which 10 are O-type stars. On the basis of radial velocity measurements collected in the WEBDA data base, García & Mermilliod (2001) estimated that the binary frequency among the 10 O-stars in IC 1805 may be as high as 80 %. Such a high binary frequency, if confirmed, would put some severe constraints on models aiming at describing the formation of massive stars in open clusters (see e.g. Bonnell & Bate 2002).

In the framework of the investigation of the non-thermal emission from massive stars, a crucial point worth considering is the presence of a γ-ray source whose position is compatible with that of IC 1805. With the advent of the Energetic Gamma Ray Experiment Telescope (EGRET) onboard the *Compton* satellite, our vision of the galactic γ-ray emission improved significantly. The third EGRET catalog (Hartman et al. 1999) contains 271 point sources detected at energies greater than 100 MeV, among which 77 sources with a galactic latitude $|b_{\rm II}| \leq 10^\circ$, thus most probably located in our Galaxy. The discovery of this large number of sources, most of them still unidentified, motivated a large number of investigations aiming at the understanding of the nature of these high-energy sources. Albeit most of these γ-ray sources may be pulsars, pulsar wind nebulae, active galactic nuclei or supernova remnants (Grenier 2004; Torres 2004), it is interesting to note that probable positional coincidences of a few number of these EGRET sources with OB associations – or even with individual massive stars – have been revealed by the study of Romero et al. (1999). In particular, these latter authors pointed out the possible link between the unidentified EGRET source 3EG J0228 +6151 and the massive star HD 15629 located in IC 1805.

Another good reason to investigate IC 1805 is the fact that it harbours a confirmed non-thermal radio emitter, namely the long period massive binary HD 15558. As the nature of the soft γ-ray emission reported by the *Compton* satellite is non-thermal as well – and should also be produced be a population of relativistic particles – there is a possibility that both non-thermal sources may be related. Moreover, independently of its possible relation with the EGRET source, HD 15558 might be responsible for the emission of a yet undetected high-energy counterpart to the non-thermal emission observed in the radio domain.

In summary, it appears that the relation between the unidentified EGRET source 3EG J0228 +6151 and the massive star content of IC 1805 cannot be excluded. In order to investigate this possibility, an intensive study of the most massive stars of this open cluster has been carried out. Even though we did not obtain new high-energy data on IC 1805, we performed a detailed optical spectroscopic study of its six most luminous O-type stars in order to investigate their multiplicity, and some aspects of their stellar and wind properties. Our results, described in three studies presented below, constitute a census of many properties of these stars that will be helpful in order to more intensively address the issue of the non-thermal emission when new high-energy data will be made available.

2.1 The early-type stars BD +60°497, BD +60°501 and BD +60°513

On the basis of a series of spectra obtained with the Aurélie spectrograph mounted on the 1.52 m telescope at the Observatoire de Haute-Provence (see Appendix A), we investigated the multiplicity of three O-stars in IC 1805: BD +60°497, BD +60°501 and BD +60°513 (for details, see Rauw & De Becker 2004). We established the first SB2 orbital solution for BD +60°497 with a period of 3.96 d, and derived O6.5V((f)) and O8.5-9.5V((f)) spectral types respectively for the primary and for the secondary. For the other two stars, we found no significant radial velocity variations on time-scales of a few days, or from one year to the next, therefore suggesting they are most probably single. This is in contradiction with the fact that the two latter targets were previsously considered as spectroscopic binaries. Using archive *ROSAT* data, we also briefly investigated the X-ray emission from these three stars, and we did not find any evidence for excess emission attributable to a wind-wind interaction. We note however that the investigation of the X-ray emission from these stars – along with other massive stars in IC 1805 – requires high quality data obtained with more recent X-ray observatories like *XMM-Newton* or *Chandra*.

A&A 421, 693–702 (2004)
DOI: 10.1051/0004-6361:20040255
© ESO 2004

Astronomy & Astrophysics

Early-type stars in the young open cluster IC 1805

I. The SB2 system BD+60° 497 and the probably single stars BD+60° 501 and BD+60° 513*

G. Rauw** and M. De Becker

Institut d'Astrophysique et de Géophysique, Université de Liège, Allée du 6 Août, Bât. B5c, 4000 Liège, Belgium

Received 12 February 2004 / Accepted 30 March 2004

Abstract. We investigate the multiplicity of three O-type stars in the very young open cluster IC 1805. All our targets were previously considered as spectroscopic binaries, but no orbital solution was available for any of them. Our results confirm the binarity of BD+60° 497 and we provide the very first orbital solution for this double-lined spectroscopic binary. This is only the second O-star binary in IC 1805, and the first SB2 system, for which an orbital solution is now available. BD+60° 497 has an orbital period of 3.96 days and consists of an evolved O6.5 V((f)) primary and an O8.5-9.5 V((f)) secondary with minimum masses of $m_1 \sin^3 i = 13.9\ M_\odot$ and $m_2 \sin^3 i = 10.9\ M_\odot$. The observed primary/secondary mass ratio (1.28) appears lower than expected from a comparison with single star evolutionary models (1.60−1.74). For the other two stars, BD+60° 501 and BD+60° 513, we find no significant radial velocity variations, suggesting that they are most probably single. Although a fraction of binaries among the early-type stars of IC 1805 as high as 80% has been advocated in the literature, our results suggest that this number might be overestimated.

Key words. stars: binaries: spectroscopic – stars: early-type – stars: fundamental parameters – stars: individual: BD+60° 497 – stars: individual: BD+60° 501 – stars: individual: BD+60° 513

1. Introduction

Studying early-type binaries in very young open clusters has the potential to provide important information on many fundamental problems of stellar astrophysics including the star and cluster formation processes, dynamical interactions in clusters and stellar evolution in general. This is especially crucial for the still poorly understood formation of the most massive stars. Unfortunately, our present knowledge of the binary properties of massive stars is still fragmentary (Mermilliod 1996). For many binaries reliable orbital solutions are still lacking and the binarity of the majority of the early-type stars has simply never been investigated.

Several years ago, our group started an investigation of a number of early-type binaries in the open clusters Trumpler 16 and NGC 6231 in the southern hemisphere. Our extensive observing campaigns already led to the discovery of several triple systems and allowed us to considerable improve the orbital solutions for a number of binaries (Rauw et al. 2000, 2001; Morrell et al. 2001; Sana et al. 2001, 2003; Albacete Colombo et al. 2002). In this context, we have also undertaken a spectroscopic monitoring of the most massive members of the IC 1805 cluster in the northern hemisphere.

IC 1805 is a rich cluster in the core of the Cas OB6 association which in turn is embedded in the molecular cloud W 4 in the Perseus spiral arm of our Galaxy. All in all, the cluster harbors about forty early-type stars from spectral type O4 through B2 (Shi & Hu 1999) and their energetic winds have created a "galactic chimney" – i.e. a cone-shaped cavity in the interstellar medium – that allows efficient transport of hot gas from the galactic disk into the halo (Normandeau et al. 1996).

Among the 10 O-stars in IC 1805, García & Mermilliod (2001, see also Ishida 1970) estimated an extremely high binary frequency of 80%. However, to date, an orbital solution is available for only one of them: HD 15558 (O5 III(f)). HD 15558 is the optically brightest star in the cluster. It is an eccentric single-line binary (SB1) system with an orbital period of 440 days, the longest of any known O-star binary (Garmany & Massey 1981).

In this paper, we present the first double-line (SB2) orbital solution for another O-type binary (BD+60° 497 = LSI +61 274) in IC 1805. Although, Underhill (1967) and Walborn (1973) already reported the presence of a secondary spectrum in their observations of BD+60° 497, no detailed investigation of this system has apparently ever been performed. Underhill (1967) further noted that Trumpler (1930)

Send offprint requests to: G. Rauw,
e-mail: `rauw@astro.ulg.ac.be`

[*] Based on observations collected at the Observatoire de Haute Provence (France).

[**] Research Associate FNRS (Belgium).

had suspected BD+60° 497 to be an SB1 with an orbital period of 25.48 days.

We also analyse the spectra and radial velocities of two other O-type stars in IC 1805: BD+60° 501 (=LSI +61 282) and BD+60° 513 (=LSI +61 296) for which we find no evidence of binarity in contradiction with previous reports of radial velocity changes for the former and apparent double lines for the latter (Underhill 1967). Our results on the earliest O-type stars in this cluster will be the subject of a forthcoming paper.

In Sect. 2, we present our new data on the program stars and we derive their spectral classification. The orbital solution of BD+60° 497 and the radial velocities of the other two targets are discussed in Sect. 3 whilst the fundamental parameters of the BD+60° 497 system are the subject of Sect. 4. Section 5 presents a brief discussion of the *ROSAT* X-ray observations of our program stars and finally, our conclusions are given in Sect. 6.

2. Spectral classification

2.1. Observations and data reduction

Spectroscopic observations were collected during several observing campaigns in 2002 and 2003 at the Observatoire de Haute-Provence (OHP). We used the Aurélie spectrograph attached to the 1.52 m telescope. The detector was a 2048 × 1024 CCD EEV 42-20#3, with a pixel size of 13.5 μm squared. Our spectra cover the wavelength range from 4455 to 4905 Å with a reciprocal dispersion of 16 Å mm^{-1}. Depending on the atmospheric conditions, the exposure times were of order 30 to 45 min (respectively 45 to 60 min.) for BD+60° 497 and BD+60° 501 (respectively BD+60° 513). The mean signal to noise ratio of individual spectra is about 200−300 in the continuum.

The data were reduced using the MIDAS software developed at ESO. For each observation, the Aurélie CCD data consist of five images of the object's spectrum obtained by means of a Bowen image slicer (see Gillet et al. 1994). These five images were treated individually, i.e. they were bias-subtracted, flat-fielded and extracted. After removing the cosmic ray events from the individual images, we combined them into a weigthed average. The resulting spectrum was wavelength-calibrated using a Th-Ar comparison exposure taken shortly before or after the observation on the sky. Finally, the spectra were normalized using properly chosen continuum windows.

2.2. BD+60° 497

The blue spectra of BD+60° 497 are dominated by He I, He II and the Hβ absorption lines of the primary. Weak metal lines due to C III, N III, O II, Mg II, Si III and Si IV are also present. Their changing wavelengths indicate that they mainly follow the orbital motion of the primary. The secondary spectrum is seen in the He I absorption lines. The visibility of the secondary lines changes with orbital phase (see Fig. 1 and below).

Several authors provided spectral classifications for BD+60° 497: O7 (Underhill 1967), O6 V(n) (Walborn 1973), O7 V (Mathys 1989), O7 V((f)) (Massey et al. 1995) and O7 V (Shi & Hu 1999). It should be noted that these results are in fair agreement with each other whilst older classifications included early B-types (see Ishida 1970, and references therein). Ishida (1970) suggested that the spread in older spectral types (from B3 to O7) might indicate a possible change of some spectral features. However, this is not confirmed by the more recent results (including our own data).

In order to determine the spectral type of both components of BD+60° 497, we deblended the classification lines by simultaneously fitting two Gaussian profiles. The average equivalenth width (*EW*) of the He I λ 4471 line in the spectrum of the primary (resp. secondary) determined in this way amounts to 0.34 ± 0.02 Å (resp. 0.22 ± 0.03 Å). For the He II λ 4542 line the situation is less clear: due to the stronger intensity contrast between the primary and secondary in this line, it was only at a few phases that we were able to deblend the lines. For the primary (resp. secondary) we find EW = 0.54 Å (resp. 0.08 Å) for this line. Due to the orbital variation of the secondary line strength (see below) and the fact that we could only deblend this line at phases when the secondary is approaching, the *EW* of the secondary line could be a lower limit. The equivalent width ratio of the He I λ 4471 and He II λ 4542 classification lines places the primary of BD+60° 497 right at the border between spectral type O6 and O6.5 (Conti 1973b), whilst the secondary would be of spectral type O9−9.5 (or of somewhat earlier spectral type if the measured *EW* of He II λ 4542 is indeed a lower limit). We have also compared the blue spectrum of BD+60° 497 to the atlas of Walborn & Fitzpatrick (1990). The primary's spectrum is intermediate between those of HD 101190 of type O6 V((f)) and HD 93146 of type O6.5 V((f)), but slightly closer to the latter. For the secondary, comparison with the spectra provided by Walborn & Fitzpatrick suggests that this star should have a spectral type later than about O8.5.

The He II λ 4686 absorption line is in rather strong absorption in the spectrum of BD+60° 497, suggesting a main sequence luminosity class for both stars (see however also Sect. 4 below). We note the presence of a very weak N III λ 4641 emission line. The line roughly moves in phase with the primary component though with a reduced radial velocity (*RV*) amplitude. We further note that the width of the line changes as a function of phase. At some phases near $\phi = 0.25$, the line deblends into two components suggesting that the reduced *RV* amplitude and the changing width are due to a blend between two emission lines associated with both components. This means that both stars probably have this line in weak emission in their spectrum.

In summary, we thus classify the primary and secondary of BD+60° 497 as O6.5 V((f)) and O8.5−9.5 V((f)) respectively.

Finally, let us briefly turn to the apparent change in the strength of the secondary's absorption lines as a function of orbital phase. Though in the mean spectra displayed in Fig. 1 the He I λ 4713 line doubles its *EW* between approaching and receding quadrature, we must note that the effect is much less clear cut in the He I λ 4471 line and moreover, the dispersion of the *EW* of He I λ 4713 measured on individual spectra at

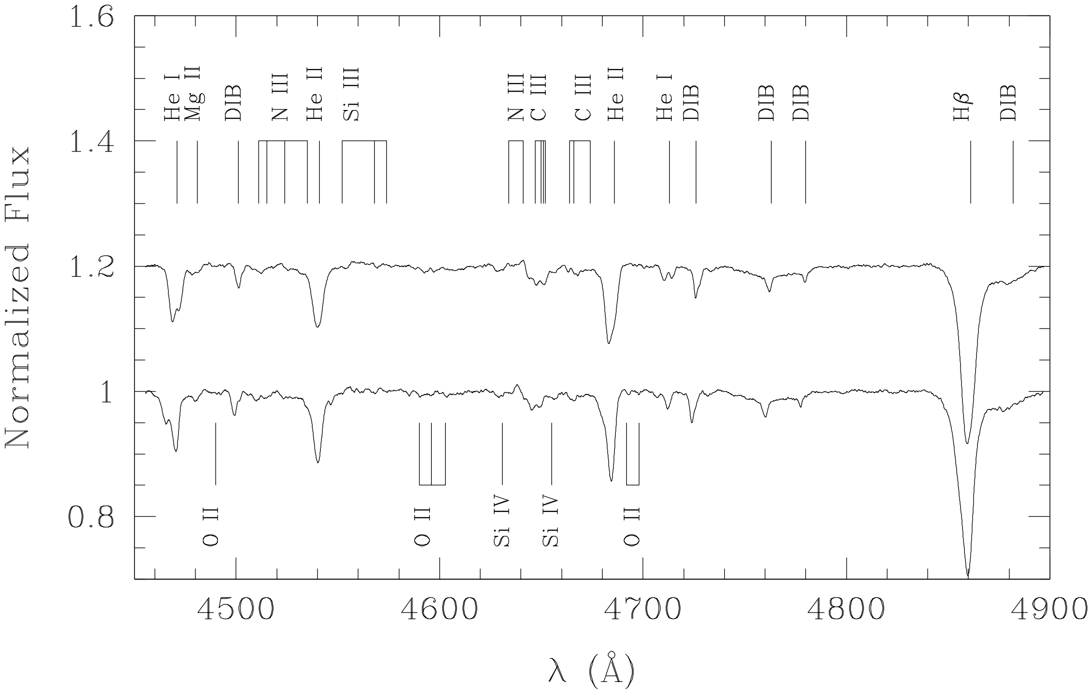

Fig. 1. Average spectrum of BD+60° 497 as observed around the phases of quadrature. The average spectrum around phases 0.65−0.85 is shifted vertically by 0.2 units with respect to the average spectrum around phases 0.1−0.35. The most prominent stellar features as well as the diffuse interstellar bands (DIBs) are identified. Note the aspect of the He I λ 4471 and λ 4713 lines that reveal clearly the signature of the secondary star. The relative importance of the secondary lines varies between the two quadratures (see text).

similar orbital phases is uncomfortably large. If real, the effect seen in Fig. 1 is such that the secondary's lines appear stronger at phases when the secondary is moving away from us compared to their intensity at approaching phases. This is the opposite situation of the so-called "Struve-Sahade" effect (SSe) which is defined as the apparent strengthening of the secondary lines at those orbital phases when the secondary is approaching and the corresponding weakening of its lines when it is receding (see e.g. Bagnuolo et al. 1999). BD+60° 497 is not the only binary where such an opposite SSe is seen. In fact, a similar behaviour was reported by Howarth et al. (1997) for HD 100213 (O7.5 V + O9.5 V).

2.3. BD+60° 501

The blue spectrum of BD+60° 501 is very similar to that of BD+60° 497 except for sharper and somewhat deeper absorptions (see Fig. 2). No indication of a secondary spectrum is found. The average *EW*s of the He I λ 4471 and He II λ 4542 classification lines are 0.57 ± 0.02 Å and 0.68 ± 0.04 Å respectively (in good agreement with the values quoted by Mathys 1989). According to the criterion provided by Conti (1973b), the ratio of these equivalent widths indicates an O7 classification. This result is confirmed by a comparison with the spectral atlas of Walborn & Fitzpatrick (1990). The strong He II λ 4686 absorption further indicates a main sequence luminosity class. Finally, we note some evidence of a very weak N III λ 4641 emission. In summary we thus assign an O7 V((f)) spectral type to BD+60° 501.

The spectral types given in the literature range from O6.5 V (Underhill 1967; Ishida 1970; Conti & Alschuler 1971) to O7 V (Walborn 1973; Mathys 1989; Shi & Hu 1999) and O7 V((f)) (Massey et al. 1995). Our result appears thus fully consistent with these classifications.

2.4. BD+60° 513

The spectrum of BD+60° 513 is similar to that of BD+60° 501 except for the much broader lines in the former (see Fig. 2). This is not unexpected since the projected rotational velocity is significantly larger for BD+60° 513 ($v \sin i \sim 300\,\mathrm{km\,s^{-1}}$) than for BD+60° 501 ($v \sin i \sim 200\,\mathrm{km\,s^{-1}}$; see Mathys 1987; Conti & Ebbets 1977). We note that the absorption lines in the spectrum of BD+60° 513 display some low-level profile variability, but no obvious indication of a secondary spectrum is found (see below). The average *EW*s of the He I λ 4471 and He II λ 4542 lines are 0.61 ± 0.04 Å and 0.56 ± 0.02 Å respectively. These values and the strength of the He II λ 4686 absorption yield an O7.5 V classification (Conti 1973b; Walborn & Fitzpatrick 1990). Again, the possibility of a very weak N III λ 4634-41 emission, finally leads to an O7.5 V((f)) spectral type for BD+60° 513.

The spectral types quoted in the literature include O7 V (Shi & Hu 1999), O7 Vn (Walborn 1973), O7.5 V (Mathys 1989; Conti & Ebbets 1977), O8 V((f)) (Massey et al. 1995),

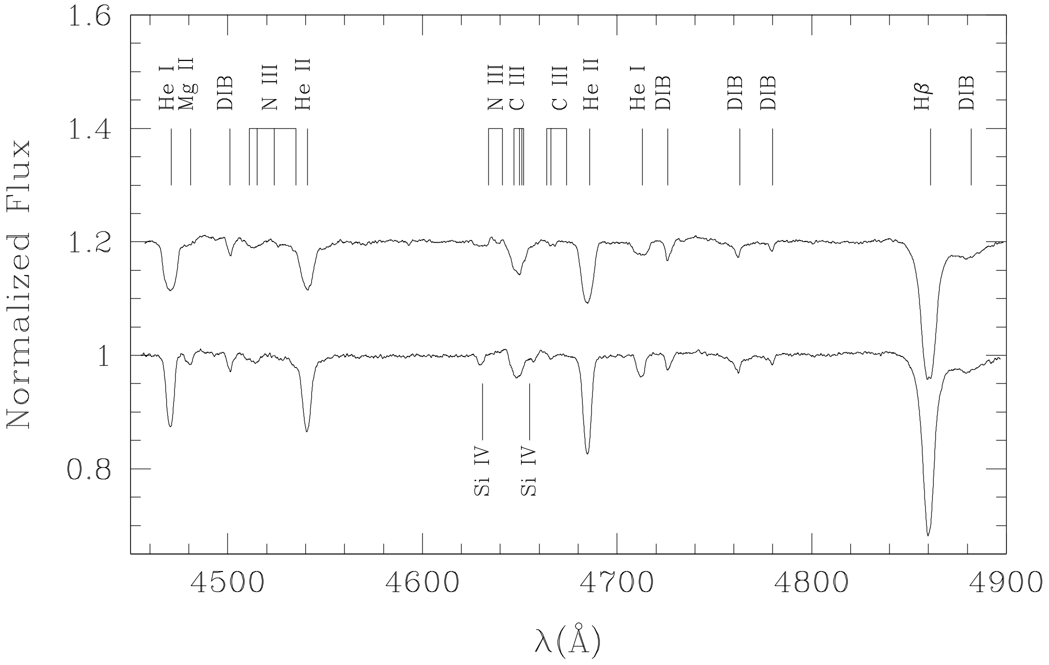

Fig. 2. Average spectra of BD+60° 501 (*bottom*) and BD+60° 513 (shifted vertically by 0.2 units). The lines of BD+60° 513 are significantly broader than those of BD+60° 501 (see text).

O9 V (Ishida 1970) and B0 (Underhill 1967). This rather wide range of spectral types most probably results from the difficulties related to the broad lines of this star and possibly some confusion problems between BD+60° 513 and BD+60° 512 in older studies (as pointed out by Conti & Leep 1974 and Mathys 1987).

3. Radial velocities and orbital solutions

3.1. BD+60° 497

Radial velocities of the components of BD+60° 497 were determined from simultaneous fits of several Gaussian profiles and through cross-correlation with a template spectrum. The results of both techniques generally agree within the uncertainties. Most lines of the binary components remain blended over large parts of the orbital cycle and the intensities of the secondary's lines change as a function of the orbital phase (Fig. 1). The secondary's signature is best seen in the He I λ4471 and λ4713 lines as well as, at some orbital phases, in Mg II λ4481. These three absorptions provide therefore the best lines to derive the radial velocities (*RV*s) of the binary components. We adopt the rest wavelengths for these lines from Underhill (1994) and the resulting *RV*s (determined by means of simultaneous Gaussian fitting) are listed in Table 1. For most measurements the typical uncertainties are of order 10–15 km s^{-1}. About twice as large uncertainties affect the data points indicated by a colon in Table 1.

We applied the generalized spectrogram technique of Heck et al. (1985; see also Gosset et al. 2001) and the trial method of Lafler & Kinman (1965) to the timeseries of our $RV_1 - RV_2$ data. Both methods consistently yield 3.96 days as the best estimate for the orbital period. This result was confirmed by a 2D period search technique (see e.g. Rauw et al. 2003) applied to the line profile changes in the spectrum of BD+60° 497. Assuming that the uncertainty on the corresponding frequency amounts to one tenth of the width of the peak in the periodogram, we estimate an uncertainty of 0.09 day on the orbital period. Our orbital period is clearly at odds with the much longer value (25.48 days) suggested by Trumpler (1930, as reported by Underhill 1967). In the following we adopt 3.96 days as the orbital period of BD+60° 497.

A circular orbital solution of BD+60° 497 yields a mass ratio $q = m_1/m_2 = 1.28$ and the minimum masses of the stars are found to be $m_1 \sin^3 i = 13.9\,M_\odot$ and $m_2 \sin^3 i = 10.9\,M_\odot$ for the primary and the secondary respectively. The systemic velocities obtained for each component are in broad agreement with each other and with the mean radial velocity of other IC 1805 cluster members (see Underhill 1967 and the cases of BD+60° 501 and BD+60° 513 below). Allowing for an eccentric orbital solution yields $e = 0.14 \pm 0.14$. Given the large errors on the eccentricity and though we cannot completely rule out a small eccentricity, in the following we assume $e = 0.0$.

3.2. BD+60° 501

We measured the *RV*s of the He I λ4471, He II $\lambda\lambda$4542, 4686 and Hβ lines in the spectra of BD+60° 501 by fitting Gaussians. These fits are of good quality and the position of the line centre is determined with an accuracy of about 1–2 km s^{-1}. The resulting mean *RV*s are listed in Table 3. Again, the rest wavelengths were adopted from Underhill (1994).

Table 1. Radial velocities of BD+60° 497 as derived from our Aurélie spectra. The orbital phases are computed with respect to HJD 2 452 935.977 with a period of 3.96 days (see Table 2).

HJD−2 450 000	ϕ	RV_1 (km s^{-1})	RV_2 (km s^{-1})
2520.644	0.118	−151.1	94.4:
2523.600	0.864	76.3	−285.2:
2524.552	0.105	−142.0:	91.9:
2527.555	0.863	92.0	−286.1
2528.533	0.110	−158.7:	77.0:
2529.562	0.370	−156.9	74.0
2531.543	0.870	91.1	−264.6
2532.534	0.120	−179.1	79.9
2533.638	0.399	−146.6	44.4
2916.583	0.103	−185.9	108.5
2918.667	0.629	50.0:	−210.6:
2919.632	0.872	78.4	−203.8
2922.677	0.641	74.3	−176.1
2925.665	0.396	−155.8:	−16.3:
2928.641	0.147	−236.3	118.0
2934.545	0.638	67.4	−189.4

Table 2. Orbital solution for BD+60° 497 assuming a circular orbit. T_0 refers to the time of conjunction with the primary being behind. γ, K and $a \sin i$ denote respectively the systemic velocity, the amplitude of the radial velocity curve and the projected separation between the centre of the star and the centre of mass of the binary system. $R_{\rm RL}$ stands for the radius of a sphere with a volume equal to that of the Roche lobe computed according to the formula of Eggleton (1983).

	Primary	Secondary
P(days)	3.96 (fixed)	
e	0.0 (adopted)	
T_0(HJD-2 450 000)	2935.977 ± 0.152	
γ (km s^{-1})	−53.7 ± 9.2	−68.9 ± 11.9
K (km s^{-1})	171.9 ± 11.9	220.6 ± 14.9
$a \sin i$ ($R_\odot$)	13.4 ± 0.9	17.3 ± 1.7
$q = m_1/m_2$	1.28 ± 0.12	
$m \sin^3 i$ ($M_\odot$)	13.9 ± 2.5	10.9 ± 2.0
$R_{\rm RL}$ $\sin i$ ($R_\odot$)	12.3 ± 0.8	11.0 ± 0.7

We find no significant variations neither over the data taken in September 2002 nor between the September 2002 and the October 2003 campaigns. This suggests that the star has a constant radial velocity over time scales of days, weeks and probably years. This result is at odds with the SB1 status (with an orbital period of 3.69 days) that Trumpler assigned to this system (see Underhill 1967). Underhill (1967) measured RVs of +1 and −57 km s^{-1} on two spectra taken two years apart. We note however that the velocities of the interstellar Ca II K-line reported by Underhill for these spectra also differ by as much as 39 km s^{-1}, confirming the caveat given by Underhill that the accuracy of her RVs was not very high.

Table 3. Radial velocities of BD+60° 501 as derived from our Aurélie spectra (see text).

HJD−2 450 000	RV (km s^{-1})
2518.633	−54.1
2520.611	−49.5
2524.527	−44.8
2527.617	−48.5
2531.572	−51.3
2532.573	−50.3
2533.602	−49.6
2919.602	−50.6
2922.588	−50.3
Mean	−49.9 ± 2.5

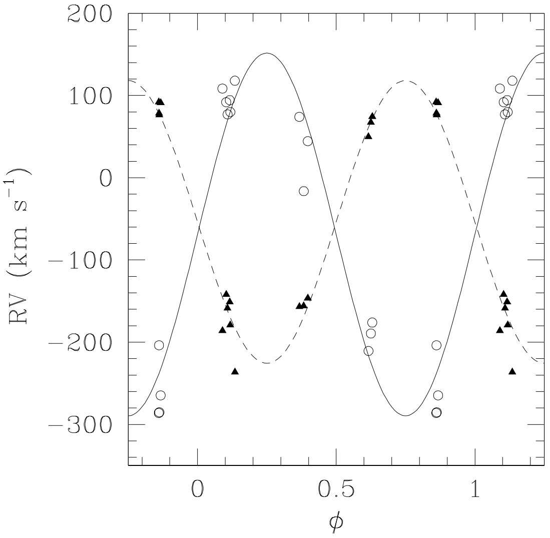

Fig. 3. Radial velocity curve of the BD+60° 497 binary system as derived from the He I $\lambda\lambda$ 4471, 4713 and Mg II λ 4481 absorption lines (see Table 1). Filled triangles and open circles stand for the primary and secondary RVs respectively. The circular orbital solution of Table 2 is shown by the solid and dashed lines.

Finally, in order to search for low level line profile variability – that could be due e.g. to non-radial pulsations, wind structures or binary effects – we have computed the time variance spectrum (TVS, Fullerton et al. 1996) of our entire data set over the spectral range 4460 to 4890 Å. The TVS hardly exceeds the expected level due to normalization errors and the S/N ratio of the data. Therefore, we conclude that no significant line profile variability is present in our data of BD+60° 501.

In summary, the RVs of BD+60° 501 as well as the lack of profile variability suggest that this is a single O7 V((f)) star.

Table 4. Same as Table 3 but for BD+60° 513.

HJD−2 450 000	RV (km s^{-1})
2520.569	−59.2
2524.609	−57.5
2527.662	−55.8
2529.602	−43.3
2531.612	−36.4
2532.619	−37.5
2533.580	−39.1
2918.631	−28.8:
2922.633	−48.9
2934.664	−36.8
Mean	−44.3 ± 10.5

3.3. BD+60° 513

Following the same procedure as for BD+60° 501 we measured the RVs of the He I λ4471, He II $\lambda\lambda$4542, 4686 and Hβ lines in the spectra of BD+60° 513 by fitting Gaussians. Due to the much broader line profiles in the spectrum of BD+60° 513, these fits are however of much poorer quality than in the case of BD+60° 501 (this is especially true for He I λ4471 and He II λ4542) leading to uncertainties of $\sim$10 km s^{-1} on the line centroids. The mean RVs of BD+60° 513 are provided in Table 4.

Though the RVs show a much wider spread than in the case of BD+60° 501, they do not reveal a clear binary behaviour. Actually, the $\sim$10 km s^{-1} dispersion in our RV data most probably reflects the difficulties related to the broadening of the lines and their distortion due to the profile variability (essentially for Hβ), whilst the star likely has a roughly constant radial velocity.

Most importantly, we do not detect any evidence for double lines contrary to the results of Trumpler reported by Underhill (1967). Underhill measured RVs of +27 and −63 km s^{-1} on two spectra separated by one year. The same remarks as for BD+60° 501 hold for these RVs especially as a result of the difficulties related to the line broadening.

An alternative possibility to explain the line broadening and the lack of significant RV changes with a binary scenario would be to assume that we observed the binary at phases between quadrature and conjunction, when the lines of the individual components are still blended. In this case, the shape of the lines (i.e. the lack of an obvious blue/red asymmetry in any of the stronger lines) would suggest that the putative binary components have to be of the same spectral type. BD+60° 513 would therefore consist of two roughly identical O7.5 V stars. It seems however rather unlikely that all our observations sample a unique orbital phase (unless the orbital period would be very long). Therefore, because of the orbital motion, we would expect the RV separation of both stars and hence the width of the various absorption lines to change. This is not the case in our data.

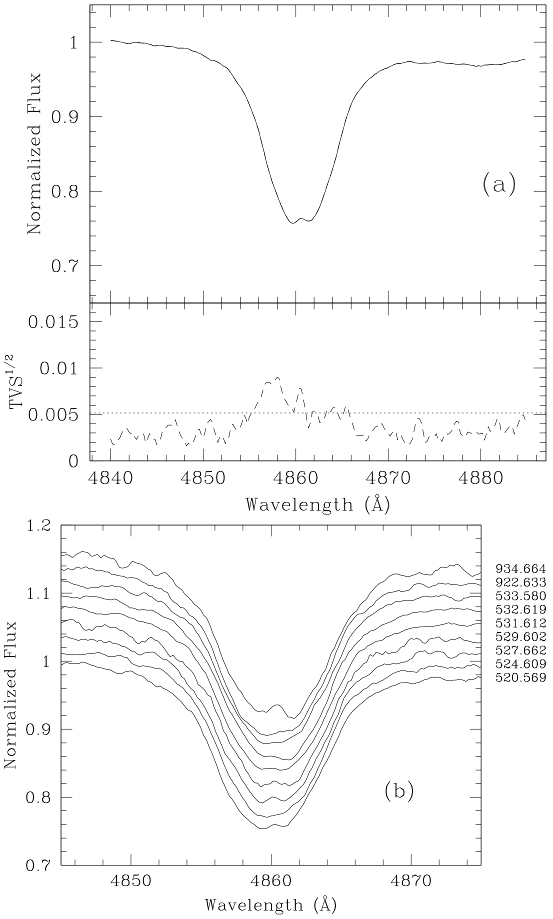

Fig. 4. Variability of the Hβ line in the spectrum of BD+60° 513. Panel **a)** yields the mean profile over our entire data set along with the square root of the TVS. The dotted line on the TVS$^{1/2}$ plot illustrates the thresholds for variations significant at the 99% level. Panel **b)** illustrates the variations of the Hβ profile as a function of time. The heliocentric Julian days are given in the format HJD−2 452 000 on the right of each spectrum. Note that the weak central emission peak in the core of the Hβ absorption is due to the contamination by the nebular emission from the IC 1805 nebula.

As mentioned above, there is some low-level line profile variability in the spectrum of BD+60° 513. In order to quantify this variability, we have computed the time variance spectrum over the entire spectral range from 4460 to 4890 Å as well as for individual lines. The TVS yields the most significant detection of variability in the blue wing of the Hβ line (see Fig. 4). The existence of this variability turns out to be robust in the sense that it remains if we omit individual spectra (one at the time) and reapply our analysis to the remaining time series. A 2D Fourier analysis (see e.g. Rauw et al. 2003) suggests time scales of 1.4 or 3.5 days for this variability. The former "period" is too short to be due to an orbital motion (there would not be enough room for a pair of O7.5 V stars in such a system). The 3.5 days period would not suffer from this problem. However, as stated above, for a short orbital period our data set would sample very different orbital phases and we would thus expect to see variations of the apparent line widths, which we do not observe here. We note that the presence of other strong peaks in the 2D periodograms suggests that the line profile variability could occur over significantly longer or shorter time scales (depending on the choice of the right alias). Unfortunately, our time series does not allow to properly investigate profile variability on these time scales.

In summary, the *RV*s of BD+60° 513 as well as the lack of line width changes suggest that this is a rather rapidly rotating single O7.5 V((f)) star. The low-level profile variability of the Hβ line could be due to non-radial pulsations maybe occuring on a time scale too short to be sampled by our data set. In fact, the rather low mass loss rate ($2.8 \times 10^{-7}\ M_{\odot}\,\mathrm{yr}^{-1}$) inferred by Llorente de Andrés et al. (1982) suggests that the stellar wind density might be too low to trigger an appreciable variability in optical lines.

4. Fundamental parameters of BD+60° 497

Moffat & Vogt (1974) quote a V magnitude of 8.84 and a $B-V$ colour of 0.51 for BD+60° 497 (their star # 27011). On the other hand, Reed (1998) presents a compilation of *UBV* measurements from different bibliographic sources (see references in Reed 1998) that yield V in the range 8.76 to 8.80 and a $B-V$ colour of 0.57. Massey et al. (1995) finally quote $V = 8.85$ and $B-V = 0.54$. In the following we adopt an average value of $V = 8.80$ and $B-V = 0.57$. The latter value yields $E(B-V) \simeq 0.90$. Using near infrared photometry, Sagar & Qian (1990) showed that $R_V = 3.0$ should be appropriate for BD+60° 497. We thus obtain an extinction of $A_{\rm V} \simeq 2.70$ in excellent agreement with the value (2.73 ± 0.05) that Sagar & Qian independently derived from their IR photometry.

Using photometry and spectroscopy of a large set of cluster members, Massey et al. (1995) inferred a distance modulus of $DM = 11.85 \pm 0.08$ and an age of 1–3 Myr for IC 1805. They also derived a mean colour excess $\overline{E(B-V)} = 0.87 \pm 0.02$ with a spread in colour excess from 0.68 to 1.29. The distance is in good agreement with the result ($DM = 11.9 \pm 0.1$) of Guetter & Vrba (1989). Therefore, we obtain an absolute V magnitude of $M_V = -5.75 \pm 0.12$ for the BD+60° 497 binary.

In order to position the components of BD+60° 497 in the Hertzsprung-Russell diagram, we need to derive the bolometric luminosity of the individual components. To do so, we first infer their relative brightness in the blue spectral range by comparing the measured *EW*s of the two components of the He I λ4471 line to the mean *EW* of this line in the spectra of single stars of same spectral type. The latter were evaluated from the compilation of *EW*s provided by Conti & Alschuler (1971) and Conti (1973a). In this way, we find that the primary must be about three times brighter than the secondary in the optical spectral range: $M_{V,1} - M_{V,2} \sim -1.14 \pm 0.16$. Combining this result with the absolute magnitude of the binary system inferred above yields $M_{V,1} = -5.42 \pm 0.13$ and $M_{V,2} = -4.28 \pm 0.17$. Finally, adopting the bolometric corrections from Humphreys & McElroy (1984), we obtain bolometric luminosities of $\log L_{\rm bol,1}/L_{\odot} = 5.55 \pm 0.05$ and $\log L_{\rm bol,2}/L_{\odot} = 4.94 \pm 0.07$ for the primary and secondary respectively.

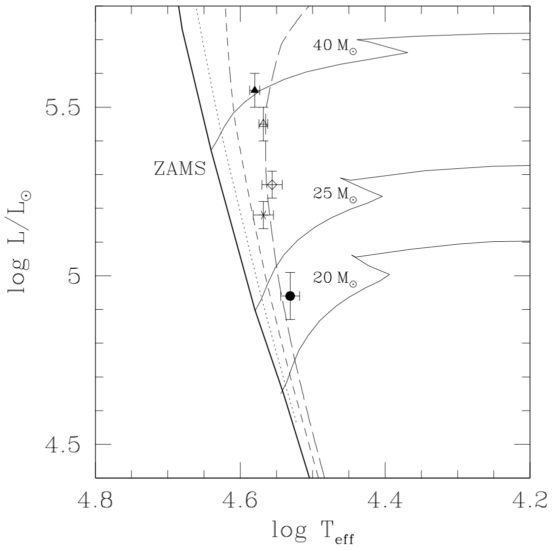

Fig. 5. Position of the primary (filled and open triangle respectively for a bolometric correction for luminosity class V or III) and secondary (filled circle) of BD+60° 497 in the Hertzsprung-Russell diagram. The evolutionary tracks for single stars of initial mass 20, 25 and 40 $M_{\odot}$ as well as the isochrones corresponding to ages of 1, 2 and 3 Myr are from Schaller et al. (1992) for solar metallicity. The locations of BD+60° 501 and BD+60° 513 are indicated by the star and open diamond respectively.

Following the temperature scale of main sequence O-type stars proposed by Martins et al. (2002), the effective temperature of the primary and secondary should be respectively ($38\,000 \pm 500$) K and ($34\,000 \pm 1000$) K. The location of the two components in the H-R diagram is illustrated in Fig. 5. Both stars appear to have evolved off the zero age main sequence (ZAMS). More precisely, whilst the absolute magnitude and the bolometric luminosity that we derived for the secondary are in good agreement with typical values of late O main sequence stars (see e.g. Howarth & Prinja 1989), the parameters of the primary are intermediate between those of a main sequence and a giant O6.5 star. Therefore, we may wonder whether it would not be more appropriate to use a luminosity class III bolometric correction for the primary. If we do so, we obtain $\log L_{\rm bol,1}/L_{\odot} = 5.45 \pm 0.05$ and $T_{\rm eff,1} = (37\,000 \pm 500)$ K. The corresponding position for the primary is also shown in Fig. 5.

In Fig. 5 we compare the properties of the components of BD+60° 497 to the single star evolutionary models of Schaller et al. (1992). We find that the primary lies almost exactly on the 40 $M_{\odot}$ initial mass evolutionary track, whilst the secondary lies between the tracks for an initial mass of 20 and 25 $M_{\odot}$. A crude interpolation between the various models yields evolutionary masses of $M_1 = (39.6 \pm 2.5)\,M_{\odot}$ and $M_2 = (22.7 \pm 1.0)\ M_{\odot}$ for the primary (adopting the main sequence bolometric correction) and secondary respectively. The corresponding evolutionary mass ratio (1.74 ± 0.13) of the system appears thus significantly larger than the observed mass ratio of 1.28 ± 0.12. This discrepancy (although slightly less severe) subsists if we adopt instead the luminosity class III bolometric correction for the primary (M_1 = (36.3 ± 1.5) $M_\odot$; M_1/M_2 = 1.60 ± 0.10).

The evolutionary tracks of Schaller et al. (1992) account for the effect of mass loss but do not include rotational mixing. Meynet & Maeder (2000) quantified the importance of rotation on the output of stellar evolution models at solar metallicity. As a consequence of rotational mixing, fast rotators appear more luminous than non-rotating stars of the same mass. However in the region of the H-R diagram where the components of BD+60° 497 are located (i.e. near the main sequence), this effect should have a rather modest impact on the stellar luminosity (≤ 0.1 in $\log L_{\rm bol}/L_\odot$ according to Fig. 8 of Meynet & Maeder 2000), probably not sufficient to reconcile the mass ratio estimated from the single star evolutionary tracks with the observed mass ratio, especially since the primary absorption lines do not reveal evidence for an exceptionally large rotational velocity.

These problems in the comparison of massive binaries to single star evolutionary theories are actually not new. Penny et al. (1996) already described the same sort of conflicts for binary systems where one component is suspected to currently undergo Roche lobe overflow (RLOF). These authors suggested that during case A RLOF, the mass-losing star is apparently hotter and more luminous than its mass would predict. Could this imply that the primary in BD+60° 497 is currently losing mass through RLOF?

From the luminosities and temperatures derived above we can estimate the radii of the two components to be (13.6 ± 0.9) $R_\odot$ and (8.5 ± 0.8) $R_\odot$ for the primary[1] and secondary respectively. Whilst the secondary probably fits well inside its critical volume, the primary component might fill its Roche lobe if the inclination is as large as 65° (or 74° for the giant parameters). BD+60° 497 is not known to display eclipses that might help to constrain the orbital inclination. Halbedel (1986) monitored BD+60° 497 over 43 night as one of two comparison stars during her observing campaign on BD+60° 562. The differential photometry failed to reveal significant variability of the program star or the comparison stars. Although for a short orbital period that close to an integer number of days the orbital cycle could under some circumstances be poorly sampled, it appears unlikely that BD+60° 497 displays strong variability attributable to photometric eclipses. We further checked this on the data of the Northern Sky Variability Survey (NSVS[2], Woźniak et al. 2004). The NSVS contains time series of data obtained in a single unfiltered photometric band with the Robotic Optical Transient Search Experiment. Though these data indicate a dispersion of 0.018 mag for BD+60° 497, they fail to reveal phase-locked variations attributable to eclipses or ellipsoidal variations. The lack of eclipses yields the condition $a \cos i \geq R_1 + R_2$. Substituting the numerical values from Table 2 and the radii of the components, we obtain $i \leq$ (54 ± 2.5)° (or $i \leq$ (55 ± 2.5)° for the giant parameters). For these values of the inclination, the Roche lobe radii (computed from the results in Table 2) would be sufficiently large so that none of the stars should be filling its Roche lobe. Moreover, though a direct comparison with binary evolutionary models is always tricky (due to the huge parameter space to explore), we note that models predict a rather complex behaviour for the evolutionary tracks during RLOF (e.g. de Loore & Vanbeveren 1994; Wellstein et al. 2001) and an overluminosity of the mass losing star during RLOF does not seem to be a general feature.

We thus conclude that there is no indication at present that the primary in BD+60° 497 is undergoing Roche lobe overflow. Alternatively, we caution that the numerical results obtained in this section (including the evolutionary masses) rest upon the various calibrations that we adopted. Recent results suggest that the effective temperature scale of mid-O stars might have to be revised downwards by as much as 6000 K (Bianchi & Garcia 2002) compared to the calibration of Martins et al. (2002) and this could of course impact on the properties derived in this section and account for some of the discrepancy between the observed and evolutionary mass ratios.

Using the same calibrations as above, we have also plotted the locations of BD+60° 501 and BD+60° 513 in the H-R diagram. For BD+60° 501, we infer on average V = 9.58 ± 0.03 and $B - V$ = 0.46 ± 0.01 (Massey et al. 1995; Reed 1998). With R_V = 3.0, we thus obtain $A_{\rm V} \simeq 2.34$ in good agreement with the value (2.24 ± 0.18) of Sagar & Qian (1990). The absolute V magnitude and bolometric luminosity of BD+60° 501 thus become M_V = −4.61 ± 0.11 and $\log L_{\rm bol}/L_\odot$ = 5.18 ± 0.04, whilst the effective temperature of an O7 V star should be (37 000 ± 500) K according to Martins et al. (2002). For BD+60° 513, we obtain in a similar fashion V = 9.40 ± 0.01 and $B - V$ = 0.49 ± 0.01. From these values we derive M_V = −4.88 ± 0.11 and $\log L_{\rm bol}/L_\odot$ = 5.27 ± 0.04 and the effective temperature is estimated as (36 000 ± 500) K. It can be noted from Fig. 5 that the location of these stars in the H-R diagram is in good agreement with the 1−3 Myr age of the cluster as determined by Massey et al. (1995).

5. *ROSAT* data

O-type stars are rather soft intrinsic X-ray emitters with luminosities that roughly follow an empirical relation between $L_{\rm X}$ and $L_{\rm bol}$ (see Berghöfer et al. 1997 and references therein). Due to an excess X-ray emission produced in the wind interaction zone, some binary systems display an X-ray luminosity above the level expected from this empirical relation. X-ray observations therefore have the potential to provide some additional hints on the multiplicity of early-type stars.

IC 1805 was observed for 8.8 ks with the PSPC instrument onboard the *ROSAT* satellite on 22−23 August 1992 (sequence number rp201263n00). We have extracted these data from the LEDAS archive and processed them using the XSELECT and XSPEC softwares. BD+60° 497 and BD+60° 501 are clearly detected with net (i.e. background corrected) count rates of $(4.6 \pm 1.3) \times 10^{-3}$ and $(6.4 \pm 1.1) \times 10^{-3}$ cts s^{-1}. BD+60° 513 is not detected in this observation and a save upper limit on its net count rate (determined from the count rate of the faintest source detected in this field) is $\sim 2 \times 10^{-3}$ cts s^{-1}.

---

[1] If we adopt the luminosity III bolometric correction for the primary, the radius becomes (12.8 ± 0.8) $R_\odot$.

[2] The NSVS was created jointly by the Los Alamos National Laboratory and the University of Michigan and was funded by the US Department of Energy, NASA and the NSF.

Although the X-ray spectra of BD+60° 497 and BD+60° 501 are of poor quality, we managed to fit them with an absorbed `mekal` optically thin thermal plasma model (Mewe et al. 1985).

For BD+60° 497 we fixed the neutral hydrogen column density at the interstellar value of $N_{\rm H}^{\rm ISM} = 0.52 \times 10^{22}\,{\rm cm}^{-2}$ and we obtained a best fitting temperature $kT = 0.34^{+.43}_{-.14}$ keV with a flux of $4.2 \times 10^{-14}\,{\rm erg\,cm^{-2}\,s^{-1}}$ in the energy band 0.1−2.0 keV. The corresponding dereddened X-ray flux over the same energy range is $3.6 \times 10^{-13}\,{\rm erg\,cm^{-2}\,s^{-1}}$. Adopting a distance of 2.3 kpc (see above), we obtain an X-ray luminosity of $L_{\rm X} = 2.4 \times 10^{32}\,{\rm erg\,s^{-1}}$ in the 0.1−2.0 keV domain. From the empirical $L_{\rm X}/L_{\rm bol}$ relation of Berghöfer et al. (1997) and the bolometric luminosities of the individual binary components derived hereabove, we expect an X-ray luminosity of the binary of $2.6 \times 10^{32}\,{\rm erg\,s^{-1}}$ in excellent agreement with the value derived from the *ROSAT* data. Therefore, we conclude that BD+60° 497 does not display any excess X-ray emission that could be attributed to a wind interaction in the binary.

For BD+60° 501 the hydrogen column density was fixed at $N_{\rm H}^{\rm ISM} = 0.45 \times 10^{22}\,{\rm cm}^{-2}$ and the best fitting temperature was found at $kT = 0.93^{+.75}_{-.59}$ keV. The corresponding observed and unabsorbed fluxes are 4.6×10^{-14} and $1.8 \times 10^{-13}\,{\rm erg\,cm^{-2}\,s^{-1}}$ in the 0.1−2.0 keV band. This corresponds to an X-ray luminosity of $L_{\rm X} = 1.1 \times 10^{32}\,{\rm erg\,s^{-1}}$. Again this value is in good agreement with the empirical $L_{\rm X}/L_{\rm bol}$ relation of Berghöfer et al. (1997) from which we expect an X-ray luminosity of $0.8 \times 10^{32}\,{\rm erg\,s^{-1}}$. On the other hand, given the bolometric luminosity of BD+60° 513 estimated above, the non-detection of the latter in the *ROSAT* data is somewhat surprising. We note that this non-detection – and consequently the lack of an X-ray luminosity excess – provides further evidence against a close binary scenario for BD+60° 513. In fact, the O7 V + O7 V binary HD 159176 displays an X-ray excess of about a factor 7 (De Becker et al. 2004) and one would expect a very similar result if BD+60° 513 were an O7.5 V + O7.5 V binary.

In summary, the *ROSAT* data do not provide any evidence for multiplicity of BD+60° 501 or BD+60° 513.

6. Summary and conclusions

Using a set of spectroscopic data we have investigated the multiplicity of three mid-O (O6−8.5) stars in the very young open cluster IC 1805. We have found that BD+60° 497 is an SB2 system consisting of an O6.5 V((f)) primary and an O8.5-9.5 V((f)) secondary. From the radial velocities of its components, we have inferred an orbital period of 3.96 ± 0.09 days and we have presented the very first orbital solution for this system. The mass ratio of the binary 1.28 ± 0.12 is smaller than the value expected from a comparison with single star evolutionary tracks. We suggest that this discrepancy stems mainly from the uncertainties that affect the current calibrations of O-star temperatures, bolometric corrections and luminosities.

The other two targets of our present study, BD+60° 501 and BD+60° 513, do not display significant radial velocity changes, suggesting that these are probably single stars. This is in contradiction with previous reports of these stars showing *RV* changes or double lines.

So far, the only confirmed spectroscopic binaries in IC 1805 are the SB1 system HD 15558 (Garmany & Massey 1981) and the SB2 system BD+60° 497 studied in the present paper. The stars investigated here provide a complete sample of mid-O type stars in IC 1805. The fraction of confirmed binaries in this mass range is thus 1/3. Our results imply therefore that the lower limit[3] on the binary fraction among the early-type stars of IC 1805 is reduced to 60% rather than the 80% quoted by Ishida (1970) and García & Mermilliod (2001) who included BD+60° 501 and BD+60° 513 in their census of massive binary stars in IC 1805. Therefore the binary fraction in this cluster appears less extreme than previously thought. Additional data on the earliest O-type stars (HD 15558, HD 15570 and HD 15629) of IC 1805 are currently being analysed and will help to further constrain the binary fraction among O-type stars in this cluster. This will be the subject of a forthcoming paper (De Becker et al. in preparation).

Acknowledgements. We are greatly indebted to the FNRS (Belgium) for multiple assistance including the financial support for the rent of the OHP telescope in 2002 through contract 1.5.051.00 “Crédit aux Chercheurs”. The travels to OHP and the rent of the telescope in 2003 were supported by the Ministère de l'Enseignement Supérieur et de la Recherche de la Communauté Française. This research is also supported in part by contract P5/36 “Pôle d'Attraction Interuniversitaire” (Belgian Federal Science Policy Office) and through the PRODEX XMM-OM and INTEGRAL contracts. We would like to thank the staff of OHP for their support. The SIMBAD and WEBDA databases have been consulted for the bibliography. We thank Dr. J.-C. Mermilliod for additional information on the WEBDA database as well as the referee Dr. C. Foellmi for a careful reading of the manuscript.

References

Albacete Colombo, J. F., Morrell, N. I., Rauw, G., et al. 2002, MNRAS, 336, 1099
Bagnuolo, W. G. Jr., Gies, D. R., Riddle, R., & Penny, L. R. 1999, ApJ, 527, 353
Berghöfer, T. W., Schmitt, J. H. M. M., Danner, R., & Cassinelli, J. P. 1997, A&A, 322, 167
Bianchi, L., & Garcia, M. 2002, ApJ, 581, 610
Conti, P. S. 1973a, ApJ, 179, 161
Conti, P. S. 1973b, ApJ, 179, 181
Conti, P. S., & Alschuler, W. R. 1971, ApJ, 170, 325
Conti, P. S., & Leep, E. M. 1974, ApJ, 193, 113
Conti, P. S., & Ebbets, D. 1977, ApJ, 213, 438
De Becker, M., Rauw, G., Pittard, J. M., et al. 2004, A&A, 416, 221
de Loore, C., & Vanbeveren, D. 1994, A&A, 292, 463
Eggleton, P. P. 1983, ApJ, 268, 368
Fullerton, A. W., Gies, D. R., & Bolton, C. T. 1996, ApJS, 103, 475
García, B., & Mermilliod, J.-C. 2001, A&A, 368, 122
Garmany, C. D., & Massey, P. 1981, PASP, 93, 500
Gillet, D., Burnage, R., Kohler, D., et al. 1994, A&AS, 108, 181
Gosset, E., Royer, P., Rauw, G., Manfroid, J., & Vreux, J.-M. 2001, MNRAS, 327, 435

---

[3] This fraction is a lower limit since we cannot rule out the existence of binaries seen under a low inclination (thus preventing us from detecting any *RV* changes).

Guetter, H. H., & Vrba, F. J. 1989, AJ, 98, 611
Halbedel, E. M. 1986, IBVS, 2884, 1
Heck, A., Manfroid, J., & Mersch, G. 1985, A&AS, 59, 63
Howarth, I. D., & Prinja, R. K. 1989, ApJS, 69, 527
Howarth, I. D., Siebert, K. W., Hussain, G. A. J., & Prinja, R. K. 1997, MNRAS, 284, 265
Humphreys, R. M., & McElroy, D. B. 1984, ApJ, 284, 565
Ishida, K. 1970, PASJ, 22, 277
Lafler, J., & Kinman, T. D. 1965, ApJS, 11, 216
Llorente de Andrés, F., Burki, G., & Ruiz del Arbol, J. A. 1982, A&A, 107, 43
Martins, F., Schaerer, D., & Hillier, D. J. 2002, A&A, 382, 999
Massey, P., Johnson, K. E., & De Gioia-Eastwood, K. 1995, ApJ, 454, 151
Mathys, G. 1987, A&AS, 71, 201
Mathys, G. 1989, A&AS, 81, 237
Mermilliod, J.-C. 1996, in The Origins, Evolution and Destinies of Binary Stars in Clusters, ed. E. F. Milone, & J.-C. Mermilliod, ASP Conf. Ser., 90, 97
Mewe, R., Gronenschild, E. H. B. M., & van den Oord, G. H. J. 1985, A&AS, 62, 197
Meynet, G., & Maeder, A. 2000, A&A, 361, 101
Moffat, A. F. J., & Vogt, N. 1974, Veröff. Astron. Inst. Bochum, 2
Morrell, N. I., Barbá, R. H., Niemela, V. S., et al. 2001, MNRAS, 326, 85
Normandeau, M., Taylor, A. R., & Dewdney, P. E. 1996, Nature, 380, 687
Penny, L. R., Gies, D. R., & Bagnuolo, W. G. Jr. 1996, in WR Stars in the Framework of Stellar Evolution, Proc. 33rd Liège Int. Astroph. Coll., ed. J.-M. Vreux, A. Detal, D. Fraipont-Caro, E. Gosset, & G. Rauw, 289
Rauw, G., Sana, H., Gosset, E., et al. 2000, A&A, 360, 1003
Rauw, G., Sana, H., Antokhin, I. I., et al. 2001, MNRAS, 326, 1149
Rauw, G., De Becker, M., & Vreux, J.-M. 2003, A&A, 399, 287
Reed, B. C. 1998, ApJS, 115, 271
Sagar, R., & Qian, Z.-Y. 1990, ApJ, 353, 174
Sana, H., Rauw, G., & Gosset, E. 2001, A&A, 370, 121
Sana, H., Hensberge, H., Rauw, G., & Gosset, E. 2003, A&A, 405, 1063
Schaller, G., Schaerer, D., Meynet, G., & Maeder, A. 1992, A&AS, 96, 269
Shi, H. M., & Hu, J. Y. 1999, A&A, 136, 313
Trumpler, R. J. 1930, Lick Obs. Bull., 14, 154
Underhill, A. B. 1967, in Determination of Radial Velocities and their Applications, ed. A. H. Batten, & J. F. Heard (London: Academic Press), Proc. IAU Symp., 30, 167
Underhill, A. B. 1994, ApJ, 420, 869
Walborn, N. R. 1973, AJ, 78, 1067
Walborn, N. R., & Fitzpatrick, E. L. 1990, PASP, 102, 379
Wellstein, S., Langer, N., & Braun, H. 2001, A&A, 369, 939
Woźniak, P. R., Vestrand, W. T., Akerlof, C. W., et al. 2004, AJ, 127, 2436

2.2 The early-type stars HD 15570 and HD15629

We investigated two of the earliest O-type stars of IC 1805, i.e. HD 15570 and HD 15629, in order to constrain their multiplicity and to study their line profile variability. Spectral time series were obtained at the Observatoire de Haute-Provence with the Aurélie spectrograph mounted on the 1.52 m telescope during five observing runs in September 2000, September 2001, September 2002, October 2003 and October 2004[1]. We investigated the line profile variability of these two stars using the techniques described in Appendix A.

Our investigation of the radial velocity of HD 15570 (O4If$^+$) did not reveal any significant variations attributable to binarity on time-scales of a few days, or from one year to the next. However, we observed a significant line profile variability of the He II λ 4686 and Hβ lines, with a recurrence time-scale of about 6 days. The profiles present correlated variations suggesting that more than one component contribute to the lines. The variations of Hβ are more significant in the emission part of its P-Cygni profile. The equivalent width of He II λ 4686 presents a somewhat marginal modulation probably with a time-scale of about 6 days as well, but we note that this time-scale is not very well defined (see De Becker & Rauw 2005a and the detailed report inserted below). Two scenarios could be envisaged to explain these profile variations:

- the variations could possibly be attributed to rotational modulations, the time-scale of 6 days being the rotational period.
- another possibility to be considered is a wind-wind interaction within a binary system seen under a low inclination, but if the rotational and orbital axes are parallel this would lead to an excessive V$_{rot}$ (V$_{rot}\sin i = 130\,\mathrm{km\,s^{-1}}$). For this reason, the rotational modulation scenario is slightly preferred.

For the O5V((f)) star HD 15629, our investigation did not reveal any significant radial velocity variations attributable to a binary motion on time-scales of a few days, or from one year to the next. However, we detected a significant variability of the profile of the He II λ 4686 and Hβ lines on a time-scale of a few days. We note that this variability is clearly detected during one observing run (September 2002) whilst it is marginal in other data sets. This suggests possible transient variations that require further investigation with more data. For details, see the detailed report inserted below.

A consequence of the lack a evidence of binarity for several stars is a revision of the claim that the binary fraction of the O-type stars in IC 1805 may be as high as about 80 %. Indeed, considering our results, all we can say is that the O-star binary fraction in IC 1805 should be at least 20 % but is most probably not exceeding 60 %.

---

[1] HD 15629 was only observed during the three latter observing runs of this campaign.

Early-type stars in the young open cluster IC 1805: II. HD 15570 and HD 15629

M. De Becker,[1] G. Rauw,[1] and P. Eenens[2]

[1]Institut d'Astrophysique et de Géophysique, Université de Liège, 17, Allée du
6 Août, B5c, B-4000 Sart Tilman, Belgium
[2]Departamento de Astronomia, Universidad de Guanajuato, Apartado 144,
36000 Guanajuato, GTO, Mexico

Abstract: We report on a spectroscopic investigation of the multiplicity and of the line profile variability in the blue spectrum of two of the earliest O-stars of the open cluster IC 1805, namely HD 15570 (O4If$^+$) and HD 15629 (O5V((f))). Our radial velocity study does not reveal any significant variations attributable to a binary motion on time scales of a few days or from one year to the next. In the case of HD 15570, we detect strong variations of the profile of the He II λ 4686 line correlated to those of Hβ with a possible time scale of about 6 d. The variability pattern of these two lines suggests that more than one component contribute to their profiles. This behaviour, along with the high plasma temperature ($\sim$ 1.25 keV) revealed by the fit of archive *ROSAT*-PSPC X-ray data with a thermal emission model, might be compatible with a wind-wind interaction scenario in an eccentric binary system. However, the very low inclination of the orbital axis – and therefore presumably of the rotational axis – required by the absence of significant radial velocity variations, would lead to an excessive rotational velocity. For this reason, we slightly favor a rotational modulation scenario. In the case of HD 15629, the He II λ 4686 and Hβ lines present a significant variability on time scales possibly compatible with a rotational modulation scenario. The study of optical and archive X-ray data suggests that this star is most probably single. Considering new and previously published results, we briefly discuss the multiplicity of O-stars in IC 1805. We find that the binary frequency among O-stars in IC 1805 has a lower limit of 20 %, and that previously published values (80 %) might be overestimated.

1 Introduction

The study of stellar populations of young open clusters has been the purpose of many works in the last years (e.g. Sagar et al. 1988; Raboud & Mermilliod 1998). One of the crucial questions addressed in this context concerns the massive star content and the binary frequency of the earliest stars harboured by these clusters. Recent numerical simulations of the stellar formation of open clusters predict a high level of mass segregation, along with the formation of the most massive stars through simultaneous accretion and stellar collisions, resulting in the presence of the most massive stars in binary systems (Bonnell & Bate, 2002). The investigation of the multiplicity of the massive star content of young open clusters is consequently of particular interest. For instance, García & Mermilliod (2001) presented radial velocity measurements for 37 O- and B-stars in the open cluster NGC 6231, and proposed binary frequencies for a series of open clusters, among which IC 1805.

IC 1805 is a young rich open cluster in the core of the Cas OB6 association, in the molecular cloud W 4 in the Perseus spiral arm of our Galaxy. Massey et al. (1995) inferred an age of 1-3 Myr for the cluster, in agreement with other previous estimates (see Feinstein et al. 1986, and references therein, although these latter authors proposed an age < 1 Myr). The spectroscopic study of Shi & Hu (1999) revealed that about 80 of the members of IC 1805 are O or B stars. García & Mermilliod (2001) (see also Ishida 1970) estimated a binary frequency of 80 % among the 10 O-stars in IC 1805. However, in a previous paper Rauw & De Becker (2004), we showed that two suspected binaries, BD +60° 501 (O7V((f))) and BD +60° 513

Table 1: Observing runs used for the line profile variability study of HD 15570 and HD 15629. The first and second columns give the name of the campaign as used in the text as well as the instrumentation used. For each star, the next columns yield the number of spectra obtained, the time elapsed between the first and the last spectrum of the run, the natural width of a peak of the power spectrum taken as $1/\Delta T$, and finally the mean signal-to-noise ratio of each data set.

		HD 15570				HD 15629			
Obs. run	Telescope	Number of spectra	ΔT (d)	$\Delta\nu_{\rm nat}$ (d^{-1})	S/N	Number of spectra	ΔT (d)	$\Delta\nu_{\rm nat}$ (d^{-1})	S/N
September 2000	OHP/1.52 m	7	9.99	0.10	390	–	–	–	–
September 2001	OHP/1.52 m	5	7.02	0.14	360	–	–	–	–
September 2002	OHP/1.52 m	10	14.94	0.07	300	9	12.99	0.08	300
October 2003	OHP/1.52 m	7	17.97	0.06	300	4	17.98	0.06	280
October 2004	OHP/1.52 m	7	9.90	0.10	260	7	9.90	0.10	260
October 2004	SPM/2.10 m	4	2.07	0.48	180	–	–	–	–

(O7.5V((f))), were most probably single stars, suggesting that the binary frequency proposed by García & Mermilliod (2001) might be overestimated. In this paper, we investigate the multiplicity and the line profile variability of another two O-stars of IC 1805: HD 15570 and HD 15629. These two stars, along with the SB1 system HD 15558 (Garmany & Massey, 1981), are the earliest O-type stars of the cluster.

HD 15570 (O4If$^+$, V = 8.10) was proposed to be the most massive member of IC 1805, and incidentally one of the most massive and most luminous stars known in our Galaxy, with a present evolutionary mass of about 80 $M_\odot$ following Herrero et al. (2000). Polcaro et al. (2003) reported on a substantial profile variability of the Hα line, with an equivalent width variation of about a factor 4. The same authors proposed to interpret this behaviour in the context of wind instabilities related to the magnetic field, though they failed to constrain the time scale of the variations. HD 15629 (O5V((f)), V = 8.42) has also been proposed to be a very massive star. According to Herrero et al. (2000), this star could have evolved from an initial mass of about 70 $M_\odot$, and presently be on the way towards evolutionary stages close to those of HD 14947 (O5If$^+$) and HD 210839 (O6I(n)fp, λ Cep). The same authors inferred a present-day evolutionary mass of about 61 $M_\odot$. For both stars, no clear evidence of binarity has been reported in the literature, even though some radial velocities quoted in the WEBDA data base[1] suggest the occurrence of variations.

This paper is organized as follows. In Sect. 2, we describe our observations. The spectra of our targets are discussed in details in Sect. 3. Next comes Sect. 4 with a discussion of the radial velocities, equivalent widths and archive photometry. Sections 5 and 6 are respectively devoted to the line profile variability and to an analysis of archive *ROSAT* data. Finally, the overall discussion of the results and the conclusions are presented in Sect. 7 and 8.

2 Observations and data reduction

Spectroscopic observations of HD 15570 and HD 15629 were collected at the Observatoire de Haute-Provence (OHP, France) during several observing runs from 2000 to 2004 for HD 15570, and from 2002 to 2004 for HD 15629. All spectra were obtained with the Aurélie spectrograph fed by the 1.52 m telescope (Gillet et al., 1994). Aurélie was equipped with a 2048×1024 CCD EEV 42-20#3, with a pixel size of 13.5 μm squared. All spectra were taken with a 600 l/mm grating allowing us to achieve a resolving

---

[1] Available at http://obswww.unige.ch/webda

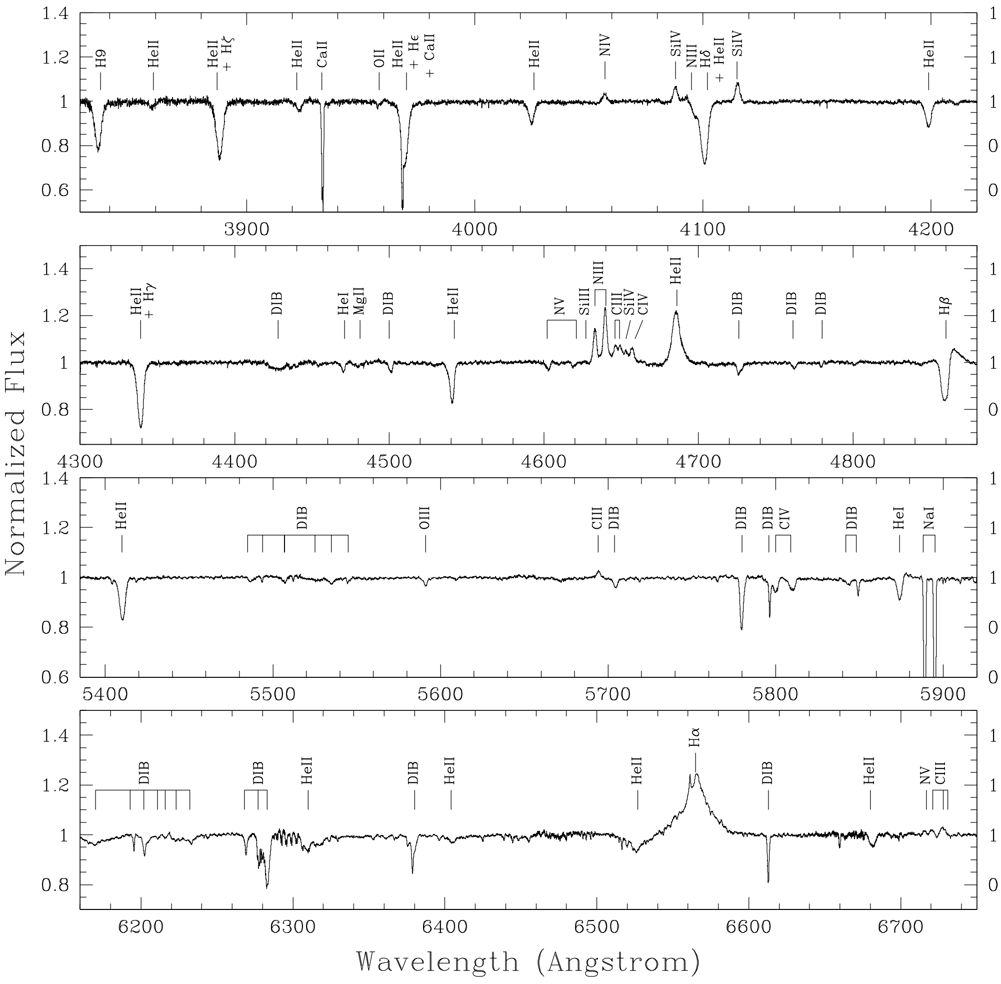

Figure 1: Mean spectrum of HD 15570 calculated from spectra obtained at SPM between HJD 2 453 287.93 and HJD 2 453 290.00.

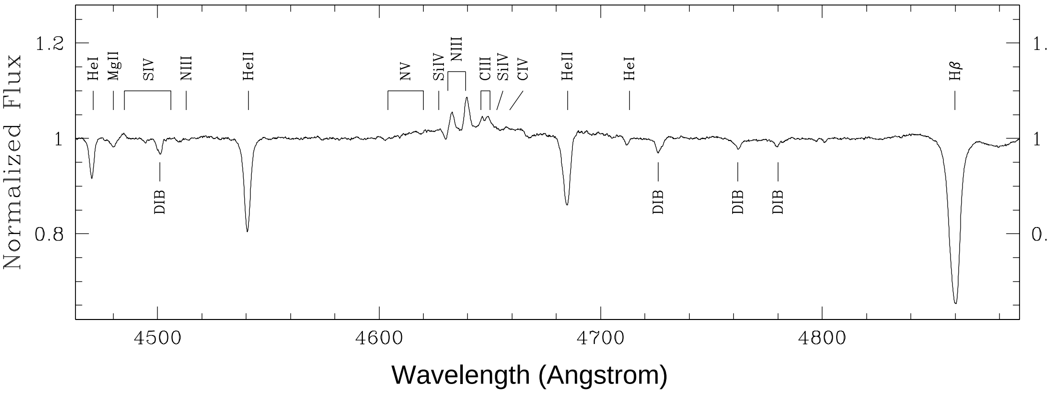

Figure 2: Mean normalized spectrum of HD 15629 between 4465 Å and 4890 Å as observed in September 2002 at OHP.

power of about 8000 in the blue range, with a reciproqual dispersion of 16 Å mm^{-1}. Our collection of spectra is described in Table 1.

We adopted the same reduction procedure as in Rauw & De Becker (2004). The data collected with the Aurélie spectrograph consist of five images of the spectrum obtained with an image slicer Gillet et al. (1994). All images were combined after individual treatment and cosmic ray removal. The wavelength calibration was performed using a Th-Ar comparison spectrum obtained shortly before or after the observation of the star. All spectra were normalized using splines calculated on the basis of properly chosen continuum windows.

We also obtained several spectra of HD 15570 with the echelle spectrograph mounted on the 2.1 m telescope at the Observatorio Astronómico Nacional of San Pedro Martir (SPM), in Mexico, with exposure times ranging between 10 and 20 minutes. The instrument covers the spectral domain between about 3800 and 6800 Å . The detector was a Site CCD with 1024 × 1024 pixels of 24 μm squared. The slit width was set to 200 μm corresponding to 2 arcsec on the sky. The data were reduced using the echelle package available within the MIDAS software. After adding consecutive spectra of a given night to reach higher signal-to-noise ratios, at the expense of time resolution, we obtained 4 spectra of HD 15570 that were normalized using carefully chosen splines.

3 Spectral classification

3.1 HD 15570

The most prominent features observed in the spectrum presented in Fig. 1 are the He II λ 4686 and Hα lines, in strong emission. The He II λ 4686 emission is one of the characteristics of the Of$^+$ type, along with Si IV $\lambda\lambda$ 4088-4115 also in emission. The other main emission lines are from N III $\lambda\lambda$ 4634-4641. We find also weaker emission lines of N IV at 4058 Å , C III at 4650 and 5696 Å , and also C IV λ 4662. The weak emission lines at 6721, 6728 and 6731 Å might be attributed to C III (Walborn & Howarth 2000; Walborn 2001). We report also on the probable presence of the Si IV λ 4656 line in weak emission, along with that of the weak N V $\lambda\lambda$ 6716,6718 emission (Walborn & Howarth 2000; Walborn 2001). The Hβ line appears as a P Cygni profile with a very deep absorption component. Other absorption lines are mainly due to He II. He I λ 4471 is very weak. We also note that the He I λ 5875 line appears as a P Cygni profile, even if the emission component is rather weak. The Mg II λ 4481 line is detected, and we also note the presence of the N V $\lambda\lambda$ 4604,4620 lines in weak absorption. Even if its presence is not obvious in the mean SPM spectrum (see Fig. 1), a weak emission feature at about 4487 Å is observed in OHP spectra and is probably due to S IV (Werner & Rauch, 2001).

The various classifications proposed in the literature for this star are O4If$^+$ (Walborn, 1972), O4If (Massey et al., 1995), O5Iaf (Ishida, 1970) and O4.5If (Shi & Hu, 1999). We measured the equivalent width (EW) of the He I λ 4471 and He II λ 4542 lines, and we obtained EW(He I λ 4471) = 0.12 ± 0.01 Å and EW(He II λ 4542) = 0.60 ± 0.02 Å. These values are averaged quantities of the EWs obtained for all observing runs. Using the classification criterion given by Mathys (1988), we infer the spectral type O4. The various emission lines discussed above lead to the O4If$^+$ spectral type for HD 15570, in agreement with Walborn's classification Walborn (1972). A comparison with the spectrum of the O4If$^+$ star HD 269698 (Walborn & Fitzpatrick, 1990) lends further support to this classification.

3.2 HD 15629

The strongest lines in the blue spectrum of HD 15629 (Fig. 2) are in order of decreasing intensity: Hβ, He II λ 4542, He II λ 4686 and He I λ 4471, all in absorption. The He I λ 4713 absorption line is very weak. The Mg II λ 4481 absorption line is also present. The N III $\lambda\lambda$ 4634-4641 lines are the strongest emission features observed in this spectrum. The C III blend at about 4650 is also present and we note the possible presence of C IV λ 4662 in weak emission. The weak emission feature at about 4487 Å is probably due to S IV (Werner & Rauch, 2001).

The classification found in the literature for this star is O5V((f)) (Walborn 1972; Massey et al. 1995; Shi & Hu 1999). From our EW measurements of the He I λ 4471 and He II λ 4542 lines (respectively 0.21 ± 0.01 Å and 0.68 ± 0.02 Å) and adopting the classification criterion porposed by Mathys (1988), we derive an O5 spectral type. Considering the fact that the N III $\lambda\lambda$ 4634-4641 features are in emission, and that He II λ 4686 is in strong absorption, we adopt the O5V((f)) spectral type for HD 15629, in agreement with previous classifications.

4 Radial velocities, equivalent widths, and photometry

4.1 Radial velocities

We have measured the radial velocity (RV) of the strongest lines for HD 15570 and HD 15629 by fitting Gaussians to the line profiles. The RVs of various lines from OHP data only are quoted in Table 2.

In the case of HD 15570, the dispersion of the RV of the He I λ 4471 line is larger than for other lines in most of our data sets, as its profile deviates significantly from a Gaussian. In the case of the He II λ 4542 line, we performed a Fourier analysis of the RVs following the method described by Heck et al. (1985). The periodogram reveals several peaks. The highest one is found at a frequency of 0.71 d^{-1}. However, the semi-amplitude is very low (about 4 km s^{-1}) compared to the typical error on the RVs. This error on the RVs, i.e. about 10 km s^{-1}, corresponds to the standard deviation determined for the radial velocity of a Diffuse Interstellar Band (DIB) at about 4762 Å. The radial velocities of the N III emission lines appear to be stable on the time scales investigated in this study. As a result, we do not detect any significant RV variation attributable to binarity on time scales of a few days, nor from one year to the next, in our OHP data. The radial velocities measured on the main absorption and emission lines observed in the SPM spectra did not reveal any significant RV change neither on a time scale of a few days, although we may note that the dispersion obtained in most cases is larger due to non-Gaussian profiles and to a poorer quality of the data. The lack of significant RV variations is not in agreement with the RV changes suggested by the data collected in the WEBDA data base. We note however that these archive RV measurements were obtained on the basis of sometimes heterogeneous line lists and with instruments of different capabilities, at very different epochs.

Table 2: Radial velocity of the main He and N lines for both stars measured on OHP spectra (expressed in km s^{-1}). The mean radial velocity along with its 1-σ standard deviations are provided for each observing run. All individual RVs can be found in the WEBDA data base at `http://obswww.unige.ch/webda`.

Data set	He I λ 4471	He II λ 4542	N III λ 4634	N III λ 4641
	HD 15570			
Sept.2000	–69.1 ± 8.2	–46.7 ± 8.7	–56.1 ± 3.9	–67.0 ± 2.8
Sept.2001	–65.1 ± 10.6	–51.1 ± 3.2	–58.6 ± 3.5	–70.3 ± 2.0
Sept.2002	–60.5 ± 13.2	–50.0 ± 5.0	–56.8 ± 4.6	–70.0 ± 3.3
Oct.2003	–59.3 ± 15.7	–46.2 ± 3.9	–55.6 ± 4.5	–67.6 ± 5.4
Oct.2004	–72.7 ± 8.3	–47.8 ± 7.0	–58.0 ± 4.7	–70.6 ± 3.7
All	–65.0 ± 12.3	–48.3 ± 5.9	–56.9 ± 4.2	–69.1 ± 3.8
	HD 15629			
Data set	He I λ 4471	He II λ 4542	N III λ 4634	N III λ 4641
Sept.2000	–	–	–	–
Sept.2001	–	–	–	–
Sept.2002	–60.6 ± 3.6	–46.9 ± 4.5	–59.9 ± 8.8	–72.1 ± 6.8
Oct.2003	–55.3 ± 4.6	–41.0 ± 1.6	–54.6 ± 3.2	–71.6 ± 2.6
Oct.2004	–58.2 ± 5.9	–50.1 ± 4.6	–63.5 ± 8.3	–74.6 ± 6.5
All	–58.7 ± 4.9	–46.8 ± 5.2	–60.1 ± 8.2	–72.9 ± 6.0

The strong profile variability undergone by the He II λ 4686 and Hβ lines, along with their noticeable asymmetry, prevented us from obtaining accurate and reliable RVs. However, we mention that the RVs measured at the top (resp. bottom) of the He II λ 4686 (resp. Hβ) line reveal rather strong wavelength shifts, which are correlated both in direction and amplitude (semi-amplitude of ~ 30 km s^{-1}) for the two lines. These RV shifts are well illustrated by the profiles presented in Fig. 3. However, the lack of significant shift for the RVs of He I λ 4471, He II λ 4542 and N III $\lambda\lambda$ 4634-4641 does not support the idea that this could be due to the orbital motion in a binary system. We finally note that the RVs measured on SPM spectra of the Balmer lines display the expected progression due to the transition from purely absorption (H9) to P-Cygni (Hβ) profiles.

For HD 15629, we measured the RV for several lines that are free from profile variability. Therefore, only the He I λ 4471, He II λ 4542, and N III $\lambda\lambda$ 4634-4641 lines are considered in this discussion. A Fourier analysis of the RVs from the three data sets reveals a highest peak at 0.08 d^{-1} (P = 12.6 d) for He I λ 4471, and at 0.16 d^{-1} (P = 6.25 d) for He II λ 4542. The periodogram for this latter line presents also a peak close to that of the He I line at 0.09 d^{-1} (P = 11.1 d). However, the amplitude of these peaks is only about 5 km s^{-1}. We detect no significant RV variations for any of the lines. This result is in contrast with the variable status reported by Underhill (1967) and Humphreys (1978). We also mention that long term RV variations were reported for this star (see the WEBDA data base), but we should consider these values with caution for the same reasons as for HD 15570 (see above). In summary, we did not find any trend pointing to a binary scenario on the time scales sampled by our data.

4.2 Equivalent widths

We estimated the EW relative to the local continuum of the strongest lines by integrating the line profiles (see Table 3). In the case of HD 15570, the EWs of the He I λ 4471 and He II λ 4542 lines do not present any significant variability. The EW of the He II λ 4686 line, and to some extent that of Hβ, present a larger dispersion. The semi-amplitude of this dispersion for a given observing run can reach about

Table 3: Mean equivalent widths (expressed in Å) of the strongest lines in the blue spectra of HD 15570 and HD 15629 for each data set. The negative values stand for a line in emission. The 1-σ dispersion is provided in each case.

Data set	HD 15570			
	He I λ 4471	He II λ 4542	He II λ 4686	Hβ
Sept. 2000	0.12 ± 0.01	0.61 ± 0.02	–1.98 ± 0.13	1.08 ± 0.06
Sept. 2001	0.11 ± 0.01	0.59 ± 0.01	–1.97 ± 0.10	1.05 ± 0.07
Sept. 2002	0.12 ± 0.01	0.59 ± 0.02	–1.95 ± 0.11	1.10 ± 0.08
Oct. 2003	0.12 ± 0.01	0.61 ± 0.01	–2.01 ± 0.09	1.08 ± 0.04
Oct. 2004	0.11 ± 0.01	0.61 ± 0.01	–2.00 ± 0.12	1.11 ± 0.04

Data set	HD 15629			
	He I λ 4471	He II λ 4542	He II λ 4686	Hβ
Sept. 2000	–	–	–	–
Sept. 2001	–	–	–	–
Sept. 2002	0.21 ± 0.01	0.68 ± 0.02	0.57 ± 0.04	1.99 ± 0.04
Oct. 2003	0.20 ± 0.01	0.69 ± 0.02	0.54 ± 0.03	1.98 ± 0.03
Oct. 2004	0.21 ± 0.01	0.67 ± 0.02	0.58 ± 0.02	2.07 ± 0.05

10 % for He II λ 4686. We note that this is lower than the amplitude (from 2.39 to 3.97 Å) reported by Polcaro et al. (2003). We performed a Fourier analysis on the EWs of the He II λ 4686 line from the complete data set. On the one hand, to optimize the consistency of our EWs, the EWs were estimated on the basis of a unit continuum, therefore including some fraction of the large emission bump[2] observed between about 4600 and 4700 Å . The periodogram is dominated by a peak at about 0.83 d^{-1} along with peaks close to 0.06 and 0.17 d^{-1}, the latter being an alias of the 0.83 d^{-1} peak. We have folded the EWs of He II λ 4686 with the time scales corresponding to these peaks, but no strong trend was observed even if the dispersion (∼ 0.2 Å) is higher than the expected uncertainty on our EWs[3]. On the other hand, we performed the same Fourier analysis on the basis of EWs determined relative to the local continuum between 4670 and 4700 Å (significantly above 1 because of the large emission bump). In this case, the periodogram is clearly dominated by a peak at about 0.17 d^{-1}. However, no obvious trend is observed when the EWs are folded with the corresponding recurrence time scale. We note that the amplitude of the dominant peak is about 0.1 Å , i.e. of the order of the expected error on the EW. We mention that χ^2-tests point to a significant variability at the 99.5 % and 90 % confidence levels for the EW time series obtained respectively relative to the unit and the local continuum. The differences in the periodograms obtained from the two approaches we followed to determine the EWs may come from the emission bump, whose nature is still not clearly understood. Indeed, when the spectra are overplotted, we see that significant changes are observed in the continuum level between 4600 and 4700 Å . If the bump presents some variability (intrinsic or due to rectification errors), it might interfere with the modulations undergone by the line itself, therfore preventing us to investigate only the line profile variations. For this reason, we consider that the EWs obtained relative to the local continuum are less affected by the bump, and therefore more relevant for the purpose of the study of the behaviour of the He II λ 4686 line.

We also note that no strong variations are observed from one year to the next. Consequently, the strong variability reported by Polcaro et al. (2003) for the EW of the He II λ 4686 line was not observed between September 2000 and October 2004. The EWs of Hα measured on SPM spectra range between

---

[2] This emission bump is not observed in Fig. 1 because the echelle spectra were rectified relative to a local continuum. Its presence is however very clear if we consider Aurélie data.

[3] We determined the typical uncertainty of the EWs by estimating the dispersion of the EW relative to a unit continuum between 4630 and 4660 Å , i.e. ∼ 0.08 Å . We selected this wavelength domain because no significant variability was detected in this range. The dispersion of the EWs is therefore expected to come from errors in the normalization.

3.7 and 4.7 Å . These values are rather close to the lowest EWs reported by Polcaro et al. (2003). The highest value for the EW of Hα is observed in the same spectrum as the largest EW of the He II λ 4686 line, whose variability seems to be correlated with that of Hα (see Fig. 6 and the discussion in Sect. 3).

In the case of HD 15629, the EWs do not show any significant variations for any of the lines. They present a larger dispersion for the He II λ 4686 and Hβ lines as compared to He I λ 4471 and He II λ 4542, but with an amplitude which is lower than in the case of HD 15570.

4.3 Photometry

We also used the *Hipparcos* and *Tycho* photometry to investigate the variability of the two stars. For both stars we fitted the three magnitudes series (i.e. V_T, B_T and H_P) with a constant and we calculated the reduced χ^2. In the case of HD 15570 our results point to a variability of the magnitudes with more than 99 % confidence. We then performed a Fourier analysis of the photometric time series using the same technique as used for EWs hereabove. However, the periodograms did not present obvious dominant peaks likely associated to a particular time scale for the variability. The amplitude of these variations might be of the order of 0.09, 0.08 and 0.012 magnitudes respectively in the V_T, B_T and H_P filters. We finally considered the highest peaks of the periodograms and we folded the magnitudes with the corresponding periods, but no obvious trend was revealed. No trend was neither observed on the recurrence time scale observed for the EWs of the He II λ 4686 line. If the variability of the *Hipparcos* and *Tycho* photometry is real, it may be non-periodic or ruled by a yet undetermined time scale. We applied the same procedure to photometric data of HD 15629 but our analysis did not reveal significant variability on the time scale covered by the *Hipparcos* and *Tycho* observations.

5 Line profile analysis

We investigated the line profile variability of HD 15570 and HD 15629 using the same approach as described for instance by Rauw & De Becker (2004) and De Becker & Rauw (2004). Our results are described in detail in this section.

5.1 HD 15570

We calculated the Time Variance Spectrum (TVS, see Fullerton et al. 1996) of our time series to search for a significant line profile variability (at the 99 % confidence level). The lines displaying the highest variability in all data sets are He II λ 4686 and Hβ. Some variability is also detected for He II λ 4542 in the case of the 2000 and 2001 data sets, but its level is much lower than that of the other two lines. We note also a marginal variability of the N III $\lambda\lambda$ 4634-4641 lines in 2000, 2002 and 2003. Our SPM spectra revealed a significant variability of the H9 line, and possibly of the Hγ line, but at a lower level. In this section, we will concentrate on the line profile analysis of the lines presenting the strongest variability in our OHP series.

The variability of the strong He II λ 4686 emission line is illustrated in Fig. 3 for the time series of September 2002. We clearly see a wavelength shift of the top of the line, along with a slight modification of the width of the profile. The most striking characteristic of this variability pattern is shown by the profile obtained at HJD 2 452 533.546. This suggests that more than one emission components contribute to the profile, with at least one of them varying in wavelength or varying in intensity for a given spectral position. This behaviour is confirmed by the profiles of the Hβ line shown in Fig. 3. If we compare night by night the profiles obtained for He II λ 4686 and Hβ, we see that their variability is strongly correlated, in agreement with the RV discussion presented in Sect. 4.

We performed a 2D Fourier analysis using the technique described by Rauw et al. (2001) for the lines displaying a significant variability. The 2D periodograms obtained in the cases of the September 2002

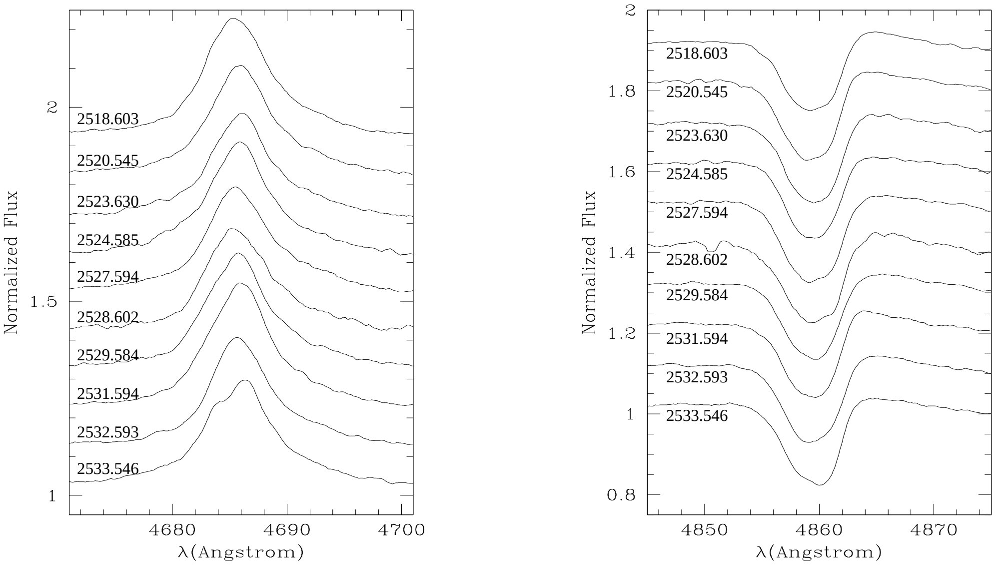

Figure 3: Time series of the He II λ 4686 and Hβ lines observed in September 2002. The line profiles undergo a significant variability on a time scale of a few days.

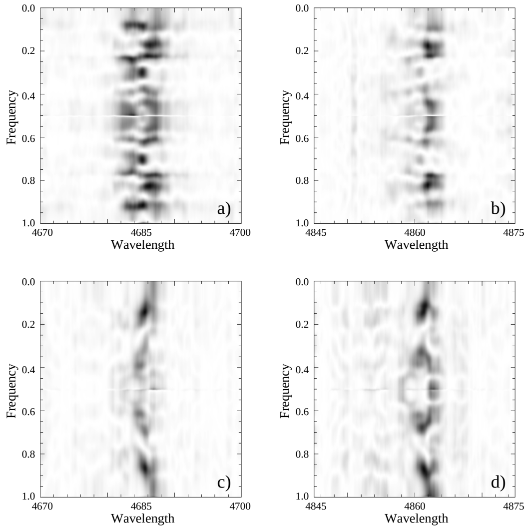

Figure 4: Two-dimensional power spectra for the He II λ 4686 line of HD 15570 in 2002 (a) and in 2004 (c), and for the Hβ line in 2002 (b) and in 2004 (d). Frequencies and wavelengths are respectively expressed in d^{-1} and in Å . The strong correlation between the variability patterns of the two lines is noticeable. As discussed in the text, the main peak in these periodograms fall at frequencies of about 0.15 - 0.18 d^{-1}. We note that the peaks observed close to 0.5 d^{-1} in September 2002, and close to 0.4 and 0.6 d^{-1} are aliases of the main peaks. The other peaks observed in September 2002 are significantly weaker and probably not relevant.

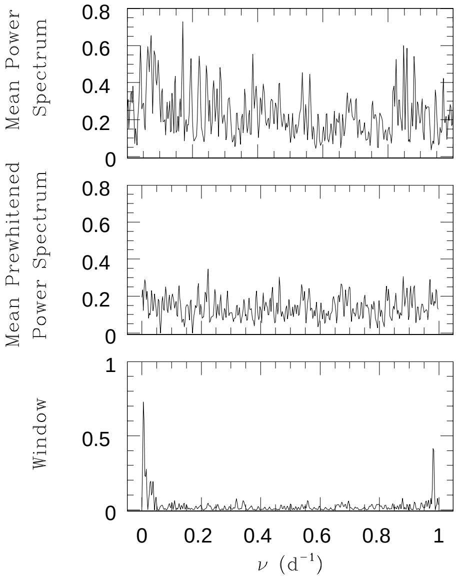

Figure 5: *Upper panel:* mean power spectrum obtained for the He II λ 4686 line of HD 15570 between 4680 Å and 4690 Å for the complete data set, up to 1.0 d^{-1}. The dominant peak corresponding to a frequency of 0.171 d^{-1} translates into a recurrence time scale of about 5.8 d. *Middle panel:* residual power spectrum obtained after prewhitening with two frequencies (0.063 and 0.171 d^{-1}). *Bottom panel:* power spectral window corresponding to the complete data set sampling.

and of the October 2004 observing runs are presented in Fig. 4. If we compare the variability pattern of the two lines for a given data set, we clearly see the strong correlation of their behaviour. The main peaks appear at the same frequencies for the He II λ 4686 and Hβ lines. Moreover, the bulk of the variability is observed in the core of the lines. For the September 2000 and the October 2004 data sets, the main peaks are found at frequencies located between 0.14 and 0.16 d^{-1} (along with the alias at 1-ν). For the September 2001 and September 2002 data sets, rather similar periodograms are obtained with main peaks at a somewhat different frequency, i.e. between about 0.17 and 0.18 d^{-1}. These sets of frequencies are found for both He II λ 4686 and Hβ. In the case of the October 2003 data set, these frequencies are however almost absent, and the main peaks are found at frequencies close to 0.07 and 0.25 d^{-1} (and their 1-ν aliases). We caution however that this latter data set is affected by the poorer sampling (only 7 spectra obtained over 18 days).

In the case of the combined data set, therefore benefitting from the longest time base, we found that the periodogram is dominated by peaks at about 0.06 and 0.17 d^{-1} (and aliases at 1-ν). Figure 5 shows the mean periodogram (upper panel) obtained for our complete data set up to 1 d^{-1}, along with the residual power spectrum (middle panel) obtained after 'prewhitening' (see Rauw et al. 2001) with two frequencies. The first one corresponds to the main peak of the periodogram (i.e. 0.171 d^{-1}), and the second one (i.e. 0.063 d^{-1}) corresponds to the main peak of the residual periodogram obtained after prewhitening with the first frequency. We note that the main peaks of the periodogram computed on the basis of the line profile fall at the same frequency as for the EWs discussed in Sect. 4.

We mention also that for the two data sets obtained with the best signal-to-noise ratio, i.e. September 2000 and September 2001, we were able to investigate the variability of the He II λ 4542 line. For September 2000, we obtain a main peak at about 0.14 d^{-1}, in agreement with the results from the two

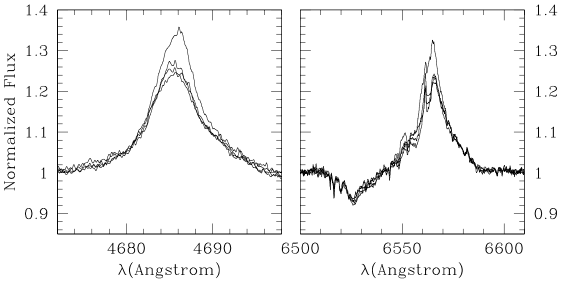

Figure 6: Line profiles of He II λ 4686 (*left*) and Hα (*right*) of HD 15570 observed during our four SPM observations. Their variability appears to be correlated.

more variable lines of the same data set. For September 2001, the results are less conclusive, probably because of the lower level of variability of the He II λ 4542 line.

The SPM data reveal a strong variability of the Hα line, possibly correlated with that of the He II λ 4686 line. Figure 6 presents the profiles displayed by these two lines for our four SPM observations. Hα appears in strong emission with a double-peaked shape. The variation in the intensity is correlated between the two lines. This apparently correlated behaviour suggests that both lines are at least partly produced in the same region.

5.2 HD 15629

HD 15629 displays a low level profile variability in the He II λ 4686 and Hβ lines. The variability of the profile of these lines in September 2002 is significant, but the putative variations in October 2003 and October 2004 are marginal, and below the 99 % confidence level for Hβ in 2003. Consequently, we will mainly discuss the line profile variability of this star on the basis of the September 2002 results, and of the complete data set resulting from the combination of the spectra from September 2002, October 2003 and October 2004.

The variability of the He II λ 4686 and Hβ lines is illustrated in Fig. 7. This figure shows clearly the lower level of the variability of the Hβ line as compared to He II λ 4686. The variability pattern seems however slightly similar for the two lines. The two-dimensional periodograms obtained for the September 2002 data set alone contains power at about the same frequencies, and over the same wavelength domain, as those presented in Fig. 7. This is not surprising as the overall variability is clearly dominated by that observed in September 2002. The main peaks appear at frequencies of about 0.29 and 0.60 d^{-1} (or their 1-ν aliases). The apparently stronger peaks at about 0.5 d^{-1} are aliases of the main frequencies mentioned hereabove, and they disappear from the residuals obtained after prewhitening with the main frequencies.

6 Archive *ROSAT* data

IC 1805 was observed with the PSPC instrument onboard the *ROSAT* satellite on 22-23 August 1992 (sequence number rp201263n00), with an exposure time of 8.8 ks. We retrieved the data from the HEASARC archive database and processed them using the XSELECT software. HD 15570 and HD 15629 are among the brightest X-ray sources in the PSPC image of IC 1805 (see Fig. 8). The two other bright sources are HD 15558 (SB1, O5III(f)) and GSC 04046-01182. A spectrum of this latter target was obtained at OHP in the blue domain during the October 2004 observing run. The spectrum presents a large number of lines, whilst its dominant feature is a broad and deep Hβ absorption line. A comparison with an atlas

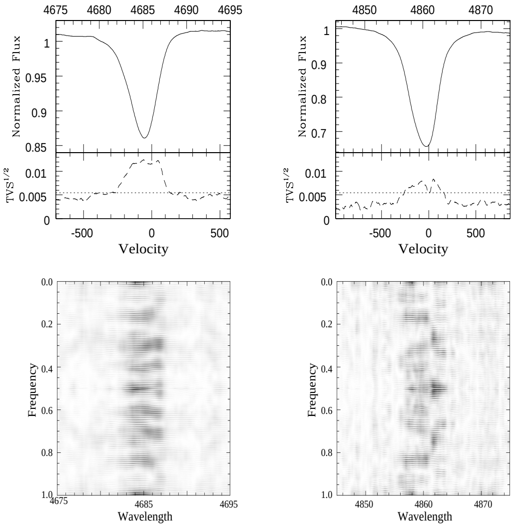

Figure 7: *Upper panels:* mean spectrum and square root of the time variance spectrum of the He II λ 4686 line (*on the left*) and for Hβ (*on the right*) of HD 15629 for the combined data set. The 99 % significance level of the TVS$^{1/2}$ is indicated by the horizontal dotted line. Velocities are expressed in km s^{-1}. *Lower panels:* the corresponding two-dimensional power spectra. The darkest regions stand for the highest peak intensities of the periodogram. Frequencies and wavelengths are respectively expressed in d^{-1} and in Å .

of stellar spectra (Montes & Martins 1998; Montes et al. 1999) reveals it could be a foreground late F or G star (main sequence or giant). These classifications are compatible with that obtained from the Two Micron All Sky Survey magnitudes and colours (2MASS, Skrutskie et al. 1997), which point towards G0III or G6V. From the typical V absolute magnitudes for these types and classes, and using $m_V = 10.4$, we derived distance moduli respectively of 9.4 and 5.3. These values lead to distances of 760 and 115 pc respectively. Using typical bolometric magnitudes (i.e. 2.8×10^{33} and 1.3×10^{35} erg s^{-1} respectively for the G6V and G0III cases), along with dereddened X-ray luminosities derived from *ROSAT*-PSPC data (i.e. 3.2×10^{29} and 1.4×10^{31} erg s^{-1} respectively for the G6V and G0III cases)[4], we obtain in both cases an L_X/L_{bol} of about 1×10^{-4}.

We extracted PSPC spectra of HD 15570 and HD 15629 over a 1 arcmin radius circle. The background was extracted in an annulus surrounding the source region covering an equal surface. We then rebinned the spectra to get at least 5 counts per bin, and we analysed the spectra with the XSPEC software. The background corrected count rates are $(1.23 \pm 0.17) \times 10^{-2}$ and $(4.2 \pm 1.4) \times 10^{-3}$ cts s^{-1} respectively for HD 15570 and HD 15629.

We fitted the X-ray spectrum of HD 15570 between 0.1 and 2.5 keV with a single temperature optically thin thermal plasma `mekal` model (Mewe et al. 1985; Kaastra 1992). We first tried to use two hydrogen columns to account for the interstellar medium (ISM) and circumstellar (wind) absorptions, but we obtained large error bars on parameters and sometimes non-physical results. The best results were obtained after freezing the local absorption column to zero. In order to evaluate the ISM column density, we first estimated the intrinsic color $(B-V)_\circ$ from the spectral type. We obtained the color excess using the observed $(B-V)$ given by Massey et al. (1995) and then we estimated the hydrogen column density from the relation given by Bohlin et al. (1978), yielding $N_{H,ISM} = 0.59 \times 10^{22}$ cm^{-2}.

---

[4] We derived these quantities following the same procedure as described hereafter in the cases of HD 15570 and HD 15629.

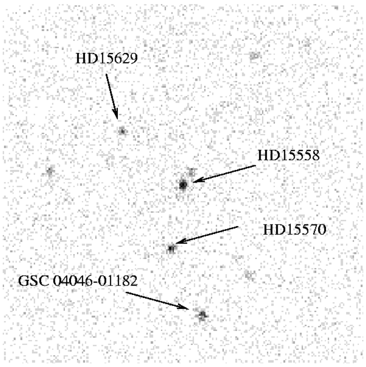

Figure 8: PSPC image of IC 1805 obtained in August 1992 with an 8.8 ks exposure time. The brightest X-ray sources are indicated. The North is up and the East is on the left.

We obtain a characteristic plasma temperature[5] (kT) of $1.25^{1.46}_{0.95}$ keV. The observed flux in the PSPC bandpass is about 1.3×10^{-13} erg cm^{-2} s^{-1}, which converts into a flux corrected for the ISM absorption of about 4.9×10^{-13} erg cm^{-2} s^{-1}. Adopting a distance of 2.34 kpc as determined by Massey et al. (1995), we obtain an X-ray luminosity corrected for ISM absorption of 3.2×10^{32} erg s^{-1}. Considering the bolometric luminosity derived by Herrero et al. (2000) from their 'spherical' model with mass loss, i.e. 5.38×10^{39} erg s^{-1}, the expected L_X should be of the order of 1.0×10^{33} erg s^{-1} (following the empirical relation of Berghöfer et al. (1997)). Consequently, HD 15570 appears to be a rather weak X-ray emitter as compared to other presumably single O-stars.

In the case of HD 15629, we followed the same procedure as described for HD 15570. We adopted an $N_{H,ISM}$ of 0.44×10^{22} cm^{-2} and we fitted the spectrum with a one-temperature `mekal` model with a kT of $0.19^{0.30}_{0.08}$ keV. We derive observed and ISM corrected fluxes of respectively 5.0×10^{-14} and 1.2×10^{-13} erg cm^{-2} s^{-1}. This latter value yields an X-ray luminosity of 7.89×10^{31} erg s^{-1}. Considering the bolometric luminosity determined by Herrero et al. (2000) (i.e. 2.52×10^{39} erg s^{-1}) we obtained an expected L_X of about 4.3×10^{32} erg s^{-1}. The actual X-ray luminosity of HD 15629 is very weak as compared to the expected X-ray emission from a single star.

In summary, the plasma temperature derived from the fit with thermal models for HD 15629 is rather low, lending further support to the single star scenario for that star. However, the plasma temperature for HD 15570 is rather high (~ 1.25 keV), higher than the typical temperatures expected for the shocked plasma of a single star wind (see e.g. Feldmeier et al. 1997). Additional X-ray observations with more sensitive instruments working up to 10.0 keV, like *XMM-Newton* or *Chandra*, are needed to clearly establish the X-ray properties of the massive stars in IC 1805.

7 Discussion

7.1 Possible interpretations

Our line profile variability analysis provided indications of a possible recurrence time of a few days in the spectrum of HD 15570. The reccurent time scale might be of about 6 days. This time scale is found

---

[5] The error bars on kT stand for the 1-σ confidence level.

consistently in the line profile modulations of He II λ 4686 and Hβ. We note that the same time scale emerges from our analysis of the EWs of the He II λ 4686 line, even if the latter variations are marginal. In HD 15629, the situation is less clear. Strong variability was only observed in our September 2002 data set which could indicate a transient perturbation of its stellar wind. Therefore, in the following, we focus on the more stable case of HD 15570.

In order to interpret the variability observed in the blue spectrum of HD 15570, we can envisage several scenarios likely to produce recurrent line profile variations. Let us consider these scenarios independently.

- *Rotational modulation.* If the winds of these stars deviate from spherical symmetry e.g. because of a putative tilted dipolar magnetic field likely to interact with the wind plasma, we can expect some variability on the time scale of the rotation period (see e.g. Stahl et al. 1996). In that case, using the relations provided for instance by De Becker & Rauw (2004), we can establish the possible interval for the rotational period, provided that some stellar parameters are known. In the case of HD 15570, from the quantities quoted in Table 4, we derived only lose constraints with minimum (P_{min}) and maximum (P_{max}) periods of 1.8 and 8.6 d respectively[6]. All the proposed time scales for this star, including the putative recurrence time scale af about 6 d, lie in the wide range of possible rotation periods and the rotational modulation can not be excluded, even if more data are needed to check the periodicity and to identify unambiguously the variability time scale(s).
- *Orbital motion in a binary system.* The apparent RV variations observed in the case of the He II λ 4686 and Hβ lines for HD 15570, along with the profile distortion, could be reminiscent of a binary motion. However, such an amplitude for the RV variations (i.e. $\sim 30\,\mathrm{km\,s^{-1}}$ for the semi-amplitude), should be observed for other lines like He II λ 4542 and N III $\lambda\lambda$ 4634-4641. The fact that the variations of HD 15570 are observed only for two lines in the blue spectrum is incompatible with a binary motion.
- *Wind-wind interaction in a binary system.* Although no RV modulation is found for the two stars studied in this paper, we can not exclude a priori a scenario where a binary system is seen under a very low inclination angle. A low amplitude radial velocity curve could also be produced by a very long period binary system, but the variability time scales would be much longer than observed in our data set. Consequently, the presence of a putative companion could possibly be unveiled by an interaction between the winds of the two components of the system. As mentioned in Sect. 5, the profiles of the He II λ 4686 line of HD 15570, and to some extent of Hβ, behave as if there were more than one component in the profile. The variation of the EW of the He II λ 4686 line is also compatible with this idea. The line profile variability observed for He II λ 4686 is somewhat reminiscent of the case of WR 20a (Rauw et al., 2005), except for the EW variations which were in that case attributed to a partial eclipse of the emitting regions. However, an eccentric orbit could be responsible for some variations like that of HD 15570 as described in Sect. 5. We also mention that the high plasma temperature derived from the fit of the *ROSAT*-PSPC spectrum might be associated with a plasma heated in the collision zone of the two winds although the X-ray luminosity is surprisingly low.

In summary, either a rotational modulation or a colliding wind system seen under a very low inclination could account for the 6 day recurrence time observed in HD 15570. Given the rather large $v \sin i$ of HD 15570, a low orbital inclination and therefore presumably also a low inclination of the rotational axis, seem less likely and we slightly favor the rotational modulation scenario. Of course, this interpretation as well as the stability of the recurrence time scale call for confirmation through future observations.

---

[6] For HD 15629, we note that P_{min} and P_{max} are respectively about 0.8 and 7.1 d.

Table 4: Stellar parameters of HD 15570 and HD 15629. All parameters are taken from Herrero et al. (2000), on the basis of their 'spherical' model with mass loss, except the projected rotational velocities which are taken from Conti & Ebbets (1977) and Penny (1996) respectively for HD 15570 and HD 15629.

	HD 15570	HD 15629
M_* ($M_\odot$)	79.6	61.4
R ($R_\odot$)	22.0	12.7
V_{rot} sini (km s^{-1})	130	90
L_{bol} ($L_\odot$)	1.38×10^6	6.46×10^5

Table 5: O-type star content of IC 1805. This first column gives the star number following Vasilevskis et al. (1965). For the multiplicity, 's' means that our investigations did not reveal any indication of binarity, '?' stands for a lack of spectroscopic monitoring, and 'IB?' stands for the fact that the star is possibly an interacting binary candidate. The references for the spectral types are the following: (1) Mermilliod (1989), (2) Rauw & De Becker (2004), (3) Garmany & Massey (1981), and (4) this study. (Notes: * the spectral type of the secondary should range between O8.5 and O9.5, ** Underhill (1967) reported on double lines for this star.)

#	ID	Sp. Type	Ref.	Status
21		O9.5V((f))	1	?
104	BD +60° 497	O6.5V((f)) + O9V((f))*	2	SB2
112	BD +60° 498	O9V	3	?**
113		O9.5V((f))	1	?
118	BD +60° 499	O9V	3	?
138	BD +60° 501	O7V((f))	2	s
148	HD 15558	O5III(f)	3	SB1
160	HD 15570	O4If$^+$	4	s,IB?
192	HD 15629	O5((f))	4	s
232	BD +60° 513	O7.5V((f))	2	s

7.2 Multiplicity in IC 1805

As mentioned in the introduction, the multiplicity of massive stars in young open clusters is a crucial question. The fact that García & Mermilliod (2001) proposed a binary frequency of 80 % for O-stars suggests that the star formation process that was at work in IC 1805 favored the formation of massive binary systems. However, in our spectroscopic study of three early-type stars of this cluster (Rauw & De Becker, 2004), we showed that only one system is a spectroscopic binary (BD +60° 497), whilst the other two are most probably single stars (BD +60° 501 and BD +60° 513), leading to the conclusion that the binary frequency claimed by García & Mermilliod (2001) might be overestimated.

In Table 5, we summarize our present knowledge of the multiplicity of the O-star members of IC 1805. At this stage, spectroscopic monitoring confirmed the binarity of only two members, i.e. HD 15558 (Garmany & Massey, 1981) and BD +60° 497 (Rauw & De Becker, 2004), and our investigations revealed no indication of binarity for three of them (BD +60° 501, BD +60° 513 and HD 15629). As shown in this study, the probability that HD 15570 being a interacting winds binary is very low. For the four remaining O-type members, the multiplicity remains an open question. Consequently, at this stage all we can say is that the O-star binary frequency in IC 1805 should be of at least 20 % but is most probably not exceeding 60 %.

8 Summary and conclusions

We analysed optical spectra to investigate the multiplicity and the line profile variability of two of the three most massive members of the young open cluster IC 1805, i.e. HD 15570 (O4If$^+$) and HD 15629 (O5V((f))). For both stars, the RVs do not present any significant trend attributable to a binary motion. For HD 15570, the RVs measured on He II λ 4686 and Hβ suggest a significant variability with a semi-amplitude of about 30 km s^{-1}. However, the lack of such a variability for other lines of the blue spectrum is incompatible with RV variations due to binarity. The variations of the EW of He II λ 4686, and the EW itself, are significantly lower than reported by Polcaro et al. (2003). We also detect a significant variability of the equivalent width of the Hα line but, once again, at a significantly lower level than reported by Polcaro et al. (2003). Consequently, we conclude that our data do not confirm the results of Polcaro et al. (2003).

The investigation of our time series led to the detection of a significant variability of He II λ 4686 and Hβ for both stars. For HD 15570, the strongest variability is observed in the case of the He II λ 4686 line, which is strongly correlated to that of Hβ, and also probably to that of Hα although more data are needed to confirm this. The line profiles of He II λ 4686 and Hβ present a significant variability on a time scale of a few days, possibly about 6 d. The same time scale emerges from our time analysis of the EWs of the He II λ 4686 line, but we note that the variations are marginal. This can be accounted for by either a rotational modulation or a colliding wind system seen under rather low inclination scenario. The high plasma temperature observed in X-rays lends some support to the colliding wind scenario, but a low inclination of both rotational and orbital axes, provided they are parallel, would therefore lead to an excessive rotational velocity. For this reason, the rotational modulation scenario is slightly favored. A better sampling of high quality optical data, along with new X-ray observations are needed to check these scenarios. As a rather evolved massive star, HD 15570 may possibly be close to evolutionary transition between Of and WR stars, and constitutes a key target to probe poorly explored aspects of the evolution of O-type stars. In the case of HD 15629, the variability is lower than for HD 15570 and occurs mainly during a single observing run. The possible time scales lie in the range of admissible rotation periods. However, we note that our time series does not allow a detailed investigation of the behaviour of the lines discussed in this study, and more data are needed.

From our new and previously published results, we briefly address the question of the multiplicity of the early-type stars in IC 1805. The binary frequency among O-stars should at least be of 20 %, since out of 10 O-stars only 2 are confirmed binaries. We conclude that the previously claimed binary frequency of 80 % was heavily overestimated, and that spectroscopic monitoring is strongly needed to address the issue of the multiplicity of massive stars in open clusters.

Acknowledgements

We are greatly indebted to the FNRS (Belgium) for multiple assistance including the financial support for the rent of the OHP telescope in 2000 and 2002 through contract 1.5.051.00 "Crédit aux chercheurs". The travels to OHP were supported by the Ministère de l'Enseignement Supérieur et de la Recherche de la Communauté Française. This research is also supported in part by contract PAI P5/36 (Belgian Federal Science Policy Office) and through the PRODEX XMM-OM Project. We would like to thank the staff of the Observatoire de Haute Provence (France) and of the San Pedro Martir Observatory (Mexico) for their technical support during the various observing runs. The SIMBAD database has been consulted for the bibliography.

References

Berghöfer T.W., Schmitt J.H.M.M., Danner R., Cassinelli J.P., 1997, A&A, 322, 167

Bieging J.H., Abbott D.C., Churchwell E., 1989, ApJ, 340, 518

Bohlin R.C., Savage B.D., Drake J.F., 1978, ApJ, 224, 132

Bonnell I.A., Bate M.R., 2002, MNRAS, 336, 659

Conti P.S., Ebbets D., 1977, ApJ, 213, 438

De Becker M., Rauw G., 2004, A&A, 427, 995

Feinstein A., Vázquez R.A., Benvenuto O.G., 1986, 159, 223

Feldmeier A., Puls J., Pauldrach A.W.A., 1997, A&A, 322, 878

Fullerton A.W., Gies D.R., Bolton C.T., 1996, ApJS, 103, 475

García B., Mermilliod J.-C., 2001, A&A, 368, 122

Garmany C.D., Massey P., 1981, PASP, 93, 500

Gillet D. et al., 1994, A&AS, 108, 181

Heck A., Manfroid J., Mersch G., 1985, A&AS, 59, 63

Herrero A., Puls J., Villamariz M.R., 2000, A&A, 354, 193

Howarth I.D., Prinja R.K., 1989, ApJS, 69, 527

Humphreys R.M., 1978, ApJ, 38, 309

Ishida K., 1970, PASJ, 22, 277

Kaastra J.S., 1992, *An X-ray spectral code for optically thin plasmas*, Internal SRON-Leiden Report

Massey P., Thompson A.B., 1991, AJ, 101, 1408

Massey P., Johnson K.E., De Gioia-Eastwood K., 1995, ApJ, 454, 151

Mathys G., 1988, A&AS, 76, 427

Mermilliod J.-C., 1989, unpublished data, available at the WEBDA data base

Mewe R., Gronenschild E.H.B.M., van den Oord G.H.J., 1985, A&AS, 62, 197

Montes D., Martin E.L., 1998, A&AS, 128, 485

Montes D., Ramsey L.W., Welty A.D., 1999, ApJS, 123, 283

Penny L.R., 1996, ApJ, 463, 737

Polcaro V.F., Viotti R., Norci L., Eenens P., Corral L., Rossi C., 2003, in *Magnetic Fields in O, B, and A stars*, ASP Conferences Series, 305, eds L.A. Balona, H.F. Henrichs, & T. Medupe, 377

Raboud D., Mermilliod J.-C., 1998, A&A, 333, 897

Rauw G., De Becker M., 2004, A&A, 421, 693

Rauw G., Morrison N.D., Vreux J.-M., Gosset E., Mulliss C.L., 2001, A&A, 366, 585

Rauw G. et al., 2005, A&A, 432, 985

Sagar R., Myakutin V.I., Piskunov A.E., Dluzhnevskaya O.B., 1988, MNRAS, 234, 831

Shi H.M., Hu J.Y., 1999, A&AS, 136, 313

Skrutskie M.F. et al., 1997, in *The Impact of Large Scale Near-IR Sky Surveys*, ed. F. Gazon et al. (Dordrecht: Kluwer Acad. Pub.), 25

Stahl O. et al.,1996, A&A, 312, 539

Stevens I.R., Blondin J.M., Pollock A.M.T., 1992, ApJ, 386, 265

Underhill A.B., 1967, in *Determination of Radial Velocities and their Applications*, eds A.H. Batten & J.F. Heard, IAU Symp. 30, 167

Vasilevskis S., Sanders W.L., Van Altena W.F., 1965, AJ, 70, 806

Walborn N.R., 1972, AJ, 77, 312

Walborn N.R., 2001, in *Eta Carinae and Other Mysterious Stars*, ASP Conference Series, 242, eds. T. Gull, S. Johansson, K. Davidson, 217

Walborn N.R., Fitzpatrick E.L., 1990, PASP, 102, 379

Walborn N.R., Howarth I.D., 2000, PASP, 112, 1446

Werner K., Rauch T., 2001, in *Eta Carinae and Other Mysterious Stars*, ASP Conference Series, 242, eds. T. Gull, S. Johansson, K. Davidson, 229

2.3 The very massive binary HD 15558

HD 15558 (m_V = 8.0) was reported to be a spectroscopic binary a few decades ago, and the first SB1 orbtital solution was proposed by Garmany & Massey (1981), revealing a highly eccentric system (e = 0.54) with a period of about 440 days, i.e. the longest of any O-type spectroscopic binary known so far. However, it appeared that this orbital solution relied on time series including a somewhat heterogeneous set of radial velocities. Garmany & Massey (1981) indeed used mean radial velocities calculated on the basis of 4 to 12 different lines. Among these lines, many are expected to be at least partly produced in their stellar wind, and might therefore not reflect the radial velocity of the star itself. The heterogeneity of the radial velocity series could have a significant impact on the orbital parameters.

We have carried out a spectroscopic campaign at the Observatoire de Haute-Provence aiming mainly at the calculation of a refined orbital solution and to the detection of the spectral signature of the companion. A total of 17 échelle spectral were obtained with the Elodie spectrograph mounted on the 1.93 m telescope (se Appendix A). The spectral series was completed by observations obtained with the Aurélie spectrograph fed by the 1.52 m telescope. Most of the Aurélie spectra were obtained during observing runs in September 2000, September 2001, September 2002, October 2003 and October 2004 (for details, see the detailed report inserted below).

On the basis of 70 radial velocity measurements, we derived a period of about 442 d and we calculated a refined SB1 orbital solution. A careful inspection of the spectra obtained close to the extrema of the radial velicity curve of the primary revealed asymmetries likely attributable to the companion. The spectral signature of the secondary was indeed clearly revealed in a few lines: He I λ 4471, He II λ 4542, C IV λ 5812 and He I λ 5876. A simultaneous fit of Gaussians to the profiles of the He I λ 4471 and He II λ 4542 lines allowed us to estimate their equivalent width, and therefore to derive the spectral types of the two stars: O5.5 and O7. Considering in addition that the He II λ 4686 line of the primary has a P-Cygni profile whilst the same line is in absorption in the case of the secondary, along with the fact that we do not observe clearly the N III λλ 4634-4641 lines in emission for the secondary, we propose that HD 15558 is an 05.5III(f) + O7V binary.

We also used these Gaussian fits to measure the radial velocity of the secondary close to the extrema of the radial velocity curve (12 Aurélie spectra were fortunately obtained very close to each extrema of the radial velocity curve). Using an estimate of the amplitude of the secondary radial velocity curve along with some parameters derived in our SB1 orbital solution, we estimated the minimum masses of the two stars to be respectively 152 ± 51 and $46 \pm 11\,M_\odot$. In order to try to determine the minimum masses following a alternative approach, we used the disentangling method proposed by González & Levato (2005) to separate the primary and secondary spectra of HD 15558 and derive the radial velocity of both stars for our complete spectral series. We then computed the first SB2 orbital solution of HD 15558. The main result is the obtaining of very high minimum masses, confirming the result already obtain from the simple fitting approach described above. We insist on the fact that the quality of the radial velocities derived for the secondary is rather poor, and the error on the minimum masses is large. However, even though the SB2 solution does not appear to be satisfactory, our data point clearly to a high mass ratio (about 3), and to a very extreme minimum mass for the primary. Our results deserve independent validation using an improved spectral disentangling technique.

The main problem considering our results is to reconcile the very extreme mass of the primary with its spectral type. It seems indeed unlikely that a very massive main-sequence (O2 or O3) star could cool down enough during its evolution to become an O5.5 giant. A alternative scenario can however be considered, where HD 15558 is not a binary but a triple system. The primary may indeed be constituted of a yet unrevealed close binary system. In this scenario, as the mass of the primary is estimated on the basis of the motion of the secondary, the primary object – i.e. the hypothetical close binary – would appear to be a massive object whose mass is the sum of the masses of two stars. Even though our data donot provide any evidence for this scenario, we estimate that at this stage it should not be rejected, and that it could constitute a valuable working hypothesis for future investigations concerning HD 15558.

Early-type stars in the young open cluster IC 1805: III. The massive binary HD 15558

M. De Becker,[1] and G. Rauw[1]

[1]Institut d'Astrophysique et de Géophysique, Université de Liège, 17, Allée du
6 Août, B5c, B-4000 Sart Tilman, Belgium

Abstract: We report on the results of an intensive spectroscopic campaign devoted to HD 15558. This massive binary has the particularity to be a non-thermal radio emitter along with the longest period O-type binary known so far. On the basis of 70 homogeneous radial velocity measurements, we derive a new SB1 orbital solution. We report also for the first time on the detection of the spectral signature of the secondary star. Following two different approaches, i.e. (i) a simultaneous fit of Gaussians to some line profiles and (ii) a spectral disentangling procedure, we derive spectral type O5.5III(f) and O7V respectively for the primary and the secondary. On the basis of the radial velocities obtained from the disentangling method, we tentatively compute a first SB2 orbital solution although the radial velocities from the secondary star should be considered with caution. The mass ratio is rather high, i.e. about 3, and it leads to very extreme minimum masses, in particular for the primary. Minimum masses of the order of 150 ± 50 and $50 \pm 15\,\mathrm{M}_\odot$ are found respectively for the primary and the secondary. We also investigate the line profile variability of HD 15558 and we find that the He II λ 4686 and Hβ undergo a significant variability on an ill-defined recurrence time-scale of the order of a few days that is mainly associated with the primary.

1 Introduction

The multiplicity of massive stars is a key point known to have a strong impact on their behaviour and evolution. For this reason, the intensive study of massive binaries is one of the most crucial aspects of the research on massive stars. Moreover, the presence of a substantial fraction of OB stars in open clusters is worth considering in the framework of recent models on the formation of massive stars (see e.g. Bonnell & Bate 2002). According to these numerical simulations, the most massive stars are formed through simultaneous accretion and stellar collisions, resulting in their presence mostly in binary systems. Besides, the observation of several open clusters suggested some of them may reach high binary frequency among their massive members (García & Mermilliod, 2001). Among these open clusters, IC 1805 was proposed to have an O-type binary fraction of about 80 % (García & Mermilliod, 2001). We initiated a spectroscopic campaign aiming at the intensive study of the early-type stellar content of IC 1805, with emphasis on the investigation of their multiplicity. In this campaign, we showed that the previously published value of 8 binaries out of 10 early-type stars might be overestimated (see Rauw & De Becker 2004 and the previous section of this chapter of the thesis). These papers revealed indeed the binary nature of BD +60° 497 (Rauw & De Becker, 2004), but showed that four other members are probably single (i.e. BD +60° 501, BD +60° 513, HD 15570 and HD 15629, see Rauw & De Becker 2004 and the previous section of this chapter of the thesis). In the present paper, we will concentrate on the most luminous member of IC 1805: HD 15558.

HD 15558 ($\mathrm{m}_V = 8.0$) was classified as an O5III(f) star by Mathys (1989). It was reported to be a spectroscopic binary with a period of about 420 d for the first time by Trumpler (according to Underhill 1967). Up to now, the only orbital solution proposed for this system is that of Garmany & Massey (1981), revealing a highly eccentric binary (e = 0.54) with a period of about 440 d, i.e. the longest of any O-type spectroscopic binary known so far. This star is also believed to be very massive. On the basis of a model taking into account mass-loss and sphericity (Santaloya-Rey et al., 1997), Herrero et al. (2000) derived spectroscopic and evolutionary masses of about 90 $M_\odot$ for HD 15558.

This star offers also the particularity to belong to the category of the non-thermal radio emitters (see (Rauw, 2004) for a review). Such emission processes require the presence of (i) a magnetic field and (ii) a population of relativistic electrons, believed to be accelerated through the first order Fermi mechanism in hydrodynamic shocks (for a discussion of the involved physical processes, see De Becker et al. 2005 and references therein). In the case of a binary system like HD 15558, the hydrodynamic shocks responsible for this acceleration come likely from the wind-wind collision occuring somewhere between the two stars (Eichler & Usov 1993; Dougherty et al. 2003). In the context of this scenario, the accurate knowledge of the orbital parameters is mandatory if one wants to investigate the non-thermal emission processes at work in the case of HD 15558. Moreover, the identification of the previously undetected companion is also very important, as the wind properties of both stars are crucial parameters in these processes. For this reason, we initiated a long-term optical campaign devoted to the spectroscopic monitoring of HD 15558.

This paper is organized as follows. In Sect. 2 we describe the observations and the data reduction procedure. Section 3 presents the spectrum of HD 15558. The orbital solution and a discussion are given in Sect. 4. The analysis of the line profile variability of the primary is provided in Sect. 5, whilst the results of the analysis of archive X-ray observation are given in Sect. 6. Section 7 consists of a discussion of our results. Finally, a summary of the main results and the conclusions are provided in Sect. 8.

2 Observations and data reduction

We observed HD 15558 at the Observatoire de Haute-Provence (OHP, France) with the 1.52 m telescope equipped with the Aurélie spectrograph (Gillet et al., 1994) during five observing runs, respectively in September 2000, September 2001, October 2002, October 2003 and October 2004. The exposure time was set between 30 and 60 minutes depending on sky and weather conditions. Aurélie was equipped with a 2048×1024 CCD EEV 42-20#3, with a pixel size of 13.5 μm squared. All spectra were taken with a 600 l/mm grating allowing us to achieve a resolving power of about 8000 in the blue range, with a reciproqual dispersion of 16 Å mm^{-1}. These data cover the spectral domain between 4455 and 4890 Å . The details concerning these observations are provided in Table 1.

We obtained also 17 spectra with the Elodie echelle spectrograph (Baranne et al., 1996) fed by the 1.93 m telescope at the Observatoire de Haute Provence, between March 2003 and February 2005 to monitor a complete orbital period. The exposure time of each of these spectra was 90 minutes. This spectrograph uses a combination of a prism and of a grism as a cross-disperser, with a blaze angle of 76°. The resolving power achieved is about 42000 between 3906 and 6811 Å in a single exposure, and the detector is a Tk1024 CCD with $24\,\mu\mathrm{m} \times 24\,\mu\mathrm{m}$ pixels. Due to some pointing constraints specific to the 1.93 m telescope, no echelle spectra were obtained between April 2004 and July 2004. We filled that gap with 6 observations with the Aurélie spectrograph mounted on the 1.52 m telescope. Two spectra out of the 6 were obtained using the same grating as described in the previous paragraph (between 4455 and 4890 Å). The four remaining spectra were obtained using a 1200 l/mm grating providing a resolving power of about 16000 in the blue range, with a reciproqual dispersion of 8 Å mm^{-1} (between 4455 and 4680 Å). The exposure time of these 6 Aurélie spectra was 60 minutes.

The Aurélie spectra consist of five images of the spectrum obtained with an image slicer, which were combined after individual treatment and cosmic removal. We used Th-Ar comparison spectra obtained shortly before or after the observation of the star to perform the wavelength calibration. The Elodie data consist in single spectra distributed over 67 orders. The data were reduced using the standard on-line automatic treatment implemented at the OHP. All spectra were noramilized using splines calculated on the basis of properly chosen continuum windows.

Table 1: Description of the data of HD 15558 obtained during the five observing runs with the 1.52 m telescope at OHP. The first and second columns give the name of the campaign as used in the text as well as the instrumentation used. The next columns yield the number of spectra obtained, the time elapsed between the first and the last spectrum of the run, the natural width of a peak of the power spectrum taken as 1/ΔT, and finally the mean signal-to-noise ratio of each data set.

Obs. run	Tel./Instr.	Number of spectra	ΔT (d)	$\Delta\nu_{\rm nat}$ (d^{-1})	S/N
Sept. 2000	1.52/Aurélie	12	10.97	0.09	530
Sept. 2001	1.52/Aurélie	12	7.02	0.14	440
Sept. 2002	1.52/Aurélie	11	14.92	0.07	430
Oct. 2003	1.52/Aurélie	7	17.95	0.06	360
Oct. 2004	1.52/Aurélie	5	7.00	0.14	450

3 The spectrum of HD 15558

In Fig. 1, we present the spectrum of HD 15558 between 3910 and 6750 Å obtained with the Elodie spectrograph on 7 January 2004, i.e. close to the maximum of the radial velocity curve presented in Fig. 2. However, we note that the orders of the echelle spectra obtained with Elodie are rather narrow, causing the rectification procedure to be somewhat difficult where the wings of several lines merge together over several tens of Å . So, for the purpose of the presentation of the optical spectrum of HD 15558, the spectral domain between 4580 and 4710 Å in Fig. 1 comes from one of the Aurélie spectra obtained during the September 2001 observing run, i.e. very close to the orbital phase of the selected Elodie spectrum.

The strongest absorption features are the hydrogen Balmer lines. The He II lines appear also in absorption, except for He II λ 4686 which displays a P-Cygni profile. The He I absorption lines at 4471 and 5875 Å are also present, along with He I λ 4713 which is very weak. The other absorption features observed in the spectrum are Mg II λ 4481, N V $\lambda\lambda$ 4604,4620, Si III λ 4627, O III λ 5592 and C IV $\lambda\lambda$ 5801,5812. The strongest emission lines are the N III $\lambda\lambda$ 4634,4641 lines. We report also on noticeable C III lines at 4650, 4652, 5696, 6721,6728 and 6731 Å . The three latter lines were qualified as selective emission lines by Walborn (2001). The rather weak N V $\lambda\lambda$ 6716,6718 emission features are other selective emission lines (Walborn & Howarth 2000; Walborn 2001). We report also on the presence of the Si IV λ 4116 emission line, along with that of the much weaker Si IV λ 4088 also in emission. The C IV λ 4662 emission line is cleary present.

4 HD 15558 as a binary system

4.1 Radial velocity time series

As mentioned in Sect. 1, the only orbital solution available for HD 15558 was proposed by Garmany & Massey (1981). These authors reported on a period of 439.3 ± 1.0 d, with an eccentricity of 0.54 ± 0.05. However, their orbital solution was based on time series including a somewhat heterogeneous set of radial velocities (RVs). They indeed used mean RVs calculated on the basis of 4 to 12 different lines. Among these lines, many are expected to be at least partly produced in the stellar wind, and might therefore not reflect the RV of the star itself. The heterogeneity of their RV time series could have a significant

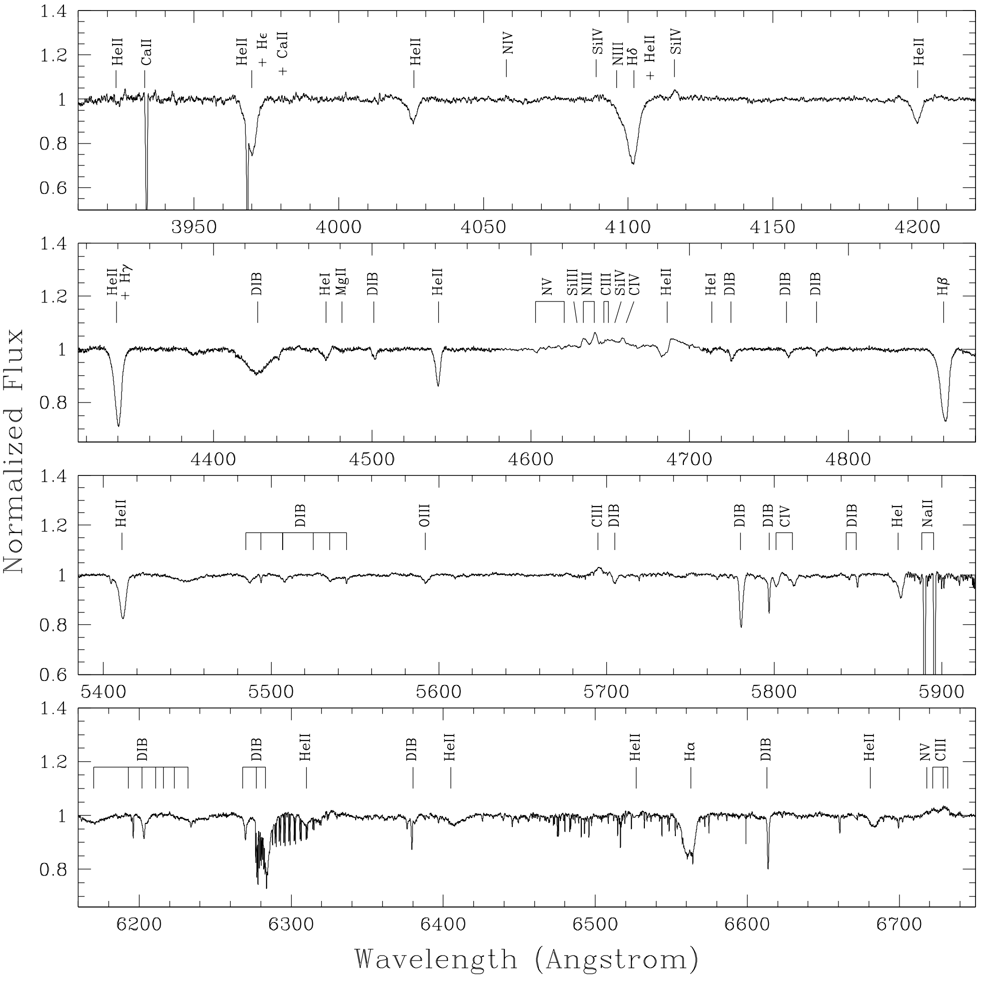

Figure 1: Spectrum of HD 15558 obtained about at phase 0.8, i.e. at the maximum of the radial velocity curve presented in Fig. 2. This spectrum was obtained with the Elodie echelle spectrograph on 7 January 2004, except for the spectral domain between 4580 and 4710 Å which is taken from one of the spectra obtained in September 2001 with the Aurélie spectrograph.

Table 2: Description of the data of HD 15558 obtained during the long-term monitoring using the 1.93 and the 1.52 m telescopes. The first column gives the date of the observation. The instrumentation used to obtain the spectrum is provided in the second column. The next column yields the resolving power of the instrumentation used, and the signal-to-noise ratio is given in the last one.

Date	Telescope/Instr.	$\lambda/\Delta\lambda$	S/N
2003/09/04	1.93 m/Elodie	42000	170
2003/10/04	1.93 m/Elodie	42000	160
2003/10/21	1.93 m/Elodie	42000	100
2004/01/07	1.93 m/Elodie	42000	180
2004/01/15	1.93 m/Elodie	42000	100
2004/02/14	1.93 m/Elodie	42000	130
2004/03/11	1.93 m/Elodie	42000	110
2004/04/04	1.93 m/Elodie	42000	110
2004/04/10	1.52 m/Aurélie	8000	330
2004/05/06	1.52 m/Aurélie	16000	160
2004/06/09	1.52 m/Aurélie	16000	290
2004/06/28	1.52 m/Aurélie	16000	360
2004/07/15	1.52 m/Aurélie	8000	550
2004/07/26	1.52 m/Aurélie	16000	360
2004/08/15	1.93 m/Elodie	42000	100
2004/08/26	1.93 m/Elodie	42000	120
2004/09/06	1.93 m/Elodie	42000	140
2004/10/07	1.93 m/Elodie	42000	130
2004/11/09	1.93 m/Elodie	42000	60
2004/11/17	1.93 m/Elodie	42000	140
2004/12/03	1.93 m/Elodie	42000	140
2005/01/27	1.93 m/Elodie	42000	100
2005/02/16	1.93 m/Elodie	42000	70

impact on the orbital parameters. In this section, we describe the procedure we adopted to establish our RV time series, and how we use it to determine the SB1 orbital parameters of the system.

First of all, we focused on the wavelength range covered by all our spectra, whatever the instrumentation used, i.e. the spectral domain between 4455 and 4680 Å . We then selected the lines whose profile did not deviate too strongly from a typical gaussian shape. Only the He II λ 4542 and the N III $\lambda\lambda$ 4634,4641 lines meet our criteria. We then determined the RVs by fitting Gaussians to the profiles. In the case of Elodie data, the He II line is simultaneously observed in two adjacent orders. We therefore measured the RV on each order and we used the mean of the two values in our time series. The RVs obtained from these three lines, along with those obtained from other lines observed only in our echelle spectra, are compiled in Table 3. In this Table, the column labeled 'Mean' contains the mean RVs obtained from the three lines discussed above. We estimate that the uncertainty on the RVs are respectively of the order of 15-20, 10-15, and 5-8 km s^{-1} respectively for low resolution Aurélie, medium resolution Aurélie, and high resolution Elodie data. These uncertainties were estimated on the basis of radial velocity measurements performed on Diffuse Interstellar Bands (DIBs).

Table 3: Radial velocities obtained from our times series of HD 15558. The second and third columns give respectively the heliocentric Julian day (–2 450 000) and the orbital phase following the parameters provided in Table 4 (left part). The next columns provide the radial velocities obtained for lines that were selected for the determination of the orbital solution. The column labelled 'Mean' contains the mean of the radial velocities obtained for the He II and the N III lines quoted respectively in the fourth and in the fifth columns. All RVs are expressed in km s^{-1}. Finally, the last column yields the weight attributed to our measurements to calculate the orbital parameters, depending on the spectral resolution of the instrument and the signal-to-noise ratio of the spectra.

#	HJD	ϕ	He II λ 4542	N III $\lambda\lambda$ 4634, 4641	Mean	Weight
1	1810.640	0.034	–85.9	–96.1	–91.0	0.25
2	1810.658	0.034	–88.0	–117.0	–102.5	0.25
3	1811.619	0.037	–86.7	–109.0	–97.9	0.25
4	1811.665	0.038	–88.8	–101.5	–95.1	0.25
5	1812.660	0.039	–87.5	–112.6	–100.0	0.25
6	1813.651	0.041	–87.8	–118.8	–103.3	0.25
7	1814.643	0.043	–91.6	–118.9	–105.2	0.25
8	1815.645	0.046	–88.9	–110.2	–99.6	0.25
9	1818.641	0.053	–86.4	–110.6	–98.5	0.25
10	1819.593	0.055	–86.8	–109.9	–98.3	0.25
11	1820.648	0.057	–83.0	–118.1	–100.6	0.25
12	1821.609	0.059	–91.2	–111.2	–101.2	0.25
13	2163.580	0.832	–1.2	–12.1	–6.7	0.25
14	2164.597	0.834	–4.3	–10.4	–7.3	0.25
15	2164.660	0.835	–0.9	–18.8	–9.9	0.25
16	2165.577	0.837	–3.5	–23.7	–13.6	0.25
17	2165.590	0.837	–0.1	–12.9	–6.5	0.25
18	2167.550	0.841	–1.9	–7.4	–4.6	0.25
19	2167.564	0.841	–6.7	–14.8	–10.7	0.25
20	2168.601	0.843	–1.8	–17.3	–9.5	0.25
21	2168.642	0.844	–6.0	–18.9	–12.4	0.25
22	2169.581	0.846	–4.2	–16.8	–10.5	0.25
23	2170.580	0.848	–7.2	–22.1	–14.6	0.25
24	2170.603	0.848	–8.1	–23.9	–16.0	0.25
25	2518.617	0.634	–27.5	–28.5	–28.0	0.25
26	2520.593	0.639	–14.8	–20.2	–17.5	0.25
27	2523.580	0.646	–11.5	–32.8	–22.2	0.25
28	2524.510	0.648	–13.8	–28.0	–20.9	0.25
29	2527.531	0.655	–12.4	–21.6	–17.0	0.25
30	2528.499	0.657	–14.5	–26.7	–20.6	0.25
31	2529.529	0.659	–10.5	–21.6	–16.1	0.25
32	2531.503	0.664	–4.9	–21.8	–13.4	0.25
33	2532.516	0.666	–8.3	–20.6	–14.5	0.25
34	2532.644	0.666	–7.9	–27.2	–17.5	0.25
35	2533.532	0.668	–12.6	–24.2	–18.4	0.25
36	2886.627	0.466	–37.0	–51.5	–44.2	1.00
37	2916.592	0.534	–29.4	–62.0	–45.7	1.00
38	2916.558	0.534	–24.7	–39.1	–31.9	0.25
39	2918.570	0.538	–25.7	–52.6	–39.2	0.25
40	2919.561	0.541	–26.6	–47.8	–37.2	0.25

Table 3: (continued)

#	HJD	ϕ	He II $\lambda\,4542$	N III $\lambda\lambda\,4634$, 4641	Mean	Weight
41	2922.566	0.547	–24.4	–34.4	–29.4	0.25
42	2926.573	0.556	–19.6	–34.8	–27.2	0.25
43	2928.593	0.561	–24.7	–39.4	–32.0	0.25
44	2934.511	0.574	–20.0	–33.2	–26.6	0.25
45	2934.481	0.574	–13.7	–47.1	–30.4	1.00
46	3012.476	0.751	–14.0	–31.5	–22.7	1.00
47	3020.329	0.768	–19.2	–20.7	–20.0	1.00
48	3050.375	0.836	–11.2	–24.6	–17.9	1.00
49	3076.317	0.895	–16.7	–34.3	–25.5	1.00
50	3100.318	0.949	–43.1	–62.1	–52.6	1.00
51	3106.340	0.963	–28.8	–47.1	–38.0	0.25
52	3132.374	0.022	–63.5	–85.2	–74.3	0.50
53	3165.550	0.097	–88.2	–114.4	–101.3	0.50
54	3184.590	0.140	–82.7	–104.4	–93.6	0.50
55	3201.593	0.178	–72.1	–98.7	–85.4	0.25
56	3212.544	0.203	–65.3	–94.9	–80.1	0.50
57	3232.579	0.248	–67.1	–87.5	–77.3	1.00
58	3244.384	0.275	–63.0	–93.0	–78.0	1.00
59	3254.630	0.298	–46.3	–78.0	–62.2	1.00
60	3286.477	0.370	–43.8	–60.1	–52.0	1.00
61	3289.570	0.377	–46.3	–62.9	–54.6	0.25
62	3290.553	0.379	–35.6	–53.3	–44.4	0.25
63	3294.603	0.388	–32.3	–46.6	–39.4	0.25
64	3295.584	0.390	–37.6	–44.2	–40.9	0.25
65	3296.569	0.393	–44.0	–56.0	–50.0	0.25
66	3318.587	0.442	–28.5	–41.8	–35.1	0.10
67	3326.508	0.460	–33.4	–56.5	–45.0	1.00
68	3343.487	0.499	–27.9	–54.4	–41.2	1.00
69	3398.308	0.623	–9.4	–33.8	–21.6	1.00
70	3418.295	0.668	–3.6	–24.5	–14.0	0.10

4.2 Period determination

We performed a Fourier analysis on our RV time series following the technique described by Heck et al. (1985), as used for instance by Rauw & De Becker (2004) and De Becker et al. (2004). We independently applied the same technique to three RV time series obtained respectively from He II λ 4542, a mean of the RVs from the two N III $\lambda\lambda$ 4634,4641 lines, and a mean of the He II and N III lines. In the three cases, the periodogram is dominated by a strong peak at a frequency of $0.00226\,\mathrm{d}^{-1}$, corresponding to a period of 442.478 d. As the time base covered by our data is about 1608 d, the typical width of the peaks of the periodograms is about $6.22 \times 10^{-4}\,\mathrm{d}^{-1}$. Considering that the uncertainty on the frequency is about 10 % of the width of the peak, we obtain an uncertainty on the period of 12.178 d. The fact that the three RV time series lead exactly to the same period is a strong argument for this value being the true period of the system.

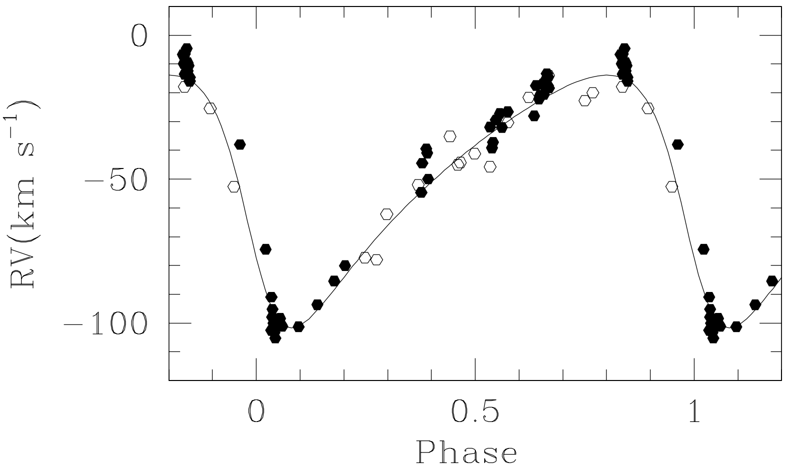

Figure 2: Radial velocity curve of HD 15558 for an orbital period of 442.478 d. The open and filled hexagons stand respectively for the primary RVs obtained with Elodie and Aurélie spectra. The solid line yields our best fit orbital solution respectively corresponding to the parameters provided by Table 4. The mean of the RVs of the He II λ 4542 and of the N III $\lambda\lambda$ 4634,4641 lines was used to computed this orbital solution.

4.3 Orbital solution

We obtained the SB1 orbital solution of HD 15558 using the method of Wolfe et al. (1967) for SB1 systems. We assigned different weights to take into account the expected uncertainties affecting our RV measurements, depending on the spectral resolution of the instrumentation used and on the signal-to-noise ratio of the spectra. These weights vary between 0.1 and 1.0 respectively for very poor quality and good quality Elodie data. Aurélie RVs get intermediate weights to take into account the fact that though the resolution of the spectrograph is rather low, the quality of the data in much better than for Elodie spectra.

We first fixed the period to the value determined from the Fourier analysis of our RV time series, i.e. 442.278 d. We obtained similar results for the orbital parameters, i.e. for most of them within the error bars, whatever the RV time series used. We also calculated the orbital solution through an iterative process allowing the period to vary, but it did not improve significantly the results. We indeed obtained a period of about 445 d, which can not be distinguished from the 442.478 d period obtained in Sect 4.2 provided the uncertainty on the period is about 12 d. Therefore, we adopted the results obtained with a period fixed to 442.478 d. The corresponding orbital parameters are summarized in Table 4 for the two series of RVs.

4.4 Searching for the companion

We inspected more carefully spectra obtained at phases close to the extrema of the radial velocity curve presented in Fig. 2. Though we did not obtain any echelle spectra close to the minimum of the primary radial velocity curve, the September 2000 and September 2001 Aurélie observing runs fall respectively very close to the minimum and maximum of the radial velocity curve. We were therefore able to perform a more careful inspection of the line profiles on the basis of our Aurélie spectra. We added together the 12 spectra obtained during each observing runs to obtain two high signal-to-noise ratio spectra, respectively of about 1000 at the minimum and 900 at the maximum. We detected opposite asymmetries at both

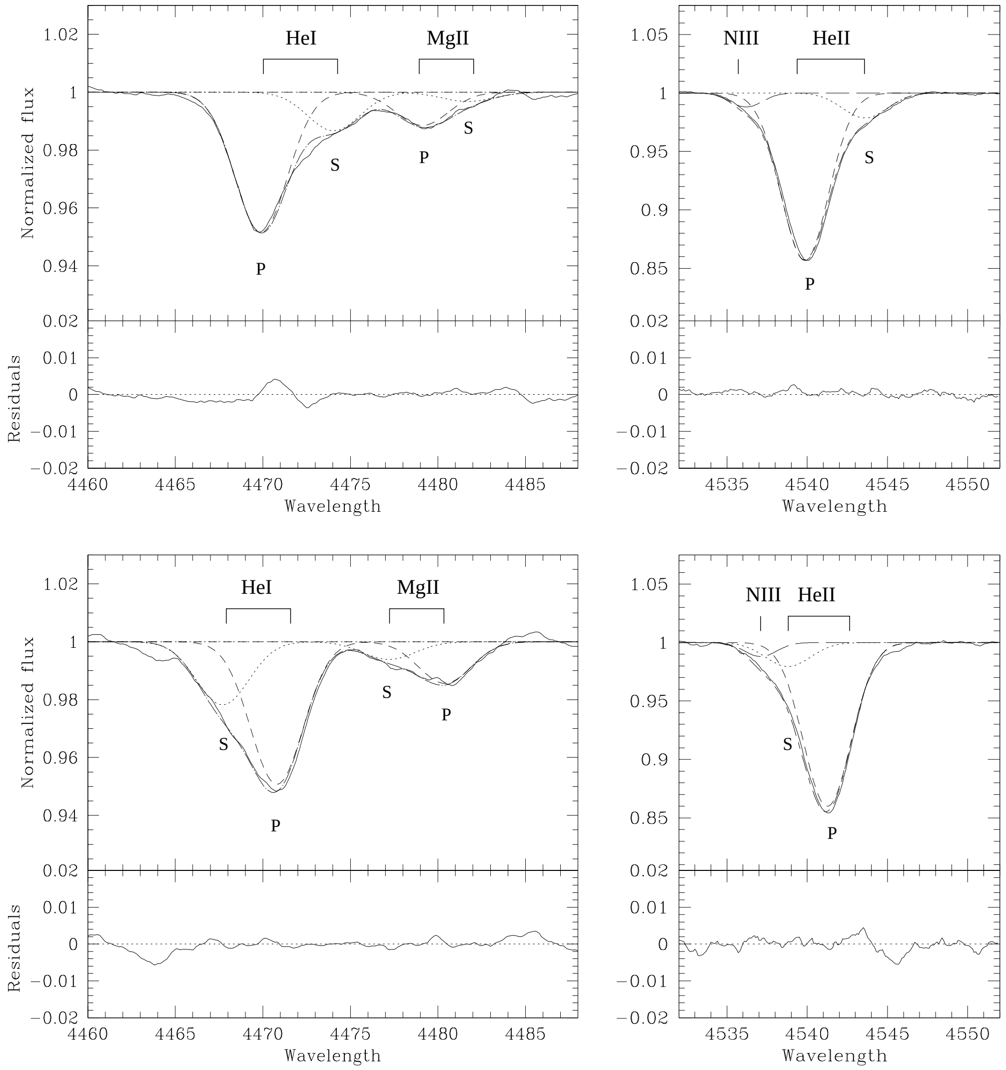

Figure 3: Distentangling of the line profiles from the two components of HD 15558 respectively at the minimum of the radial velocity curve (*upper part of the figure*), and at the maximum of the radial velocity curve (*lower part of the figure*). The two data sets correspond to the mean spectra obtained respectively during the September 2000 and September 2001 observing runs with the 1.52 m OHP telescope. The profiles of the He I λ 4471, the Mg II λ 4481, and the He II λ 4542 lines are displayed, along with the best-fit functions (dotted-dashed lines). The individual Gaussians are also displayed, with the dashed and dotted lines standing respectively for the primary (P) and the secondary (S). The bottom part of each panel represents the residuals.

Table 4: Orbital parameters of the SB1 solution of HD 15558. $T_\circ$ refers to the time of periastron passage. γ, K, and $a \sin i$ denote respectively the systemic velocity, the amplitude of the radial velocity curve, and the projected separation between the centre of the star and the centre of mass of the binary system. The last row provides the mass function. The orbital elements are given for the solutions obtained respectively from the mean of the RVs of the He II λ 4542 and N III $\lambda\lambda$ 4634,4641 lines, and from the RVs of He II λ 4542 only.

	He II λ 4542 N III $\lambda\lambda$ 4634,4641	He II λ 4542
P (days)	442.478 (fixed)	
e	0.39 ± 0.03	0.40 ± 0.03
$T_\circ$ (HJD–2 450 000)	1795.400 ± 6.556	1798.385 ± 7.207
γ (km s^{-1})	–50.2 ± 1.1	–40.1 ± 1.1
K (km s^{-1})	43.9 ± 1.8	41.3 ± 1.8
ω	116° ± 6°	121° ± 7°
$a \sin i$ ($R_\odot$)	350.0 ± 15.2	331.2 ± 15.2
$f(m)$ ($M_\odot$)	3.0 ± 0.4	2.5 ± 0.3

extrema for the profiles of the He I λ 4471, Mg II λ 4481 and He II λ 4542 lines, suggesting clearly the presence of the secondary. The inspection of the Elodie spectrum closest to the maximum of the primary RV curve reveals also the signature of the secondary in the profile of the C IV λ 5812 and He I λ 5876 lines.

The upper and lower panels of Fig. 3 show the profile of the He I λ 4471, Mg II λ 4481 and He II λ 4542 lines respectively at the minimum and at the maximum of the primary radial velocity curve. We disentangled the profiles from the primary and the secondary by fitting Gaussians following an iterative process. We constructed fitting functions of the form given by Eq. 1:

$$P(\lambda) = \sum_{j}^{\mathrm{N}} \frac{N_j}{\sigma_j\sqrt{2\pi}} \exp\Big[-\frac{(\lambda-\lambda_{c,j})^2}{2\sigma_j^2})\Big] \quad (1)$$

with N = 2,3,4 following the complexity of the blended profile. The three parameters to be determined for each Gaussian are respectively the normalization factor (N_j), the standard deviation of the Gaussian (σ_j), and the central position ($\lambda_{c,j}$). We iteratively changed the values for the three parameters with N = 2 to obtain a first order fit of the primary and of the secondary for the helium lines. We then increased the number of Gaussian components in our fit to account for the presence of the N III λ 4537 line on the blue side of the He II λ 4542 line. We optimized the fit of the He II line by fitting the N III line in the blend at the minimum of the radial velocity curve of the primary, i.e. when the secondary He II line is shifted to the red and consequently well separated from the N III line. We then fixed the width and the normalization factor of the N III line to the same values to fit the helium components of the blended profile at the maximum of the RV curve. We used a N = 4 function to fit the blend of the He I λ 4471 line with that of Mg II at 4481 Å (primary and secondary). The synthetic profiles obtained on the basis of Eq. 1 are overplotted on the observed profiles in Fig 3. While performing these fits, we first fixed the width and the normalization coefficient of the primary component to the same values at both extrema. We then improved the fits by allowing these parameters to vary.

On the basis of our best fits, we estimated the equivalenth width (EW) of the He I and He II lines to obtain a spectral classification of the two components of the system. At the maximum of the RV curve, we obtain EWs of 0.18 ± 0.02 and 0.53 ± 0.03 Å respectively for the He I λ 4471 and He II λ 4542 lines of the primary. At the same phase but for the secondary, we obtain respectively EWs of 0.05 ± 0.02 and 0.08 ± 0.02 Å . Using the classification criteria proposed by Mathys (1988), we obtain

O5 and O6.5 spectral types respectively for the primary and the secondary. The best-fit parameters obtained at the phase corresponding to the minimum of the SB1 RV curve lead to EWs of 0.19 ± 0.02 and 0.52 ± 0.03 Å (respectively 0.08 ± 0.02 and 0.07 ± 0.03 Å) for the He I and He II lines of the primary (resp. secondary). In this case, the spectral types of the two components of HD 15558 are O5.5 and O7.5. Considering mean values of the EWs obtained at the extreme phases of the orbit, the classification of the two components of the system are O5.5 and O7 respectively for the primary and the secondary.

We note that the EW of He I λ 4471 undergoes a significant decrease ($\sim$40%) as the secondary is receding from the obsever. Such a decrease is also marginally observed for the Mg II line, but no such behaviour is detected for the He II λ 4542 line. However, the EWs of the primary remains steady from one extremum to the other. This behaviour is quite reminiscent of the so-called Struve-Sahade effect observed in the case of several massive binary system (see e.g. Bagnuolo et al. 1999). However, we note that it might be due to errors in the normalization of the spectra and more data are needed to confirm this trend.

4.5 Estimation of the masses of the components of HD 15558

As we were able to separate the primary and secondary components from the profiles of a few lines at both extrema of the RV curve, we obtained a first estimate of the amplitude of the secondary RV curve. In the case of the He II λ 4542 line, we estimated that the RV of the secondary was determined with an uncertainty of about 15 km s^{-1} at its maximum, and about 20 km s^{-1} at its minimum. This difference is due to the fact that the blend with the N III makes the determination of the parameters of the secondary component of the He II line more difficult (see bottom left panel of Fig. 3). According to our fit, and using the K value derived from our SB1 fit (see Table 4), we obtain a mass ratio of 3.3 ± 0.4. The explicite expression of the mass function as a function of the period (P), the eccentricity (e), the primary RV semi-amplitude (K) and the mass ratio (q) allowed us to estimate the minimum masses of the two components. Considering some error propagation calculation, we obtain minimum masses of 152 ± 51 and 46 ± 11 M$_\odot$ respectively for the primary and the secondary. We note that the large errors on the minimum masses are clearly dominated by the large uncertainty on the mass ratio.

The very large masses of the two stars, mainly of the primary, are compatible with the large values already mentioned in the litterature for this star (see e.g. Herrero et al. 2000). This is the first time that spectroscopic data lend support to this assertion. However, we emphasize that the minimum masses are poorly constrained. The critical issue regarding our results is the estimate of the mass ratio. More RV measurements are needed close to the extrema of the radial velocity curve to reduce the uncertainty on q, and accordingly reduce the error bars on the minimum masses. In order to address this issue and to tentatively derive the first SB2 orbital solution for this system, we applied a distentangling method to our spectral time series.

4.6 Disentangling of the primary and secondary spectra of HD 15558

We used the spectral disentangling method described by González & Levato (2005). It consists in an iterative procedure allowing to compute the spectra and RVs of the two components of a binary system. At the starting point, a flat spectrum is adopted for the secondary, and the mean on the observed spectra is used as the starting primary spectrum. At each iteration, the spectra of the primary and the secondary obtained at the prevous step are subtracted from the observed spectra, and the radial velocities are determined on the residuals through a cross-correlation procedure using a template including a series of lines. The advantage of this procedure is the fact that it does not require any accurate a priori knowledge of the spectrum of the two stars.

As our spectral time series include data obtained with different instrumentations, we once again limited our investigation to a wavelength domain covered by all our data. We applied the disentangling procedure to our 70 spectra between 4456 and 4567 Å , in order to include the He I λ 4471, the Mg II λ

Table 5: Orbital parameters of the SB2 solution of HD 15558 determined from the RVs computed with the disentangling procedure of González & Levato (2005). We started the iteration procedure with the mean of the He II λ 4542 and the N III $\lambda\lambda$ 4634-4641 lines (*left part*) and of the He II λ 4542 line alone (*right part*). The parameters have the same meaning as in Table 4. $R_{\rm RL}$ stands for the radius of a sphere with a volume equal to that of the Roche lobe computed according to the formula of Eggleton (1983).

	He II & N III		He II	
	Primary	Secondary	Primary	Secondary
P (days)	442.478 (fixed)			
e	0.41 ± 0.06		0.37 ± 0.07	
T$_\circ$ (HJD–2 450 000)	1790.377 ± 11.935		1796.271 ± 12.970	
ω	100° ± 10°		120° ± 12°	
γ (km s^{-1})	–54.1 ± 8.2	0.6 ± 11.4	–51.5 ± 12.3	-10.2 ± 15.3
K (km s^{-1})	48.3 ± 4.6	157.9 ± 15.2	43.3 ± 6.3	135.9 ± 19.7
$a \sin i$ (R$_\odot$)	385.6 ± 38.8	1259.5 ± 126.6	351.4 ± 52.0	1101.3 ± 163.0
$m \sin^3 i$ (M$_\odot$)	234.0 ± 61.4	71.6 ± 15.8	159.5 ± 58.4	50.9 ± 14.4
$q = m_1/m_2$	3.27 ± 0.45		3.13 ± 0.71	
$R_{\rm RL} \sin i$ (R$_\odot$)	186.5 ± 19.3	355.8 ± 37.9	168.6 ± 26.0	314.6 ± 52.3

4482 and the He II λ 4542 lines. These lines were selected because they display rather clearly the signature of both components of the system. Starting from the two sets of RVs used to obtain the SB1 solutions described in Table 4, we applied this technique in three different situations:

(a) First, we used all our spectra and we allowed both primary and secondary RVs to vary. The RVs obtained after 20 iterations were used to compute an SB2 orbital solution. The orbital parameters are given in Table 5. The most striking results are the huge minimum masses for the stars, mostly for the primary, in agreement with the values discussed in Sect. 4.5. We see that most parameters have values close to those obtained for the SB1 orbital solution (see Table 4). Even the difference in the semi-amplitude of the primary radial velocity curve is rather small, whilst the RVs were estimated on the basis of two very different approaches. The Gaussian fit used for the SB1 case is likely to slightly underestimate the amplitude of the RV curve, but Fig. 3 suggests that the shift between the blended profile and the primary component centroids should be very small. In the case of the mean He II and N III (resp. He II alone) RVs, we note that the disentangling of four (resp. one) spectra gave unsatisfactory results as the derived RVs deviated strongly from these of other spectra obtained only a few days before or after. For this reason, we discarded these spectra from the computation of the orbital solutions presented in Table 5. In Fig. 4, we present the radial velocity curves obtained for both components of the system. We see that the agreement between the data and the computed RV curve for the secondary is rather poor, mostly at phases where the separation between the two components is small. The separated spectra of the primary and of the secondary in the wavelength domain used for the disentangling procedure are individually displayed in Fig. 5.

(b) We then applied the same procedure, but we fixed the radial velocities of the primary to the values initially given. We obtained rather similar results as in case (a) although the RVs derived for the secondary in the case of several spectra were not acceptable.

(c) We finally applied the spectral disentangling method to a reduced spectral series, including only 32 spectra obtained at phases close the extrema of the radial velocity curve, i.e. between phases 0.05 and 0.25 and between phases 0.75 and 0.95. We selected these spectra in order to obtain an estimate of the mass ratio unaffected by the data obtained when the primary and secondary components are not well separated. This approach leads to a mass ratio of 3.7 ± 1.2, but we note that this value

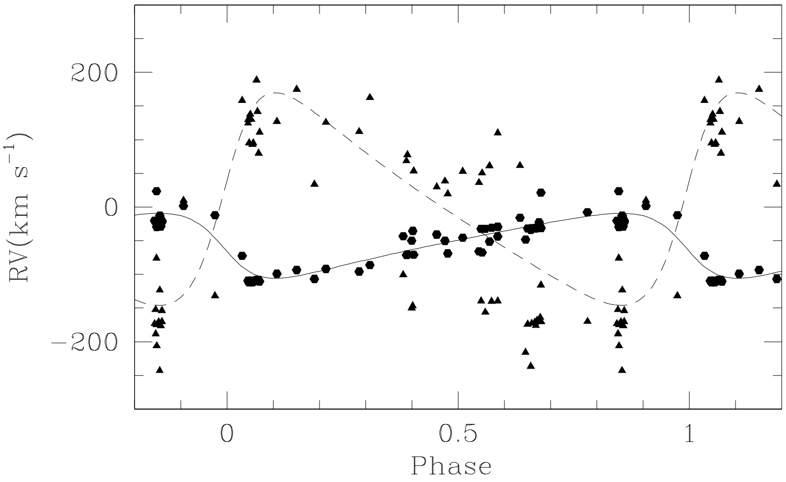

Figure 4: Radial velocity curves of the two components of HD 15558 for an orbital period of 442.478 d. The hexagons (resp. triangles) stand for the primary (resp. secondary) RVs. The solid and dashed line yield our best fit orbital solution respectively for the primary and the secondary, with the parameters provided in the left part of Table 5.

should be considered with caution as the eccentricity (0.1 ± 0.1) and the T_o deviate significantly from the values derived from the SB1 and the SB2 (cases a and b) solutions.

In summary, we find that the mass ratio of the two components of the system obtained from radial velocities determined on the basis of the disentangling method is of the order of 3, whatever the initial RVs considered as starting point of the procedure. This value is in agreement with the mass ratio derived from the simultaneous fit of Gaussians discussed in Sect. 4.5, but we failed to reduce the uncertainty on q. Consequently, the minimum masses estimated with both approaches are similar. The extreme minimum masses seem therefore to be robust. For initial RVs obtained with the He II λ 4542 line, both methods provide minimum masses of the order of 150 ± 50 and $50 \pm 15\,M_\odot$ respectively for the primary and the secondary. For RVs obtained from the He II and N III lines, the minimum masses are somewhat larger with a larger standard deviation. Although the uncertainty on the secondary radial velocities is large, the fact that our results rely partly on several spectra obtained close to the extrema of the radial velocity curves lends some support to the mass ratios derived by our analysis.

5 Line profile analysis

We investigated the line profile variability of HD 15558 using the same approach as described for instance by Rauw & De Becker (2004), De Becker & Rauw (2004) and in the previous section of this chapter in the thesis. We first calculated the Time Variance Spectrum (TVS, see Fullerton et al. 1996) of our time series to search for a significant line profile variability (at the 99 % confidence level). The lines displaying the strongest variability in all data sets are He II λ 4686 and Hβ.

We then performed a 2D Fourier analysis using the technique described by Rauw et al. (2001) and used for instance by De Becker & Rauw (2004) for the lines displaying a significant variability. We used the unequally spaced data Fourier analysis technique as described by Heck et al. (1985). The periodograms were inspected to identify the main peaks. As a next step the data were 'prewhitened' for

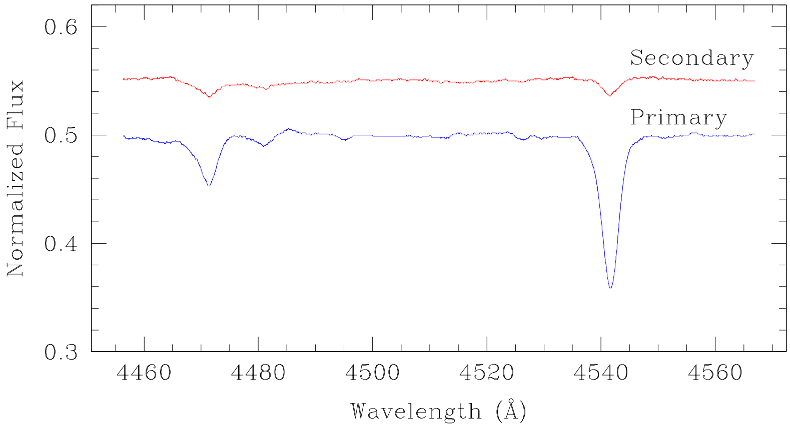

Figure 5: Separated spectra of the primary (*lower spectrum*) and of the secondary (*upper sepctrum*) of HD 15558 in the wavelength domain used for the disentangling procedure.

the variations occurring at the corresponding frequencies. The frequencies which give the best results, i.e. a periodogram without significant peaks after prewhitening, were then considered in the purpose to identify the time-scales of the line profile variations.

In Fig. 6, we have represented the mean profile, the Time Variance Spectrum, and the two-dimension periodogram of the He II λ 4686 and Hβ lines respectively for the September 2000, September 2001, September 2002 and October 2003 Aurélie data sets (see Table 1). In each case, we see that both lines display a significant variability, with a higher variability level in the case of the He II λ 4686 line. We note also that the variability level is not the same at the different epochs. We did not include the results from the October 2004 observing run because they were much less conclusive. This latter data set contains indeed only five spectra, and the variability of the He II line appears to be only marginal.

The comparison of the TVS from September 2000 and September 2001, respectively corresponding to the minimum and maximum of the radial velocity curve of the primary (see Fig. 2), shows that the variability is mostly associated with the primary. The profile of the He II λ 4686 primary clearly shows a P-Cygni shape, whilst that of the secondary is probably in absorption, or another P-Cygni profile dominated by its absorption component. It is rather obvious in the case of the September 2001 data set, where the emission component of the primary P-Cygni is rather weak, and nearly absent. This should be due to the superposition of the emission component of the primary P-Cygni with the absorption profile of the secondary.

The periodograms obtained for both lines present sometimes similarities suggesting that their variability may at least be partly correlated, even though significant differences are found. In September 2000, strong peaks are found at frequencies close to 0.12 and 0.4 d^{-1} (with their $1-\nu$ aliases) for He II λ 4686, and mainly close to 0.1 (or 0.9) d^{-1} in the case of Hβ. In September 2001, the periodogram obtained for the He II λ 4686 line displays strong peaks at frequencies of about 0.15 or 0.85 d^{-1}, whilst for Hβ the strongest peaks fall at about 0.2 and 0.8 d^{-1}. For the same data, we report also on a significant, although weak, variability of the He II λ 4542 line with a frequecy of 0.22 (or 0.78) d^{-1}. In September 2002, the situation is rather clear. Fig. 7 shows the mean periodogram obtained in the case of the He II λ 4686 line, between 4681 and 4685.5 Å, along with the residuals obtained after prewhitening with a frequency of about 0.21 d^{-1}. For Hβ of the same data set, the main frequency is about 0.24 d^{-1}. The

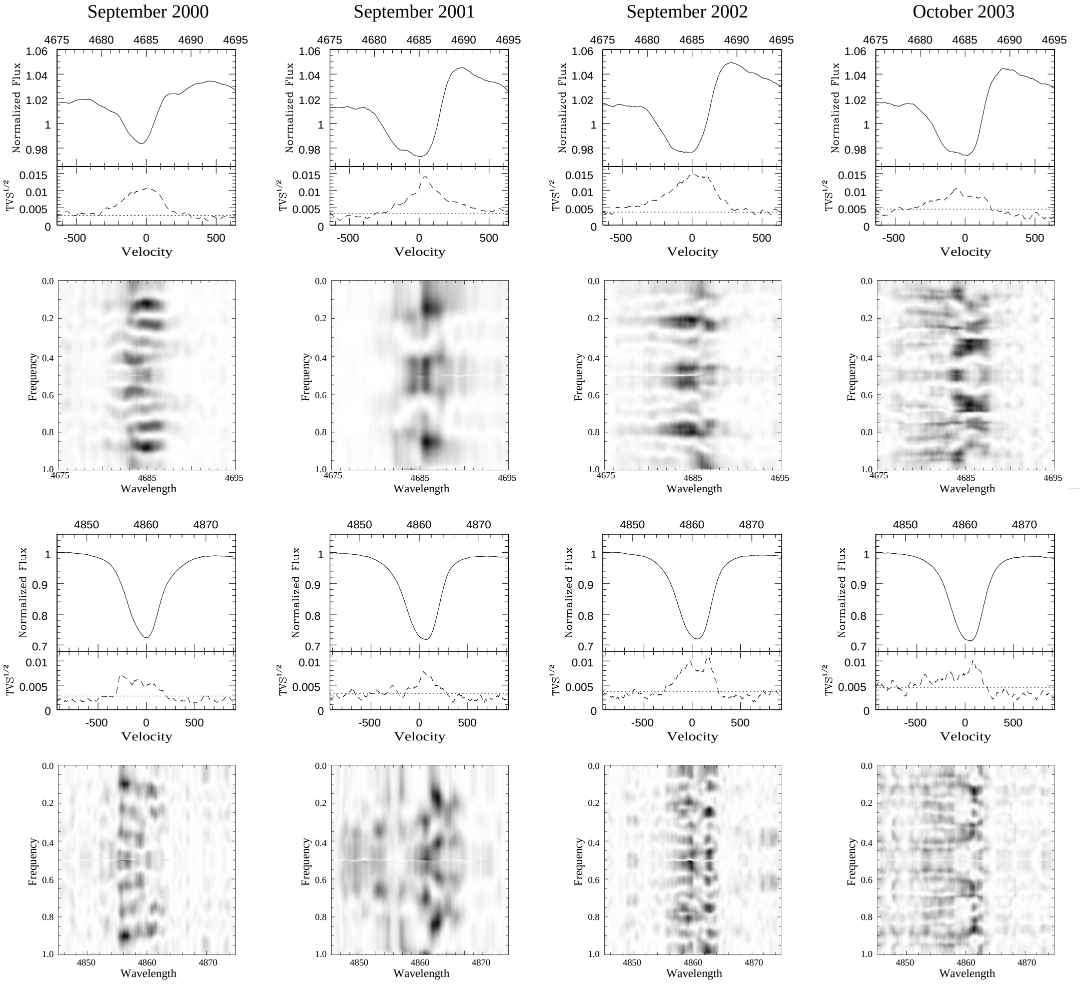

Figure 6: Investigation of the profile variability of the He II λ 4686 line between 4675 Å and 4695 Å (*upper part*) and of Hβ between 4845 Å and 4875 Å (*lower part*) for HD 15558. The data are taken respectively from the September 2000, the September 2001, the September 2002 and the October 2003 Aurélie data sets. *Upper panel:* mean spectrum and square root of the time variance spectrum. The 99 % significance level of the TVS$^{1/2}$ is indicated by the horizontal dotted line. Velocities are expressed in km s^{-1}. *Lower panel:* the corresponding two-dimensional power spectra. The darkest regions stand for the highest peak intensities of the periodogram. Frequencies and wavelengths are respectively expressed in d^{-1} and in Å .

situation is much less clear in October 2003 where He II λ 4686 gives main peaks at frequencies between 0.3 and 0.4 d^{-1} (along with their $1-\nu$ aliases), albeit Hβ presents a dominant peak at about 0.13 (or 0.87) d^{-1}. We note that the peaks found at frequencies close to 0.5 d^{-1} are most probably aliases of the main peaks discussed above as they disappeared most of the time when we prewhitened our time series with the main frequencies.

Considering these results, we see that no particularly stable recurrence time-scale has been revealed by the temporal analysis of our spectral time series. The only robust result is the discovery of a significant variability on a yet ill-defined time-scale of a few days, and concentrated mainly in the primary component. Such a behaviour is reminiscent of the case of the Oef star BD +60° 2522 that displays a significant variability for the same lines with a changing variability level and an apparently variable recurrence time-scale (?). At this stage, such changing variability patterns are not yet elucidated.

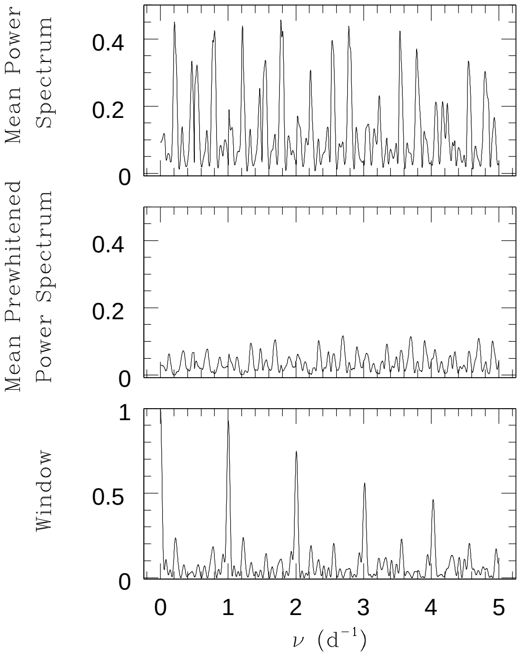

Figure 7: *Upper panel:* mean power spectrum obtained for the He II λ 4686 line of HD 15558 between 4681 Å and 4685.5 Å for the September 2002 data set, up to 5.0 d^{-1}. *Middle panel:* residual power spectrum obtained after prewhitening with one frequency (0.2085 d^{-1}). A similar result is obtained if the $1-\nu$ alias at 0.7995 d^{-1} is used to prewhite the data. We note that the peaks appearing at frequencies of about 0.45 and 0.55 d^{-1} (see Fig 6) are aliases of the main peaks obtained at about 0.2 and 0.8 d^{-1}. *Bottom panel:* power spectral window corresponding to the September 2002 data set sampling.

6 Archive *ROSAT* data

IC 1805 was observed with the PSPC instrument onboard the *ROSAT* satellite on 22-23 August 1992 (sequence number rp201263n00), with an exposure time of 8.8 ks. We retrieved the data from the HEASARC archive database and processed them using the XSELECT software. HD 15558 is the brightest X-ray source in the *ROSAT* field of view. We extracted the PSPC spectrum of HD 15558 over a 1 arcmin radius circle. The background was extracted from an annulus surrounding the source region and covering an equal surface. The spectrum was then rebinned to get at least 5 counts per bin, and we analysed it using the XSPEC software. The PSPC count rate of HD 15558 corrected for the background between 0.1 and 2.5 keV is $(2.35\pm 0.24)\times 10^{-2}$ cts s^{-1}.

We fitted the X-ray spectrum of HD 15558 between 0.1 and 2.5 keV with a single temperature optically thin thermal plasma `mekal` model (Mewe et al. 1985; Kaastra 1992). The best results were obtained when using only one absorption column frozen to the interstellar value. In order to estimate this ISM column density, we first estimated the intrinsic color $(B-V)_\circ$ from the spectral type. We obtained the color excess using the observed $(B-V)=0.5$ given by Massey et al. (1995), i.e. $E(B-V)=0.71$, and then we estimated the hydrogen column density from the gas to dust ratio given by Bohlin et al. (1978), yielding $N_{H,ISM}=0.47\times 10^{22}$ cm^{-2}. The best-fit plasma temperature is $kT=0.77^{0.99}_{0.58}$ keV, where the confidence interval is given at 90 %. The observed flux is about 2.0×10^{-13} erg cm^{-2} s^{-1} whilst the flux corrected for the ISM absorption is about 8.5×10^{-13} erg cm^{-2} s^{-1}. Assuming that the distance to IC 1805 is 2.34 kpc (Massey et al., 1995), the corrected X-ray flux converts into an X-ray unabsorbed luminosity of about 5.6×10^{32} erg s^{-1}. Considering the empirical relation given by Berghöfer et al. (1997), the expected X-ray luminosity for an O-type star with a bolometric luminosity of 5.6×10^{39} erg s^{-1} (Herrero et al., 2000) should be 1.1×10^{33} erg s^{-1}. Consequently, HD 15558 does not appear to be overluminous in X-rays. However, we note that the *ROSAT*-PSPC bandpass is not ideal to investigate the X-ray emission from massive binaries likely to emit significantly above 2.0 keV. X-ray observations with X-ray telescopes like *XMM-Newton* or *Chandra* are strongly needed to establish the spectral properties of HD 15558 above 2.0 keV.

7 Discussion

7.1 Spectral classification

As mentioned in Sect. 5, the He II λ 4686 line shows a P-Cygni profile for the primary and is in absorption for the secondary. These profiles, along with the luminosity contrast between the primary and the secondary, are compatible with a difference of one luminosity class between the two stars. Considering the fact that Hα is in absorption (see Fig. 1), it is unlikely that the primary is a supergiant and we therefore propose giant and main-sequence luminosity classes respectively for the primary and the secondary. On the other hand, it is not clear whether the N III $\lambda\lambda$ 4634,4641 lines are in emission for the secondary as well. Consequently, we propose that the massive binary HD 15558 is formed of an O5.5III(f) primary with an O7V secondary.

7.2 A very massive primary?

The most interesting – and also puzzling – result presented in Sect. 4 is undoubtedly the very high mass derived for the primary, especially considering its spectral type. On the one hand, the most massive star whose mass was determined using spectroscopic and photometric data is the massive binary WR20a, with masses of 82 and 83 M$_\odot$ respectively for the primary and the secondary (Rauw et al. 2004; Bonanos et al. 2004). On the other hand, other very high stellar masses were proposed (i) for the Pistol Star, close to the Galactic center, with a mass around 200 - 250 M$_\odot$ (Figer et al., 1998), and (ii) for the most massive star in the Large Magellanic Cloud with a mass of the order of 120 - 200 M$_\odot$ (Massey & Hunter, 1998).

The fact that we derive such a high mass for the primary raises the question of the so-called stellar 'upper mass limit'. Massive stars are expected to be vibrationally unstable above a given critical mass which depends on the evolutionary state. For zero-age main sequence stars, the most accurate calculations resulted in critical masses between about 90 and 440 solar masses (see Appenzeller 1987 for a review). Oey & Clarke (2005) statistically demonstrated that the local census of massive stars oberved so far (Milky Way + Magellanic Clouds) exhibits a 'universal' upper mass cutoff around 120 -

200 $M_\odot$ for a Salpeter initial mass function (IMF). Considering that the largest stellar mass observed in IC 1805 is about 100 $M_\odot$, the same authors estimate that the probability that the stellar population of IC 1805 extends to 150 $M_\odot$ (resp. 200 $M_\odot$) is about 0.63 (resp. 0.51). As a consequence, a stellar mass of $150 \pm 50\,M_\odot$, assuming the minimum masses derived above are close to the true masses ($i \sim 90°$), does not disagree with both the theoretical and the statistical approaches of the stellar upper mass limit.

However, extrapolating the empirical mass-luminosity relation ($L \propto M^p$, e.g. with $p = 3.0$) up to such a high stellar mass, we derive a luminosity of about $1.3 \times 10^{40}\,\mathrm{erg\,s^{-1}}$ which converts into an absolute bolometric magnitude of –11.57. From the observed V magnitude of HD 15558 and considering a reddening law with $R_V = 3.1$ and a color excess E(B - V) = 0.71 (see Sect. 6), we derive an extinction A_V equal to 2.20, leading to an apparent dereddened V magnitude equal to 5.70. Using the relation given by Howarth & Prinja (1989), we obtain a bolometric correction of –3.86, yielding a dereddened apparent bolometric magnitude equal to 1.84. With these absolute and apparent bolometric magnitudes, we derive therefore a distance of about 4.8 kpc! Such a distance would cast doubt on the membership of HD 15558 in IC 1805, which seems very unlikely. If we consider an exponent p for the mass-luminosity relation larger than 3, the problem is getting worse. If one considers on the contrary that HD 15558 belongs indeed to IC 1805, i.e. that it is located at a distance of about 2.3 kpc (see Massey et al. 1995), the exponent p in this high mass regime should be about 2.7. This may point to a possible inadequacy of the available mass-luminosity relation for such a high mass regime, generally established on the basis of populations of lower mass stars. This can be understood if one considers the scarcity of stars with masses above a few tens of solar masses, making this high mass domain poorly explored observationally.

Provided the mass derived for the primary is indeed of the order of 150 $M_\odot$, the main issue comes from its spectral type. We may indeed expect the most massive stars to be also the earliest ones. Considering for instance the typical masses given by Howarth & Prinja (1989), we see that the expected masses for O5.5 stars should lie between 50 and 80 $M_\odot$ depending to the luminosity class. An O5.5III star with a mass of about 150 $M_\odot$ – i.e. about a factor 2 too high – constitutes therefore an severe anomaly with respect to the usual classification adopted for O-type stars.

Let us consider an alternative scenario, where HD 15558 is not a binary but a triple system. The primary may be constituted of a yet unrevealed close binary system. In this scenario, as the mass of the primary is estimated on the basis of the motion of the secondary, the primary object – i.e. the hypothetical close binary – would appear to be a massive object whose mass is the sum of the masses of two stars. Provided the spectral type derived from our spectra for the primary is typical of the two stars constituting the close binary, we possibly are observing the merged spectrum of two similar O-stars, in addition to that of the secondary object whose spectral type should be O7. This scenario offers the possibility to explain the unexpected high mass of the primary object, and to reconcile its mass with its spectral type. However, the triple system scenario still needs to solve the following issue: our spectral time series did not reveal any binary motion on a time-scale of a few days. If the primary is indeed constituted of two stars, the short period orbit might be seen under a very low inclination angle. We might also consider the possibility that the time-scale of this orbit is a few weeks or so, and therefore poorly sampled by our spectral time series. However, we note that the radial velocity curve plotted in Fig. 2 does not present any strong dispersion likely to be due to an orbital motion on a time-scale significantly shorter than the main period of 442 d. In addition, we might expect some additional X-rays to be produced by an interaction between the winds of the two stars constituting the primary. High quality data obtained for instance with *XMM-Newton* are strongly needed to investigate the X-ray emission from HD 15558 and discuss its origin in detail. In summary, even though our data do not provide any strong evidence supporting the triple scenario, this scenario may reconcile the mass derived for the primary and its spectral type.

On the other hand, an initially extremely massive and very hot early-type (i.e. spectral type O2) main sequence star will cool down a bit during its evolution towards the giant luminosity class. For instance, according to the evolutionary models of Schaller et al. (1992), a star of initial mass 120 $M_\odot$ starts its evolution with an effective temperature of 53000 K. When the effective temperature reaches

38000 K, typical for an O5.5 giant (Martins et al., 2005), the stellar mass has decreased to about 85 $M_\odot$. Moreover, at this evolutionary stage, the hydrogen surface abundance should already be reduced, whilst helium should be enhanced. The main conclusion here is that a very massive star would have to lose a substantial fraction of its initial mass before reaching the effective temperature of an O5.5 giant. This would then imply an extremely large initial mass for the primary of HD 15558.

7.3 An open cluster with unusually large stellar masses?

The existence of such a massive star is worth discussing in the context of the massive star population of IC 1805, which should not be addressed without considering the presence of the most evolved known object in the vicinity: the microquasar LSI +61°303. This high mass X-ray binary producing a collimated relativistic jet consists of a Be star and of a compact object whose nature (neutron star or black hole) is not yet established (Massi, 2004). LSI +61°303 is believed to have been ejected out of IC 1805 during the supernova explosion of the initially most massive component of the binary (Mirabel, 2004). If the progenitor of LSI +61°303 was formed at the same epoch as the other O-stars in IC 1805, among which HD 15558, its primary component may have been more massive than the primary of HD 15558. Alternatively, if LSI +61°303 was part of an older population of stars, its supernova explosion might have triggered the formation of the current population of O-type stars.

Two additional stars of this cluster are believed to have very large stellar masses, namely HD 15570 and HD 15629 (see (Herrero et al., 2000), even though their masses have up to now only been estimated through model atmosphere fits. Unfortunately, as these two stars are probably single (see the previous section of this chapter in the thesis), an independant mass determination through the study of a binary motion is unlikely.

This series of presumably very massive objects suggests that IC 1805 harbours a population of particularly massive stars as compared to other open clusters. According to Massey et al. (1995), a large number of very massive stars in an open cluster may be explained by its a very young massive star population. Indeed, the age of the massive star population in IC 1805 was estimated to be equal to 2 ± 1 Myr. Consequently, the apparently large stellar masses found in IC 1805 as compared to other clusters or assocations might be explained by the fact that it is a very young open cluster. Its most massive members have therefore not yet evolved to compact objects.

8 Summary and conclusions

We have presented the results of an intensive spectroscopic study of the massive binary HD 15558. On the basis of 70 homogeneous radial velocity measurements, we have derived a SB1 orbital solution with significantly refined parameters as compared to those obtained by Garmany & Massey (1981). The system appears to be eccentric (e ∼ 0.4) and we obtain a period of 442 ± 12 d.

A careful inspection of the spectra obtained close to the extrema of the radial velocity curve reveals the presence of the companion in the profiles of the He I λ 4471, He II λ 4542, C IV λ 5812 and He I λ 5876 lines. We have simultaneously fitted Gaussians to the profiles of the He I λ 4471 and He II λ 4542 lines in order to separate the primary and secondary components. The determination of the equivalent width of these two lines allowed us to derive O5.5 and O7 spectral types respectively for both stars. Considering in addition that He II λ 4686 of the primary has a P-Cygni profile whilst the same line is in absorption in the case of the secondary, along with the fact that we do not observe clearly the N III $\lambda\lambda$ 4634-4641 lines in emission for the secondary, we propose that HD 15558 is an 05.5III(f) + O7V binary.

We estimated the radial velocities of the secondary following two approaches: (1) a simultaneous fit of line profiles and (2) a disentangling method. Both approaches allowed us to determine minimum masses of the order of 150 ± 50 and 50 ± 15 $M_\odot$ respectively for the primary and the secondary. We also obtained the first SB2 orbital solution for HD 15558. Although we note that the quality of this SB2 solution is rather poor, we insist on the fact that our data point clearly to a rather high mass ratio (about 3), leading to an extreme minimum mass for the primary. Our results deserve independent validation using an improved disentangling procedure.

The main problem considering our results is to reconcile the very extreme mass of the primary with its spectral type. It is indeed unlikely that a very massive main-sequence star could cool down enough during its evolution to become an O5.5 giant. A possible scenario can however be considered, where HD 15558 is not a binary but a triple system. The primary may indeed be constituted of a yet unrevealed close binary system. In this scenario, as the mass of the primary is estimated on the basis of the motion of the secondary, the primary object – i.e. the hypothetical close binary – would appear to be a massive object whose mass is the sum of the masses of two stars. Even though our data donot provide any evidence for this scenario, we estimate that at this stage it should not be rejected, and that it could constitute a valuable working hypothesis for future investigations concerning this system.

Acknowledgements

We want to express our gratitute to the staff at OHP for the good job and their useful advices that helped us to define the best strategy to carry out the monitoring of HD 15558. Our thanks go also to all the astronomers that contributed to the service mode observations. We are greatly indebted to the FNRS (Belgium) for multiple assistance including the financial support for the rent of the OHP telescope in 2000 and 2002 through contract 1.5.051.00 "Crédit aux chercheurs". The travels to OHP were supported by the Ministère de l'Enseignement Supérieur et de la Recherche de la Communauté Française. This research is also supported in part by contract PAI P5/36 (Belgian Federal Science Policy Office) and through the PRODEX XMM/INTEGRAL contract. We would like to thank the staff of the Observatoire de Haute Provence for their technical support during the various observing runs. The SIMBAD database has been consulted for the bibliography.

References

Appenzeller I., 1987, in *Instabilities in Luminous Early-Type Stars*, eds. H.J.G.L.M. Lamers and C.W.H. de Loore, Dordrecht: Reidel, 56

Bagnuolo W.G.Jr., Gies D.R., Riddle R., Penny L.R., 1999, ApJ, 527, 35

Baranne, A., Queloz, D., Mayor, M., et al. 1996, A&AS, 119, 373

Berghöfer T.W., Schmitt J.H.M.M., Danner R., Cassinelli J.P., 1997, A&A, 322, 167

Bohlin R.C., Savage B.D., Drake J.F., 1978, ApJ, 224, 132

Bonanos A.Z., Stanek K.Z., Udalski A. et al., 2004, ApJ, 611, L33

Bonnell I.A., Bate M.R., 2002, MNRAS, 336, 659

De Becker M., Rauw G., 2004, A&A, 427, 995

De Becker M., Rauw G., Manfroid J., 2004, A&A, 424, L39

De Becker M., Rauw G., Swings J.-P., 2005, Ap&SS, 297, 291

Dougherty S.M., Pittard J.M., Kasian L., Coker R.F., Williams P.M., Lloyd H.M., 2003, A&A, 409, 217

Eichler D., Usov V., 1993, ApJ, 402, 271

Eggleton P.P., 1983, ApJ, 268, 368

Figer D.F., Najarro F., Morris M. et al., 1998, ApJ, 506, 384

Fullerton A.W., Gies D.R., Bolton C.T., 1996, ApJS, 103, 475

García B., Mermilliod J.-C., 2001, A&A, 368, 122

Garmany C.D., Massey P., 1981, PASP, 93, 500

Gillet D. et al., 1994, A&AS, 108, 181

González J.F., Levato H., 2005, A&A, in press

Heck A., Manfroid J., Mersch G., 1985, A&AS, 59, 63

Herrero A., Puls J., Villamariz M.R., 2000, A&A, 354, 193

Howarth I.D., Prinja R.K., 1989, ApJS, 69, 527

Kaastra J.S., 1992, *An X-ray spectral code for optically thin plasmas*, Internal SRON-Leiden Report

Martins F., Schaerer D., Hillier D.J., 2005, A&A, 436, 1049

Massey P., Hunter D.A., 1998, ApJ, 493, 180

Massey P., Johnson K.E., De Gioia-Eastwood K., 1995, ApJ, 454, 151

Mathys G., 1988, A&AS, 76, 427

Massi M., 2004, in *7th Symposium of the European VLBI Network on New Developments in VLBI Science and Technology*, eds. R. Bachiller, F. Colomer, J.-F. Desmurs, P. de Vicente, 215

Mathys G., 1988, A&AS, 76, 427

Mathys G., 1989, A&AS, 81, 237

Mewe R., Gronenschild E.H.B.M., van den Oord G.H.J., 1985, A&AS, 62, 197

Mirabel I.F., Rodrigues I., Liu Q.Z., 2004, A&A, L29

Oey M.S., Clarke C.J., 2005, ApJ, 620, L43

Rauw G., 2004, in *Cosmic Gamma-Ray Sources*, eds. K.S. Cheng and G.E. Romero, Kluwer Academic Publishers, Dordrecht, 105

Rauw G., De Becker M., 2004, A&A, 421, 693

Rauw G., Morrison N.D., Vreux J.-M., Gosset E., Mulliss C.L., 2001, A&A, 366, 585

Rauw G. et al., 2004, A&A, 420, L9

Santolaya-Rey A.E., Puls J., Herrero A., 1997, A&A, 488, 512

Schaller G., Schaerer D., Meynet G., Maeder A., 1992, A&AS, 96, 269

Underhill A.B., 1967, in *Determination of Radial Velocities and their Applications*, eds A.H. Batten & J.F. Heard, IAU Symp. 30, 167

Walborn N.R., 2001, in *Eta Carinae and Other Mysterious Stars*, ASP Conference Series, 242, eds. T. Gull, S. Johansson, K. Davidson, 217

Walborn N.R., Howarth I.D., 2000, PASP, 112, 1446

Wolfe R.H.Jr., Horak H.G., Storer N.W., 1967, in Modern Astrophysics, ed. M. Hack, Gordon & Branch, New York, 251

Chapter 3

The colliding wind binary HD 159176

> As discussed in Chapter 1, the physics of wind collisions is likely to play a significant role in the processes responsible for the non-thermal emission from massive stars. For this reason, before investigating with details the X-ray emission from non-thermal radio emitters in the next two chapters, it is worth discussing the X-ray properties of colliding wind binaries. In this chapter, we study the X-ray emission of the short period massive binary HD 159176 that is not a non-thermal radio emitter. The thermal X-ray emission will be investigated on the basis of two different modelling approaches. From the results obtained from high quality *XMM-Newton* data, we will see that the case of HD 159176 is unexpectedly worth considering in the context of the campaign devoted to the non-thermal emission from massive stars.

The massive binary HD 159176 ($V = 5.7$) is located in the core of the young open cluster NGC 6383. It consists of a close binary system constituted of two O7V stars, evolving on a circular orbit with a period of 3.367 d. The study of this cluster based on *XMM-Newton* observations revealed the presence of a number of X-ray sources mainly concentrated close to HD 159176 (Rauw et al. 2003a). The overall properties of many of these X-ray sources suggest that they may be candidates for low-mass pre-main sequence stars.

Our *XMM-Newton* data allowed us to carry out a detailed analysis of the X-ray properties of HD 159176. Using both EPIC and RGS data, we studied the X-ray spectrum on the basis of several models. As we are dealing with a massive binary system, a thermal X-ray emission is expected to be produced by:

- the plasma heated by intrinsic hydrodynamic shocks in individual stellar winds of the two stars.
- the plasma heated by the colliding winds between the two stars.

In order to model such emission components, we used classical optically thin plasma thermal models, i.e. `mekal` models (see De Becker et al. 2004c, included hereafter for details). We obtained reasonable fits of our RGS and EPIC spectra between 0.4 and 5.0 keV with a two-component model with temperatures of 0.2–0.3 keV for the soft component, and 0.6 or 1.0 keV for the hard one. The latter temperatures are compatible with those we may expect for a close binary whose winds have not reached their terminal velocities before they collide. Using the canonical relation proposed by Berghoefer et al. (1997), we found that HD 159176 is a factor 7 overluminous in X-rays. This excess is most probably produced by the plasma heated by the colliding winds.

We also adopted a different modelling approach using a composite model made of one `mekal` component along with a colliding wind emission component based on the geometrical steady-state colliding-wind model developed by Antokhin et al. (2004). This model assumes that the radiative cooling is strong, therefore leading to a total conversion of the kinetic power of the winds into radiation. Such a model should be well adapted to the case of HD 159176 as it was developed for colliding winds characterized by radiative shocks, mainly found in the case of short period massive binaries. This latter approach yielded satisfactory results below 5.0 keV, but we failed to obtain a reasonable fit when we tried to model our EPIC spectra up to 10.0 keV. We explored a wide range of the parameter space of the colliding wind model – the main parameters being the mass loss rates and the terminal velocities – to try to reconcile the composite model with our data, but a high-energy tail remained unfitted. We improved significantly the fit by adding a power law component. It appeared that this power law – characterized by a photon index of about 2.5 – was necessary to obtain a very good fit of the EPIC spectra in the whole bandpass. This strongly suggests that a non-thermal component has been detected. If the identification of this hard X-ray emission as being non-thermal is confirmed, HD 159176 might be the first O + O system reported to be a non-thermal X-ray emitter. An additional point worth mentioning is the fact that we observed an X-ray emission from the colliding wind component that is at least 4 times weaker than predicted by the steady-state model of Antokhin et al. (2004). This means that at least 75 % of the kinetic energy injected in the shocks is not converted into X-rays. At this stage, as discussed in De Becker et al. (2004c), the origin of this discrepancy is still unknown. However, we propose that a fraction of this kinetic energy might be used to accelerate electrons through the first order Fermi mechanism.

Considering this unexpected result, one may wonder how we could consider the case of HD 159176 in the context of the study of the non-thermal radio emitters. Indeed, this should be considered in order to address one the main questions formulated in the introduction of this work, i.e. the issue of the detection of a non-thermal emission in the high-energy domain. In this context, the somewhat puzzling point is that HD 159176 is not known to be a non-thermal radio emitter. This may suggest that, for some massive stars, non-thermal emission processes might be at work even if they are not revealed by radio observations. To address this issue, and tentatively imagine a general scenario likely to reconcile these new pieces with the general puzzle of the non-thermal emission from massive stars, we need to gather more information relative to confirmed non-thermal radio emitters. This can be achieved by having a look at another young open cluster, namely NGC 6604 (see Chapter 4).

A&A 416, 221–233 (2004)
DOI: 10.1051/0004-6361:20031710

Astronomy & Astrophysics

An *XMM-Newton* observation of the massive binary HD 159176[⋆]

M. De Becker[1], G. Rauw[1,⋆⋆], J. M. Pittard[2], I. I. Antokhin[3,4], I. R. Stevens[5], E. Gosset[1,⋆⋆], and S. P. Owocki[6]

[1] Institut d'Astrophysique, Université de Liège, Allée du 6 Août, Bât B5c, 4000 Liège (Sart Tilman), Belgium
[2] Department of Physics & Astronomy, University of Leeds, Leeds LS2 9JT, UK
[3] Department of Physics & Astronomy, University of Glasgow, Kelvin Building, Glasgow G12 8QQ, Scotland, UK
[4] On leave from: Sternberg Astronomical Institute, Moscow University, Universitetskij Prospect, 13, Moscow 119899, Russia
[5] School of Physics & Astronomy, University of Birmingham, Edgbaston Birmingham B15 2TT, UK
[6] Bartol Research Institute, University of Delaware, Newark, DE 19716, USA

Received 14 February 2003 / Accepted 28 November 2003

Abstract. We report the analysis of an *XMM-Newton* observation of the close binary HD 159176 (O7 V + O7 V). The observed L_X/L_{bol} ratio reveals an X-ray luminosity exceeding by a factor ∼7 the expected value for X-ray emission from single O-stars, therefore suggesting a wind-wind interaction scenario. EPIC and RGS spectra are fitted consistently with a two temperature `mekal` optically thin thermal plasma model, with temperatures ranging from ~ 2 to 6×10^6 K. At first sight, these rather low temperatures are consistent with the expectations for a close binary system where the winds collide well before reaching their terminal velocities. We also investigate the variability of the X-ray light curve of HD 159176 on various short time scales. No significant variability is found and we conclude that if hydrodynamical instabilities exist in the wind interaction region of HD 159176, they are not sufficient to produce an observable signature in the X-ray emission. Hydrodynamic simulations using wind parameters from the literature reveal some puzzling discrepancies. The most striking one concerns the predicted X-ray luminosity which is one or more orders of magnitude larger than the observed one. A significant reduction of the mass loss rate of the components compared to the values quoted in the literature alleviates the discrepancy but is not sufficient to fully account for the observed luminosity. Because hydrodynamical models are best for the adiabatic case whereas the colliding winds in HD 159176 are most likely highly radiative, a totally new approach has been envisaged, using a geometrical steady-state colliding wind model suitable for the case of radiative winds. This model successfully reproduces the spectral shape of the EPIC spectrum, but further developments are still needed to alleviate the disagreement between theoretical and observed X-ray luminosities.

Key words. stars: early-type – stars: individual: HD 159176 – stars: winds, outflow – stars: binaries: general – X-rays: stars

1. Introduction

HD 159176 is a relatively bright ($m_v = 5.7$) double-lined spectroscopic binary (Trumpler 1930) in the young open cluster NGC 6383. The system has been well studied in the visible and UV wavelengths. Conti et al. (1975) derived an orbital solution that was subsequently improved by Seggewiss & de Groot (1976), Lloyd Evans (1979) and most recently by Stickland et al. (1993). The binary has an orbital period of 3.367 days and consists of two nearly identical O-stars in a circular orbit.

Conti et al. suggested that both stars are O7 stars that have evolved off the main-sequence and nearly fill up their Roche lobes. However, Stickland et al. argued that the stars were probably not evolved. Although the system does not display photometric eclipses, Thomas & Pachoulakis (1994) reported ellipsoidal variability with an amplitude of about 0.05 mag in the optical and UV wavebands. These light curves were analysed by Pachoulakis (1996) who inferred radii of both stars of order $0.25\,a$, where a is the orbital separation. According to these results, the stars do not fill up their critical volume and are thus not very deformed.

Several observations point towards the existence of a wind interaction process in HD 159176. For instance, the optical spectrum of the system displays the so-called Struve-Sahade effect, i.e. the absorption lines of the approaching star appear stronger (Conti et al. 1975; Seggewiss & de Groot 1976; Lloyd Evans 1979), although the reverse effect is seen in the UV (Stickland et al. 1993). Though the origin of this effect is as yet not established, a commonly proposed scenario involves the existence of an interaction process within the binary system (Gies et al. 1997).

Analysing UV resonance line profiles of HD 159176 as observed with *IUE*, Pachoulakis (1996) derived a mass-loss rate of about $3 \times 10^{-6}\ M_\odot\ \mathrm{yr}^{-1}$ for each star (note that this value is

---

[⋆] Based on observations with *XMM-Newton*, an ESA Science Mission with instruments and contributions directly funded by ESA Member States and the USA (NASA).

[⋆⋆] Research Associate FNRS (Belgium).

Table 1. Relevant parameters of the HD 159176 binary system adopted throughout this paper unless otherwise stated. The numbers are taken from Pachoulakis (1996, P96) and Diplas & Savage (1994, DS).

Parameter	Prim.	Sec.	Ref.
$a \sin i\,(R_\odot)$	28.9		P96
$M\ (M_\odot)$	31.9	31.6	P96
$i\,(^\circ)$	$\sim$50		P96
$T_{\rm eff}$ (K)	42 500	35 000	P96
$R_*\ (R_\odot)$	9.8	9.3	P96
v_∞ (km s^{-1})	2850		P96
$\dot{M}\ (M_\odot\,{\rm yr}^{-1})$	3.2×10^{-6}	2.6×10^{-6}	P96
$\log N_{\rm H,ISM}$ (cm^{-2})	21.23		DS

a factor five larger than the one derived by Howarth & Prinja 1989). The stellar winds of the components of HD 159176 are therefore probably sufficiently energetic to interact. The interaction region is expected to be located roughly mid-way between the stars and it prevents the wind of each star from deploying into the direction towards the other star. This situation has an impact on the UV resonance line profiles and the UV light curve (Pachoulakis 1996; Pfeiffer et al. 1997). Pfeiffer et al. analysed the variations of the UV resonance lines and concluded that there exists a source of extra emission between the stars. These authors associated this extra emission with resonant scattering of photospheric light by the material inside a colliding wind region. According to their analysis, this shock region is slightly wrapped around the secondary star.

HD 159176 was detected as a rather bright X-ray source with *EINSTEIN* (0.157 ± 0.008 cts s^{-1} with the IPC, Chlebowski et al. 1989) and *ROSAT* (0.291 ± 0.034 cts s^{-1} during the All Sky Survey, Berghöfer et al. 1996). Chlebowski & Garmany (1991) suggested that the excess X-ray emission observed in many O-type binaries compared to the expected intrinsic contribution of the individual components is produced by the collision of the stellar winds (see also e.g. Stevens et al. 1992). Therefore, it seems likely that at least part of the X-ray flux of HD 159176 may originate in the wind interaction region. In contrast with this picture, Pfeiffer et al. (1997) suggest that the bulk of the X-ray emission arises primarily from the intrinsic emission of the individual components, rather than from a colliding wind interaction.

To clarify this situation, we obtained an AO1 *XMM-Newton* observation of HD 159176. Since the system is X-ray bright, it is well suited to investigate the X-ray properties of a short-period early-type binary.

2. Observations

The observation of HD 159176 with *XMM-Newton* (Jansen et al. 2001) took place during revolution 229, in March 2001 (JD 2 451 977.903–2 451 978.338). According to the ephemeris given by Stickland et al. (1993), the whole observation covered phases between 0.53 and 0.66 (phase 0.0 corresponding to the maximum radial velocity of the primary component).

The total observation was split into three exposures. During the first exposure (Obs. ID 0001730401), the satellite was still inside the radiation belts and only the RGS instruments were used for on-target observations. The total on-target EPIC exposure time of the other two exposures (Obs. IDs 0001730201 and 0001730301) is about 26 ks.

The three EPIC instruments were operated in the full frame mode (Turner et al. 2001; Strüder et al. 2001). All three EPIC instruments used the thick filter to reject optical light. The two RGS instruments were operated in the default spectroscopy mode (den Herder et al. 2001).

We used version 5.2 of the *XMM-Newton* Science Analysis System (SAS) to reduce the raw EPIC data. For each EPIC camera, the observation data files (ODFs) of the two exposures were merged by the *XMM-Newton* Science Operation Center (SOC) into a single set of observation data files. In order to process the EPIC-MOS files with the "emproc" pipeline chain, we had to manually correct some keywords in the ODF summary file generated by the "odfingest" task. For the pn camera, the merged ODF had to be reprocessed by the *XMM-Newton* SOC to generate an event list.

The only events considered in our analysis were those with pattern 0–12 for EPIC-MOS and 0 for EPIC-pn respectively (Turner et al. 2001). We found no event with pattern 26–31, so that we conclude that no significant pile-up affects our data.

In this paper, we discuss only the X-ray data for HD 159176. The other X-ray sources found in the EPIC field of view and associated with the open cluster NGC 6383 are discussed in a separate paper (Rauw et al. 2003). The response matrices used for the EPIC spectra of HD 159176 were those provided by the SOC. No difference was found between spectra obtained with these response matrices and those obtained with the SAS-generated ones.

For the RGS data, separate ODFs were provided for each of the three observations. The three data sets yield exposure times of respectively about 10, 16 and 9 ks. The RGS data were processed with version 5.3 of the SAS. The raw data were run through the "rgsproc" pipeline meta-task. Appropriate response matrices were generated using the "rgsrmfgen" SAS task.

3. Dealing with high background level episodes

We extracted a light curve at very high energies (Pulse Invariant (*PI*) channel numbers $> 10\,000$) that revealed a high level of soft proton background. The soft protons responsible for these flares are thought to be accelerated by magnetospheric reconnection events unrelated to solar flares (Lumb 2002). Unfortunately this high-level background affects a significant fraction of the exposures. Indeed, nearly one half of the total EPIC observation is affected. For this reason, one has to check whether a bad time interval rejection is necessary, or whether the background correction of spectra could take these undesired events properly into account. As a convincing test, we generated EPIC spectra on the basis of the whole event lists (including events occurring during the flare). On the other hand, we filtered the event lists for time intervals with high-energy ($PI > 10\,000$) count rates exceeding thresholds of 0.20 and 1.10 cts s^{-1}, for the MOS and pn cameras respectively, in order to reject the flares and obtain filtered spectra. Of course, the spectra obtained with the complete event list have a better

Table 2. Performed and useful exposure times for all *XMM-Newton* instruments. The useful RGS exposure time is considerably reduced due to a strong flare of soft protons. The fourth column yields the background-corrected count rate for the source, between 0.4 and 10 keV for EPIC, and between 0.3 and 2.5 keV for RGS. In the case of the RGS instruments, only exposure 0001730201 is considered. The error bars on the count rate represent the ±1 σ standard deviation.

Instrument	Performed duration (s)	Effective exposure (s)	Background-corrected count rate (count s^{-1})
MOS1	25 901	25 435	0.512 ± 0.005
MOS2	25 906	25 473	0.532 ± 0.005
pn	22 759	20 402	1.303 ± 0.009
RGS1	16 495	7490	0.085 ± 0.006
RGS2	16 535	6838	0.101 ± 0.006

signal-to-noise ratio than the spectra obtained from the filtered one because of the longer exposure time (about 25 ks for the whole exposure, instead of about 13 ks for the filtered data).

Following detailed comparison of the results from the two approaches, we did not find any significant difference between the fitting results (see Sect. 4) relevant to both cases. For this reason, we decided not to reject the flare intervals from our EPIC data set, and the effective exposure times (see Table 2) are thus close to the performed observation duration.

Timing analysis of the flare events was also performed to evaluate their impact on the lower energy ($PI < 10\,000$) light curves. We extracted EPIC-pn events with boxes covering the 12 CCDs, but excluding the sources appearing in the field. Light curves were extracted, between *PI* 400 and 10 000, with a *PI* width of 400 units and time bins ranging from 50 to 1000 s. These light curves show that the mean level of flare contribution to the background is only about twice the mean level of the proton unaffected background. Figure 2 shows the count rate versus *PI*, where each point stands for a 400 *PI* channel interval, for the time interval affected by the main flare. The count rate of this background decreases by about a factor 10 from *PI* 400 to 10 000. The bump near *PI* 8000 is due to fluorescent emission lines produced by interaction of charged particles with the camera body material (Lumb 2002). Comparing the overall background level (including the flare) to the count rate in the source region over $PI \in [400 : 800]$, i.e. over the energy range with the highest background level, we find that, at its peak level, the total background contributes only for about 0.9% of the corrected source count rate. The same calculations performed in other energy bands reveal that the background contribution below 5 keV is always at least 4 times lower than the source count rate. This result confirms that the rejection of the soft proton time intervals is irrelevant for the analysis of HD 159176, and that the flare is properly taken into account by the background subtraction step.

However, this conclusion does not hold for RGS data. Indeed, the comparison of spectra obtained with and without the flare epochs revealed significant differences. As a consequence, low-background good time intervals were selected by application of count thresholds to the high energy light curves. These thresholds were evaluated, on the basis of a visual inspection of the light curves. The third (9 ks) exposure was almost completely contaminated by high background, whereas the first (10 ks) observation gave only about 3 ks of useful time. Only the 16 ks exposure could be used, although more than half of it had also to be rejected. For this reason, the effective RGS exposure time is severely reduced, as shown in Table 2.

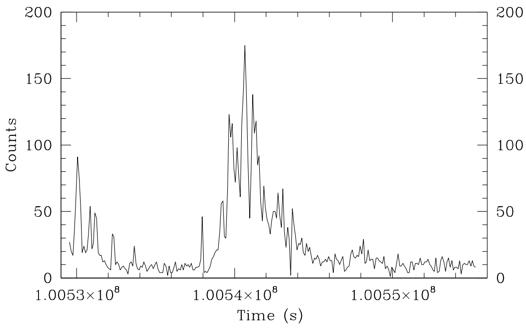

Fig. 1. Light curve for events with $PI > 10\,000$ obtained for the EPIC-MOS2 field and covering the two exposures where the EPIC instruments were operating. A time bin of 100 s was adopted.

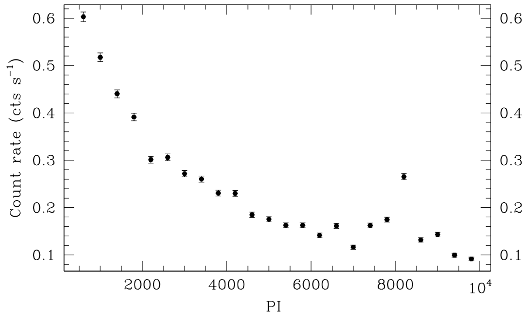

Fig. 2. EPIC-pn count rates versus *PI* for the global background (including the soft proton flares) for a ~350 arcmin^2 area (about a half of the whole detector plane area). The background is much stronger in low energy bands than at higher energies. The bump seen near $PI = 8000$ is due to fluorescent emission lines produced by charged particles interacting with the camera body material. The error bars represent the ±1 σ standard deviation.

4. The EPIC spectrum of HD 159176

The source spectrum was extracted within a circular region of 60 arcsec radius. The intersection with a circular region of radius 15 arcsec centered on a faint point source located at RA = 17:34:40 and Dec = −32:34:33 (Equinox J2000) was rejected. The background was selected within an annular region centered on HD 159176, with an outer radius 1.414 times larger than for the source region. Again, the intersections with 15 arcsec circles centered on two point sources (at RA = 17:34:48, Dec = −32:34:24 and RA = 17:34:48, Dec = −32:35:21) were rejected. Consequently, source and background regions extend nearly over the same area. We also tried to select alternative background regions with boxes distributed near the source region, and avoiding the numerous point sources of the field. This selection did not give a significant difference in the background

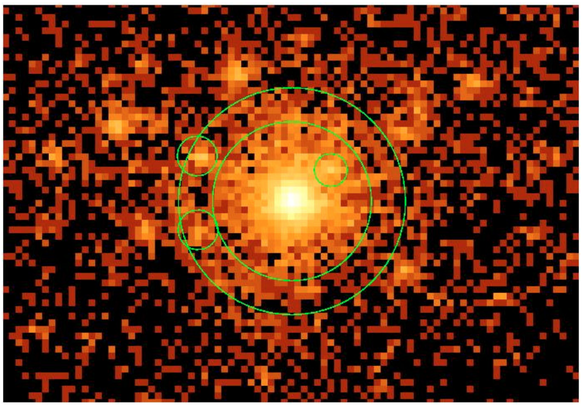

Fig. 3. EPIC-MOS1 source and background regions selected for spectrum extraction. Note the crowded aspect of the field around HD 159176. The source intensities are displayed using a logarithmic scale.

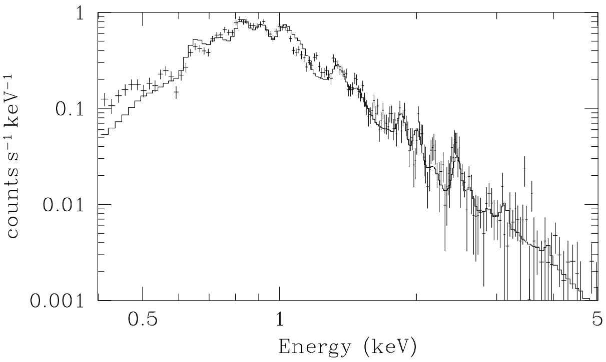

Fig. 4. EPIC-MOS1 spectrum of HD 159176 fitted with the two-temperature `mekal` model between 0.4 and 5.0 keV.

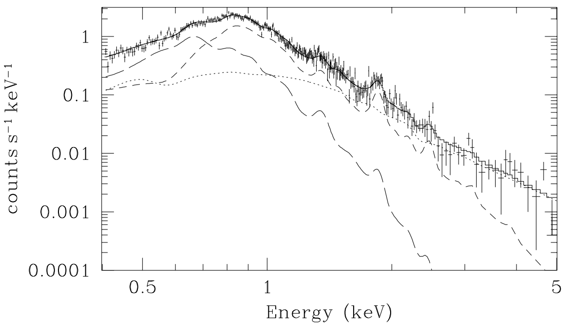

Fig. 5. EPIC-pn spectrum of HD 159176 fitted with the two `mekal` components + power law model between 0.4 and 5.0 keV. The three components are also individually displayed. The power law begins to dominate the spectrum at energies above 2 keV.

corrected spectrum. In the case of the pn camera, an additional difficulty arises from the gaps between the CCDs of the pn detector. We excluded the gaps manually from the source and background regions.

Figure 3 shows the EPIC-MOS1 field with the selected regions for the source and the background in the annular case. The small circular regions are used for the exclusion of the point sources located inside these source and background regions.

The emission lines of the RGS spectrum (see the next section) indicate that at least the low energy X-ray emission of HD 159176 is dominated by a thermal plasma emission. On the other hand, the shock region in a colliding wind binary might accelerate free electrons up to relativistic velocities and in combination with the intense UV radiation fields of the two stars, these particles could produce a hard non-thermal X-ray emission through inverse Compton scattering (see Chen & White 1991; Eichler & Usov 1993). Therefore, we tested various models combining optically thin thermal plasma models with a non-thermal power law component. In the framework of a model where the X-ray emission arises from shocks (either in the wind interaction or in instabilities of the individual winds), one should observe a range of plasma temperatures corresponding to the distribution of the pre-shock wind velocities. Therefore, one expects a priori that more than one thermal component is required to fit the observed spectrum. So, the spectra have been fitted either with two temperature `mekal` thermal plasma models (Mewe et al. 1985; Kaastra 1992) or with models containing a single temperature `mekal` component along with a non-thermal power law component. For each thermal component, solar metallicity was assumed.

The spectra were rebinned to achieve a minimum of 9 and 25 counts per energy bin for the MOS and pn data respectively and then fitted with the XSPEC software (version 11.1.0). For each model, we used an interstellar neutral hydrogen column density of $N_{\mathrm{H}} = 0.17 \times 10^{22}\,\mathrm{cm}^{-2}$ (Diplas & Savage 1994), and a second absorption component to account for circumstellar absorption. The results are listed in Table 3. We note that the best-fitting power law components turn out to be rather steep with photon indices (Γ) above 3.8. This situation is very much reminiscent of the results obtained for the O4 V star 9 Sgr (see Rauw et al. 2002b). Figure 4 illustrates the spectrum of HD 159176 as observed with the MOS1 instrument. Note that including different absorption columns for the individual model components does not improve the quality of the fits. In fact, XSPEC fails to fit at least one of the column densities.

Another model was fitted with some success to the EPIC-pn data. This model consists of three components: 2 thermal `mekal` components and a non-thermal power law component (see Sect. 8 for a possible interpretation of this component). This fit yields a better χ^2_ν, albeit the value obtained for the photon index is once more rather large. The results are summarized in Table 4 for the two background regions selected. One can see that both background techniques yield very similar results. This comforts us with the idea that background selection is not a critical issue for this source, and that the annular region with parasite sources excluded provides a satisfactory description of the actual background. Figure 5 displays the pn spectrum along with the best-fit corresponding to this latter model. We note that this three component model yields a significantly better fit to the EPIC-pn spectrum above 2 keV than the two component models.

Table 3. Fitted model parameters for EPIC spectra of HD 159176. The upper part of the table concerns the `wabs`$_{\rm ISM}$`*wabs`$_{\rm WIND}$`*(mekal + mekal)` model, whilst the bottom part summarizes the results for the `wabs`$_{\rm ISM}$`*wabs`$_{\rm WIND}$`*(mekal + power)` model. The $N_{\rm H}$ given in the table refers to the circumstellar (i.e. wind) column assumed to be neutral. The interstellar column density is frozen at 0.17×10^{22} cm^{-2} for all models. The Norm parameter of the `mekal` component is defined as $(10^{-14}/(4\,\pi\,D^2)) \int n_{\rm e}\, n_{\rm H}\, {\rm d}V$, where D, $n_{\rm e}$ and $n_{\rm H}$ are respectively the distance to the source (in cm), and the electron and hydrogen densities (in cm^{-3}), whereas for the power law this parameter corresponds to the photon flux at 1 keV. The error bars represent the 1 σ confidence interval.

	$N_{\rm H}$ (10^{22} cm^{-2})	kT^1 (keV)	Norm^1	kT^2 (keV)	Norm^2	χ^2_ν d.o.f.
MOS1	0.41	0.22	2.04×10^{-2}	1.05	1.51×10^{-3}	2.19
	±0.03	±0.04	$\pm 0.38 \times 10^{-2}$	±0.02	$\pm 0.09 \times 10^{-3}$	197
MOS2	0.39	0.21	2.11×10^{-2}	1.00	1.58×10^{-3}	2.65
	±0.03	±0.04	$\pm 0.40 \times 10^{-2}$	±0.02	$\pm 0.09 \times 10^{-3}$	198
pn	0.35	0.18	1.88×10^{-2}	0.59	2.98×10^{-3}	1.87
	±0.02	±0.03	$\pm 0.26 \times 10^{-2}$	±0.01	$\pm 0.17 \times 10^{-3}$	321

	$N_{\rm H}$ (10^{22} cm^{-2})	kT (keV)	Norm^1	Γ	Norm^2	χ^2_ν d.o.f.
MOS1	0.26	0.30	4.69×10^{-3}	4.01	1.87×10^{-3}	1.65
	±0.02	±0.01	$\pm 0.84 \times 10^{-3}$	±0.09	$\pm 0.18 \times 10^{-3}$	197
MOS2	0.24	0.29	5.08×10^{-3}	3.80	1.69×10^{-3}	1.99
	±0.02	±0.01	$\pm 0.89 \times 10^{-3}$	±0.08	$\pm 0.16 \times 10^{-3}$	198
pn	0.28	0.28	6.72×10^{-3}	4.09	1.67×10^{-3}	1.70
	±0.01	±0.01	$\pm 0.80 \times 10^{-3}$	±0.08	$\pm 0.14 \times 10^{-3}$	321

Table 4. Fitted model parameters for the EPIC-pn spectrum of HD 159176 for two different background estimation techniques. The adopted model is `wabs`$_{\rm ISM}$`*wabs`$_{\rm WIND}$`*(mekal + mekal + power)`. The column densities given in the table refer to the circumstellar material. The interstellar column density is frozen at 0.17×10^{22} cm^{-2}. The error bars represent the 1 σ confidence interval.

	$N_{\rm H}$ (10^{22} cm^{-2})	kT^1 (keV)	Norm^1	kT^2 (keV)	Norm^2	Γ	Norm^3	χ^2_ν d.o.f.
Annulus	0.20	0.20	4.39×10^{-3}	0.58	1.79×10^{-3}	3.50	7.35×10^{-4}	1.11
	±0.02	±0.01	$\pm 1.05 \times 10^{-3}$	±0.01	$\pm 0.19 \times 10^{-3}$	±0.12	$\pm 1.25 \times 10^{-4}$	319
Boxes	0.18	0.21	3.66×10^{-3}	0.59	1.72×10^{-3}	3.43	8.12×10^{-4}	1.09
	±0.01	±0.01	$\pm 0.83 \times 10^{-3}$	±0.01	$\pm 0.18 \times 10^{-3}$	±0.10	$\pm 1.13 \times 10^{-4}$	319

The main motivation behind these fits is to provide an overall description of the observed spectral distribution that can then be used to derive fluxes and to check for consistency with previous observations. With the parameter values obtained for these fits, we can determine the flux emitted by HD 159176 between 0.4 and 10.0 keV. For this purpose we adopt the best fitting model obtained for EPIC-pn, i.e. the three component model whose parameters are shown in Table 4. The flux corrected for interstellar absorption only is 5.52×10^{-12} erg cm^{-2} s^{-1}. If we adopt a distance to NGC 6383 of 1.5 kpc, we obtain a luminosity of 1.48×10^{33} erg s^{-1}. This value can be compared to X-ray luminosities obtained with *EINSTEIN* (Chlebowski et al. 1989) and *ROSAT* (Berghöfer et al. 1996). In the case of *EINSTEIN*, Chlebowski et al. converted the IPC count rates between 0.2 and 3.5 keV into fluxes, assuming a 0.5 keV thermal bremsstrahlung model and an absorption column (0.209×10^{22} cm^{-2}) calculated on the basis of the color excess $E(B-V)$ determined through a relation given by Mihalas & Binney (1981) for an intrinsic color index $(B-V)_0$ of −0.309 and an observed $(B-V)$ color index of +0.04. For *ROSAT*, Berghöfer et al. converted the PSPC count rate (between 0.1 and 2.4 keV) into a flux assuming a 0.73 keV Raymond & Smith (1977) optically thin plasma model. The same absorption column as for *EINSTEIN* was used. The X-ray luminosities scaled to the 1.5 kpc distance are shown in the second column of Table 5 for *EINSTEIN*, *ROSAT*, and *XMM*.

The luminosities derived from the different satellites are quite different. These discrepancies cannot be explained by the differences in the sensitivity ranges of the various instruments. Instead, it seems more likely that the model assumptions used to convert the *EINSTEIN*-IPC and *ROSAT*-PSPC count rates into luminosities are responsible for the discrepant luminosities. To check this, we have used XSPEC to simulate *EINSTEIN*-IPC and *ROSAT*-PSPC spectra of HD 159176.

Table 5. X-ray luminosities and luminosity ratios from *EINSTEIN*, *ROSAT* and *XMM* observations of HD 159176. Luminosities are calculated for a 1.5 kpc distance. The Obs. CR column gives the count rates from Chlebowski et al. (1989) and Berghöfer et al. (1996) respectively for *EINSTEIN* and *ROSAT*, as well as our value for EPIC-pn. The Th. CR column provides the theoretical count rates calculated on the basis of the individual instrument response matrices for the 3 component model of Table 4 (see text).

Satellite	L_X (erg s^{-1})	$L_X/L_{\rm bol}$	Obs. CR (cts s^{-1})	Th. CR (cts s^{-1})
EINSTEIN	4.33×10^{33}	2.89×10^{-6}	0.157	0.138
ROSAT	8.43×10^{32}	5.64×10^{-7}	0.291	0.287
XMM	1.48×10^{33}	9.93×10^{-7}	1.303	1.328

The three component model derived from the fit of the EPIC-pn data (see Table 4) was folded through the response matrices of the IPC and PSPC instruments. The corresponding theoretical count rates, 0.138 cts s^{-1} for the IPC and 0.287 cts s^{-1} for the PSPC, are in very good agreement with the observed values (see Table 5). Therefore, we conclude that the archive data do not reveal evidence for long-term variability of the X-ray flux of HD 159176.

Since the orbit of HD 159176 does not have a significant eccentricity, it is expected that a possible orbital modulation of the X-ray emission from a colliding wind interaction zone would be due entirely to the changing circumstellar column density along the line of sight. However, given the rather low inclination ($i \sim 50°$, Table 1), we expect only a marginal orbital modulation of the X-ray flux at energies above 0.4 keV. At this stage, it is worth recalling that our *XMM* observation of HD 159176 was obtained during orbital phases 0.53–0.66, i.e. shortly after quadrature. Therefore, we expect no strong occultation effect of the X-ray emission from either component or from the wind interaction region: our value of the luminosity should thus reflect the typical X-ray emission of HD 159176.

We use the total bolometric luminosity of HD 159176 as derived from the parameters in Table 1, i.e. 1.49×10^{39} erg s^{-1}, to compute the $L_X/L_{\rm bol}$ ratios given in Table 5. On the other hand, we estimate the X-ray luminosity of the individual components by means of the empirical relation of Berghöfer et al. (1997). The ratio of the sum of the expected X-ray luminosities and the total bolometric luminosity amounts to 1.48×10^{-7}, which is about a factor 7 inferior to the *XMM* value listed in Table 5, suggesting that there exists indeed a moderate excess X-ray emission in HD 159176.

5. The RGS spectrum of HD 159176

Because of the strong soft proton activity and since it turned out to be impossible to merge event lists from separate RGS exposures, we had to restrict our analysis to the results of the pipeline processing of the 16 ks exposure. We extracted first order spectra of HD 159176 via the "rgsspectrum" SAS task. Figure 6 shows RGS1 and RGS2 spectra. The most prominent features in the RGS spectrum are the Lyα lines of Ne X and O VIII, as well as the He-like triplet of O VII and some strong Fe XVII lines. The Ne IX He-like triplet is also present, but the poor quality of our data as well as the blend with many iron lines from various ionization stages hamper the analysis of this part of the spectrum. The temperatures of maximum emissivity of the lines seen in the RGS spectra of HD 159176 span a range from ~2 to ~6×10^6 K (i.e. $kT \sim 0.17$–0.52 keV, see the APED database, Smith & Brickhouse 2000).

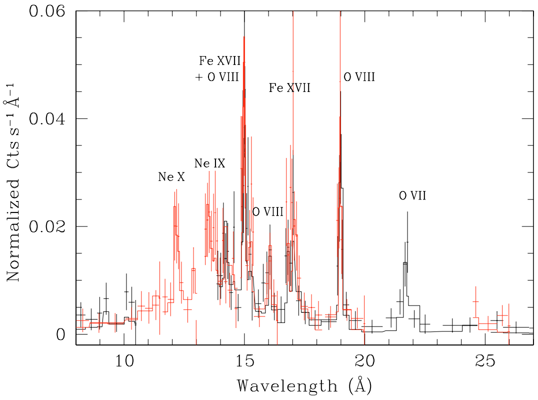

Fig. 6. Combined fit of RGS1 and RGS2 spectra between 8 and 27 Å for a two-temperature `mekal` model. The strongest lines are labelled.

Models were fitted to the RGS spectra. The model including the two-temperature `mekal` component yields the best fits. The combined fit of RGS1 and RGS2 spectra by a two-temperature `mekal` thermal model is also illustrated in Fig. 6. The best fitting parameter values are given in Table 6. With reasonable χ^2_ν values, we obtain temperatures (about 0.16 and 0.60 keV) consistent with the fit parameters of the EPIC pn spectrum. It is interesting to note that these temperatures correspond to the extreme values of the range inferred hereabove from the maximum emissivities of the lines identified in the spectrum. The interstellar column density appears also comparable within the error bars to the EPIC results for the same two-temperature model.

The agreement between the RGS and EPIC pn parameters suggests that we can attempt a simultaneous fit of the spectra from different instruments. For this purpose, we used the two-temperature `mekal` model. The results are summarized in Table 6. First, we fitted the three EPIC spectra together. Next, we also included the RGS spectra.

We see that, in the first case, best fitting parameter values are very close to the results obtained hereabove for the MOS spectra (which are somewhat different from the best fitting parameters of the pn spectrum). On the other hand, including also the RGS spectra in the fit, we obtain a value of the second temperature which is also in good agreement with that obtained for the MOS spectra fitted individually. Finally, we note that fitting the EPIC + RGS data with a differential emission measure model (i.e. the `c6pmekl` model in XSPEC, see Singh et al. 1996) yields a differential emission measure with a very broad maximum spanning from about 0.15 to 1.2 keV, again in reasonable agreement with the temperature ranges inferred from the RGS line spectrum.

Table 6. Model parameters for a two-temperature `mekal` model fitted to the RGS1 and RGS2 spectra of HD 159176, to the three EPIC spectra considered simultaneously and finally to all the *XMM* data taken together. The adopted model is `wabs`$_{\rm ISM}$`*wabs`$_{\rm WIND}$`*(mekal + mekal)`. The column density given in the Table refers to the local (i.e. circumstellar) absorption. The interstellar column density is frozen at 0.17×10^{22} cm^{-2}. The error bars represent the 1 σ confidence interval.

	$N_{\rm H}$ (10^{22} cm^{-2})	kT^1 (keV)	Norm^1	kT^2 (keV)	Norm^2	χ^2_ν d.o.f.
RGS1	0.32	0.16	1.66×10^{-2}	0.62	3.96×10^{-3}	1.36
	±0.11	±0.01	$\pm 1.70 \times 10^{-2}$	±0.04	$\pm 1.81 \times 10^{-3}$	61
RGS2	0.27	0.16	1.37×10^{-2}	0.59	2.67×10^{-3}	1.45
	±0.09	±0.01	$\pm 0.26 \times 10^{-2}$	±0.03	$\pm 1.05 \times 10^{-3}$	71
EPIC	0.40	0.21	2.19×10^{-2}	0.97	1.48×10^{-3}	2.41
	±0.14	±0.02	$\pm 0.23 \times 10^{-2}$	±0.01	$\pm 0.05 \times 10^{-3}$	726
EPIC	0.40	0.21	2.22×10^{-2}	0.96	1.54×10^{-3}	2.28
+ RGS	±0.01	±0.02	$\pm 0.22 \times 10^{-2}$	±0.01	$\pm 0.05 \times 10^{-3}$	862

The best fitting temperatures of the X-ray spectra of HD 159176 are rather low. In fact, these temperatures are roughly typical for presumably single O-stars. On the other hand, for an O + O colliding wind binary, one expects a priori to find harder X-ray emission from the wind interaction region. For instance, in the spectrum of HD 93403, Rauw et al. (2002a) found a hot thermal component with $kT \sim 0.92{-}1.25$ keV, which is significantly hotter than the temperature of the harder component in the EPIC and RGS spectra of HD 159176. However, the smaller orbital separation of HD 159176 (as compared to HD 93403) prevents the stellar winds of its components from reaching their terminal velocities before they collide, leading to lower temperatures in the wind interaction region.

Given the rather poor signal-to-noise ratio of our RGS data, nothing reliable can be said about the morphology of the emission lines. For instance, the strongest line of the spectrum, the O VIII Ly α line at 18.97 Å, is illustrated in Fig. 7. This line appears to be significantly broadened. In fact, the line's *FWHM* estimated from Fig. 7 is about 2500 km s^{-1}, while the *FWHM*s of the instrumental profiles at this wavelength are about 0.06 and 0.07 Å (i.e. 950 and 1100 km s^{-1}) for RGS1 and RGS2 respectively (den Herder et al. 2001). The line appears therefore significantly larger than what would be expected for a coronal emission model (see Owocki & Cohen 2001). We also note that the line profile is neither Gaussian nor Lorentzian. Theoretical models of line emission from either single O-type stars or colliding wind binaries (e.g. Owocki & Cohen 2001; Feldmeier et al. 2003; Henley et al. 2003) predict rather flat-topped profiles with asymmetries depending on the amount of wind absorption and, in the case of binary systems, on the orbital phase. The detection of an orbital modulation of the X-ray line profiles such as predicted by Henley et al. would provide a clear evidence that the lines are formed in the wind collision zone. However, since we have only a single *XMM-Newton* observation of HD 159176 at our disposal, we cannot make any statement about the existence or not of such a modulation. Unfortunately, our current data set does not have the quality needed to perform a detailed comparison between the observed lines and the predictions from the various models. All we can state is that the O VIII Ly α line is slightly blue-shifted by about 300–600 km s^{-1}, though the highest peak in the profile is found near the rest wavelength. Within the error bars, these features are in reasonable agreement with some of the line profiles predicted by Owocki & Cohen (2001) for a single O star wind. On the other hand, the agreement with line profiles formed in a wind interaction zone for a wind momentum ratio of $\eta \sim 1$ (see below) and an orbital phase of 0.53–0.66 (corresponding to $\theta \in [98°, 130°]$ in the formalism of Henley et al. 2003) is slightly less good. At these phases, the colliding wind models predict the highest peak to occur with a significant blue-shift (Henley et al.). We caution however that the line profiles presented by Henley et al. were computed assuming an adiabatic wind interaction, while the wind interaction zone in HD 159176 is most likely radiative (see below).

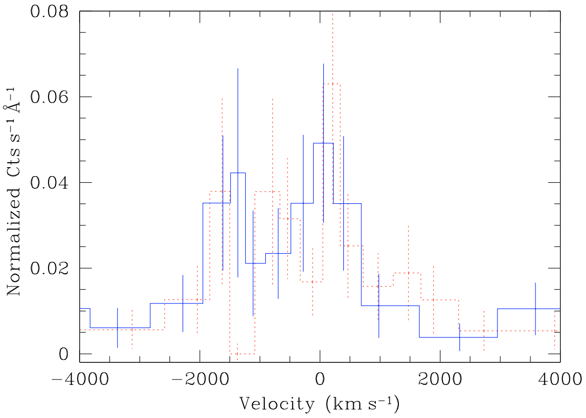

Fig. 7. The O VIII Ly α line at 18.97 Å as seen with the RGS1 (dotted line) and RGS2 (solid line) instrument.

Another noteworthy feature of the RGS spectra of HD 159176 is the fact that the forbidden (f) component of the O VII He-like triplet is very weak. Inspection of the spectrum reveals no significant excess of counts above the level of the pseudo-continuum at the wavelength of the f line, whereas the intercombination (i) and resonance (r) lines are clearly detected at a level of about 7×10^{-5} and 3×10^{-5} photons cm^{-2} s^{-1}

respectively. Unfortunately, the limited quality of our data does not allow us to perform sophisticated fits of the triplet. Nevertheless, we have fitted the triplet by three Gaussians plus a constant (to mimic the pseudo-continuum) where we requested that the three Gaussians should have the same Doppler shift and the same width. This fit yields an f/i ratio of 0.08 which can probably be considered as a safe upper limit. A low f/i ratio is not unexpected. In fact, in the winds of hot early-type stars, the intense UV radiation induces a strong coupling between the upper level of the forbidden line and the upper level of the intercombination line, leading to an enhancement of the i and a decrease of the f component (Porquet et al. 2001). For the O VII He-like triplet, Porquet et al. calculate an f/i ratio of less than 3×10^{-3} for a star with a radiation temperature $\geq 30\,000$ K and for a dilution factor $w \geq 0.1$. In HD 159176, this mechanism can act on the intrinsic X-ray emission of the individual binary components as well as on the X-ray emission from the colliding wind region. Indeed, assuming that the wind-interaction zone lies about half-way between the two stars, the UV radiation field of each star is diluted by $w = 0.15$ at the location of the colliding wind region. The enhanced plasma density in the colliding wind region could further reduce the f/i ratio (Porquet et al. 2001), though this is likely to be only a second order effect in the case of a hot, close binary such as HD 159176.

Finally, a further comparison of the RGS spectrum (Fig. 6) with RGS spectra obtained for stars such as 9 Sgr (Rauw et al. 2002b) or ζ Pup (Kahn et al. 2001) shows that the HD 159176 spectrum does not display the N VII λ 24.8 Å line. To find out whether this is due to a reduced N abundance or not, we fitted simultaneously RGS1 and RGS2 spectra with variable abundance `mekal` models, allowing the nitrogen abundance to vary (with other abundances frozen at the solar value). The resulting fit suggests a slightly (2.85 ± 1.26) enhanced N abundance (with respect to solar abundance) while we recover the temperatures for the RGS fits within the error bars. Moreover, the N VII λ 24.8 Å line appears clearly in the theoretical RGS spectrum of HD 159176 when the absorption columns are set to zero, albeit this line nearly completely disappears when the absorption components are set to the values derived in our fit. Therefore, the absence of the N VII line in our observed spectrum is due to the strong absorption that photons at this rather low energy suffer when they encounter the circumstellar or interstellar medium. Also, the relative intensities of oxygen lines compared to other elements seem quite higher in the spectrum of HD 159176. At this stage, it is worth recalling that ζ Pup is an evolved object and the line intensities in its RGS spectrum reflect the signature of the CNO process (Kahn et al. 2001). On the other hand, we do not expect to see such an effect in the spectrum of a relatively unevolved system such as HD 159176.

6. Short-term variability of the X-ray flux

Hydrodynamic models of colliding wind binaries predict the existence of various kinds of dynamical instabilities that should affect the wind interaction region (Stevens et al. 1992; Pittard & Stevens 1997) and manifest themselves through a rapid variability of the emerging X-ray flux in addition to the much slower orbital phase-locked modulation. Theoretical considerations (Stevens et al. 1992) indicate that the nature of these instabilities depends on the efficiency of radiative cooling in the shocked region which is a function of the orbital separation and of the wind properties of the components of the binary system. Previous X-ray satellites lacked the required sensitivity to look for the signature of these variations. Owing to the large collecting area of the X-ray mirrors onboard *XMM-Newton* and since HD 159176 is rather X-ray bright, we can use our present data set to seek for the signature of these instabilities.

To investigate the putative short-term variability of HD 159176, we divided the effective exposure into short time intervals. In the case of the MOS instruments, we used 2.1 ks time intervals. We obtained 9 and 10 equal time intervals respectively for MOS1 and MOS2. Because the good time intervals (GTIs) of the different instruments are not strictly identical, the time bins of the time series of the two instruments do not match exactly. A spectrum was extracted for each time bin through the same procedure as described in Sect. 4. Each spectrum was rebinned, to get at least 4 counts per energy channel, and fitted with a two temperature `mekal` model.

Some parameters seem indeed to change with time but no correlation is found between MOS1 and MOS2. In each case, the lower temperature does not vary significantly while the higher temperature component displays larger variations. No systematic trend is found for these variations. The same study was carried out for EPIC-pn data using the two models described in Sect. 3 for time intervals of 2 ks. In this case, we do not observe any significant variation in the model parameters either.

A more model-independent way to check for variability consists in studying the run of count rates for particular time bins, over different energy ranges: see for instance Fig. 8 for count rates between 0.4 and 10.0 keV within 1 ks time bins. This figure does not reveal any significant correlation between the different EPIC instruments. The same conclusion applies also for narrower energy ranges selected within this same interval. Moreover, we see that count rates in all energy bands are nearly constant within 2 σ for all instruments.

Finally, we extracted light curves for the three EPIC instruments with smaller time bins of 200 s and 100 s, within spatial regions corresponding to the source and the background areas selected for spectra extraction (Sect. 4). Because of standard GTIs, some of the time intervals were shorter than 200 s (or 100 s) and we therefore scaled the count rates to the effective exposure time within each bin. The background corrected count rates display some fluctuations but do not reveal any correlation between the various instruments. χ^2 tests performed on these corrected light curves confirm this lack of short time scale variability.

7. Confrontation with theoretical models

To complete our study, we can compare the overall properties of the observed spectrum of HD 159176 with the predictions of colliding wind models.

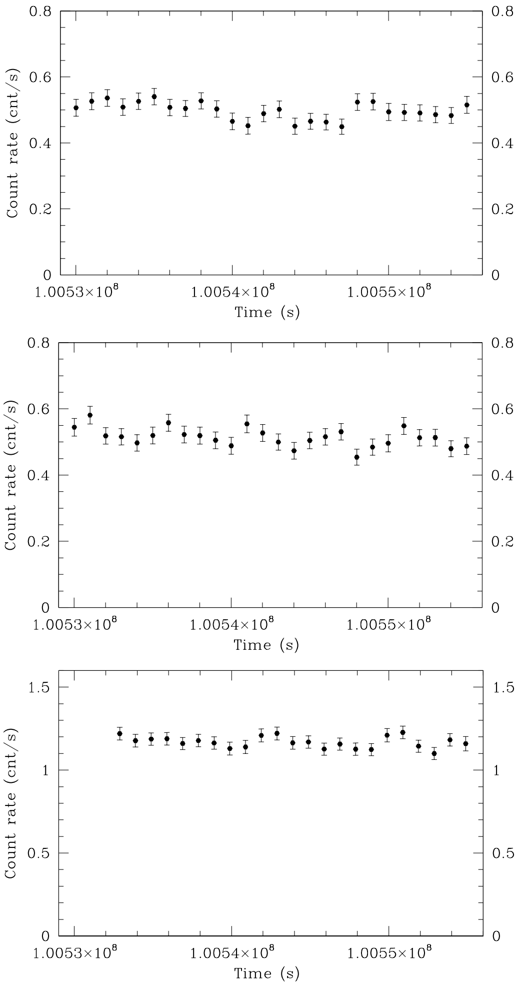

Fig. 8. Count rates evaluated in the 0.4–10.0 keV energy band versus time for MOS1 (upper panel), MOS2 (middle panel) and pn (bottom panel). The time bin used is 1000 s for all instruments. The error bars represent the $\pm 1\,\sigma$ standard deviation.

7.1. Analytical and hydrodynamical estimates of the X-ray luminosity

A relevant quantity which should be introduced here is the cooling parameter:

$$\chi = \frac{t_{\rm cool}}{t_{\rm esc}} = \frac{v_3^4\, d_7}{\dot{M}_{-7}}$$

where $t_{\rm cool}$, $t_{\rm esc}$, v_3, d_7, and $\dot{M}_{-7}$ are respectively the cooling time, the escape time from the shock region near the line of the centers, the pre-shock velocity in units of 1000 km s^{-1}, the distance from the stellar center to the shock in units of 10^7 km, and the mass loss rate in units of $10^{-7}\,M_\odot\,{\rm yr}^{-1}$ (see Stevens et al. 1992). Depending on the binary parameters, the gas in a colliding wind region could be either adiabatic ($\chi \geq 1$) or radiative ($\chi < 1$). While present day hydrodynamical models probably provide a safe estimate of the X-ray emission in adiabatic winds, their use in a highly radiative situation is more problematic. In fact, for values of χ lower than about 2 or 3, the numerical simulations fail to spatially resolve the cooling length in the wind interaction region. Moreover, the thin-shell instabilities that appear in the simulation of these shocks introduce a mixing of hot and cool material that further complicates the prediction of the X-ray emission. Therefore, in the radiative case, it seems more appropriate to use analytical results to estimate the X-ray luminosity.

Turning back to HD 159176, we can estimate the value of the relevant cooling parameter using the binary parameters given in Table 1. In a close binary such as HD 159176, the stellar winds do not reach v_∞ before they collide. The pre-shock velocity should be in the range 850–2000 km s^{-1}. The upper boundary of this range is obtained assuming a "standard" wind velocity law with $\beta = 0.6$ and $v_\infty = 2850$ km s^{-1}; the lower boundary corresponds to the value expected if we account for radiative inhibition effects for equal stars with a separation of about 40 $R_\odot$ (see Fig. 4 of Stevens & Pollock 1994). These pre-shock velocity values are derived along the line connecting the centers of the stars, where the bulk of the X-ray emission is generated.

Therefore, adopting the parameters of Table 1 and a pre-shock velocity lower than 2000 km s^{-1}, the resulting value of χ is typical of radiative winds. The corresponding intrinsic X-ray luminosity can be estimated for each component of the binary through the following relation taken from Pittard & Stevens (2002):

$$L_{\rm X,intr} \sim 0.5\,\Xi\,\dot{M}\,v^2$$

where Ξ accounts for a geometrical factor (1/6 for equal winds) and a small inefficiency factor (hence we used $\Xi = 0.1$), and v is the wind speed at the contact surface. In the conditions described hereabove, $L_{\rm X,intr}$ is significantly larger than our observed value. For a pre-shock velocity of 2000 km s^{-1}, $L_{\rm X,intr}$ ($\approx 8 \times 10^{35}$ erg s^{-1}) is more than a factor 400 too high. Note that the intrinsic luminosity needs to be corrected for stellar wind absorption before it can be compared to the observed luminosity. However, as we will see below, this correction hardly exceeds a factor of a few tens and is therefore not sufficient to account for such a huge discrepancy. If we reduce the pre-shock velocity to 850 km s^{-1}, the intrinsic luminosity becomes $L_{\rm X,intr} \approx 10^{35}$ erg s^{-1}, which is still much too large.

In order for our predicted luminosity to match the observed value of $L_{\rm X}$, we need to reduce the mass-loss rates. As a second step, we therefore adopt $\dot{M} = 6 \times 10^{-7}\,M_\odot\,{\rm yr}^{-1}$ for both stars as suggested by Howarth & Prinja (1989). With a pre-shock velocity of 2000 km s^{-1}, χ amounts to ~3.5, allowing us to derive the X-ray flux from a hydrodynamical simulation. For this purpose, we used the code of Pittard & Stevens (1997) which is based on the VH-1 numerical code (see Blondin et al. 1990). This code uses a lagrangian piecewise parabolic method to solve the partial differential equations of hydrodynamics followed by a remap onto a fixed grid after each time step (for details see the references in Pittard & Stevens 1997). The simulations do not include radiative driving and assume instead constant wind speeds. A theoretical attenuated X-ray spectrum was generated from a 3D radiative transfer calculation on the hydrodynamical results, and we found $L_{\rm X,att} \sim 2 \times 10^{34}$ erg s^{-1}. Hence it seems that $\dot{M}$ must be reduced below the Howarth & Prinja (1989) value in order to account for the observed L_X.

In order to explore a wider range of the wind parameter space, we decided to test an alternative approach that allows us to overcome some of the practical limitations encountered hereabove. This is described in the following section.

7.2. Steady-state colliding wind model

The main problem when modelling the X-ray emission from a close binary system like HD 159176 is that the wind-wind collision can be highly radiative. Since it is difficult, if not impossible, to resolve the width of such shocks in hydrodynamical calculations, the necessary information to compute the X-ray emission is lost. For this reason, Antokhin et al. (2004, in preparation) have developed a steady-state model able to account for the physics of radiative shocks in a way suitable to lead to a relevant discussion of colliding wind X-ray emission from close binary systems.

In this approach, Antokhin et al. (2004) completely neglect instabilities and orbital rotation. Assuming a strong radiative cooling, both shocks generated in the primary and the secondary winds are thin. The pre-shock wind velocities are specified by a $\beta-$law, and the shape of the contact surface is computed. The wind density and normal velocity are calculated at the exact position of the shock. The 1D hydrodynamic equations are then solved for the case of a radiative post-shock flow. The X-ray spectrum is computed, and the process is repeated along the contact surface to obtain an integrated spectrum. The absorption of the X-ray radiation by the winds and by the shocks is determined using warm material opacity tables obtained with the CLOUDY v.94.00 code (`http://thunder.pa.uky.edu/cloudy/`). This model neglects any dissipative process and assumes that all the kinetic energy of the winds is radiated, thus giving an upper limit to the actual X-ray luminosity. For further details about this model, we refer the reader to Antokhin et al. (2004).

7.2.1. Equal winds

Following this approach, a grid of models was generated and converted into a table model suitable to be used within XSPEC. As a first step, the assumption of equal winds was adopted. The parameters of the model are the mass loss rate and the terminal velocity. The parameter space covers $\dot{M}$ values from 2.5×10^{-8} to 6.0×10^{-6} $M_\odot$ yr^{-1}, and v_∞ values between 1700 and 2450 km s^{-1}. The luminosities computed by the model were converted into fluxes assuming a distance of 1.5 kpc. The model normalization which scales as the inverse of the distance squared should be unity if all the model assumptions are correct and the distance is indeed equal to 1.5 kpc. Figure 9 shows the emerging (i.e. after absorption by circumstellar material) luminosity between 0.5 and 10.0 keV versus the mass loss rate and the terminal velocity. This figure shows clearly that the general trend followed by the luminosity is to decrease as the velocity decreases. For $\dot{M}$ values lower than about 8.5×10^{-7} $M_\odot$ yr^{-1}, L_X increases as the mass loss rate increases, but it decreases with increasing mass loss rate for higher $\dot{M}$ values. This turnover in the behaviour of the luminosity versus $\dot{M}$ is due to the increase of the optical depth of the warm wind material as the wind density increases.

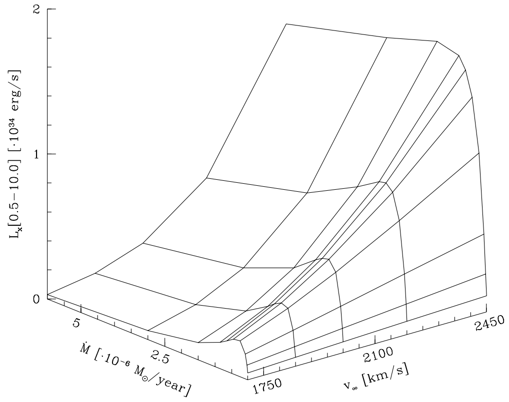

Fig. 9. Emerging X-ray luminosity between 0.5 and 10.0 keV as a function of the mass loss rate and the terminal velocity as computed for a distance of 1.5 kpc. The parameter space covers values between 2.5×10^{-8} and 6.0×10^{-6} $M_\odot$ yr^{-1} for the mass loss rate, and between 1700 and 2450 km s^{-1} for the terminal velocity.

To take into account the fact that intrinsic emission of the individual winds is supposed to contribute to the observed spectrum, we used a `mekal` thermal plasma component in addition to the colliding wind component. Interstellar absorption is accounted for by using an absorption column frozen to the value used in Sect. 4. The best fit of our EPIC-pn spectrum requires an additional power law component to fit the high energy tail already mentioned in the framework of the EPIC-pn spectral analysis in Sect. 4. The physical motivation of this power law is discussed in Sect. 8[1]. Figure 10 shows the fit obtained between 0.4 and 10.0 keV where the three individual components are displayed. The fluxes of the three components in the 0.4–10.0 keV band are 1.5×10^{-12} erg s^{-1}, 3.8×10^{-12} erg s^{-1} and 5.7×10^{-13} erg s^{-1} respectively for the `mekal`, the colliding wind and the power law components. This fit corresponds to $\log \dot{M} = -6.67 \pm 0.09$, $v_\infty = 1905 \pm 50$ km s^{-1}, and a normalization parameter of 0.24 ± 0.04. In the best fit model, the `mekal` component has a temperature of 0.29 ± 0.01 keV, and the power law has a photon index of 2.50 ± 0.22. While this model provides an acceptable fit to the data – the reduced χ^2_ν is 1.14 for 319 d.o.f. – we note that the best fit value of the normalization parameter is a factor 4 lower than expected. Because of the membership of HD 159176 to the open cluster NGC 6383, it seems quite unlikely that the distance could be off by as much as a factor 2. Moreover, in order to explain the low normalization parameter, the actual distance of HD 159176 would have to be larger by a factor 2 whereas an estimate of the distance on the basis of the expected absolute magnitude of an O7V + O7V binary rather suggests that the distance of HD 159176 might be

---

[1] We explored higher velocity values to try to fit this high energy tail with the colliding wind model. However, these models yield an increase of the intensity of the Fe K line at about 6.7 keV up to a level that is totally inconsistent with our data.

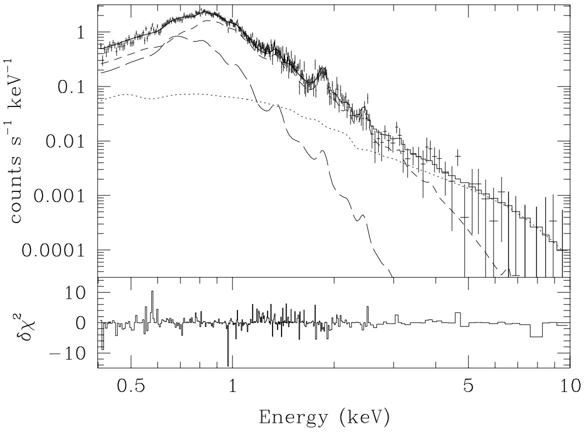

Fig. 10. EPIC-pn spectrum of HD 159176 fitted with a `mekal` + colliding wind + power law model between 0.4 and 10.0 keV in the case of equal winds. The contributions of the three components are also individually displayed: the long-dashed, short-dashed, and dotted lines are respectively the `mekal`, wind-collision, and power law components.

less than 1.5 kpc[2]. If the normalization value is frozen to one, the model clearly overestimates the data mostly between 1 and 5 keV, leading to an unacceptable χ^2. Therefore, the low normalization value probably means that the model predicts, for the derived $\log\dot{M}$ and v_∞, a luminosity which is too large by about a factor of 4. A similar result is obtained for a simultaneous fit of MOS1 and MOS2 data with the same model. The only difference is a somewhat higher terminal velocity (v_∞ = 2190 ± 50 km s^{-1}), compatible with the higher temperature obtained for `mekal` models described in Sect. 4, and a stronger disagreement of the normalization parameter which is a factor about 8 too low.

The results of this subsection can be summarized as follows. Exploring a domain of the parameter space that includes the full range of reasonable values of $\dot{M}$ and v_∞ for stars of spectral type O7 ± one subclass, we have found a model where the interplay between emission and circumstellar absorption allows to reproduce the observed spectral shape. However, this model as well as all other combinations of $\dot{M}$ and v_∞ in this domain of the parameter space fail to reproduce the observed luminosity. The most likely explanation for this failure is that one or several of the model assumptions break down in the case of HD 159176. One possibility that we briefly explore in the following section could be that the stars have winds of unequal strengths.

7.2.2. Unequal winds

Although Pachoulakis (1996) inferred only slightly different wind momenta (see Table 1), we note that the stellar parameters ($T_{\rm eff}$, $L_{\rm bol}$) derived by Pachoulakis yield very different values of $\dot{M}$ (9×10^{-7} and 1×10^{-7} $M_\odot$ yr^{-1}) when passed through the relation of Vink et al. (2001). Such large differences in $\dot{M}$, and hence wind strength, are however at odds with the essentially equal spectral types inferred from optical spectroscopy. Nevertheless, we attempted to establish whether an unequal wind CWB model could reconcile the predicted and observed luminosities. We thus developed a grid of models depending on four parameters: the terminal velocity of the primary ($v_{\infty,1}$), the mass loss rate of the primary ($\dot{M}_1$), the terminal velocity of the secondary ($v_{\infty,2}$), and finally the wind momentum ratio defined as

$$\eta = \frac{\dot{M}_1\, v_{\infty,1}}{\dot{M}_2\, v_{\infty,2}}.$$

This latter parameter is used to control the ratio of the wind strengths, to avoid any collision of the primary wind with the photosphere of the secondary. An additional normalization parameter as described for the equal wind case is also used.

The velocity parameters are allowed to vary in a range between 1700 and 2500 km s^{-1}, and the allowed values for $\dot{M}_1$ are taken between 3.0×10^{-8} $M_\odot$ yr^{-1} and 6.0×10^{-6} $M_\odot$ yr^{-1}. The parameter η can vary between 1.0 and 1.44. Beyond this upper boundary the stronger wind of the primary crashes onto the secondary surface.

The result of the fit seems only weakly sensitive to the value of η (note that the range covered is quite narrow). If η is frozen to unity and velocities constrained to be equal, the same fitting result as described for the equal wind case is obtained. However, we were not able, with the current model, to obtain a satisfactory fit with a norm parameter close to unity. This result illustrates again the impossibility to reconcile the observed spectrum with the model at its current stage of development, at least within the parameter space we explored.

8. Summary and conclusions

The main results from our study of the *XMM-Newton* data of HD 159176 are the following:

- The study of EPIC and RGS data reveals a soft spectrum which is consistently fitted with a two temperature thermal model. The hottest component is at about 0.6 keV for EPIC-pn and RGS, and about 1.0 keV for EPIC-MOS data. The X-ray luminosity is rather low, with a value of $L_{\rm X}/L_{\rm bol}$ showing a moderate excess (~7) compared to what is expected for isolated stars with the same bolometric luminosity but without any wind-wind interaction.
- Our analysis of RGS data reveals that lines are significantly broadened. For instance, the O VIII Ly α line at 19.0 Å has a full width at half maximum of about 2500 km s^{-1}, in agreement with X-ray lines originating either from shocks distributed throughout the wind or from a colliding wind zone.
- The study of EPIC light curves failed to reveal any significant variability on time scales of 100–2000 s. This indicates that, at least in a system like HD 159176, the hydrodynamic instabilities that might exist in the region of the shocked winds are not able to produce a clear variability of the X-ray emission.

---

[2] With m_V = 5.64 (FitzGerald et al. 1978) corrected for the reddening (A_V = 1.12) and M_V = −4.8 (Conti & Alschuler 1971) for a typical O7V star, leading to M_V = −5.55 for an O7V + O7V system, we infer a distance of about 1.0 kpc only. With M_V = −5.2 (Schmidt-Kaler 1982), the calculated distance is about 1.2 kpc.

- The EPIC spectrum reveals a high energy tail which can not be fitted by thermal models (`mekal` or colliding wind). This hard X-ray emission component was fitted with a power law with a photon index of about 2.5. Its presence could reflect a non-thermal process such as inverse Compton scattering (Pollock 1987; Chen & White 1991). The photon index is not too far from the 1.5 value expected for an X-ray spectrum arising from a population of relativistic electrons generated through an acceleration mechanism involving strong shocks. The possibility of a non-thermal X-ray component was already suggested for instance for a system like WR 110 by Skinner et al. (2002). So far, the most prominent indication of relativistic electrons in stellar winds of early-type stars have been found in the radio domain where a significant fraction of the stars were found to display a non-thermal, probably synchrotron, emission (e.g. Bieging et al. 1989). In the case of HD 159176, radio observations failed to reveal such a non-thermal component, providing only an upper limit on the radio flux at 6 cm (Bieging et al. 1989). However, this does not rule out the possibility that relativistic electrons could be accelerated at the wind collision shock. In fact, the acceleration site would be buried so deeply within the radio photosphere that no synchrotron emission could escape and we would therefore observe HD 159176 as a thermal radio emitter.
- Besides the non-thermal tail, the observed spectral shape can be consistently reproduced using a steady-state colliding wind model with a mass loss rate value of about $1.7{-}2.6 \times 10^{-7}\ M_{\odot}\,\mathrm{yr}^{-1}$ and a terminal velocity ranging between 1850 and 1950 $\mathrm{km\,s}^{-1}$ (or between 2140 and 2240 $\mathrm{km\,s}^{-1}$ for EPIC-MOS data). However, this model is unable to predict X-ray luminosities compatible with the observed spectrum of HD 159176. Theoretical values are systematically higher than the observed X-ray luminosities. This disagreement between theory and observation is discussed hereafter.

The disagreement between our *XMM-Newton* observation and the theoretical predictions could possibly be explained by several factors. First, let us recall that the kinetic power of the collision should be considered as an upper limit on the X-ray luminosity even in a highly radiative system. For instance, some of the collision energy might be taken away by the shocked gas which ends up with negligible velocity and pressure near the line of centers. In order not to pile up at the "stagnation point", this gas must be advected from the system, and the work needed to lift it out of the gravitational potential of the system could take away energy at the expense of X-ray emission. Second, higher values of the parameter η (see the unequal wind case, Sect. 7.2.2) should be considered. Although the current version of the model is unable to deal with the case where the primary wind crashes onto the secondary photosphere, this scenario should be envisaged. Let us emphasize however that the optical spectrum of HD 159176 does not provide support for very large values of η. Third, diffusive mixing between hot and cool material is likely to exist due to the instability of the shock front. As a consequence, the material tends to emit a much softer spectrum (i.e. EUV, or even UV), at the expense of X-rays. Unfortunately, current simulations lack the needed resolution to accurately deal with this mixing. Note that thermal conduction (Myasnikov & Zhekov 1998) is also expected to produce a softer spectrum. Finally, further developments of the current model are needed to address this issue. An improvement of the current steady-state model would be for instance to consider the effect of mechanisms able to lower the predicted luminosities like sudden radiative braking (Gayley et al. 1997), which can potentially occur every time unequal winds interact in a close binary system. In addition, orbital effects should also be included to study such systems.

HD 159176 is the first short period colliding O + O binary studied with the high sensitivity of the instruments on board the *XMM-Newton* satellite. The major point of this system is that the shocks associated with the wind collision are radiative, making them very difficult to simulate with current hydrodynamic models. For the first time, an alternative model has been used to address this case, following a steady-state geometrical approach leading to promising results. To achieve a better understanding of the special case of radiative colliding wind shocks, other close binary systems should be observed in conjunction with further developments of the new theoretical approach followed in this study.

Acknowledgements. Our thanks go to Mathias Ehle (*XMM*-SOC) for his help in processing the EPIC data and to Alain Detal (Liège) for his help in installing the SAS. We wish to thank Andy Pollock (ESA) for discussion. The Liège team acknowledges support from the Fonds National de la Recherche Scientifique (Belgium) and through the PRODEX XMM-OM and Integral Projects. This research is also supported in part by contracts P4/05 and P5/36 "Pôle d'Attraction Interuniversitaire" (SSTC-Belgium). J.M.P. gratefully acknowledges funding from PPARC for a PDRA position. I.I.A. acknowledges support from the Russian Foundation for Basic Research (grant 02-02-17524). This research has made use of the SIMBAD database, operated at CDS, Strasbourg, France and of the NASA's Astrophysics Data System Abstract Service.

References

Antokhin, I. I., Owocki, S. P., & Brown, J. 2004, in preparation

Berghöfer, T. W., Schmitt, J. H. M. M., & Cassinelli, J. P. 1996, A&AS, 118, 481

Berghöfer, T. W., Schmitt, J. H. M. M., Danner, R., & Cassinelli, J. P. 1997, A&A, 322, 167

Bieging, J. H., Abbott, D. C, & Churchwell, E. B. 1989, ApJ, 340, 518

Blondin, J. M., Kallman, T. R., Fryxell, B. A., & Taam, R. E. 1990, ApJ, 356, 591

Chen, W., & White, R. L. 1991, ApJ, 366, 512

Chlebowski, T., & Garmany, C. D. 1991, ApJ, 368, 241

Chlebowski, T., Harnden, F. R. Jr., & Sciortino, S. 1989, ApJ, 341, 427

Conti, P. S., & Alschuler, W. R. 1971, ApJ, 170, 325

Conti, P. S., Cowley, A. P., & Johnson, G. B. 1975, PASP, 87, 327

den Herder, J. W., Brinkman, A. C., Kahn, S. M., et al. 2001, A&A, 365, L7

Diplas, A., & Savage, B. D. 1994, ApJS, 93, 211

Eichler, D., & Usov, V. 1993, ApJ, 402, 271

Feldmeier, A., Oskinova, L., & Hamann, W. R. 2003, A&A, 403, 217

FitzGerald, M. P., Jackson, P. D., Luiken, M., Grayzeck, E. J., & Moffat, A. F. J. 1978, MNRAS, 182, 607

Gayley, K. G., Owocki, S. P., & Cranmer, S. R. 1997, ApJ, 475, 786

Gies, D. R., Bagnuolo, W. G. Jr., & Penny, L. R. 1997, ApJ, 479, 408

Henley, D. B., Stevens, I. R., & Pittard, J. M. 2003, MNRAS, 346, 773

Howarth, I. D., & Prinja, R. K. 1989, ApJS, 69, 527

Jansen, F., Lumb, D., Altieri, B., et al. 2001, A&A, 365, L1

Kaastra, J. S. 1992, An X-ray spectral code for optically thin plasmas, Internal SRON-Leiden Report

Kahn, S. M., Leutenegger, M. A., Cottam, J., et al. 2001, A&A, 365, L312

Lloyd Evans, T. 1979, MNRAS, 186, 13

Lumb, D. 2002, EPIC background files, XMM-SOC-CAL TN-0016

Mewe, R., Gronenschild, E. H. B. M., & van den Oord, G. H. J. 1985, A&AS, 62, 197

Mihalas, D., & Binney, J. 1981, Galactic Astronomy, Structure and Kinematics (San Francisco: Freeman)

Myasnikov, A. N., & Zhekov, S. A. 1998, MNRAS, 300, 686

Owocki, S. P., & Cohen, D. H. 2001, ApJ, 559, 1108

Pachoulakis, I. 1996, MNRAS, 280, 153

Pfeiffer, R. J., Pachoulakis, I., Koch, R. H., & Stickland, D. J. 1997, The Observatory, 117, 301

Pittard, J. M., & Stevens, I. R. 1997, MNRAS, 292, 298

Pittard, J. M., & Stevens, I. R. 2002, A&A, 388, L20

Pollock, A. M. T. 1987, ApJ, 320, 283

Porquet, D., Mewe, R., Dubau, J., Raassen, A. J. J., & Kaastra, J. S. 2001, A&A, 376, 1113

Rauw, G., Vreux, J.-M., Stevens, I. R., et al. 2002a, A&A, 388, 552

Rauw, G., Blomme, R., Waldron, W. L., et al. 2002b, A&A, 394, 993

Rauw, G., De Becker, M., Gosset, E., Pittard, J. M., & Stevens, I. R. 2003, A&A, 407, 925

Raymond, J. C., & Smith, B. W. 1977, ApJS, 35, 419

Schmidt-Kaler, Th. 1982, Physical Parameters of the Stars, Landolt-Börnstein: Numerical Data and Functional Relationships in Science and Technology, New series, Group VI, vol. 2b (Berlin: Springer-Verlag)

Seggewiss, W., & de Groot, M. 1976, A&A, 51, 195

Singh, K. P., White, N. E., & Drake, S. A. 1996, ApJ, 456, 766

Skinner, S. L., Zhekov, S. A., Güdel, M., & Schmutz, W. 2002, ApJ, 572, 477

Smith, R. K., & Brickhouse, N. S. 2000, Rev. Mex. Astron. Astrofis. Ser. Conf., 9, 134

Stevens, I. R., & Pollock, A. M. T. 1994, MNRAS, 269, 226

Stevens, I. R., Blondin, J. M., & Pollock, A. M. T. 1992, ApJ, 386, 265

Stickland, D. J., Koch, R. H., Pachoulakis, I., & Pfeiffer, R. J. 1993, The Observatory, 113, 204

Strüder, L., Briel, U., Dennerl, K., et al. 2001, A&A, 365, L18

Thomas, J. C., & Pachoulakis, I. 1994, IBVS, 4115, 1

Trumpler, R. J. 1930, PASP, 42, 342

Turner, M. J. L., Abbey, A., Arnaud, M., et al. 2001, A&A, 365, L27

Vink, J. S., de Koter, A., & Lamers, H. J. G. L. M. 2001, A&A, 369, 574

Chapter 4

NGC 6604, a young open cluster containing two non-thermal radio emitters

> In the context of this dissertation, the study of NGC 6604 is of particular interest since this cluster harbours two non-thermal radio emitters: HD 168112 and HD 167971. Mainly on the basis of *XMM-Newton* observations, we successively study the X-ray properties of these two targets. Several results obtained in the radio domain (in collaboration with the ROB) will also be discussed in order to constrain the mechanism responsible for the non-thermal radio emission. Considering these results, along with previous ones resulting from the studies of another non-thermal radio emitter (9 Sgr) and also from the analysis of HD 159176 (see the previous chapter), the main elements of a general scenario for the non-thermal emission from massive stars will be proposed.

NGC 6604 is a rather compact open cluster lying in the Ser OB2 association. The age of the cluster, located at a distance of about 1.7 kpc, was estimated to be 5 ± 2 Myr by Barbon et al. (2000). We obtained two *XMM-Newton* observations of the NGC 6604 open cluster separated by about five months to investigate the X-ray properties of HD 168112 and HD 167971, and our analysis revealed also the presence of several fainter X-ray sources. Most of these sources are probably located in the cluster, and some of them present properties attributable to pre-main sequence candidates. We separated our X-ray study of NGC 6604 in two papers: the first one is devoted to HD 168112 (De Becker et al. 2004a), and in the second one we describe the results we obtained for HD 167971 and for the fainter X-ray sources detected in the *XMM-Newton* field of view (De Becker et al. 2005a). The aim-point of the two *XMM-Newton* observations was set is such a way as to observe simultaneously the two radio non-thermal emitters within a single EPIC field of view. As a consequence, the two targets were observed off-axis and we did not obtain RGS data for any of them.

4.1 The non-thermal radio emitter HD 168112

When this campaign started, there was no information available concerning the multiplicity of HD 168112, and it was therefore considered to be a single star. We intensively investigated its X-ray properties in order to (i) constrain its thermal X-ray emission following the same mechanisms as discussed in Chapter 3, and (ii) search for any putative non-thermal X-ray component in the EPIC bandpass. Moreover, in the context of our collaboration with the ROB, we also obtained crucial information from quasi-simultaneous radio observations of HD 168112 with the VLA. As we obtained two observations of NGC 6604, we were also able to investigate the X-ray and radio variability of HD 168112 on a time-scale of a few months.

In the *X-ray domain*, we obtained good quality spectra most probably pointing to a thermal origin of the X-rays, even though the nature of the hard component is not clearly established. Provided that the hard X-ray emission is thermal, it is characterized by a kT of about 2–3 keV, i.e. too high a temperature to be explained by the intrinsic shocks of individual stellar winds. Moreover, the X-ray flux appears to be highly variable as it decreases by about 30% between our two *XMM-Newton* observations, mostly at energies higher than about 1 keV. Such a behaviour is not compatible with our present knowledge of individual stellar winds, but could possibly be an indication of colliding winds in the presence of a yet unidentified companion.

In the *radio domain*, HD 168112 presents also a strong variability. The radio flux increases by a factor 5–7 between the two VLA observations. Moreover, the radio emission switches from an intermediate spectral index in April 2002 to a non-thermal one in September 2002. This behaviour is clearly what one could expect from a non-thermal radio emitter. Once again, at the time of writing of this dissertation, there is no known mechanism likely to produce such results in the context of single stars.

Considering these results, it appears that HD 168112 might be a rather long period eccentric binary system. In this scenario, the variability in the X-rays can be explained by a variation of the emission measure as a function of the orbital phase. In the radio domain, the variability could also be explained via an eccentric system where the properties of the collision zone undergo some modulations as a function of the orbital phase. Moreover, the alternating detection and non-detection of HD 168112 at 20 cm could be explained if the wind interaction zone would take place outside the radius of the sphere where τ is equal to one at 20 cm at apastron, whilst it would be buried within that sphere at periastron passage.

More recently, Blomme et al. (2005) investigated all the archive VLA and ATCA data available on HD 168112 to try to constrain the time-scale of the long term variations in the radio domain. This study confirmed the highly variable behaviour of HD 168112, and several time-scales ranging between 1 and 2 years were proposed. These time-scales were confronted to the variations suggested by the archive X-ray data discussed by De Becker et al. (2004a). As a result, a recurrent time-scale of about 1.4 yr was proposed, but we note that the archive X-ray data should be considered with caution because of some possible calibration deviations between *ROSAT*-HRI and *ROSAT*-PSPC.

In order to find some unambigous evidence for the binarity of HD 168112, a spectroscopic campaign in the visible is going on. The aim is to check whether significant radial velocity variations attributable to a binary motion can be detected. At the time of the publication of our quasi-simultaneous X-ray and radio observations of HD 168112 (De Becker et al. 2004a), only a few optical spectra were available. The sampling was not optimal to investigate time-scales of a few months to a few years, and all that we could say is that the amplitude of the radial velocity variations should be low. Consequently, the putative

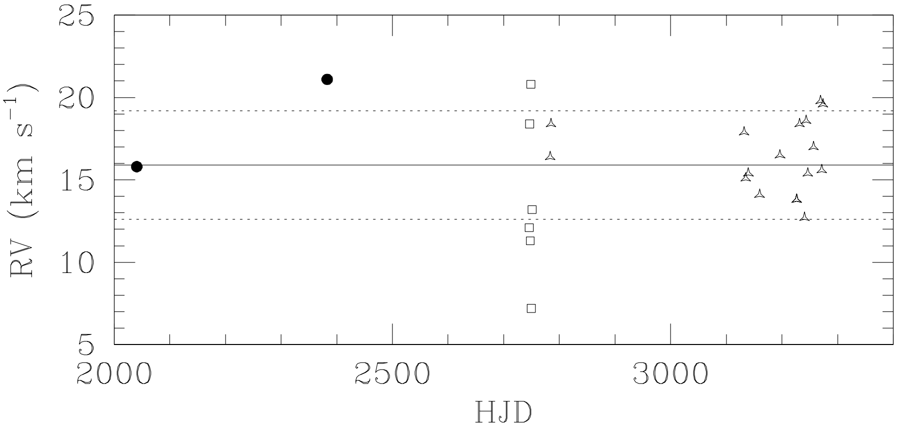

Figure 4.1: Radial velocities of HD 168112 as determined from a set of nine absorption lines (as a function of the heliocentric Julian day –2 450 000). The different symbols stand from different instruments: filled dots for the FEROS echelle spectrograph mounted on the La Silla 1.5 m telescope, open squares for the echelle spectrograph at SPM in Mexico, and triangles for FEROS mounted on the 2.2 m telescope on La Silla.

binary system should be seen under a very low inclination angle. Since then, more optical data have been obtained and we were able to put some constraints on the radial velocity curve of HD 168112 (Rauw et al. 2005b). The conclusion is that we did not detect any significant radial velocity variations on time-scales of a few days, or several months, nor between 1.5 and about 4 years. Our results yield only an upper limit of about 6.6 km s^{-1} (2 σ) on the amplitude of the RV variations. A plot of our radial velocity time series is given in Fig. 4.1.

If HD 168112 is indeed a binary system, the fact that we donot observe any significant radial velocity variations puts stringent limits on the inclination i of the orbital axis of the system relative to the line of sight. Rauw et al. (2005b) estimated the probability that i is lower than the largest inclination (i_{lim}) that can be accommodated within our upper limit on the semi-amplitude of the radial velocity curve, assuming a random distribution of orbital directions in space. For instance, in the case of a period of 500 d, i.e. close to the period of 1.4 yr proposed by Blomme et al. (2005), the inclination should be less than about 20° for a mass ratio of the two companions lower than 5, in order to have a wind interaction as proposed by De Becker et al. (2004a). In this scenario, the probability to have a binary system with an inclination lower than about 20° is only a few percent. The value of i_{lim} increases as longer periods are considered and hence the probability to have an inclination lower than i_{lim} increases slightly.

A&A 420, 1061–1077 (2004)
DOI: 10.1051/0004-6361:20041030

Astronomy & Astrophysics

Quasi-simultaneous *XMM-Newton* and VLA observation of the non-thermal radio emitter HD 168112 (O5.5III(f^+))*

M. De Becker[1], G. Rauw[1,**], R. Blomme[2], W. L. Waldron[3], H. Sana[1,***], J. M. Pittard[4], P. Eenens[1,5], I. R. Stevens[6], M. C. Runacres[2], S. Van Loo[2], and A. M. T. Pollock[7]

[1] Institut d'Astrophysique, Université de Liège, Allée du 6 Août, Bât. B5c, 4000 Liège (Sart Tilman), Belgium
[2] Royal Observatory of Belgium, Avenue Circulaire 3, 1180 Brussels, Belgium
[3] L-3 Communications Government Services, Inc., 1801 McCormick Drive, Suite 170, Largo, MD 20774, USA
[4] Department of Physics & Astronomy, University of Leeds, Leeds LS2 9JT, UK
[5] Departamento de Astronomia, Universidad de Guanajuato, Apartado 144, 36000 Guanajuato, GTO, Mexico
[6] School of Physics & Astronomy, University of Birmingham, Edgbaston Birmingham B15 2TT, UK
[7] ESA/Vilspa, Apartado 50727, 28080 Madrid, Spain

Received 14 January 2004 / Accepted 10 March 2004

Abstract. We report the results of a multiwavelength study of the non-thermal radio emitter HD 168112 (O5.5III(f^+)). The detailed analysis of two quasi-simultaneous *XMM-Newton* and VLA observations reveals strong variability of this star both in the X-ray and radio ranges. The X-ray observations separated by five months reveal a *decrease* of the X-ray flux of ~30%. The radio emission on the other hand *increases* by a factor 5–7 between the two observations obtained roughly simultaneously with the *XMM-Newton* pointings. The X-ray data reveal a hard emission that is most likely produced by a thermal plasma at $kT \sim 2$–3 keV while the VLA data confirm the non-thermal status of this star in the radio waveband. Comparison with archive X-ray and radio data confirms the variability of this source in both wavelength ranges over a yet ill defined time scale. The properties of HD 168112 in the X-ray and radio domain point towards a binary system with a significant eccentricity and an orbital period of a few years. However, our optical spectra reveal no significant changes of the star's radial velocity suggesting that if HD 168112 is indeed a binary, it must be seen under a fairly low inclination.

Key words. radiation mechanisms: non-thermal – stars: early-type – X-rays: stars – radio continuum: stars – stars: individual: HD 168112

1. Introduction

Over the last two decades, X-ray and radio emission of O-type and Wolf-Rayet stars have been intensively studied (e.g., Raassen et al. 2003, Table 9; Cappa et al. 2004). Among the early-type stars detected at radio wavelengths, a subset display unusually high radio flux levels with spectral shapes that deviate significantly from the expectations for thermal free-free emission (Bieging et al. 1989; Williams 1996). This feature is attributed to non-thermal emission, probably synchrotron radiation (White 1985). Such an emission from stellar winds allows us to state that a magnetic field and a population of relativistic electrons exist in the radio emission region. Due to the large opacity of the stellar wind at radio wavelengths, the detected non-thermal free-free emission must arise far away from the stellar surface (~100 R_*), outside the radio photosphere.

Two scenarios have been proposed where relativistic electrons are accelerated through the first order Fermi mechanism occurring in shocks. In the first one, the star is single and electrons are accelerated by shocks distributed across the stellar wind (Chen & White 1991a, and references therein), and arising from the line-driving instability (also known as the deshadowing instability, Feldmeier 2001). In the second scenario, the star is a binary and the shock responsible for the acceleration of electrons to relativistic velocities results from the collision of the stellar winds of the binary components (van der Hucht et al. 1992; Eichler & Usov 1993; Dougherty et al. 2003).

The existence of a population of relativistic electrons implies that *high energy* non-thermal emission could be produced within the stellar winds and/or a within a wind-wind binary collision zone (Pollock 1987; Chen & White 1991a). The idea is

---

Send offprint requests to: M. De Becker,
e-mail: `debecker@astro.ulg.ac.be`

[*] Based on observations with XMM-Newton, an ESA Science Mission with instruments and contributions directly funded by ESA Member states and the USA (NASA). Also based on observations collected with the VLA, an instrument of the National Radio Astronomy Observatory, which is a facility of the National Science Foundation operated by Associated Universities, Inc. Optical data were collected at the European Southern Observatory (La Silla, Chile), and at the Observatorio Astronómico Nacional of San Pedro Mártir (Mexico).

[**] Research Associate FNRS (Belgium).

[***] Research Fellow FNRS (Belgium).

that Fermi accelerated relativistic electrons could be thermalized by the strong UV flux from the hot star through Inverse Compton (IC) scattering thereby generating non-thermal X-ray and γ-ray emission. Following this model, X-ray spectra of such objects should display the signature of IC scattering emission through a hard power law tail in the high energy spectrum (above ~3 keV).

Dougherty & Williams (2000) showed that out of nine non-thermal radio-emitting Wolf-Rayet (WR) stars, seven are visual or spectroscopic binaries. Although the fraction of binaries among the non-thermal emitting O-stars is much less constrained, one may wonder whether binarity is indeed a necessary condition for the occurrence of non-thermal emission and whether these stars exhibit also non-thermal X-ray emission. In an attempt to answer this question, Rauw et al. (2002) investigated the case of the O4((f$^+$)) star 9 Sgr (HD 164794). This presumably single star is indeed a well-known non-thermal radio emitter, and consequently a good candidate to search for a high energy non-thermal counterpart. While 9 Sgr indeed exhibits a hard emission tail in its X-ray spectrum, the thermal or non-thermal nature of this tail could not be established. On the other hand, the optical spectra analysed by Rauw et al. (2002) show some clues that 9 Sgr might be a long period binary.

In the framework of the same campaign, we investigated the case of another presumably single non-thermal radio emitter: HD 168112. In this purpose, we obtained two sets of quasi simultaneous observations (March/April and September 2002) with the *XMM-Newton* satellite and the NRAO Very Large Array (VLA) radio observatory, as well as optical data spread over two years. This rather luminous star ($m_{\rm V}$ = 8.55) lies inside NGC 6604, which is a fairly compact open cluster lying at the core of the HII region S54 (Georgelin et al. 1973). Conti & Ebbets (1977) derived an O5.5((f)) spectral type for HD 168112, while Walborn (1973) assigned an O5 III type. This star is known as a non-thermal radio emitter, with a negative radio spectral index, and a flux level at 6 cm ranging between 1.3 and 5.4 mJy (Bieging et al. 1989).

This paper is devoted to HD 168112. The analysis of the observations of other members of the NGC 6604 cluster, among which the luminous multiple star HD 167971 (O5/8V + O5/8V (+ O8I), Leitherer et al. 1987), will be addressed in a forthcoming paper. In Sect. 2, we describe the *XMM-Newton*, VLA, and optical observations. Sections 3 and 4 are respectively devoted to the analysis of the X-ray spectra and the X-ray variability between our two *XMM-Newton* observations. Section 5 briefly discusses former observations of HD 168112 in the X-ray domain whilst Sects. 6 and 7 deal with the analysis of the radio and optical data. The discussion and conclusions are respectively presented in Sects. 8 and 9.

2. Observations

2.1. X-ray data

NGC 6604 was observed with *XMM-Newton* (Jansen et al. 2001) during revolution 426, on April 6, 2002 (Obs. ID 0008820301, JD 2 452 372.477 – .637), and revolution 504, on September 9 (Obs. ID 0008820601, JD 2 452 526.694 – .868). All three EPIC instruments (MOS1, MOS2, and pn) were operated in the full frame mode (Turner et al. 2001; Strüder et al. 2001), and used the thick filter to reject optical light. We did not obtain any RGS data because HD 167971 and HD 168112 were observed off-axis to make sure that they appear simultaneously in the EPIC field of view. Because of the brightness of the sources in the field, the Optical Monitor was closed during the observations.

The data reduction was performed with version 5.3.1 of the *XMM* Science Analysis System (SAS). The raw files were processed through the "emproc" and "epproc" tasks respectively for EPIC-MOS and EPIC-pn. For EPIC-MOS data analysis, we considered only events with pattern 0–12, and no significant pile-up was found (pattern 26–31). The case of EPIC-pn was more difficult. Indeed, we first applied too severe screening criteria (pattern 0–4, flag = 0), such that bad columns and bad pixels disappeared, as well as pixels along the CCD gaps. Unfortunately, because of the position of HD 168112, the source region is crossed by a gap, and a bad column. As a consequence, only a few percent of the star events remained, which was not sufficient for a reliable analysis to be performed. We therefore relaxed the selection criteria, and selected events with pattern 0–12. Consequently, we have to consider our EPIC-pn spectra of HD 168112 with some caution. Nevertheless, the pn data will be compared to the MOS data in the following sections. Finally, response matrices and ancillary files were generated through the "rmfgen" and "arfgen" tasks respectively.

The combined EPIC image in Fig. 1 shows that the two brightest sources are, in order of increasing luminosity, HD 168112 and HD 167971. Other point sources, presumably belonging to the NGC 6604 open cluster also appear in the field. As already mentioned, the analysis of these sources is postponed to a forthcoming study.

2.2. Radio data

Table 1 presents the log of the NRAO VLA observations. The two observing runs were performed close to the *XMM-Newton* ones: the first VLA observation took place 14 days before the corresponding *XMM-Newton* pointing and the second VLA observation was obtained 2 days after the second X-ray run. For both epochs, data were obtained at 3.6 cm (*X*-band), 6 cm (*C*-band) and 20 cm (*L*-band). For the second epoch we also observed at 18 cm. Fluxes at each wavelength were calibrated on the flux calibrator 3C 48 = 0137+331 (J2000). The fluxes assigned to the flux calibrator are given in Table 2. Each observation of HD 168112 was preceeded and followed by an observation of the phase calibrator 1832-105 (J2000) for the 3.6 and 6 cm bands, and of 1834-126 (J2000) for the 18 and 20 cm ones. All observations were made in two sidebands (denoted IF1 and IF2), each of which has a bandwidth of 50 MHz.

The data reduction was done using the Astronomical Image Processing System (AIPS), developed by NRAO. The observed visibilities of the calibrators were used to determine the instrumental gains. These were then interpolated in time and applied to the HD 168112 visibilities. The Fourier transform of the calibrated visibilities (using robust uniform weighting – see

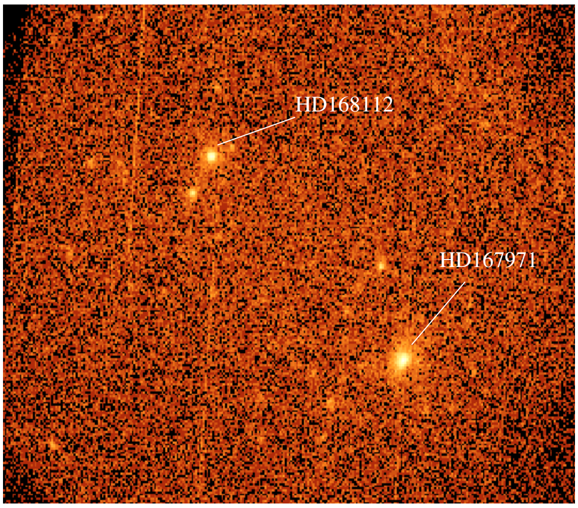

Fig. 1. Combined EPIC (MOS1, MOS2 and pn) image obtained for the first exposure (April 2002). The brightest source is the eclipsing binary HD 167971. HD 168112 is the second brightest source of the field. Other members of the NGC 6604 open cluster appear also as X-ray emitters. The width of the field is about 30 arcmin. The North is up, and the East is on the left.

Table 1. Log of VLA observations. The date, programme and configuration are listed, as well as the wavelength observed and the integration time on HD 168112 (in min). Fluxes are given in Table 10.

Date	Progr.	Config.	λ (cm)	Int. time (min)
2002-Mar.-24	AB1048	A	3.6	11.0
(JD = 2 452 358.089-.148)			6.	10.8
			20.	5.0
2002-Sep.-11	AB1065	CnB[a]	3.6	8.5
(JD = 2 452 528.662-.723)			6.	8.3
			18.	5.0
			20.	4.7

[a]: North arm is in B configuration, East and West arm are in C configuration but with 3 antennas still in B-type positions.

Briggs 1995) resulted in an intensity map, which was then cleaned to remove the effect of the beam.

As HD 168112 is close to the Galactic plane, background structure is expected to be present at radio wavelengths. Only the lower-resolution 18 and 20 cm maps taken on the second epoch show some background. To eliminate this, we dropped all observational data taken on the shortest baselines for these two observations.

2.3. Optical data

Four echelle spectra of HD 168112 were gathered with the Fiber-fed Extended Range Optical Spectrograph (FEROS, Kaufer et al. 1999). In May 2001 and April 2002 the spectrograph was attached to the ESO 1.52 m telescope at La Silla, while in May 2003, it was used at the 2.2 m ESO/MPE telescope at La Silla. The exposure times varied between 25 and 45 min. The spectral resolving power of the FEROS instrument is 48 000. The detector was an EEV CCD with 2048 × 4096 pixels of 15 μm × 15 μm. We used an improved version of the FEROS context within the MIDAS package provided by ESO to reduce the data.

Table 2. Fluxes of the flux calibrator 3C48, based on the 1995.2 VLA coefficients (Perley & Taylor 1999). The two values for each entry correspond to the two 50 MHz sidebands (IF1 and IF2).

λ	Frequency (GHz)		Flux (Jy)	
(cm)	IF1	IF2	IF1	IF2
3.6	8.485	8.435	3.1449	3.1637
6.	4.885	4.835	5.4054	5.4585
18.	1.665	1.635	13.9788	14.1852
20.	1.465	1.385	15.4935	16.1955

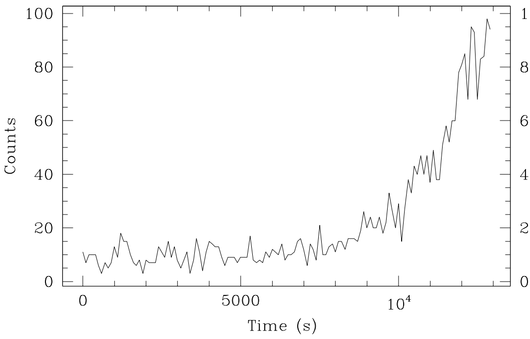

Fig. 2. Raw light curve for events with *PI* > 10 000 for MOS1 during the first exposure, obtained with a time bin of 100 s. The second part of the exposure (after time 9000 s) is strongly affected by the flare.

A series of spectra of HD 168112 were also obtained in April 2003 with the echelle spectrograph at the 2 m telescope of the Observatorio Astronómico Nacional of San Pedro Mártir (SPM). The detector was a Site CCD with 1024 × 1024 pixels of 24 μm squared. The slit width was set to 150 μm corresponding to 2″ on the sky. The data were reduced using the MIDAS echelle package and the individual wavelength-calibrated echelle orders were rectified using carefully selected continuum windows.

3. The EPIC spectrum of HD 168112

3.1. Dealing with high background level episodes

A raw light curve extracted at very high energies (Pulse Invariant (*PI*) channel numbers > 10 000) revealed a strong soft proton flare (Lumb 2002) during the second half of the first exposure as shown in Fig. 2.

The level of the overall background during the flare was estimated following the same procedure as described by De Becker et al. (2004) in the case of the *XMM-Newton* observation of the colliding wind binary HD 159176. We selected events occuring on the whole EPIC-pn detector with boxes

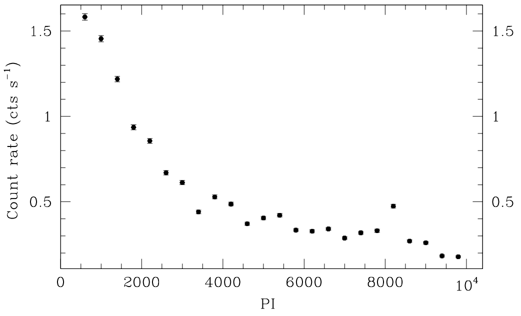

Fig. 3. Total count rate over the 350 arcmin^2 background area (see text) versus PI during the soft proton flare of the first exposure with $PI \in$ [400:10 000] for EPIC-pn. The general shape of the curve is the same as for the mean background before the flare but displays an intensity level that is a factor about 2.5 times higher. The bump near PI 8000 is produced by fluorescent lines generated by the interaction of charged particles with the body of the pn detector (Lumb 2002). The error bars represent the 1-σ standard deviation.

excluding point sources, gaps, and bad columns, leading to a total extraction area of about 350 arcmin^2 (∼half of the EPIC-pn field area). This event list was then used to obtain light curves over intervals 400 PI channels wide, with $PI \in$ [400:10 000]. This operation was performed both on the low background and on the flare parts of the first observation to get a rough estimate of the overall background as a function of the energy. A comparison of these two results reveals that the mean overall background level during the flare is about 2.5 times higher than the mean level during the quiet background period. The overall background count rate is maximum at lower energies and decreases rapidly as PI increases, as shown in Fig. 3. After applying the suitable area scaling factor, we compared the count rates of the overall background and of the background corrected source region in each PI interval. It appeared that the background level during the flare is of the same order of magnitude as the source at energies below 5 keV.

Table 3. Performed duration and effective exposure time of both observations (April and September 2002). The difference between the performed and effective duration of the exposures is only due to overheads.

Instrument	Obs. 1		Obs. 2	
	Performed duration (s)	Effective exposure (s)	Performed duration (s)	Effective exposure (s)
MOS1	13 122	12 855	13 667	13 402
MOS2	13 122	12 896	13 667	13 406
pn	10 546	9525	12 046	10 771

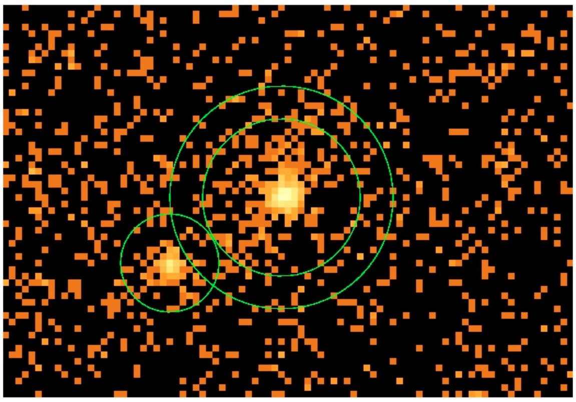

Fig. 4. EPIC-MOS1 source and background regions selected for spectrum extraction. The point source near HD 168112 is excluded from the background annulus region.

We rejected the bad time interval by applying a threshold of 0.16 cts s^{-1} in the case of EPIC-MOS, and 1.10 cts s^{-1} for EPIC-pn to obtain the filtered event list. The first exposure (∼13 ks) was strongly affected by the flare and only about 7 ks were usable for data analysis after filtering. The whole second exposure (∼14 ks) was free from flaring events and no time filtering was considered. To check for the impact of this flare on our spectral analysis of the April 2002 data, we extracted spectra from our filtered and unfiltered event lists for the three EPIC instruments. Both sets of spectra were fitted with some of the models described in Sect. 3.2. The results we obtained were identical within the error bars for both spectral sets. This is because the background subtraction (which is a part of our reduction procedure) cancels the effect of the soft proton flare. As a consequence, we consider that the spectral analysis, at least for a source as bright as HD 168112, can be performed on the whole data set. In the following, all fitting results will refer to the whole exposure for the April observation, without any filtering for soft proton contaminated time intervals. As a consequence, the effective exposure time is very close to the performed duration of the exposure, as shown in Table 3.

3.2. Spectral analysis

The HD 168112 EPIC spectra were extracted within a circular region of radius 60 arcsec. The actual background spectrum was derived from an annulus centered on the source (the external radius is about 85 arcsec), excluding its intersection with a circular region centered on a point source (RA = 18:18:44.3 and Dec = −12:07:51.5, Equinox 2000.0). Figure 4 shows the source and background regions selected in the case of EPIC-MOS1 data. In the EPIC-pn case, a rectangular region was also considered to exclude the gap between CCDs which crosses the source and/or background regions.

EPIC-MOS and EPIC-pn spectra were rebinned to get a minimum of 9 and 16 counts respectively in each energy channel. We fitted spectra within XSPEC (release 11.1.0) using different components including optically thin thermal plasma `mekal` models (Mewe et al. 1985; Kaastra 1992), as well as power laws. On the one hand, the choice of the `mekal` model was motivated by the fact that massive stars are known to display rather soft thermal spectra, as confirmed for example by RGS spectra of ζ Pup (Kahn et al. 2001) or HD 159176 (De Becker et al. 2004). This thermal emission is nowadays attributed to shock heated plasma resulting either from instability-induced shocks distributed throughout the stellar wind (Feldmeier et al. 1997) or from a colliding wind interaction in a binary system (Stevens et al. 1992). On the other hand, as HD 168112 is known as a non-thermal radio emitter, one should also consider the possibility of a non-thermal X-ray counterpart, which would dominate the spectrum at hard energies and should then be modelled by a power law component (Pollock 1987; Chen & White 1991a).

The quality of our fittings was estimated through the χ^2 minimization, and the estimation of the model parameters was obtained on the basis of the resulting best fit. However, one could ask whether the χ^2 statistic is applicable to the case of bins containing a small number of counts. For this reason, we checked the consistency of our results with those obtained with the C-statistic (Cash 1979). For a specific spectral model, this method provides a alternative approach for parameter estimation in the case of small count numbers. Another technique which was considered is a χ^2 statistic with a Churazov weighting, also well designed for small count numbers (Churazov et al. 1996). As a result, we obtained parameter values which are in agreement with the values given in Tables 5 and 6 within the error bars. For this reason, only the standard χ^2 technique is considered in Sect. 3.2.2.

3.2.1. Absorption columns

Different combinations of the above emission components (mekal + power) were tried, to fit the whole X-ray emission within the EPIC bandpass, i.e. between about 0.4 and 10.0 keV. We also included in our fittings the absorption due to both the interstellar medium (ISM) and the wind material.

The ISM absorption column was frozen at 0.58×10^{22} cm^{-2}. This value was obtained assuming $N_{\rm H} = 5.8 \times 10^{21} \times E(B-V)$ cm^{-2} as given by Bohlin et al. (1978). The colour excess was evaluated from an observed $(B-V)$ of +0.69 (Chlebowski et al. 1989), and an intrinsic colour $(B-V)_{\rm o}$ of −0.309 (following e.g. Mihalas & Binney (1981) for an O5 star).

The local absorption column, related to the wind material, has been considered following two approaches. The first one consisted in considering a cold neutral absorption column, as for the case of the interstellar column. In the second approach, we treated the X-ray absorption by the wind in a more realistic way using a stellar wind model (Waldron et al. 1998). The purpose of this model is to deal with the absorption by warm ionized material, taking into account the fact that ionization edges of ionized elements are significantly shifted to higher energies as compared to those of neutral elements. The wind column density above a given radius is calculated assuming a spherically symmetric wind and a standard β velocity law. Cross sections for such a wind model differ essentially from those of cold material below about 1 keV. The stellar parameters used to model the wind opacity of HD 168112 are given in Table 4. On the basis of these opacities, a FITS table was generated in a format suitable to be used within XSPEC as a multiplicative model. The only free parameter of this model is the wind column density ($N_{\rm W}$). In the remaining of the text, this wind absorption model will be referred to as the `wind` component. For both cold and warm absorption columns, solar abundances are assumed.

Table 4. Stellar parameters of HD 168112 taken from Leitherer (1988).

M ($M_\odot$)	70
R_* ($R_\odot$)	16
v_∞ (km s^{-1})	3250
$\dot{M}$ ($M_\odot$ yr^{-1})	2.5×10^{-6}
$L_{\rm bol}$ (erg s^{-1})	3.0×10^{39}
d (kpc)	2

Because of its more realistic treatment of wind absorption, emphasis will be put on the results obtained with the ionized material absorption column. Nevertheless both approaches will be discussed in the next section.

3.2.2. Spectral fittings

We first tried to fit both individual and combined EPIC-MOS spectra, with a cold local absorption component. A single temperature model appeared to be ineffective to fit data above about 3 keV ($\chi^2_\nu \geq 1.3$). Better results were achieved with a two-temperature model. The temperatures, consistent from one exposure to the other, are of the order of 0.2 keV and 2–3 keV for EPIC-MOS data (about 2.3×10^6 K and 3×10^7 K respectively). Only the emission measures suffer a decrease between the two observations. For the second observation, we noted some inconsistencies between the fitting parameters of the MOS1 and MOS2 spectra, especially for the absorption component and the normalization parameter of the softest component. This problem occurred also for the fittings with the `wind` model and it turned out that it was due to a local minimum in the parameter space of the MOS2 spectral fit. To avoid such problems and to improve the statistics of our fittings we shall therefore focus on combined MOS1 + MOS2 fittings.

As stated in Sect. 2, our EPIC-pn data are to be considered with some caution. We first fitted pn spectra under the same conditions as for EPIC-MOS data. The results reveal spectral properties very similar to the EPIC-MOS ones, consisting of a soft component of 0.2 keV and a hard thermal component of about 2–2.5 keV. Because of the quality of the fit and its rather good consistency with EPIC-MOS results, we decided to consider EPIC-pn results as well in our overall discussion of the X-ray spectrum of HD 168112.

As a second step, we performed the same fittings but using a warm local absorption component. The results are summarized in Table 5. Figure 5 shows combined EPIC-MOS1 and EPIC-MOS2 spectra as obtained respectively for the two observations in the case of a two-component thermal model. The temperatures obtained are about 0.3 keV and 2–3 keV (about 3.5×10^6 K and 3×10^7 K respectively), in rather good agreement with those obtained for the cold absorption model. As could be expected, the soft emission component is mostly

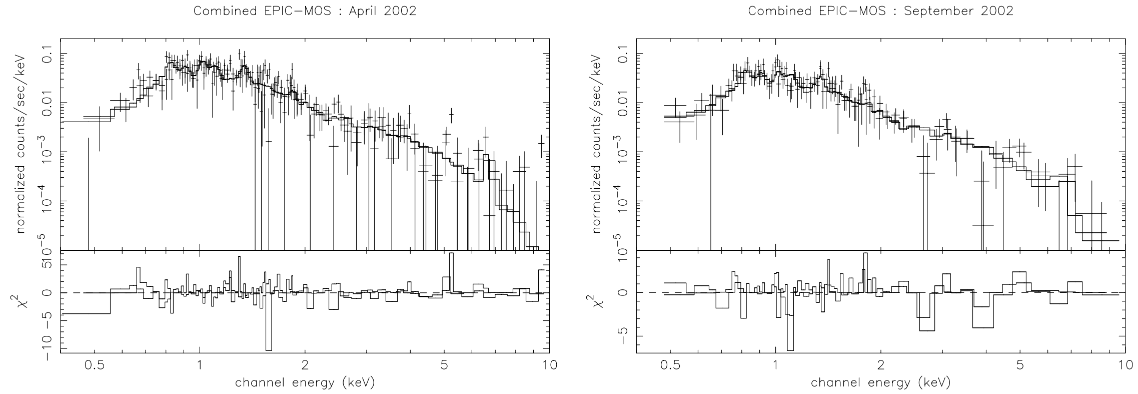

Fig. 5. Combined EPIC-MOS1 and EPIC-MOS2 spectra of HD 168112 fitted with a `wabs`$_{\rm ISM}$`*wind*(2-T mekal)` model between 0.4 and 10.0 keV. The ISM absorption component is frozen at 0.58×10^{22} cm^{-2}. The two model-lines appearing in the upper part are due to the fact that the response matrices of the two instruments are different. *Left panel*: observation 1. *Right panel*: observation 2.

Table 5. Best-fit parameters for EPIC spectra of HD 168112 in the case of a `wabs`$_{\rm ISM}$`*wind*(2-T mekal)` model. Results are given for combined MOS, pn, and combined EPIC spectra. The upper and bottom parts of the table concern the first and second observation respectively. The ISM absorption component (`wabs`$_{\rm ISM}$) is frozen at 0.58×10^{22} cm^{-2}. The quoted circumstellar absorption column is ionized, with $N_{\rm W}$ expressed in cm^{-2}. The last column gives the observed flux between 0.4 and 10.0 keV for each fitting result. The normalization parameter (Norm) of the `mekal` component is defined as $(10^{-14}/(4\,\pi\,D^2)) \int n_{\rm e}\, n_{\rm H}\, {\rm d}V$, where D, $n_{\rm e}$ and $n_{\rm H}$ are respectively the distance to the source (in cm), and the electron and hydrogen number densities (in cm^{-3}). The error bars represent the 1-σ confidence interval.

	Log $N_{\rm W}$	kT_1 (keV)	Norm$_1$	kT_2 (keV)	Norm$_2$	χ^2_ν d.o.f.	Obs. flux (erg cm^{-2} s^{-1})
MOS1 + MOS2	21.90	0.29	5.36×10^{-3}	2.72	3.33×10^{-4}	0.98	4.77×10^{-13}
	±0.07	±0.02	$\pm 2.93 \times 10^{-3}$	±0.62	$\pm 1.01 \times 10^{-4}$	174	
pn	21.89	0.27	5.59×10^{-3}	2.00	4.77×10^{-4}	1.07	4.78×10^{-13}
	±0.07	±0.02	$\pm 3.29 \times 10^{-3}$	±0.33	$\pm 1.14 \times 10^{-4}$	136	
MOS1 + MOS2	21.90	0.28	5.57×10^{-3}	2.29	4.06×10^{-4}	1.01	4.79×10^{-13}
+ pn	±0.05	±0.02	$\pm 2.25 \times 10^{-3}$	±0.31	$\pm 0.76 \times 10^{-4}$	315	
MOS1 + MOS2	21.88	0.26	5.14×10^{-3}	2.36	2.93×10^{-4}	0.90	3.59×10^{-13}
	±0.08	±0.02	$\pm 3.44 \times 10^{-3}$	±0.49	$\pm 0.82 \times 10^{-4}$	116	
pn	21.96	0.25	6.68×10^{-3}	2.16	2.97×10^{-4}	1.01	3.34×10^{-13}
	±0.06	±0.01	$\pm 3.06 \times 10^{-3}$	±0.42	$\pm 0.83 \times 10^{-4}$	89	
MOS1 + MOS2	21.93	0.25	6.14×10^{-3}	2.23	2.97×10^{-4}	0.94	3.44×10^{-13}
+ pn	±0.05	±0.01	$\pm 2.41 \times 10^{-3}$	±0.32	$\pm 0.59 \times 10^{-4}$	210	

affected by the change of the absorption model. We emphasize on the compatibility between the parameters of the combined EPIC-MOS and the combined EPIC-MOS/pn fittings.

We also tried to fit similar models but using two local absorption components, one for each individual `mekal` component. However, it turned out that one of the absorption components could not be constrained by the fit. For this reason, we do not consider the results of this multiple absorption components model in our discussion.

Another uncertainty affects our analysis of the EPIC data with the models discussed hereabove. This issue concerns the fact that the fit results described are related to a local minimum. The other local minimum gave a temperature for the soft component of about 0.55–0.60 keV. The quality of the fit was very similar to that of the previous one obtained with the same data sets. However, it appeared that in some cases this local minimum gave rise to inconsistent values for the warm local absorption component, with rather large error bars as compared to those quoted in Table 5. For this reason, only the results relevant to the local minimum described in Table 5 are considered.

A third `mekal` component was finally added to the model discussed above. This trial yielded temperatures of about 0.30, 0.74 and 3.6 keV for the EPIC-MOS data simultaneously, and of about 0.28, 0.68 and 3.1 keV for the simultaneous fit of the three EPIC data sets. However, this additional component did not improve the χ^2_ν and was therefore not considered in the following.

To illustrate the effect of the various models on our fittings, we consider how these models fit specific lines appearing in our EPIC spectra. In the case of the combined fit of EPIC-MOS data for the first observation, Fig. 7 shows the 1.2 to 2.1 keV region, where two of the most prominent lines of

Table 6. Best-fit parameter values for a `wabs`$_{\rm ISM}$`*wind*(mekal+power)` model for the combined EPIC-MOS data, EPIC-pn, and the three EPIC spectra together. The ISM absorption component is frozen at 0.58×10^{22} cm^{-2}. The local absorption column accounts for the ionization of the wind, with $N_{\rm W}$ expressed in cm^{-2}. The upper and lower parts of the table refer to the first and second observation respectively. For the power law component, the normalization parameter (Norm$_2$) corresponds to the photon flux at 1 keV. The error bars represent the 1-σ confidence interval.

	Log $N_{\rm w}$	kT_1 (keV)	Norm$_1$	Γ	Norm$_2$	χ^2_ν d.o.f.
MOS1 + MOS2	21.86	0.30	4.37×10^{-3}	2.58	2.12×10^{-4}	0.99
	±0.09	±0.03	$\pm 3.02 \times 10^{-3}$	±0.32	$\pm 1.35 \times 10^{-4}$	174
pn	21.80	0.28	3.56×10^{-3}	3.02	3.78×10^{-4}	1.05
	±0.15	±0.03	$\pm 3.94 \times 10^{-3}$	±0.30	$\pm 1.82 \times 10^{-4}$	136
MOS1 + MOS2	21.84	0.29	4.18×10^{-3}	2.82	2.85×10^{-4}	1.01
+ pn	±0.08	±0.02	$\pm 2.55 \times 10^{-3}$	±0.22	$\pm 1.15 \times 10^{-4}$	315
MOS1 + MOS2	21.71	0.26	2.57×10^{-3}	2.97	2.47×10^{-4}	0.82
	±0.21	±0.03	$\pm 3.63 \times 10^{-3}$	±0.27	$\pm 1.15 \times 10^{-4}$	116
pn	21.89	0.26	4.55×10^{-3}	2.93	2.23×10^{-4}	1.00
	±0.87	±0.02	$\pm 3.36 \times 10^{-3}$	±0.32	$\pm 1.41 \times 10^{-4}$	89
MOS1 + MOS2	21.86	0.26	4.30×10^{-3}	2.93	2.33×10^{-4}	0.89
+ pn	±0.70	±0.01	$\pm 2.46 \times 10^{-3}$	±0.22	$\pm 0.96 \times 10^{-4}$	210

the spectrum lie. These lines are Mg XI at about 1.34 keV and Si XIII at about 1.86 keV. The three panels of Fig. 7 show respectively the results from the 2-T model using the cold local absorption, the 2-T model using the warm local absorption, and the 3-T model using the warm local absorption. If the first model reproduces the Si XIII line rather poorly, the situation is significantly improved when the warm material model is used, as seen in the second and third panels. Indeed, for the 2-T model, the soft component temperature is higher in the case of the warm absorption. Consequently, the model describes a plasma whose temperature is closer to the temperature of maximum emissivity ($\sim 10^7$ K) of this Si XIII line, and the same is true for the 3-T model which leads to even higher temperatures. If the Si bundance is allowed to vary (using a 2T-`vmekal` model available within XSPEC), the fit points to a possible overabundance of Si relative to the solar composition (a factor <2), giving rise to a better fit of the Si XIII line without the need to increase the plasma temperature. For the Mg XI line, the model seems to better reproduce the line strength in the case of the 2-T model with warm absorption as well. Allowing the Mg abundance to vary does not significantly improve the quality of the fit. According to the APED database (Smith & Brickhouse 2000) and the SPEX line list (Kaastra et al. 2004), the region between the two lines discussed hereabove harbours a number of other lines (Mg XII at about 1.47 keV being the strongest one, many other lines being due to Fe XXIII and Fe XXIV). Some of these may be responsible for the residuals in Fig. 7.

As stated at the beginning of this section, models including a power law component were also investigated. The results that we obtained are listed in Table 6 for combined EPIC-MOS data, and for EPIC-pn, and finally for the three EPIC instruments together. In this model, a `mekal` thermal component is used along with a power law component. Parameters get values which are very consistent between different data sets, and from one exposure to the other. The typical value of the temperature and of the photon index are respectively ~0.3 keV and ~3 for all instruments. We may note that this photon index value is significantly larger than the value ($\Gamma \sim 1.5$) predicted for IC X-ray emission from relativistic electrons accelerated by strong shocks (Chen & White 1991a). The problem of the local minima encountered in the case of purely thermal models was even more obvious in the case of this model. As it was the case for the 2-T model, the second local minimum gives a temperature for the thermal component of about 0.5–0.6 keV, with the photon index of the power law nearly unchanged. This local minimum was rejected because of the impossibility to obtain a reasonable value of $N_{\rm w}$ for the second exposure, and because of a wider dispersion of the normalization values of all emission components.

We note that the fittings with either purely thermal or thermal + non-thermal models yield essentially equivalent χ^2. However, the likely presence of a moderately strong Fe-K line at about 6.5 keV is not accounted for by models including power laws. If the detection of this line is real (it appears in EPIC-MOS (see Fig. 5) and EPIC-pn spectra (see Fig. 6)), at least for the first observation) and is confirmed by future observations, its presence argues in favour of a thermal origin of the high energy tail of the EPIC spectra.

A word of caution is however necessary here. In fact, the formation of lines mainly occurs through the collisional excitation produced by ions colliding with free electrons. Non-thermal electrons may therefore also contribute to the excitation of several transitions (see e.g. Gabriel et al. 1991; Mewe 1985). Assuming that the iron Kα line is mainly produced by the 1 s–2 p resonance transition of Fe XXV, we have calculated the collisional excitation rates following the formalism outlined in Mewe (1985). It turns out that the ratio between the thermal and non-thermal excitation rates is strongly dependent on the low-energy cut-off energy of the power law distribution of the

Table 7. X-ray fluxes and luminosities of HD 168112. The third column gives the absorbed flux, and the fourth one yields the flux corrected for interstellar absorption. Luminosities corrected for interstellar absorption were determined for the two exposures between 0.4 and 10.0 keV and are given in the fifth column. These luminosities were calculated adopting a 2 kpc distance (see Table 4).

Observation	Data set	Abs. flux (erg cm^{-2} s^{-1})	Corr. Flux (erg cm^{-2} s^{-1})	Corr. luminosity (erg s^{-1})
April 2002	MOS1 + MOS2	4.77×10^{-13}	1.93×10^{-12}	9.15×10^{32}
	MOS1 + MOS2 + pn	4.79×10^{-13}	1.98×10^{-12}	9.38×10^{32}
Sept. 2002	MOS1 + MOS2	3.59×10^{-13}	1.84×10^{-12}	8.72×10^{32}
	MOS1 + MOS2 + pn	3.44×10^{-13}	1.79×10^{-12}	8.48×10^{32}

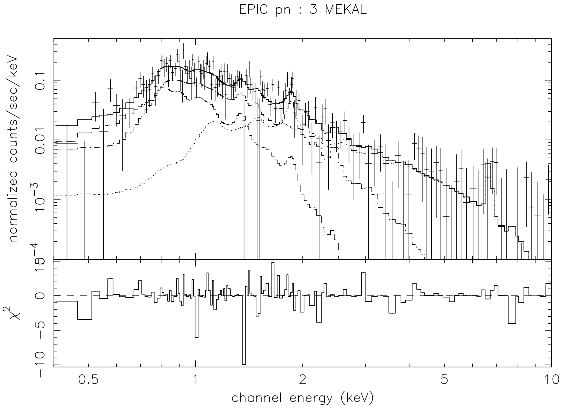

Fig. 6. EPIC-pn spectrum of HD 168112 fitted with a `wabs`$_{\rm ISM}$`*wind*(3-T mekal)` model (solid line) between 0.4 and 10.0 keV for the first observation (April 2002). The ISM absorption component is frozen at 0.58×10^{22} cm^{-2}. The three thermal components are displayed individually (dotted, dashed-dotted, and dashed lines).

relativistic electrons. For most values of this cut-off energy, the excitation rates are comparable. As a result, the contribution of non-thermal electrons to the line formation will be of the same order as the fraction of these electrons to the total number of electrons. Therefore, if the relativistic electrons make up a small fraction (~1%) of the total number of free electrons, their contribution to the Fe K α line should be rather marginal. In summary, the fact that the Fe K line and the high energy continuum can both be reproduced by a 2–3 keV thermal component argues in favour of a thermal origin for this high energy component in the HD 168112 EPIC spectrum.

3.2.3. X-ray fluxes

Based on the best-fit parameters for the two-temperature `mekal` model, we evaluated the fluxes between 0.4 and 10.0 keV. These are listed in Table 5. The fluxes for the combined EPIC-MOS and EPIC-MOS/pn fit, as well as the corresponding luminosities calculated adopting a 2 kpc distance (Bieging et al. 1989), are also given in Table 7. The absorbed X-ray flux suffered a decrease of about 25–30% from April to September. To check for possible systematic errors due to the somewhat different location of the source on the detector from one pointing to the other, we evaluated the exposure map at the position of the source on the detector. Between the two observations, the net exposure difference amounts to about 0.5% for EPIC-MOS1, 2% for EPIC-MOS2, and 3% for EPIC-pn. These differences are too small to explain the amplitude of the flux variation observed for HD 168112. We may note that the fluxes obtained in the case of cold material local absorption are similar to those quoted in Table 5.

Table 8. EPIC-MOS and EPIC-pn count rates obtained for HD 168112 during the two *XMM-Newton* observations between 0.4 and 10.0 keV. The error bars represent the 1-σ confidence interval.

Observation	EPIC MOS1 (cts s^{-1})	EPIC MOS2 (cts s^{-1})	EPIC pn (cts s^{-1})
April 2002	0.060	0.057	0.157
	±0.003	±0.003	±0.006
Sept. 2002	0.037	0.039	0.111
	±0.002	±0.002	±0.004

We compared the luminosities from the two observations to the value expected for a single O star following the relation given by Berghöfer et al. (1997). To do so, we used the bolometric luminosity given by Leitherer (1988), i.e. 3.0×10^{39} erg s^{-1}, and we obtained an expected $L_{\rm X}$ of about 5.3×10^{32} erg s^{-1}. As a result, the expected $L_{\rm X}/L_{\rm bol}$ ratio is 1.75×10^{-7}. We then computed the $L_{\rm X}/L_{\rm bol}$ ratio for both exposures using the $L_{\rm X}$ values given in Table 7. These calculations yield 3.1×10^{-7} and 2.8×10^{-7} respectively for the two observations. As a consequence, we detect no significant luminosity excess. Indeed, for both observations the X-ray level is within a factor 1.7 of what is expected for a single star. This is well within the intrinsic dispersion of the relation given by Berghöfer et al. (1997), which is about a factor 2.

4. Variability of the X-ray flux

As mentioned in Sect. 3.2.3, HD 168112 shows a substantial decrease in its observed flux from the first observation to the second one. This reduction in the X-ray emission is clearly shown by the count rates in Table 8 that drop between the two exposures. Considering the mean combined EPIC-MOS count rate, the decrease is of the order of 35% compared to the first observation value.

The flux determinations in the previous section require a more detailed discussion. Between 0.4 and 10.0 keV, it

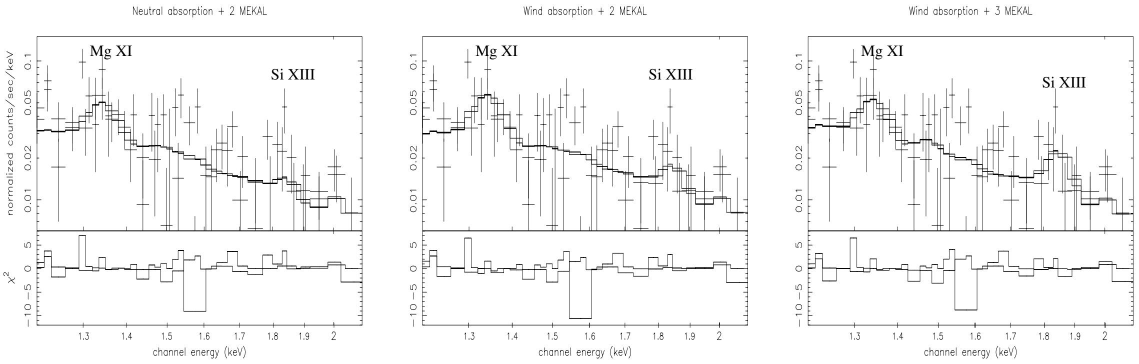

Fig. 7. Combined EPIC-MOS1 and EPIC-MOS2 spectra of HD 168112 fitted with a purely thermal model displayed between 1.2 and 2.1 keV. Data are taken from the April observation. The two model-lines appearing in the upper part are due to the fact that the response matrices of the two instruments are different. The two most prominent lines are Mg XI at about 1.34 keV and Si XIII at about 1.86 keV. The ISM absorption component is frozen at $N_H = 0.58 \times 10^{22}$ cm^{-2}. *Left panel*: `wabs`$_{\rm ISM}$`*wabs*(2-T mekal)`. *Middle panel*: `wabs`$_{\rm ISM}$`*wind*(2-T mekal)`. *Right panel*: `wabs`$_{\rm ISM}$`*wind*(3-T mekal)`.

appears that the variability observed for the combined EPIC-MOS and EPIC-MOS/pn data is about 25–30% for absorbed fluxes, whilst the dereddened fluxes vary by only about 5–10% (see Table 7). However, at energies above ~0.8 keV, the absorbed and dereddened fluxes display the same level of variability. The discrepancy in the variability of flux over the entire energy range arises therefore from the lowest energy bins. In fact, the correction for the interstellar absorption amounts to a factor about 35 to 100 at energies of 0.5–0.7 keV. Thus, although the energy bins below 0.8 keV contribute only to a marginal fraction of the total observed flux (of the order 5%), they account for almost half of the total dereddened flux when corrected for the ISM absorption. Therefore, any variations occurring predominantly at higher energy (typically above 0.8 keV), will be diluted while considering the whole EPIC bandpass of an ISM absorption corrected spectrum and will consequently lose most of its significance. Moreover, fluxes estimated in the soft part of the spectrum are very sensitive to the quality of the data, which in our case is quite poor because of the low count rate in this energy band. We may also emphasize that a moderate uncertainty on the ISM column density could have a considerable impact on the dereddened flux in the lowest energy bins. Considering all these limitations, we decided to focus our discussion on the energy range above 0.8 keV that is less drastically affected by the correction of the ISM absorption.

Table 9 gives the observed (absorbed) fluxes estimated from the two temperature model with the warm wind absorption fitted to the combined EPIC-MOS data. The quoted fluxes are given in three energy bands that were chosen to clearly illustrate the dependence of the variability as a function of the energy band. The softer band (0.8–1.0 keV) displays a variability of about 20%, and between 1.0 and 5.0 keV the variability is about 28%[1]. These values suggest that the variability is somewhat stronger in the hard part of the spectrum. We may also note that the reported variability levels remain unchanged within one or two percent, if we consider fluxes corrected for the interstellar medium.

Table 9. Observed fluxes estimated in the case of the model resulting from combined EPIC-MOS data fitted with the two-temperature model, in the case of the warm local absorption model.

Energy (keV)	April 2002 (erg cm^{-2} s^{-1})	Sept. 2002 (erg cm^{-2} s^{-1})	Variability
0.8–10.0	4.61×10^{-13}	3.30×10^{-13}	~27%
0.8–1.0	0.66×10^{-13}	0.53×10^{-13}	~20%
1.0–5.0	3.24×10^{-13}	2.33×10^{-13}	~28%

Beside the variability observed between the two *XMM-Newton* observing periods, we also looked for short term variations (i.e. variations within a single exposure). We extracted light curves in the four energy bands, respectively (1) 0.4–1.0 keV, (2) 1.0–2.5 keV, (3) 2.5–10.0 keV and 0.4–10.0 keV. For each energy range, event lists were binned with 200 s, 500 s, 1000 s, and 2000 s time intervals. For each time bin of the light curves, and for each energy range (expressed in *PI* channel numbers, considering that 1 *PI* channel corresponds approximately to 1 eV), count rates were calculated with their corresponding standard deviation. These light curves were extracted within the same source and background regions used for spectral analysis (Sect. 3), and all source light curves were corrected for background and Good Time Intervals (GTIs)[2]. Figure 8 shows light curves obtained for a time bin of 1000 s between 0.4 and 10.0 keV for EPIC-MOS and EPIC-pn instruments for the two observations. We do not see any correlation between the fluctuations of the count rate of the three instruments. Moreover, variability tests (χ^2, Kolmogorov-Smirnov, and pov-test as described by

---

[1] We do not consider flux values above 5.0 keV for two reasons: firstly only a few photons are detected in that region of the spectrum, and secondly this energy band is the most strongly affected by the soft proton flare which occurred during the April observation.

[2] Even if no flare contaminated time interval was rejected, standard GTIs are anyway always applied to *XMM-Newton* data, and must be taken into account in every timing analysis.

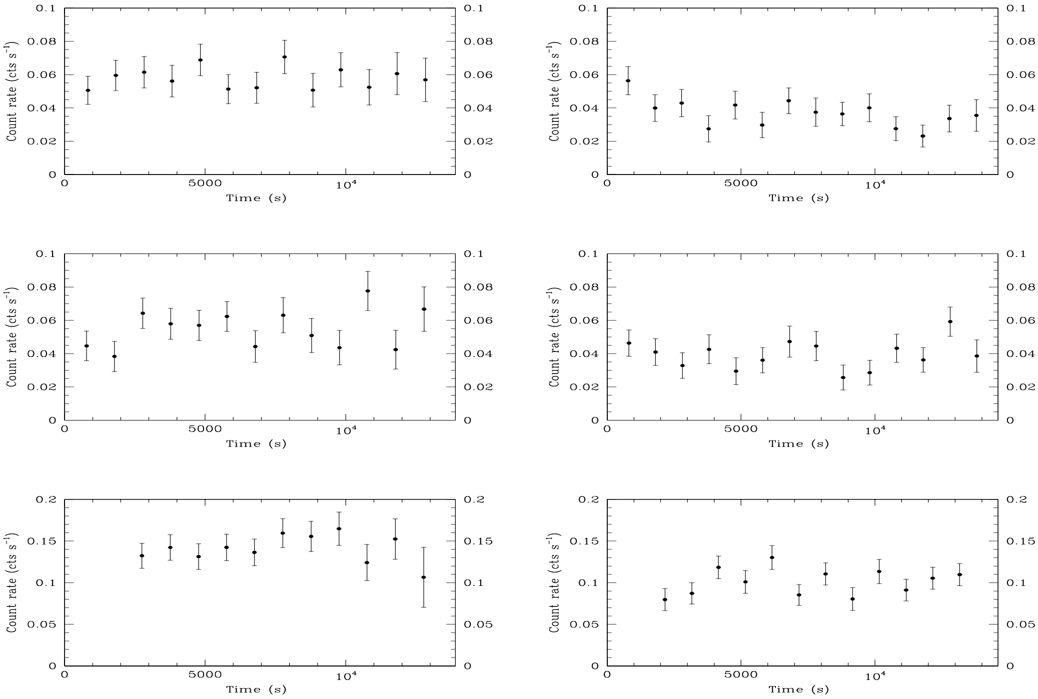

Fig. 8. Light curves obtained for a 1000 s time bin between 0.4 and 10.0 keV for observation 1 (*on the left*) and observation 2 (*on the right*). No correlation is found between the fluctuations observed for the three EPIC instruments. *Top panel*: MOS1. *Middle panel*: MOS2. *Bottom panel*: pn. The error bars represent the 1-σ poissonian standard deviation.

Sana et al. 2004) applied to all our data sets did not reveal any significant variability on time scales shorter than the duration of an exposure, except the one due to the soft proton flare of the first observation (see Sect. 3.1).

5. Comparison with previous X-ray observations

Prior to the present *XMM-Newton* observations, HD 168112 was observed with *EINSTEIN* (Chlebowski et al. 1989) and the estimated X-ray luminosity (between 0.2 and 3.5 keV) was about 2.04 × 10^{33} erg s^{-1} for a 2 kpc distance. The *EINSTEIN* count rate was about 0.018 ± 0.004 cts s^{-1}, for a 7591.5 s exposure (*EINSTEIN* sequence number 5960; observed on March 14, 1981).

Because of the differences in the adopted model hypotheses for the *EINSTEIN* and our luminosity estimates, X-ray luminosities are not directly comparable. To achieve a more suitable comparison, we folded our *XMM-Newton* best fit 2-T models through the response matrix of the IPC instrument. The corresponding equivalent IPC count rates estimated between 0.2 and 3.5 keV are 0.013 ± 0.003 cts s^{-1} and 0.009 ± 0.003 cts s^{-1} respectively for our two exposures. The results for both exposures are thus lower than the actual IPC count rate given by Chlebowski et al. (1989), indicating that the flux during the *EINSTEIN* observation was higher than at the time of our two *XMM-Newton* pointings.

We also retrieved *ROSAT*-PSPC data (rp500298n00, 9.5 ks; obtained between September 13 and September 15, 1993) and we inferred a count rate of 0.054 ± 0.003 cts s^{-1}. The same procedure as described hereabove for *EINSTEIN* data but using the *ROSAT*-PSPC response matrix was applied. The equivalent PSPC count rates corresponding to our two *XMM-Newton* observations are respectively 0.027 ± 0.002 cts s^{-1} and 0.019 ± 0.002 cts s^{-1}. These results suggest that the *ROSAT*-PSPC observation of HD 168112 was performed at a time when the star was in a higher emission state than during the *EINSTEIN* and *XMM-Newton* observations.

Finally, according to the ROSHRI database (see e.g. ledas-`www.star.le.ac.uk/rosat/rra`), the vignetting corrected count rate of a *ROSAT*-HRI observation performed between September 12 and October 9, 1995 (rh201995n00, 36.3 ks) is (7.8 ± 0.6) × 10^{-3} cts s^{-1}. The same procedure as for PSPC was applied using the HRI response matrix and we obtain equivalent HRI count rates of (10.4 ± 0.1) × 10^{-3} and (7.6 ± 0.1) × 10^{-3} cts s^{-1} respectively for our two *XMM* exposures, suggesting that during the *ROSAT*-HRI observation HD 168112 was in an X-ray emission state similar to what was observed with *XMM-Newton* in September 2002.

In summary, as a result of this comparison with previous observations, we see that the X-ray flux of HD 168112 undergoes a quite strong long-term variability. Figure 9 shows the X-ray count rate from these observations, normalized relative to the *XMM-Newton* count rate in April 2002 arbitrarily set to unity. It is clear from Fig. 9 that the data coverage is insufficient to provide a detailed description of this behaviour. X-ray monitoring of HD 168112 at a sampling time scale of a few weeks or months would certainly help to better constrain the phenomenon.

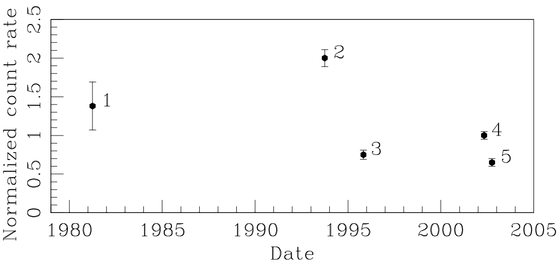

Fig. 9. Normalized equivalent X-ray count rates arising from different observatories, as a function of time. 1: *EINSTEIN*-IPC, March 1981. 2: *ROSAT*-PSPC, September 1993. 3: *ROSAT*-HRI, September and October 1995. 4: *XMM-Newton*-EPIC, April 2002. 5: *XMM-Newton*-EPIC, September 2002.

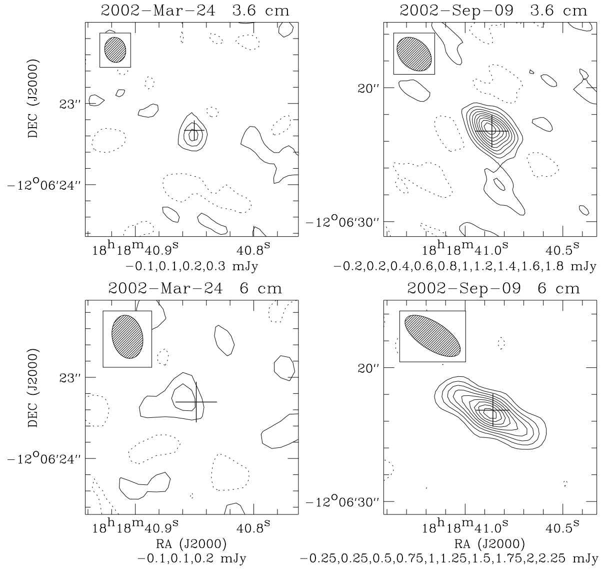

Fig. 10. VLA maps of HD 168112 at 3.6 and 6 cm for both epochs. Note the different spatial scales used. The synthesized beam is shown in the upper left corner of each panel. The cross indicates the optical ICRS 2000.0 position (from SIMBAD). Contour levels are listed at the bottom of each panel. The first contour line is at a flux level of ~2× the rms of the map. The negative contour is indicated by the dashed line.

6. VLA observations

For both epochs, HD 168112 is detected at 3.6 and 6 cm (see Fig. 10), but not at 18 and 20 cm. For the detections, we measured the flux by fitting an elliptical Gaussian to the source. The Gaussian has the same shape as the cleaned beam, so the position and total intensity are the only parameters fitted. The error bar on the flux due to *random* errors is given by the root-mean-square (rms) in the map. To get a feeling for the *systematic* errors, we repeated the reduction, systematically dropping one antenna, using different weightings of distant visibilities, or natural weighting instead of robust uniform, or doubling or halving the number of clean components. The error bars given in Table 10 show the range of results found by these various reductions, or the rms error bar when it is larger. For each observation, we also compared the peak intensity of the source to the flux derived from the Gaussian fit. There is very good agreement for March data, showing that the sources are indeed point sources. For September, however, the peak intensities are higher than the Gaussian fluxes by about 1-σ. The error bars of the 3.6 and 6 cm observations include a 2% calibration error (Perley & Taylor 1999).

For the non-detections at 18 and 20 cm, Table 10 gives an upper limit of three times the rms measured in a box of 100 × 100 pixels centered on HD 168112. Because of interference at 18 cm, the rms at that wavelength is higher than at 20 cm. The influence of the background structure on the 18 cm and 20 cm maps for September 2002 is rather limited. Various combinations of dropping the shortest baselines and depth of cleaning give maps that are acceptably smooth, showing that all background effects have been removed. The upper limits listed in Table 10 are based on the highest rms found in the set of acceptable maps.

The major new result from the present observations is the clear difference in flux level between both epochs. The fluxes of September are roughly in agreement with some of the Bieging et al. (1989) observations. The March fluxes, however, are substantially lower than their observations by a factor of 5–7.

We explored the possibility that these low fluxes are due to poor phase calibration (Thompson et al. 1986, pp. 428–432). Phase errors increase with baseline length, so the A configuration used in March is the most sensitive to this effect. At 3.6 cm, most gain phases between the two calibration observations bracketing HD 168112 change by <20°, with only a few showing higher values up to 50°. At 6 cm, the gain phases change by about 30°. Comparison with previous work (Blomme et al. 2002, 2003) suggests that, for such changes, some flux might be lost, but not a substantial amount. The effect is certainly not large enough to explain the factor 5–7 difference in the fluxes.

Another possibility is that we could be resolving the star. However, Blomme et al. (2003) showed that for the much closer star ζ Pup the flux lost in this way only amounts to ~10%. Furthermore, one of a number of unpublished VLA archive data taken in C configuration shows a flux for HD 168112 that is as low as our March observation: 0.3 ± 0.05 mJy at 3.6 cm (Blomme et al. 2004, in preparation). One may also wonder whether the change in resolution between the two observations could explain the flux variation. As mentioned above, low fluxes were already observed with the C configuration, although our high flux measurement was also obtained with the C configuration. Moreover, by throwing away some of the data, a lower-resolution observation can be simulated with the March data, but that does not change the flux significantly.

Table 10 also lists the spectral index (α, where $F_\nu \propto \lambda^{-\alpha}$) based on our 3.6 and 6 cm observations. For September, α is significantly different from the value expected for thermal emission (+0.6), showing that the emission at that time was definitely non-thermal. For March, the result is less clear due to the large error bar on α. It is possible that at that time HD 168112 was showing a thermal spectrum. However, using the mass loss rate, terminal velocity and distance from Table 4,

Table 10. VLA fluxes and spectral index.

Date	Flux (mJy)					Spectral	Reference
	2 cm	3.6 cm	6 cm	18 cm	20 cm	index	
Data from this paper							
2002-Mar.-24	–	0.3 ± 0.1	0.3 ± 0.1	–	<0.6	0.0 ± 0.9	
2002-Sep.-11	–	1.8 ± 0.2	2.1 ± 0.3	<2.4	<1.2	−0.3 ± 0.4	
Data from literature							
1984-Mar.-09	–	–	1.3 ± 0.1	–	–	–	Bieging et al. (1989)
1984-Apr.-04	1.2 ± 0.2	–	1.9 ± 0.1	–	–	−0.4 ± 0.2	Bieging et al. (1989)
1984-Dec.-21	1.3 ± 0.1	–	5.4 ± 0.1	–	8.2 ± 0.3	−0.8 ± 0.5	Bieging et al. (1989)
1989-Nov.-10	–	–	–	< 2.4	–	–	Phillips & Titus (1990)

the Wright & Barlow (1975) formula predicts a 6 cm flux of only 0.03 mJy. Even the observed flux in March is a factor ten larger than this value. Therefore, we are definitely not seeing the underlying free-free emission of the stellar wind.

Combining our data with published values shows considerable variability (0.3–5.4 mJy at 6 cm and <1.2–8.2 mJy at 20 cm). This variability in fluxes and in spectral index is consistent with the way other non-thermal emitters, such as Cyg OB2 No. 9 (Waldron et al. 1998) and WR 140 (Williams et al. 1994), behave.

7. Optical observations

The mean spectrum of HD 168112 as observed at SPM is shown in Fig. 11. The most prominent absorption lines belong to H I, He I, He II as well as to some metal ions (e.g. O III, C III, C IV, N III,...). The equivalent width (*EW*) ratio of the He I λ4471 and He II λ4542 absorption lines ($W' = EW(4471)/EW(4542) = 0.41$) yields an O5.5 spectral type according to the criterion of Conti (1973). The strength of the He II λ4686 absorption ($EW = 0.49$ Å) as well as its slightly asymmetric shape with a steeper red wing suggest a giant luminosity class.

There are also a few narrow emission lines: N III $\lambda\lambda$4634–41 with equivalent widths of −0.17 and −0.26 Å respectively, as well as C III λ5696 ($EW = -0.30$ Å). The Si IV λ4116 line is also seen as an extremely faint emission ($EW \sim -0.08$ Å), whereas Si IV λ4089 is seen as a very faint absorption ($EW \sim 0.07$ Å). This situation is similar to what is found in 9 Sgr (Rauw et al. 2002) and is usually interpreted as the λ4089 absorption and emission almost canceling each other (see Walborn 2001). We note also the presence of the two very weak S IV emissions at 4485 and 4504 Å (Werner & Rauch 2001) and of a weak C III $\lambda\lambda$ 4647–50 blend. Finally, we note that the core of the Hα absorption line is partially filled in by emission. The *EW* of the Hα line as measured on our spectra (1.94 ± 0.11 Å) is in excellent agreement with the value (2 Å) adopted by Leitherer (1988).

Considering these spectral properties, we classify HD 168112 as O5.5 III(f$^+$), in excellent agreement with classifications published in the literature (see Mathys 1988 and references therein).

Table 11. Average radial velocities of nine absorption lines in the spectrum of HD 168112 as measured on our SPM and FEROS data. The third column yields the instrumentation used for the observation: echelle spectrograph at San Pedro (SPM), FEROS at the 1.5 m telescope (F1.5) or FEROS at the 2.2 m telescope (F2.2).

Date HJD − 2 450 000	$\overline{RV}$ (km s^{-1})	Inst.
2040.746	15.8	F1.5
2382.900	21.1	F1.5
2745.919	12.1	SPM
2746.875	18.4	SPM
2747.867	11.3	SPM
2748.842	20.8	SPM
2749.876	7.2	SPM
2750.864	13.2	SPM
2783.820	16.4	F2.2
2784.815	18.4	F2.2

So far, there exists basically no information on the multiplicity of HD 168112 in the literature. We have measured the heliocentric radial velocities (*RV*s) of the strongest absorption lines in our spectra. We then averaged the *RV*s of nine of them (Hγ, Hβ, He II $\lambda\lambda$4200, 4542, 4686, 5412; He I λ5876 and C IV $\lambda\lambda$5801, 5812). The rest wavelengths of these lines were adopted from Underhill (1994).

The results listed in Table 11 do not reveal any significant *RV* changes. For instance, the mean *RV* averaged over the SPM data set amounts to 13.8 ± 5.0 km s^{-1}, whilst this mean is 15.5 ± 4.5 km s^{-1} over the entire data set. No obvious trend appears in the *RV*s over the six nights of the SPM campaign or between the various FEROS campaigns. The lack of significant *RV* variations suggests that HD 168112 is either single or it could be a binary system with a rather large mass ratio seen under a low inclination angle.

Finally, we also consider archive photometric data of HD 168112. A set of such data was collected between 1982 and 1990 in the framework of the Long Term Photometry of Variables (LTPV) programme at ESO (Manfroid et al. 1991; Sterken et al. 1993). HD 168112 was used as a comparison star

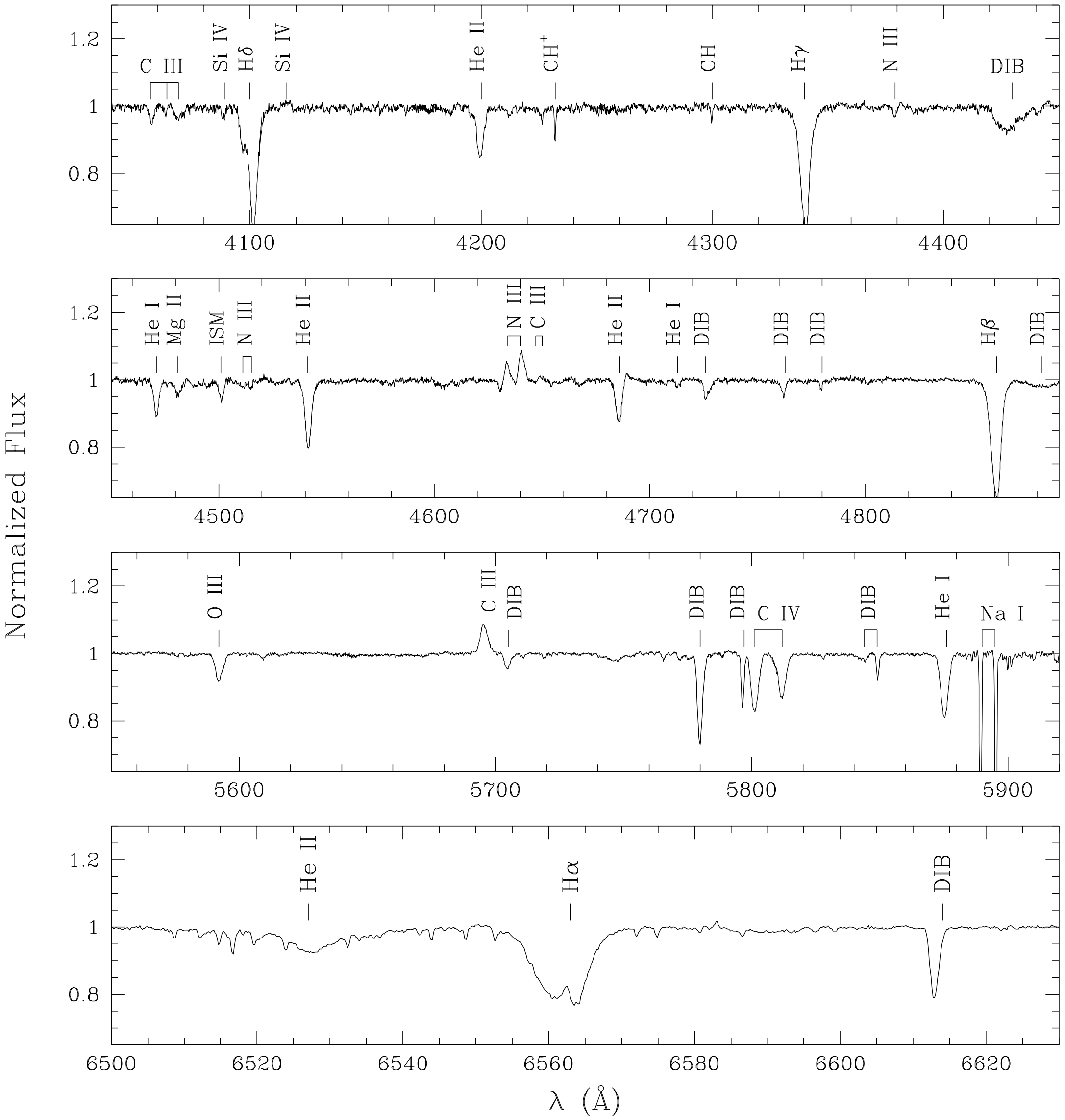

Fig. 11. Mean optical spectrum of HD 168112 as observed from SPM in April 2003. The most prominent stellar and interstellar lines as well as diffuse interstellar bands (DIBs) are indicated.

designated A 5020 in the context of the LTPV. The data were obtained in the Strömgren system with various telescopes and photometers at the La Silla observatory (see Manfroid et al. 1991). We have retrieved the data from this campaign and we analysed the differential photometry of A 5020 − B 5020, where B 5020 is a second comparison star (=HD 168135, B9 V) that was observed immediately after or before HD 168112. Since each telescope and instrumental configuration has its specific properties, we analysed the corresponding data separately. The results are presented in Table 12. The 1-σ dispersions of the differential magnitudes are always small (except perhaps for the *u* filter and instrumental system 6) and are comparable to typical results of the LTPV campaign (Manfroid et al. 1991). There is no significant trend in the data points either. We conclude that the existing photometric data do not display any significant variations that could be attributed e.g. to the effects of binarity.

In summary, our optical analysis failed to reveal any evidence of binarity on time scales of weeks, or from one year to the next. Moreover, photometric data do not show any variation either. These results suggest three possible scenarios. Firstly, the binary system, if any, could be seen under a very low inclination angle, preventing us from seeing any radial velocity or photometric variations. Secondly, the orbital period of the suspected binary system could be very long, or the sampling of our *RV* measurements could be too sparse to reveal the actual *RV* change. Thirdly, HD 168112 could be a single star.

Table 12. Differential LTPV photometry of HD 168112. The quoted magnitudes and 1-σ dispersions correspond to the difference A 5020 − B 5020 (where A 5020 is the magnitude of HD 168112 and B 5020 that of HD 168135). The first column yields the code of the telescope + instrument configuration (see Manfroid et al. 1991) and the second column indicates the number of data points for each set-up.

Telescope	N	u	v	b	y
5	26	0.780 ± 0.011	1.205 ± 0.005	0.976 ± 0.004	0.570 ± 0.005
6	39	0.747 ± 0.053	1.192 ± 0.012	0.962 ± 0.008	0.568 ± 0.010
7	30	0.873 ± 0.010	1.252 ± 0.010	0.966 ± 0.010	0.580 ± 0.009

8. Discussion

8.1. Scenarios for a thermal hard X-ray emission from HD 168112

It appears that the bulk of the X-rays have a thermal origin. Indeed the continuum is well fitted by bremsstrahlung emission, while there is clear evidence for thermal line emission (e.g. Mg XI at 1.34 keV, Si XIII at 1.86 keV and the Fe K blend at 6.5 keV). While a non-thermal component may also make a small contribution (this possibility is discussed further in Sect. 8.2), we will concentrate first on possible explanations for the observed thermal emission.

8.1.1. The single star scenario

Two features of the X-ray data of HD 168112 are rather unusual for a single O-star. On the one hand, the X-ray flux appears to be variable by a factor of a few. Such a variability is not expected for presumably single O-stars, as stated by Berghöfer & Schmitt (1995) on the basis of *ROSAT* data. On the other hand, all our spectral fittings with two temperature thermal models suggest plasma temperatures for the hard component of the order of 2–3 keV, i.e. in the range 2.3–3.5 × 10^7 K. The X-ray emission for single hot stars is usually attributed to the effects of instabilities and shocks arising in their stellar winds. While these shocks may produce some emission at energies comparable to those seen in HD 168112, the emission measure associated with this very hot plasma is likely to be rather low. More importantly, when we compare our EPIC spectra with X-ray spectra of presumably single O-stars such as ζ Pup (Kahn et al. 2001), we clearly notice that the latter are dominated by a soft thermal emission. In order to check whether this impression could be biased by the much lower interstellar column towards ζ Pup (compared to HD 168112), we have extracted the *ASCA* SIS spectra of this star[3]. The spectrum was fitted with a thermal model with a temperature of about 0.65 keV, and this model was then reddened by the same ISM column as HD 168112. Clearly this fake reddened ζ Pup spectrum does not exhibit a hard tail similar to that seen in HD 168112. We therefore conclude that such a hard emission is not seen in the spectrum of a presumably single star like ζ Pup.

One way to account for the high plasma temperatures derived in our fittings could possibly result from the confinement of the wind by a magnetic field. Babel & Montmerle (1997) suggest that a moderate magnetic field could deviate the stellar winds from either hemisphere towards the magnetic equator, where they would collide, thereby producing a plasma at temperatures as high as several 10^7 K. In the case of HD 168112, a magnetic field is indeed expected to be present since we observe synchrotron radio emission.

8.1.2. The binary scenario

A striking property of the X-ray emission of HD 168112 is its strong variability between the two observations. The X-ray flux suffered a decrease of about 25–30% between April 2002 and September 2002. Comparison with archive data confirms the existence of a substantial variability of the X-ray flux of HD 168112. This long term variability is compatible with a binary scenario for HD 168112. This idea is reinforced by the fact that this variability is mostly observed in the hard EPIC bandpass, i.e. in the part of the spectrum presumably mostly influenced by a putative wind-wind collision X-ray emission in a O+O-type binary. In a colliding wind scenario, we do not expect strong variability in the soft part of the spectrum as it is mostly produced by the intrinsic emission from both components. In this context, the observed variability could be due for instance to a significant orbital eccentricity. In fact, the emission measure of the hot post-shock plasma in an adiabatic wind collision zone varies roughly as $1/D$ where D is the orbital separation of the binary components (Stevens et al. 1992; Pittard & Stevens 1997). Therefore, an orbital eccentricity of $e \geq 0.5$ would allow to account for the factor 3 variability of the X-ray fluxes as seen in Fig. 9. The variations seen in the latter figure are compatible with a possible orbital period of several years. Moreover, the fact that this variability seems to be most significant at higher energies is compatible with a variation of an X-ray emission component originating from a wind-wind interaction.

Finally, we emphasize that the temperatures of the hard component in the 2-T fittings imply pre-shock velocities of the order of 1300–1600 km s^{-1}. Such values are indeed typical for relatively wide colliding wind binaries (Pittard & Stevens 1997) where the winds collide with velocities near v_∞.

8.2. HD 168112 as a non-thermal emitter

HD 168112 is known to be a variable non-thermal radio emitter, and this is reconfirmed by our new data. Combining our results with those of Bieging et al. (1989), we find spectral indices

---

[3] ζ Pup was observed with the *ASCA* satellite in October 1993 during about 30 ks (P.I.: Dr. T. G. Tsuru). Screened event files were retrieved from the ARNIE database at Leicester University and reduced using the XSELECT software (version 1.4b).

that vary between 0.0 and −0.8 with a 6 cm flux ranging between 0.3 mJy and 5.4 mJy. As non-thermal processes require the existence of relativistic electrons, thermal electrons must be accelerated to relativistic velocities. This could in principle be done by the first order Fermi mechanism: it requires an acceleration time of only a few minutes to generate relativistic electrons that emit synchrotron radiation in the observable radio region (Van Loo et al. 2004). Both synchrotron emission and Fermi mechanism require the existence of a moderate magnetic field (e.g. Longair 1992). Magnetic fields associated with OB stars have been measured using spectropolarimetric methods in the case of β Cep and θ^1 Ori C (Donati et al. 2001, 2002). The acceleration of relativistic electrons by the Fermi mechanism can occur either in the shocks due to intrinsic instabilities of the wind of a single star or in a colliding wind binary, and in the following sections we discuss these models in greater depth.

8.2.1. The single star scenario

At the present stage of the study of HD 168112, this star is not known as a binary system. As stated in the introduction, the only known mechanism for a single O-star to accelerate relativistic electrons is by means of hydrodynamic shocks inside its stellar wind. However, since the optical depth of the wind at radio wavelengths is very large, the radio photosphere is located far from the visible photosphere and relativistic electrons accelerated in the inner regions of the wind would have to travel over large distances before they could produce observable synchrotron radio emission. Due to the intense UV stellar radiation field, the time scale for IC thermalization of relativistic electrons is quite short. This implies that the relativistic electrons responsible for the observed synchrotron emission must be accelerated in situ, i.e. the shocks responsible for this acceleration must subsist at large distances from the stellar surface (Chen & White 1994). On the other hand, shocks occuring in the inner wind where the UV flux is strongest could also accelerate electrons to relativistic energies. These relativistic electrons could produce a power law tail in the hard X-ray to soft γ-ray energy range through IC scattering (Chen & White 1991a,b). However, one should emphasize that in this case the population of relativistic electrons responsible for the non-thermal X-rays would be distinct from that producing the synchrotron emission.

Our EPIC spectral fittings with power law models yield photon indices of the order of 3. In the framework of the first order Fermi mechanism, the index of the electron distribution is related to the shock properties through the following relation: $n = (\chi + 2)/(\chi - 1)$ where n is the index of the relativistic electrons population and χ is the compression ratio, defined as the ratio between the velocity of the preshock and postshock regions (Bell 1978a,b). This electron index is related to the photon index of the IC emission as follows: $\Gamma = (n + 1)/2$, where Γ is the photon index. For a photon index of $\approx$3, this leads to $n \approx 5$ and $\chi \approx 1.75$. We note that the value for strong shocks is $\chi = 4$. If the hard X-rays in the spectrum of HD 168112 actually result from the above scenario, then the properties of the shocks inside the wind deviate from those of strong shocks. This situation is very similar to the case of 9 Sgr (Rauw et al. 2002) where the possible photon index was found to be larger than 2.9. The disagreement between our results and the hypothesis adopted by Chen & White (1991a) could mean that the stellar winds harbour a distribution of hydrodynamical shocks characterized by different strengths (Feldmeier et al. 1997). The assumption of strong shocks with $\chi = 4$ only might therefore not hold in the case of a shock distribution. If the power law fitted as a second emission component in Sect. 3.2 expresses any physical reality, the compression ratio deduced from our *XMM-Newton* observations should be considered as a mean value, typical of the shock distribution existing in the non-thermal X-ray emission region. At this stage, we emphasize nevertheless that the occurrence of a non-thermal emission process in the X-ray domain is not established. The possible reasons responsible for the non detection of inverse Compton scattering in X-rays are discussed in Sect. 9.

Although the variability in the X-ray domain is likely not compatible with the single star scenario, the radio variability could be explained by a variable magnetic field. Another possibility comes from shocks of different strengths crossing the relevant geometric region. The strongest shocks produce more radio emission than weaker ones, because they accelerate more of the electrons into the momentum range where synchrotron radiation is emitted at radio wavelengths (Van Loo et al. 2004).

8.2.2. The binary scenario

If HD 168112 is a binary, in the case of a non-thermal hard X-ray emission, the discussion relevant to the photon index developed hereabove remains valid, but the shocks responsible for the electron acceleration are most probably associated with the wind-wind interaction (Williams et al. 1990; Eichler & Usov 1993; Dougherty et al. 2003). The rather low value of the compression ratio derived in the previous section (χ = 1.75), compared to the strong shock value ($\chi_{\rm str}$ = 4), could possibly be explained by heat conduction unopposed by magnetic field in the wind collision zone (Myasnikov & Zhekov 1998). Moreover, in a colliding wind binary, the non-thermal X-ray and radio emission would arise in the same region, i.e. they would be produced by the same population of relativistic electrons. In such a case, the determination of both radio (synchrotron) and X-ray (IC) luminosities could lead to a straightforward estimate of the magnetic field strength (see e.g. Benaglia & Romero 2003).

We should note also that the strong variability of the non-thermal radio emitters is probably more compatible with binarity. Indeed, the observed variability for these objects can possibly be related to changes due to the orbital phase, like in WR 140 (Williams et al. 1994).

For instance in an eccentric binary, seen under a low inclination, the strong variability of the radio emission could result from the synchrotron emission site, i.e. the wind interaction zone, moving in and out of the primary's free-free radio photosphere. Adopting the stellar parameters from Table 4, we estimate radii for the photospheres at 3.6, 6, and 20 cm of 2.6, 3.8 and 8.8 AU respectively. As discussed in Sect. 8.1, the variations of the X-ray flux suggest an eccentricity of ≥0.5 for a putative binary system. The alternating detection and non-detection of HD 168112 at 20 cm (see Table 10) could be explained if the wind interaction zone lies outside the radio photosphere at apastron, whilst it would be buried within the photosphere at periastron passage. This translates into

$$a\,(1\,-\,e) \leq R_{\tau=1}(20\,\mathrm{cm}) \leq a\,(1\,+\,e).$$

If $e = 0.5$, one gets 5.9 AU ≤ a ≤ 17.6 AU which corresponds to an orbital period 1.7 yrs ≤ P ≤ 8.9 yrs for $M_1 + M_2 = 70\,M_\odot$, which is the stellar mass given by Leitherer (1988).

9. Conclusions

The major points of our multiwavelength investigation of HD 168112 can be summarized as follows:

- Our VLA data confirm the non-thermal nature of the radio emission from HD 168112, and reveal also strong variability of the radio flux at 3.6 and 6 cm. However, our target was not detected at 18 and 20 cm.
- Our *XMM-Newton* data reveal what is most likely a thermal spectrum, with plasma temperatures up to 2–3 keV. We failed to unambigously detect a high energy power law tail associated with a putative non-thermal component.
- The X-ray flux shows strong variability between our two *XMM-Newton* observations (∼30%), mostly at energies above ∼1 keV. If we assume that the X-ray and radio fluxes vary on time scales of months, our quasi-simultaneous *XMM-Newton* and VLA data suggest that the X-ray and radio fluxes vary in opposite directions: whereas the radio flux increased between March and September 2002, the X-ray flux had decreased.
- Our optical data failed to reveal a signature of binarity.

Although the failure to detect radial velocity variations argues against HD 168112 being a binary, it should be emphasized that many of the other properties of this system could be readily explained by a wind-wind interaction in a wide eccentric binary with a period of several years and seen under a low inclination angle. In fact, the radio and X-ray variations could result from the change in orbital separation between the two binary components. In this scenario, we could expect to measure the largest X-ray flux when the separation between the stars is minimum (i.e. around periastron), whereas the synchrotron radio emission would be strongest when the separation is larger, i.e. when the wind interaction zone lies well outside the radio photosphere of the primary star.

How could we establish the nature of HD 168112? The best way to do this would probably be through a regular monitoring of the star in the radio domain. For instance, one radio observation every two months over ∼5 years might be sufficient to establish a recurrence in the radio light curve that might help us constrain the orbital period of a putative binary. A radio light curve with a quality comparable to that of WR 140 (Williams et al. 1994; White & Becker 1995) would undoubtedly provide new insight into the nature of this star. Another interesting test to be performed would be a high angular resolution optical interferometric observation of HD 168112. At a distance of 2 kpc an interferometer with an angular resolution of ∼1 mas would be able to resolve a secondary component if it lies at a distance of at least ∼2 AU from the primary. This technique was recently succesfully applied to the case of two spectroscopic binaries (Monnier et al. 2004).

Finally, it is important to ask the following question: what could be the reason for our failure to detect an inverse Compton X-ray emission although we knew all the ingredients required to produce such an emission to be present in HD 168112 and 9 Sgr (Rauw et al. 2002)? Several factors could contribute to hide or inhibit such an inverse Compton X-ray emission:

1. *An overwhelming thermal X-ray emission.* This could be an issue especially for binary systems where the interaction region could produce a fair amount of hard thermal X-rays. In this respect, observations in the γ-ray energy range will be extremely useful. A detection of early-type stars with the *INTEGRAL* observatory would not be affected by the thermal emission from the colliding wind region and would provide an unambigous evidence for the inverse Compton mechanism.
2. *Too large a dilution of the photospheric UV flux at the site of the relativistic electron acceleration.* Again, this is more likely to be an issue in a binary system with a wide orbital separation where the electron acceleration takes place in the wind interaction zone, i.e. several tens or hundreds of stellar radii away from the UV photosphere.
3. *Too large a magnetic field.* If the non-thermal X-ray and radio emission arise from the same population of relativistic electrons, the ratio between the IC and synchrotron luminosities should depend on the magnetic field strengths:

$$\frac{L_{\mathrm{sync}}}{L_{\mathrm{IC}}} \propto \frac{B^2\,d^2}{L}$$

where L_{sync}, L_{IC}, B, d, and L are respectively the radio synchrotron luminosity, the inverse Compton luminosity, the strength of the magnetic field, the distance to the star, and its bolometric luminosity (Benaglia & Romero 2003). Therefore, for a rather large value of B, the synchrotron luminosity could be large, whereas the IC X-ray emission would remain undetectable.

Clearly more work is needed on the theoretical side to provide simulated inverse Compton X-ray and γ-ray spectra of single and binary early-type stars suitable for a comparison with the new data that are now available.

Acknowledgements. Our thanks go to Alain Detal (Liège) for his help in installing the SAS. The authors wish also to thank Dr. Eric Gosset for instructive discussions, as well as Prof. Rolf Mewe for very helpful instructions concerning the transition rate calculations. The Liège team acknowledges support from the Fonds National de la Recherche Scientifique (Belgium) and through the PRODEX XMM-OM and Integral Projects. This research is also supported in part by contracts P4/05 and P5/36 "Pôle d'Attraction Interuniversitaire" (SSTC-Belgium). J.M.P. gratefully acknowledges funding from PPARC for a PDRA position. S.V.L. gratefully acknowledges a doctoral research grant by the Belgian State, Federal Office for Scientific, Technical and Cultural Affairs (OSTC). This research has made use of the SIMBAD database, operated at CDS, Strasbourg, France and NASA's Astrophysics Data System Abstract Service.

References

Babel, J., & Montmerle, T. 1997, A&A, 323, 121

Barbon, R., Carraro, G., Munari, U., Zwitter, T., & Tomasella, L. 2000, A&AS, 144, 451

Bell, A. R. 1978a, MNRAS, 182, 147

Bell, A. R. 1978b, MNRAS, 182, 443

Benaglia, P., & Romero, G. E. 2003, A&A, 399, 1121

Berghöfer, T. W., & Schmitt, J. H. M. M. 1995, Adv. Space Res., 16, 163

Berghöfer, T. W., Schmitt, J. H. M. M., Danner, R., & Cassinelli, J. P. 1997, A&A, 322, 167

Bieging, J. H., Abbott, D. C., & Churchwell, E. B. 1989, ApJ, 340, 518

Blomme, R., Prinja, R. K., Runacres, M. C., & Colley, S. 2002, A&A, 382, 921

Blomme, R., Van de Steene, G. C., Prinja, R. K., Runacres, M. C., & Clark, J. S. 2003, A&A, 408, 715

Bohlin, R. C., Savage, B. D., & Drake, J. F. 1978, ApJ, 224, 132

Briggs, D. S. 1995, High Fidelity Deconvolution of Moderately Resolved Sources, Ph.D. Thesis, The New Mexico Institute of Mining and Technology, Socorro, New Mexico

Cappa, C. E., Goss, W. M., & van der Hucht, K. A. 2004, AJ, in press [`arXiv:astro-ph/0401571`]

Cash, W. 1979, ApJ, 228, 939

Chen, W., & White, R. L. 1991a, ApJ, 366, 512

Chen, W., & White, R. L. 1991b, ApJ, 381, L63

Chen, W., & White, R. L. 1994, Ap&SS, 221, 259

Chlebowski, T., Harnden, F. R. Jr., & Sciortino, S. 1989, ApJ, 341, 427

Churazov, E., Gilfano, M., Forman., W., & Jones, C. 1996, ApJ, 471, 673

Conti, P. S. 1973, ApJ, 179, 181

Conti, P. S., & Ebbets, D. 1977, ApJ, 213, 438

Davidge, T. J., & Forbes, D. 1988, MNRAS, 235, 797

Davidson, K., & Ostriker, J. P. 1973, ApJ, 179, 585

De Becker, M., Rauw, G., Pittard, J. M., et al. 2004, A&A, 416, 221

Donati, J.-F., Wade, G. A., Babel, J., et al. 2001, MNRAS, 326, 1265

Donati, J.-F., Babel, J., Harries, T. J., et al. 2002, MNRAS, 333, 55

Dougherty, S. M., & Williams, P. M. 2000, MNRAS, 319, 1005

Dougherty, S. M., Pittard, J. M., & Kasian, L. 2003, A&A, 409, 217

Eichler, D., & Usov, V. 1993, ApJ, 402, 271

Feldmeier, A. 2001, Hydrodynamics of astrophysical winds driven by scattering in spectral lines, Habilitation Thesis, Potsdam University

Feldmeier, A., Puls, J., & Pauldrach, A. W. A. 1997, A&A, 322, 878

Gabriel, A. H., Bely-Dubau, F., Faucher P., et al. 1991, ApJ, 378, 444

Georgelin, Y. M., Georgelin, Y. P., & Roux, S. 1973, A&A, 25, 337

Jansen, F., Lumb, D., Altieri, B., et al. 2001, A&A, 365, L1

Kaastra, J. S. 1992, An X-ray spectral code for optically thin plasmas, Internal SRON-Leiden Report

Kaastra, J. S., Mewe, R., & Raassen, A. J. J. 2004, in New Visions of the X-ray Universe in the XMM-Newton and Chandra Era, ed. F. Jansen, ESA, SP-488, in press

Kahn, S. M., Leutenegger, M. A., Cottam, J., et al. 2001, A&A, 365, L312

Kaufer, A., Stahl, O., Tubbesing, S., et al. 1999, The Messenger, 95, 8

Leitherer, C. 1988, ApJ, 326, 356

Leitherer, C., Forbes, D., Gilmore, A. C., et al. 1987, A&A, 185, 121

Longair, M. S. 1992, High Energy Astrophysics (Cambridge University Press)

Lumb, D. 2002, EPIC background files, XMM-SOC-CAL TN-0016

Manfroid, J., Sterken, C., Bruch, A., et al. 1991, A&AS, 87, 481

Mathys, G. 1988, A&AS, 76, 427

Mewe, R., Gronenschild, E. H. B. M., & van den Oord, G. H. J. 1985, A&AS, 62, 197

Mewe, R. 1999, in X-ray spectroscopy in astrophysics, EADN School X, Amsterdam, Lectures notes in physics, ed. J. van Paradijs, & J. A. M. Bleeker (Berlin: Springer), 520, 109

Mihalas, D., & Binney, J. 1981, Galactic Astronomy, Structure and Kinematics (San Francisco: Freeman)

Monnier, J. D., Traub, W., Schloerb, F. P., et al. 2004, ApJ, 602, L57

Myasnikov, A. V., & Zhekov, S. A. 1998, MNRAS, 300, 686

Perley, R. A., & Taylor, G. B. 1999, The VLA Calibrator Manual (`http://www.aoc.nrao.edu/~gtaylor/calib.html`)

Phillips, R. B., & Titus, M. A. 1990, ApJ, 359, L15

Pittard, J. M., & Stevens, I. R. 1997, MNRAS, 292, 298

Pollock, A. M. T. 1987, ApJ, 320, 283

Raassen, A. J. J., van der Hucht, K. A., Mewe, R., et al. 2003, A&A, 402, 653

Rauw, G., Blomme, R., Waldron, W. L., et al. 2002, A&A, 394, 993

Sana, H., Stevens, I. R. S., Gosset, E., Rauw, G., & Vreux, J.-M. 2004, MNRAS, in press

Singh, K. P., White, N. E., & Drake, S. A. 1996, ApJ, 456, 766

Smith, R. K., & Brickhouse, N. S. 2000, Rev. Mex. Astron. Astrofis., Ser. Conf., 9, 134

Sterken, C., Manfroid, J., Anton, K., et al. 1993, A&AS, 102, 79

Stevens, I. R., Blondin, J. M., & Pollock, A. M. T. 1992, ApJ, 386, 265

Strüder, L., Briel, U., Dennerl, K., et al. 2001, A&A, 365, L18

Thompson, A. R., Moran, J. M., & Swenson, G. W. Jr. 1986, Interferometry and Synthesis in Radio Astronomy (New York: Wiley-Interscience)

Turner, M. J. L., Abbey, A., Arnaud, M., et al. 2001, A&A, 365, L27

Underhill, A. B. 1994, ApJ, 420, 869

van der Hucht, K. A., Williams, P. M., Spoelstra, T. A. Th, & de Bruyn, A. G. 1992, in Non-isotropic and Variable Outflows from Stars, ed. L. Drissen, C. Leitherer, & A. Nota, ASP Conf. Ser., 22, 253

Van Loo, S., Runacres, M. C., & Blomme, R. 2004, A&A, 418, 717

Walborn, N. R. 1973, AJ, 78, 1067

Walborn, N. R. 2001, in Eta Carinae and Other Mysterious Stars: The hidden opportunities of emission spectroscopy, ed. T. R. Gull, S. Johannson, & K. Davidson, ASP Conf. Ser., 242, 217

Waldron, W. L., Corcoran, M. F., Drake, S. A., & Smale, A. P. 1998, ApJS, 118, 217

Werner, K., & Rauch, T. 2001, in Eta Carinae and Other Mysterious Stars: The hidden opportunities of emission spectroscopy, ed. T. R. Gull, S. Johannson, & K. Davidson, ASP Conf. Ser., 242, 229

White, R. L. 1985, ApJ, 289, 698

White, R. L., & Becker, R. H. 1995, ApJ, 451, 352

Williams, P. M. 1996, in Radio Emission from the Stars and the Sun, ed. J. Parades, & A. R. Taylor, ASP Conf. Ser., 93, 15

Williams, P. M., van der Hucht, K. A., Pollock, A. M. T., et al. 1990, MNRAS, 243, 662

Williams, P. M., van der Hucht, K. A., & Spoelstra, T. A. Th. 1994, A&A, 291, 805

Wright, A. E., & Barlow, M. J. 1975, MNRAS, 170, 41

4.2 The multiple system HD 167971

HD 167971 was proposed to consist of a close eclipsing binary system made up of two similar O-stars of spectral type O5-8V, with a third more luminous and more distant O-type companion of spectral type O8I (Leitherer et al. 1987). The period of the eclipsing binary is about 3.32 d. The presence of the third component was revealed by a non-zero third light in the photometric solution, although there is still no strong evidence for a gravitational link between the third star and the close eclipsing binary. The interesting particularity of HD 167971 is that it is a strong non-thermal radio emitter – the strongest of the survey of Bieging et al. (1989) – with a radio spectral index of –0.6 and a flux density at 6 cm ranging between 13.8 and 17.0 mJy (Williams 1996).

On the basis of our two *XMM-Newton* observations of NGC 6604, we investigated in detail the X-ray emission from HD 167971. We obtained good quality EPIC spectra for both observations. First, we fitted the spectra with two kinds of composite models, both of them including two absorption components accounting respectively for neutral interstellar aborption and for the absorption by the ionized material of the stellar winds. The first model we used was a thermal model including three `mekal` components, and the second one included two thermal `mekal` components and an additional power law. These two models yielded very satisfactory results with characteristic temperatures respectively of 2×10^6 and 9×10^6 K for the two soft thermal components. However, the nature of the hard part of the spectrum is not unambigously revealed by our data. If the hard emission is thermal, the characteristic temperature of the third emission component is about 2.3×10^7 to 4.6×10^7 K. On the basis of this model, we estimated the overall X-ray luminosity and we find an excess of about a factor 4 as compared to the expected X-ray emission from isolated stars of the same bolometric luminosity for both observations. Such an excess, although weak, is significant considering the scatter of the relation of Berghoefer et al. (1997) used to estimate this excess, suggesting therefore that HD 167971 is overluminous in X-rays. On the other hand, if the hard emission is of non-thermal origin, the photon index of the power law is about 3, which is rather large and reminiscent of the case of other non-thermal radio emitters such as 9 Sgr (Rauw et al. 2002).

We investigated the variability of the X-ray emission from HD 167971. We did not find any variation on time-scales of a few hundreds to a few thousands of seconds in our *XMM-Newton* data. However, the fact that we obtained two observations separated by about five months allowed us to investigate the X-ray variability on a longer time-scale. Even though the comparison of our two observations relied on somewhat heterogenous data sets and therefore should be considered with caution (see the discussion in De Becker et al. 2005a), we found that the X-ray flux in September 2002 was about 10 % lower than in April 2002. Considering the ephemeris determined by Leitherer et al. (1987), and provided the observed variation is real, the X-ray flux variation can possibly be attributed to an eclipse occurring during the second observation. However, we note that the extrapolation of this ephemeris to the epoch of our observations should be considered with caution, especially for such a short period.

Provided the nature of the hard X-ray emission from HD 167971 is thermal, our results can be considered in the following scenario partly illustrated by Fig. 4.2. As the plasma temperature of a few 10^7 K is unlikely for individual winds, it should be characteristic of a plasma heated by a wind-wind collision. Moreover, the slight X-ray luminosity excess reported above can also be attributed to X-rays emitted by colliding winds, in addition

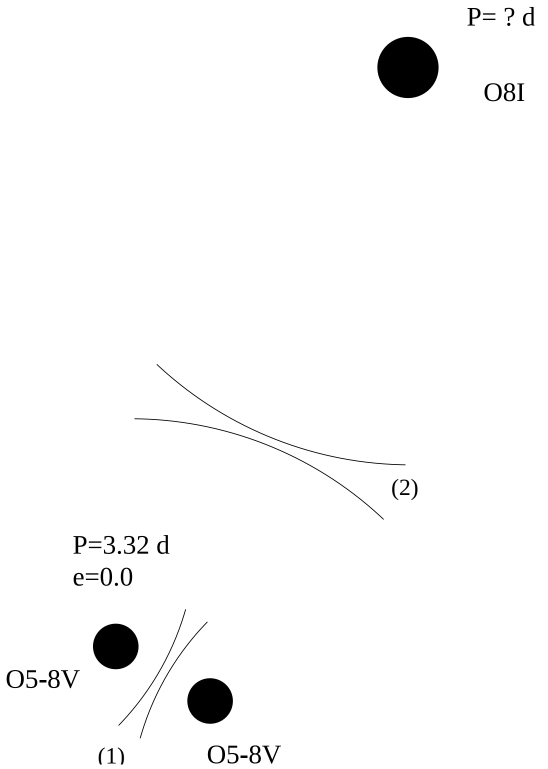

Figure 4.2: Schematic representation of HD 167971. The close eclipsing binary and the third star are represented. In the scenario where the three stars are gravitationally bound, the two wind-wind interactions individually labelled (1) and (2) can be envisaged. The size of the stars, their relative separation, and the position of the interaction zones are arbitrarily chosen.

to those emitted by individual stellar winds (see the brief discussion of these processes in Sect. 1.1). In the context of a multiple system such as HD 167971 – even though there is still no evidence that the third star is gravitationally linked to the close binary – two wind-wind interactions should be envisaged:

- a collision between the winds of the two stars constituting the close binary system (label (1) in Fig. 4.2).
- a collision between the wind of the third more distant star and the combined winds of the close binary system (label (2) in Fig. 4.2) .

In the case of the close binary system (1), the period is very short and therefore the separation between the two stars should be small. As a consequence, the winds of the two O5-8V stars do not have enough space to reach their terminal velocities in a way that is reminiscent of the case of HD 159176 (similar spectral types, similar period). Such a situation is not likely to lead to post-shock temperatures of the order of those found for the hottest thermal component of the model we used to fit the X-ray spectrum of HD 167971. However, the interaction of the combined winds of the eclipsing binary with that of the more distant third star (2) might lead to higher temperatures as the winds may reach their terminal velocities before they collide. In summary, we find some evidence for the occurrence of a wind-wind collision in our X-ray data, most probably attributable to an interaction involving the third star. In order to produce a detectable interaction, the third star should not be located too far from the close eclipsing binary. This suggests that the third star might therefore be gravitationally linked to the two O5-8V stars, indicating that HD 167971 is indeed a triple system as illustrated by the schematic representation of Fig. 4.2.

As mentioned above, our results do not allow us to claim that a non-thermal emission components has been detected in the X-ray spectrum of HD 167971. However, the non-thermal emission in the radio domain is well-established. Provided we find a probable wind collision signature in the X-rays, the wind-wind interaction is once again likely to be responsible for the non-thermal emission observed in the radio domain. As the period – and therefore the separation – of the eclipsing binary harboured by HD 167971 is very short, the putative synchrotron radio emission produced at position (1) in the schematic representation of Fig. 4.2 should not be detected as it would most probably be absorbed by the material of the winds. On the other hand, a non-thermal radio emission produced at position (2) in Fig. 4.2 should not be totally absorbed. The strong non-thermal radio emission observed for HD 167971 should come from this latter interaction zone.

At this stage of our study of the X-ray emission of non-thermal radio emitters, a census of what we have learned so far should be made. In Sect. 5.3 of De Becker et al. (2005a) inserted below, we propose a discussion based on a comparison of mainly four targets: 9 Sgr (Rauw et al. 2002), HD 168112 (De Becker et al. 2004a, included in this dissertation), HD 167971 (De Becker et al. 2005a, included in this dissertation), and HD 159176 (De Becker et al. 2004c, included in this dissertation). Although the presentation of the observational results of this work is not yet complete, it is interesting to present such a discussion – leading to one of the major conclusions of this thesis – as it will be crucial in our interpretation of the results presented in the next chapter devoted to Cyg OB2.

As suggested by the census of non-thermal emitting O and WR stars in the introduction of this work, the multiplicity seems to play a significant role in the production of non-thermal emission from massive stars. This idea is strongly supported by the sample of stars enumerated above. Indeed, all of them are at least suspected binaries (HD 168112), or even confirmed binaries (9 Sgr) or triple systems (HD 167971). A noticeable characteristic of the three non-thermal radio emitters of this sample is that the possible orbital periods are rather long (from a few months up to a few years). Moreover, we did not unambigously detect any high-energy counterpart to the non-thermal emission already detected in the radio domain. On the other side, HD 159176 – a short period binary – appears to be the only O + O system presenting a putative non-thermal emission component in its X-ray spectrum, whilst it is not known to be a non-thermal radio emitter.

We propose that this rather strict distinction between two regimes could be interpreted as follows. On the one hand, short period binaries like HD 159176 may produce a non-thermal emission through inverse Compton scattering along with a soft thermal X-ray emission originating from the collision zone (in addition to the individual contributions of the two stars). As the thermal emission is soft, the non-thermal emission can be unveiled in the hard part of the EPIC spectrum. In the radio domain, the putative synchrotron emission should be completely absorbed by the wind material and therefore not detected. On the other hand, the separation between stars constituting long period binaries allows the synchrotron radio emission to escape partly from the wind material, and such systems are therefore observed as non-thermal radio emitters. In the X-rays, the thermal emission from the wind-wind interaction is quite hard since the winds collide once they have reached their terminal velocities, and the putative non-thermal emission is completely overwhelmed by the thermal component. As a consequence, it appears that *the simultaneous observation of non-thermal radiation in the X-ray (below about 10.0 keV) and radio domains is rather unlikely.* This important result will be considered in order to interpret the data analysis described in Chapter 5, and will also constitute one of the crucial aspects of the discussion and of the conclusions developed in Chapter 6.

A&A 437, 1029–1046 (2005)
DOI: 10.1051/0004-6361:20052810
© ESO 2005

Astronomy & Astrophysics

An *XMM-Newton* observation of the multiple system HD 167971 (O5-8V + O5-8V + (O8I)) and the young open cluster NGC 6604⋆

M. De Becker[1], G. Rauw[1,⋆⋆], R. Blomme[2], J. M. Pittard[3], I. R. Stevens[4], and M. C. Runacres[2]

[1] Institut d'Astrophysique, Université de Liège, Allée du 6 Août, Bât. B5c, 4000 Liège (Sart Tilman), Belgium
e-mail: `debecker@astro.ulg.ac.be`
[2] Royal Observatory of Belgium, Avenue Circulaire 3, 1180 Brussels, Belgium
[3] Department of Physics & Astronomy, University of Leeds, Leeds LS2 9JT, UK
[4] School of Physics & Astronomy, University of Birmingham, Edgbaston Birmingham B15 2TT, UK

Received 3 February 2005 / Accepted 19 March 2005

Abstract. We discuss the results of two *XMM-Newton* observations of the open cluster NGC 6604 obtained in April and September 2002. We concentrate mainly on the multiple system HD 167971 (O5-8V + O5-8V + (O8I)). The soft part of the EPIC spectrum of this system is thermal with typical temperatures of about 2×10^6 to 9×10^6 K. The nature (thermal vs. non-thermal) of the hard part of the spectrum is not unambiguously revealed by our data. If the emission is thermal, the high temperature of the plasma ($\sim 2.3 \times 10^7$ to 4.6×10^7 K) would be typical of what should be expected from a wind-wind interaction zone within a long period binary system. This emission could arise from an interaction between the combined winds of the O5-8V + O5-8V close binary system and that of the more distant O8I companion. Assuming instead that the hard part of the spectrum is non-thermal, the photon index would be rather steep (~3). Moreover, a marginal variability between our two *XMM-Newton* pointings could be attributed to an eclipse of the O5-8V + O5-8V system. The overall X-ray luminosity points to a significant X-ray luminosity excess of about a factor 4 possibly due to colliding winds. Considering HD 167971 along with several recent X-ray and radio observations, we propose that the simultaneous observation of non-thermal radiation in the X-ray (below 10.0 keV) and radio domains appears rather unlikely. Our investigation of our *XMM-Newton* data of NGC 6604 reveals a rather sparse distribution of X-ray emitters. Including the two bright non-thermal radio emitters HD 168112 and HD 167971, we present a list of 31 X-ray sources along with the results of the cross-correlation with optical and infrared catalogues. A more complete spectral analysis is presented for the brightest X-ray sources. Some of the members of NGC 6604 present some characteristics suggesting they may be pre-main sequence star candidates.

Key words. radiation mechanisms: non-thermal – stars: early-type – stars: individual: HD 167971 – stars: winds, outflows – X-rays: stars

1. Introduction

The nature of the X-ray emission from hot stars has been the subject of many discussions over the last three decades. The bulk of the X-ray emission of single O-stars arises in a hot optically thin thermal plasma inside the stellar wind. These plasmas are believed to be heated up to several 10^6 K by shocks resulting from instabilites related to the line driving mechanism responsible for the mass loss of massive stars (see e.g. Owocki & Rybicki 1985; Feldmeier et al. 1997). The case of massive binaries is more complex, because they harbour a wind interaction zone that can produce a substantial additional X-ray emission (Stevens et al. 1992). Such a wind collision is expected to heat the shocked plasma to temperatures of several 10^7 K.

Some massive stars are known to display non-thermal emission in the radio domain (see e.g. Bieging et al. 1989; Williams 1996). Dougherty & Williams (2000) showed that most of the non-thermal radio emitting Wolf-Rayet (WR) stars are binaries, suggesting that the non-thermal phenomenon might be intimately related to multiplicity. However, the situation for O-stars is much less clear as the binary fraction among O-type non-thermal radio emitters is apparently lower than for WR stars (see Rauw 2004).

The non-thermal radio emission, which is thought to be synchrotron emission (White 1985), requires the presence of a population of relativistic electrons inside the radio emitting region, as well as the existence of a moderate magnetic field. On the one hand, high energy electrons could be accelerated through the first order Fermi mechanism in shocks (Pollock 1987; Chen & White 1991; Eichler & Usov 1993). On the

---

⋆ Based on observations with XMM-Newton, an ESA Science Mission with instruments and contributions directly funded by ESA Member states and the USA (NASA). Partly based on observations collected at the European Southern Observatory (La Silla, Chile).

⋆⋆ Research Associate FNRS (Belgium).

other hand, the existence of magnetic fields of a few hundred Gauss has recently been confirmed in the case of a few massive stars (Donati et al. 2001, 2002). For a discussion of the physical processes involved in this scenario, see e.g. De Becker et al. (2005). If the ingredients required for non-thermal radio emission are present, one may wonder whether the relativistic electrons could produce a signature at other, essentially higher, energies. Indeed, the intense UV flux from massive stars could interact with relativistic electrons through Inverse Compton (IC) scattering resulting in a power law X-ray emission component (Eichler & Usov 1993; Chen & White 1994). Such a scenario could apply both to single and binary systems, since both types of objects are believed to harbour hydrodynamic shocks that could accelerate particles. There are two major questions to be addressed in order to fully understand non-thermal phenomena in early-type stars: (1) one has to establish whether non-thermal X-ray emission really occurs; and (2) one has to check whether single stars are indeed able to produce non-thermal radiation.

In the framework of these considerations, non-thermal radio emitting massive stars are a priori privileged targets to search for an X-ray counterpart to this non-thermal radio emission. We therefore initiated a joint X-ray and radio campaign aiming at a better understanding of the emission processes in non-thermal radio emitters. The first target of this campaign observed with *XMM-Newton* was the O4V((f$^+$)) star 9 Sgr (Rauw et al. 2002). Whilst the X-ray spectrum of 9 Sgr displays indeed a hard emission tail, the very nature of the latter, thermal or non-thermal, could not be fully established. Optical spectra of 9 Sgr revealed long term radial velocity variations suggesting that 9 Sgr could indeed be a long-period binary system. The second object considered was HD 168112 (De Becker et al. 2004b). This O5.5III(f$^+$) star, belonging to the NGC 6604 cluster (Barbon et al. 2000), also shows some evidence for binarity although no radial velocity variations were found. Indeed, De Becker et al. (2004b) report changes of the nature of the radio emission (going from composite to strongly non-thermal, with a flux variation by a factor 5–7) simultaneously with a significant decrease of the X-ray flux (about 30%), suggesting that a wind collision occurs in an eccentric long period binary system seen under low inclination. Blomme et al. (2005a) suggest a ∼1.4 yr period for the radio fluxes. These results lend further support to the idea that binarity might be a necessary condition for non-thermal radio emission, also in O-stars. This paper is mainly devoted to the study of HD 167971, another non-thermal radio emitter which is known to be a multiple system (Leitherer et al. 1987), and belongs also to NGC 6604.

HD 167971 was first classified as an O8f star (Hiltner 1956). This system has been a target of several photometric studies (i.e. Johnson 1965; Moffat & Vogt 1975; Leitherer & Wolf 1984). The IR study of Bertout et al. (1985) yielded $\dot{M} \sim 9.4 \times 10^{-6} M_\odot\,\mathrm{yr}^{-1}$ and $v_\infty \sim 2120\,\mathrm{km\,s}^{-1}$. In a more recent photometric and spectrometric study, Leitherer et al. (1987) proposed this system to consist of a close eclipsing binary made up of 2 similar O-stars, with a third more luminous and more distant O-type companion (O5-8V + O5-8V + (O8I)). Their analysis of the light curve revealed a 3.3213 days period for the eclipsing binary. They found a mass loss rate of $\sim 2 \times 10^{-6} M_\odot\,\mathrm{yr}^{-1}$ and a terminal velocity of $3100\,\mathrm{km\,s}^{-1}$ for the brightest third star. The study of Davidge & Forbes (1988) confirmed the orbital period of the close binary system. Their photometric solution, which is in better agreement with observations, has non-zero third light, suggesting that HD 167971 is indeed a multiple system. However, we note that at this stage there is no evidence of a gravitational link between the third star and the eclipsing binary.

In his review of radio emitting hot stars, Williams (1996) lists HD 167971 as a non-thermal emitter, with a radio spectral index of −0.6 and a 6 cm flux level ranging between 13.8 and 17.0 mJy. It is the strongest non-thermal radio emitter reported in the study of Bieging et al. (1989). This star appears consequently to be a good candidate to study the implication of binarity on non-thermal emission processes. This paper is devoted to the analysis of two *XMM-Newton* pointings obtained in 2002. The radio results from the VLA, as well as a discussion of archive radio data, will be presented in a separate paper (Blomme et al. 2005b, in preparation).

NGC 6604 is a rather compact open cluster lying at the core of the HII region S54 (Georgelin et al. 1973), in the Ser OB2 association (Forbes 2000). The study of Forbes & DuPuy (1978) revealed that it is rather young (∼4 Myr) as suggested also by the possible presence of pre-main sequence (PMS) objects. However, the study of Barbon et al. (2000) did not confirm the existence of pre-main sequence stars, although these authors also derived an age of the cluster of about 5 ± 2 Myr. The same authors derive a distance to the cluster of about 1.7 kpc. In addition to the study of the two non-thermal radio emitters mentioned hereabove, the X-ray observation of NGC 6604 offers also the possibility to study the stellar population of the cluster. Indeed, recent *XMM-Newton* observations of NGC 6383 (Rauw et al. 2003) and NGC 6231 (Sana et al. 2005) reveal a strong concentration of X-ray selected PMS stars around the most massive cluster members that are found in the cluster core. Such mass segregated clusters with a concentration of low-mass PMS objects could indicate that the most massive stars have formed through a combination of gas accretion and stellar collisions in the very dense core of the cluster (Bonnell et al. 1998; Bonnell & Bate 2002; Bonnell et al. 2003). The *XMM-Newton* observation of NGC 6604 is expected to bring new insight on the existence of low-mass PMS stars in this cluster.

This paper is organized as follows. In Sect. 2, we briefly discuss the data reduction. Section 3 describes the X-ray spectral analysis, as well as some considerations relevant to the colliding winds context. In Sect. 4 we compare our results for HD 167971 with archival X-ray observations. Section 5 is devoted to a general discussion of HD 167971. The X-ray emission from the other sources in the field of view is discussed in Sect. 6. Finally, our conclusions are presented in Sect. 7.

2. Observations

We obtained two *XMM-Newton* (Jansen et al. 2001) observations of the NGC 6604 open cluster during revolution 426,

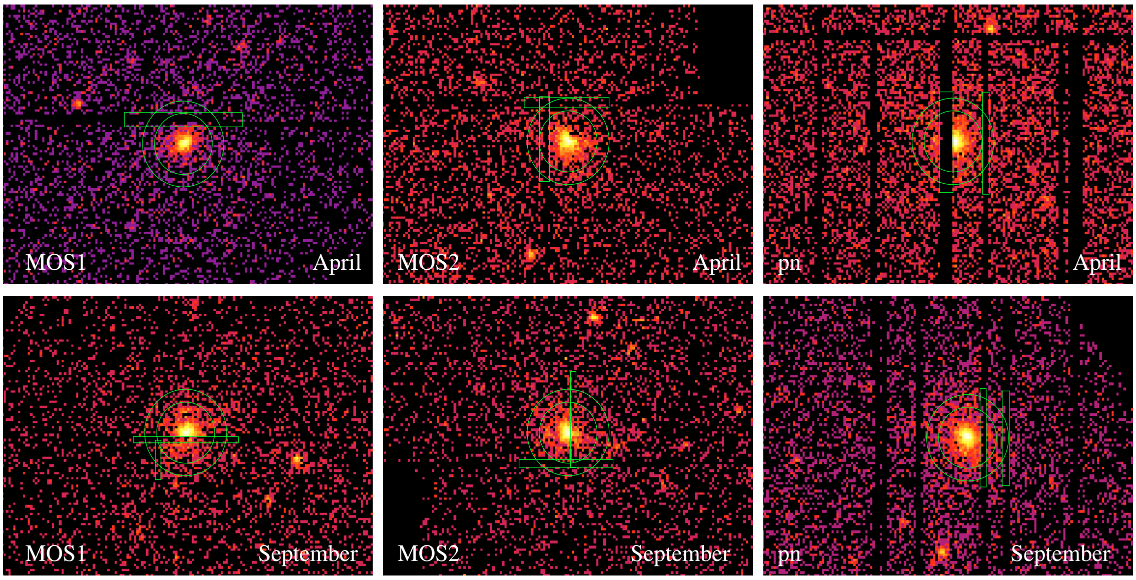

Fig. 1. Source (circle) and background (annulus) regions selected for the spectrum extraction of HD 167971. Boxes were used to exclude the CCD gaps and bad columns. We see clearly that some observations are strongly affected by the presence of these gaps. The images are displayed in detector coordinates.

in April 2002 (Obs. ID 0008820301, JD 2 452 372.477–2 452 372.637), and revolution 504, in September 2002 (Obs. ID 0008820601, JD 2 452 526.694–2 452 526.868). The aim-point of these observations was set in such a way as to monitor simultaneously the two non-thermal radio emitters HD 168112 and HD 167971 within a single EPIC field of view. The exposure time for both observations was about 13 ks. For details on these exposures and on the reduction procedure, we refer to the paper devoted to HD 168112 (De Becker et al. 2004b).

The X-ray events of HD 167971 were selected from inside a 60 arcsec radius circular region centered on the star. The background was extracted from an annular region around the source. The inner and outer radius of this annulus were chosen to obtain a surface area roughly equal to the source region area. Both regions are shown in Fig. 1 in the case of the three EPIC fields, for both observations. In each case, the source region is affected by at least one gap, which was excluded by means of a rectangular box. These boxes were adjusted following a careful inspection of the adequate exposure maps. Unfortunately these gaps sometimes cross the source region close to its center, strongly affecting the results discussed hereafter. In the case of the EPIC-pn data sets, the background region is crossed by a bad column which was also removed with a box.

3. The EPIC spectrum of HD 167971

3.1. Spectral analysis

As already stated by De Becker et al. (2004b), the end of the April 2002 exposure is affected by a strong soft proton flare (see Lumb 2002). However, it appears that the background subtraction provides an efficient correction, and the contaminated time interval was therefore not rejected. Indeed, the level of the background is at least a factor 2 lower than the mean count rate inside the source region[1].

To carry out this spectral analysis, we followed the same procedure as already applied to other targets like HD 159176 (De Becker et al. 2004a) and HD 168112 (De Becker et al. 2004b). We chose a list of models including thermal and non-thermal emission components. Massive stars are known to display thermal spectra with strong and broad emission lines (e.g. ζ Pup, Kahn et al. 2001; τ Sco, Cohen et al. 2003). Most current models consider that, in the case of single O-stars, such hot plasmas are produced by strong shocks inside the stellar wind (Feldmeier et al. 1997). To model the emission spectrum arising from such plasmas, we used an optically thin thermal plasma `mekal` model (Mewe et al. 1985; Kaastra 1992) available within XSPEC. In the case of massive binaries, colliding winds can also heat the plasma in the wind interaction zone to a temperature of up to a few times 10^7 K. The emission from the wind interaction zone can also be modelled with optically thin thermal plasma codes (see e.g. the case of HD 159176, De Becker et al. 2004a). Moreover, to account for the possibility of non-thermal emission arising from the Inverse Compton (IC) scattering of UV photons due to the presence of a population of relativistic electrons (Pollock 1987; Chen & White 1991; Eichler & Usov 1993), power law models were also considered. Our grid of models therefore includes pure thermal models, and thermal plus non-thermal models.

---

[1] In the case of HD 168112 (De Becker et al. 2004b), the soft proton flare did not affect significantly the spectral analysis although the background level was of the same order of magnitude as the source count rate.

The χ^2 minimization technique was used to estimate the quality of the fits described in the following paragraphs of this section. The parameter values quoted in Tables 2 and 3 are obtained through this method. However, to check the consistency of our approach, we confronted these results with those obtained with other techniques. Indeed, when one deals with small count numbers the parameter estimation could be achieved through the C-statistic (Cash 1979), or alternatively with the χ^2 statistic using a Churazov weighting (Churazov et al. 1996). Both methods yield results compatible with those quoted in Tables 2 and 3 within the error bars.

3.1.1. Wind absorption

In each case, two separate absorption columns were used to account for interstellar (ISM) and circumstellar (wind material) absorption respectively. The first absorption component is due to neutral material and the hydrogen column density was fixed at 0.63×10^{22} cm^{-2}. This value was obtained through the gas to dust ratio given by Bohlin et al. (1978), using a ($B - V$) color index of +0.77 (Chlebowski et al. 1989) and an intrinsic color index $(B - V)_0$ of –0.31 estimated for an O8 star (see e.g. Mihalas & Binney 1981). For the second absorption column, left as a free parameter while fitting the spectra, we used the ionized wind model already presented by Nazé et al. (2004). This model considers the absorption by the 10 most abundant elements (H, He, C, N, O, Ne, Mg, Si, S and Fe) fixed at their solar abundances (Anders & Grevesse 1989). We used the stellar fluxes from the Kurucz library of spectra, and a standard wind velocity law with $\beta = 0.8$.

The main problem to model the wind properties of HD 167971 with this model is that it only accounts for the geometry of a single star wind, although we know that our target is a triple system. The choice of the parameters adequate for our purpose is therefore not straightforward. To check the sensitivity of the wind opacity calculated by this model regarding the stellar parameters, we computed several opacity tables covering a parameter space typical for a range of spectral types including that of the components of HD 167971. This grid was calculated for mass loss rates ranging from 10^{-6} to $10^{-5}\,M_\odot\,\mathrm{yr}^{-1}$, and terminal velocities between 2200 and 3100 km s^{-1}. These domains cover different values proposed by some authors for the parameters of HD 167971 (Bertout et al. 1985; Leitherer et al. 1987). We used also three different Kurucz spectra, respectively referred to as *low* (T_{eff} = 30 000; $\log g$ = 3.5), *medium* (T_{eff} = 35 000; $\log g$ = 4.0), and *high* (T_{eff} = 40 000; $\log g$ = 4.5), and we computed the optical depth (τ) as a function of the energy for X-ray emitting shells located between 1.5 and 100 stellar radii. The opacities resulting from the normalization of τ by the hydrogen column of the wind is very similar whatever the case considered within this parameter space. Consequently, any set of parameters located within the boundaries discussed hereabove appears to be adequate. In the next section, we will discuss spectral fittings using the opacities we obtained from the *high* Kurucz spectrum, and the parameters quoted in Table 1. The parameters were selected on the basis of the values used or derived by Leitherer et al. (1987) in the computation of synthetic Hα profiles for this star. Figure 2 shows the normalized τ as a function of the energy for the ionized wind (solid line), along with the same quantity for neutral material (dashed line). We see that the largest deviation between the neutral and ionized cases is observed at low energies. The opacity table obtained with the parameters listed in Table 1 was converted into a FITS table in a format suitable to be used as a multiplicative absorption model within the XSPEC software. It will be referred to as the `wind` absorption model in the remainder of this paper.

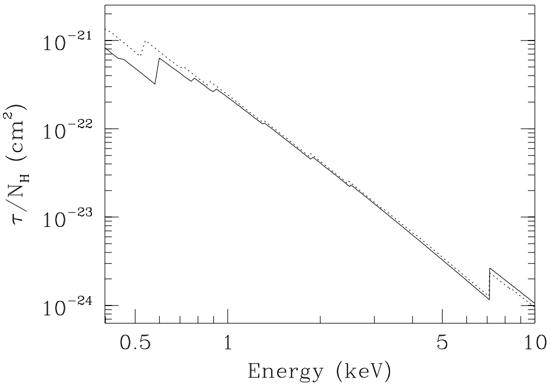

Fig. 2. Opacity resulting from the normalization of the optical depth by the hydrogen column density as a function of the energy for ionized (solid line) and neutral (dashed line) wind material.

Table 1. Parameters selected to compute the opacity table used for the modelling of the absorption of X-rays by the ionized wind material.

T_{eff} (K)	35 000
$\log g$	4.0
$\dot{M}$ ($M_\odot$ yr^{-1})	5×10^{-6}
V_∞ (km s^{-1})	3100
R_{shell} (R_*)	5

3.1.2. Spectral fittings

As previously mentioned, most of our data sets are strongly affected by the presence of gaps and/or bad columns. Only the EPIC-MOS1 and EPIC-MOS2 observations of April, and to some extent the EPIC-pn observation of September appear to be only slightly affected. In all other cases, the CCD gaps lie very close to the center of the PSF of the source. Since the data seriously affected by gaps yield unreliable spectral fits, we consider only the spectral fits for those data that are least affected.

Two-component models were used as a first step with some success, but it appeared that those models were unable to fit data above about 4–5 keV. As a consequence, we used three component models, each one having two `mekal` thermal components, plus another thermal or power law component. Solar abundances are assumed throughout our fitting procedure. The results obtained with these two models are summarized in Tables 2 and 3. The last column of these tables yields the observed (i.e. absorbed) flux integrated between 0.4 and 10.0 keV

Table 2. Parameters for EPIC spectra of HD 167971 in the case of a `wabs*wind*(mekal+mekal+mekal)` model. Results are given for MOS1, MOS2, combined MOS in the case of the April observation, and for EPIC-pn only in the case of the September one. The first absorption component is frozen at 0.63×10^{22} cm^{-2}. The second absorption column, quoted as N_w (in cm^{-2}), stands for the absorption by the ionized wind material. The last column gives the observed flux between 0.4 and 10.0 keV. The normalization parameter (Norm) of the `mekal` component is defined as $(10^{-14}/(4\,\pi\,D^2)) \int n_\mathrm{e}\, n_\mathrm{H}\, \mathrm{d}V$, where D, n_e and n_H are respectively the distance to the source (in cm), and the electron and hydrogen number densities (in cm^{-3}). The error bars represent the 1-σ confidence interval.

	Log N_w	kT_1 (keV)	Norm$_1$	kT_2 (keV)	Norm$_2$	kT_3 (keV)	Norm$_3$	χ^2_ν d.o.f.	Obs. flux (erg cm^{-2} s^{-1})
April									
MOS1	21.77	0.27	1.38×10^{-2}	0.79	2.05×10^{-3}	3.30	6.38×10^{-4}	0.867	1.79×10^{-12}
	±0.08	±0.02	$\pm 0.67 \times 10^{-2}$	±0.08	$\pm 0.72 \times 10^{-3}$	±1.32	$\pm 3.86 \times 10^{-4}$	120	
MOS2	21.78	0.24	1.68×10^{-2}	0.77	2.62×10^{-3}	3.96	4.26×10^{-4}	1.115	1.69×10^{-12}
	±0.07	±0.02	$\pm 0.76 \times 10^{-2}$	±0.06	$\pm 0.76 \times 10^{-3}$	±2.68	$\pm 3.81 \times 10^{-4}$	116	
MOS1	21.78	0.25	1.52×10^{-2}	0.78	2.35×10^{-3}	3.57	5.21×10^{-4}	0.973	1.70×10^{-12}
+ MOS2	±0.05	±0.01	$\pm 0.50 \times 10^{-2}$	±0.05	$\pm 0.52 \times 10^{-3}$	±1.25	$\pm 2.73 \times 10^{-4}$	243	
September									
pn	21.69	0.27	9.55×10^{-3}	0.77	1.87×10^{-3}	2.40	5.47×10^{-4}	1.089	1.49×10^{-12}
	±0.06	±0.01	$\pm 2.86 \times 10^{-3}$	±0.05	$\pm 0.43 \times 10^{-3}$	±0.43	$\pm 2.32 \times 10^{-4}$	244	

Table 3. Same as Table 2, but in the case of a `wabs*wind*(mekal+mekal+power)` model. For the power law component, the normalization parameter (Norm$_3$) corresponds to the photon flux at 1 keV.

	Log N_w	kT_1 (keV)	Norm$_1$	kT_2 (keV)	Norm$_2$	Γ	Norm$_3$	χ^2_ν d.o.f.	Obs. flux (erg cm^{-2} s^{-1})
April									
MOS1	21.48	0.31	4.24×10^{-3}	0.75	1.36×10^{-3}	3.04	8.47×10^{-4}	0.851	1.70×10^{-12}
	±0.28	±0.05	$\pm 5.77 \times 10^{-3}$	±0.08	$\pm 0.78 \times 10^{-3}$	±0.282	$\pm 5.09 \times 10^{-4}$	120	
MOS2	21.66	0.25	9.54×10^{-3}	0.75	2.04×10^{-3}	2.95	6.07×10^{-4}	1.095	1.63×10^{-12}
	±0.14	±0.02	$\pm 6.66 \times 10^{-3}$	±0.06	$\pm 0.94 \times 10^{-3}$	±0.426	$\pm 6.25 \times 10^{-4}$	116	
MOS1	21.63	0.27	8.02×10^{-3}	0.76	1.78×10^{-3}	2.94	6.78×10^{-4}	0.954	1.70×10^{-12}
+ MOS2	±0.11	±0.02	$\pm 4.65 \times 10^{-3}$	±0.05	$\pm 0.64 \times 10^{-3}$	±0.268	$\pm 4.21 \times 10^{-4}$	243	
September									
pn	21.68	0.27	9.08×10^{-3}	0.78	1.84×10^{-3}	2.51	2.96×10^{-4}	1.072	1.52×10^{-12}
	±0.07	±0.01	$\pm 3.18 \times 10^{-3}$	±0.05	$\pm 0.47 \times 10^{-3}$	±0.33	$\pm 2.78 \times 10^{-4}$	244	

for each set of model parameters. The dispersion on the flux was evaluated from the range of fluxes for the models with parameters covering the confidence intervals quoted in Tables 2 and 3. According to this approach, the error on the flux in that energy band is expected to be about 5%.

First, the EPIC-MOS1 and EPIC-MOS2 results of the April observation appear to be very consistent, and our models were also fitted to the two data sets simultaneously. A comparison between the results of the two models reveals no significant differences in the quality of the fit. Both models are nearly equivalent within the error bars for the two first thermal `mekal` components. The χ^2_ν values obtained and used as goodness-of-fit criterion are very similar for all EPIC instruments, either considered independently or combined. Moreover, the fluxes estimated on the basis of these two models are similar within the error bars, reinforcing the idea that both models reproduce the spectral shape rather consistently. Unfortunately, the poor quality of the data above 5 keV does not allow us to unambiguously check for the presence of the Fe K line that could help constrain the nature of the hard spectral component. These results show that the ambiguity of the nature of the hard part of the spectrum (thermal versus non-thermal) can not be alleviated with our data. This case is reminiscent of the results of the *XMM-Newton* observations obtained in the case of other non-thermal radio emitters (see e.g. 9 Sgr, Rauw et al. 2002).

The EPIC-pn observation of September gives results very similar to those of the EPIC-MOS ones of April. Even if some systematic deviations could be expected as the EPIC-MOS and EPIC-pn instruments are somewhat different, we see that the overall spectral shape remained more or less steady between

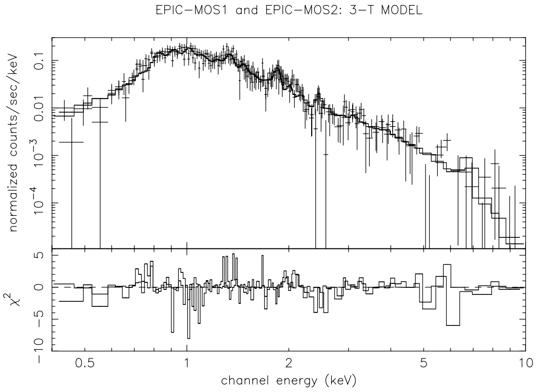

Fig. 3. Combined EPIC-MOS1 and EPIC-MOS2 spectra of HD 167971 for the April 2002 observation, fitted with a `wabs*wind*(mekal+mekal+mekal)` model between 0.4 and 10.0 keV.

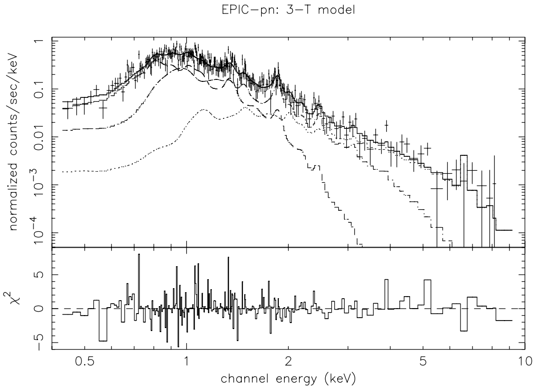

Fig. 4. EPIC-pn spectrum of HD 167971 of the September 2002 observation, fitted with a `wabs*wind*(mekal+mekal+mekal)` model between 0.4 and 10.0 keV. The three components are individualy displayed.

the two observations. If we consider the three-temperature model, we see that the emission measure of the soft thermal component decreases from April to September. This decrease is responsible for the lower flux quoted in Table 2 for the September pointing. However, if we consider the model described in Table 3, it is the normalization factor of the power law which decreases between the two pointings whilst the parameters of the two thermal components remain steady.

3.2. X-ray luminosity of HD 167971

3.2.1. X-ray variability

When investigating the X-ray variability of a system like HD 167971, one has to consider several scenarios likely to produce variations in the X-ray luminosity. Variability could indeed be expected for several reasons. First, the interaction of the stellar winds of the two components of the O5-8V + O5-8V close binary system could vary with the phase. Since the close binary has a circular orbit (van Genderen et al. 1988), the only way to produce a modulation of the X-ray flux from the wind-interaction zone would come from a change in the column density along the line of sight as a function of the orbital phase. The resulting change in absorption would then mostly affect the soft part of the EPIC spectrum. Nevertheless, no significant change appears in the spectrum or in the absorption component of the model used to fit the data between the first and the second exposure. A second possible origin could be the putative wind-wind interaction due to the presence of the third star, if the system in indeed triple. The stellar wind of the third component is indeed likely to produce a second interaction zone by colliding with the winds of the stars of the close binary system. Finally, variability could possibly result from the eclipse of the O5-8V + O5-8V binary system. According to the ephemeris derived by Leitherer et al. (1987), the April observation was performed between phases 0.64 and 0.69, and the September one between phases 0.04 and 0.12. As phase zero corresponds to the primary eclipse, we see that the September *XMM-Newton* observation was performed when the primary was partially hidden by the secondary, allowing us to possibly expect a lower X-ray flux than during the April observation when no eclipse occurred. However, the extrapolation of this ephemeris to the epoch of our observations must be considered with caution, especially for such a short period. To clarify this question, we investigated the X-ray variability of HD 167971 on the basis of the results of our two *XMM-Newton* observations, along with a confrontation to archive data (see Sect. 4).

Table 4. Observed count rates for the three EPIC instruments evaluated between 0.4 and 10.0 keV. The error bars on the count rates represent the 1-σ confidence interval.

Observation	MOS1 CR (cts s^{-1})	MOS2 CR (cts s^{-1})	pn CR (cts s^{-1})
April 2002	0.146 ±0.004	0.143 ±0.004	–
September 2002	–	–	0.465 ±0.008

Count rates of HD 167971 between 0.4 and 10.0 keV are presented in Table 4. Since CCD gaps (see Fig. 1) affect the area of the effective source region considered for the event selection, the variability between our two observations can not be discussed on the basis of count rates.

To obtain a more consistent, although model dependent way to quantify the X-ray emission, absorbed fluxes and fluxes corrected for interstellar absorption were evaluated on the basis of the pure thermal model. The fluxes quoted in Table 2 give a rough idea of the behaviour of HD 167971 between April and September 2002. If we make the assumption that we can compare the fluxes obtained separately with the EPIC-MOS and EPIC-pn instruments, we observe a slight decrease of the X-ray flux (∼12%). However, we remind that the error on the flux estimate is about 5%, and that such a heterogeneous comparison may introduce another systematic error of a few percent. Therefore, the variability of HD 167971 between the two *XMM-Newton* observations is of rather low level. If this slight variation is real, it can be due to the eclipse occurring during the second observation as pointed out above. We note however that the decrease of the emission measure is observed mostly for the soft component in the case of the three-temperature model, whilst the case of V444 Cyg discussed by Pittard (2002) shows that the eclipse would indeed be expected to reduce mainly the flux in the hard part of the X-ray spectrum. A detailed modelling of the effect of the absorption by the winds, of the occultation of the colliding zone, and of the dynamic of the stellar winds including radiative inhibitaion effects is needed to investigate the effect of the eclipse on the observed X-ray spectrum.

The variability on shorter time scales was also investigated. Light curves were generated in different energy bands between 0.4 and 10.0 keV, with time bins ranging from 100 s to 1000 s. These light curves were background corrected, and each time bin accounts for Good Time Intervals (GTIs)[2]. Variability tests (chi-square, *pov*-test[3]) were applied to all of them and no significant short term variability was found.

3.2.2. Overall luminosity

To obtain an estimate of the overall X-ray luminosity corrected for the ISM absorption, let us consider the model parameters obtained in the case of EPIC-MOS for the first observation, and EPIC-pn for the second one. This yields an L_X of about 4.3×10^{33} and 3.8×10^{33} erg s^{-1} respectively for the April and September observations, for a distance of 2 kpc. According to the bolometric magnitudes given by van Genderen et al. (1988) for the three components of this presumably triple system, we can infer bolometric luminosities of 1.5×10^{39} erg s^{-1} for each star of the close binary system, and 3.0×10^{39} erg s^{-1} for the third component. This yields a total bolometric luminosity of about 6.0×10^{39} erg s^{-1}. Following the empirical relation given by Berghöfer et al. (1997) applied to the three members of the multiple system, we infer expected individual X-ray luminosities and add them to obtain a total X-ray luminosity of about 1.0×10^{33} erg s^{-1} corresponding to an expected $L_X/L_{\rm bol}$ ratio of about 1.7×10^{-7}. Following the X-ray luminosities derived hereabove, the observed $L_X/L_{\rm bol}$ ratio goes from 7.2×10^{-7} to 6.3×10^{-7} respectively for the April and the September *XMM-Newton* observations. These values yield X-ray luminosity excesses of about a factor 4.2 and 3.7 for both observations respectively. These values are significant considering the scatter of the relation of Berghöfer et al. (1997), suggesting that HD 167971 is overluminous in X-rays.

4. Comparison with previous observations

HD 167971 was observed with the *EINSTEIN* satellite on 31 March 1981 (sequence number 4240, 5.22 ks). Chlebowski et al. (1989) reported an X-ray luminosity of 5.8×10^{33} erg s^{-1} for a 2 kpc distance. This value is slightly larger than our *XMM-Newton* results. However, we compared the *EINSTEIN* results to ours following a more model independent way. We passed the model obtained in the case of the three thermal `mekal` components through the *EINSTEIN* response matrix to obtain a simulated IPC spectrum. The model parameters are taken from the simultaneous EPIC-MOS fit for the April observation, and from EPIC-pn for the September one (see Table 2). Count rates were estimated between 0.2 and 3.5 keV (the energy range of the IPC instrument) on the basis of these simulated spectra, and we obtained 0.049 ± 0.001 cts s^{-1} and 0.047 ± 0.001 cts s^{-1} respectively for the April and the September 2002 exposures. These values are in excellent agreement with the count rate given by Chlebowski et al. (1989), i.e. 0.050 ± 0.005 cts s^{-1}. This result suggests that at the time of the *EINSTEIN* observation, HD 167971 was in an emission state similar to our *XMM-Newton* observations.

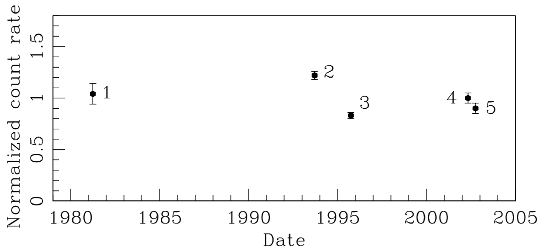

Fig. 5. Normalized equivalent X-ray count rates of HD 167971 arising from different observatories, as a function of time. 1: *EINSTEIN*-IPC, March 1981. 2: *ROSAT*-PSPC, September 1993. 3: *ROSAT*-HRI, September and October 1995. 4: *XMM-Newton*-EPIC, April 2002. 5: *XMM-Newton*-EPIC, September 2002. We note that the *ROSAT* and *EINSTEIN* points are averaged values from several observations spread over a few hours to a few days.

This target was also observed with *ROSAT*. A PSPC observation (rp500298n00, 9.29 ks, performed between 13 September and 15 September 1993) reports a count rate of 0.129 ± 0.004 cts s^{-1}. By folding the three-temperature model obtained for the fit of our EPIC data through the PSPC response matrix, we obtain 0.106 ± 0.002 cts s^{-1} and 0.103 ± 0.002 cts s^{-1} respectively for our two *XMM-Newton* observations between 0.1 and 2.5 keV (the PSPC bandpass). These results suggest that HD 167971 was in a higher emission state at the time of the *ROSAT* observation. The same procedure was applied in the case of a HRI observation performed between 12 September and 10 October 1995 (rh201995n00, 36.3 ks). The reported HRI count rate is 0.035 ± 0.001 cts s^{-1}. The results we obtain by passing the model through the HRI response matrix are 0.042 ± 0.001 cts s^{-1} and 0.041 ± 0.001 cts s^{-1} respectively for the April 2002 and the September 2002 *XMM-Newton* observations, suggesting that at the moment of the HRI observation, HD 167971 was in an emission state somewhat lower than that observed with *XMM-Newton*.

In summary, these results from archive data and from our *XMM-Newton* observations are plotted in Fig. 5. We note that we do not expect any confusion with other X-ray sources to affect the archive count rates quoted in this section. The count rates are normalized relative to the *XMM-Newton* count rate of April 2002 arbitrarily set to unity. The normalized count rate of the September 2002 *XMM-Newton* observation is

---

[2] Even if no flare contaminated time interval was rejected, standard GTIs are anyway always applied to *XMM-Newton* data, and should be taken into account in every timing analysis.

[3] See Sana et al. (2004) for a detailed discussion of this variability test.

determined following the flux ratio observed between 0.4 and 10.0 keV for the three-temperature model. The error bars on the *XMM-Newton* count rates are set to about 5% in Fig. 4. We consider that this value is more realistic than the standard deviations quoted in Table 4. We see that the X-ray flux of HD 167971 undergoes a significant variability with a peak to peak amplitude of about 40%. However, we note that this apparent variability relies mostly on the position of the *ROSAT*-PSPC point in Fig. 5, as other count rates suggest a more or less constant level. Moreover, we want to draw attention to the fact that the overall shape of the light curve plotted in Fig. 5 is very similar to that presented in Fig. 9 of De Becker et al. (2004b) for HD 168112, even if the amplitude of the apparent variability was larger in that case. Consequently this apparent variability might be attributed to some systematic effects affecting the various observations (common to HD 168112 and HD 167971) mentioned in this section. A detailed description of this behaviour requires a better data coverage than that available at the time of this study.

5. Discussion

5.1. Search for a colliding-wind signature

As HD 167971 is a multiple system whose components are O-stars, a wind-wind interaction is expected. Do our *XMM-Newton* data reveal the signature of colliding winds? Several questions should be considered to address this point:

– *Plasma temperature.* The results of the fittings with the three-temperature model point to a plasma temperature for the hardest component of about 2–4 keV, i.e. about 2.3×10^7 to 4.6×10^7 K. Such high temperatures are usually not expected for the emission from shocks due to intrinsic wind instabilities, but are expected for shocks between the winds within a binary system (see e.g. Stevens et al. 1992). These post-shock temperatures correspond to pre-shock velocities of about 1300–1800 km s^{-1}, typical for winds colliding at speeds near the terminal velocity, as should be expected for long period wide binaries (Pittard & Stevens 1997). For short period binary systems like the O5-8V + O5-8V pair in HD 167971 ($P \sim 3.32$ d), the winds have not reached their terminal velocities before they collide, and the temperatures are not expected to be so high. Such systems yield typical temperatures of at most 1×10^7 K. For instance, HD 159176 (O7V + O7V) with a period of 3.367 d displays temperatures of about 2×10^6 to 6×10^6 K (De Becker et al. 2004a), whilst the O7.5(f)III + O7.5(f)III close binary HD 152248 (5.816 d period) has plasma temperatures lower than 1×10^7 K (Sana et al. 2004). So, if the high temperatures we derived from our spectral fittings have a physical meaning, they are most probably related to the interaction between the wind of the O8I component and the combined winds of the close O5-8V + O5-8V binary system. We note however that high plasma temperatures can arise in the winds of individual stars if the magnetic field of the star is able to confine the stellar wind near the magnetic equatorial plane (Babel & Montmerle 1997).

– *X-ray luminosity.* The luminosities we derived from our spectral fittings point to an excess attributable to a wind-wind interaction. This is compatible with a scenario where the colliding winds bring a significant contribution to the overall X-ray luminosity, in addition to the emission from the intrinsic shocks of the individual winds of the components of HD 167971.

– *X-ray variability.* As discussed in Sect. 3.2.1, the question of the variability of the X-ray flux is rather complex. We do not detect any strong variability in the X-ray flux between our two *XMM-Newton* observations. Only a slight decrease possibly due to the eclipse of the O5-8V + O5-8V close binary system is observed. However, our discussion of archive data reveals that HD 167971 possibly shows some variability, even if the data coverage is insufficient to constrain the time scale of this variability. If not due to some undetermined systematic effect (see last paragraph of Sect. 4), the amplitude of this apparent variability seems to be rather high (~40%). Even if there is no clear evidence that the three stars are physically related, this variability might be compatible with what could be expected from a long period and eccentric binary system. The count rates from *ROSAT* and *EINSTEIN* result indeed from a combination of several observations spanning different phases of the orbit of the O5-8V + O5-8V binary system, and consequently are phase averaged values. Moreover, most of the count rates quoted in Fig. 5 point to a low level, although it is not reasonable to think that all the pointings except that of *ROSAT*-PSPC fall at the moment of an eclipse. For these reasons, we do not expect the eclipse of the close binary system to be responsible for the variability illustrated in Fig. 5. However, considering the lack of reliability of this putative long term variability, we decided to attribute only little weight to this argument.

Regarding these results, we realize that we find a probable signature of a wind-wind collision. Some clues, like the high plasma temperature in the context of the thermal model, point to a possible detection of the interaction between the close system and the third more luminous companion. With the large separations characterizing this interaction, the shocks of the collision zone are expected to be strongly adiabatic, resulting in a phase-locked X-ray variability scaling with 1/D, with D being the distance from one of the two components to the interaction zone (see Stevens et al. 1992; Pittard & Stevens 1997). According to this scenario, the X-ray emission should peak close to the periastron passage. Such a high temperature for the hard component of the spectrum, if it is thermal, was also reported in the case of HD 168112 which is possibly a wide and eccentric binary system (De Becker et al. 2004b; Blomme et al. 2005a). In the case of HD 167971, the X-ray luminosity excess attributed to the wind collision is much more significant.

Quantifying the respective contributions from the two expected collision zones is not an easy task. To address such an issue, an accurate knowledge of the stellar properties of the three stars along with a better idea of their relative positions is needed. We can however tentatively adopt the following semi-quantitative approach. From Sect. 3.2.2, we can assume

Table 5. Comparison of the cases of 9 Sgr (Rauw et al. 2004), HD 168112 (De Becker et al. 2004b), HD 167971 (this study), and HD 159176 (De Becker et al. 2004a). The question marks for the multiplicity and the period stem from the fact that these are not well established.

	9 Sgr	HD 168112	HD 167971	HD 159176
Multiplicity	binary?	binary?	triple	binary
Period	long period?	long period (1.4 yr)?	3.3213 d + long period	3.367 d
Thermal X-rays	soft + hard	soft + hard	soft + hard	soft
Hard X-rays	ambiguous	most probably thermal	ambiguous	possible power law tail
Synchrotron radio emission	yes	yes	yes	no

that the cumulated intrinsic contributions from the three stars is about 10^{33} erg s^{-1}. As the overluminosity factor is about 4, the X-rays arising from the collision zone(s) amount to about 3×10^{33} erg s^{-1}. On the other hand, for the O7V + O7V close binary system HD 159176 (De Becker et al. 2004a) rather similar to the eclipsing binary harboured by HD 167971[4], the same considerations lead to an X-ray luminosity for the collision zone of about 1.3×10^{33} erg s^{-1}. If the O5-8V + O5-8V binary within HD 167971 produces the same amount of X-rays, we estimate that the putative collision zone due to the third companion may produce more than twice as much X-rays as that of the close eclipsing binary. We mention however that the highest temperature component of the thermal model used to fit the EPIC spectra accounts for only about 10% of this quantity, suggesting that the softest components account significantly for the putative wind-wind collision with the third star.

5.2. Non-thermal emission from HD 167971

In the radio domain, the non-thermal nature of the emission from HD 167971 is well established (Bieging et al. 1989; Blomme et al. 2005b). The high non-thermal radio flux suggests that it comes from the interaction between the close eclipsing binary and the third star. However, in the X-ray domain, the nature of the hard component of the spectrum is still unclear. As discussed in Sect. 3.1, the pure thermal model and that including the power law yield results of similar quality. This ambiguity is a common feature in the study of X-ray spectra of massive stars (see e.g. De Becker 2001; Rauw et al. 2002; De Becker et al. 2004b). If we make the assumption that a non-thermal emission component is responsible for the hard part of the spectrum of HD 167971, we obtain photon index values close to 3, which is rather steep as compared to the value, i.e. 1.5, considered by Chen & White (1991) for X-rays produced through Inverse Compton scattering from relativistic electrons accelerated in strong shocks. For a discussion of such high values of the photon index, we refer to De Becker et al. (2004b).

5.3. Comparison with other early-type stars

Up to now, our campaign devoted to non-thermal radio emitters includes the observations of three targets: 9 Sgr (Rauw et al. 2004), HD 168112 (De Becker et al. 2004b), and HD 167971 (this study). The next targets of this campaign are the non-thermal radio emitters of the Cyg OB2 association (#8A, #9 and #5, see e.g. Waldron et al. 1998). Forthcoming studies based on *XMM-Newton* and *INTEGRAL* observations of these stars will bring new elements to the overall discussion of the high energy emission from massive stars. For instance, Cyg OB2 #8A is a well known non-thermal radio emitter that has recently been identified as a binary system by De Becker et al. (2004c), lending further support to the scenario where binarity is a necessary condition to observe non-thermal emission from massive stars. This idea is also supported by the results of Benaglia & Koribalski (2005) who discuss the case of four southern non-thermal radio emitters, among which three are confirmed binary systems. The need for a binary scenario to explain the non-thermal radio emission has independently been demonstrated by Van Loo (2005) following a theoretical approach. Several works has recently been devoted to the non-thermal radio emission from massive binaries (Dougherty et al. 2003; Pittard et al. 2005). These recent models take into account several physical effects likely to affect the observed synchrotron spectrum (Razin effect, free-free absorption, IC cooling). Future developments of these models are expected to lead to an estimate of the non-thermal high-energy emission from massive binaries.

At this stage, it could be interesting to confront the results obtained in the case of the first three targets studied in this campaign. The summary of the results arising from these studies is provided in Table 5. For these three objects, our analyses did not reveal any unambiguous power-law emission component in the X-ray spectra. A striking characteristic of their X-ray spectra is that the fit with thermal models reveals a rather hard emission, with plasma temperatures of a few 10^7 K. HD 167971 is a known multiple system and such high plasma temperature could be explained by a wind-wind interaction. HD 168112 is not known to be a binary system, but was proposed to be a binary candidate by De Becker et al. (2004b). The results of the study of Blomme et al. (2005a) lend further support to this idea, suggesting a period of about 1.4 yr based on archival radio and X-ray data, even if no unambiguous evidence of

---

[4] The bolometric luminosity provided by van Genderen et al. (1988) for the latter stars is intermediate between those given by Howarth & Prinja (1989) for the O5.5V and O6V spectral types.

binarity has been found in the optical domain. In the case of 9 Sgr, low amplitude radial velocity variations in the optical spectrum suggest it is a binary with a yet undetermined period (Rauw et al. 2002). If the high plasma temperatures observed for these three stars are indeed due to wind collisions within binary systems, the observed post-shock temperatures are related to rather high pre-shock wind velocities (typically at least $\sim$1000 km s^{-1}). Such high velocities can only be achieved in binary systems where the winds collide after they have reached their terminal velocity, i.e. in systems with periods exceeding several days. In this scenario, the non-thermal radio emission is produced by a population of relativistic electrons accelerated in the shock due to the same wind-wind interaction. The putative non-thermal X-ray counterpart to this non-thermal radio emission has little chance to be detected, as it would probably be overwhelmed by the hard thermal component produced by the wind collision. If on the contrary the period were shorter, the pre-shock velocities would be lower and the X-ray thermal emission would be softer, allowing consequently the putative non-thermal X-ray emission to be detected in the hard part of the spectrum. However, the shorter orbital period required to possibly observe the non-thermal X-ray emission could cause the wind collision zone to be deeply embedded in the stellar wind material, thereby leading to a severe absorption of the synchrotron radio emission.

The fact that the conditions for detecting a non-thermal emission in the radio domain may be different from those for such a detection in the X-rays raises an interesting question. We may indeed wonder whether non-thermal radio emitters are ideal candidates to search for a non-thermal X-ray counterpart. To address this issue, let us consider some results obtained for other massive stars recently observed in the X-ray domain.

In the case of the short period massive binary HD 159176 (OV7 + OV7), a high energy tail is observed in the X-ray spectrum. It can not be fitted with a thermal model[5], but can be approximated with a power law (De Becker et al. 2004a). For that system, the typical temperature of the X-ray emitting plasma is sufficiently low to prevent the putative power law tail to be overwhelmed by the thermal X-rays from the colliding wind zone. This is due to the fact that the winds collide as they have not reached their terminal velocities. The non-detection of HD 159176 (Bieging et al. 1989) in the radio domain is compatible with the rather low flux expected for purely thermal radio emitters, and can be explained by the fact that any putative synchrotron emitting zone would be deeply embedded within the stellar winds. We mention also the case of WR 110 (HD 165688) whose binarity has not yet been established. Skinner et al. (2002) reported a soft thermal X-ray spectrum, along with a high energy power law tail, whilst its radio spectrum is purely thermal.

Considering these recent results, we propose that the non-thermal radio emission could ideally be detected in the case of binaries with periods larger than several weeks. For instance, the shortest period well-established non-thermal radio emitter is Cyg OB2 #8A, with an orbital period of about 21.9 d (De Becker et al. 2004c). On the other hand, short period binaries are not expected to display a non-thermal radio emission because of the strong absorption by the wind material. However, their rather soft thermal X-ray emission could possibly unveil a power law component produced by inverse Compton scattering of UV photons. Moreover, the less diluted UV radiation field in the shock region of close binary systems is expected to lead to the production of a higher non-thermal X-ray flux, favoring its detection. In the context of this scenario, the simultaneous observation of non-thermal radiation in the X-ray (below 10.0 keV) and radio domains appears rather unlikely.

6. Other X-ray sources in the field of view

6.1. Source list

Beside HD 167971 discussed in the previous sections, and HD168112 (De Becker et al. 2004b), other fainter X-ray sources are observed in the field of the EPIC cameras. To investigate the X-ray emission from these sources, we processed our data with the version 6.0.0 of the Science Analysis Software (SAS) to benefit from the latest version of the *edetect_chain* metatask. We filtered the event lists of the April observation to reject the end of the exposure contaminated by a soft proton flare (see Sect. 3.1 of De Becker et al. 2004b), thereby reducing the effective exposure time to about 9 and 6 ks for EPIC-MOS and EPIC-pn respectively. Adding together the two observations and considering that EPIC-pn is about twice as sensitive as EPIC-MOS, we obtain an EPIC-MOS equivalent combined exposure time of about 80 ks on NGC 6604.

We first applied the source detection simultaneously to the data from the three EPIC instruments of our two observations to improve the detection efficiency. We used three energy bands respectively refered to as S (0.5–1.0 keV), M (1.0–2.5 keV), and H (2.5–10.0 keV). The images in these three energy bands were extracted on the basis of the merged event lists of the two observations, for the three EPIC instruments respectively. We obtained a first source list using a detection likelihood threshold of 40. We then inspected each source of the list by eye to reject false detections due to background fluctuations and instrumental artifacts following the same approach as Rauw et al. (2003) and Nazé et al. (2004). Adopting the formalism described by Sana et al. (2005), we determined the likelihood thresholds adequate for individual datasets. The likelihood thresholds we finally adopted are 40 for the combined EPIC data sets, 40 for combined EPIC-MOS, 10 for individual EPIC-MOS, and 10 for EPIC-pn. After applying the same procedure to data sets resulting from individual instruments and/or observations, we added a few more sources to the list obtained for the full combined data set. We finally obtain a catalogue of 31 X-ray sources presented in Table 6 by order of increasing right ascension. The position of these sources in the EPIC field is shown in Fig. 6. All sources are identified following the naming conventions recommended by the *XMM SOC* and the IAU.

---

[5] Optically thin plasma model (Mewe et al. 1985; Kaastra 1992) or colliding wind model (Antokhin et al. 2004).

Table 6. Characteristics of the X-ray sources in the field of view. The 31 sources are sorted by order of increasing right ascension. Source #1 was identified as an extended source, and the 30 next ones as point sources. The count rates corrected for the exposure map are quoted for all three EPIC instruments. The missing values are due to a strong deviation from those of the other instruments because of CCD gaps. The hardness ratios are given for EPIC-pn only. The quoted counterparts are located within 4.5″ of the X-ray sources. Nr is the number of counterparts within the correlation radius, and *d* is the angular separation between the X-ray source and its nearest counterpart. The error bars on the count rate represent the ±1 σ Poissonian standard deviation.

#	XMMU	MOS1 CR	MOS2 CR	pn CR	HR_1	HR_2	GSC 2.2						2MASS					USNO B1.0		
		10^{-3} cts s^{-1}	10^{-3} cts s^{-1}	10^{-3} cts s^{-1}			No.	$d('')$	Cat. id.	R	B	V	No.	$d('')$	J	H	K_S	No.	$d('')$	Cat. id.
(1)	(2)	(3)	(4)	(5)	(6)	(7)	(8)	(9)	(10)	(11)	(12)	(13)	(14)	(15)	(16)	(17)	(18)	(19)	(20)	(21)
1	J181731.4–120622.2[a]			311.0 ± 15.3	0.34 ± 0.05	–0.67 ± 0.05	1	4.4	S3001223315		10.6	9.7	1	4.5	7.3	7.1	6.9	1	4.4	0778-0542759
2	J181746.1–120542.3	6.1 ± 1.0	5.8 ± 1.0	13.1 ± 1.9	0.55 ± 0.14	–0.17 ± 0.16	1	2.0	S300122014588	17.9			2	1.9	15.0	13.9	12.6	1	2.3	0779-0530036
														2.8	14.7	13.8	12.2			
3	J181750.7–120400.4	4.4 ± 1.0	2.6 ± 0.9	12.1 ± 1.9	0.51 ± 0.14	–0.62 ± 0.20	1	2.2	S3001220900	13.0	14.4	13.3	1	1.5	11.4	11.1	10.9	1	1.9	0779-0530128
4	J181750.7–120506.3	3.5 ± 0.8	4.2 ± 0.8*	11.8 ± 1.8	0.30 ± 0.14	–0.47 ± 0.22	1	1.7	S300122015025	15.7	18.7	16.3	1	1.4	13.4	12.6	12.4	1	2.3	0779-0530127
5	J181806.0–121433.8[b]	231.4 ± 4.4*	229.6 ± 4.1*	673.3 ± 8.3*	0.23 ± 0.01*	–0.75 ± 0.01*	1	1.6	S30012201153		8.3	7.6	1	1.6	5.5	5.3	5.1	1	1.6	0777-0543906
6	J181808.4–120824.9	1.3 ± 0.4	1.2 ± 0.4	5.7 ± 0.9	0.51 ± 0.31	0.42 ± 0.15	1	2.6	S300122012953	17.9			1	2.2	15.6	15.2	14.7	0		
7	J181808.6–120851.2	2.6 ± 0.5	2.1 ± 0.4	3.6 ± 0.8*	1.00 ± 0.43*	0.53 ± 0.20*	0						1	2.6	15.2	13.8	13.4	1	3.2	0778-0543325
8	J181810.0–121048.5[c]	12.5 ± 0.8	13.1 ± 0.9	36.6 ± 1.9*	0.38 ± 0.05*	–0.80 ± 0.05*	1	2.1	S3001220165		10.0	9.3	1	2.2	7.7	7.5	7.4	1	2.1	0778-0543346
9	J181810.6–120409.3	2.1 ± 0.5	2.8 ± 0.6	7.7 ± 1.2	0.75 ± 0.16	–0.16 ± 0.17	1	1.8	S300122015589	14.3	16.8	15.3	1	1.5	11.3	10.2	9.4	1	1.5	0779-0530455
10	J181813.1–121503.1	4.6 ± 0.7	4.2 ± 0.7	3.8 ± 0.9	0.89 ± 0.16	–0.82 ± 0.23	1	4.4	S30012209459	17.5			1	3.3	15.3	14.4	14.3	1	3.5	0777-0544085
11	J181815.3–121148.7	4.6 ± 0.6	4.5 ± 0.6	13.4 ± 1.2	0.72 ± 0.08	–0.13 ± 0.09	1	1.2	S300122011032	18.5			1	1.3	15.2	14.2	14.0	0		
12	J181815.7–120842.8	1.2 ± 0.4	1.5 ± 0.4	2.6 ± 0.7	1.00 ± 0.31	0.34 ± 0.24	0						0					0		
13	J181816.9–121617.4	3.3 ± 0.6	1.2 ± 0.5	3.7 ± 0.9*	1.00 ± 0.39*	0.08 ± 0.27*	0						0					0		
14	J181819.3–121616.9	5.4 ± 0.8	3.6 ± 0.6	13.3 ± 1.7*	0.54 ± 0.12*	–0.41 ± 0.14*	0						0					0		
15	J181820.5–121736.3	1.7 ± 0.5	0.6 ± 0.3	4.2 ± 0.9	1.00 ± 0.12	0.16 ± 0.21	0						0					1	1.1	0777-0544362
16	J181822.6–121503.4	7.3 ± 0.8	6.6 ± 0.7	15.2 ± 1.5*	0.85 ± 0.17*	0.45 ± 0.08*	0						0					0		
17	J181823.2–120719.4	1.1 ± 0.4	2.2 ± 0.4	4.1 ± 0.8	0.38 ± 0.33	0.42 ± 0.18	0						0					1	2.5	0778-0543806
18	J181827.3–120613.4	3.0 ± 0.5	3.5 ± 0.5*	11.9 ± 1.2	0.45 ± 0.09	–0.67 ± 0.11	1	0.9	S300122014289	18.1			1	0.1	15.2	14.1	13.8	1	0.2	0778-0544019
19	J181830.3–121359.1	4.1 ± 0.5	3.5 ± 0.5	10.4 ± 1.0	0.61 ± 0.08	–0.37 ± 0.11	1	1.6	S30012209935	17.2			1	1.6	15.2	14.3	14.0	1	1.6	0777-0545005
20	J181832.0–121740.3	1.6 ± 0.5	1.4 ± 0.5*	4.3 ± 1.0	0.60 ± 0.20	–0.60 ± 0.27	1	2.4	S30012208102	15.2	18.9	17.7	2	1.4	13.8	12.9	13.3	2	2.3	0777-0545104
														2.8	13.5	12.6	13.1		2.9	0777-0545111
21	J181832.1–121605.0	3.5 ± 0.6	2.4 ± 0.6*	7.6 ± 1.1	0.54 ± 0.12	–0.51 ± 0.16	1	3.5	S300122028708	18.4			2	2.6	14.7	13.8	13.5	1	3.3	0777-0545106
														4.0	14.2	13.2	12.8			
22	J181837.1–120601.7	1.6 ± 0.4	1.3 ± 0.4	8.1 ± 1.0*	0.09 ± 0.12*	–1.00 ± 0.10*	1	2.6	S300122014474	14.1	16.2	15.6	1	1.5	13.5	12.9	12.9	1	2.8	0779-0531112
23	J181839.5–120935.3	1.3 ± 0.3	1.3 ± 3.3	5.2 ± 0.9*	0.60 ± 0.16*	–0.30 ± 0.19*	1	3.8	S30012201041	13.5	14.5	13.8	2	1.6	14.2	13.0	12.3	1	3.5	0778-0544645
														4.0	12.5	12.2	12.1			
24	J181840.9–120623.7[d]	55.3 ± 1.8	59.2 ± 1.9				1	0.6	S3001220959		9.2	8.6	1	0.6	6.9	6.7	6.6	1	0.6	0778-0544725
25	J181844.3–120752.3	12.1 ± 0.9	13.5 ± 0.9	45.6 ± 1.9	–0.37 ± 0.04	–0.89 ± 0.06	0						0					0		
26	J181901.2–120050.8	4.6 ± 0.9	3.9 ± 0.8	16.4 ± 2.2	0.76 ± 0.12	–0.06 ± 0.14	1	1.0	S300122017698	15.2	18.5	16.6	1	1.2	12.0	11.0	10.5	1	1.0	0779-0532345
27	J181903.0–120638.4	4.3 ± 0.8	3.2 ± 0.6	12.2 ± 1.5	–0.26 ± 0.11	–0.70 ± 0.27	2	2.3	S3001220971		10.5	9.8	2	2.4	8.3	8.1	8.0	1	2.3	0778-0546021
								3.4	S300122014341	12.0				4.2	13.8	12.9	12.7			
28	J181904.9–120918.7[e]		2.8 ± 0.6	7.3 ± 1.3*	1.00 ± 0.18*	0.54 ± 0.13*	0						1	2.0	14.2	13.1	12.8	0		
29	J181905.2–120306.5	2.9 ± 0.7	5.1 ± 0.9	9.1 ± 1.7	0.99 ± 0.09	–0.07 ± 0.18	0						2	0.9	15.0	14.0	13.5	2	1.1	0779-0532614
														3.8	15.3	14.3	14.0		2.6	0779-0532625
30	J181906.8–121018.2	5.4 ± 0.9	7.0 ± 0.9	18.0 ± 1.9*	0.60 ± 0.19*	0.60 ± 0.08*	0						1	4.5	15.4	14.6	14.1	1	3.0	0778-0546278
31	J181909.9–121753.4	5.7 ± 1.1	8.2 ± 1.3	12.8 ± 2.1	1.00 ± 0.05	–0.23 ± 0.17	1	1.0	S300122028430	17.3			1	1.3	15.1	14.2	13.9	1	1.1	0777-0547481

[a] This X-ray source is associated to the O6V((f)) star HD 167834 (BD –12° 4969). We quote the count rates obtained as an extended source detection. The X-ray properties quoted are from EPIC-pn data of the April observation only, as this source was not in the field of the other data sets.

[b] HD 167971. The large difference between the count rates quoted for this star in this table and the observed ones given in Table 4 are explained by the exposure map correction applied during the source detection procedure.

[c] BD –12° 4982 (O9.5I or III, see text).

[d] HD 168112: the EPIC-pn count rate is not quoted as a CCD gap crosses the sources region. The analysis described by De Becker et al. (2004b) was performed with different screening criteria than for the current analysis to deal with the EPIC-pn data.

[e] We note that even if no optical counterpart was found in the catalogues used for the correlation, a star appears clearly on the DSS image centered on this position.

[*] This value is possibly affected by a CCD gap located at <10 arcsec, but is nevertheless quoted.

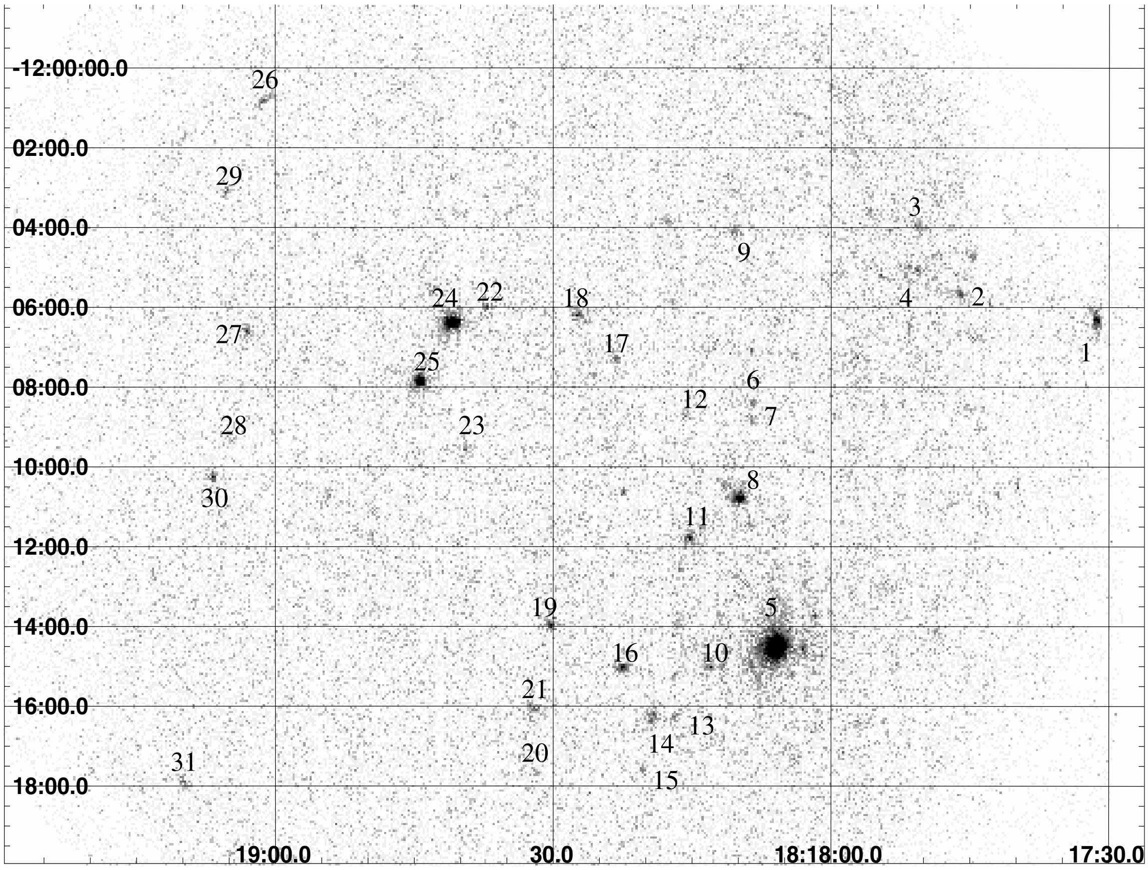

Fig. 6. Image of the NGC 6604 open cluster from the combined EPIC data sets of the two observations. The X-ray sources listed in Table 6 are labelled. The pixel size is 2.5″. The right ascension is increasing from the right to the left, and the declination is increasing from the bottom to the top. The width of the field is about 30′.

6.2. Source identification

The position of the 31 X-ray sources were cross-correlated with three catalogues: the Guide Star Catalogue (GSC, version 2.2)[6], the Two Micron All Sky Survey (2MASS, Skrutskie et al. 1997), and the US Naval Observatory (USNO-B1.0, Monet et al. 2003). We derived the optimal correlation radius following the procedure described by Jeffries et al. (1997). In this way, we find that a cross-correlation radius of 4.5 arcsec includes the majority of the true correlations while rejecting most of the spurious correlations. With a radius of 4.5 arcsec we expect to achieve at least 23 true and only about 2 spurious correlations. We also assume that the position of the source on the detector has little impact on the correlation radius. We should however keep in mind that this assumption is mostly valid close to the center of the field for a given instrument, but could possibly bias our source identification procedure for large off-axis angles.

Among the 31 X-ray sources quoted in Table 6, five sources (#12, #13, #14, #16 and #25) have neither a GSC, 2MASS nor USNO counterpart. 20 (respectively 23) have at least one optical counterpart in the GSC (resp. USNO) catalogue, and some sources have possibly two optical (#20, #27 and #29) counterparts. No other positive correlations were found with the sources included in the photometric survey of Forbes & DuPuy (1978) within a 10 arcsec radius. A total of 18 EPIC sources in the field of view of NGC 6604 have a single 2MASS counterpart while another 6 sources have two infrared counterparts. In Fig. 8, we show the JHK colour–colour diagram of those objects that have quality flags A or B for the measurements of all three individual near-IR magnitudes. We used the March 2003 update of the colour transformations, initially derived by Carpenter (2001) and available on the 2MASS website[7], to convert the $J - H$ and $H - K_s$ colours to the homogenized photometric system introduced by Bessell & Brett (1988). We thus exclude all objects that have colours and magnitudes that are either subject to large uncertainties or are only upper limits due to non-detections. Using the extinction law of Rieke & Lebofsky (1985) and assuming $R_V = A_V/E(B - V) = 3.1$ (Barbon et al. 2000), we also show the reddening vector for

---

[6] The Guide Star Catalogue-II is a joint project of the Space Telescope Institute and the Osservatorio Astronomico di Torino.

[7] `http://www.ipac.caltech.edu/2mass/index.html`

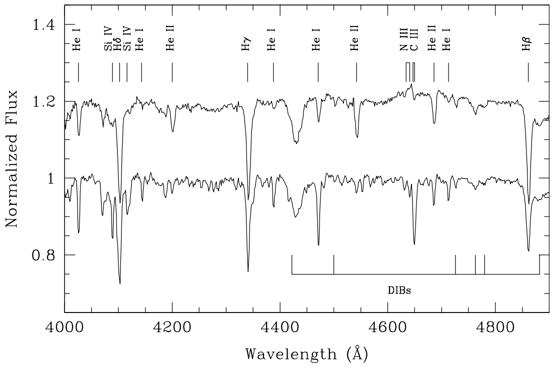

Fig. 7. Optical normalized spectra obtained between 4000 and 4900 Å respectively for the sources #1 (HD 167834, *top spectrum*) and #8 (BD −12° 4982, *bottom spectrum*).

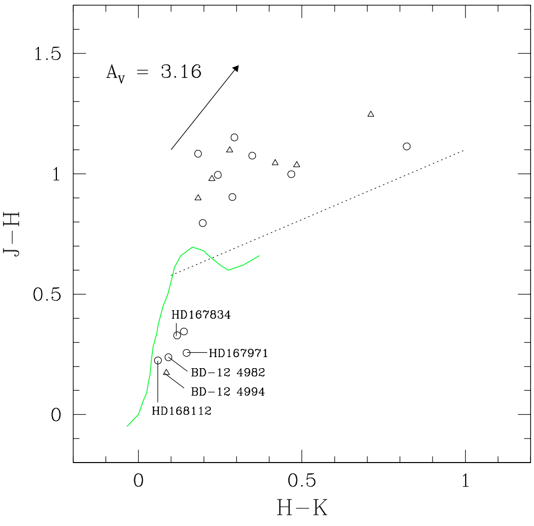

Fig. 8. *JHK* colour–colour diagram of the 2MASS counterparts of the X-ray sources in the EPIC field of view around NGC 6604. The heavy solid line yields the intrinsic near-IR colours of main sequence stars following Bessell & Brett (1988), whereas the reddening vector is illustrated for $A_V = 3.16$. Open circles and triangles stand for EPIC sources having respectivley a single or two 2MASS counterpart(s). The dotted straight line yields the locus of dereddened colours of classical T Tauri stars according to Meyer et al. (1997).

$E(B - V) = 1.02$ as was found to be appropriate for NGC 6604 (Barbon et al. 2000).

There are three broad groups that appear in Fig. 8. The first group consists of five sources that are clearly associated with early-type stars: #1 (HD 167834), #5 (HD 167971), #8 (BD −12° 4982), #24 (HD 168112) and #27 (BD −12° 4994). In the second group, we find objects around $H - K \sim 0.3$ and $J - H \sim 1.0$. These objects have colours that are consistent with slightly reddened late type (early G to late K) main-sequence or giant stars. Finally, a small group of objects (#9, #26 and one of the two counterparts of the three sources #21, #23 and #29) have $H - K > 0.4$. Assuming that they are affected by the same reddening as NGC 6608 ($E(B - V) = 1.02$), these objects would be associated with very late (mostly late M) main sequence stars. If these sources were normal main sequence stars belonging to NGC 6604, it seems rather unlikely that we would be able to detect their X-ray emission. An alternative possibility could be that they are X-ray bright pre-main sequence stars with a moderate IR excess. In fact, their dereddened infrared colours are in broad agreement with the intrinsic colours of classical T Tauri stars (Meyer et al. 1997).

Of course, a fraction of the X-ray selected objects might in fact be foreground stars or background sources. NGC 6604 ($l_{\rm II}$ = 18.26°, $b_{\rm II}$ = 1.69°) lies very close to the Galactic plane and the total Galactic neutral hydrogen column density along this direction must therefore be quite large. This should produce a substantial absorption of X-ray photons from extragalactic background sources. Because of the Galactic coordinates of NGC 6604, estimating this column density accurately is a very difficult task. For instance, the *DIRBE*/*IRAS* extinction maps provided by Schlegel et al. (1998) yield a good estimate of the total Galactic $E(B - V)$ at Galactic latitudes above $|b_{\rm II}| \geq 5°$, but are subject to very large uncertainties near the Galactic plane. With these limitations in mind, the maps of Schlegel et al. (1998) suggest $E(B - V) \sim 3.5 \pm 0.5$ for NGC 6604 (corresponding to $N_{\rm H} \sim 2 \times 10^{22}$ cm^{-2}). Assuming that extragalactic background sources have a power-law spectrum with a photon index of 1.4, and are subject to a total interstellar absorption of 2×10^{22} cm^{-2}, the detection limits $\sim 4.0 \times 10^{-3}$ and 1.5×10^{-3} cts s^{-1} for the pn and MOS detectors translate into unabsorbed fluxes of 2.1×10^{-14} erg cm^{-2} s^{-1} and 6.0×10^{-14} erg cm^{-2} s^{-1} in the 0.5–2.0 keV and 2.0–10 keV band respectively. From the $\log N - \log S$ relation of Giacconi et al. (2001), we would expect to first order to detect around 8–10 extragalactic sources over the EPIC field of view. We emphasize that these objects should be detected as rather hard sources. Hence, several of the hard sources quoted in Table 6 that lack an optical counterpart may actually be associated with AGN.

Optical spectra of the counterparts of EPIC sources #1, #8 and #14 were obtained on June 22, 2004 with the EMMI instrument mounted on ESO's 3.5 m New Technology Telescope (NTT) at La Silla. The EMMI instrument was used in the RILD low dispersion spectroscopic mode with grism # 5 (600 grooves mm^{-1}) providing a wavelength coverage from about 3800 to 7020 Å with a spectral resolution of 5.0 Å (`FWHM` of the He–Ar lines). The slit width was set to 1 arcsec and the exposure times were 1 min for the two bright sources #1 and #4, and 40 min for the counterpart of source #14. The data were reduced in the standard way using the `long` context of the MIDAS package.

The optical spectrum of source #1 (HD 167834) is given in the top part of Fig. 7. We obtain equivalent widths (*EW*) of 0.36 and 0.69 Å respectively for the He I λ 4471 and He II λ 4542 lines. We estimate that the typical error on the estimate of *EW*s is about 5–10%. According to the classification criterion given by Mathys (1988), and considering that the N III $\lambda\lambda$ 4634-41 lines are in emission and the He II λ 4686 line is in strong absorption, we derive an O6V((f)) spectral type. We note also that the C III λ 5696 line is in weak emission. In the

Table 7. Parameters for models fitted to the spectra of sources #1 between 0.4 and 10.0 keV, and #8 and #25 between 0.4 and 5.0 keV. The data are from the EPIC-pn observation for source #1, and from the three EPIC instruments for sources #8 and #25. The parameters have the same meaning as in Tables 2 and 3. For sources #1 and #8, two absorption columns were used accounting respectively for the ISM and the local absorption (same ionized wind absorption model as for HD 167971, left as a free parameter). The ISM columns were frozen at 0.73×10^{22} and 0.55×10^{22} cm^{-2} respectively for sources #1 and #8. In the case of source #25, a unique absorption column (ISM + local) was used and left as a free parameter. The error bars represent the 90% confidence interval. The upper and lower parts of the table are respectively devoted to the purely thermal models and to the model including a power law. The observed fluxes quoted in the last column are affected by large errors due to the large relative error on the normalization parameters (Norm$_1$ and Norm$_2$), and no significant variability between the April and September observations can be claimed on the basis of these values.

Source	Obs.	N_H (10^{22} cm^{-2})	kT_1 (keV)	Norm$_1$	kT_2 (keV)	Norm$_2$	χ^2_ν (d.o.f.)	Obs. flux (erg cm^{-2} s^{-1})
#1	April	$0.91^{1.18}_{0.56}$	$0.19^{0.23}_{0.17}$	$6.20^{15.09}_{1.68} \times 10^{-2}$	$1.38^{2.02}_{1.07}$	$1.20^{1.57}_{0.81} \times 10^{-3}$	0.97 (78)	8.0×10^{-13}
#8	April	$0.71^{1.06}_{0.43}$	$0.71^{0.86}_{0.62}$	$0.26^{4.75}_{2.73} \times 10^{-3}$	–	–	0.73 (66)	6.8×10^{-14}
	September	$0.69^{0.86}_{0.49}$	$0.71^{0.80}_{0.64}$	$0.30^{3.84}_{2.12} \times 10^{-3}$	–	–	0.85 (178)	7.9×10^{-14}
#25	April	$0.72^{0.84}_{0.51}$	$0.23^{0.33}_{0.19}$	$1.12^{3.51}_{0.00} \times 10^{-3}$	–	–	0.63 (95)	7.9×10^{-14}
	September	$0.76^{0.93}_{0.59}$	$0.24^{0.32}_{0.18}$	$0.90^{4.14}_{0.00} \times 10^{-3}$	–	–	0.87 (133)	6.1×10^{-14}
		N_H (10^{22} cm^{-2})	kT (keV)	Norm$_1$	Γ	Norm$_2$	χ^2_ν (d.o.f.)	Obs. Flux (erg cm^{-2} s^{-1})
#1	April	$0.20^{1.24}_{0.00}$	$0.58^{0.66}_{0.46}$	$1.43^{2.61}_{0.47} \times 10^{-3}$	$2.98^{7.28}_{1.19}$	$4.04^{12.96}_{2.31} \times 10^{-4}$	1.16 (78)	7.9×10^{-13}

case of source #8 (BD –12° 4982, bottom spectrum of Fig. 7), the ratio of the *EW* of the He I λ 4471 and He II λ 4542 lines leads to an O9.5 spectral type. This spectral type is in excellent agreement with that given by Barbon et al. (2000, their source #32). Following the *EW*s of the He I λ 4388 line (0.36 Å) and of the He II λ 4686 line (0.31 Å), we derive a supergiant luminosity class, whilst the *EW*s of the Si IV λ 4088 line (0.54 Å) and of the He I λ 4143 line (0.29 Å) point to a giant luminosity class. We note however that the spectrum of this star is very similar to that of the O9.7Iab star μ Nor (HD 149038) given by Walborn & Fitzpatrick (1990). Finally, for the source #14, possibly associated to Cl* NGC 6604 FD 61 (following the nomenclature proposed by Forbes & DuPuy 1978) even if no optical counterpart is quoted in Table 6, we derive a G6 spectral type, with an uncertainty of about 2 spectral types. We note that this optical counterpart is however located at about 6 arcsec of the X-ray source #14. Two possible 2MASS infrared counterparts are approximately located at the position, but the precision of their photometry is very poor.

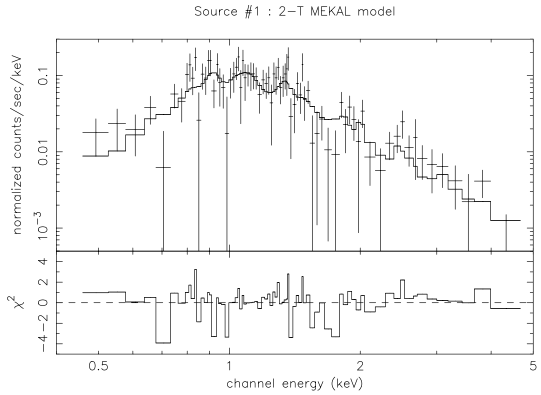

Fig. 9. EPIC-pn spectrum of source #1 (HD 167834) obtained in April 2002, fitted with a `wabs`$_{\rm ISM}$`*wind*(mekal+mekal)` model. The ISM absorption column was frozen at 0.73×10^{22} cm^{-2}

6.3. X-ray properties

Using the count rates obtained in the three energy bands mentioned in Sect. 6.1, we obtained hardness ratios (see Cols. 6 and 7 of Table 6) defined respectively as

$$HR_1 = \frac{M - S}{M + S}$$

$$HR_2 = \frac{H - M}{H + M}\cdot$$

We find that some sources present rather extreme hardness ratios, suggesting very hard X-ray spectra. Sources #7, #12, #13, #15, #28, #29 and #31 have HR_1 values larger than 0.90 as shown in Col. 6 of Table 6 for EPIC-pn. We note that high hardness ratios are also obtained from EPIC-MOS instruments for these sources. Some of these sources may be extragalctic sources as discussed above.

We selected the brightest sources, and performed a spectral analysis of our EPIC data from the April and September observations.

Source #1 is likely associated with the O6V((f)) star HD 167834 (BD –12° 4969). This X-ray source was detected by the *EINSTEIN* satellite with a count rate of

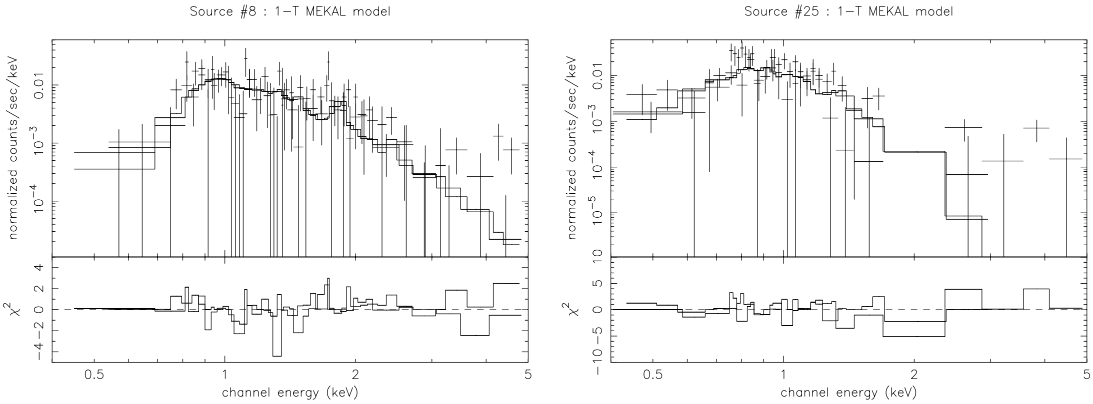

Fig. 10. Combined EPIC-MOS1 and EPIC-MOS2 spectra of the September 2002 observation, fitted with a `wabs`$_{\rm ISM}$`*wind*mekal` model for source #8 (*left*) and a `wabs*mekal` model for source #25 (*right*). In the case of source #8, the ISM absorption column was frozen at 0.55×10^{22} cm^{-2}.

0.012 ± 0.004 cts s^{-1}, leading to a flux[8] of about 3.4×10^{-13} erg cm^{-2} s^{-1} (Grillo et al. 1992). If we take into account the exposure map correction, this source is the second brightest X-ray emitter in NGC 6604, after HD 167971 and before HD 168112.

Source #8 has a single counterpart in the three catalogues used for the source identification, and is most probably associated to the O9.5I or III star BD −12° 4982. No optical or infrared counterpart was found for source #25. No information on the X-ray emission of these two objects has been found in the literature.

In the case of #1, a 50″ radius circular region was used to extract the spectrum. The EPIC-pn spectrum was binned to have a minimum of 9 counts per channel. For #8 and #25, the spectra were extracted within a circular region with a radius of 40″. For the three sources, the background was extracted within an annulus centered on the source and covering the same area as the source region. Gaps and bad columns were excluded by rejecting properly adjusted rectangular boxes. The spectra were fitted following the same approach as described in Sect. 3.1.2. For sources #8 and #25 we obtained very similar fitting results from the EPIC-MOS and EPIC-pn spectra. All spectra from sources #8 and #25 were binned to reach a minimum of 5 counts per channel. The main results from the spectral analysis of these sources are summarized herebelow and in Table 7:

- #1. From the $(B-V) = 0.95$ color given by Forbes (2000) for this star, and the intrinsic color typical for an O6.5 star (Mihalas & Binney 1981), we followed the same procedure as described in Sect. 3.1.1 to derive $E(B-V) = 1.26$, yielding an ISM $N_{\rm H}$ of 0.73×10^{22} cm^{-2}. We used the same ionized wind absorption model as for HD 167971 to account for local absorption, and we left it as a free parameter. The EPIC-pn spectrum is best fitted with a two-temperature thermal `mekal` model (see Fig. 9), with characteristic temperatures of about 0.2 and 1.4 keV. The rather high temperature for the hotter component suggests that the intrinsic X-ray emission from the shocks in the stellar wind of the OB star (see e.g. Feldmeier et al. 1997) is not the only process responsible for the observed X-rays. From this model, we derive an observed flux of $\sim 8.0 \times 10^{-13}$ erg cm^{-2} s^{-1} between 0.4 and 10.0 keV. Assuming that the distance to the star is 1.7 kpc (Barbon et al. 2000), we obtain an $L_{\rm X}$ corrected for the ISM absorption of 4.4×10^{33} erg s^{-1}. If we consider the color excess derived above in this paragraph, the V magnitude from Table 6, the distance to NGC 6604 provided by Barbon et al. (2000), and the typical bolometric correction for an O6V star (Vacca et al. 1996), we obtain a bolometric luminosity of about 1.7×10^{39} erg s^{-1}. This yields an $L_{\rm X}/L_{\rm bol}$ ratio of 2.6×10^{-6}. Considering the X-ray luminosity expected from the empirical relation of Berghöfer et al. (1997), e.g. $\sim 2.8 \times 10^{32}$ erg s^{-1}, we obtain an X-ray luminosity excess of about 16! We mention that if we use the typical bolometric luminosity for a single O6V star (i.e. 9.8×10^{38} erg s^{-1}, Howarth & Prinja 1989), HD 167834 appears a factor 30 overluminous in X-rays. The spectrum of this source is also compatible with a model including a thermal component and a power law, but the quality of the fit is somewhat poorer than that obtained for the purely thermal model (see Table 7). The possible explanations to produce additional X-rays associated to a plasma temperature of a few 10^7 K could be an interaction between the winds of two OB stars in a binary system (see e.g. Stevens et al. 1992), or possibly a magnetic confinement scenario as proposed by Babel & Montmerle (1997). However, the huge luminosity excess can more probably be explained by the binary scenario. Higher quality data are needed to discuss the physical origin of this X-ray emission.
- #8. We adopted the same approach as for source #1 to establish the value of the ISM hydrogen column density. With a $(B-V) = 0.64$ (Forbes 2000), we derive an ISM $N_{\rm H}$ of

---

[8] The flux was estimated assuming a thermal model with $kT = 0.5$ keV and a neutral absorption column obtained by integrating a model of the hydrogen particle spatial distribution in the Galaxy. The procedure is described in Grillo et al. (1992).

0.55×10^{22} cm^{-2}. A second absorption column was left as a free parameter to account for the absorption by the wind material. The best fit is obtained between 0.4 and 5.0 keV with a single temperature `mekal` model, with a characteristic temperature of about 0.7 keV. We do not find any significant difference in the model parameters obtained for our two observations. We obtain an oberved flux between 0.4 and 5.0 keV of 7–8 × 10^{-14} erg cm^{-2} s^{-1}. The fact that this source presents a rather soft spectrum is consistent with the rather modest hardness ratios reported in Table 6. The combined fit of EPIC-MOS spectra is shown in Fig 10.

– #25. As no optical counterpart was found for this source, we were not able to determine a priori an ISM hydrogen column density in its direction. So we used a unique absorption column which was left as a free parameter. The spectral analysis of this source between 0.4 and 5.0 keV reveals a very soft spectrum fitted with a one-temperature model with a kT of about 0.2 keV, which is very consistent with the HR_1 and HR_2 values quoted in Table 6. We did not find any indication for a significant variability of the model parameters between our April and September observations. Figure 10 shows the EPIC-MOS spectra fitted simultaneously with the 1-T model.

6.4. X-ray variability

We ran the `edetect_chain` metatask on the three EPIC data sets simultaneously, separately for the two observations, and we carefully inspected the images in both cases to check whether the sources listed in Table 6 are detected at both epochs. Most of the apparent variability observed for the X-ray sources can be explained by the fact that the effective exposure times of our two pointings are significantly different (∼6 ks in April and ∼11 ks in September for EPIC-pn, and ∼9 ks in April and ∼13 ks in September for EPIC-MOS), and to some extent can also be due to gaps or bad columns. However, it appears that the sources #19 and #21 are only detected in September 2002, whilst sources #15, #28 and #31 are detected only in April 2002. This strong variability suggests a flaring behaviour. We extracted light curves to investigate their variability with more details, but these sources are too faint to provide conclusive results. Source #31 presents apparently a sufficiently high count rate to give a valuable light curve, but we note that this source lies very close to the border of the EPIC field. Consequently, the observed count rate is about a factor of 3 lower than the exposure corrected value quoted in Table 6. Among these targets, only #15, #28 and #31 present a very high hardness ratio HR_1. A comparison of the count rates obtained from the two separate observations reveals no significant variability for the other X-ray sources detected with *XMM-Newton*.

We finally searched for a short time scale variability in the cases of the X-ray sources discussed in Section 6.3, i.e. #1, #8, and #25. We extracted light curves with time bins ranging from 100 s to 1000 s following the same approach as used in the case of HD 167971 (see Sect. 3.2.1). Variability tests (chi-square, *pov*-test) performed on these light curves did not reveal any significant variability during our two *XMM-Newton* observations for any of the three EPIC instruments.

6.5. Star formation in NGC 6604?

As mentioned in the previous subsections, several indicators (possible flaring activity, position in the JHK_S diagram...) suggest some of the X-ray emitters in NGC 6604 may be candidate PMS stars (Feigelson & Montmerle 1999). This fact is at first sight contradictory to the statement of Barbon et al. (2000) that pre-ZAMS objects are not detected in NGC 6604. However, this lack of detection could be partly explained by the fact that the study of these authors was limited to an area of only 2.1 × 3.3 arcmin^2 centered on HD 167971. Most of the X-ray sources we detect are indeed located outside this area.

The fact that our investigation is only able to reveal the brightest X-ray emitters harboured by NGC 6604 could strongly bias our investigation of PMS activity in the cluster. Let us consider the faintest X-ray sources of our list. Assuming a simple thermal model with a kT of about 0.5 keV[9], we obtain an unabsorbed flux between 0.4 and 10.0 keV of about 1.0×10^{-14} erg cm^{-2} s^{-1}. For a distance to the cluster of about 1.7 kpc (Barbon et al. 2000), this unabsorbed flux leads to a luminosity for the faintest source detected in our data of about 3.5×10^{30} erg s^{-1}. This value is of the order of the highest typical luminosities expected for PMS stars when no flare is occuring (Feigelson & Montmerle 1999). This suggests that our data only allow a detection of the more luminous PMS candidates within NGC 6604, and possibly during flaring stages, i.e. at their highest X-ray emission state. Deeper X-ray observations are needed to investigate the PMS populations in NGC 6604.

Unlike the situation in NGC 6383 (Rauw et al. 2003) and NGC 6231 (Sana et al. 2005), the X-ray sources in NGC 6604 reveal no concentration around the more massive cluster members. In NGC 6383 and NGC 6231, the fainter X-ray sources are mainly associated to PMS stars, thereby suggesting a close relationship between the formation of low-mass and high-mass stars. In NGC 6604, the rather sparse spatial distribution of the members of the cluster already noted in the visible domain, show that this is not a mass-segregated open cluster. Following the *N*-body simulations performed by Bonnell & Bate (2002), gas accretion should indeed have led to a strong contraction of the cluster responsible for a significant mass segregation. A possible explanation for the absence of notable mass segregation in open clusters was proposed by Vine & Bonnell (2003). According to these authors, the strong stellar winds of O and B stars in young open clusters result in a significant gas removal from the core, where the OB stars are preferentially formed. Their simulations show that the changes in the gravitational potential of the core as a result of this gas expulsion is able to break the mass segregation (*core dissolution*), allowing stars to drift away from the core. The apparently different dynamical stages between NGC 6604 and NGC 6383 is not

---

[9] With an absorbing interstellar column of about 0.6×10^{22} cm^{-2}, i.e. an approximate mean value of those used for the spectral analysis of HD 168112 and HD 167971.

unexpected regarding their ages, i.e. respectively 5 ± 2 (Barbon et al. 2000) and 1.7 ± 0.4 Myr (FitzGerald et al. 1978).

7. Summary and conclusions

The analysis of our *XMM-Newton* data from HD 167971 reveals that the soft part of the X-ray spectrum is thermal with typical plasma temperatures of about 0.2 to 0.8 keV, i.e. 2×10^6 to 9×10^6 K. The harder part of the spectrum is fitted equally well with a thermal or a power law component. On the one hand, if the higher energy emission is thermal, the plasma temperatures ($\sim 2.3 \times 10^7$ to 4.6×10^7 K) are compatible with those expected for a shock heated plasma in a wind-wind collision zone, where the winds have reached speeds close to their terminal velocities. If we consider the short period of the close binary system, such velocities are not expected at the position of the collision zone of the winds of the O5-8V components. Provided the three components are indeed physically connected, this argues in favour of an interaction with the third more distant companion. On the other hand, if the hard energy emission component is non-thermal, the photon index is rather high (~3), which is reminiscent of the case of other non-thermal radio emitters like 9 Sgr (Rauw et al. 2002) or HD 168112 (De Becker et al. 2004b). The X-ray luminosity exceeds the value expected for the "canonical" $L_X/L_{\rm bol}$ relation by a factor 4. This excess is larger than that found for HD 168112 (De Becker et al. 2004b). Finally, we report on a weak decrease of the X-ray flux between our two observations separated by about five months possibly due to an eclipse of the O5-8V + O5-8V close binary system.

By considering several results from recent observations of massive stars with X-ray satellites (*XMM-Newton*) and radio telescopes (e.g. VLA), we note that the non-thermal radio emitters are possibly not the best candidates to display a non-thermal emission in the bandpass of current X-ray observatories like *XMM-Newton* or *Chandra*. In a scenario where non-thermal radio emission requires a wind-wind collision in a binary system, wide binaries produce too hard a thermal spectrum to allow the detection of any putative hard non-thermal contribution. On the contrary, short period binaries are not expected to produce an observable synchrotron radio spectrum because of the huge opacity of the wind material for radio photons. They are however likely to produce a softer thermal X-ray spectrum than long period binaries, offering the possibility to unveil the expected hard non-thermal X-ray emission component. In other words, the simultaneous detection of a non-thermal emission in the radio and X-ray domains seems rather unlikely. More X-ray and radio observations of massive binaries (O and WR), whatever the thermal or non-thermal nature of their radio emission, are needed to interpret the non-thermal emission from massive stars.

Finally, our investigation of the X-ray emission from NGC 6604 led to the detection of 29 sources in addition to HD 168112 and HD 167971. The cross-correlation of the position of these sources with the GSC, the 2MASS and the USNO catalogues revealed that most of them have at least one optical or infrared counterpart. We describe a more complete spectral analysis in the case of the three brightest objects of our source list. Two of them are associated to BD –12° 4982 (O9.5I or III) and HD 167834 (O6.5V((f))) respectively, and the third one has no known optical or infrared counterpart. Some indicators of stellar formation activity suggest a few sources of our list may be PMS objects. Unfortunately most of the sources detected in NGC 6604 are too faint to be investigated in details in the context of this study. Finally, the X-ray emitters of NGC 6604 detected with *XMM-Newton* are not concentrated close to the most massive stars of the cluster. This rather sparse spatial distribution contrasts with that observed in other open clusters like NGC 6383 and NGC 6231 where young stellar objects detected in X-rays are mainly concentrated close to the most massive stars.

Acknowledgements. Our thanks go to Alain Detal (Liège) for his help in installing the SAS, to Hugues Sana for helpful discussions on the X-ray source detection procedure, and to Yaël Nazé for providing the wind absorption model routines and for helpful discussions. The Liège team acknowledges support from the Fonds National de la Recherche Scientifique (Belgium) and through the PRODEX XMM-OM and Integral Projects. This research is also supported in part by contract P5/36 "Pôle d'Attraction Interuniversitaire" (Belspo). This research has made use of the SIMBAD database, operated at CDS, Strasbourg, France and NASA's ADS Abstract Service. This publication makes use of data products from the Two Micron All Sky Survey, which is a joint project of the University of Massachusetts and the IPAC/California Institute of Technology, funded by NASA and the NSF.

References

Anders, E., & Grevesse, N. 1989, Geochim. Cosmochim. Acta, 53, 197

Antokhin, I. I., Owocki, S. P., & Brown, J. C. 2004, ApJ, 611, 434

Babel, J., & Montmerle, T. 1997, A&A, 323, 121

Barbon, R., Carraro, G., Munari, U., Zwitter, T., & Tomasella, L. 2000, A&AS, 144, 451

Benaglia, P., & Koribalski, B. 2005, in Massive Stars in Interacting Binaries, ed. A. F. J. Moffat, & N. St-Louis, in press

Berghöfer, T. W., Schmitt, J. H. M. M., Danner, R., & Cassinelli, J. P. 1997, A&A, 322, 167

Bertout, C., Leitherer, C., Stahl, O., & Wolf, B. 1985, A&A, 144, 87

Bessell, M. S., & Brett, J. M. 1988, PASP, 100, 1134

Bieging, J. H., Abbott, D. C., & Churchwell, E. B. 1989, ApJ, 340, 518

Blomme, R., Van Loo, S., De Becker, M., et al. 2005a, A&A, 436, 1033

Blomme, R., et al. 2005b, A&A, in preparation

Bohlin, R. C., Savage, B. D., & Drake, J. F. 1978, ApJ, 224, 132

Bonnell, I. A., & Bate, M. R. 2002, MNRAS, 336, 659

Bonnell, I. A., Bate, M. R., & Zinnecker, H. 1998, MNRAS, 298, 93

Bonnell, I. A., Bate, M. R., & Vine, S. G. 2003, MNRAS, 343, 413

Carpenter, J. M. 2001, AJ, 121, 2851

Cash, W. 1979, ApJ, 228, 939

Chen, W., & White, R. L. 1991, ApJ, 366, 512

Chen, W., & White, R. L. 1994, Ap&SS, 221, 259

Chlebowski, T., Harnden, F. R. Jr., & Sciortino, S. 1989, ApJ, 341, 427

Churazov, E., Gilfano, M., Forman, W., & Jones, C. 1996, ApJ, 471, 673

Cohen, D. H., de Messières, G. E., MacFarlane, J. J., et al. 2003, ApJ, 586, 495

Davidge, T. J., & Forbes, D. 1988, MNRAS, 235, 797

De Becker, M. 2001, Master Thesis, University of Liège

De Becker, M., Rauw, G., Pittard, J. M., et al. 2004a, A&A, 416, 221

De Becker, M., Rauw, G., Blomme, R., et al. 2004b, A&A, 420, 1061

De Becker, M., Rauw, G., & Manfroid, J. 2004c, A&A, 424, L39

De Becker, M., Rauw, G., & Swings, J.-P. 2005, Ap&SS, in press

Donati, J.-F., Wade, G. A., Babel, J., et al. 2001, MNRAS, 326, 1265

Donati, J.-F., Babel, J., Harries, T. J., et al. 2002, MNRAS, 333, 55

Dougherty, S. M., & Williams, P. M. 2000, MNRAS, 319, 1005

Dougherty, S. M., Pittard, J. M., Kasian, L., et al. 2003, A&A, 409, 217

Eichler, D., & Usov, V. 1993, ApJ, 402, 271

Feigelson, E. D., & Montmerle, T. 1999, ARA&A, 37, 363

Feldmeier, A., Puls, J., & Pauldrach, A. W. A. 1997, A&A, 322, 878

FitzGerald, M.P., Jackson, P. D., Luiken, M., Grayzeck, E. J., & Moffat, A. F. J. 1978, MNRAS, 182, 607

Forbes, D. 2000, AJ, 120, 2594

Forbes, D., & DuPuy, D. 1978, AJ, 83, 266

Georgelin, Y. M., Georgelin, Y. P., & Roux, S. 1973, A&A, 25, 337

Giacconi, R., Rosati, P., Tozzi, P., et al. 2001, ApJ, 551, 624

Grillo, F., Sciortino, S., Micela, G., Vaiana, G. S., & Harnden, F. R. 1992, ApJS, 81, 795

Hiltner, W. A. 1956, ApJS, 2, 389

Howarth, I. D., & Prinja, R. K. 1989, ApJS, 69, 527

Jansen, F., Lumb, D., Altieri, B., et al. 2001, A&A, 365, L1

Jeffries, R. D., Thurston, M. R., & Pye, J. P. 1997, MNRAS, 287, 350

Johnson, H. L. 1965, ApJ, 141, 923

Kaastra, J. S. 1992, An X-ray spectral code for optically thin plasmas, Internal SRON-Leiden Report

Kaastra, J. S., Mewe, R., & Raassen, A. J. J. 2004, in New Visions of the X-ray Universe in the *XMM-Newton* and *Chandra* Era, ed. F. Jansen, ESA, SP-488, in press

Kahn, S. M., Leutenegger, M. A., Cottam, J., et al. 2001, A&A, 365, L312

Leitherer, C., & Wolf, B. 1984, A&A, 132, 151

Leitherer, C., Forbes, D., Gilmore, A. C., et al. 1987, A&A, 185, 121

Lumb, D. 2002, EPIC background files, XMM-SOC-CAL TN-0016

Mathys, G. 1988, A&AS, 76, 427

Mewe, R., Gronenschild, E. H. B. M., & van den Oord, G. H. J. 1985, A&AS, 62, 197

Meyer, M. R., Calvet, N., & Hillenbrand, L. A. 1997, AJ, 114, 288

Mihalas, D., & Binney, J. 1981, Galactic Astronomy, Structure and Kinematics (San Francisco: Freeman)

Moffat, A. F. J., & Vogt, N. 1975, A&AS, 20, 155

Monet, D., Levine, S. E., Canzian, B., et al. 2003, AJ, 125, 984

Nazé, Y., Rauw, G., Vreux, J.-M., & De Becker, M. 2004, A&A, 417, 667

Owocki, S. P., & Rybicki, G. B. 1985, ApJ, 299, 265

Pittard, J. M. 2002, in Interacting Winds from Massive Stars, ed. A. F. J. Moffat, & N. St-Louis (San Francisco: Astron. Soc. Pac.), ASP Conf. Ser., 260, 627

Pittard, J. M., & Stevens, I. R. 1997, MNRAS, 292, 298

Pittard, J. M., Dougherty, S. M., & Coker, R. F. 2005, in Massive Stars in Interacting Binaries, ed. A. F. J. Moffat, & N. St-Louis, in press

Pollock, A. M. T. 1987, ApJ, 320, 283

Raboud, D., & Mermilliod, J.-C. 1998, A&A, 333, 897

Rauw, G. 2004, in Cosmic Gamma-Ray Sources, ed. K. S. Cheng, & G. E. Romero (Dordrecht: Kluwer Academic Publishers), 105

Rauw, G., Blomme, R., Waldron, W. L., et al. 2002, A&A, 394, 993

Rauw, G., De Becker, M., Gosset, E., Pittard, J. M., & Stevens, I. R. 2003, A&A, 407, 925

Rieke, G. H., & Lebofsky, M. J. 1985, ApJ, 288, 618

Sana, H., Stevens, I. R., Gosset, E., Rauw, G., & Vreux, J.-M. 2004, MNRAS, 350, 809

Sana, H., Gosset, E., Rauw, G., Sung, H., & Vreux, J.-M. 2005, A&A, submitted

Schlegel, D. J., Finkbeiner, D. P., & Davis, M. 1998, ApJ, 500, 525

Skinner, S. L., Zhekov, S. A., Güdel, M., & Schmutz, W. 2002, ApJ, 572, 477

Skrutskie, M. F., Schneider, S. E., Stiening, R., et al. 1997, in The Impact of Large Scale Near-IR Sky Surveys, ed. F. Gazon et al. (Dordrecht: Kluwer Acad. Pub.), 25

Smith, R. K., & Brickhouse, N. S. 2000, Rev. Mex. Astron. Astrofis. Serie de Conferencias, 9, 134

Stevens, I. R., Blondin, J. M., & Pollock, A. M. T. 1992, ApJ, 386, 265

Vacca, W. D., Garmany, C. D., & Shull, J. M. 1996, ApJ, 460, 914

van Genderen, A. M., van Amerongen, S., ven der Bij, M. D. P., et al. 1988, A&AS, 74, 467

Van Loo, S. 2005, in Massive Stars in Interacting Binaries, ed. A. F. J. Moffat, & N. St-Louis, in press

Vine, S. G., & Bonnell, I. A. 2003, MNRAS, 342, 314

Walborn, N. R., & Fitzpatrick, E. L. 1990, PASP, 102, 379

Waldron, W. L., Corcoran, M. F., Drake, S. A., & Smale, A. P. 1998, ApJS, 118, 217

White, R. L. 1985, ApJ, 289, 698

Williams, P. M. 1996, in Radio Emission from the Stars and the Sun, ed. J. Parades, & A. R. Taylor (San Francisco: Astron. Soc. Pac.), ASP Conf. Ser., 93, 15

Chapter 5

Cyg OB2, a very young globular cluster harbouring three non-thermal radio emitters

> In this chapter, we will concentrate on the results we obtained concerning the Cyg OB2 association. The massive binary Cyg OB2 #8A will be discussed in detail mainly on the basis of optical data that led to the discovery of its binarity, and also on the basis of X-ray data. A procedure to estimate the non-thermal high-energy emission will be described and applied to this system. Some optical and X-ray results will be presented for another non-thermal radio emitter located in Cyg OB2, i.e. Cyg OB2 #9. The last section of this chapter will be devoted to the *INTEGRAL* observations of the Cyg OB2 region.

Cygnus OB2 (VI Cygni) is a rich OB association that has been proposed to be a very young globular cluster (Knödlseder 2000). It is characterized by a rich population of massive stars, among which three non-thermal radio emitters: Cyg OB2 #5, Cyg OB2 #8A and Cyg OB2 #9. These three stars, along with Cyg OB2 #12, were discovered to be bright X-ray emitters by the *Einstein* observatory (Harnden et al. 1979). Another particularity of Cyg OB2 is that it harbours an unidentified EGRET γ-ray source, namely 3EG J2033+4118, whose relation with the O-stars in Cyg OB2 cannot be excluded. All these characteristics suggest that this association is an ideal location for a multi-wavelength investigation of the non-thermal emission from massive stars.

The study of Rauw et al. (1999) revealed that Cyg OB2 #5 is mainly constituted of a 6.6 d close binary consisting of an O6-7f supergiant and a more evolved Ofpe/WN9 transition object. On the other side, Contreras et al. (1997) presented results from radio observations, along with some indications of the presence of a third B-type star located about 0.95 arcsec away from the close binary. These observations reveal that the nature of the radio emission near the position of the B-type companion is non-thermal, whilst that of the two hottest stars is (mainly) thermal. This is consistent with a scenario where the strongest winds of the earliest stars interact with that of the B star very close to the latter, therefore producing non-thermal emission close to the shock where the relativistic electrons are accelerated. On the basis of this idea, Benaglia et al. (2001b) followed the approach described by Eichler & Usov (1993) to estimate the expected amount of high-energy photons produced by IC scattering and likely contributing to the unidentified

EGRET source 3EG J2033 +4118.

In the case of the other two non-thermal emitting O stars harboured by Cyg OB2, the situation was not as clear. For this reason, we investigated the cases of Cyg OB2 #8A and Cyg OB2 #9 to constrain the conditions ruling their non-thermal radio emission. First, we will present our results on Cyg OB2 #8A. Our optical campaign devoted to this star led to the discovery of its binarity. The first orbital solution, along with strong evidences for a wind-wind interaction in the visible and X-ray domains, are presented in this dissertation. For Cyg OB2 #9, some preliminary optical and X-ray results will be presented as well, though the optical campaign is still going on. At the time of writing of this study, the multiplicity of this star remains an open question, even though some properties of its X-ray and radio emissions point to a possible rather long period binary scenario.

5.1 The non-thermal radio emitter Cyg OB2 #8A

5.1.1 Discovery of a new binary system

We observed Cyg OB2 #8A (V = 9.1) with the Aurélie spectrograph mounted on the 1.52 m telescope at the Observatoire de Haute-Provence during four observing runs in September 2000, September 2001, September 2002 and October 2003. All our spectra were obtained with the same setup, in the same wavelength domain (4460 – 4890 Å).

After a careful inspection of the profiles of the He I λ 4471 and He II λ 4542 lines, we noted asymmetries strongly suggesting the presence of a companion star. Moreover, the profiles of the strongest lines in the blue spectrum presented a significant variability on a time scale of about 22 d. A systematic investigation of all our spectra revealed undoubtedly the binary signature of Cyg OB2 #8A, and we determined its first SB2 orbital solution along with the spectral types of the two components. The primary and the secondary are respectively O6 and O5.5 type stars, the primary being one luminosity class brighter than the secondary (De Becker et al. 2004b, see the paper included on the next page). From 35 radial velocity mesurements of the primary and the secondary, we determined a period of 21.908 ± 0.040 d, along with an eccentricity of 0.24 ± 0.04. We must mention that 5 additional spectra obtained in October 2004 present profiles in agreement with our orbital solution.

The major impact of the discovery of the binarity of this star concerns its non-thermal radio emission. The binary nature of this target lends indeed further support to the scenario where the non-thermal emission from massive stars is produced in binary systems. Another important point to be considered is the fact that Cyg OB2 #8A is the shortest period non-thermal radio emitter known so far. This fact seems at first sight to constitute a challenge considering the strong absorption due to the wind material undergone by radio photons. Indeed, in a rather short period binary system, and provided that the non-thermal radio emission is produced in the wind-wind interaction region, the non-thermal emission region is deeply embedded inside the wind material. This apparent issue can possibly be alleviated following some geometrical considerations (inclination angle of the system, longitude of the periastron, size of the emitting region...).

A&A 424, L39–L42 (2004)
DOI: 10.1051/0004-6361:200400049

Astronomy & Astrophysics

A Spectroscopic study of the non-thermal radio emitter Cyg OB2 #8A: Discovery of a new binary system*

M. De Becker, G. Rauw**, and J. Manfroid***

Institut d'Astrophysique et de Géophysique, Université de Liège, 17, Allée du 6 Août, B5c, 4000 Sart Tilman, Belgium
e-mail: `debecker@astro.ulg.ac.be`

Received 7 May 2004 / Accepted 2 August 2004

Abstract. We present the results of a spectroscopic campaign revealing that the non-thermal radio emitter Cyg OB2 #8A is an O6 + O5.5 binary system. We propose the very first orbital solution indicating a period of about 21.9 days. The system appears to be eccentric (0.24 ± 0.04) and is likely seen under a rather low inclination angle. The mass ratio of the components is close to unity. The impact of the binarity of this star in the framework of our understanding of non-thermal radio emission from early-type stars is briefly discussed.

Key words. binaries: spectroscopic – stars: early-type – stars: fundamental parameters – stars: individual: Cyg OB2 #8A

1. Introduction

Cyg OB2 is one of the most interesting OB association of our Galaxy. It is known to harbour a huge number of OB stars, among which about 100 O-stars (Knödlseder 2000; Comerón et al. 2002). Considering its mass, density and size, Knödlseder (2000) suggested to re-classify it as a young globular cluster, the first object of this class in our Galaxy. However, the extremely large and non-uniform reddening towards Cyg OB2 renders its study at optical wavelengths extremely difficult.

One of the optically brightest O-stars in Cyg OB2 is Cyg OB2 #8A (BD +40° 4227, $m_V = 9.06$). This star is classified as O5.5I(f) (Massey & Thompson 1991). Cyg OB2 #8A is one of the first early-type stars discovered to be an X-ray emitter with *Einstein* (Harnden et al. 1979). Its X-ray emission was subsequently investigated with *ROSAT* (Waldron et al. 1998) and *ASCA* (Kitamoto & Mukai 1996; De Becker 2001).

A peculiarity of this star is that it is a non-thermal radio emitter (Bieging et al. 1989). This non-thermal emission requires the existence of a population of relativistic electrons, believed to be accelerated in shocks through the Fermi mechanism (Chen & White 1994). An important question is what is the nature of the shocks responsible for this acceleration process: intrinsic shocks due to radiative instabilities within the wind of a single star (e.g. Chen & White 1994), or a wind-wind collision within binary systems (e.g. Eichler & Usov 1993)? Concerning the latter scenario we note that while the majority of non-thermal radio emitting Wolf-Rayet stars are indeed binaries (Dougherty & Williams 2000), the situation is less clear for O-stars (De Becker et al. 2004). In particular, up to now no evidence for binarity was put forward for Cyg OB2 #8A. For instance, Lortet et al. (1987) did not detect any bright ($\Delta m \leq 3$ mag) visual companion with an angular separation in the range 0.04 to 1.5 arcsec.

In this paper, we present the first spectroscopic monitoring of Cyg OB2 #8A revealing that it is a binary system. The observations are described in Sect. 2. The spectrum is discussed in Sect. 3 and in Sect. 4 we present our period determination, as well as the first orbital solution proposed for this system. The conclusions and prospects are finally given in Sect. 5.

2. Observations and data reduction

Spectroscopic observations of Cyg OB2 #8A were collected at the Observatoire de Haute-Provence (OHP, France) during four observing runs in September 2000, September 2001, September 2002 and October 2003. All observations were carried out with the Aurélie spectrograph fed by the 1.52 m telescope (Gillet et al. 1994). Aurélie was equipped with a 2048 × 1024 CCD EEV 42-20#3, with a pixel size of 13.5 μm squared. All spectra were taken with a 600 l/mm grating with a reciprocal dispersion of 16 Å mm^{-1}, allowing us to achieve a spectral resolution of about 8000 in the blue range.

A total of 35 spectra were obtained over the wavelength range between about 4455 and 4900 Å. The data were reduced using the MIDAS software developed at ESO, with the same procedure as described by Rauw & De Becker (2004). Table 1 gives the journal of our observations, including the radial velocity measured on the He I λ 4471 line (see Sect. 4.1).

---

* Based on observations collected at the Observatoire de Haute Provence, France.

** Research Associate FNRS (Belgium).

*** Research Director FNRS (Belgium).

Table 1. Journal of our observations of Cyg OB2 #8A. The first column provides the heliocentric julian date (in the format HJD − 2 450 000). The second column gives the phase according to our orbital solution (see Table 2). The third and fourth columns yield the radial velocities measured on the He I λ 4471 line for the two components of the binary system. The last column gives the weight assigned to the various *RV* values in the orbital solution. The *RV*s with a weight superior to 0.5 are those which were determined through the simultaneous fit of two Gaussians with the *simplex method*.

Date	Phase	RV_1 (km s^{-1})	RV_2 (km s^{-1})	Weight
1810.466	0.152	23.4	–74.6	0.1
1811.468	0.198	55.2	–97.0	0.1
1812.475	0.244	36.3	–110.6	0.3
1813.523	0.291	54.7	–84.7	0.3
1814.510	0.336	59.9	–111.1	0.3
1815.503	0.382	56.3	–121.5	1.0
1819.462	0.563	34.7	–86.1	0.3
1821.488	0.655	10.1	–58.9	0.1
2163.394	0.261	39.4	–97.2	0.5
2164.382	0.307	53.1	–104.4	1.0
2165.361	0.351	72.3	–80.5	1.0
2167.367	0.443	53.7	–84.4	0.7
2168.376	0.489	38.7	–44.5	0.3
2169.371	0.535	17.0	–32.6	0.1
2170.351	0.579	0.7	–42.9	0.1
2170.446	0.584	0.5	–33.0	0.1
2518.409	0.466	29.9	–90.7	0.1
2520.369	0.556	21.4	–76.4	0.1
2522.361	0.647	–1.2	–44.8	0.1
2524.354	0.738	–60.8	34.2	0.1
2529.394	0.968	–110.5	65.2	1.0
2532.340	0.103	6.9	–54.8	0.1
2532.421	0.106	9.4	–25.5	0.1
2533.318	0.148	18.8	–87.1	0.1
2533.432	0.153	21.1	–81.5	0.1
2919.402	0.771	–66.0	41.2	0.1
2922.388	0.907	–85.9	114.4	1.0
2923.336	0.950	–113.6	84.2	1.0
2925.407	0.045	–50.4	17.9	0.05
2926.671	0.103	–43.9	11.1	0.1
2928.349	0.179	37.0	–84.4	0.7
2929.283	0.221	59.0	–83.1	0.3
2930.334	0.270	36.6	–91.4	0.3
2934.286	0.450	62.2	–102.0	0.7

The mean signal-to-noise ratio of individual spectra of our data set, estimated over a region devoid of lines, is about 250.

3. Spectral analysis

The inspection of our time series of spectra reveals that some lines display variations pointing towards Cyg OB2 #8A being a binary system. This is most obvious for the He I λ 4471 and He II λ 4686 lines. The former shows indeed a (partial) deblending of lines compatible with a binary system, and the latter undergoes strong variability even if no clear deblending is observed.

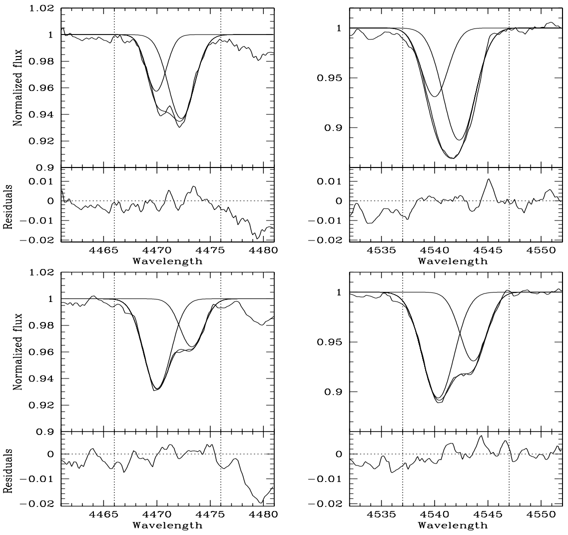

Fig. 1. Results of the fit of two Gaussians to the He I λ 4471 (*left*) and He II λ 4542 (*right*) lines for the spectra obtained on HJD 2 452 164.382 and HJD 2 452 922.388 respectively for the upper and lower figures. These profiles correspond respectively to phases 0.307 and 0.907 ouf our orbital solution. The individual components are overplotted. The vertical dashed lines give the boundaries of the domain where the fit was performed. The lower panels provide the residuals of the fit.

We measured the equivalent widths (*EW*s) of the He I λ 4471 and He II λ 4542 lines to determine the spectral types of both components. To separate the lines of the two stars, we performed the measurements on the spectra displaying the most pronounced separation between the components (HJD 2 452 922.388). We simultaneously fitted two Gaussians to the profile, allowing the central position, the width, and the normalization factor of both lines to vary. The best fit parameters were obtained using an *N*-dimensional *downhill simplex method* (Nelder & Mead 1965), with *N* being the number of free parameters (6 in our case). The integration of the two individual Gaussians gives the *EW*s of the lines of the components of the binary. Figure 1 shows the results obtained for the He I λ 4471 and He II λ 4542 lines at the date near quadrature selected for the spectral type determination. Using the classification criterion of Mathys (1988), the *EW* ratios obtained from these fits allow us to infer O6 and O5.5 spectral types respectively for the primary and the secondary. We note that spectra obtained at the opposite quadrature display similar intensities for both components. For instance, the profiles displayed in Fig. 1 give intensities (as well as widths and consequently *EW*s) which do not differ by more than about 5–6%. Consequently, we do not find evidence for a significant "Struve-Sahade" effect (see e.g. Bagnuolo et al. 1999). The intensities of the lines in the spectra of the two components roughly yield a visual brightness ratio of 2 between the primary and the secondary. Since the spectral types of both components are similar, this suggests that their luminosity classes might be different. With an O6I + O5.5III binary system, the large M_V mentioned by Herrero et al. (2002) is readily explained.

4. Cyg OB2 #8A as a binary system

4.1. Period determination

As a first step, we searched for the period of the system through a study of the line profile variability of our time series. A Time Variance Spectrum (TVS, Fullerton et al. 1996) computed between 4455 and 4890 Å on all our spectra reveals a significant variability for He i λ 4471, He ii $\lambda\lambda$ 4542, 4686, Hβ and N iii $\lambda\lambda$ 4634, 4641. In each case, the TVS displays a double peaked profile suggesting a simultaneous variability of the wings of these lines, compatible with a binary scenario. We performed a Fourier analysis on our times series using the method described by Heck et al. (1985), and used e.g. by Rauw & De Becker (2004) for BD +60° 497. All periodograms display peaks at frequencies of 0.043 and 0.094 d^{-1}, except for the He ii λ 4686 line which does not show the 0.094 d^{-1} peak. Prewhitening of the periodogram (see e.g. Rauw et al. 2001) reveals that these frequencies are harmonics, corresponding respectively to P = 23.26 d and about $P/2$. The former period is more compatible with our data even though $P/2$ gives often the strongest peak. This could be explained by the typical duration of our observing runs (max. 16 d), shorter than the actual period.

As a second step, we measured the radial velocities of both components of the system[1] using the fitting method described in the previous section when the separation of the lines was sufficient. When the lines were too heavily blended, we set the line widths and intensities to their values determined from the fits near quadrature and we used an iterative scheme where the line positions were first estimated by eye and subsequently changed to improve the residuals. These measurements were performed only for the He i λ 4471 line, as the other lines were not sufficiently separated. The typical error on the RVs is about 10 km s^{-1} for the cases where we were able to fit Gaussians[2], and we estimate that it can reach about 25–35 km s^{-1} at phases where the lines are severely blended. The Heck et al. (1985) Fourier technique was then applied to our RV time series of the primary (RV_1), the secondary (RV_2), and to the difference RV_1–RV_2. The periodograms of the RV_1 and RV_2 series present both highest peaks corresponding to periods of 23.31 and 21.88 d (±0.04 d). These values emerge also from the RV_1–RV_2 data set. However, we have folded our RVs with these two periods with some success and both values were used as first guesses in our search for an orbital solution.

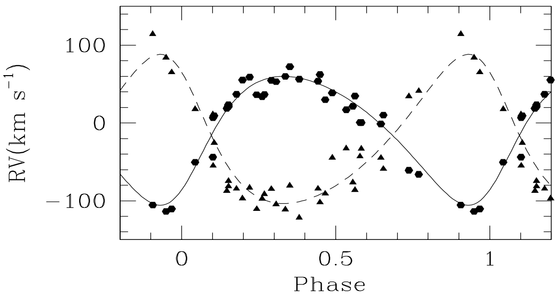

Fig. 2. Radial velocity curve of Cyg OB2 #8A for an orbital period of 21.908 d. The hexagons (resp. triangles) stand for the primary (resp. secondary) RVs. The solid and dashed lines yield our best fit orbital solution respectively for the primary and the secondary.

Table 2. Orbital solution for Cyg OB2 #8A. $T_\circ$ refers to the time of periastron passage. γ, K, and a sin i denote respectively the systemic velocity, the amplitude of the radial velocity curve, and the projected separation between the centre of the star and the centre of mass of the binary system. $R_{\rm RL}$ stands for the radius of a sphere with a volume equal to that of the Roche lobe computed according to the formula of Eggleton (1983).

	Primary	Secondary
P (days)	21.908 (fixed)	
e	0.24 ± 0.04	
$T_\circ$ (HJD–2 450 000)	1807.139 ± 0.894	
γ (km s^{-1})	–8.1 ± 3.3	–25.0 ± 3.6
K (km s^{-1})	82.8 ± 3.5	95.8 ± 4.0
a sin i ($R_\odot$)	34.8 ± 1.5	40.3 ± 1.7
$q = m_1/m_2$	1.16 ± 0.06	
m sin^3 i ($M_\odot$)	6.4 ± 0.6	5.5 ± 0.5
$R_{\rm RL}$ sin i ($R_\odot$)	13.6 ± 0.2	14.8 ± 0.2

4.2. Orbital solution

We obtained the first orbital solution for this system using the method described by Sana et al. (2003), and used e.g. by Rauw & De Becker (2004). We assigned various weights to our data to take into account the different errors affecting our RV measurements. Due to the intensity ratio of the lines of the two components (∼2), there was no ambiguity on the identification of the lines respectively of the primary and the secondary. Table 2 yields the main parameters of the system according to our best orbital solution[3]. As can be seen from Fig. 2, the system is eccentric with e = 0.24 ± 0.04. However, we emphasize that the error we obtain on the eccentricity underestimates the actual error as a result of the rather heterogeneous phase coverage of our time series (see Fig. 2).

The rather low values of the RV amplitude (K), along with the modest values of m sin^3 i as compared to the typical masses of stars of that spectral type, suggest that the system is seen under a rather low inclination angle, which would explain why the lines remain strongly blended over large parts of the orbital cycle. Consequently, Cyg OB2 #8A is unlikely to display eclipses. The projected Roche lobe radii ($R_{\rm RL}$ sin i, computed for an actual orbital separation equal to the semi-major axis) do not suggest any mass transfer through Roche lobe overflow.

We note that the accuracy of this orbital solution is affected by several factors. First, we measured RVs only for the He i λ 4471 line, because of the strong blending of all other

---

[1] One of our spectra was dropped because of a strong contamination of the He i λ 4471 line profile by a cosmic.

[2] This error on the radial velocity corresponds to the standard deviation determined for the radial velocity of a Diffuse Interstellar Band (DIB) at about 4762 Å obtained for spectra of similar S/N ratio.

[3] The orbital solution with the period of about 23.3 d turned out to be incompatible with a spectrum kindly provided by Dr. A. Herrero (private communication).

lines. Second, our data do not allow us to state that a simple two-Gaussian model is adequate at all orbital phases. Indeed, individual lines can present intrinsic variability independent of their motion due to binarity. In that case, individual line profiles should not be Gaussian anymore. Moreover, our data do not allow us to reject completely the possibility of a third component that could account for some discrepancies between the data and our orbital solution. More data obtained with a larger telescope, and with a better spectral resolution are necessary to address these issues.

5. Conclusions and future work

We present for the first time spectroscopic data revealing that Cyg OB2 #8A is an O6 + O5.5 binary system with a period of 21.9 d, likely seen under a rather low inclination angle. The two components are probably of different luminosity classes. The system appears to be eccentric, with a mass ratio of the two components close to 1. The binarity of Cyg OB2 #8A implies that the fundamental parameters derived through application of a single-star model atmosphere code (Herrero et al. 2002) will have to be revised.

The He ii λ 4686 line presents a strong line profile variability which will be investigated in a subsequent paper to search for the signature of a putative wind-wind interaction.

The binarity of this system is crucial in the framework of the study of non-thermal radio emitters. In fact, 4 out of 8 O-stars displaying non-thermal radio emission listed by Rauw (2004) are now confirmed binaries, while 2 more are suspected binaries. This lends further support to the idea that multiplicity and hence colliding winds are fundamental ingredients for the acceleration of the relativistic electrons (Eichler & Usov 1993) that generate the synchrotron radio emission (White 1985). *ASCA* data reveal that the X-ray spectrum of Cyg OB2 #8A shows a hard emission component with a temperature of more than 15×10^6 K (De Becker 2001). Provided that the thermal nature of this hard component is confirmed by our forthcoming observations with *XMM-Newton*, this temperature could be compatible with a plasma heated by a wind-wind collision (Stevens et al. 1992).

However, the short period of this system raises questions regarding the detectability of synchrotron radiation in the radio domain. The radio photospheres, even at 3.6 cm, are huge (more than 1000 and 700 $R_\odot$ respectively for the primary and the secondary) and the collision zone of the two winds is deeply embedded therein. A similar situation occurs however in the case of WR 104 ($P \sim 1$ yr), where synchrotron radiation originates well within the dense wind of the Wolf-Rayet component (Monnier et al. 2002). Considering this result, with a mass loss rate lowered by a factor of about 5–10 as expected for O stars compared to WR stars, even with a shorter separation, we expect that a non-thermal radio spectrum could be detected in the case of Cyg OB2 #8A. Information on the filling factors of the two winds (if they are clumpy) and on their geometry (if they are not spherical) are needed to understand this unexpected transparency. Additional studies are foreseen to address this issue, including an intense radio monitoring of Cyg OB2 #8A to search for a putative variability correlated with our orbital period.

Finally, as a binary system harbouring a small population of relativistic electrons, Cyg OB2 #8A may also contribute to the yet unidentified EGRET gamma-ray source 3EG J2033+4118 (Benaglia et al. 2001) through inverse Compton scattering of photospheric UV photons. This hypothesis will be investigated through forthcoming observations of the Cyg OB2 region with the *INTEGRAL* satellite.

Acknowledgements. We thank the referee Dr. Artemio Herrero for his careful reading and useful comments. We are greatly indebted to the FNRS (Belgium) for the financial support for the rent of the OHP telescope in 2000 and 2002 through contract 1.5.051.00 "Crédit aux chercheurs". The travels to OHP were supported by the Ministère de l'Enseignement Supérieur et de la Recherche de la Communauté Française. This research is also supported in part by contract PAI P5/36 (Belgian Federal Science Policy Office) and through the PRODEX XMM-OM Project. Our thanks go to Hugues Sana for helpful discussions on the orbital solution method.

References

Bagnuolo, W. G., Jr., Gies, D. R., Riddle, R., & Penny, L. R. 1999, ApJ, 527, 353
Benaglia, P., Romero, G. E., Stevens, I. R., & Torres, D. F. 2001, A&A, 366, 605
Bieging, J. H., Abbott, D. C., & Churchwell, E. 1989, ApJ, 340, 518
Chen, W., & White, R. L. 1994, Ap&SS, 221, 259
Comerón, F., Paquali, A., Rodighiero, G., et al. 2002, A&A, 389, 874
De Becker, M. 2001, Master thesis, University of Liège
De Becker, M., Rauw, G., Blomme, R., et al. 2004, A&A, 420, 1061
Dougherty, S. M., & Williams, P. M. 2000, MNRAS, 319, 1005
Eggleton, P. P. 1983, ApJ, 268, 368
Eichler, D., & Usov, V. 1993, ApJ, 402, 271
Fullerton, A. W., Gies, D. R., & Bolton, C. T. 1996, ApJS, 103, 475
Gillet, D., Burnage, R., Kohler, D., et al. 1994, A&AS, 108, 181
Harnden, F. R., Branduardi, G., Elvis, M., et al. 1979, ApJ, 234, L51
Heck, A., Manfroid, J., & Mersch, G. 1985, A&AS, 59, 63
Herrero, A., Puls, J., & Najarro, F. 2002, A&A, 396, 949
Kitamoto, S., & Mukai, K. 1996, PASJ, 48, 813
Knödlseder, J. 2000, A&A, 360, 539
Lortet, M. C., Blazit, A., Bonneau, D., & Foy, R. 1987, A&A, 180, 111
Massey, P., & Thompson, A. B. 1991, AJ, 101, 1408
Mathys, G. 1988, A&AS, 76, 427
Monnier, J. D., Greenhill, L. J., Tuthill, P. G., & Danchi, W. C. 2002, in Interacting Winds from Massive Stars, ed. A. F. J. Moffat, & N. St-Louis (San Francisco: Astron. Soc. Pac.), ASP Conf. Ser., 260
Nelder, J. A., & Mead, R. 1965, Computer J., 73, 308
Rauw, G. 2004, in Cosmic Gamma-Ray Sources, ed. K. S. Cheng, & G. Romero, in press
Rauw, G., Morrison, N. D., Vreux, J.-M., Gosset, E., & Mulliss, C. L. 2001, A&A, 366, 585
Rauw, G., & De Becker, M. 2004, A&A, 421, 693
Sana, H., Hensberge, H., Rauw, G., & Gosset, E. 2003, A&A, 405, 1063
Stevens, I. R., Blondin, J. M., & Pollock, A. M. T. 1992, ApJ, 386, 265
Waldron, W. L., Corcoran, M. F., Drake, S. A., & Smale, A. P. 1998, ApJS, 118, 217
White, R. L. 1985, ApJ, 289, 698

5.1.2 Optical spectrum and wind interaction

We observed Cyg OB2 #8A with the échelle spectrograph mounted on the 2.2 m telescope at San Pedro Mártir (in collaboration with P. Eenens, Mexico). Four observations spread over three days were obtained in October 2004, with exposure times ranging between 10 and 20 minutes (for details on the instrumentation used, see Appendix A). The spectra were normalized using carefully chosen splines. We added all the spectra to obtain the good signal to noise spectrum presented in Fig. 5.1. We note that these spectra were taken at orbital phases close to 0.7, i.e. when the separation of the lines of the two components is minimum.

All hydrogen Balmer lines from H 9 to Hβ are in absorption. Hα appears also in absorption in Fig. 5.1. We note however that the normalization of the échelle spectra should be considered with caution, as it could indeed 'remove' a weak emission component. If we consider this line as observed on classical spectra obtained with Aurélie at OHP, we see that it presents a broad emission profile with a deep absorption component at the centre (see the end of this section). All He II lines are in absorption, except He II λ 4686 that displays a more complicated profile (see the discussion further in this section). We also note the presence of significant absorption from the He I lines at 4471 and 5875 Å , and from Mg II λ 4481, O III λ 5592 and C IV $\lambda\lambda$ 5802,5812.

Emission lines are also observed: the strongest ones being N III $\lambda\lambda$ 4634,4641. Other noticeable emission lines are seen for Si IV λ 4118 and C III λ 5695. In the blue part of the spectrum, weaker emission features are also observed: C III at 4650 Å , Si IV at 4656 Å , and probably C IV at 4662 Å . In the red part of the spectrum, the weak lines at 6721, 6728 and 6731 Å could be attributed to C III (see Walborn & Howarth 2000; Walborn 2001). We report also on the presence of a weak N V $\lambda\lambda$ 6716,6718 emission (see Walborn & Howarth 2000; Walborn 2001), though we note that other N V lines are not observed at 4604 and 4620 Å .

The shape of several lines undergoes significant variations as a function of the orbital phase. To illustrate these variations, we present the profiles of the He I λ 4471 and He II λ 4542 lines respectively in Figs. 5.2 and 5.3. The inversion of the asymmetry of the line profiles is obvious on these figures. The data, obtained at OHP with Aurélie from September 2000 to October 2004, consist mainly in the spectra used for the determination of the orbital parameters of the system. As already mentioned by De Becker et al. (2004b), the equivalent widths measured on these profiles lead to the determination of O6 and O5.5 spectral types respectively for the primary and the secondary. Additional information can be obtained concerning the spectral types of the stars from N III profiles at 4634 and 4641 Å . In Fig. 5.4, we have plotted the profiles of these lines for all our Aurélie spectra. We clearly see that both components display these lines in emission. The separation of the N III lines is obvious at phases 0.85–0.95. Consequently, according to Walborn's criterion (1971), the spectral classification can be improved by adding an "f" to both components of the system.

As we are dealing with a binary system, one could wonder whether any wind-wind interaction might be revealed by profile variations of some lines. On the basis of our Aurélie time series, we investigated the line profile variability of the He II λ 4686 and Hα lines. A study of the line profile variability of the He II λ 4686 line was already presented by De Becker & Rauw (2005c) for the data obtained from September 2000 to October 2003, but the discussion given here includes also additional data from the October 2004 campaign.

In the case of He II λ 4686, we have performed a Fourier analysis of the line profiles

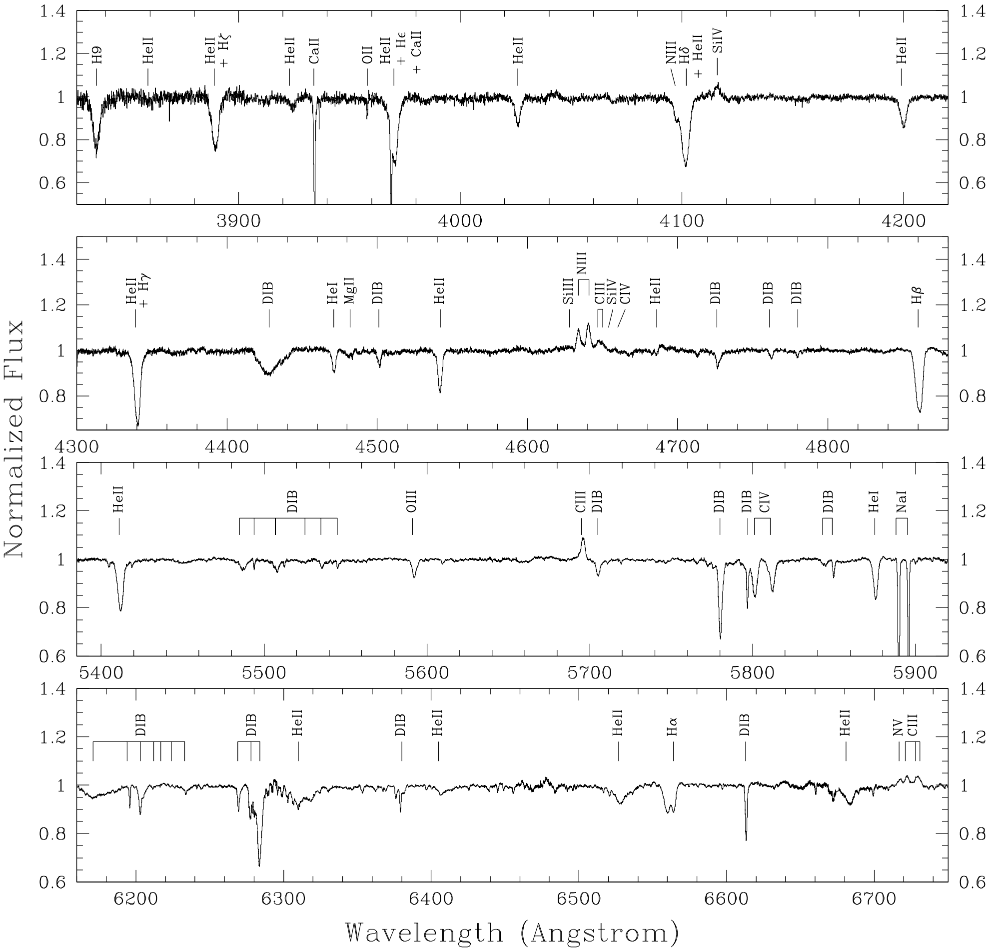

Figure 5.1: Optical spectrum of Cyg OB2 #8A obtained at the San Pedro Mártir observatory. We note that the lack of significant emission in the Hα profile is most likely due to the continuum normalization.

and we found a recurrence time-scale equal to the orbital period. Consequently, the strong variations undergone by the line are phase-locked, and we plotted the profiles as a function of the orbital phase in Fig. 5.5. For the sake of the interpretation, in each case we have plotted open and filled circles at the position of the centroid of the components of the line associated respectively to the primary and to the secondary. These positions were determined on the basis of the orbital solution presented in Sect. 5.1.1. We find that most of the time, the profile attributed to the primary displays a P-Cygni shape. The profile of the secondary seems most probably to be in absorption. Consequently, according to the classification criteria proposed by Walborn (1971), we obtained spectral types of O6f and O5.5(f) respectively for the primary and the secondary.

Even though most of the variability can be explained by the blend of the two lines due to the orbital motion, we observe also some significant deviations from a P-Cygni profile for the primary. These deviations are obvious if one considers for instance the profiles obtained at orbital phases close to 0.77 or 0.95. In some cases, the absorption components

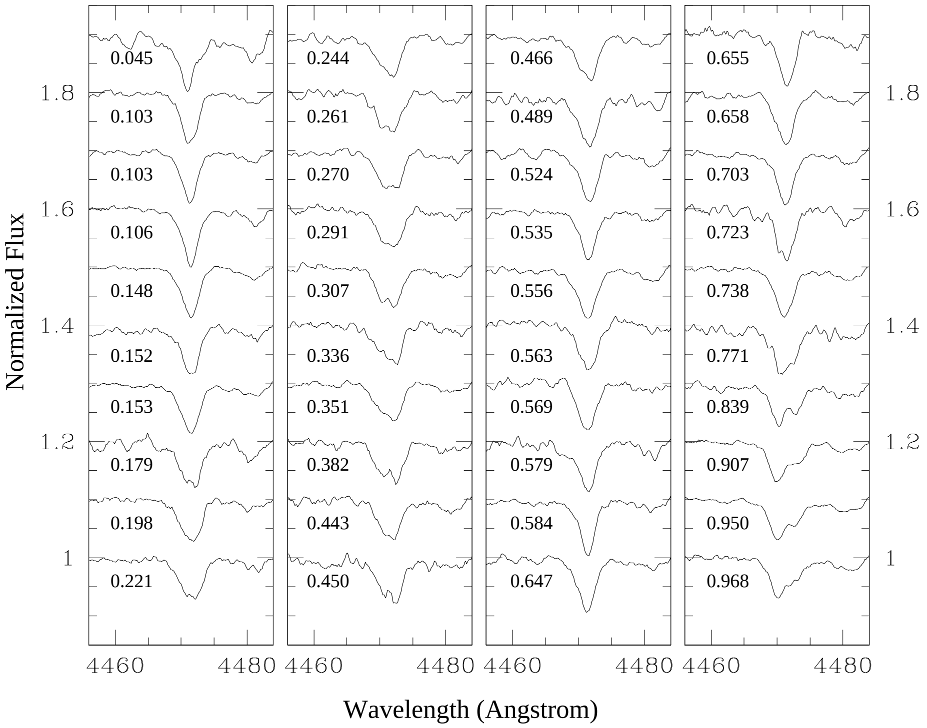

Figure 5.2: Profile series of the He I λ 4471 line of Cyg OB2 #8A obtained at OHP with the Aurélie spectrograph. The orbital phase is given in each case.

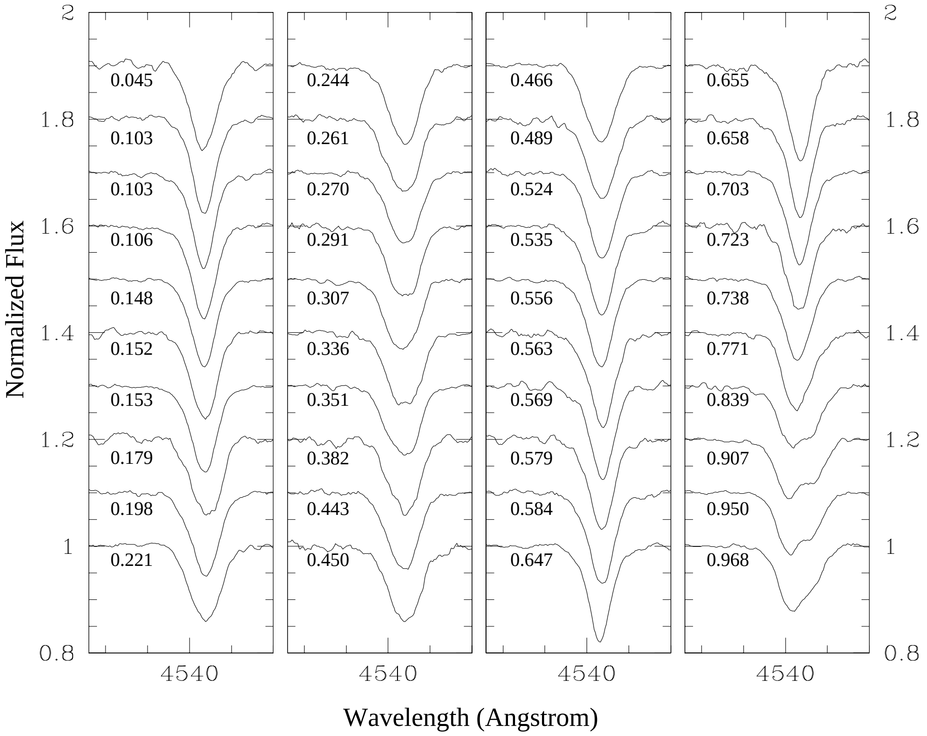

Figure 5.3: Same as Fig. 5.2 but for the He II λ 4542 line.

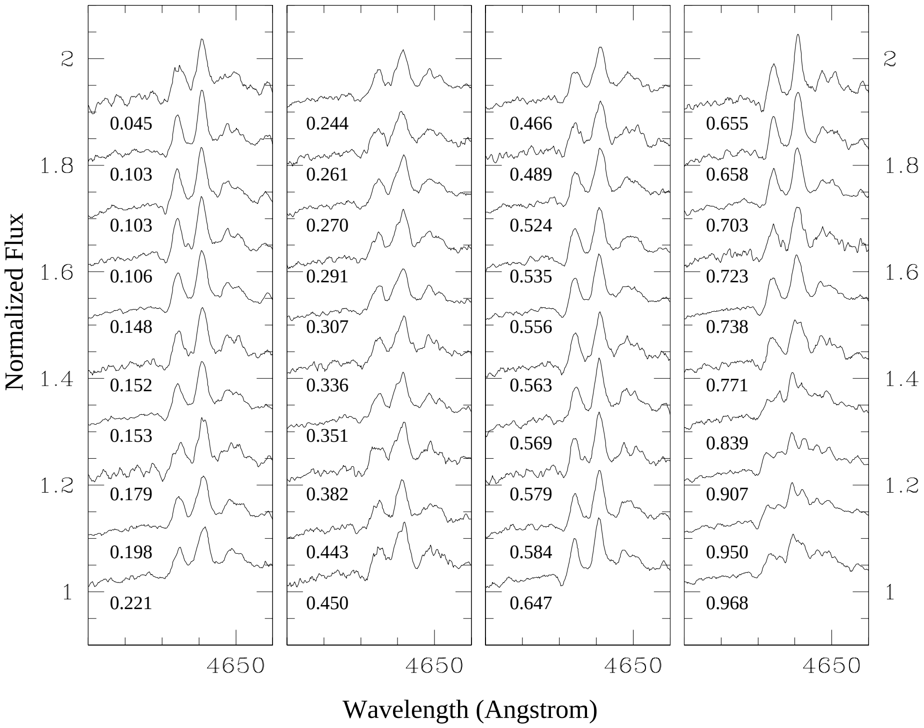

Figure 5.4: Same as Fig. 5.2 but for the N III λλ 4634-4641 lines.

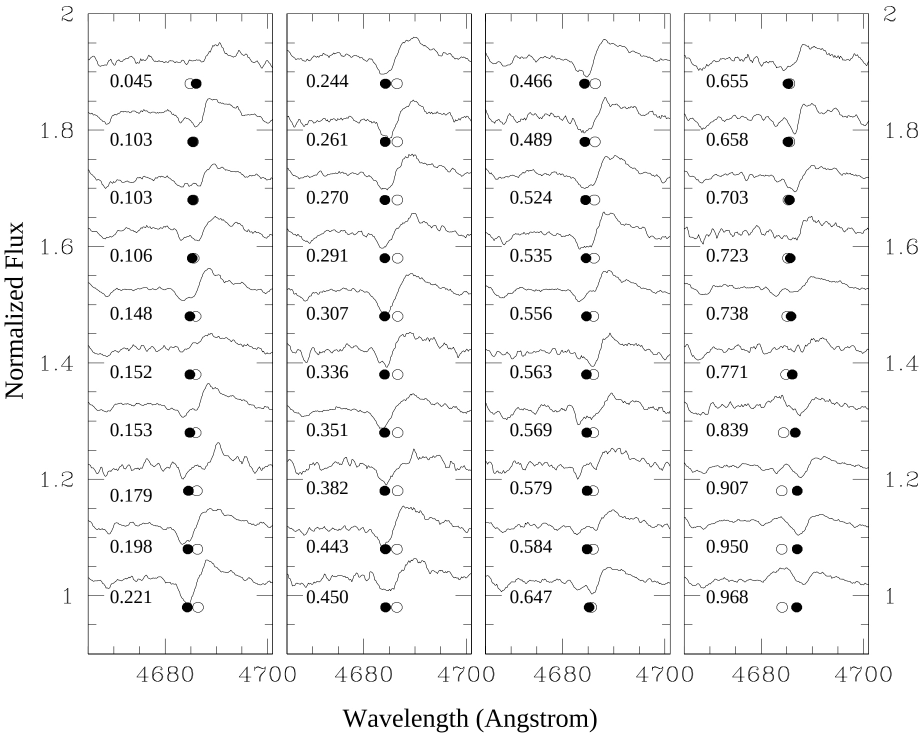

Figure 5.5: Same as Fig. 5.2 but for the He II λ 4686 line. The open and filled circles stand respectively for the position of the primary and secondary line centroids.

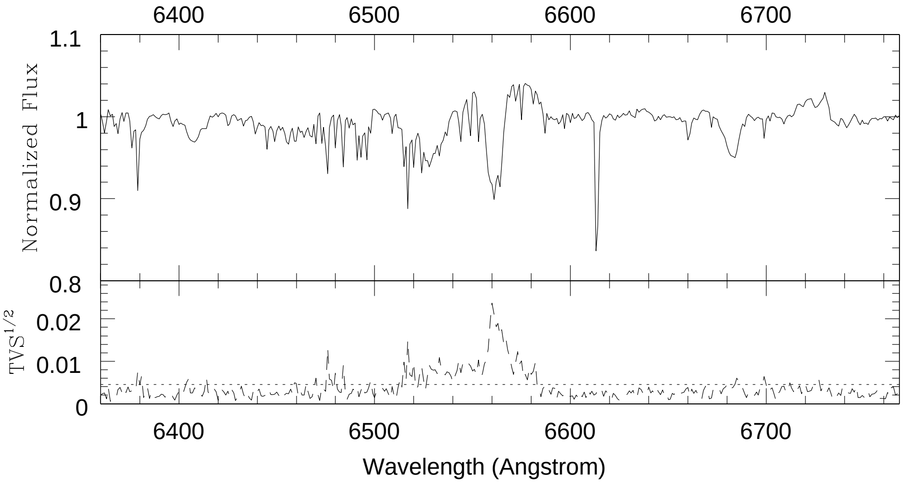

Figure 5.6: *Upper panel:* mean Aurélie spectrum of Cyg OB2 #8A between 6360 and 6770 Å obtained in summer 2005. *Lower panel:* square root of the time variance spectrum. The dotted horoizontal line stands for the 99 % confidence level. The strong peak at the position of the Hα line points to a significant variability of this line during that observing run.

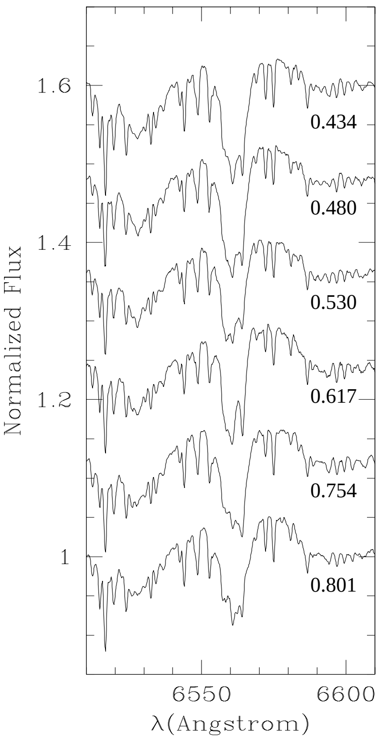

Figure 5.7: Hα profile of Cyg OB2 #8A obtained in summer 2005 at OHP. The orbital phase is specified in each case. The profile can be considered as the combination of an emission component due to the primary and an absorption component associated with the secondary. The narrow absorption features are due to atmospheric water.

seem to be filled by some additional emission whose origin is not clearly associated to one of the stars. Consequently, it becomes clear that the variations undergone by the He II λ 4686 profile cannot be explained by the simple periodic blend of the individual lines of both stars. We propose that these deviations may be due to the alteration of the line emission region by a wind-wind interaction.

In the case of the Hα line, the six spectra collected at OHP with the Aurélie spectrograph in summer 2005 do not cover a complete orbital cycle, but we detect a significant variability as shown in Fig. 5.6 where the TVS (see Appendix B) presents a strong peak at the position of the line. The profiles are individually displayed as a function of orbital phase in Fig. 5.7. More data are however needed to check whether these strong variations occur on a time-scale equal to the orbital period. Besides these variations, the important point here is the shape of the line itself. We see from Figures 5.6 and 5.7 that the profile can be considered as a combination of a broad emission component and a narrower absorption component. These emission and absorption components might be attributed respectively to the primary (i.e. the brightest star) and to the secondary. As mentioned in Sect. 5.1.1, there is a factor 2 in luminosity between the two stars, which translates into a difference between them of one luminosity class. With a large Hα emission, the primary should be a supergiant. We therefore propose the O6If and O5.5III(f) classifications respectively for the primary and the secondary components of Cyg OB2 #8A. We note that such classifications agree with the large luminosity reported for Cyg OB2 #8A (see Herrero et al. 2002). We finally note that we cannot reject the possibility that a fraction of the emission component of Hα could be produced by the wind-wind interaction.

5.1.3 Estimation of the high-energy emission from Cyg OB2 #8A

In order to investigate to issue of the high-energy counterpart to the non-thermal emission of massive stars observed in the radio domain, it would be helpful to adopt a somewhat more quantitative approach – although simplified – of the physical processes believed to be responsible for the non-thermal emission of radiation in the particular case of binary systems. The example of Cyg OB2 #8A is particularly interesting as a lot of information have been gathered on the geometry of this system, and on the stellar and wind properties of the stars it contains. For this reason, De Becker et al. (2005c) estimated the expected IC luminosity of Cyg OB2 #8A following the same approach as that adopted by Benaglia et al. (2001b) for the case of Cyg OB2 #5. Here, we describe a similar but somewhat refined approach benefitting in particular from the better constrained wind and stellar parameters discussed above in this section. These considerations will then be applied to the particular case of Cyg OB2 #8A. We note that the approach that will be described below should be considered as a simplified approach, used only to give an idea of the impact of several physical parameters on some quantities such as the IC luminosity. A more complete and quantitative approach would require sophisticated models including more physics than used below.

Geometry of the system

Separation between the stars. Within an eccentric binary system, we can derive the relative distance between the two stars. The relative separation, i.e. the distance in units of the semi-major axis of the orbit, is given by Eq. 5.1

$$r = \frac{1-e^2}{1+e\,\cos v} \tag{5.1}$$

where v is the true anomaly, i.e. the angle between the vector radius and the direction to periastron, and e is the eccentricity of the orbit. In order to obtain the relative separation as a function of the phase of the orbit, a relation between the true anomaly and the orbital phase is needed. As a first step, let us consider the expression of the true anomaly (v) as a function of the eccentric anomaly (E). These two angles are defined in Fig. 5.8.

$$v = 2\,\arctan\left[\left(\frac{1+e}{1-e}\right)^{\frac{1}{2}}\,\tan\,\frac{E}{2}\right] \tag{5.2}$$

The determination of the eccentric anomaly corresponding to a given orbital phase is less straightforward. If phase zero is defined to correspond to periastron, the mean anomaly (M) is directly related to the orbital phase (ϕ) : $M = 2\,\pi\,\phi$. A method to relate the eccentric anomaly to the phase is through Kepler's equation, i.e. the relation between the mean anomaly and the eccentric anomaly:

$$E - e\,\sin\,E = M \tag{5.3}$$

The numerical resolution of Eq. 5.3 allows to obtain the value of E for a given orbital phase. Then the successive application of Eqs. 5.2 and 5.1 provides the relative separation between the two components of the binary system.

The projected semi-major axes ($a_1\,\sin\,i$ and $a_2\,\sin\,i$) for the two components can be obtained from the orbital solution of the binary system. Provided an estimate of the inclination angle i is available, the multiplication of the relative separation (r) by the sum $a_1 + a_2$ yields the separation (D) between the two stars.

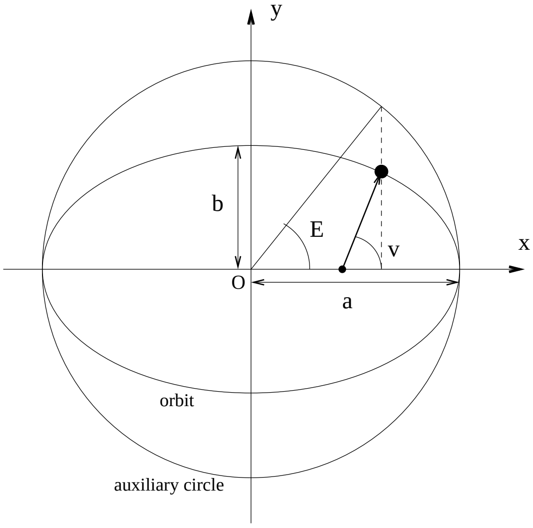

Figure 5.8: Schematic representation of an eccentric orbit. The true anomaly (v) is indicated, along with the eccentric anomaly (E) defined as the angle between the projection of the position of the star on the auxiliary circle and the direction of the periastron, measured from the center (O) of the auxiliary circle. a and b are respectively the semi-major and semi-minor axes of the elliptical orbit.

Wind momentum equilibrium. The collision between the stellar winds of the two components of a binary system occurs at a position which is set by the relative strengths of the winds. If the winds have similar strengths, the collision zone is a plane perpendicular to the line of centres, at equal distance from the two stars. On the contrary, if the winds are not equal, the collision zone is a cone-shaped layer of shocked gas partially folded around the star producing the weaker wind.

If we assume that the spherical winds of the two components flow nearly radially out to the shocks, we can derive the distances from the stars where these winds meet. At the position of the collision zone, the wind momenta are balanced, yielding

$$r_1 = \frac{1}{1+\eta^{\frac{1}{2}}}\,D\,,\; r_2 = \frac{\eta^{\frac{1}{2}}}{1+\eta^{\frac{1}{2}}}\,D \tag{5.4}$$

where r_1, r_2, D and η are respectively the distances to the collision zone from the primary and the secondary, the separation between the stars (see above), and a dimensionless parameter expressed as

$$\eta = \frac{\dot{M}_2\,V_{\infty,2}}{\dot{M}_1\,V_{\infty,1}} \tag{5.5}$$

where $\dot{M}$ and V_∞ stand for the mass loss rate and the terminal velocity respectively. The parameter η thus expresses the ratio of the momentum flux of the two winds (Stevens et al. 1992).

Estimation of the Inverse Compton (IC) luminosity

Local magnetic field. The surface magnetic field strength (B_s) is probably one of the most critical and poorly known physical quantities for massive stars (see the discussion in Chapter 1). Moreover, provided that B_s is determined, the behaviour of the magnetic field as a function of the distance to the star in the ionized material of the stellar wind still needs to be established.

Some relations providing the dependence of the strength and geometry of the magnetic field as a function of the radial distance (r) to the star in the outflowing gas are given for instance by Usov & Melrose (1992). Three regimes can be envisaged: (1) *dipolar*, (2) *radial*, and (3) *toroidal*. The equations for these three regimes, along with their conditions of application, are given below:

$$B = B_s \times \begin{cases} \left(\frac{R}{r}\right)^3 & \mathrm{for\,R} \leq \mathrm{r} < \mathrm{r_A} \qquad \mathrm{(dipolar)} \\ \frac{R^3}{r_A\,r^2} & \mathrm{for\,r_A} < \mathrm{r} < \mathrm{R}\,\frac{\mathrm{V_\infty}}{\mathrm{V_{rot}}} \qquad \mathrm{(radial)} \\ \frac{V_\infty}{V_{rot}}\,\frac{R^2}{r_A\,r} & \mathrm{for\,R}\,\frac{\mathrm{V_\infty}}{\mathrm{V_{rot}}} < \mathrm{r} \qquad \mathrm{(toroidal)} \end{cases} \tag{5.6}$$

In these relations, V_{rot} and V_∞ are respectively the stellar rotational velocity and the wind terminal velocity. R is the stellar radius, and r_A is the Alfvén radius which can be defined as the radius where the kinetic and magnetic energy densities are balanced. The Alfvén radius can be expressed as follows:

$$r_A \sim R \times \begin{cases} 1+\xi & for\,\xi \ll 1, \\ \xi^{1/4} & for\,\xi \gg 1 \end{cases} \tag{5.7}$$

with the parameter ξ expressed by

$$\xi = \frac{B_s^2\,R^2}{2\,\dot{M}\,V_\infty} \tag{5.8}$$

From these relations, we can see that the typical Alfvén radius for early-type stars is in the range from $\sim R$ to $\sim 2-3\,R$ (Usov & Melrose 1992). The best approach consists in using the well-established or expected wind and stellar parameters to estimate which regime is suitable, before applying the corresponding relation to estimate the local magnetic field strength at a given distance r from the center of the star.

When the strength of the magnetic field at the distance of the shock zone is obtained from Eq. 5.6, one can ask whether it is affected by the hydrodynamic conditions close to the shock. In the case of a strong shock, the compression ratio (χ) is expected to be equal to 4 (see Sect. 1.1). The magnetic field strength dependence on the density could be of the order of $\rho^{2/3}$ (Tassoul 1976), and can be used to determine some kind of concentration factor ϵ. Consequently, the magnetic field strength could increase up to a factor of 2.5 in the post-shock region of a strong shock. Moreover, the magnetic fields from both stars are expected to contribute to the local magnetic field strength at the collision zone. Let us therefore consider that the mean local magnetic field can be obtained using the following relation:

$$B_{col} \;=\; \epsilon\,\frac{B_1 + B_2}{2} \tag{5.9}$$

where B_1 and B_2 are the local magnetic field from the primary and the secondary respectively, expressed in Gauss. Our approach is thus significantly different from previous ones (Eichler & Usov 1993; Benaglia et al. 2001b) where the local magnetic field was considered to come from the secondary star only, as those authors dealt with cases where the collision zone was very close to the secondary. We insist on the fact that the way we deal with the magnetic field is only an assumption. A detailed investigation of the magneto-hydrodynamic conditions at the collision zone is far beyond the scope of this work.

Radio luminosity. In the literature, radio emission levels are mostly provided as flux densities expressed in mJy at a given frequency (S_ν). This flux density can be converted into more conventional units (cgs) following the procedure described below.

We first need to establish a relation yielding the flux density in a given frequency interval. This can be done through an integration of the flux density between two frequencies ν_1 and ν_2:

$$S \;=\; \int_{\nu_1}^{\nu_2} S_\nu\, d\nu \tag{5.10}$$

As we know that the radio spectrum is a power law with a spectral index α, we can establish the following relation:

$$S_\nu \;=\; S_{\nu'}\left(\frac{\nu}{\nu'}\right)^{\alpha}$$

where ν' is a frequency for which we have a measure of the flux density. Inserting this relation in Eq. 5.10, we obtain

$$S \;=\; \frac{S_{\nu'}}{\nu'^{\alpha}}\int_{\nu_1}^{\nu_2} \nu^{\alpha}\, d\nu$$

and we derive the integrated flux density:

$$S \;=\; \frac{S_{\nu'}}{(\alpha+1)\,\nu'^{\alpha}}\,(\nu_2^{\alpha+1} - \nu_1^{\alpha+1}) \tag{5.11}$$

As a final step, considering that $1\,\mathrm{mJy} = 10^{-29}\,\mathrm{W\,m^{-2}\,Hz^{-1}} = 10^{-22}\,\mathrm{erg\,s^{-1}\,m^{-2}\,Hz^{-1}}$ $= 10^{-26}\,\mathrm{erg\,s^{-1}\,cm^{-2}\,Hz^{-1}}$, and multiplying both sides of Eq. 5.11 by $4\,\pi\,d^2$, we obtain a relation giving the radio luminosity in cgs units integrated between two frequencies ν_1 and ν_2:

$$L_{radio} = 4\,\pi\,d^2\,10^{-26}\,\frac{S_{\nu'}}{(\alpha+1)\,\nu'^{\alpha}}\,(\nu_2^{\alpha+1}-\nu_1^{\alpha+1}) \tag{5.12}$$

where $S_{\nu'}$, ν' and d are respectively expressed in mJy, in Hz and in cm. To calculate this quantity, the flux density at a given frequency (ν'), the distance to the star, and the spectral index are thus needed.

Lower limit on the synchrotron radio luminosity. In a binary system producing a non-thermal radio emission, the total radio spectrum has essentially three origins: (1) the thermal emission from the wind of the primary, i.e $L_{ff,1}$, (2) the thermal emission from the wind of the secondary, i.e $L_{ff,2}$, and (3) the non-thermal emission from the collision zone between the two stars, i.e L_{synch}. This third part is likely to be embedded inside the combined winds and therefore undergoes a free-free absorption characterized by a given optical depth (τ). We note that a thermal radio emission component is also expected to be produced by colliding winds (see Pittard et al. 2006), but we neglect it in our simplified approach. Consequently, the observed radio luminosity can be expressed as follows:

$$L_{radioobs.} = L_{ff,1} + L_{ff,2} + L_{synch}\,e^{-\tau} \tag{5.13}$$

In order to estimate the non-thermal contribution to the radio spectrum, we need to estimate the free-free thermal contributions from the primary and the secondary respectively. These quantities can be calculated on the basis of the relations given for example by Leitherer et al. (1995), according to the free-free radio emission theory established by Wright & Barlow (1975) and Panagia & Felli (1975):

$$S_{\nu} = 2.32\,\times\,10^4\left(\frac{\dot{M}\,Z}{V_{\infty}\,\mu}\right)^{4/3}\left(\frac{\gamma\,g_{\nu}\,\nu}{D^3}\right)^{2/3} \tag{5.14}$$

where g_{ν} is the Gaunt factor obtained through the following relation:

$$g_{\nu} = 9.77\left(1 + 0.13\,\log\frac{T_e^{3/2}}{Z\,\nu}\right)$$

The various quantities used in these two relations are

$\dot{M}$: the mass loss rate in $\mathrm{M}_{\odot}\,\mathrm{yr}^{-1}$

V_{∞} : the terminal velocity in $\mathrm{km\,s}^{-1}$

ν : the frequency in Hz

D : the distance to the star in kpc

T_e : the electron temperature expressed as a fraction of the effective temperature, e.g. $0.5 \times T_{eff}$

μ : the mean molecular weight, i.e. $\frac{\sum A_i\,M_i}{\sum A_i}$, where A_i and M_i are respectively the abundance and the molecular weight of the ith ionic species. For a plasma containing 77 % hydrogen and 23 % helium, $\mu = 1.69$

Z : the rms ionic charge, i.e. $\frac{(\sum A_i\,Z_i^2)^{1/2}}{\sum A_i}$, where Z_i is the ionic charge of the ith ionic species. For the same abundances as above, $Z = 1.3$

γ : the mean number of electrons per ion, i.e. $\frac{\sum A_i\, Z_i}{\sum A_i}$. For the same abundances as above, $\gamma = 1.23$

Following this approach, the thermal flux density from both components of the binary system can be calculated. Using Eq. 5.12 with a spectral index α of 0.6, these quantities can be converted into radio luminosities expressed in erg s^{-1}.

Applying Eq. 5.12 using $S_{\nu'}$ and α obtained from the observation, the observed radio luminosity can be calculated as well. The difference between these observed (mixed thermal and non-thermal) and theoretical (thermal) quantities provides a lower limit on the luminosity ($L_{synch,min}$) of the intrinsic synchrotron emission produced at the collision zone:

$$L_{synch,min} \;=\; L_{synch}\, e^{-\tau} \tag{5.15}$$

where τ is an optical depth characteristic of the total absorption undergone by the synchrotron radiation produced globally in the emission region located at the collision zone. This optical depth results from the integration of the opacity along the line of sight over all the emitting volume. The determination of such a quantity is not straightforward and requires an accurate knowledge of the geometrical and wind parameters of the system. This absorption factor ($e^{-\tau}$) is likely to have a large impact on the synchrotron luminosity, mostly in the cases of close binary systems and systems including stars with dense stellar winds (e.g. WR stars). For instance, an optical depth τ of about 2.3 would be responsible for an attenuation of the synchrotron luminosity by a factor 10. Moreover, we note that the fact that we neglect here the Razin effect (see Sect. 1.4.1) leads the intrinsic synchrotron luminosity to be underestimated.

Inverse Compton luminosity. The radio synchrotron luminosity and the inverse Compton luminosity can be related by a unique equation, provided both emission mechanisms arise from the same population of relativistic electrons (White & Chen 1995). Such a relation derives from the fact that for either process the total energy lost by a high-energy electron can be expressed by similar relations depending on the energy density respectively of the magnetic field (U_B) and of the radiation field (U_{ph}). This leads to the following equation for the ratio between L_{synch} and L_{IC}:

$$\frac{L_{synch}}{L_{IC}} \;=\; \frac{U_B}{U_{ph}} \tag{5.16}$$

We can use this luminosity ratio to obtain an expression of the IC luminosity as a function of the synchrotron radio luminosity, taking into account the fact that both stars of the binary system contribute to the photon energy density:

$$L_{IC} \;=\; \frac{2}{c}\,\frac{L_{synch}}{B_{col}^2}\left(\frac{L_{bol,1}}{r_1^2} + \frac{L_{bol,2}}{r_2^2}\right) \tag{5.17}$$

where $L_{bol,1}$ (respectively $L_{bol,2}$) and r_1 (resp. r_2) stand for the bolometric luminosity and for the distance from the center of the star to the collision zone for the primary (resp. the secondary). B_{col} is the strength of the magnetic field in the acceleration region of relativistic particles (which is also the emitting region of the synchrotron and IC photons, i.e. the collision zone). c is the speed of light.

We note that this approach is very similar to that of Eichler & Usov (1993) and Benaglia et al. (2001b). However, these latter studies took into account only one term for the photon density. This approximation was valid because those authors had to deal with asymmetric binary systems where the winds collide close to the secondary. Consequently, the primary photon density could be neglected compared to that of the secondary. Eq. 5.17 is therefore more general than that used by Eichler & Usov (1993) and Benaglia et al. (2001b), and it should preferentially be used each time one has to deal with binary systems characterized by a momentum ratio (η) that is not significantly smaller than 1. We finally note that, when using the minimum synchrotron luminosity as defined by Eq. 5.15, our approach leads to a lower limit on the high-energy IC luminosity.

Estimate of the high-energy cutoff of the non-thermal spectrum

The electrons are accelerated through the first-order Fermi mechanism, and a valuable quantity worth to be estimated is the maximum energy reached by the electrons under given circumstances. As non-thermal radiation processes provide the most effective cooling mechanisms of relativistic electrons, a high-energy cutoff is obtained when the rate of energy gain of the particles is balanced by the rate of energy loss by radiative processes like IC scattering and synchrotron emission. We note that relativistic electrons may also lose energy through Coulomb collisions with thermal ions, but this cooling process is not expected to be significant (see e.g. Pittard et al. 2006) and we decided to neglect it.

On the one hand, we can use the relation given by Dougherty et al. (2003) for the rate of IC loss of energy of relativistic electrons, e.g. electrons whose Lorentz factor γ is $\gg 1$, and the relation provided by Rybicki & Lightman (1979) for the energy loss by synchrotron emission:

$$\frac{d\,E}{d\,t}\bigg|_{IC} = \frac{\sigma_T\,\gamma^2}{3\,\pi}\,\frac{L_{bol}}{r^2} \tag{5.18}$$

$$\frac{d\,E}{d\,t}\bigg|_{synch} = \frac{\sigma_T\,\gamma^2}{6\,\pi}\,c\,B^2 \tag{5.19}$$

where σ_T is the Thomson cross section whose value is $6.6524 \times 10^{-25}\,\mathrm{cm}^{-2}$. L_{bol} and r are respectively the stellar bolometric luminosity and the distance from the star to the shock region. To take into account the radiation from the two stars of the binary system, the last factor of Eq. 5.18 should be written $(\frac{L_{bol,1}}{r_1^2} + \frac{L_{bol,2}}{r_2^2})$.

On the other hand, the rate of energy gain through the Fermi acceleration mechanism given by Baring et al. (1999) can be expressed in cgs units as follows:

$$\frac{d\,E}{d\,t}\bigg|_{Fermi} = A\,\frac{\chi - 1}{\chi\,(1 + g\,\chi)}\,\frac{Q}{\theta}\,B\,V_{sh}^2 \tag{5.20}$$

where A is a constant $\sim 1.6 \times 10^{-20}$.

In this relation, χ is the compression ratio of the shock, B is the local magnetic field in Gauss, V_{sh} is the speed of the shock in $\mathrm{cm\,s^{-1}}$, g is the ratio between the upstream and downstream diffusion coefficients of the high-energy particles generally considered equal to $1/\chi$, and θ is the ratio of the mean free path of the particles over the gyroradius. This latter parameter is considered to be constant accross the acceleration zone, independent of the particle and energy, and it characterizes the turbulence. Its minimum value is one (for the case of strong hydromagnetic turbulence), and it was considered to be about 3 by Eichler & Usov (1993) in the case of the wind collision zone of WR + O binary systems. A low θ value means that the turbulence is high enough to reduce substantially the mean free path of the particles, therefore confining them in the acceleration region. Q is the mean electric charge.

The particles are accelerated as far as the rate of energy gain is not overwhelmed by the rate of energy loss. The maximum Lorentz factor of the relativistic electrons is consequently provided by the condition:

$$\frac{d\,E}{d\,t}\Big|_{IC} + \frac{d\,E}{d\,t}\Big|_{synch} = \frac{d\,E}{d\,t}\Big|_{Fermi}$$

which translates to

$$\gamma^2 \leq \frac{3\,\pi\,A\,(\chi-1)\,Q\,B\,V_{sh}^2}{\sigma_T\,\chi\,(1+g\,\chi)\,\theta\left(\frac{L_{bol,1}}{r_1^2}+\frac{L_{bol,2}}{r_2^2}+\frac{c\,B^2}{2}\right)} \tag{5.21}$$

The maximum Lorentz factor (γ_{max}) expressed by the right hand side of Eq. 5.21 corresponds to an electron energy of $\gamma\,m_e\,c^2$, where m_e is the mass of the electron. For a γ_{max} of the order or 10^4, the maximum energy reached by the electrons is about 5 GeV. When the maximum Lorentz factor is estimated, one can determine the maximum frequency of the photons produced by inverse Compton scattering, through the following relation:

$$\nu_{max} = \frac{4}{3}\,\gamma_{max}^2\,\nu_* \tag{5.22}$$

where ν_* is the typical frequency of the seed stellar photons. This quantity can be estimated from Wien's law providing the frequency of the maximum of Planck's function for a black body temperature corresponding to the effective temperature of the star.

In Eq. 5.21, both inverse Compton scattering and synchrotron emission are considered. However, in most cases only IC scattering will significantly contribute to the energy loss of the relativistic particles, and the third term between brackets in the denominator of Eq. 5.21 vanishes. The reason is that the UV and visible radiation fields from the stars are strong, and that the synchrotron mechanism would require too high a local magnetic field strength to become significant.

If we equal Eq. 5.18 and Eq. 5.19, taking into account a parameter f expressing the relative efficiency of the synchrotron radiation mechanism as compared to the IC scattering for the cooling of the relativistic particles, we can write:

$$\frac{d\,E}{d\,t}\Big|_{synch} = f\,\frac{d\,E}{d\,t}\Big|_{IC}$$

It follows that

$$B_{min,f} = \left\{\frac{2\,f}{c}\left(\frac{L_1}{r_1^2}+\frac{L_2}{r_2^2}\right)\right\}^{\frac{1}{2}} \tag{5.23}$$

In this relation, the parameter f can take values between 0 and 1. This relation allows to estimate the minimum strength of the magnetic field, assuming that the rate of synchrotron energy loss becomes significant if it contributes to a fraction f of the energy loss due to IC scattering. A rapid handling of Eq. 5.23 yields an expression for f, provided that an estimate of the local magnetic field strength is available. The following expressions provide the fraction of the total non-thermal emission from the system, respectively of IC and synchrotron origin, as a function of f:

$$F_{IC} = \frac{1}{1+f} \tag{5.24}$$

$$F_S = \frac{f}{1+f} \tag{5.25}$$

with both quantities satisfying the condition $F_{IC} + F_S = 1$.

Application to the case of Cyg OB2 #8A

On the basis of the spectral types and luminosity classes determined above in this chapter, we can derive some fundamental parameters needed to estimate the non-thermal high-energy emission from Cyg OB2 #8A. Typical masses, radii and effective temperatures for an O6 supergiant and an O5.5 giant can be obtained from Howarth & Prinja (1989). We calculated the typical bolometric luminosities for the two stars on the basis of their radii and effective temperatures. The mass loss rates were computed using the relation given by Vink et al. (2000), and the terminal velocities were estimated assuming that it amounts to 2.6 times the escape velocity of the star (Lamers et al. 1995). All these parameters are collected in Table 5.1.

At this stage, it may be worth checking whether a priori ”reasonable” values were attributed to some of the parameters listed in Table 5.1. We converted the total bolometric luminosity, i.e. the sum of the individual bolometric luminosities derived for the primary and the secondary, into an absolute bolometric magnitude equal to –10.78. Assuming a distance to Cyg OB2 #8A of 1.8 kpc (Bieging et al. 1989), we obtain a dereddened apparent bolometric magnitude equal to 0.5. We estimated the bolometric correction using the relation given by Howarth & Prinja (1989) for a mean effective temperature of 40 kK (BC = 3.7), and we applied it to the dereddened bolometric magnitude to derive a dereddened V magnitude of 4.2. In addition, assuming the extinction toward Cyg OB2 is similar to the mean Galactic extinction (Torres-Dodgen et al. 1991), i.e. considering that $A_V = 3.1 \times E(B\text{- }V)$ with E(B - V) = 1.6 (Torres-Dodgen et al. 1991), we derive an extinction $A_V = 4.96$. These quantities lead to an apparent V magnitude equal to 9.16, which is very similar to the value of 9.09 measured by Torres-Dodgen et al. (1991). These numbers point to a very good agreement between the observed value for the apparent V magnitude and the one calculated on the basis of our assumptions on the individual bolometric luminosities, which are critical parameters for the estimate of the IC luminosity below. As these bolometric luminosities were derived from the radii and effective temperatures of the stars, we conclude that the values attributed to these parameters (and hopefully to other parameters as well) are valid.

Table 5.1: Fundamental stellar and wind parameters of the primary and secondary components of Cyg OB2 #8A.

	Primary	Secondary
Sp. type	O6If	O5.5III(f)
$M_\star$ ($M_\odot$)	73	59
$R_\star$ ($R_\odot$)	23	14
$T_{\rm eff}$ (K)	39000	42000
$L_{\rm bol}$ (erg s^{-1})	4.2×10^{39}	2.1×10^{39}
$\dot{M}$ ($M_\odot$ yr^{-1})	8.5×10^{-6}	2.6×10^{-6}
V_∞ (km s^{-1})	2267	2891

Provided the masses and minimum masses (see De Becker et al. 2004b) are known, we obtain an inclination (i) of the line of sight relative to the orbital axis of the system of 26° ± 5°. Using the projected semi-major axes given by De Becker et al. (2004b), we can use Eqs. 5.1 to 5.3 to compute the separation between the two stars as a function of the orbital phase (see the upper panel of Fig. 5.9). We derived a wind momentum ratio η (Eq. 5.5) equal to 0.39, and we then computed the distances between the center of each star and the interaction zone (Eqs. 5.4).

According to Eq. 5.6, the magnetic regime of both stars is radial. The middle panel of Fig. 5.9 plots the magnetic field at the collision zone for two surface magnetic field strengths respectively of 1 and 100 G. In both cases, we considered that the magnetic field strength is the same for both stars, and we used Eq. 5.9 with ϵ equal to 2.5 to obtain the magnetic field strength at the collision zone as a function of the orbital phase.

On the one hand, assuming a distance to Cyg OB2 #8A of 1.8 kpc (Bieging et al. 1989), we used Eq. 5.14 to obtain thermal radio flux densities of 0.32 and 0.05 mJy respectively for the primary and the secondary. Using Eq. 5.12 and assuming a thermal spectral index of 0.6, these values convert into luminosities of 1.16×10^{28} erg s^{-1} for the primary and 1.72×10^{27} erg s^{-1} for the secondary. On the other hand, Bieging et al. (1989) reported on a radio observation of Cyg OB2 #8A performed on 21 December 1984, yielding a flux density at 6 cm of 0.4 ± 0.1 mJy with a non-thermal spectral index of -0.9 ± 0.2. We also converted these data into a radio luminosity in cgs units, i.e. 2.40×10^{28} erg s^{-1}. Using individual thermal radio luminosities along with the value of the observed radio luminosity in Eq. 5.13, we derive a minimum synchrotron luminosity of 1.06×10^{28} erg s^{-1}.

As already mentioned in this section, up to now the estimate of the non-thermal high-energy emission from massive binaries has been obtained only for asymmetric systems, i.e. binary systems whose stellar winds of the primary and secondary are very different, therefore leading to a wind interaction zone very close to the secondary star. This is typically the case of binary systems constituted of a Wolf-Rayet primary, with an OB secondary (see e.g. Eichler & Usov 1993). As a result, in previous studies, the magnetic and radiation fields were neglected in the estimation of the IC scattering emission from the interaction zone. In the case of Cyg OB2 #8A, the situation is not as simple since the wind momentum ratio is of 0.39, and all the terms included in Eqs. 5.17 and 5.21 must be taken into account. The results of the application of Eq. 5.17 for surface magnetic fields of 1 and 100 G respectively are plotted in the bottom panel of Fig. 5.9. We can summarize the results as follows:

- first, provided the synchrotron luminosity is constant along the orbit (see the discussion below), the maximum of the IC luminosity is found at apastron and the minimum at periastron, with an amplitude difference larger than a factor 2. This is due to the r^{-2} decrease of the local magnetic field strength (radial regime, see Eq. 5.6). As L_{IC} is proportional to B^{-2}, the amplitude of the variations of L_{IC} vs r is rather large, even though the variation of r is not so large.

- second, the IC luminosity obtained with a surface magnetic field of 1 G is about 10^4 times larger than that obtained for a surface magnetic field of 100 G. This is a consequence of the fact that $L_{IC} \propto B^{-2}$ in Eq. 5.17. We insist however on the fact that this does not mean that the IC luminosity decreases as B increases. It means that *for a given synchrotron luminosity*, a large magnetic field will lead Eq. 5.17 to predict a low IC luminosity. This apparent misleading behaviour can be clarified if one keeps in mind the fact that only the synchrotron emission depends on the magnetic field strength, and not the IC emission (see Eqs. 5.18 and 5.19).

In addition to estimating the IC luminosity of Cyg OB2 #8A, we can roughly determine the maximum energy of the relativistic electrons produced by the colliding winds through the first order Fermi mechanism. Using Eq. 5.21, we obtain maximum Lorentz

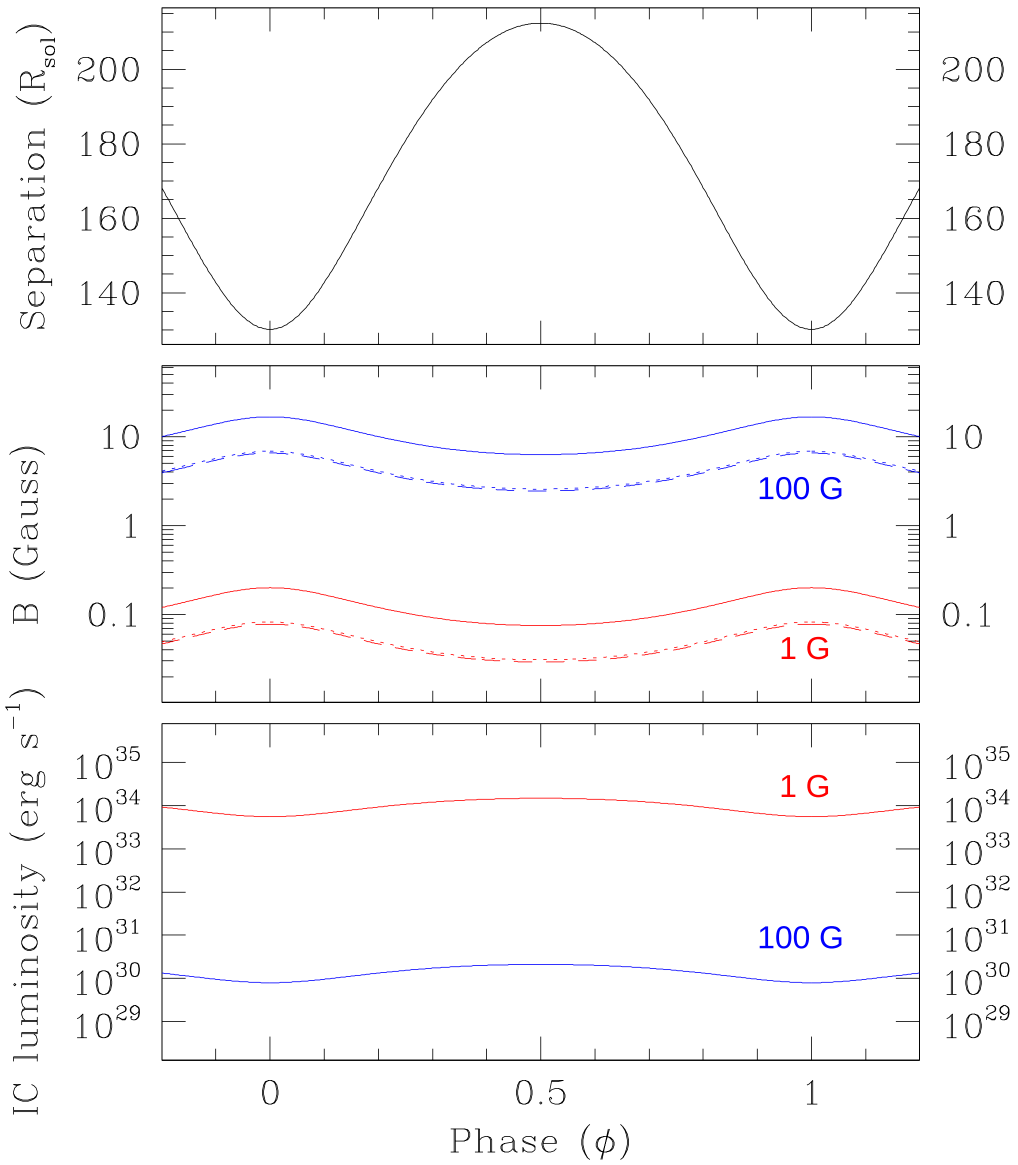

Figure 5.9: Results of the estimate of the IC scattering luminosity of Cyg OB2 #8A as a function of the orbital phase respectively for surface magnetic fields of 1 G (*red*) and 100 G (*blue*). *Upper panels*: separation between the two stars. *Middle panels*: magnetic field strength at the wind-wind interaction zone (solid line). The primary (dashed line) and secondary (dotted line) contributions are also individually displayed. *Bottom panels*: minimum IC luminosity expected from the simplified approach described in this section for the parameters quoted in Table 5.1.

factors for the electrons of about 1200 and 11000 respectively for surface magnetic fields of 1 and 100 G. These Lorentz factors respectively convert into energies of 0.6 and 6 GeV. Considering typical frequencies of about 4.1×10^{15} Hz for the photons emitted at the photospheres of the two stars of the system[1], Eq. 5.22 predicts that such relativistic electrons are able to produce high-energy photons up to energies of about 300 MeV and 2 GeV if the surface magnetic field is of the order of 1 and 100 G respectively. As a consequence, Cyg OB2 #8A is theoretically able to contribute to some extent to the unidentified EGRET source 3EG J2033 +4118, since that instrument was sensitive to photons with energies higher than about 100 MeV.

We note that Eq. 5.22 includes terms taking IC scattering and synchrotron mechanisms into account for the cooling of relativistic electrons. As noted earlier in this section, this cooling is expected to be dominated by IC scattering. However, if the local magnetic field is high enough, synchrotron cooling may provide a significant contribution as well. Let's consider that synchrotron cooling is significant if it contributes for about 10 % of the global cooling of relativistic electrons, i.e. $F_S = 0.1$ and $F_{IC} = 0.9$. This assumption converts into a factor f of about 0.11 that can be used in Eq. 5.23 to derive a minimum strength of the local magnetic field of about 30 and 50 G respectively at apastron and at periastron. In other words, in a binary system such as Cyg OB2 #8A, a surface magnetic field of a few hundreds of Gauss is enough to allow the synchrotron emission to contribute significantly to the cooling of the relativistic electrons accelerated at the collision zone between the winds of the two stars. Considering the values mentioned in Chapter 1 for the strength of the surface magnetic field of a few massive stars – even though these examples might not be representative of most of OB stars – it appears that considering IC scattering alone may be a poor approximation. Once again, a determination of the magnetic field of massive stars is strongly needed to check the validity of such an approximation in each particular case.

The approach we followed to investigate the question of the non-thermal emission of Cyg OB2 #8A is affected by several limitations worth mentioning. Some of them have already been pointed out above, but we provide here a more complete census of these issues:

- *The estimate of the surface magnetic field.* As shown in Fig. 5.9, the IC luminosity obtained from Eq. 5.17 is strongly affected by the estimate of the surface magnetic field.

- *The estimate of the local magnetic field.* The dependence of the magnetic field on the radial distance to the star in the stellar wind's plasma is not well-established. Moreover, the hydrodynamics of the interaction zone between the two stellar winds may also affect the local magnetic field in a way that differs significantly from our simplified approach illustrated by Eq. 5.9.

- *The dependence of the synchrotron luminosity as a function of orbital phase.* It is obvious that considering that the synchrotron luminosity is the same at all orbital phases is an approximation that is quite not justified. In an eccentric binary system, the synchrotron luminosity is indeed expected to change as the local magnetic field strength vary with the orbital phase.

---

[1] This frequency was obtained from Wien's law considering a characteristic effective temperature of 40000 K, intermediate between those of the two components of Cyg OB2 #8A.

- *The estimation of the intrinsic synchrotron luminosity.* Ideally, we would like to estimate the IC luminosity but here we obtained only its lower limit, based on a lower limit of the synchrotron luminosity. A radiative transfer code is needed to estimate the impact of the absorption of radio photons by the wind material on the synchrotron luminosity as a function of the orbital phase. In a case such as Cyg OB2 #8A, as the orbital and wind parameters are rather well constrained, τ (see Eq. 5.15) can be estimated at any orbital phase. Consequently, a radio monitoring of the system during a complete orbital cycle may provide a series of measurements of the emergent synchrotron luminosity that could be converted into intrinsic synchrotron luminosities. More realistic IC luminosities may therefore be obtained through Eq. 5.17.

Throughout this discussion, we have shown that the relation between the magnetic field and the non-thermal emission from massive stars is tight. As a result, one may wonder – as already mentioned in the introduction – whether the investigation of the non-thermal emission from massive binaries could lead to an indirect method to estimate the magnetic field, at least close to the interaction region. Here, we have estimated the IC emission level for a given strength of the surface magnetic field. If on the contrary we may obtain a direct value of the IC luminosity from high-energy observations, provided an determination of the synchrotron luminosity is also available, the same equations as used above may allow us to estimate the local magnetic field. This is only possible in the case of non-thermal emission produced by binary systems, as in this case both non-thermal radio and high-energy emission processes arise in the same place and hence involve the same population of relativistic electrons. In practice, we need to investigate the X-ray and soft γ-ray emissions from massive binaries such as Cyg OB2 #8A in order to (i) identify a high-energy non-thermal emission component and (ii) determine its luminosity. For this reason, we obtained *XMM-Newton* and *INTEGRAL* observations of the Cyg OB2 region and the results of these studies are described below.

5.1.4 X-ray emission from Cyg OB2 #8A

The observation of Cyg X-3 with the *EINSTEIN* X-ray observatory revealed serendipitously the presence of bright X-ray point sources whose counterparts were found to be O-type stars of Cyg OB2, the brightest one being Cyg OB2 #8A. Later on, additional observations of Cyg OB2 with *ROSAT* (Waldron et al. 1998) and *ASCA* (Kitamoto & Mukai 1996; De Becker 2001) improved our knowledge of the X-ray emission from its massive star contents. More recently, a study based on *Chandra* data on these stars was published by Waldron et al. (2004). However, these studies did not consider the binary scenario in order to interpret the X-ray emission from Cyg OB2 #8A.

In order to study in detail the X-ray emission from the early-type stars in Cyg OB2, we obtained four *XMM-Newton* observations separated by about ten days in October - November 2004. The exposure times were about 20 ks, although the fourth exposure was reduced to about 10 ks because of a very high background level due to a strong soft proton flare (for details, see De Becker et al. 2005b). The aim-point was set at the position of Cyg OB2 #8A in order to obtain RGS data for this star, in addition to the EPIC data. We reduced and analyzed the data using the SAS v. 6.0.0 software, following the same approach as adopted and described in Chapters 3 and 4.

We obtained the best fit of the EPIC spectra using a three-component thermal model, along with two absorption components accounting for the interstellar and circumstellar absorption respectively. The characteristic plasma temperatures are of the order of 3×10^6, 9×10^6 and 20×10^6 K respectively for the three components. On the basis of this model, we derived an intrinsic – corrected for the ISM absorption – X-ray luminosity of the order of 10^{34} erg s^{-1}, leading to an overluminosity factor of 13–18 during our four observations. We note that the most obvious characteristic of the EPIC spectrum is the strong Fe K blend at about 6.7 keV, strongly supporting the thermal nature of the hard X-ray emission of Cyg OB2 #8A. We tried to replace the third thermal component with a power law, but the resulting composite model failed to reproduce successfully the general shape of the observed spectrum. Such characteristics for the X-ray emission from Cyg OB2 #8A completely agree with the scenario where a large fraction of the X-ray emission is produced by a wind-wind interaction located between the two stars of the binary system.

In this context, binarity in an eccentric system is also expected to lead to a significant variability of the X-ray flux as a function of the orbital phase. Accordingly, the X-ray flux can vary for two main reasons:

- a variation of the absorption along the line of sight (mainly in the soft part of the EPIC spectrum).
- the eccentricity, likely to cause the physical conditions of the collision zone to change with the orbital phase. If some variability is detected in the harder part of the spectrum, it should essentially come from this process.

We first investigated the variability by comparing the fluxes (and count rates) obtained in several energy bands. We found that the flux undergoes a variation of the order of 20 %, and we found also strong evidence for differences in the variability level in the soft and hard parts of the spectrum (see De Becker & Rauw 2005b and De Becker et al. 2005b).

We also performed a refined analysis of archive *ROSAT* and *ASCA* data, and we combined these results with those obtained with *XMM-Newton* to obtain a phase-folded X-ray light curve. In this light curve (see Fig. 6 of De Becker et al. 2005b), the maximum of the X-ray emission falls close to phase 0.75, and the minimum is located shortly after the periastron passage. The reasonable agreement between the count rates obtained with the various instruments at different epochs strongly argues in favor of a phase-locked variability with the orbital period of 21.908 days determined by De Becker et al. (2004b). Hydrodynamic simulations lead to predicted luminosities overestimated by about a factor 5 as compared to observed values. We propose that this may be explained mostly by the fact that we did not take radiative inhibition effects into account in our simulations. Moreover, we note that a decrease of the mass loss rate may also reduce the predicted X-ray luminosity. The detailed description of the procedure we used to investigate the phase-locked variability of Cyg OB2 #8A can be found in De Becker et al. (2005b, inserted hereafter). This latter paper is intended to be submitted in the near future.

The fact that we did not find any evidence for a non-thermal counterpart in the X-ray spectrum between 0.5 and 10.0 keV agrees completely with the idea already mentioned in Chapter 4 that it is unlikely to observe simultaneously non-thermal radiation in the X-ray (below 10.0 keV) and radio domains. Indeed, in the scenario where some non-thermal X-rays are produced by the colliding winds of the binary system, the high temperature thermal component produced by the same wind-wind interaction region may overwhelm the non-thermal component, therefore preventing us from detecting it. However, we should consider the fact that the colliding winds are unlikely to produce thermal X-rays at energies above 10.0 keV. The observation of a system such as Cyg OB2 #8A at higher energies is thus strongly needed to investigate the issue of the non-thermal emission from massive stars. For this reason, we obtained *INTEGRAL* observations whose analysis will be described later in this chapter.

Mon. Not. R. Astron. Soc. **000**, 000–000 (0000) Printed 14 November 2005 (MN LATEX style file v2.2)

XMM-Newton observations of the massive colliding wind binary and non-thermal radio emitter Cyg OB2 #8A (O6If + O5.5III(f))[⋆]

M. De Becker,[1]† G. Rauw,[1]‡ H. Sana,[1] A.M.T. Pollock[2], J.M. Pittard[3], R. Blomme[4], I.R. Stevens[5], S. Van Loo[3]
[1] *Institut d'Astrophysique et de Géophysique, Université de Liège, 17, Allée du 6 Août, B5c, B-4000 Sart Tilman, Belgium*
[2] *European Space Agency XMM-Newton Science Operation Centre, European Space Astronomy Centre, Apartado 50727, Villafranca del Castillo, 28080 Madrid, Spain*
[3] *School of Physics and Astronomy, The University of Leeds, Woodhouse Lane, Leeds LS2 9JT, UK*
[4] *Royal Observatory of Belgium, Avenue Circulaire 3, 1180 Brussels, Belgium*
[5] *School of Physics and Astronomy, University of Birmingham, Edgbaston Birmingham B15 2TT, UK*

14 November 2005

ABSTRACT

We report on the results of four *XMM-Newton* observations separated by about ten days of Cyg OB2 #8A (O6If + O5.5III(f)). This massive colliding wind binary has the particularity to be a very bright X-ray emitter – one of the first X-ray emitting O-stars discovered by the *Einstein* satellite – and also to be a confirmed non-thermal radio emitter whose binarity was discovered quite recently (De Becker et al. 2004c). The X-ray spectrum between 0.5 and 10.0 keV is essentially thermal, and is best fitted with a three-component model with temperatures of about 3, 9 and 20 MK. The X-ray luminosity corrected for the interstellar absorption is rather large, i.e. about 10^{34} erg s^{-1}. Compared to the 'canonical' $L_{\rm X}/L_{\rm bol}$ ratio of O-type stars, Cyg OB2 #8A was a factor 13–19 overluminous in X-rays during our observations. The high plasma temperature and X-ray luminosity point to a thermal emission produced by the plasma heated by the collision between the winds of the two stars. The EPIC spectra did not reveal any evidence for the presence of a non-thermal contribution in X-rays. This is not unexpected considering the idea proposed by De Becker et al. (2005b) that the simultaneous detections of non-thermal radiation in the radio and soft X-ray (below 10.0 keV) domains is unlikely. Our data reveal a significant decrease in the X-ray flux from apastron to periastron with an amplitude of about 20 %. Combining our *XMM-Newton* results with those from previous *ROSAT*-PSPC and *ASCA*-SIS observations, we obtain a light curve suggesting a phase-locked X-ray variability. The maximum emission level occurs around phase 0.75, and the minimum is probably seen shortly after the periastron passage. Using hydrodynamic simulations, we find a maximum of the X-ray emission close to phase 0.75 as well, but the X-ray luminosity is overestimated by about a factor 5. We propose that at least part of this discrepancy may be explained by the fact that higher order effects, such as radiative inhibition, were not taken into account in our simulations. The strong phase-locked variability and the spectral shape of the X-ray emission of Cyg OB2 #8A revealed by our investigation point undoubtedly to X-ray emission dominated by colliding winds.

Key words: stars: early-type – stars: winds, outflows – stars: individual: Cyg OB2 #8A – X-rays: stars – stars: binaries: general

1 INTRODUCTION

The Cyg OB2 (VI Cygni) association has several particularities that stimulated the interest of astronomers. It has a diameter of about 2°, corresponding to about 60 pc at a distance of 1.7 kpc (Knödlseder 2000). It harbours a huge number of early type stars: about 100 O-type and probably more than 2000 B-type stars (Knödlseder 2000; Comerón et al. 2002). Considering its mass, density and size, Knödlseder (2000) proposed it may be the first object in the Galaxy

---

[⋆] Based on observations with XMM-Newton, an ESA Science Mission with instruments and contributions directly funded by ESA Member states and the USA (NASA).
† E-mail: debecker@astro.ulg.ac.be
‡ Research Associate FNRS (Belgium)

to be re-classified as a young globular cluster. However, a complete census of the massive star content of Cyg OB2 is not easy to achieve because of the heavy extinction in this direction (Comerón et al. 2002). So far, a spectral classification has only been proposed for its brightest and bluest members (Massey & Thompson 1991).

Another particularity of Cyg OB2 is that it contains some of the brightest OB stars of our Galaxy (see e.g. Herrero et al. 2002), among which we find some of the brightest X-ray emitting early-type stars. Historically, the *Einstein* X-ray observatory discovered the first X-ray sources whose optical counterparts were known to be massive stars in Cyg OB2, i.e. Cyg OB2 #5, #8A, #9, and #12 (Harnden et al. 1979). The same field was further investigated with various X-ray observatories since the discovery of the *Einstein* satellite: *ROSAT* (Waldron et al. 1998), *ASCA* (Kitamoto & Mukai 1996; De Becker 2001) and more recently *Chandra* (Waldron et al. 2004). This paper is the first of a series presenting the *XMM-Newton* view of Cyg OB2. It will focus on its brightest X-ray emitter, i.e. Cyg OB2 #8A (BD +40° 4227).

Cyg OB2 #8A was recently discovered to be a binary system consisting of an O6I(f) primary and an O5.5III(f) secondary (De Becker et al. 2004c; De Becker & Rauw 2005). The system is eccentric ($e = 0.24 \pm 0.04$) with a period of 21.908 ± 0.040 d. The fact that Cyg OB2 #8A is a binary system could reconcile the high bolometric luminosity reported by Herrero et al. (2002) with its spectral classification, believed so far to be a single O5.5I(f) star. The analysis of a time series of the He II λ 4686 line revealed a phase-locked profile variability likely attributed to a wind-wind interaction (De Becker & Rauw 2005).

In the framework of the campaign devoted to the multiwavelength study of non-thermal radio emitters (see De Becker 2005), Cyg OB2 #8A is a particularly interesting target. The non-thermal radio emission, supposed to be synchrotron radiation (White 1985), requires (i) the presence of a magnetic field and (ii) the existence of a population of relativistic electrons. However, although in the past few years the first direct measurements of surface magnetic fields have been performed for a few early-type stars, e.g. β Cep (Donati et al. 2001), θ^1 Ori C (Donati et al. 2002) and ζ Cas (Neiner et al. 2003), the estimation of the strength of the magnetic field of massive stars remains a difficult task. Therefore our knowledge of magnetic fields in early-type stars is at most fragmentary. The relativistic electrons are supposed to be accelerated through the first order Fermi mechanism described for instance by Bell (1978), and applied to the case of massive stars by Pollock (1987), Chen & White (1994) and Eichler & Usov (1993). This process requires the presence of hydrodynamic shocks. We mention that an alternative scenario was proposed by Jardine et al. (1996), but we will assume that the first order Fermi mechanism in the presence of hydrodynamic shocks (the so-called Diffusive Shock Acceleration - DSA - mechanism) is the dominant process. For a discussion of the physical processes involved in the general scenario of the non-thermal emission from massive stars, we refer e.g. to De Becker et al. (2005a) and references therein. The issue to be addressed here is that of the nature of these shocks: are they intrinsic to the stellar winds (see e.g. Feldmeier et al. 1997), or are they due to the wind-wind collision in a binary system (see e.g. Stevens et al. 1992). In the case of Wolf-Rayet (WR) stars, the non-thermal radio emitters are mostly binary systems (see Dougherty & Williams 2000 and Rauw 2004 for reviews). But for O-stars, the situation is less clear even though the fraction of binaries (confirmed or suspected) among non-thermal radio emitters has recently evolved to a value closer to that of WR stars (see De Becker 2005). The recent discovery of the binarity of Cyg OB2 #8A lends further support to the scenario where the population of relativistic electrons, and consequently the non-thermal radio emission, is produced in the interaction zone between the winds of two stars (in this binary system).

In addition, one can wonder whether non-thermal radiation can be produced in the high-energy domain as a counterpart of this non-thermal emission in the radio waveband. Indeed, as relativistic electrons are present close to a source of UV photons, i.e. the photosphere of the star(s), other mechanisms such as inverse Compton (IC) scattering are expected to play a significant role in their cooling. As a result, these stars could be non-thermal emitters both in the X-ray and soft γ-ray domains. In this context, several targets have been investigated in the X-ray domain with *XMM-Newton*: 9 Sgr (Rauw et al. 2002), HD 168112 (De Becker et al. 2004b) and HD 167971 (De Becker et al. 2005b). Up to now, no unambiguous detection of non-thermal X-ray emission has been revealed by the X-ray observations of non-thermal radio emitters. In the γ-ray domain, De Becker et al. (2005a) estimated that IC scattering in the collision zone of Cyg OB2 #8A could possibly contribute up to about 10 % of the γ-ray emission (> 100 MeV) of the unidentified EGRET source 3EG J2033+4118. The forthcoming analysis of the Cyg OB2 data collected with the *INTEGRAL* satellite will possibly provide new insight into the high-energy emission from its massive star content (see De Becker 2005).

Beside this putative non-thermal emission, the X-ray spectrum of massive binaries like Cyg OB2 #8A is expected to be dominated by thermal emission produced by the plasma heated by hydrodynamic shocks due to intrinsic instabilities or to the wind-wind collision. As a colliding wind binary, Cyg OB2 #8A might be compared to other massive binaries where the colliding winds contribute significantly to the thermal X-ray emission (see for instance WR 140, Pollock et al. 2005; and WR 25, Pollock & Corcoran 2005). In this context, the possibility to detect a non-thermal emission component as discussed hereabove will depend strongly on the properties of the thermal emission contributions. De Becker et al. (2005b) discussed the unlikelihood of the simultaneous detection of non-thermal radio and soft X-ray emission and proposed that short period binaries (a few days) were more likely to present a non-thermal X-ray emission below 10.0 keV than wide binaries. To investigate the X-ray emission of the massive members of Cyg OB2, we obtained four pointings with the *XMM-Newton* X-ray observatory. This paper is devoted to the massive binary Cyg OB2 #8A. The study of the other bright X-ray emitting massive stars, along with that of other fainter sources of the field, is postponed to forthcoming papers.

The present paper is organized as follows. Section 2 describes the observations and the data reduction procedure. The spectral analysis of EPIC and RGS data of Cyg OB2 #8A is discussed in Sect. 3, whilst Sect. 4 is devoted to a discussion of the X-ray luminosity and to its variability. The discussion of archive X-ray data is provided in Sect. 5. Section 6 is devoted to a general discussion. Finally, Sect. 7 summarizes the main results of this analysis and presents the conclusions.

2 OBSERVATIONS

As already stated, we obtained observations of Cyg OB2 with the *XMM-Newton* satellite, with a separation of about ten days between two consecutive pointings. The information relative to the four pointings are provided in Table 1. The aim-point was set to the position of Cyg OB2 #8A in order to obtain high resolution RGS spectra of this system. Because of the brightness of the massive stars located in the field of view we used the EPIC medium filter to reject optical light.

2.1 EPIC data

2.1.1 Data reduction

All three EPIC-MOS1, EPIC-MOS2 and EPIC-pn instruments were operated in the full frame mode (Turner et al. 2001, Strüder et al. 2001). We used the version 6.0.0 of the *XMM* Science Analysis System (SAS) for the data reduction. The raw EPIC data of the four pointings were processed through the `emproc` and `epproc` tasks. The event lists were screened in the standard way: we considered only events with pattern 0–12 and pattern 0–4 respectively for EPIC-MOS and EPIC-pn.

We selected the source X-ray events from inside a 60 arcsec radius circular region centered on Cyg OB2 #8A, excluding its intersection with a circular 15 arcsec radius region centered on Cyg OB2 #8C (RA = 20:33:17.9 and DEC = + 41:18:29.5, Equinox 2000.0). The background region was defined as an annulus centered on the source and covering the same area as the circular source region, excluding its intersection with a 15 arcsec circular region centered on a point source (RA = 20:33:13.9 and DEC = + 41:20:21.4, Equinox 2000.0). For EPIC-MOS2 data, we excluded the intersection of these two regions (source and background) with a rectangular box to reject a bad column that crosses the central CCD, at slightly more than 30 arcsec away from the center of the source region. We did the same in the case of EPIC-pn data to avoid a CCD gap located at about 40 arcsec from Cyg OB2 #8A. In each case, the boxes were adjusted after a careful inspection of the relevant exposure maps. Fig. 1 shows the source and background regions used for the three EPIC instruments in the case of Observation 1. The regions for the other observations differ only by the rotation angle. We generated the response matrix file (RMF) with the `rmfgen` task for EPIC-MOS data. For EPIC-pn data, because of a problem with `rmfgen`[1], we used the canned response matrix for on-axis sources provided by the SOC. The ancilliary response files (ARF) were generated with the `arfgen` task. We finally rebinned our spectra to get at least 9 and 16 counts per energy bin respectively for EPIC-MOS and EPIC-pn. All our spectra were then analysed using the XSPEC software (see Sect. 3.1).

2.1.2 High level background episodes

Before the spectra extraction and the analysis, we extracted a high energy light curve (Pulse Invariant – PI – channel numbers $> 10\,000$, i.e. photon energies above ~ 10 keV) from the complete event lists to investigate the behaviour of the background level during the four pointings. High background time intervals are known to occur because of solar soft proton flares (Lumb 2002). We detected high background level episodes mostly in the fourth pointing. Even though such a high background level is not expected to affect significantly the spectral analysis of sources as bright as Cyg OB2 #8A (see e.g. De Becker et al. 2004a; 2004b), we decided to filter our data sets to reject the most affected time intervals. This allows to obtain the cleanest possible spectra thereby increasing the reliability of our analysis. As can be seen from the spectra shown for instance by De Becker et al. (2004b), the background correction produces spectra with large error bars on the normalized flux for spectral bins strongly affected by a high background level. In the case of bright sources like Cyg OB2 #8A, the data analysis does not suffer critically from the rejection of a fraction of the exposure time. After inspection of the light curves from the four data sets, we selected the time intervals below a threshold of 20 cts s^{-1} for EPIC-MOS and 75 cts s^{-1} for EPIC-pn. As a consequence, the effective exposure times are reduced (see Table 2) as compared to the values provided by the last column of Table 1.

Table 1. Observations of Cyg OB2 performed in 2004 with *XMM-Newton*. The columns yield respectively the (1) revolution number, (2) the observation ID, (3) the observation date, (4) the beginning and ending times expressed in Julian days, (5) the orbital phase at mid-exposure according to the ephemeris determined by De Becker et al. (2004c), and finally (6) the performed exposure time expressed in ks.

Rev. (1)	Obs. ID (2)	Date (3)	JD –2 453 300 (4)	ϕ (5)	Exp. (ks) (6)
896	0200450201	10/29-30	8.458 – 8.701	0.534	21
901	0200450301	11/08-09	18.425 – 18.691	0.989	23
906	0200450401	11/18-19	28.399 – 28.688	0.445	25
911	0200450501	11/28-29	38.372 – 38.639	0.900	23

Table 2. Effective exposure time of the Cyg OB2 observations after rejection of the flare contaminated time intervals.

	Obs. 1	Obs. 2	Obs. 3	Obs. 4
EPIC-MOS1	18.6 ks	20.9 ks	22.9 ks	12.6 ks
EPIC-MOS2	18.2 ks	20.3 ks	22.6 ks	12.9 ks
EPIC-pn	14.9 ks	15.2 ks	19.0 ks	9.0 ks
RGS1	18.0 ks	19.7 ks	20.1 ks	12.2 ks
RGS2	17.9 ks	19.1 ks	19.8 ks	12.2 ks

2.1.3 Pile-up?

Considering the X-ray brightness of Cyg OB2 #8A, one can wonder whether the EPIC data are affected by pile-up. According to the *XMM-Newton* User's Handbook, the count rate threshold above which pile-up may affect the data of point sources in full frame mode are about 0.7 and 8.0 cts s^{-1} respectively for EPIC-MOS and EPIC-pn in full frame mode. As will be shown farther (see Table 7), the critical value is reached for some EPIC-MOS data sets, and we have to check whether our data are affected.

First, we generated pattern histograms and searched for the presence of patterns 26-29 expected to be due to pile-up. We did not find such patterns for any of our data sets. Next, we used the `epatplot` task to draw curves of the singlet and doublet events as a function of PI. We obtained a first series of curves on the basis of event lists filtered using the standard screening criteria and the spatial filter described hereabove for the source region. A second series of curves was then built on the basis of event lists obtained with a slightly modified spatial filter, where the core of the point spread function (PSF) was excluded. Since pile-up is expected to occur mainly in the core of the PSF, these latter event lists should

---

[1] The `rmfgen` task may work unproperly when confronted to somewhat comlicated source regions made of circles and boxes such as shown in Fig. 1.

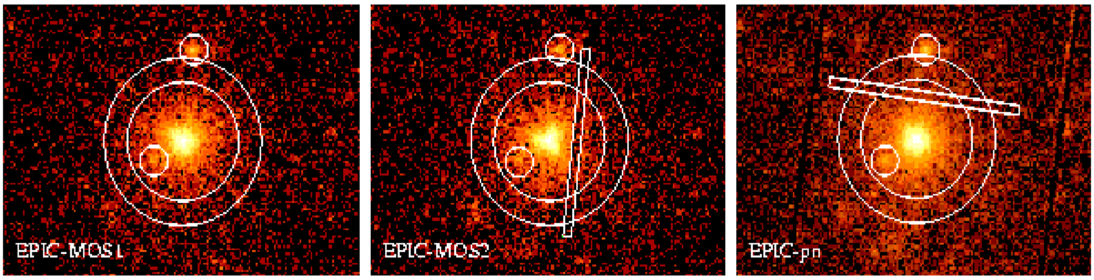

Figure 1. Source (circle) and background (annulus) regions selected for the spectrum extraction of Cyg OB2 #8A for the first *XMM-Newton* observation. Boxes were used to exclude the CCD gap for EPIC-pn and the bad column for EPIC-MOS2. Small circular regions were used to exclude faint point sources close to Cyg OB2 #8A. The EPIC-pn image was corrected for Out Of Time (OOT) events. The inner circle has a radius of 60 arcsec. North is up and East is to the left.

essentially be unaffected. As the curves built using `epatplot` are supposed to be pile-up sensitive, we may expect some differences between the two sets of curves if our data are indeed affected. However, no significant differences were found. Consequently, we consider that our data are unaffected by pile-up.

2.2 RGS data

2.2.1 *Data reduction*

The two RGS instruments were operated in Spectroscopy mode during the four observations (den Herder et al. 2001). The raw data were processed with the SAS version 6.0.0 through the `rgsproc` task. The first and second order spectra of the source were extracted using the `rgsspectrum` task. We selected the background events from a region spatially offset from the source region. The response matrices were constructed through the `rgsrmfgen` task for RGS1 and RGS2 data of the four pointings.

2.2.2 *High background level episodes*

We followed the same procedure as described in Sect. 2.1.2 to select good time intervals (GTIs) unaffected by soft proton flares. However, as the mean level of the light curves was different according to the data set and also to the instrument, we refrained from adopting the same count rate threshold for all the data. After rejection of the time intervals contaminated by the high background, we obtained the effective exposure times quoted in Table 2. Like in the case of EPIC data, the pointing whose exposure time is the most severely reduced is the fourth one.

3 ANALYSIS OF CYG OB2 #8A DATA

3.1 Spectral analysis

As briefly discussed in Sect. 1, several physical mechanisms are expected to be responsible for the X-ray emission of massive stars. On the one hand, the heating of the plasma of the stellar winds by hydrodynamic shocks is responsible for a thermal emission. These shocks may occur in stellar winds of individual stars (see e.g. Feldmeier et al. 1997) or in the wind-wind collision zone of binary systems (see e.g. Stevens et al. 1992). These two types of hydrodynamic shocks are able to produce plasma with characteristic temperatures of the order of a few 10^6 and of a few 10^7 K respectively.

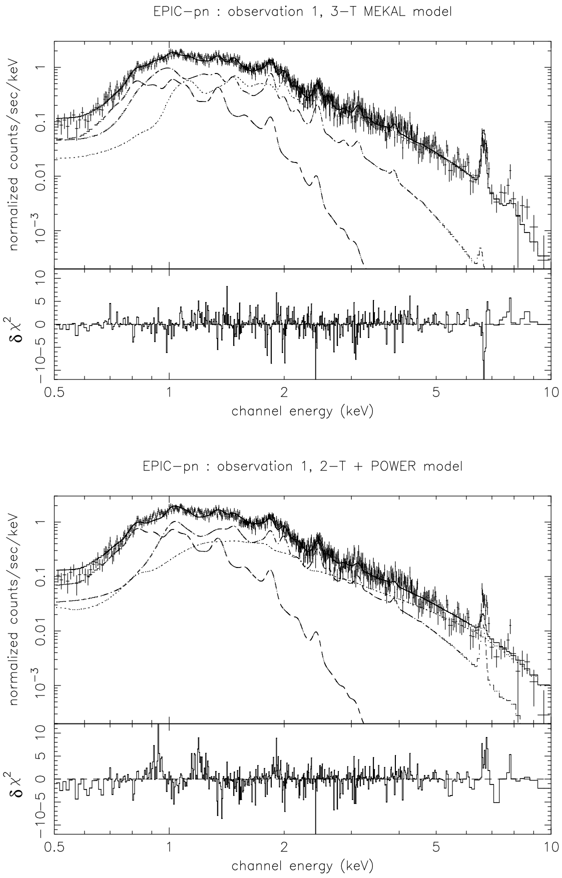

Figure 2. EPIC-pn spectrum of Cyg OB2 #8A of Observation 1, fitted with a $\texttt{wabs}_{\rm ISM}\texttt{*wind*(mekal}_1\texttt{+mekal}_2\texttt{+mekal}_3\texttt{)}$ (*Upper panel*) and a $\texttt{wabs}_{\rm ISM}\texttt{*wind*(mekal}_1\texttt{+mekal}_2\texttt{+power)}$ (*Bottom panel*) model between 0.5 and 10.0 keV. The three components are individually displayed in both cases. The Fe K blend at about 6.7 keV is the most obvious feature in the spectrum. The bottom window of each panel shows the contributions of individual bins to the χ^2 of the fit. The contributions are carried over with the sign of the deviation (in the sense data minus model).

Table 3. Parameters of the two components of Cyg OB2 #8A mainly estimated on the basis of a comparison with typical values provided by Howarth & Prinja (1989).

	Primary	Secondary
Sp. Type	O6If	O5.5III(f)
$T_{\rm eff}$ (K)	39 000	42 000
$R_\star$ ($R_\odot$)	23	14
$M_\star$ ($M_\odot$)	73	59
$L_{\rm bol}$ (erg s^{-1})	4.2×10^{39}	2.1×10^{39}
$\log g$	3.58	3.85
$\dot{M}$ ($M_\odot$ yr^{-1})	8.5×10^{-6}	2.6×10^{-6}
V_∞ (km s^{-1})*	2267	2891

* The terminal velocities of both stars were estimated to be 2.6 times the escape velocities of the stars (Vink et al. 2000, 2001), calculated on the basis of the typical masses and radii given by Howarth & Prinja (1989).

To first approximation, such a thermal emission can be modelled by optically thin thermal plasma models (`mekal` model: Mewe et al. 1985; Kaastra 1992). On the other hand, non-thermal emission processes like IC scattering are expected to produce a `power` law component in the X-ray spectrum. In this section, we will use composite models made of `mekal` and power law models. We note that solar abundances (Anders & Gevesse 1989) are assumed for the plasma throughout this paper.

3.2 ISM and wind absorption

Absorption models are required to account for the fact that both local circumstellar (wind) and interstellar (ISM) material are likely to absorb a significant fraction of the X-rays. The ISM absorption column was fixed to a value of $N_{\rm H} = 0.94 \times 10^{22}$ cm^{-2} obtained from the dust-to-gas ratio given by Bohlin et al. (1978), using the color excess ($E(B-V)$ = 1.6) provided by Torres-Dodgen et al. (1991).

To account for the fact that the wind material is ionized, an ionized wind absorption model was used for the local absorption component. We adopted the same opacity table as in the case of the multiple system HD 167971 (De Becker et al. 2005b), obtained with the wind absorption model described by Nazé et al. (2004). In De Becker et al. (2005b), we showed that there were no significant difference between opacities derived from various sets of parameters covering at least spectral types from O5 to O8. From the optical data already presented in De Becker et al. (2004c), we can estimate some crucial stellar and wind parameters of the stars in Cyg OB2 #8A. Following the spectral types of the two components, i.e. O6If and O5.5III(f), we adopted typical stellar radii and effective temperatures from Howarth & Prinja (1989), allowing us to estimate the bolometric luminosity of the two stars. The mass loss rates and terminal wind velocities were then obtained from the mass loss recipes of Vink et al. (2000, 2001). These parameters are quoted in Table 3. Provided that the stellar parameters of Cyg OB2 #8A lie within the parameter space discussed by De Becker et al. (2005b), we estimate that the `wind` absorption model that we used for HD 167971 suits the local absorption of Cyg OB2 #8A as well.

3.3 EPIC spectra

In order to fit the EPIC spectra, we tried different models including `mekal` and power law components. The quality of the fits was estimated using the χ^2 minimization technique and the best-fit parameter values we quoted in Table 4. We checked the consistency of our results with both the Cash statistic (Cash 1979) and the χ^2 statistic using a Churazov weighting (Churazov et al. 1996). We did not find any significant differences in the results obtained with the three methods. This was not unexpected as we are dealing with good quality spectra containing not so small numbers of counts per energy bin.

The best fits between 0.5 and 10.0 keV were obtained using a three-temperature thermal model. In the case of EPIC-MOS2, our fits pointed to normalization parameter values that deviated significantly from those of EPIC-MOS1 and EPIC-pn. This might be due to the bad column crossing the source region in the case EPIC-MOS2 (see Fig. 1), resulting in serious problems in obtaining a valuable ARF. For this reason, we discarded the EPIC-MOS2 data from our discussion and we will concentrate on EPIC-MOS1 and EPIC-pn data. As quoted in Table 4, the reduced χ^2 lies between 1.01 and 1.56 according to the instrument and to the data set. The characteristic temperature of the three thermal emission components are respectively about 3×10^6, 9×10^6 and 20×10^6 K. We note the good agreement achieved for the four observations, with a slightly lower temperature for the hard component of the second observation. The upper panel of Fig. 2 shows the EPIC-pn spectrum of Cyg OB2 #8A between 0.5 and 10.0 keV fitted by the three-temperature thermal model. Clearly, the most spectacular feature of this spectrum is the Fe K blend at about 6.7 keV. This spectral feature is observed for all instruments and in all data sets. As discussed by De Becker et al. (2004b), a large amount of relativistic electrons would be needed to produce such a line in a non-thermal plasma, and we therefore estimate that it might be considered as a signature of the thermal nature of the hot X-ray emission component observed in our EPIC spectra.

The results obtained with models including `power` laws were rather poor. Even though in some cases the replacement of the hardest thermal component discussed herebefore by a power law led to a slightly improved reduced χ^2, these models were rejected because they failed to fit the iron line at about 6.7 keV. The bottom panel of Fig. 2 shows the result of the fit of the EPIC-pn spectrum of Observation 1 with such a model. We see that the iron blend is poorly fitted, and that the fit of the softer part of the spectrum is less satisfactory than is the case of the upper panel of the same figure. In this case, the two thermal components yield kT of about 0.26 and 1.20 keV, whilst the power law has a photon index of about 3. We note also that we tried to use more sophisticated models with `wind` absorption columns affected to each emission component. However, this did not improve the quality of the fits and in most cases we obtained similar values (within the 1-σ error bars) for every local absorption component. For these reasons, we used only one local absorption column as described in Table 4.

Finally, in order to model our X-ray spectra of Cyg OB2 #8A, we adopted an alternative approach relying on a different physical interpretation of the thermal X-ray emission from shocked plasma. As discussed by Pollock et al. (2005), it is likely that the shocked plasma is not in equilibrium. We therefore tried to fit the EPIC spectra with the non-equilibrium ionization (NEI) plasma model (`vpshock` model available in XSPEC) initially developed for supernova remnants (see Borkowski et al. 2001), even though such

Table 4. Parameters for EPIC spectra of Cyg OB2 #8A in the case of a `wabs`$_{\rm ISM}$`*wind*(mekal`$_1$`+mekal`$_2$`+mekal`$_3$`)` model. Results are given for MOS1, pn, and combined MOS1+pn ('EPIC') in the case of the four observations. The first absorption component (`wabs`$_{\rm ISM}$) is frozen at the ISM value: 0.94 × 10^{22} cm^{-2}. The second absorption column, quoted as $N_{\rm w}$ (in cm^{-2}), stands for the absorption by the ionized wind material. The normalization parameter (Norm) of the `mekal` components is defined as $(10^{-14}/(4\,\pi\,D^2))\int n_{\rm e}\,n_{\rm H}\,dV$, where D, $n_{\rm e}$ and $n_{\rm H}$ are respectively the distance to the source (in cm), and the electron and hydrogen number densities (in cm^{-3}). The error bars represent the 90 % confidence interval. The last two columns give respectively the observed flux and the flux corrected for the ISM absorption between 0.5 and 10.0 keV.

	Log $N_{\rm w}$	kT_1 (keV)	Norm$_1$ (10^{-2})	kT_2 (keV)	Norm$_2$ (10^{-3})	kT_3 (keV)	Norm$_3$ (10^{-3})	χ^2_ν (d.o.f.)	Obs.Flux (erg cm^{-2} s^{-1})	Corr.Flux (erg cm^{-2} s^{-1})
Observation 1										
MOS1	$21.74^{21.82}_{21.67}$	$0.23^{0.27}_{0.20}$	$4.94^{10.35}_{2.57}$	$1.03^{1.10}_{0.87}$	$9.67^{12.21}_{5.95}$	$1.98^{2.60}_{1.66}$	$4.93^{8.26}_{2.72}$	1.26 (281)	6.23 × 10^{-12}	3.36 × 10^{-11}
pn	$21.68^{21.73}_{21.62}$	$0.26^{0.29}_{0.23}$	$2.66^{4.10}_{1.68}$	$0.79^{0.83}_{0.76}$	$9.87^{10.83}_{8.97}$	$1.84^{1.91}_{1.77}$	$7.59^{8.16}_{7.06}$	1.24 (636)	6.85 × 10^{-12}	3.07 × 10^{-11}
EPIC	$21.70^{21.74}_{21.66}$	$0.25^{0.28}_{0.23}$	$3.23^{4.40}_{2.24}$	$0.83^{0.87}_{0.79}$	$8.81^{9.58}_{8.06}$	$1.81^{1.87}_{1.75}$	$7.51^{8.05}_{7.04}$	1.39 (924)	6.61 × 10^{-12}	3.09 × 10^{-11}
Observation 2										
MOS1	$21.96^{22.01}_{21.90}$	$0.23^{0.27}_{0.20}$	$9.00^{17.88}_{4.05}$	$0.82^{0.97}_{0.75}$	$10.11^{12.00}_{8.37}$	$1.67^{1.90}_{1.53}$	$5.44^{6.76}_{4.07}$	1.01 (265)	4.87 × 10^{-12}	2.71 × 10^{-11}
pn	$21.90^{21.93}_{21.86}$	$0.24^{0.28}_{0.23}$	$6.16^{8.90}_{3.67}$	$0.79^{0.85}_{0.74}$	$9.74^{10.92}_{8.56}$	$1.57^{1.66}_{1.50}$	$6.60^{7.46}_{5.70}$	1.05 (580)	5.22 × 10^{-12}	2.64 × 10^{-11}
EPIC	$21.91^{21.95}_{21.89}$	$0.24^{0.26}_{0.22}$	$6.55^{9.66}_{4.53}$	$0.80^{0.85}_{0.75}$	$9.76^{10.77}_{8.77}$	$1.60^{1.68}_{1.53}$	$6.24^{6.96}_{5.49}$	1.12 (852)	5.15 × 10^{-12}	2.64 × 10^{-11}
Observation 3										
MOS1	$21.80^{21.85}_{21.72}$	$0.27^{0.29}_{0.23}$	$3.67^{6.08}_{2.20}$	$0.89^{0.98}_{0.82}$	$7.71^{8.86}_{6.60}$	$1.92^{2.20}_{1.80}$	$6.20^{6.90}_{4.44}$	1.37 (296)	5.85 × 10^{-12}	2.53 × 10^{-11}
pn	$21.70^{21.75}_{21.66}$	$0.28^{0.30}_{0.26}$	$2.55^{3.43}_{1.94}$	$0.81^{0.85}_{0.78}$	$9.34^{10.14}_{8.60}$	$1.91^{1.98}_{1.85}$	$7.18^{7.59}_{6.74}$	1.21 (686)	6.75 × 10^{-12}	2.88 × 10^{-11}
EPIC	$21.72^{21.79}_{21.69}$	$0.28^{0.30}_{0.26}$	$2.71^{4.41}_{2.10}$	$0.83^{0.87}_{0.79}$	$8.75^{9.48}_{8.01}$	$1.92^{1.98}_{1.86}$	$6.84^{7.22}_{6.41}$	1.49 (989)	6.47 × 10^{-12}	2.76 × 10^{-11}
Observation 4										
MOS1	$21.96^{22.01}_{21.89}$	$0.22^{0.24}_{0.19}$	$14.94^{27.73}_{8.27}$	$0.88^{1.00}_{0.78}$	$10.36^{12.31}_{8.04}$	$1.72^{2.16}_{1.53}$	$5.32^{7.16}_{2.77}$	1.17 (225)	5.38 × 10^{-12}	3.89 × 10^{-11}
pn	$21.86^{21.89}_{21.80}$	$0.24^{0.28}_{0.23}$	$8.38^{10.89}_{4.31}$	$0.87^{0.92}_{0.81}$	$11.78^{13.00}_{10.21}$	$1.82^{1.92}_{1.69}$	$5.44^{6.52}_{4.84}$	1.33 (506)	6.31 × 10^{-12}	3.74 × 10^{-11}
EPIC	$21.89^{21.92}_{21.85}$	$0.23^{0.25}_{0.22}$	$9.93^{13.28}_{6.97}$	$0.87^{0.92}_{0.82}$	$11.38^{12.38}_{10.10}$	$1.82^{1.90}_{1.69}$	$5.21^{6.16}_{4.68}$	1.56 (738)	5.91 × 10^{-12}	3.73 × 10^{-11}

a model was not calculated for colliding wind binary conditions. We obtained reasonable fits of the spectra with statistic values as good or better than those reported in Table 4, although this model failed to fit the soft part of the EPIC spectrum. However, the physical interpretation of these fits is not straightforward considering the parameters of the model, i.e. the chemical abundances and the ionization age of the plasma. Our fits suggest abundances of several elements lower than solar, that might reflect the strength of the continuum.

3.4 RGS spectra

As a first step, we combined the first and second order spectra in order to inspect the main spectral features and to identify the spectral lines. Above about 18 Å, the spectrum is very absorbed and we concentrated our analysis on the spectral domain below this wavelength. We identified the prominent lines through a comparison with the `aped` (Smith & Brickhouse 2000) and `spex` (Kaastra et al. 2004) line lists (see Table 5). In order to perform a more detailed analysis of the RGS data, we obtained fluxed (RGS1 + RGS2) spectra for our four observations. A closer look to the line profiles displayed in Fig. 3 suggests that some of them undergo a significant variability.

As a second step, we subtracted the background to individual spectra and then applied the response matrix for a global fitting between 5 and 35 Å. The analysis of first order RGS1 spectra was severely limited as a dead CCD falls between about 10 and 14 Å. For first order RGS2 data the dead CCD is located in the absorbed part of the spectrum and has no impact on the present analysis. Consequently, the observed count rates quoted in Table 7 for RGS1 and RGS2 are significantly different. We note that for the second order spectra, the dead CCDs fall in both cases in the less absorbed part of the spectrum, and no such differences are observed in the count rates from both instruments. We obtained the best-fit with a two-component `mekal` model. The χ^2 are slightly better if we use three thermal emission components but the error bars in the resulting fit parameters increase substantially. As we are dealing here with spectra containing sometimes small numbers of counts per energy bin, we used the Cash statistic (Cash 1979) to compare the results obtained with the χ^2 statistic. We did not find any significant differences between the results obtained with the two approaches. We obtained typical temperatures of about 2 × 10^6 and 8-12 × 10^6 K. These temperatures are close to the values obtained for the two softer thermal components of the 3-T model fitted to the EPIC data (see Sect. 3.3). The fact that a third emission component is not needed for data from the RGS instruments is explained by their different bandpass, i.e. $0.4 < {\rm E} < 2.5$ keV, whilst the $\sim 20 \times 10^6$ K thermal component is mostly required for higher energies. We checked the consistency of the results obtained between EPIC and RGS data through a simultaneous fit of the spectra from the four instruments, i.e. EPIC-MOS1, EPIC-pn, RGS1 and RGS2. We used the same three-temperature model as in Sect. 3.3 and we obtained parameter values (see Table 6) very close to those

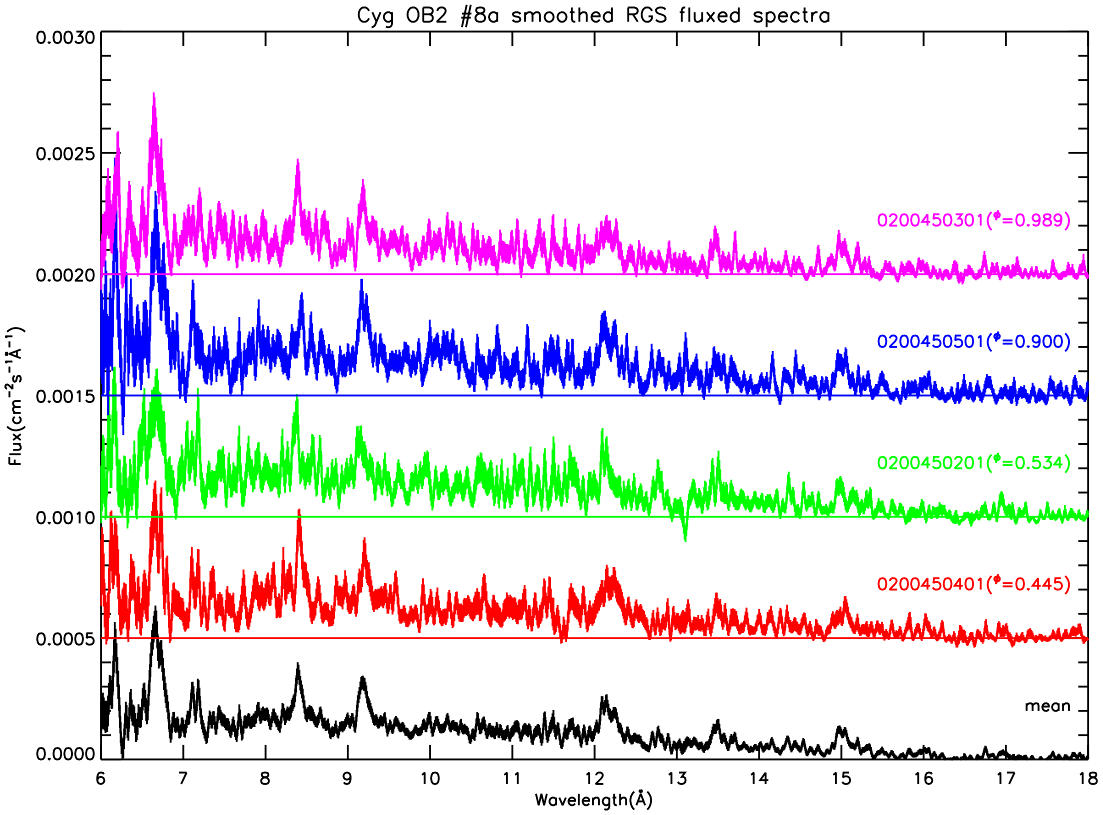

Figure 3. Smoothed RGS fluxed spectra of Cyg OB2 #8A obtained for our four observations between 6 and 18 Å . The orbital phase is specified in each case. The lower panel represents the mean RGS spectrum. The five spectra are respectively vertically shifted by 0.0005 in flux units. The prominent lines observed in the spectra are listed in Table 5.

Table 5. Identification of the prominent lines in the RGS sepctrum of Cyg OB2 #8A between 6 and 18 Å .

Ion	Wavelength (Å)
Si XIV (Ly α)	6.180
Si XIII (He-like)	6.648
Mg XII	7.106
Mg XII (Ly α)	8.419
Mg XI (He-like)	9.169
Fe XVII	10.000
Ne X (Ly α)	12.132
Ne IX (He-like)	13.447
Fe XVII	15.014

presented in Table 4 for the simultaneous fit of EPIC-MOS1 and EPIC-pn spectra, with similar or slightly larger reduced χ^2.

4 X-RAY LUMINOSITY OF CYG OB2 #8A

4.1 Variability analysis from XMM-Newton data

The count rates obtained with the five instruments on board *XMM-Newton* for the four observations are quoted in Table 7. We observe significant variability of Cyg OB2 #8A on a time-scale of about ten days, i.e. the typical separation between two pointings in our series. The largest variation is found between Observations 1 and 2, with an amplitude of about 20 %. We emphasize that the variations we observe for all instruments are correlated. To illustrate the variability observed between the different observations (see Fig. 4), we compared the count rates obtained in several energy bands in Observation 1 with those obtained in Observation 2 (*left panels*), Observation 3 (*middle panels*), and Observation 4 (*right panels*), respectively for EPIC-MOS1 (*upper part*) and EPIC-pn (*lower part*). In each of these plots labelled (a) to (f), the upper section displays the count rates and the lower section shows the relative variability of the observed count rate. Albeit it is not shown here, we note that the same comparison was performed for the X-ray fluxes, estimated on the basis of the 3-T model with parameters given in Table 4. A plot of the relative variability of the observed X-ray flux of Cyg OB2 #8A for EPIC-pn has been presented by De Becker & Rauw (2005). We clearly see that there is a decrease in the X-ray count rate (flux) between the first and the second observation in the

Table 6. Same as Table 4 but for RGS data fitted by a `wabs`$_{\rm ISM}$`*wind*(mekal+mekal)` model between 5 and 35 Å. For each observation, the results are provided for the simultaneous fit (RGS1 + RGS2) of first order, second order, and first + second order spectra. The last line for each observation gives the parameters obtained for the simultaneous fit of combined RGS (2 instruments, 2 orders) and EPIC (MOS1 and pn) data with a `wabs`$_{\rm ISM}$`*wind*(mekal+mekal+mekal)` model between 0.5 and 10.0 keV.

	Log $N_{\rm w}$	kT_1 (keV)	Norm$_1$ (10^{-2})	kT_2 (keV)	Norm$_2$ (10^{-2})	kT_3 (keV)	Norm$_3$ (10^{-3})	χ^2_ν (d.o.f.)
Observation 1								
RGS: Order 1	$21.88_{21.81}^{21.95}$	$0.19_{0.18}^{0.22}$	$13.77_{6.12}^{24.14}$	$1.00_{0.94}^{1.06}$	$1.52_{1.35}^{1.70}$	–	–	1.17 (229)
RGS: Order 2	$21.76_{21.41}^{21.96}$	$0.20_{0.17}^{0.27}$	$8.64_{1.20}^{27.02}$	$1.38_{1.25}^{1.64}$	$1.18_{0.96}^{1.41}$	–	–	0.93 (109)
RGS: Ord. 1 & 2	$21.87_{21.78}^{21.94}$	$0.19_{0.18}^{0.20}$	$16.28_{8.71}^{25.83}$	$1.26_{1.18}^{1.33}$	$1.37_{1.23}^{1.49}$	–	–	1.15 (343)
EPIC + RGS	$21.65_{21.60}^{21.70}$	$0.24_{0.22}^{0.26}$	$2.71_{1.89}^{3.82}$	$0.78_{0.76}^{0.82}$	$0.85_{0.78}^{0.93}$	$1.76_{1.71}^{1.81}$	$8.13_{7.63}^{8.59}$	1.39 (1243)
Observation 2								
RGS: Order 1	$22.03_{21.99}^{22.09}$	$0.23_{0.19}^{0.32}$	$9.44_{3.00}^{21.63}$	$1.19_{0.98}^{1.14}$	$1.69_{1.56}^{2.05}$	–	–	1.59 (217)
RGS: Order 2	$21.99_{21.90}^{22.08}$	$0.22_{0.18}^{0.28}$	$10.41_{3.28}^{22.73}$	$1.01_{0.69}^{1.40}$	$1.23_{0.98}^{1.56}$	–	–	0.89 (110)
RGS: Ord. 1 & 2	$22.03_{21.98}^{22.08}$	$0.23_{0.20}^{0.27}$	$10.12_{5.18}^{18.95}$	$1.04_{0.98}^{1.10}$	$1.64_{1.46}^{1.83}$	–	–	1.37 (332)
EPIC + RGS	$21.90_{21.87}^{21.92}$	$0.24_{0.22}^{0.25}$	$5.70_{4.10}^{7.46}$	$0.78_{0.74}^{0.81}$	$1.00_{0.91}^{1.08}$	$1.57_{1.52}^{1.64}$	$6.49_{5.84}^{7.11}$	1.17 (1151)
Observation 3								
RGS: Order 1	$21.84_{21.75}^{21.92}$	$0.22_{0.18}^{0.30}$	$4.05_{1.29}^{11.09}$	$1.05_{1.00}^{1.11}$	$1.35_{1.18}^{1.53}$	–	–	1.13 (240)
RGS: Order 2	$21.84_{21.71}^{21.96}$	$0.24_{0.19}^{0.31}$	$3.17_{1.17}^{10.83}$	$1.01_{0.96}^{1.07}$	$1.25_{1.15}^{1.46}$	–	–	1.03 (121)
RGS: Ord. 1 & 2	$21.84_{21.77}^{21.91}$	$0.22_{0.18}^{0.30}$	$3.85_{1.37}^{11.71}$	$1.04_{0.99}^{1.08}$	$1.32_{1.18}^{1.47}$	–	–	1.09 (366)
EPIC + RGS	$21.62_{21.57}^{21.66}$	$0.27_{0.25}^{0.33}$	$15.05_{8.89}^{20.56}$	$0.80_{0.77}^{0.82}$	$0.85_{0.78}^{0.90}$	$1.88_{1.84}^{1.94}$	$7.13_{6.81}^{7.46}$	1.54 (1324)
Observation 4								
RGS: Order 1	$22.00_{21.93}^{21.08}$	$0.23_{0.19}^{0.34}$	$10.30_{2.59}^{26.41}$	$0.92_{0.78}^{1.00}$	$1.62_{1.39}^{2.16}$	–	–	1.17 (153)
RGS: Order 2	$21.78_{21.60}^{21.92}$	$0.33_{0.24}^{0.41}$	$0.73_{0.34}^{17.15}$	$0.77_{0.69}^{0.87}$	$1.58_{1.36}^{1.97}$	–	–	0.91 (76)
RGS: Ord. 1 & 2	$21.94_{21.87}^{22.02}$	$0.29_{0.19}^{0.41}$	$3.18_{1.31}^{16.13}$	$0.83_{0.77}^{0.91}$	$1.65_{1.45}^{2.01}$	–	–	1.09 (234)
EPIC + RGS	$21.87_{21.83}^{21.90}$	$0.23_{0.22}^{0.25}$	$7.81_{5.56}^{10.54}$	$0.86_{0.81}^{0.88}$	$1.21_{1.10}^{1.30}$	$1.83_{1.72}^{1.91}$	$5.18_{4.73}^{5.94}$	1.54 (954)

Table 7. Observed count rates of Cyg OB2 #8A for the five *XMM-Newton* instruments, expressed in cts s^{-1}.

	EPIC-MOS1	EPIC-MOS2	EPIC-pn	RGS1	RGS2
Observation 1	0.741 ± 0.007	0.737 ± 0.007	2.141 ± 0.013	0.034 ± 0.002	0.056 ± 0.002
Observation 2	0.592 ± 0.006	0.598 ± 0.006	1.697 ± 0.012	0.027 ± 0.002	0.040 ± 0.002
Observation 3	0.699 ± 0.006	0.692 ± 0.006	2.038 ± 0.011	0.032 ± 0.002	0.048 ± 0.002
Observation 4	0.688 ± 0.008	0.667 ± 0.008	2.009 ± 0.015	0.035 ± 0.002	0.049 ± 0.002

whole EPIC bandpass. The first and third observations appear to be very similar. In the case of the fourth observation, we see that the count rate decreases only in the hard energy band (above about 2.0 keV). We note that all the variability trends discussed here are consistent if we consider count rates and observed fluxes, or EPIC-MOS and EPIC-pn data.

We finally searched for short term variability, i.e. within a single exposure. We have binned the event lists into 100 s, 200 s, 500 s and 1000 s time intervals in four energy bands, respectively 0.5–10.0 keV, 0.5–1.0 keV, 1.0–2.5 keV and 2.5–10.0 keV. We calculated the count rates in each time bin, along with their standard deviation, after subtraction of a background scaled according to the respective surface areas of the source and background regions (the same as used for the spectra extraction, see Sect. 2.1.1). Good Time Intervals (GTIs) were considered to compute the count rates using effective time bin lengths. A first inspection of the light curves does not reveal any significant variability correlated between the EPIC instruments on time-scales shorter than single exposures. This lack of significant variation is confirmed by variability tests applied to every light curve (χ^2 and pov-test as described by Sana et al. 2004).

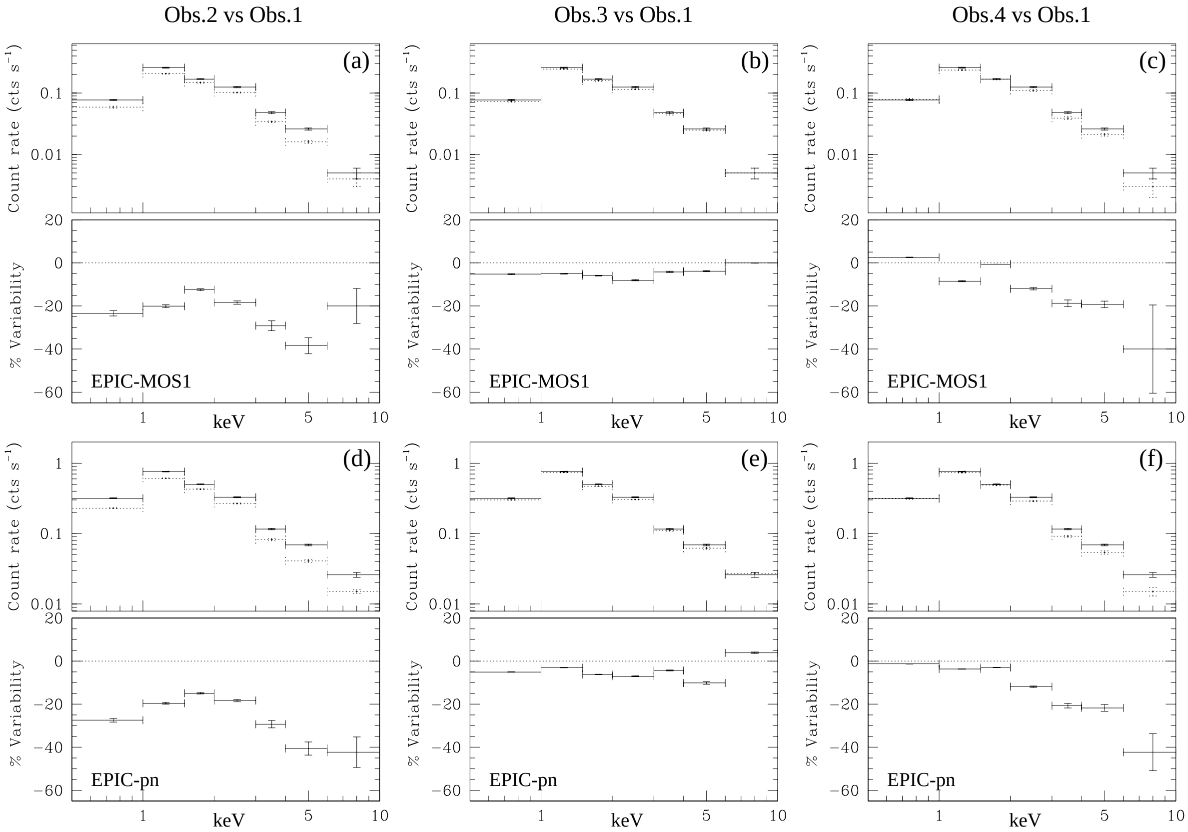

Figure 4. Relative variability of Cyg OB2 #8A for EPIC-MOS1 and EPIC-pn between 0.5 and 10.0 keV. For each part of the figure labelled a, b, c, d, e or f, we have represented: (i) *Upper panels:* Observed count rate of the first observation (solid symbols) as compared to the *n*th observation (dotted symbols) with *n* being the number of the observation, i.e. 2, 3 or 4. (ii) *Lower panels:* Relative variability of the observed count rate. A negative value stands for a decrease in the X-ray flux as compared to Obs. 1. The vertical error bars on the count rates stand for the 1-σ confidence interval, while the horizontal bars give the energy interval considered.

4.2 Overall luminosity

On the basis of the best-fit parameters presented in Table 4 for the three-temperature model, we have evaluated the fluxes between 0.5 and 10.0 keV for the four exposures. The observed, i.e. absorbed, fluxes are provided in the last but one column of Table 4. Considering a distance to Cyg OB2 #8A of 1.8 kpc (Bieging et al. 1989), we computed its unabsorbed X-ray luminosity, i.e. corrected for the ISM absorption, in the case of the simultaneous fit of EPIC-MOS1 and EPIC-pn data. The results are collected in Table 8. In this table, we also provide the $L_\mathrm{X}/L_\mathrm{bol}$ ratio. On the basis of the bolometric luminosities given in Table 3, we also computed the expected intrinsic X-ray luminosity using the empirical relation proposed by Sana et al. (2005). Although this latter relation relies on a rather small sample of O-type stars as compared to that of Berghöfer et al. (1997), we prefered to use this one because of its limited dispersion ($\sim$ 40 %, as compared to about a factor 2 for Berghöfer et al. 1997), and also because the empirical relation of Sana et al. (2005) was established after a careful individual investigation of each O-star of their sample in the same energy domain as for the present analysis, i.e. between 0.5 and 10.0 keV. We therefore obtain X-ray luminosities of 5.17 × 10^{32} and 2.58 × 10^{32} erg s^{-1} respectively for the primary and the secondary. The sum of these two quantities, i.e. L_X of 7.75 × 10^{32} erg s^{-1}, allowed us to calculate overluminosity factors ranging between about 13 and 19 (see column (4) of Table 8).

Table 8. X-ray luminosity of Cyg OB2 #8A. The columns (1) and (2) yield respectively the flux and the luminosity between 0.5 and 10.0 keV, corrected for the ISM absorption, and derived from the simultaneous fit of EPIC-MOS1 and EPIC-pn instruments with the 3-T model. The luminosities are computed considering a distance of 1.8 kpc (Bieging et al. 1989). Column (3) gives the $L_\mathrm{X}/L_\mathrm{bol}$ ratio, and finally the X-ray luminosity excess is provided in column (4).

	Corr. flux (erg cm^{-2} s^{-1}) (1)	Corr. L_X (erg s^{-1}) (2)	$L_\mathrm{X}/L_\mathrm{bol}$ (3)	excess (4)
Obs. 1	3.09×10^{-11}	1.20×10^{34}	1.9×10^{-6}	15.5
Obs. 2	2.64×10^{-11}	1.02×10^{34}	1.6×10^{-6}	13.2
Obs. 3	2.76×10^{-11}	1.07×10^{34}	1.7×10^{-6}	13.8
Obs. 4	3.73×10^{-11}	1.45×10^{34}	2.3×10^{-6}	18.7

Table 9. Observed count rates (CR) of Cyg OB2 #8A for the *ROSAT*-PSPC observations expressed in cts s^{-1}. The orbital phase is computed at mid-exposure according to the ephemeris of De Becker et al. (2004c).

Observation	JD (–2 400 000)	ϕ	CR (cts s^{-1})
rp200109n00	48 368.074	0.022	0.187 ± 0.008
rp900314n00 #1	49 107.104	0.756	0.306 ± 0.014
rp900314n00 #2	49 109.310	0.856	0.282 ± 0.010
rp900314n00 #3	49 110.218	0.898	0.295 ± 0.007
rp900314n00 #4	49 110.972	0.932	0.245 ± 0.008

5 ARCHIVE X-RAY DATA

5.1 *ROSAT*-PSPC data

Cyg OB2 has been observed twice with the *ROSAT*-PSPC instrument. A first observation was performed on 1991 April 21 (sequence number rp200109n00, ∼ 3.5 ks), and the second one between 1993 April 29 and 1993 May 5 (sequence number rp900314n00, ∼ 19 ks). The latter consisted mainly of four exposures spread over about five days. The analysis of Waldron et al. (1998) revealed a significant variation of the soft X-ray flux (below 2 keV) between the 1991 and the 1993 observations, with the highest emission level observed in 1993. We retrieved the screened data from the archive and we used the `xselect` software to analyze the data of Cyg OB2 #8A. We extracted a light curve of this observation and we split it by applying time filters to obtain four separated data sets with effective exposure times of about 3–4 ks. We selected the source events within a 1 arcmin circular region. The background was selected in an annular region around the source region of the same area, excluding its intersection with a 30 arcsec circular region centered on a point source located to the North relative to Cyg OB2 #8A (RA = 20:33:13.9 and DEC = + 41:20:21.4, Equinox 2000.0). We used the `xspec` software to analyse the spectra and we obtained reasonable fits with a single temperature `mekal` model, with a kT of about 0.5–0.7 keV. We determined the count rates for each subexposure in the 0.4–2.5 keV energy band and we collected them in Table 9, along with the time of each exposure.

5.2 *ASCA*-SIS data

The Cyg OB2 association was observed with *ASCA* (Tanaka et al. 1994) during the performance verification phase on 1993 April 29 (sequence number 20003000, ∼ 30 ks). A first analysis of these data was reported by Kitamoto & Mukai (1996). These authors already pointed out the need to use two thermal emission components, with characteristic temperatures of the order of 0.6 and 1.5 keV respectively, in order to model reasonably the data of Cyg OB2 #8A. We retrieved the raw data and processed them using the `xselect` software. Even though both gas-imaging spectrometers (GIS) and solid-state imaging spectrometers (SIS) were operated during the observation, we only used SIS data because of their better spatial resolution. We extracted the source events within a 2.21 and 2.95 arcmin radius circular region respectively for SIS0 and SIS1. In both cases, we selected the background events from a rectangular box located a few arcmin to the East of Cyg OB2 #8A. As the source region crosses over two CCDs, we constructed two response matrix files (RMF), i.e. one for each CCD, and we obtained the effective RMF through a weighted sum of the two individual response matrices.

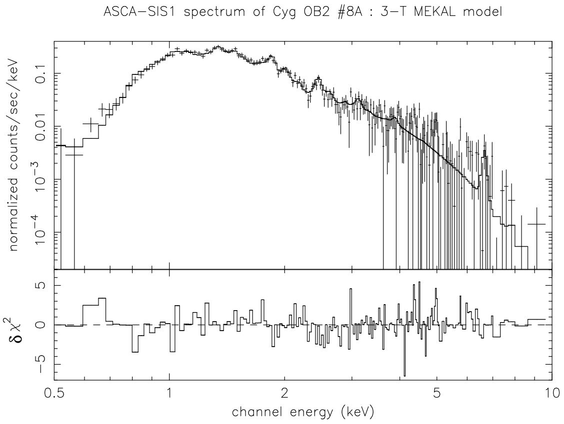

Figure 5. *ASCA*-SIS1 spectrum of Cyg OB2 #8A fitted with a `wabs`$_{\rm ISM}$`*wind*(mekal`$_1$`+mekal`$_2$`+mekal`$_3$`)` model between 0.5 and 10.0 keV. The lower part of the figure has the same meaning as for Fig. 2.

The spectral analysis was performed with the `xspec` software, and the best-fit results were obtained with the three-temperature thermal model described in Sect. 3.3. We note that we obtained a lower value of the reduced χ^2 by replacing the third thermal component by a power law, but we estimate that this apparently better result is only due to the rather poor quality of the data in the hard part of the spectrum, unlikely to reveal the Fe K line clearly present in our *XMM-Newton* EPIC spectra. As the quality of the SIS0 data appeared to be significantly poorer than that of SIS1, we considered only the latter in our spectral analysis. The best-fit parameters obtained with the 3-T thermal model between 0.5 and 10.0 keV are given in Table 10. The SIS1 spectrum and the corresponding model are presented in Fig. 5. From this model, we obtained an absorption corrected $L_{\rm X}$ of 1.86×10^{34} erg s^{-1} between 0.5 and 10.0 keV, leading to an X-ray luminosity excess of about 24. We finally note that the observed count rate in the same energy band is 0.331 ± 0.004 cts s^{-1} for SIS1.

6 DISCUSSION

6.1 Orbital modulation of the X-ray flux

6.1.1 Observational material

As Cyg OB2 #8A is a binary system, one could wonder whether a modulation of the X-ray flux is likely to be revealed by the existing X-ray observations. This issue was adressed by De Becker et al. (2005a) where the results from several X-ray observations (*ROSAT* and *ASCA*) were combined to obtain a phase-folded light curve, on the basis of the ephemeris published by De Becker et al. (2004c). The light curve suggested a phase-locked modulation of the X-ray flux, probably due to the combined effect of the variation of the absorption along the line of sight and of the X-ray emission itself as a function of orbital phase. Because of inconsistencies between *ROSAT*-HRI and -PSPC count rates and because of a poor sampling of the orbital cycle, this preliminary light curve did not allow us to draw any firm conclusion. However, we mention that

Table 10. Parameters for the *ASCA*-SIS1 spectrum of Cyg OB2 #8A fitted with a `wabs`$_{\rm ISM}$`*wind*(mekal`$_1$`+mekal`$_2$`+mekal`$_3$`)` model between 0.5 and 10.0 keV. The parameters have the same meaning as in Table 4.

Log $N_{\rm w}$	$21.82_{21.73}^{21.92}$
kT$_1$ (keV)	$0.23_{0.19}^{0.29}$
Norm$_1$	$9.91_{3.98}^{30.18} \times 10^{-2}$
kT$_2$ (keV)	$0.83_{0.73}^{1.04}$
Norm$_2$	$1.30_{1.00}^{1.64} \times 10^{-2}$
kT$_3$ (keV)	$1.66_{1.46}^{2.06}$
Norm$_3$	$7.61_{1.47}^{9.83} \times 10^{-3}$
χ^2_ν (d.o.f.)	1.05 (180)
Obs. Flux (erg cm^{-2} s^{-1})	7.42×10^{-12}
Corr. Flux (erg cm^{-2} s^{-1})	4.88×10^{-11}
Corr. $L_{\rm X}$ (erg s^{-1})	1.86×10^{34}
$L_{\rm X}/L_{\rm bol}$	2.94×10^{-6}
$L_{\rm X}$ excess	~ 24

the light curve presented by De Becker et al. (2005a) suggests clearly that the *ROSAT*-HRI count rates show a phase modulation similar to that of the PSPC data.

Using our four *XMM-Newton* observations, along with the results from archive *ROSAT*-PSPC and *ASCA*-SIS1 data[2], we constructed a new light curve. To compare the count rates from the different instruments in a consistent way, we used the 3-T model with the parameters obtained for the simultaneous fit of EPIC-MOS1 and EPIC-pn data for Observation 1, and we convolved it with the respective response matrices of *ROSAT*-PSPC and *ASCA*-SIS1 to obtain faked spectra. We obtained count rates of 0.250 ± 0.004 and 0.270 ± 0.001 cts s^{-1} respectively for both instruments. On the basis of these values, and of the count rates obtained in Sect. 5, we compared the X-ray emission level from all observations after normalization with respect to the *XMM-Newton* Observation 1. The normalized X-ray count rates obtained this way are plotted as a function of the orbital phase in Fig. 6. We note that this light curve does not suggest any large error on the orbital parameters derived by De Becker et al. (2004c), considering the short period and the large time interval separating some of the observations discussed here. Over the time range between 1991 and 2004, an error of 0.040 d on the period would indeed lead to an error on the orbital phase of the order of 0.4. This suggests that the error of 0.040 d given for the 21.908 d period might be a somewhat conservative value, reinforcing our trust in the orbital parameters proposed by De Becker et al. (2004c).

This curve presents a maximum at an orbital phase close to 0.75. We note the relative consistency of the various observations that contribute to the rather steep decrease in the X-ray emission between phases 0.75 and 1.0. We note however a discrepancy between the EPIC and PSPC points close to phase 0.9. Unfortunately, the lack of observations between phases 0.0 and 0.4 prevents us from constraining the position of the minimum, likely located shortly after phase zero. A somewhat more detailed view of the variability of

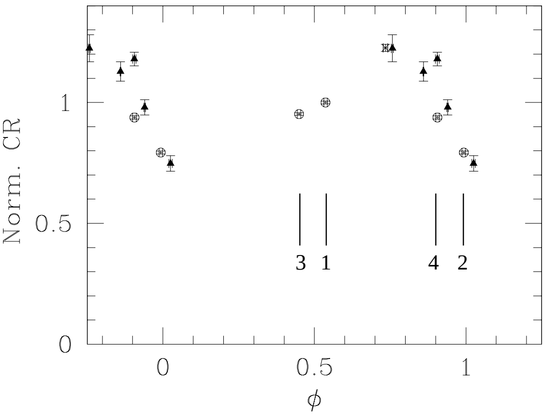

Figure 6. Normalized (see text) equivalent X-ray count rate of Cyg OB2 #8A from different observations as a function of the orbital phase following the ephemeris of De Becker et al. (2004c). *ROSAT*-PSPC: filled triangles. *ASCA*-SIS1: cross. *XMM-Newton*-EPIC: open circles. The vertical lines point to the four *XMM-Newton* observations labelled by their number.

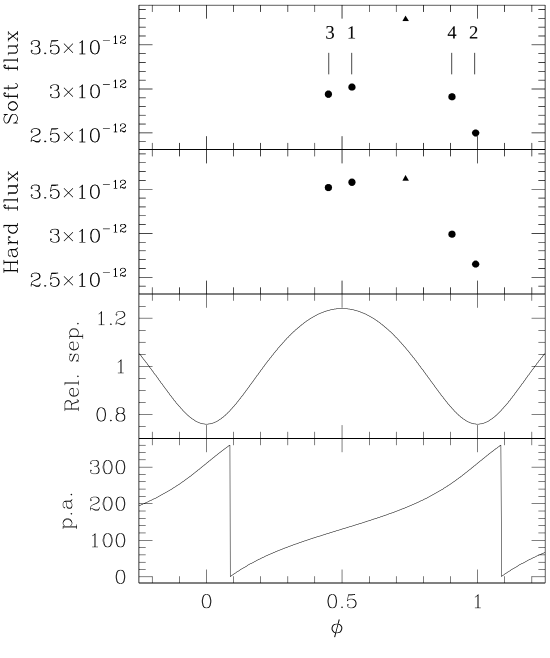

Figure 7. Variability of the X-ray flux of Cyg OB2 #8A as a function of the orbital phase observed with *XMM-Newton* (filled circles) and *ASCA* (filled triangle). The four *XMM-Newton* observations are individually labelled by their number. The four panels provide respectively (from top to bottom), the flux between 0.5 and 2.0 keV in erg cm^{-2} s^{-1}, the flux between 2.0 and 10.0 keV in erg cm^{-2} s^{-1}, the relative separation between the primary and the secondary, and the position angle of the system in degrees.

---

[2] As we suspect some problems in the calibrations of the HRI instruments relative the the PSPC, we do not consider *ROSAT*-HRI count rates in our discussion.

the observed X-ray flux can be obtained on the basis of Fig. 7. The X-ray fluxes in the soft (0.5 – 2.0 keV) and hard (2.0 – 10.0 keV) bands are individually plotted as a function of the orbital phase in the two upper panels. In order to investigate the variability in the hard part of the X-ray spectrum, we used only *XMM-Newton* and *ASCA* data. The separation between the two stars in Cyg OB2 #8A and the position angle (p.a.)[3] are also provided. The decrease of the X-ray flux between apastron and periastron is particularly obvious in the hard energy band. The maximum close to phase 0.75 suggested by Fig. 6 comes mainly from the soft band, as shown by the upper panel of Fig. 7.

In addition to the decrease in the X-ray flux, the comparison between the *XMM-Newton* Observations 1 and 2 reveals a significant decrease in the characteristic plasma temperature of the hottest thermal component (see Table 4). As these two observations are respectively close to phases 0.5 (largest separation) and 0.0 (shortest separation), the decrease in the post-shock plasma temperature could be related to the decrease in the pre-shock velocity at the position of the collision zone. For this rather close binary system, the winds will indeed not yet have reached their terminal velocity before they collide. Using our estimate of the orbital (De Becker et al. 2004c) and wind (Table 3) parameters and adopting a $\beta = 1$ wind velocity law, we calculate the distance between the stagnation point (i.e. the location of the wind-wind interaction on the binary axis) and and the centre of each star. Following an estimate of the inclination angle of the system[4], i.e. about 26 ± 5 degress, we infer absolute distances of about 131 and 81 $R_\odot$ respectively for the primary and the secondary at apastron (resp. 80 and 50 $R_\odot$ at periastron). Using the corresponding pre-shock velocities, we expect the post shock temperature to vary (on axis) between about 65×10^6K and 49×10^6K from phases 0.5 to 0.0[5]. According to the values quoted in Table 4, the observed temperature for the hottest thermal component is about 21×10^6 and 18×10^6 K respectively for Observations 1 and 2. The fact that the predicted and observed temperatures are so different (about a factor 3) may suggest that the effective pre-shock velocity is lower than predicted by about a factor 1.7. However, as the EPIC bandpass does not extend further than 10 keV, we should bear in mind that our spectral fits may underestimate the characteristic temperature of the post-shock plasma. Moreover, some fraction of the emission is expected to come from off-axis where the shocks are oblique, leading the averaged observed emission to have a lower characteristic temperature than anticipated at the stagnation point. Finally, some radiative inhibition may be at work close to the line of centres of the binary system, therefore reducing the speed of the wind flows before they collide (Stevens & Pollock 1994).

Some explanation to the variability described in Sect. 4.1 (see Fig. 4) and in Fig. 6 and 7 can be given on the basis of the different orbital phases of our *XMM-Newton* observations. In the case of a binary system like Cyg OB2 #8A, we can expect some variability in the X-ray domain mainly for two reasons[6]:

- the variation of the absorption along the orbital cycle, likely to affect mostly the softer part of the spectrum (i.e. below about 2.0 keV).
- the variation of the separation between the two stars, as the orbit is eccentric, likely to affect the physical conditions in the colliding wind zone. If some variability is observed in the harder part of the spectrum, it should most probably come from this process.

Considering the strong differences between Observations 1 and 2 in the whole EPIC bandpass (parts a and d of Fig. 4), both factors might play a significant role. Considering only *XMM-Newton* results, this decrease is more spectacular in the hard part of the spectrum (Fig. 4 and Fig. 7). This should be due to the variation of the separation between the two stars. The fact that Observation 2 occurs when the primary is 'in front' of the secondary (position angle close to 0 degrees), i.e. at an orbital phase where the absorption should be larger, may explain the decrease in the soft part of the spectrum. The parameters quoted in Table 4 point indeed to a higher local absorption column in the case of Observation 2 as compared to the first one. The same trend is also suggested by the fits of RGS spectra (see Table 6). The lack of significant variability between Observations 1 and 3 (parts (b) and (e) of Fig. 4) is compatible with the fact that they fall nearly at the same phase close to apastron. Finally, the decrease in the X-ray emission observed above 2.0 keV in Observation 4 (parts (c) and (f) of Fig. 4, and Fig 7) might be explained by the decrease in the separation, lowering the X-ray emission from the collision zone. The somewhat higher local absorption in the case of Observation 4 suggested by the `wind` absorption parameter given in Table 4 may be an artecfact of the fit, where the apparent higher absorption is compensated for by the larger normalization parameter of the same observation.

6.1.2 Hydrodynamic simulations

Considering the light curves presented above (see Fig. 6 and Fig. 7), it is obvious that the X-ray emission from Cyg OB2 #8A presents orbital modulations which are worth to be further investigated. For a better understanding of the physical processes responsible for this orbital modulation, we compared our *XMM-Newton* observations with the predictions of detailed hydrodynamic simulations using the same approach as Sana et al. (2004). In this method, the VH-1 numerical code based on the Piece-wise Parabolic Method (Colella & Woodward 1984), is used to solve the partial differential equations of hydrodynamics followed by a remap onto a fixed grid after each time step. A radiative energy loss term is included in the hydrodynamic equations in order to treat the cooling self-consistently. For details see Stevens et al. (1992), Pittard & Stevens (1997) and Sana et al. (2004).

Briefly, two spherically symmetric ionized winds of constant velocity are assumed, resulting in an axi-symmetric geometry around the lines of centres where the hydrodynamic problem is reduced to a two-dimensional flow. The orbital motion is neglected. As the acceleration of the wind is not taken into account,

---

[3] This position angle is 0° when the primary is in front of the secondary, and it gets the value 180° in the reverse situation. The longitude of the periastron (ω), that is required to compute the position angle, is equal to $220° \pm 12°$. This result was not mentioned in De Becker et al. (2004c).

[4] We estimated the inclination angle by comparing the minimum masses given by De Becker et al. (2004c) and the typical masses given by Howarth & Prinja (1989) for stars of the spectral type and luminosity classes of the components of Cyg OB2 #8A.

[5] These temperatures correspond to the mean of the post-shock temperatures obtained respectively for the primary and the secondary.

[6] We also mention that some variability may be expected if the wind collision crashes onto the surface of the secondary (see e.g. Pittard 1998 and Sana et al. 2005), but we do not expect this scenario to occur in the case of Cyg OB2 #8A as the wind collision zone is not located close enough to the surface of the secondary.

Table 11. Pre-shock velocities calculated at the three orbital phases selected for the hydrodynamic simulations respectively for the primary and the secondary of the system. The velocities were calculated on the basis of the terminal velocities and radii provided in Table 3, using a $\beta = 1.0$ velocity law. We note that, as the estimate of the pre-shock velocities depends on the radius of the stars, the uncertainty on this latter quantity might be responsible for uncertainties on the calculated pre-shock velocities, and therefore on the post-shock temperatures as well.

Phase (ϕ)	$V_{pre-shock,1}$ (km s^{-1})	$V_{pre-shock,2}$ (km s^{-1})
0.5	1870	2400
0.75	1800	2310
0.0	1620	2080

Table 12. Predicted absorbed fluxes of Cyg OB2 #8A at three characteristic phases of the orbital cycle. The observed X-ray fluxes obtained close to the three phases are also quoted for comparison. For this latter quantity, the satellite is specified in each case. The observed fluxes are taken from Tables 4 and 10.

Phase (ϕ)	$f_{\rm X,sim}$ (erg s^{-1})	$f_{\rm X,obs}$ (erg s^{-1})
0.5	$(5.46 \pm 1.49) \times 10^{-11}$	0.66×10^{-11} (XMM #1)
0.75	$(4.81 \pm 1.06) \times 10^{-11}$	0.74×10^{-11} (ASCA)
0.0	$(2.95 \pm 0.43) \times 10^{-11}$	0.52×10^{-11} (XMM #2)

the pre-shock velocity is estimated on the basis of a classical velocity law (β = 1.0), for a terminal velocity estimated to be 2.6 times the escape velocity (Vink et al. 2000). We adopted a square grid size of 300 × 300 cells, corresponding to physical distances of $1.5 \times 1.5\, 10^{13}$ cm and we let the flow evolve a time long enough so that the system relaxes from the initial conditions. At each step, grids of density, pressure, radial and axial velocities are obtained, and therefore grids of temperature can be calculated. The X-ray emission from the system is evaluated by summing up the emissivity of each cell of the grid at each time step. The column of absorbing material was computed following a three-dimensional geometry taking into account the inclination of the system and the orientation of the line of sight with respect to the system (see Sana et al. 2004 for details).

We chose three different system configurations to evaluate the evolution of the X-ray flux between 0.5 and 10.0 keV along the orbital cycle: (i) apastron ($\phi = 0.5$), (ii) intermediate ($\phi = 0.75$), and (iii) periastron ($\phi = 0.0$). The pre-shock velocities estimated in each case are given in Table 11 for both stars of the system. In the three cases, the collision zone relaxes from initial conditions after about 2500 steps, i.e. about 3×10^5 s, and turns out to be highly unstable. This instability is however not expected to come from the cooling as the shocks in Cyg OB2 #8A are rather adiabatic (the cooling parameter (χ) for the primary and the secondary are respectively of the order of 0.5-1.3 and 2.5-7.3, the lowest value corresponding to periastron and the highest one to apastron). It could instead result from shear instabilities as the winds in Cyg OB2 #8A have different velocities. However, at this stage we cannot exclude a numerical origin for these instabilities.

The mean and standard deviation of the X-ray luminosity are computed over a large number ($\sim$ 5500) of time steps after relaxation from the initial conditions. The averaged predicted X-ray luminosities, absorbed by both the wind and the interstellar material (using $N_{\rm H} = 0.94 \times 10^{22}$ cm^{-2}, see Sect. 3.2), are given in the second column of Table 12. The comparison of the predicted and observed X-ray luminosities reveals that the theoretical modelling overestimates the X-ray luminosity by about a factor 5 to 8. Possibly, an overestimation of the terminal velocities and more probably the neglect of some physical processes such as radiative inhibition (Stevens & Pollock 1994) likely to occur in the case of Cyg OB2 #8A, might be partly responsible for this discrepancy. We note also that, as the X-ray luminosity is proportional to $\dot{M}^2$ for adiabatic systems, a small error on the mass loss rate will have a strong impact on the predicted X-ray luminosities. Moreover, a fraction of the kinetic energy of the shocks may be involved in the acceleration of particles (electrons and protons), but at this stage models likely to provide an estimate of this energy fraction are still lacking. However, the simulations predict indeed a minimum of the X-ray luminosity at periastron that is consistent with what we observe (see Fig. 6). The rather high emission level observed close to phase 0.75 is also predicted. We mention that the amplitude of the variation between phases 0.75 and 0.0 is very similar for observed and predicted luminosities. The X-ray luminosity observed at apastron appears however significantly lower than at phase 0.75, whilst the simulations lead to similar values at both phases. We note that the standard deviation on the predicted X-ray luminosity is the largest at apastron, suggesting that the X-ray emission could be more variable at this orbital phase, which would be averaged in a 3D condiguration. However, this could also be an artefact from our 2D simulation which leads to amplified variations. In addition, the relative emission levels obtained at the three orbital phases selected for our simulations are in agreement with the fluxes plotted in Fig. 7 in the hard energy band, i.e. the spectral domain where the colliding winds are mainly expected to produce X-rays. Although this should be considered as preliminary results as we performed the simulations at only three orbital phases, the rather good agreement between the predicted and observed variabilities confirms that the observed orbital modulations of the X-ray flux are produced by the line of sight absorption and by the variation of the separation between the two stars, as these two effects are dominent in our simulations.

6.2 Non-thermal emission

Cyg OB2 #8A is known as a bright non-thermal radio emitter (Bieging et al. 1989). The fact that it is a confirmed binary system suggests that the non-thermal emission is produced in the wind interaction zone. This has recently been confirmed by Blomme (2005) who presented a phase-folded radio light curve built on the basis of new data showing a strong phase-locked variability of the radio flux density. This is in agreement with the results of the study of Van Loo (2005) who showed that the production of the observed non-thermal emission from isolated stars is unlikely. In this scenario, electrons are accelerated through the first order Fermi mechanism up to relativistic velocities (Eichler & Usov 1993). This population of relativistic electrons is expected to interact with the local magnetic field, likely originating from the two stars, to produce synchrotron radiation in the radio domain (White 1985). New developments in the modelling of non-thermal radio emission from massive binaries have been described by Dougherty et al. (2003)

and Pittard et al. (2005). These recent models take into account several physical effects like free-free absorption, the Razin effect and IC cooling.

The latter process is particularly interesting in the sense that the cooling of relativistic electrons by UV photospheric photons through IC scattering is likely to produce a non-thermal high-energy emission component. However, we did not find any evidence for a power law emission component attributable to a non-thermal emission in our *XMM-Newton*-EPIC spectra of Cyg OB2 #8A. This was not unexpected as any putative non-thermal emission component would probably be overwhelmed by the strong thermal emission arising from the wind-wind interaction zone. The unlikelihood of the detection of a power law emission below 10.0 keV in the case of non-thermal radio emitting massive binaries was indeed pointed out by De Becker et al. (2005b). However, such a non-thermal emission could possibly be detected in very hard X-rays and soft γ-rays, where the spectra are not expected to be contaminated by thermal emission. For instance, De Becker et al. (2005a) estimated that the possible contribution of Cyg OB2 #8A to the γ-ray emission from the yet unidentified EGRET source 3EG J2033+4118 could amount up to about 10 %. However, these estimations need to be refined using more sophisticated models (see e.g. Pittard & Dougherty 2006). The observation of the Cyg OB2 region with the IBIS(ISGRI) imager onboard the *INTEGRAL* observatory will possibly provide new insight into the high-energy emission from its non-thermal radio emitting massive stars, among which Cyg OB2 #8A.

7 SUMMARY AND CONCLUSIONS

In this paper, we presented the results of four *XMM-Newton* observations of the massive binary Cyg OB2 #8A separated by about ten days. The best fits of the X-ray spectra were obtained using a three-temperature thermal model, with characteristic plasma temperatures for the three components of about 3×10^6, 9×10^6 and 20×10^6 K. The hottest component is most probably attributed to the thermal X-ray emission from the collision zone between the winds of the two stars. The nature of the X-ray emission appears to be purely thermal, and we failed to fit power law models to the hard part of the spectrum. This is in agremeent with the idea proposed by De Becker et al. (2005b) that non-thermal radio emitters are not likely to display a non-thermal emission component in their X-ray spectrum below 10.0 keV. We note also that the EPIC spectrum of Cyg OB2 #8A is reasonably fitted by non-equilibrium ionization models such as used by Pollock et al. (2005) in the case of WR 140. The X-ray luminosity is very high (about 10^{34} erg s^{-1}, leading to an overluminosity factor of 13–19 during our observations). This rather high X-ray emission level is in disagreement with the statement by Waldron et al. (2004) that the X-ray emission in Cyg OB2 #8A is probably not different from that expected from isolated O-stars.

The analysis of high spectral resolution RGS data reveals an absorbed spectrum with prominent lines mainly from Si XIV, Si XIII, Mg XII, Mg XI, Ne X, Ne IX and Fe XVII. The comparison of the spectra obtained at different orbital phases reveals a significant variability of some line profiles. Provided the variations of these lines are phase-locked, it may suggest that the plasma heated by the colliding winds contributes significantly to their production, but a better phase coverage of the orbital cycle is needed to investigate this behaviour in detail.

We folded the count rates from our *XMM-Newton* observations, along with those from archive *ROSAT*-PSPC and *ASCA*-PSPC observations, with the ephemeris given by De Becker et al. (2004c). We observe a variability of the count rate and of the X-ray flux of about 20 % between apastron and periastron. The light curve as a function of the orbital phase points to a maximum at about phase 0.75, and suggests a minimum shortly after the periastron passage. The shape of the light curve might be explained by the combined effect of absorption and varying separation along the orbital cycle, this latter factor being responsible for the lower pre-shock velocity reached by the winds at periastron with respect to apastron. Using hydrodynamic simulations, we also find a lower emission level close to phase 0.0, but the predicted X-ray luminosities are overestimated by about a factor 5. Such a discrepancy may be explained partly by somewhat excessive terminal velocities and/or mass loss rates, and mostly by the fact that we did not take radiative inhibition effects into account in our simulations. As a main conclucion, we state that the strong phase-locked variability – along with the spectral shape – of the X-ray emission of Cyg OB2 #8A revealed by our investigation points undoubtedly to X-ray emission dominated by colliding winds.

The investigation of the high-energy emission from Cyg OB2 #8A is likely to provide a wealth of information on the physics of interacting stellar winds. With a period of only about 22 days and such a large X-ray brightness, Cyg OB2 #8A offers the unique opportunity to monitor easily and intensively its X-ray emission during a complete orbit, and therefore to perform a detailed study of the interaction between stellar winds in massive binaries. The forthcoming study of *INTEGRAL*-ISGRI data will possibly constrain its high-energy emission above 20.0 keV, and allow us to evaluate its putative contribution to the unidentified EGRET γ-ray source 3EG J2033+4118. In the future, Cyg OB2 #8A appears to be an ideal target for the Wide band X-ray Imager (WXI) and the Soft Gamma-ray Detector (SGD) onboard the Next generation X-ray Telescope satellite *NeXT* (Takahashi et al. 2004). On the other hand, the results from the radio monitoring of Cyg OB2 #8A (Blomme 2005) might be used in parallel with state-of-the-art models to evaluate the non-thermal emission level in the high-energy domain. Moreover, provided that the relativistic electrons are accelerated in the collision zone of massive binaries, the simultaneous determination of the non-thermal luminosity both in the radio and high-energy domains is expected to provide an independent approach to estimate the local magnetic field in the interaction zone of the colliding winds.

ACKNOWLEDGEMENTS

Our thanks go to Alain Detal (Liège) for his help in installing the SAS. The Liège team acknowledges support from the Fonds National de la Recherche Scientifique (Belgium) and through the PRODEX XMM and INTEGRAL Projects. This research is also supported in part by contract P5/36 “Pôle d’Attraction Interuniversitaire” (Belspo). This research has made use of the SIMBAD database, operated at CDS, Strasbourg, France and NASA’s ADS Abstract Service.

REFERENCES

Anders E., & Grevesse N., 1989, Geochimica Cosmochimica Acta, 53, 197

Bell A.R., 1978, MNRAS, 182, 147

Berghöfer T.W., Schmitt J.H.M.M., Danner R., Cassinelli J.P., 1997, A&A, 322, 167

Bieging J.H., Abbott D.C., Churchwell E.B., 1989, ApJ, 340, 518

Blomme R., 2005c, in *Massive stars and High-Energy Emission in OB Associations*, Proc. JENAM 2005, in press

Bohlin R.C., Savage B.D., Drake J.F., 1978, ApJ, 224, 132

Borkowski K.J., Lyerli W.J., Reynolds S.P., 2001, ApJ, 548, 820

Cash W., 1979, ApJ, 228, 939

Chen W., White R.L., 1994, Ap&SS, 221, 259

Churazov E., Gilfano M., Forman W., Jones C., 1996, ApJ, 471, 673

Colella P., Woodward P.R., 1984, J. Comput. Phys., 54, 174

Comerón F., Paquali A., Rodighiero G. et al., 2002, A&A, 389, 874

De Becker M., 2001, Master thesis, University of Liège

De Becker M., 2005, PhD thesis, University of Liège, in preparation

De Becker M., Rauw G., 2005, in *Massive Stars in Interacting Binaries*, eds. A.F.J. Moffat & N. St-Louis, in press

De Becker M., Rauw G., 2005, in *Massive stars and high-energy emission in OB associations*, JENAM 2005, in press

De Becker M., Rauw G., Pittard J.M., Antokhin I.I., Stevens I.R., Gosset E., Owocki S.P., 2004a, A&A, 416, 221

De Becker M. et al., 2004b, A&A, 420, 1061

De Becker M., Rauw G., Manfroid J., 2004c, A&A, 424, L39

De Becker M., Rauw G., Swings J.-P., 2005a, Ap&SS, 297, 291

De Becker M., Rauw G., Blomme R., Pittard J.M., Stevens I.R., Runacres M.C, 2005b, A&A, 437, 1029

den Herder J.W. et al., 2001, A&A, 365, L7

Donati J.-F. et al., 2001, MNRAS, 326, 1265

Donati J.-F. et al., 2002, MNRAS, 333, 55

Dougherty S.M., Williams P.M., 2000, MNRAS, 319, 1005

Dougherty S.M., Pittard J.M., Kasian L., Coker R.F., Williams P.M., Lloyd H.M., 2003, A&A, 409, 217

Eichler D., Usov V., 1993, ApJ, 402, 271

Feldmeier A., Puls J., Pauldrach A.W.A., 1997, A&A, 322, 878

Gosset E. et al., 2006, in preparation

Harnden F.R. et al., 1979, ApJ, 234, L51

Herrero A., Puls, J. Najarro F., 2002, A&A, 396, 949

Howarth I.D., Prinja R.K., 1989, ApJS, 69, 527

Jardine, M., Allen, H.R., Pollock, A.M.T., 1996, A&A, 314, 594

Kaastra J.S., 1992, *An X-ray spectral code for optically thin plasmas*, Internal SRON-Leiden Report

Kaastra J.S., Mewe R., Raassen A.J.J., 2004, in New Visions of the X-ray Universe in the *XMM-Newton* and *Chandra* Era, ed. F. Jansen, ESA, SP-488, in press

Kahn S.M. et al., 2001, A&A, 365, L312

Kitamoto S., Mukai K., 1996, PASJ, 48, 813

Knödlseder J., 2000, A&A, 360, 539

Lumb D., 2002, *EPIC background files*, XMM-SOC-CAL TN-0016

Massey P., Thompson A.B., 1991, AJ, 101, 1408

Mewe R., Gronenschild E.H.B.M., van den Oord G.H.J., 1985, A&AS, 62, 197

Nazé Y., Rauw G., Vreux J.-M., De Becker M., 2004, A&A, 417, 667

Neiner C., Geers V.C., Henrichs H.F., Floquet M., Frémat Y., Hubert A.-M., Preuss O., Wiersema K., 2003, A&A, 406, 1019

Pittard J.M., 1998, MNRAS, 300, 479

Pittard J.M., Dougherty S.M., 2006, MNRAS, in preparation

Pittard J.M., Stevens I.R., 1997, MNRAS, 292, 298

Pittard J.M., Dougherty S.M., Coker R.F., O'Connor E., Bolingbroke N.J., 2005, A&A, in press

Pollock A.M.T., 1987, ApJ, 320, 283

Pollock A.M.T., Corcoran M.F., 2005, A&A, in press

Pollock A.M.T., Corcoran M.F., Stevens I.R., Williams P.M., 2005, ApJ, 629, 482

Rauw G., 2004, in *Cosmic Gamma-Ray Sources*, eds. K.S. Cheng and G.E. Romero, Kluwer Academic Publishers, Dordrecht, 105

Rauw G. et al., 2002, A&A, 394, 993

Sana H., Antokhina E., Royer P., Manfroid J., Gosset, E., Rauw G., Vreux J.-M., 2005, A&A, 441, 213

Sana H., Stevens I.R., Gosset E., Rauw G., Vreux J.-M., 2004, MNRAS, 350, 809

Sana H., Rauw G., Nazé Y., Gosset E., Vreux J.-M., 2005, MNRAS, submitted

Smith R.K., Brickhouse N.S., 2000, RevMexAA Serie de Conferencias, 9, 134

Stevens I.R., Blondin J.M., Pollock A.M.T., 1992, ApJ, 386, 265

Stevens I.R., Pollock A.M.T., 1994, MNRAS, 269, 226

Strüder et al., 2001, A&A, 365, L18

Takahashi T. et al., 2004, SPIE, 5488, 549

Tanaka Y., Inoue H., Holt S.S., 1994, PASJ, 46, L37

Torres-Dodgen A.V., Tapia M., Carroll M., 1991, MNRAS, 249, 1

Turner M.J.L. et al., 2001, A&A, 365, L27

Van Loo S., 2005, in *Massive Stars in Interacting Binaries*, eds. A.F.J. Moffat & N. St-Louis, in press

Vink J.S., de Koter A., Lamers H.J.G.L.M., 2000, A&A, 362, 295

Vink J.S., de Koter A., Lamers H.J.G.L.M., 2001, A&A, 369, 574

Waldron W.L., Corcoran M.F., Drake S.A., Smale A.P., 1998, ApJS, 118, 217

Waldron W.L., Cassinelli J.P., Miller N.A., MacFarlane J.J., Reiter J.C., 2004, ApJ, 616, 542

White R.L., 1985, ApJ, 289, 698

This paper has been typeset from a TEX/ LATEX file prepared by the author.

5.2 The non-thermal radio emitter Cyg OB2 #9

5.2.1 First results from the optical campaign

Cyg OB2 #9 (V = 10.8) was classified as an O5If star (Torres-Dodgen et al. 1991). We observed this star at the Observatoire de Haute-Provence with the Aurélie spectrograph mounted on the 1.52 m telescope in October 2003, October 2004, and in Summer 2005. The duration of each observing run was about 10 days. This star is heavily reddened and our series of 20 spectra was therefore obtained in the spectral domain between 6360 and 6780 Å . As shown in Fig. 5.10, the spectrum is dominated by the strong emission of the Hα line. We report also the presence of He II absorption lines at 6405, 6528 and 6683 Å . The weak emission at about 6718 Å is due to N V, and the emission lines at 6721, 6728 and 6731 Å may be attributed to C III (see Walborn & Howarth 2000; Walborn 2001).

We note that our spectra are significantly affected by telluric lines due to the presence of water vapor in the atmosphere. The contamination of our spectra reaches various levels according to the weather conditions and the airmass. We applied a first order correction for these telluric lines (assuming that their strength scale linearly with the airmass) to all our spectra but we note that this correction is not perfect, and the corrected spectra are therefore still significantly perturbed as can be seen in the line profiles plotted in Fig. 5.11.

We searched for a significant variability in our spectral times series using the techniques described in Appendix B. The mean spectrum of Cyg OB2 #9 and the square root of the TVS for all our data sets are plotted in Fig. 5.10. Some of the TVS peaks above the significance level are due to the telluric lines. However, some part of the variations can be attributed to the Hα line. This is more obvious for the Summer 2005 data set. The high level of the significance threshold in October 2003 is due to the poor signal-to-noise of the spectra obtained during that observing run. The fact that the variations are observed in individual data sets suggests that they occur on a time-scale of a few days. Moreover, the variability is unambigously revealed in the Summer 2005 data set which benifits from the best signal-to-noise ratio. A closer look at the profiles plotted in Fig. 5.11 reveals a slight variability of the intensity of the narrow absorption component observed at about 6560 Å . This is mostly observed in the profiles obtained in October 2003, although the TVS lies below the significance level for this data set (see Fig. 5.10). The lack of variability observed in October 2004 may be partly explained by the poor sampling, as only 5 spectra were obtained during 12 days. We note however that a transient variability cannot at this stage be completely excluded.

We also measured the radial velocities in order to search for variations attributable to a binary motion. We selected the He II λ 6683 line because its shape does not deviate too much from a Gaussian, with respect to the other lines observed in the spectrum (upper panel of Fig. 5.10). We did not find any significant variation in the radial velocities on a time-scale of a few days. We also calculated the mean and the standard deviations of the radial velocities obtained in each observing run, and the results are -10 ± 5.7, -4.2 ± 4.9 and -6.5 ± 12.7 km s^{-1} respectively in October 2003, in October 2004 and in Summer 2005. These values donot suggest any significant variation on a time-scale of a few months or of about one year. Consequently, if Cyg OB2 #9 is a binary system, the period should be rather long (at least a few years) and/or the system should be seen under a low inclination angle.

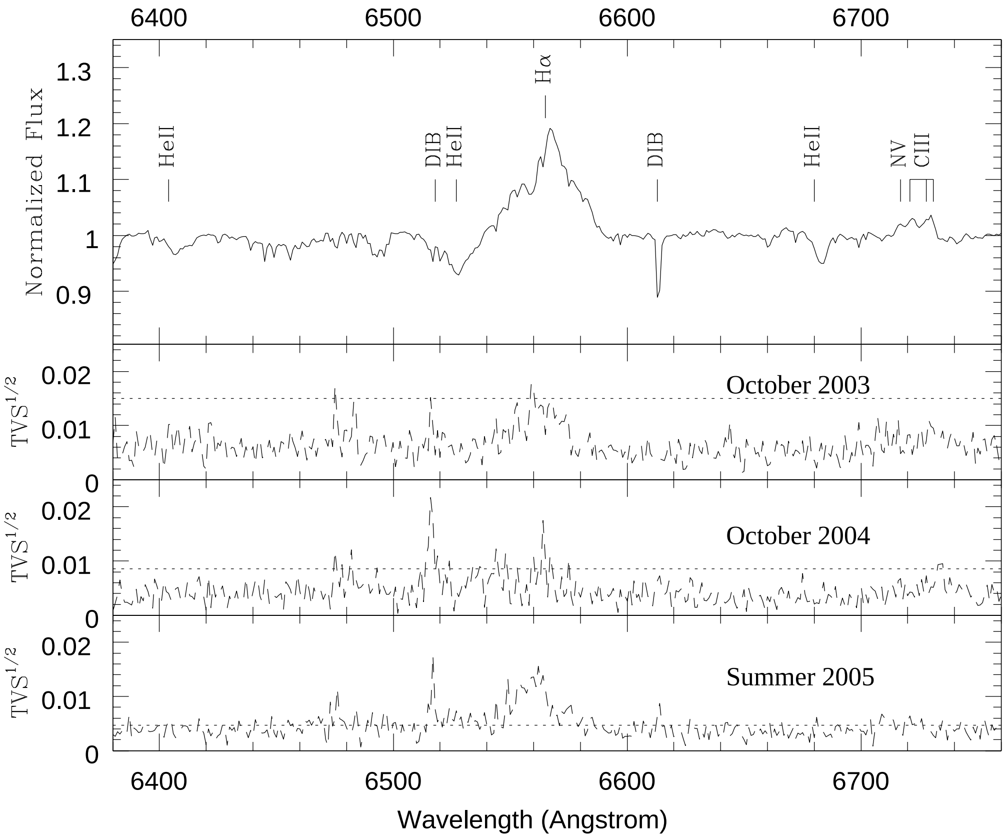

Figure 5.10: *Upper panel:* mean Aurélie spectrum of Cyg OB2 #9 between 6380 and 6760 Å obtained on the basis of the spectra taken in October 2003, October 2004 and in Summer 2005. *Lower panels:* square root of the time variance spectrum obtained respectively (from top to bottom) in October 2003, in October 2004 and in Summer 2005. The dotted horizontal line stands for the 99 % confidence level. The numerous peaks are due mostly to the fact that the intensity of the telluric lines was different for each observation because of very different weather conditions. The peaks obtained at the position of the Diffuse Interstellar Bands (DIBs) are probably due to the correction applied to our spectra to reduce the impact of the telluric lines. The TVS above the significance level at the position of the Hα line in Summer 2005 suggests that a significant variability is detected.

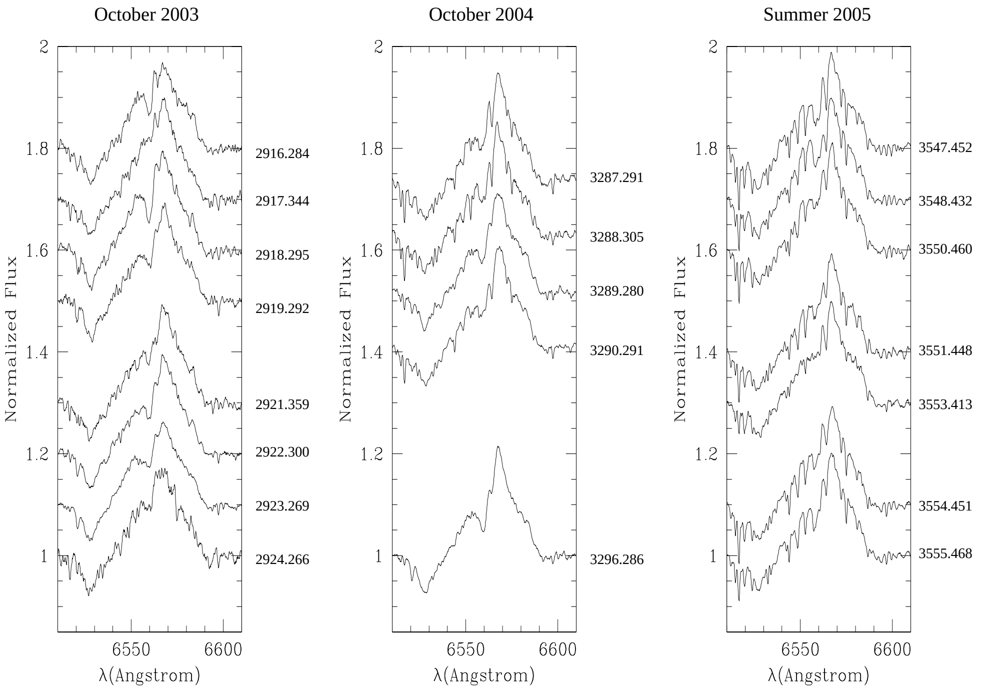

Figure 5.11: Hα profiles of Cyg OB2 #9 obtained respectively in October 2003, in October 2004 and in Summer 2005. The heliocentric Julian day (HJD - 2 450 000) is specified in each case.

5.2.2 X-ray emission from Cyg OB2 #9

As Cyg OB2 #9 was present in the EPIC field of view of our four *XMM-Newton* observations of Cyg OB2, we were able to investigate its X-ray properties following a similar approach as for Cyg OB2 #8A in Sect. 5.1.4 (see De Becker et al. 2005b). The main results were presented by Rauw et al. (2005a).

The EPIC spectra are rather well fitted by an absorbed 2-T thermal plasma model (see Fig. 5.12). While the lower temperature ($kT_1 = 0.63 \pm 0.03$ keV) is typical of the X-ray emission from isolated O-type stars, the second temperature reaches a significantly higher value ($kT_2 = 2.4 \pm 0.20$ keV) which corresponds by far to the hottest plasma in the O-type stars of Cyg OB2. This feature is quite consistent with a colliding-wind scenario in a binary system where the winds reach their terminal velocities before they collide. Moreover, the obvious presence of the Fe K blend at 6.7 keV argues in favor of the thermal nature of the hard X-ray emission observed in the EPIC bandpass.

5.2.3 Radio emission from Cyg OB2 #9

Even though we did not contribute to the observations of Cyg OB2 #9 in the radio domain, we find it useful to mention here the main result obtained quite recently on this star. This information will be helpful in the context of the general discussion presented on Chapter 6.

On the basis of all available archive radio data on Cyg OB2 #9, Van Loo (2005) presented a light curve strongly suggesting that the radio emission is variable on a time-scale of about 2.4 yr. These variations point to a colliding-wind scenario where the synchrotron radio emission is produced in a long period binary system.

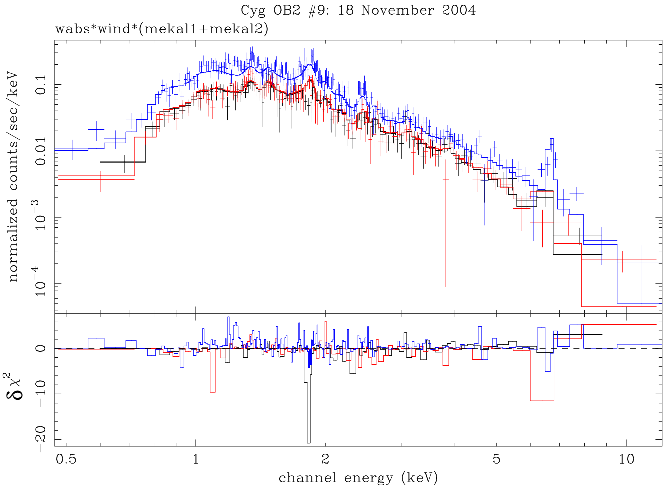

Figure 5.12: EPIC spectra of Cyg OB2 #9 as observed on 18 November 2004. The data were fitted with an absorbed two temperature optically-thin thermal plasma model. Note the prominent Fe K line at 6.7 keV.

5.3 INTEGRAL observations of the Cyg OB2 region

Time was granted to observe the Cyg OB2 region with the IBIS imager onboard the International Gamma-Ray Laboratory (*INTEGRAL*) during revolution 0080 (Announcement of Opportunity number 1, AO1), and in revolutions 0191, 0210, 0211, 0212, 0213, 0214, 0215, 0216, 0218, 0251, 0252, 0253, 0254 and 0255 (AO2) (see Appendix A). These observations consisted in series of rather short exposures of about 50 minutes (Science Windows), separated by slews. In total, the complete data set (Observing Group) contains 637 Science Windows, for a total observation time of about 2100 ks. As we were mostly interested in the hard X-ray and soft γ-ray emissions from massive stars, we did not use the high-energy detector layer (PICsIT) data, and we restricted our analysis to the low-energy detector layer, i.e. ISGRI.

Briefly, the standard analysis of ISGRI data leading to the construction of a mosaic image and to the detection of the sources in the field of view follows a well-defined sequence of steps described below (see the IBIS user's manual for details):

1. **Data correction**. Noisy pixels are flagged and energy corrections are applied to the events. The output consists mainly in an event list with the photon energy expressed in keV.
2. **Good time handling**. Good time intervals (GTIs), i.e. time intervals considered to be suitable for the data analysis, are selected and merged into a unique total GTI, corresponding to the total effective exposure time.
3. **Dead time calculation**. This step consists in the calculation of the total time interval during which the incoming photons may be lost due to the processing of the previous events.
4. **Event binning**. All events are sorted into energy bins (either default or specified by the user).

5. **Background correction**. At this stage, background maps are created in the energy bands specified in the previous step.

6. **Catalogue source selection**. Sources in the field of view are selected from an input catalogue, and an output list including their location is created. This selection is useful for the source detection procedure performed in the next step. The source selection is the first step of the so-called high-level data analysis for IBIS.

7. **Image reconstruction**. The shadowgrams, i.e. the projection through the coded mask of the sky image on the detector plane, are deconvolved to produce sky images and the source detection procedure is applied to each Science Window. Mosaic images are then constructed in each energy band on the basis of all individual images, and the source detection procedure is once again applied to the mosaic.

As a first approach, we used the offline scientific analysis (OSA) software v. 4.2 and we worked with all the Science Windows to search for the presence of point sources. We therefore obtained a first view of the Cyg OB2 region including the fully coded field of view (FCFOV) and the partially coded field of view (PCFOV). We distributed the events detected by ISGRI in three energy bands: 20 – 60 keV, 60 – 100 keV, and 100 – 1000 keV. The data analysis and the image extraction procedure were applied to each Science Window. We then constructed a mosaic of the images and we applied the source detection procedure using the input catalogue provided by the Integral Science Data Center (ISDC, Courvoisier et al. 2003) with the v. 4.2 release of the data analysis software (17th catalogue of high-energy sources). The detection threshold was fixed at $5\,\sigma$. As a result, we report on the detection of the following point sources:

- **Cyg X-1**. This source is the brightest high-energy emitter in the vicinity of Cyg OB2. It was the first binary system in which the presence of a black hole was suggested, with an O9.7 supergiant companion (HDE 226868). Comparing high precision VLBI astrometry for Cyg X-1 and *Hipparcos* astrometry for the members of Cyg OB3, Mirabel & Rodrigues (2003) convincingly demonstrated that Cyg X-1 shares common proper motion with the Cyg OB3 association, located at a distance of about 2.15 kpc (Massey et al. 1995). Ziółkowski (2005) proposed that the system might have evolved from a 80 – 100 $\mathrm{M}_\odot$ primary with a 40 – 50 $\mathrm{M}_\odot$ secondary, to become the present High-Mass X-Ray Binary (HMXRB) with masses of $20 \pm 5\,\mathrm{M}_\odot$ and $40 \pm 5\,\mathrm{M}_\odot$ respectively for the black hole and for the massive supergiant. Cyg X-1 has been previously observed with *INTEGRAL* during the performance and verification phase (Bazzano et al. 2003).

- **Cyg X-2**. This rather bright high-energy source, located at a distance of about 8 kpc, is a Low-Mass X-Ray Binary (LMXRB) with a neutron star primary (Orosz & Kuulkers 1999). The spectral type of its companion (V1341 Cyg) was reported to be in the range of A5 to F2 (Cowley et al. 1979). The first results obtained with IBIS for Cyg X-2 were described by Natalucci et al. (2003).

- **Cyg X-3**. Because of the heavy absorption, making the identification of its optical counterpart very difficult, the nature of this X-ray binary is not yet completely understood. However, some indications suggest that the companion of the compact object may be a Wolf-Rayet star (see Lommen et al. 2005, and references therein), probably making this object the only WR X-ray binary known so far. The detection of radio outbursts jet-like structures led Cyg X-3 to be classified as a microquasar. Cyg X-3 is the bright high-energy source closest to Cyg OB2 on the sky plane. The first results of the observation of this X-ray binary with *INTEGRAL* were reported by Goldoni et al. (2003).

- **EXO 2030+375**. This high-mass X-ray binary consists of a neutron star orbiting a Be companion with a period of about 46 d (Wilson et al. 2002). According to the standard model of Be/X-ray binaries, the high-energy radiation is produced by the accretion mechanism that takes place when the compact object interacts with the circumstellar disk of the Be star at each periastron passage. The results of *INTEGRAL* observations of EXO 2030+375 have been reported by Kuznetsov et al. (2003) and Camero Arranz et al. (2005).

- **SAX J2103.5+4545**. This high-mass X-ray binary pulsar (pulse period $\sim$358 s) was detected for the first time by the *Beppo Sax* observatory in 1997 (Hulleman et al. 1998). Baykal et al. (2000) discovered that the pulsar is member of an eccentric (e = 0.4) binary system orbiting with a period of about 12.68 d. According to Reig et al. (2004), the likely optical counterpart is a B0Ve star, making SAX J2103.5+4545 the Be/X-ray with the shortest orbital period known. Results from *INTEGRAL* observations of this object were for instance presented by Sidoli et al. (2005).

- **KS 1947+300**. The high-mass X-ray binary was discovered by the X-ray spectrometer onboard the *Mir* orbiting space station in 1989 (Borordin et al. 1990). The spectroscopic and photometric study performed by Negueruela et al. (2003) revealed that the optical counterpart is an early B0Ve star located at a distance of about 10 kpc, confirming therefore the Be/X-ray transient nature of KS 1947+300. According to the study of Galloway et al. (2004), the orbital period of the system is equal to 40.42 d and the orbit is almost circular.

- **QSO B1957+405**. Contrary to the high-energy sources detected with our *INTEGRAL* data discussed above, this one is not an X-ray binary. It corresponds to the powerful radio galaxy called Cyg A.

- **IGR J21247+5058**. This is one of the high-energy point sources detected for the first time by *INTEGRAL* (Walter et al. 2004). It has been associated with the radio source 4C50.55 by Ribo et al. (2004). The follow-up study performed by Masetti et al. (2004) to reveal the nature of this source suggests that it is indeed a background radio galaxy at $z = 0.02$.

We note also that the mosaic image suggests the presence of two additional rather weak point sources (see S1 and S2 in Table 5.2 and in Fig. 5.14), even though the detection procedure failed to detect them. The unidentified EGRET source 3EG J2033+4118, whose position on the mosaic image is specified in Fig 5.14, is not detected. Moreover, the mosaic image built on the basis of all individual images obtained for each Science Window displays artificial structures centered on the brightest source of the field, i.e. Cyg X-1. The amplitude of these structures suggests that they could inhibit the detection of weak sources such as 3EG J2033+4118. Indeed, the detection procedure on the mosaic image reveals several false detections close to Cyg X-1. The intensity of these fake sources can be as high as that of some of the well-established point sources listed above.

When the next release of the OSA software (v.5.0) became available, we reprocessed the data from the most fundamental screening steps up to the image reconstruction and the source detection level. The improvement of the v.5.0 release as compared to v.4.2 is twofold: (1) the background maps are significantly refined, therefore leading to a more efficient source detection procedure and (2) the treatment of bad pixels is improved. Briefly, the following screening and analysis criteria were applied:

- we used only the Science Windows where the position of 3EG J2033+4118 appeared in the FCFOV. As a consequence, we used 487 Science Windows, corresponding to a total GTI of about 1675 ks. This selection offers the advantages of decreasing the processing time and of reducing the impact of noise and artefacts at the position of 3EG J2033+4118.
- we selected the same 3 energy bands as above: 20 – 60 keV, 60 – 100 keV and 100 – 1000 keV.
- we did not use the catalogue provided with OSA v.5.0 (i.e. the 20th catalog of high-energy source). To optimize the source detection procedure and therefore reduce the processing time, we constructed a reduced catalogue including 17 point sources. The seven point sources discussed above and 3EG J2033+4118 are the main sources of this catalogue. We also added the two point sources S1 and S2. We also included the unidentified TeV source discussed by Aharonian et al. (2005), along with the four Wolf-Rayet stars present in the field of view. Finally, we added the O-star HD193322, whose position coincides with the North-West source revealed by the investigation of ISGRI data of γ Cygni described by Bykov et al. (2004). This catalogue is presented in Table 5.2.
- we forced the detection procedure to search only for the sources included in the catalogue described in Table 5.2. This mode is useful when dealing with noisy Science Windows and in case many fake new sources may be detected.
- we selected a way to calculate fluxes in the mosaic image that optimizes the signal-to-noise, and therefore the source detection. This mode put the whole pixel count of a Science Window into one pixel of the mosaic, i.e. there is no spread of the flux during the mosaic construction step. The drawback of this approach is a less accurate position estimate of the sources.

We obtained results very similar to those presented above for the complete data set of 639 Science Windows. We detected the seven point sources enumerated above, but we failed to detect 3EG J2033+4118. Moreover, the structures around Cyg X-1 are also observed as can be seen in Fig. 5.13. As these structures do not disappear when we use the improved background maps provided with OSA v.5.0, their origin should be searched for elsewhere.

We carefully inspected all the individual sky images obtained for each of the 487 Science Windows to search for anomalies likely to produce unwanted large scale features in the mosaic image. It is not straightforward to predict exactly which kind of features are likely to produce large concentric artificial structures in the mosaic, but our individual inspection of Science Window images revealed indeed a lot of artefacts mainly associated to the presence of Cyg X-1. The artefacts were mainly observed as Cyg X-1 was located off-axis. The images presented in Fig. 5.15 show different kinds of anomalies revealed by our inspection. After rejection of the most affected Science Windows (labelled ‘s’ and ‘m’ in Appendix C), we obtained an Observing Group containing 324 Science Windows (the total GTI is of about 1100 ks) and we built other mosaic images in the same energy bands as specified above. Unfortunately, significant artificial structures were still present in the mosaic images. As a last step, we rejected the Science Windows that appear to be only

Table 5.2: Input catalogue used for the high-level analysis of the FCFOV around the expected position of 3EG J2033+4118. The last three columns provide the significance of the detection of the sources respectively in the three energy bands selected for the data analysis. The detection threshold was fixed at 5 σ.

Source	α (J2000)	δ (J2000)	Status	σ_1	σ_2	σ_3
Cyg X-1	19h 58m 21.7s	+35° 12' 06"	Detected	3442	1218	399
Cyg X-2	21h 44m 41.2s	+38° 19' 18"	Detected	51	–	–
Cyg X-3	20h 32m 26.6s	+40° 57' 09"	Detected	1043	91	15
EXO 2030+375	20h 32m 15.2s	+37° 38' 15"	Detected	127	15	–
SAX J2103.5+4545	21h 03m 33.0s	+45° 45' 00"	Detected	31	–	–
KS 1947+300	19h 49m 35.6s	+30° 12' 31"	Detected	42	9	–
QSO B1957+405	19h 59m 28.4s	+40° 44' 02"	Detected	25	8	–
IGR J21247+558	21h 24m 42.0s	+50° 59' 00"	Detected	17	–	–
3EG J2033+4118	20h 33m 36.0s	+41° 19' 00"	Not detected	–	–	–
S1	21h 33m 50.1s	+51° 09' 22"	Not detected	–	–	–
S2	21h 42m 48.0s	+43° 34' 36"	Not detected	–	–	–
TeV J2033+4130	20h 32m 07.0s	+41° 30' 30"	Not detected	–	–	–
WR 140	20h 20m 28.0s	+43° 51' 16"	Not detected	–	–	–
WR 144	20h 32m 03.0s	+41° 15' 20"	Not detected	–	–	–
WR 146	20h 35m 45.1s	+41° 22' 44"	Not detected	–	–	–
WR 147	20h 36m 43.7s	+40° 21' 07"	Not detected	–	–	–
HD193322	20h 18m 17.0s	+40° 43' 55"	Not detected	–	–	–

weakly affected by artefacts (labelled 'w' in Appendix C) as well. The resulting Observing Group contained then 141 Science Windows and the total GTI was of about 480 ks. Once again, the mosaic images presented structures similar as those obtained above. At this stage, the origin of these artefacts is not yet understood.

The main result of our investigation of the *INTEGRAL* data of the Cyg OB2 region is that we failed to detect the unidentified EGRET source 3EG J2033+4118, which may be related to the massive stars harboured by the Cyg OB2 association. The main reason should be that we are dealing with an a priori faint high-energy source located in a field polulated by several bright sources, among which the very bright high-energy emitter Cyg X-1. Cyg X-1 appears to be responsible for the presence of large scale artificial structures likely able to inhibit the efficiency of the source detection procedure. The level of some of these structures on the sky intensity maps is indeed of the same order as that of some of the rather bright sources we detected with our data. In addition, we cannot reject a possible difficulty of the source detection algorithm to detect a faint source (i.e. 3EG J2033+4118) so close to a source as bright as Cyg X-3 (see the right panel of Fig. 5.14). We note also that our analysis failed to reveal the presence of the other point source candidates we tentatively introduced in the input catlogue (see the 8 last entries of Table 5.2). This non-detection suggests that these targets are not hard X-ray nor soft γ-ray emitters, or that their detection was inhibited by the same factors as for 3EG J2033+4118.

Even though our analysis did not lead to the detection of 3EG J2033+4118, our data may be used to derive an upper limit on the flux in the energy bands selected for the analysis.

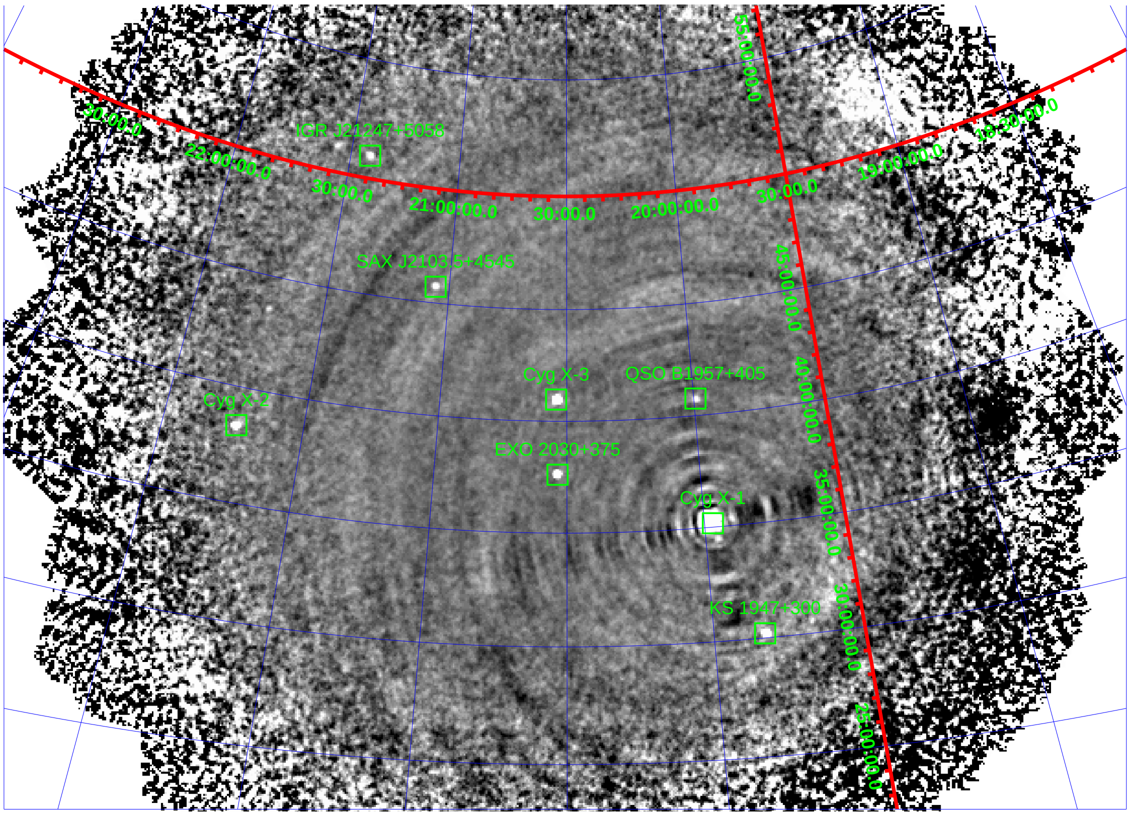

Figure 5.13: IBIS-ISGRI mosaic image constructed on the basis of the 487 Science Windows (FCFOV) between 20 and 60 keV. The point sources detected in the field of view are individually pointed out. The large structures centered on Cyg X-1 are artificial. The coordinate grid specifies the right ascension and the declination.

As we did not improve the quality of the image by removing Science Windows apparently affected by artefacts, we used the mosaic image obtained from the Observing Group containing 487 Science Windows. We first fitted a Gaussian at the expected fixed position of 3EG J2033+4118 (Central fit) in order to measure a count rate in each energy band. We repeated the same procedure by shifting the position of the Gaussian by 12 arcmin, i.e. the expected angular resolution of IBIS. Four shifts were applied respectively in the North, South, East and West directions, in order to check the consistency of the results of the fit across the typical positional error box of IBIS. Variations may be expected if the background is not homogenous in that part of the image. For 3EG J2033+4118, we noticed that the count rate obtained 12 arcmin in the South direction from its expected position deviated significantly from the four other ones. This is probably due to the proximity of the bright source Cyg X-3 in that direction. However, the Central, North, East and West fits gave identical results, and we considered that these fits were not affected by inhomogeneities in the background. As we obtained standard deviations on the count rate of the same value as the count rate itself, we obtained the $3\,\sigma$ upper limit on the count rate simply by multiplying the count rate by a factor 4. These values are quoted in Table 5.3.

As a second step, we converted this upper limit on the count rate into fluxes expressed in more physical units, i.e. in $\mathrm{erg\,cm^{-2}\,s^{-1}}$. It is therefore necessary at this stage to make an assumption on the model of the high-energy emission in the energy bands used in

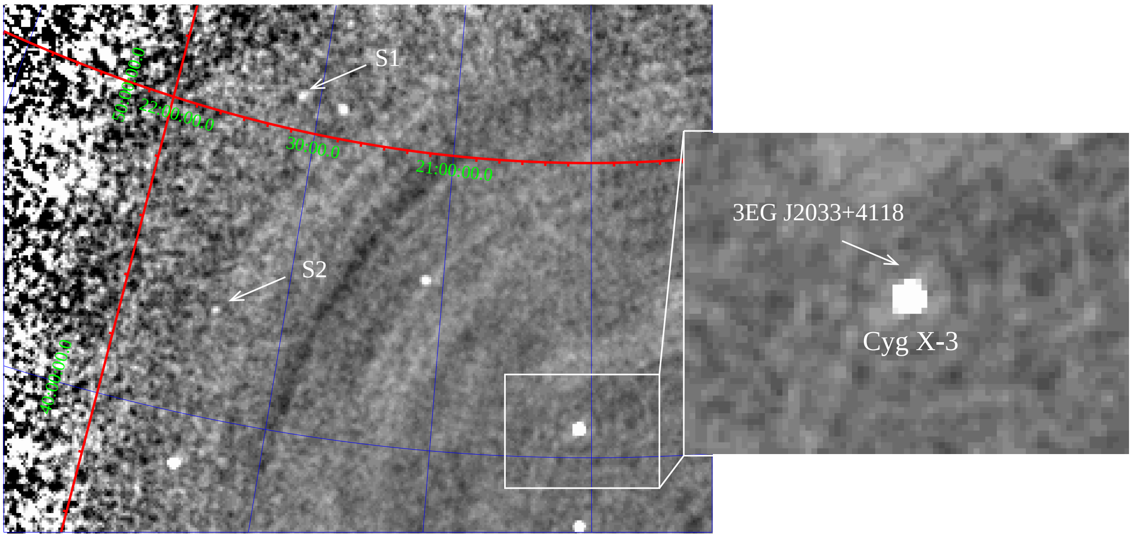

Figure 5.14: Fraction of the IBIS-ISGRI mosaic image constructed on the basis of the 487 Science Windows (FCFOV) between 20 and 60 keV. The positions of the two point sources S1 and S2 are shown by the white arrows. The right panel is centered on Cyg X-3 in order to show more explicitely the expected position of the unidentified EGRET source 3EG J2033+4118.

our ISGRI data analysis. Considering that the high-energy emission is produced by IC scattering, we may expect an emission ruled by a power law with a photon index equal to 1.5 (this value is expected for IC emission produced by a population of relativistic electrons accelerated by the DSA mechanism in the presence of strong shocks, see the discussion in Chapter 6). We folded a synthetic model with the response matrices of ISGRI (response matrix and ancilliary response) using the XSPEC software, and a power law affected by an arbitrary normalization parameter. We then estimated the count rate in each energy band in order to scale the normalization parameter to match the desired count rate provided by our Gaussian fits. The flux was then estimated on the basis of this scaled synthetic model in each energy band. The upper limits on the flux are given in Table 5.3.

Table 5.3: Upper limits at $3\,\sigma$ on the count rate and on the flux in three energy bands for 3EG J2033+4118.

	Upper limits ($3\,\sigma$)	
Energy band (keV)	Count rate ($\mathrm{cts\,s^{-1}}$)	Flux ($\mathrm{erg\,cm^{-2}\,s^{-1}}$)
20 – 60	0.091	3.8×10^{-12}
60 – 100	0.061	1.8×10^{-12}
100 – 1000	0.086	2.4×10^{-11}

We note that we also estimated the upper limits on the flux following the same procedure in the case of the WR stars included in our catalogue. In the case of WR 140, the five estimates performed at different positions across the error box on the image gave different values for the upper limit on the count rate, although a closer inspection of the image at

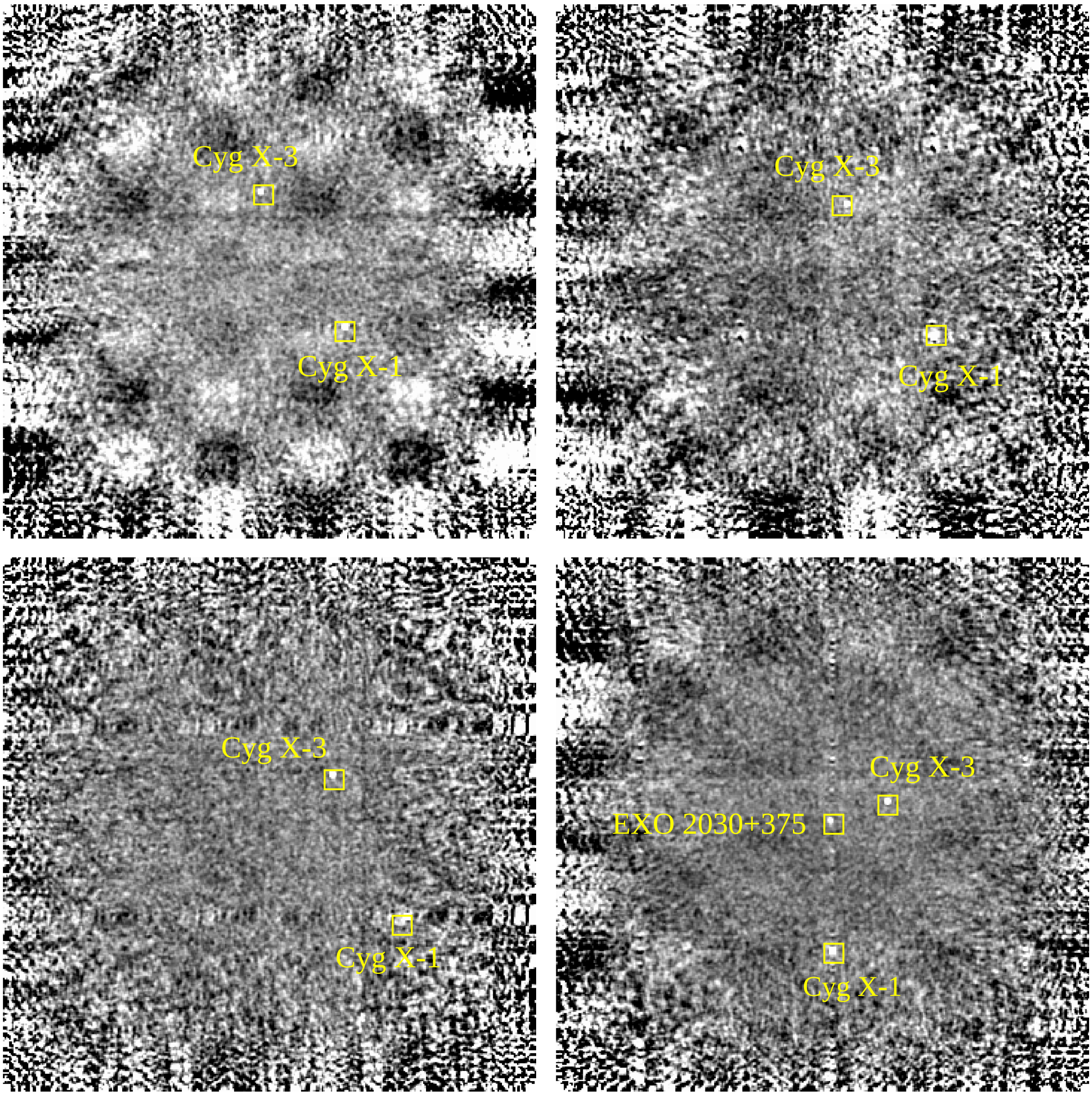

Figure 5.15: Examples of ISGRI images obtained for individual Science Windows: **Upper left:** chessboard-like shadowgram made of alternating bright and dark zones. **Upper right:** confused shadowgram presenting some features similar to the previous case. **Lower left:** shadowgram affected by horizontal structures related to Cyg X-1. The bright spot at the position of Cyg X-1 and three ghost images are respectively located at the corners of a square. Such structures are significantly amplified when Cyg X-1 is located off-axis. **Lower right:** a vertical structure crosses the spots of Cyg X-1 and EXO 2030+375. Such structures appear sometimes when two bright sources are aligned horizontally or vertically on the image.

that position did not reveal any inhomogeneity likely to produce such differences. For the other Wolf-Rayet stars, the upper limits are the same as in the case of 3EG J2033+4118, suggesting that the background reaches a rather uniform level in the region of the image where these targets are located. Finally, due to the proximity of Cyg X-3, we did not obtain any consistent fit for WR 144.

Chapter 6

Discussion and conclusions

In the previous four chapters, we have presented the results of several observational studies mainly devoted to a sample of non-thermal radio emitting O-type stars. In this chapter, we will discuss our main results and use them to draw general conclusions, following the main questions presented in the introduction. Our conclusions will then be confronted to the non-thermal radio emitters presented in the introduction that have not been intensively studied in this thesis, in order to check whether the conclusions drawn on the basis of the selected sample can be extrapolated to the complete catalogue of non-thermal radio emitters. Finally, we will summarize our three main conclusions related to the non-thermal emission from massive stars.

6.1 General discussion

On the basis of the multiwavelength investigation described in this thesis, we can come back to the main questions raised in the introduction to evaluate what we have learned concerning the non-thermal emission from massive stars. The three questions will be addressed in detail separately.

Question 1: is binarity a necessary condition to produce a non-thermal emission in the radio domain?

In Chapter 1 we have shown that, in order to accelerate relativistic electrons through the first order Fermi – or DSA – mechanism, hydrodynamic shocks are needed. In the context of massive stars, these shocks may be produced by intrinsic instabilities in individual stellar winds, or by collisions between stellar winds in a binary system.

A first inspection of the multiplicity of the stars – WR or O-type – listed in Tables 1 and 2 reveals that a significant fraction of the non-thermal radio emitters are binary or higher multiplicity systems, therefore suggesting that binarity may play a crucial role in the non-thermal emission from massive stars. On the other hand, the theoretical results obtained by Van Loo (2005) suggest indeed that isolated stars are unlikely to produce a non-thermal radio emission such as the one we observe.

In the present work, we have gathered direct or indirect information concerning the multiplicity of non-thermal radio emitters. Among the targets studied in the previous chapters, a few were thought to be isolated stars before the start of the observational studies described in this thesis.

As a first example, let us consider Cyg OB2 #8A. Our optical campaign revealed that this star is indeed a binary system, and we derived its first orbital solution, obtaining a period of about 22 d. In the case of HD 168112, our optical spectra did not provide any strong evidence for binarity but our combined X-ray and radio campaign yielded strong indications suggesting the presence of a companion orbiting with a period of several months up to a few years. The case of HD 167971 was clearer as it was already a confirmed eclipsing binary possibly bound to a third more distant star. Our X-ray observations allowed us to obtain some indications that the wind of the third star interacts with that of the close binary system, therefore suggesting that the three stars are indeed gravitationally bound and confirming that it is a triple system. In the case of Cyg OB2 #9, the situation, however, is not as clear since our ongoing optical campaign did not bring any evidence for a binary motion, even though *XMM-Newton* observations suggest that colliding winds are responsible for a fraction of the X-ray emission of this star. The case of HD 15558 was already elucidated before the beginning of this campaign as its binarity has been revealed about twenty years ago.

As a consequence, we see that the binary fraction among non-thermal radio emitting O-type stars has evolved in the last few years and is now approaching that for WR stars. The results presented in this thesis concerning the multiplicity of non-thermal radio emitting O-type stars bring some additional confirmation to the idea that *multiplicity plays a crucial role in the non-thermal radio emission from massive stars.*

Question 2: is there any possibility to detect a high-energy counterpart to the non-thermal radio emission?

As discussed in Chapter 1, in the presence of a population of relativistic electrons, high-energy photons can be produced through IC scattering. The relativistic electrons can indeed transfer some of their energy to the UV and visible photons coming from the photosphere to produce X-rays and soft γ-rays. However, even though such a process exists, the issue of the detection of such a non-thermal high-energy radiation should be discussed with more details.

On the basis of the results of *XMM-Newton* observations of non-thermal radio emitters – 9 Sgr (Rauw et al. 2002), Cyg OB2 #9 (Rauw et al. 2005a) or HD 168112, HD 167971 and Cyg OB2 #8A (this thesis) – we see that no non-thermal emission component has unambigously been revealed for O-type stars between 0.5 and 10.0 keV. In most cases, the hard part of the X-ray spectrum is most probably thermal. However, we cannot conclude that this lack of detection of non-thermal radiation in the X-ray domain can be considered as a strong evidence that it is not produced.

According to the answer tentatively given to the first question above, non-thermal radio emitters are most probably binary systems. HD 168112 is indeed possibly a binary system. HD 167971 is a confirmed binary probably gravitationally bound to a third star, and Cyg OB2 #8A is a confirmed binary system as well. The multiplicity of Cyg OB2 #9 is not yet fully elucidated, but considering (1) its X-ray properties, (2) its long term variability in the radio domain, and (3) the assumption that non-thermal radio emitters are binaries, we will consider in this discussion that Cyg OB2 #9 is a binary candidate. In the four cases, the X-ray emission is characterized by a significant emission in the hard part of the EPIC bandpass, in addition to the thermal soft X-ray emission observed in the case of every O-type stars observed so far. In the context of the colliding-wind binary model, the hard X-ray emission may be produced by the interaction of the winds of the stars constituting the binary – or higher multiplicity – system. The X-ray emission from the collision zone is thus produced by the plasma heated by the interaction between the winds up to a characteristic temperature of a few 10^7 K, i.e. these X-rays are thermal. Indeed, the thermal signature of the hard X-ray emission component is confirmed in the cases of HD 168112, Cyg OB2 #8A and Cyg OB2 #9, although the situation is not as clear in the case of HD 167971. For the massive star 9 Sgr studied by Rauw et al. (2002), the situation is not clear either. In these last two cases, the hard part of the spectrum can be reasonably fitted by a power law (i.e. non-thermal) with a photon index of 3.0 – 4.0. Such high values for the photon index are unexpected considering the fact that strong shocks should produce relativistic electrons characterized by an electron index equal to 2 (see Eq. 1.4). Indeed, the spectral index (α) of the non-thermal emission (synchrotron or IC) is related to the electron index (n) by the following relation:

$$\alpha = \frac{n-1}{2} \tag{6.1}$$

This leads to an expected spectral index of 0.5, corresponding to a photon index (Γ) equal to 1.5 ($\Gamma = \alpha + 1$, see e.g. De Becker 2001). The photon index obtained by fitting a power law to X-ray spectra is therefore significantly larger than expected. In the scenario where these values are physical, it may suggest that the hydrodynamic shocks responsible for the acceleration of the electrons are characterized by compression ratios significantly lower than 4 (see for instance the discussion in Rauw et al. 2002).

However, as we did not find any strong evidence for the detection of a non-thermal emission component in the X-ray domain for the colliding-wind binaries, the most reasonable conclusion is that the nature of their X-ray emission mentioned above is essentially thermal. In this context, whilst the theory suggests that all the conditions needed to produce a non-thermal high-energy emission are fulfilled, we should investigate the probable reason responsible for this non-detection.

In fact, the most plausible reason was already mentioned above in this discussion: *the existence of a thermal X-ray emission from the colliding-wind region.* The characteristic temperature of the emitting plasma in the interaction zone depends mainly on the pre-shock velocity of the plasma flows that collide: the larger the pre-shock velocity, the higher the post-shock temperature, and therefore also the higher the typical energy of the X-rays produced by the hot plasma. As a consequence, we should distinguish between two main regimes in relation to the thermal X-ray emission from the collision zone, respectively referred to as the *hard* and the *soft* regimes. In the *hard* regime, the winds collide as they have reached their terminal velocities, or at least a large fraction of it. The post-shock gas will therefore reach a high characteristic temperature – typically a few 10^7 K or kT ∼ 2–3 keV – and will produce harder X-rays that will significantly contribute to a thermal emission component at energies above 2.0 keV. Such a scenario is likely to occur in the case of rather long period binaries, typically of a few weeks or more, in order to have a separation between the two stars that is large enough to allow the acceleration of the winds. In the *soft* regime, the separation between the two stars is smaller and the collision occurs in the acceleration zone of the stellar winds. The pre-shock velocities are therefore lower, and the post-shock temperature will produce X-ray photons, with kT probably not higher than about 1.0 keV or so. Typically, such systems may be characterized by orbital periods of a few days at most. *In summary, these two regimes will thus be distinguished in the X-ray domain by the hardness of the thermal spectrum.*

If one wishes to detect any putative non-thermal emission component in the X-ray spectrum, a necessary condition is that it is not overwhelmed by the thermal emission. *So, the relative intensities of the thermal and non-thermal emission components in a given energy domain is critical.* Let us consider these two quantities separately:

- **The thermal component.** The thermal emission from the interaction zone will depend mainly on the mass loss rate of the stars of the binary system and on the pre-shock velocities of their stellar winds. Higher mass loss rates and pre-shock velocities will increase the X-ray luminosity of the thermal component. For a given pair of stars with given mass loss rates, the luminosity of the colliding-wind thermal component will depend on the pre-shock velocity, and therefore on the separation as the collision may occur in the acceleration zone of the winds in the case of short period binaries.

- **The non-thermal component.** For a given population of relativistic electrons, the IC scattering will depend on the intensity of UV and visible radiation field from the photospheres of the stars. As a consequence, it will reach a higher level in the case of short period systems characterized by smaller separations[1].

Two extreme situations can therefore be considered as illustrated in Fig. 6.1. In the four cases, synthetic spectra have been represented. These spectra were built on the basis of three-component emission models convolved with the response matrices of the EPIC-pn instrument in order to simulate *XMM-Newton* observations. The individual components of the model are a soft thermal emission component, a hotter thermal emission component, and a power law. The soft thermal component is the same in the four cases. The power law in panels (a) and (b) is characterized by a photon index equal to 2.5, which is the value obtained in the case of HD 159176 (see Chapter 3), whereas we have chosen to use the theoretically expected value of 1.5 in panels (c) and (d). The only difference between left and right panels is the characteristic temperature of the hot thermal emission component: one is rather soft (0.8 keV) and the other one is harder (2.0 keV). In the soft case (on the left), the power law is not completely hidden by the thermal emission. In the hard case (on the right), the hot thermal component dominates the spectrum in the hard energy band and the non-thermal component has no chance to be detected. Even in the case of the flatter photon index (case (d)), the thermal emission in the hard part of the spectrum is revealed by the Fe K line although the power law has a rather high intensity in this energy band. It is also interesting to note that the non-thermal emission in the X-ray domain has less chance to be detected if the photon index is equal to 2.5 (case (b)) as compared to the situation where the power law is flatter (case (d)). In summary, it appears that the combined effect of a steep photon index and of a hard thermal emission is likely to prevent the putative non-thermal X-ray emission from being detected below 10.0 keV. *We must keep in mind the fact that we describe here general trends that should be modulated according to the model parameters characterizing the emission components considered in this discussion.*

As a consequence, we see that in the hard regime, the observation of the putative non-thermal emission component in the typical X-ray domain ranging between 0.5 and 10.0 keV is unlikely. On the contrary, binary systems in the soft regime may reveal such a non-thermal X-ray emission contribution. It is crucial to note that the sample of non-thermal

---

[1] We note that this simplified discussion neglects the dependence of the efficiency of the acceleration mechanism as a function of the properties of the shocks that should vary with the separation between the stars.

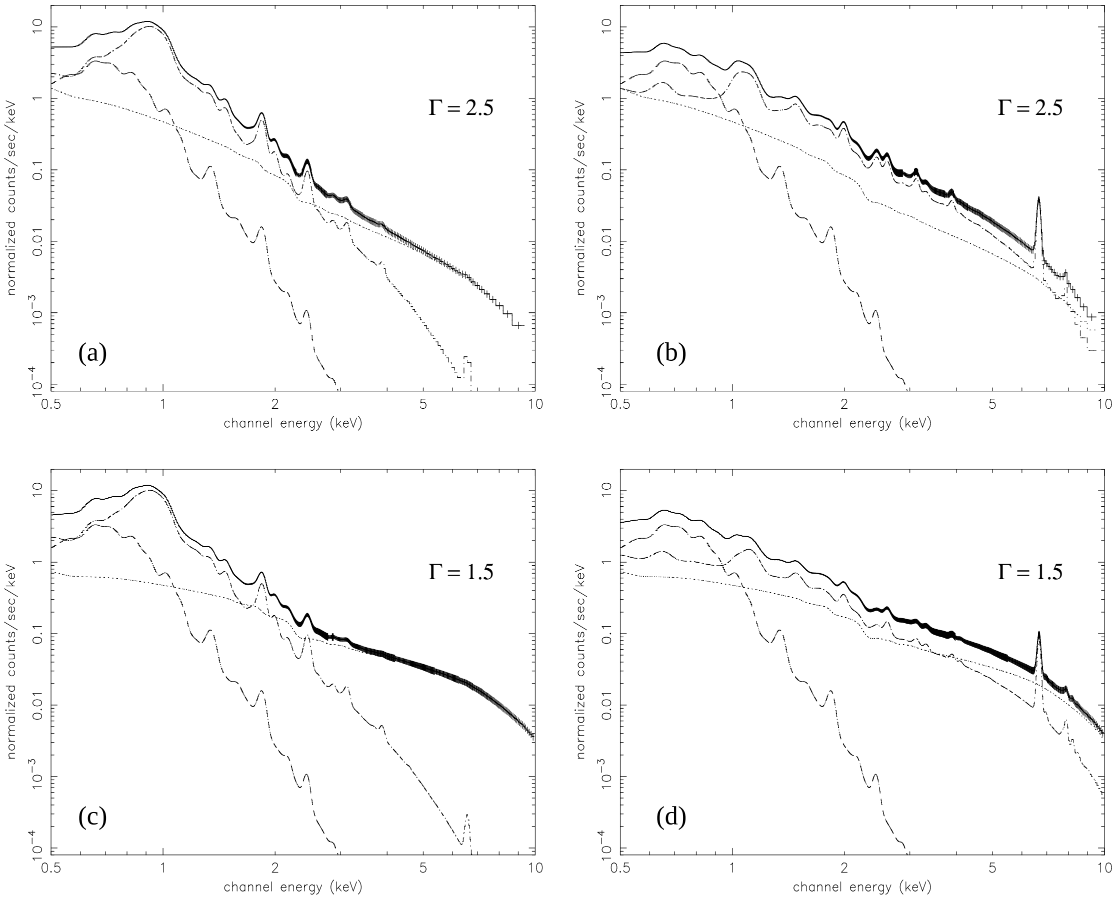

Figure 6.1: Illustration of the impact of the hardness of the thermal X-ray emission from a colliding-wind binary. Four synthetic spectra made of three emission components are represented between 0.5 and 10.0 keV. In each case, a thermal component characterized by a kT of 0.3 keV is used to model the softer contribution of the thermal emission. A power law is used to model the putative non-thermal emission component with a photon index equal to 2.5 (i.e. the same as obtained for HD 159176, see Chapter 3) in cases (a) and (b), and to 1.5 (i.e. the expected value for strong shocks, see above) in cases (c) and (d). The third component is a hotter thermal emission characterized by a different temperature in the two cases. All components are individually displayed: the two dotted-dashed lines stand for the thermal components and the dotted line represents the power law. The solid line represents the resulting model overplotted on the points of the fake spectrum. *Left panels:* the thermal emission from the wind collision zone is soft (*soft* regime), and the kT of the hot component is equal to 0.8 keV. Such a value is typical of that expected in the situation of close binaries where stellar winds have not reached their terminal velocities before they collide. In the hard part of the spectrum, the power law is not completely overwhelmed by the thermal emission and it may be detected, whatever the photon index considered. *Right panels:* the thermal emission from the wind collision zone is hard (*hard* regime), and the kT of the hot component is equal to 2.0 keV, more typical of winds colliding with large pre-shock velocities such as in longer period systems. In these cases, the hard thermal emission is too strong to allow the non-thermal emission to be undoubtedly revealed by X-ray observations in this energy domain. We note the presence of the rather strong Fe K line at about 6.7 keV, in agreement with what is observed in the cases of HD 168112, Cyg OB2 #8A and Cyg OB2 #9.

radio emitters investigated with *XMM-Newton* in this thesis is representative of the hard regime, and our targets do not reveal any non-thermal emission in the EPIC bandpass. On the other hand, the binary HD 159176 has a very short period – it is therefore typical of the soft regime – and it is the only example of probable non-thermal high-energy emitter in the EPIC energy domain.

The discussion above concerns the high-energy emission from massive binary systems, but what about the non-thermal radio emission? The ionized material constituting the stellar winds is known to absorb efficiently radio photons (see Wright & Barlow 1975 and Panagia & Felli 1975). As the emission region of the non-thermal radio photons coincides with the interaction zone of the stellar winds, we should expect a significant fraction of these non-thermal photons to be absorbed by the wind material. As a first approximation, two extreme regimes can also be envisaged: a strongly absorbed regime and a less absorbed one. In the first case, the synchrotron emission produced in the wind collision zone is nearly completely absorbed. Such systems are therefore unable to reveal their non-thermal radio emission. This situation is likely to occur when the emission zone is deeply surrounded by absorbing material, mainly if the separation between the two stars is small. On the contrary, if the separation is larger, a significant fraction of the non-thermal radio photons is likely to escape from their emission region, and the system may be classified as a non-thermal radio emitter. Besides these two extreme situations, an intermediate regime may be observed where the non-thermal emission component is not completely absorbed, although too weak to be undoubtedly revealed. Such a composite radio emission is indeed observed for several systems presented in Tables 1 and 2. The level at which these systems deviate from the archetypal non-thermal emission (negative spectral index, strong variability, high radio luminosity) will depend on the effect of the absorption of this non-thermal radio component, which depends itself on the column of wind material along the line of sight towards the emission region. For this reason, this discussion should only be considered as a qualitative approach to the non-thermal radio emission. A more quantitative approach requires an accurate knowledge of the wind properties of the stars (mass loss rate, temperature, composition...), and of the geometry of the system (separation, inclination...). In summary, non-thermal radio emitters are systems from which the synchrotron radiation is able to escape, i.e. their orbital period needs to be long enough.

Putting together the criteria that should be fulfilled to observe a non-thermal emission in the high-energy and radio domains, we obtain the following results: *long period systems are likely to reveal their non-thermal emission in the radio domain, but are unlikely to appear as non-thermal emitters in the X-ray domain between 0.5 and 10.0 keV. On the contrary, a non-thermal X-ray emission might be detected in the same energy domain in the case of short period binaries, but such systems will probably not reveal any non-thermal emission in the radio domain. Therefore, it appears that the simultaneous detection of non-thermal emission in the high-energy (below about 10.0 keV) and radio domains is unlikely.* It is important to note that we cannot a priori reject intermediate situations where both non-thermal radio and X-ray emissions might be detected, although we estimate that such situations are less probable. In addition, situations where neither of these non-thermal radiations is detected seem a priori quite plausible. The point here is to note that our investigation of non-thermal radio emitters allows us to draw only a general qualitative scenario. A more quantitative description of the phenomenon is beyond the scope of the present observational work (see however Chapter 7 for a discussion)

Considering this result, it appears that the non-thermal radio emitters will probably not reveal any high-energy non-thermal counterpart in the X-ray domain investigated intensively in this work, i.e. between 0.5 and 10.0 keV. However, at higher energies – above 10.0 keV – the plasma heated by the colliding winds is unlikely to emit a significant amount of thermal X-rays. *As a consequence, we cannot reject the possibility to detect a non-thermal high-energy emission in the hard X-ray (above 10.0 keV) or in the soft γ-ray domains. In these latter high-energy ranges, the nature of the emission would be undoubtedly non-thermal.* We emphasize however that our *INTEGRAL* data (the deepest on any cluster of massive stars) failed to reveal such an emission.

Question 3: could the observation of non-thermal processes provide an indirect way to estimate the magnetic field strength of massive stars?

As discussed in Chapter 1, the magnetic field plays a crucial role in the physical processes related to the non-thermal emission from massive stars. This role was particularly emphasized in Chapter 5 while discussing the putative IC emission from Cyg OB2 #8A. It appears from this latter simplified approach that the IC and synchrotron luminosities may be related through an equation including the magnetic field strength in the colliding-wind region (see Eq. 5.17). As a result, the simultaneous knowledge of the non-thermal luminosities in the radio and high-energy domains is likely to lead to a possible method to estimate the strength of the local magnetic field.

However, we have demonstrated that a simultaneous detection in the radio and soft X-ray domains is unlikely. Estimating the local magnetic field therefore seems compromised if we limit ourselves to the investigation of the non-thermal high-energy emission below 10.0 keV. *So, an indirect estimation of the local magnetic field in the colliding-wind region can be envisaged, provided that simultaneous measurements of the synchrotron (radio) and IC (high-energy, above 10.0 keV) luminosities are available.*

We note that such an estimation would require an accurate knowledge of several parameters that are still unknown for most of the objects listed in Tables 1 and 2. As shown in Sect. 5.1.3, most of the relevant quantities vary as a function of the orbital phase, and the orbital parameters of the system therefore need to be firmly established. Moreover, some stellar parameters such as the mass loss rate, the terminal velocities, the stellar masses and radii need also to be determined. For this reason, among O-type stars, Cyg OB2 #8A is currently the best system to carry out such an investigation. In addition, this approach is likely to lead to an estimate of the local magnetic field strength in the colliding-wind region only. The simplified way we dealt with the magnetic field in Sect. 5.1.3 is most probably not sufficient if one wants to derive estimates of the surface stellar magnetic fields. A detailed investigation of the magneto-hydrodynamic conditions at the collision zone is required in order to obtain reasonable estimates of the surface magnetic fields through this method.

6.2 From the sample to the catalogue

In the introduction, we have presented what we may call two catalogues of non-thermal radio emitting massive stars: a first one for Wolf-Rayet stars (Table 1) and a second one for O-type stars (Table 2). In Chapters 2 to 5, we have investigated in detail the case of a sample of O-type non-thermal radio emitters, and our main conclusions were drawn on the basis of this sample. At this stage, it may be helpful to evaluate how our conclusions can be extrapolated to the full catalogue of non-thermal radio emitters. For this purpose, all members of the O-type catalogue will be briefly considered separately.

Cyg OB2 #5

The non-thermal ($\alpha = -0.18 \pm 0.19$) radio emission from Cyg OB2 #5 is most probably produced in the collision zone between the combined wind of the 6.6 d binary and that of a more distant B-type star (Contreras et al. 1997). The combined stellar winds of the close binary appear to be a source of thermal radio radiation ($\alpha = 0.30 \pm 0.01$). The slight deviation between the spectral index of this latter component and the expected value for thermal radio emission may be explained by the presence of a thermal contribution originating from the colliding winds of the close binary. Indeed, as pointed out by Pittard et al. (2006), the combination of a partly absorbed thermal emission from colliding winds and of the thermal unshocked emission from the individual stellar winds of a system whose separation is not too large can mimic a composite spectrum by lowering the observed spectral index, even though the radio emission is completely thermal. This deviation is not expected to be explained by a composite (thermal + non-thermal) radio spectrum as the putative synchrotron emission produced in the close binary should be totally absorbed by the stellar wind material.

As a non-thermal radio emission is observed from Cyg OB2 #5, we donot expect to observe any non-thermal emission from it in the X-ray domain between 0.5 and 10.0 keV. The wind-wind interaction between the close binary and the B-type star is indeed likely to produce a hard thermal emission, strong enough to overwhelm the putative non-thermal X-ray emission produced either by the colliding-wind region involving the B-type star, or that located within the close binary. The investigation of the *XMM-Newton*-EPIC data of Cyg OB2 #5 by Rauw et al. (2005a) reveals indeed that its X-ray spectrum is thermal.

Cyg OB2 #8A

As discussed in detail in Chapter 5, this 22 d period binary system is a non-thermal radio emitter, and a thermal X-ray emitter between 0.5 and 10.0 keV, in agreement with the idea already discussed in Chapter 4 and developed in this chapter that the simultaneous detection of non-thermal radiation in these two domains is unlikely. Cyg OB2 #8A is the shortest period non-thermal radio emitter known so far, but the separation is large enough to allow the winds to reach a large fraction of their terminal velocities, therefore producing a hard thermal X-ray component.

The monitoring of this system in the radio domain (Blomme 2005) reveals a strong phase-locked variability with extrema of the radio emission inverted with respect to those revealed by our X-ray investigation. The detailed discussion of the radio monitoring of Cyg OB2 #8A will be described in Blomme et al. (2006a, in preparation). The fact that we observe the synchrotron emission from Cyg OB2 #8A, although the wind material should absorb it significantly, may be explained partly by the particularly favorable orientation of the system, allowing the synchrotron emitting region to be seen from a direction where the column density is lower.

Cyg OB2 #9

No evidence for binarity has been found so far for Cyg OB2 #9, but the results from *XMM-Newton* observations (Rauw et al. 2005a) indicate a hard thermal X-ray emission, suggesting it might be a binary system in the hard regime discussed in the previous section.

Indeed, according to the formalism described above, only such systems may reveal their non-thermal radio emission. In addition, the radio investigation described by Van Loo (2005) suggests a strong variation of the X-ray flux on a time-scale of about 2.4 yr, in agreement with the long period binary scenario. Although the ongoing optical campaign failed so far to provide strong evidence for binarity, more data are needed to address the issue of the multiplicity of this non-thermal radio emitter.

Cyg OB2 - 335

The multiplicity of this star has not yet been investigated. If the main ideas derived from our discussion are correct, X-ray observations are expected to reveal a multi-temperature thermal spectrum with the hottest component characterized by a plasma temperature higher than 1.0 keV.

9 Sgr

The investigation of Rauw et al. (2005b) revealed that this non-thermal radio emitter is a binary with a period of several years. The ambiguity on the nature of the hard X-ray emission discussed by Rauw et al. (2002) may therefore be lifted, since the results of our work suggest that it should be thermal. A long term radio monitoring of this system could be useful in order to confirm the relation between the non-thermal radio emission from this binary system and its binarity.

15 Mon

As a confirmed long period binary, 15 Mon agrees with our general scenario. Once again, X-ray observations should reveal a thermal emission, or at least no non-thermal emission component in the high-energy domain below 10.0 keV.

δ Ori A

δ Ori A is a multiple system including a spectroscopic and eclipsing binary with a period of about 5.7 d, along with at least one visual B-type companion (Harvin et al. 2002). It was classified as a possible non-thermal radio emitter by Bieging et al. (1989) because of a significant variability of its radio flux. The non-detection of this system in the radio domain reported by Drake (1990) may be attributed to its variability. However, additional radio observations are required to confirm the non-thermal nature of at least a fraction of the radio emission from δ Ori A.

σ Ori AB

According to the speckle interferometry study performed by Hartkopf et al. (1996), a visual companion is found with an orbital period of about 155 yr. However, the binary signature found by Bolton (1974) points to the presence of another companion orbiting with a shorter period. According to Drake (1990), σ Ori AB could consist of at least four stars. Even though the multiplicity of σ Ori AB has not yet been completely investigated, there is no doubt that it is a multiple system.

The *XMM-Newton* observation reported by Sanz-Forcada et al. (2004) points however to a rather soft-X-ray emission, in contradiction with the scenario where non-thermal radio emitters should be rather hard thermal X-ray emitters in the energy range between 0.5 and 10.0 keV. This multiple system deserves therefore a detailed additional investigation of its X-ray emission. A possible explanation could be that the orbital separation is so large that the X-ray luminosity of the colliding-wind region is much smaller than the intrinsic emission of σ Ori AB.

HD 15558

This long period binary has never been observed with recent X-ray observatories such as *XMM-Newton* or *Chandra*, and therefore its X-ray emission between 0.5 and 10.0 keV has not yet been investigated. However, considering the general scenario proposed in this thesis, we may expect this system to produce a hard thermal emission component likely to prevent any putative IC emission component from being detected. X-ray observations are needed to check the validity of this latter suggestion.

HD 93129A

This star is known as a visual binary, since the discovery of an early-type companion by Nelan et al. (2004) about 55 mas away, which corresponds to a separation of about 154 AU assuming a distance of 2.8 kpc. Such a separation is large enough to allow a significant fraction of the synchrotron emission produced in the collision zone to escape from the wind material. In this scenario, the thermal X-ray emission from the colliding winds between 0.5 and 10.0 keV is expected to be hard enough to conceal the putative non-thermal X-ray emission.

HD 93250

The X-ray investigation reported by Rauw et al. (2003c) revealed a hard thermal emission, along with a significant variability of the X-ray flux strongly suggesting the presence of a companion. Once again, HD 93250 should produce its non-thermal radio emission in the wind-wind interaction zone located somewhere between two stars. A spectroscopic monitoring in the visible domain is needed to confirm the binarity of HD 93250, determine its period, and therefore confirm the agreement with our general scenario for the non-thermal emission from massive stars.

HD 124314

This star has been classified as an SB1 system by Gies (1987), but a spectroscopic monitoring is needed to determine the period and the nature of the companion. As HD 124314 is a non-thermal radio emitter, the period should be longer than a few days, otherwise the synchrotron emission would not be detected.

HD 150136

HD 150136 is known as a binary system with a period of about 2.7 d, which is too short to allow a significant fraction of the synchrotron emission produced in the wind-collision zone to escape. However, it seems that the optical spectrum of this system presents some indication of the presence of a third star (Niemela & Gamen 2005). The existence of a third companion orbiting with a period of at least a few weeks has recently been confirmed (Gosset 2005). As a consequence, it is more likely that the synchrotron emission arises from the collision zone located somewhere between the close binary and the third star in a way that is similar to the cases of Cyg OB2 #5 and HD 167971.

The results of the *Chandra* observations of this system (Skinner et al. 2005) reveals indeed a thermal emission, with a hot emission component characterized by a kT of about 1.6 keV. Such a temperature is probably too high to be explained by the interaction between the winds of the stars of the close binary system, and should be indicative of an interaction involving the third star whose classification is not yet established. Even though this is not mentioned in the paper of Skinner et al. (2005), we estimate that a non-thermal emission should not be revealed by their *Chandra* X-ray data.

HD 167971

This triple system is the strongest non-thermal radio emitter in our sample of O-type stars. The hard X-ray emission, probably thermal, is expected to be produced in the collision zone between the O5-8V + O5-8V close binary and the more distant O8I star. The same wind interaction region is most probably responsible for the production of the non-thermal radio emission. The wind collision region between the two O5-8V stars orbiting with a period of about 3.3 d is unlikely to produce the hard thermal emission that is observed in our *XMM-Newton* data. The recent investigation of Blomme et al. (2006b, in preparation) reveals a strong variability of the non-thermal radio flux on a time-scale of several years, in agreement with the scenario where the O8 supergiant is gravitationally bound to the close binary and orbiting with a long period.

HD 168112

Although our spectroscopic monitoring of this system failed to reveal the presence of any companion, our quasi-simultaneous X-ray and radio observations of HD 168112 strongly suggest that it is a long period binary. The significant long-term variability of the radio emission revealed by Blomme et al. (2005) points to the binary scenario as well.

BD -47° 4551

The multiplicity of this non-thermal radio emitter has so far never been investigated. If the general scenario discussed in this work in valid, it should be a binary system with a period longer than a few days unlikely to reveal any non-thermal X-ray emission below 10.0 keV.

6.3 Main conclusions

From the discussion above, we find that the three main conclusions of this work, as far as non-thermal phenomena in massive stars are concerned, can be summarized as follows:

Conclusion 1:
The binary – or higher multiplicity – scenario seems to be the most appropriate in order to explain the non-thermal radio emission of massive stars.

Conclusion 2:
The simultaneous observation of non-thermal emission in the radio domain and in the high-energy domain below 10.0 keV is unlikely. Such a simultaenous detection is however more likely if we investigate the higher energy domain (very hard X-rays and soft γ-rays) with a sufficient sensitivity. In addition, it appears that the detection of non-thermal emission below 10.0 keV should not be excluded in the case of close binaries. As a result, the existence of non-thermal X-ray emitters without a radio synchrotron counterpart can be envisaged.

Conclusion 3:
An indirect estimation of the local magnetic field strength, i.e. in the colliding-wind region, can be envisaged only if a simultaneous detection of the non-thermal emission is possible in the radio and high-energy domains. This requires to investigate non-thermal radio emitters in the very hard X-rays and in the soft γ-rays (at energies between about 10.0 keV and 1.0 MeV).

Chapter 7

Prospects for future works

The studies reported in this thesis – along with other studies mentioned throughout the different parts of this work – raised a number of new questions. The main ideas proposed here need to be confronted to additional observational and theoretical results in order to be validated or refined. A non-exhaustive list of ways of investigation relevant to the theme of this thesis are suggested in this chapter.

7.1 The multiplicity of non-thermal radio emitters

As discussed in detail in the previous chapter, the multiplicity of some of the non-thermal radio emitters is still poorly established. Considering the results presented in this thesis, the fact that these stars are non-thermal radio emitters should be considered as a strong motivation to investigate more carefully their multiplicity. In fact, the fundamental stellar and wind parameters are crucial ingredients if one wishes to build quantitative models of the phenomenon. One of the main problems relevant to the issue of the multiplicity of stars in general is the strong bias that affects the census of known binaries. This probelm is twofold:

- a first origin of this observational bias is the problem of the orbital period. Typical observing runs last a few days, and are often separated by several months or years. A consequence is that most of the known binaries have periods of a few days, and sometimes are just referred to as long period binary candidates because long term radial velocity shifts were detected on time-scales of one or several years. That is the reason why we have only little information on the multiplicity of several targets discussed in this work. It appears that intensive spectroscopic monitorings should be performed to investigate poorly explored regions of the orbital parameter space, in order to probe some of the fundamental properties of massive stars. This could be achieved by conducting service mode observing programmes with telescopes equiped with medium to high-resolution spectrometers. A good example of such specific spectroscopic monitoring is that of HD 15558 discussed in Chapter 2. Even though this campaign was motivated by the fact that HD 15558 is a non-thermal radio emitter, we have shown that it led to the interesting – and somewhat puzzling – large minimum mass mostly for the primary. Further investigations, possibly using more sophisticated disentangling methods are envisaged to provide some additional validation of the preliminary results presented in this thesis. Moreover, some of the systems quoted in Table 2 appear to be multiple systems whose spectroscopic investigation is not straightforward, pointing out the necessity to develop or improve disentangling tools such as those used in the case of the study of HD 15558.

- a second origin of this observational bias is the inclination of the systems we are talking about. As most of the binaries are revealed by spectroscopic monitorings aiming at the measurement of radial velocity excursions, systems characterized by low inclinations are most of the time not revealed. In this context, a promising technique likely to provide a wealth of crucial information is interferometry. Using the high-angular resolution capability of long baseline interferometers such as the Very Large Telescope Interferometer (VLTI, in Cerro Paranal, Chile) with the AMBER instrument, we may for instance confirm the binary status of some stars (e.g. HD 168112), and study the orbital motion of long period systems whose orbital parameters have not yet been investigated (e.g. HD 167971). In this context, an interferometric campaign has been initiated to investigate the multiplicity of non-thermal radio emitters using the VLTI. A first proposal (PI: M. De Becker) has been recently submitted to observe the triple system HD 167971. The aims of these first observations are to (1) try to detect the third star, (2) detect the orbital motion on the basis of two observations separated by about three months, and (3) put first constraints on the separation between the O8 supergiant and the close eclipsing binary. Depending on the results of these first observations – provided the time will be granted – we will define a strategy to obtain complementary observations aiming at the study of the orbital motion of this long period system. HD 167971 was selected as a first target for this interferometic campaign mainly because of its brightness that facilitates the observations with instruments such as AMBER, but the observation of other targets is obviously envisaged in the future. We note that, considering the current angular resolution of long baseline interferometers (of the order of a few mas), interferometry would be devoted to multiple systems characterized by rather large separations (at a distance of 1 kpc, 1 AU of linear separation corresponds to only about 1 mas).

7.2 Future high-energy observations of non-thermal radio emitters

A significant part of this thesis was devoted to the analysis and to the discussion of results obtained on the basis of X-ray data between 0.5 and 10.0 keV. As expressed by one of our main conclusions, the discovery of a high-energy counterpart of the non-thermal radio emission in this latter energy domain is unlikely, but it might be possible at higher energies. Unfortunately, our *INTEGRAL* observations of the Cyg OB2 region did not provide any conclusive results. As discussed in Sect. 5.3, *INTEGRAL* is possibly not the best observatory to investigate the high-energy emission from faint sources such as non-thermal emitting massive stars. However, the investigation of the non-thermal emission from massive stars in the high-energy domain is not finished, and probably it is only at its starting point. Indeed, several forthcoming observatories may bring new insight:

- **GLAST.** The Gamma-ray Large Aperture Space Telescope is a project mainly funded by the United States, with participations from France, Italy, Japan, and Sweden. The primary instrument of *GLAST* is the Large Area Telescope (LAT) which is sensitive at energies from 20 MeV to 300 GeV. The γ-ray photons will be detected through their conversion to electron-positron pairs and their energy will be measured using a calorimeter. Briefly, the photons interact with the 16 layers of lead of a tracker that allow to determine their incident direction. The basic principle of *GLAST* is therefore similar to that of EGRET on board the Compton Gamma-Ray Observatory (CGRO). The angular resolution of LAT will range between 3.4° and 0.09° depending on the energy domain. Its effective area will be more than 6 times larger than that of EGRET, and it is expected to have a two orders of magnitude improved sensitivity. More information can be found in McEnery et al. (2004). LAT should be considered as the successor of EGRET, with an improved sensitivity and better imaging capabilities (field of view, angular resolution). Such an instrument will be crucial to investigate the nature of still unidentified EGRET sources such as 3EG J2033+4118, along with other high-energy sources possibly related to the non-thermal emission from massive stars. Its unprecedented sensitivity in that energy domain will certainly lead to the detection of many new high-energy sources.

- **NeXT.** The Non-thermal Energy eXploration Telescope mission has been proposed as a successor to the *Suzaku* (Astro-E2) mission by the Space Agency of Japan. It is expected to carry three hard X-ray telescopes (HXTs) for the wide band imager (WXI), one soft X-ray telescope (SXT) for the soft-X-ray spectrometer (SXS), and a soft γ-ray detector (SGD). The main characteristic of this mission is that it is expected to achieve two orders of magnitude improvement in the sensitivity in the hard X-ray region as compared to *Suzaku*. *NeXT* is expected to provide spectra and images with a typical angular resolution of about 30 arcsec between 0.5 and 80.0 keV, along with spectra in the soft γ-ray domain up to about 1.0 MeV with much higher sensitivity than present instruments. Details can be found in Takahashi et al. (2004).

- **SIMBOL-X.** *SIMBOL-X* is a project proposed by a consortium of European laboratories in response to the 2004 call for ideas of CNES. This project is based on the principle of a pair of spacecraft in a formation flying configuration. It uses for the first time a $\sim$30 m focal length X-ray mirror to focus X-rays above 10.0 keV, resulting in two orders of magnitude improvement in angular resolution and sensitivity in the hard X-ray domain with respect to non-focusing techniques. It is expected to operate between about 0.5 and 70 keV. *SIMBOL-X* will not be launched before 2012. For details on the instrumentation, see Ferrando et al. (2004).

7.3 Searching for non-thermal X-ray emitters without non-thermal radio counterpart

As suggested by our investigation of the X-ray emission of HD 159176 (see Chapter 3) and by our discussion in Chapter 6, a non-thermal X-ray emission below 10.0 keV may be observed in the case of close massive binaries. In the case of such systems, the detection of a non-thermal radio emission is unlikely as the synchrotron radiation would most probably be absorbed by the wind material. This situation leads to the somewhat unexpected prospect to discover a particular kind of sources, namely non-thermal X-ray emitters without a non-thermal radio counterpart.

HD 159176 may be the first example of this kind, but other examples may be discovered by investigating in detail the X-ray properties of close binary systems. In this context, binaries with periods of at most a few days are good candidates for two reasons: (1) the thermal emission is not expected to be too hard, and (2) the IC luminosity should be rather high as the collision zone would be very close to the photospheres of the two stars. Future X-ray investigations of short period binaries with observatories such as *XMM-Newton* or

Chandra should consider this possibility.

7.4 Theoretical developments

In Sect. 5.1.3, we have used a simplified approach to calculate the IC luminosity from Cyg OB2 #8A on the basis of an estimate of the synchrotron luminosity obtained through radio observations. However, as already mentioned, this approach is mostly useful for a qualitative discussion of the non-thermal processes at work in massive binaries, and to obtain a rough idea on the link between several physical parameters such as the magnetic field strength, the synchrotron luminosity and the IC luminosity, along with their dependence on the orbital phase as we are dealing with binary systems. However, this latter approach is severely limited, and some problems were already mentioned in Sect. 5.1.3.

In order to derive more quantitative results, more sophisticated theoretical models are strongly needed. Pittard et al. (2005, 2006) have developed radio emission models including several physical effects likely to influence the synchrotron emission from colliding-wind binaries (absorption, Razin effect, IC cooling...). Such models should be confronted to the case of O-type binaries such as Cyg OB2 #8A.

On the other hand, the acceleration of particles itself is not included self-consistently in the latter models. Very recently, Reimer et al. (2006) have submitted a paper describing a study aiming at the investigation of the non-thermal high-energy emission from colliding winds in massive binaries. Their model computes the energy distribution of relativistic electrons by including the DSA mechanism in the particular physical and geometrical conditions of colliding-wind binaries. The high-energy emission is then calculated following a rigorous treatment of non-thermal emission processes.

A more complete model including all these aspects of the physics of non-thermal emission from colliding winds (particle acceleration, synchrotron emission, IC emission) should be considered as the next step. The application of such a model to the case of non-thermal emitting massive stars may lead to significant advances in our understanding of the physical processes affecting the hydrodynamics of stellar winds along with the emission of radiation in several energy domains.

7.5 Parts of the work still in progress

Several parts of this work have not yet provided final results but are expected to be completed in the near future:

- *The X-ray investigation of Cyg OB2 #8A.* The analysis of *XMM-Newton* data presented in Sect. 5.1.4 still needs to be complemented by a more detailed study of the RGS data. The variability suggested by the spectra presented in De Becker et al. (2005b) for some lines needs to be investigated in order to check whether it may be related to a possible change of the ionization conditions as a function of the separation between the stars in the binary system.
- *The radio investigation of Cyg OB2 #8A.* The radio light curve presented by Blomme (2005) is likely to provide crucial information on the synchrotron emission from Cyg OB2 #8A. A VLA proposal has been recently submitted (PI: R. Blomme) aiming at obtaining additional data at more than one frequency, in order to study the variation of the slope of the radio spectrum as a function of the orbital phase.

- *The optical data on HD 15558.* As discussed in Chapter 2, our spectroscopic monitoring of HD 15558 led to the detection of the secondary, and to estimates of the minimum masses suggesting the primary might be the most massive O-type star known so far. However, this result still needs to be validated using additional techniques likely to provide a better separation of the spectra of the two components of the system. An alternative scenario where HD 15558 is a triple system should also be considered in future investigations as it may reconcile the very extreme mass of the primary object with its spectral type.

- *The line profile variability of O-type stars.* Even though this topic is not directly related to the study of the non-thermal emission from massive stars, the study presented in Appendix B shows that important advances should be made in order to interpret the line profile variability of optical lines. The line profile variability study of the massive stars in IC 1805 described in Chapter 2 provides additional examples of spectral variations somewhat difficult to characterize, and even more difficult to interpret. Possibly, some part of this variability is related to the rotation of the stars in the presence of a strong magnetic field. The combined effect of fast rotation and a magnetic field may produce large-scale structures in the stellar winds responsible for the variability in the profiles of some optical lines. In order to investigate the variability of line profiles in the optical spectra of massive stars a little further, a campaign has recently been initiated at the Observatoire de Haute-Provence in France. The selected targets are O-type supergiants (mainly Of$^+$ stars) and ON stars. Up to now, three observing runs have been devoted to this campaign (PI: M. De Becker) but more data are expected to be obtained in the future to complete our spectral time series. These data will be mainly used in order to (1) investigate the line profile variability of these stars and (2) to investigate their multiplicity on various time-scales.

Appendix A

Observational material

A.1 Optical spectroscopy

Throughout this dissertation, we presented results obtained on the basis of optical spectroscopic data. Here, we describe with more details the instrumentation used and the way we dealt with these data in the frame of this work.

Observatoire de Haute-Provence

Most of the spectroscopic data used in the context of this work have been obtained at the Observatoire de Haute-Provence (OHP) in France. The studies that made use of these data are described in Chapter 2, in Chapter 5, and in Appendix B.

On the one hand, many spectra were obtained with the Aurélie spectrograph mounted on the 1.52 m telescope (Gillet et al. 1994). The detector is a 2048 × 1024 CCD EEV 42-20#3, with a pixel size of 13.5 μm squared. For each observation, the data consist of five images of the object's spectrum obtained by means of a Bowen image slicer. Most of our data were obtained with grating #3 (600 l mm^{-1}) covering a spectral domain 450 Å wide, with a reciprocal dispersion of 16 Å mm^{-1} and a resolving power of 8000 - 11000. We used this setup mainly with two different central wavelengths, i.e. 4670 and 6560 Å . A few spectra were also obtained with grating #2 (1200 l mm^{-1}) centered at a wavelength of 4560 Å , offering a reciprocal dispersion of about 8 Å mm^{-1} and a resolving power of about 20000.

For our visitor mode observing runs (PIs: M. De Becker and G. Rauw), the strategy consisted in obtaining a Th-Ar comparison spectrum exposure shortly before or after every observation on the sky. Series of tungstene exposures for flat-fielding were obtained at the beginning, during, and at the end of each night. The data were reduced using the MIDAS software developed at ESO. After removing cosmic ray events from the five individual images of each observation, we combined them and the resulting spectra were wavelength calibrated. We normalized the spectra using properly chosen continuum windows.

On the other hand, we also obtained a series of spectra with the Elodie échelle spectrograph mounted on the 1.93 m telescope (Baranne et al. 1996) in service observing mode (PI: M. De Becker). This spectrograph uses a combination of a prism and of a grism as cross-disperser, with a blaze angle of 76°. The detector is a Tk1024 CCD with 24 μm squared pixels. The resolving power achieved is 42 000 between 3906 and 6811 Å in a single exposure. The Elodie data consist in single spectra distributed in 67 orders. These spectra were reduced using the automatic treatment implemented at the OHP, and were normalized using splines calculated on the basis of properly chosen continuum windows.

European Southern Observatory – La Silla

In Chapter 4, we used some spectra obtained by H. Sana with the Fiber-fed Extended Range Optical Spectrograph (FEROS, Kaufer et al. 1999) on La Silla (Chile). In May 2001 and April 2002, the échelle spectrograph was mounted on the ESO 1.52 m telescope, while in May 2003 it was fed by the 2.2 m ESO/MPE telescope. The detector was a Site CCD with 2048 × 4096 pixels of $15\,\mu \times 15\,\mu$. The spectral resolving power is 48 000. An improved version of the FEROS context within the MIDAS software was used to reduce the data.

Observatorio Astronómico Nacional of San Pedro Mártyr

In Chapters 2, 4 and 5, we used some spectra obtained by P. Eenens with the échelle spectrograph fed by the 2 m telescope at the Observatorio Astronómico Nacional of San Pedro Mártyr (SPM), in Mexico. The spectra are distributed in 26 orders covering the spectral domain between 3800 and 6800 Å . The detector was a Site CCD with 1024 × 1024 pixels of $24\,\mu$m × $24\,\mu$m, and the slit width was set to 150 or 200 μm depending on the observation. The data were reduced using the echelle package available within the MIDAS software.

A.2 Optical photometry

We did not apply for observing time specifically dedicated to this work, but we used available archive photometric data and we included related results in some papers inserted in this dissertation.

La Silla Observatory

The non-thermal radio emitter HD 168112 (see Chapter 4) has been used as a comparison star in the context of the Long Term Photometry of Variables (LTPV) programme at ESO (Manfroid et al. 1991; Sterken et al. 1993). The data were obtained with various telescopes and photometers at La Silla in the Strömgren system. These photometric data were used by G. Rauw to search for variations attributable to binarity.

Hipparcos and Tycho

For some stars studied in Chapter 2, we used the V_T, B_T and H_P magnitudes series to search for significant photometric variations. These archive data were retrieved by querying the Simbad data base available from `http://simbad.u-strasbg.fr/Simbad`.

A.3 X-ray observations

Most of the targets studied in this work have been observed in X-rays, and we reported on several results obtained with various X-ray observatories. Even though our main results come from *XMM-Newton* observations, some information are also given on archive *ROSAT* and *ASCA* observations.

XMM-Newton

The European Space Agency's X-ray Multi-Mirror Mission (*XMM-Newton*, Jansen et al. 2001) was launched on December 10, 1999. It carries three high throughput Wolter Type I grazing incidence X-ray telescopes characterized by an unprecedented surface area. The instruments consist mainly in three X-ray European Photon Imaging Camera (EPIC), i.e. the two MOS (Turner et al. 2001) and the pn (Strüder et al. 2001) instruments, both operating between about 0.4 and 10.0 keV, along with a Reflection Grating Spectrometer (RGS, den Herder et al. 2001) working between about 0.35 and 2.5 keV. An Optical Monitor (OM, Mason et al. 2001) observing between 180 and 650 nm is also mounted on the satellite.

In the context of this work, three main targets have been observed with *XMM-Newton*, namely NGC 6383, NGC 6604 and Cyg OB2.

- NGC 6383 (PI: G. Rauw): the observation of NGC 6383 took place during revolution 229, in March 2001. The total observation time was split into three exposures. As the satellite was still inside the radiation belts during the first one, the EPIC instruments were operated only during the second and the third exposures for a total observing time of about 26 ks. As the aim-point of the observations was set to the main target of the NGC 6383 open cluster, i.e. the X-ray bright massive binary HD 159176, RGS data were also obtained. The results of these observations for HD 159176 are described in Chapter 3 (De Becker et al. 2004c), and the results for the other X-ray sources in the field of view can be found in Rauw et al. (2003a).

- NGC 6604 (PI: G. Rauw): two observations of the young open cluster NGC 6604 were obtained during revolutions 426 and 504, respectively in April 2002 and in September 2002. The two main targets were the non-thermal radio emitters HD 168112 and HD 167971 (see Chapter 4). The exposure times were of the order of 13 ks for both observations for both EPIC-MOS instruments, and of about 10 ks for EPIC-pn.

- Cyg OB2 (PI: G. Rauw): four observations of the Cyg OB2 association were obtained in October - November 2004 (revolutions 896, 901, 906 and 911), with exposure times of about 20 ks each. The EPIC and RGS instruments were operated during the observations, with the aim-point set at the position of Cyg OB2 #8A (the main target of these observations). The results of the analysis of the Cyg OB2 #8A data are presented in Chapter 5.

All these data sets benefitted from the large experience in X-ray data reduction gathered by the High-Energy Astrophysics Group in Liège, using the Science Analysis Software developed by ESA and dedicated to the analysis of data obtained with *XMM-Newton*.

ROSAT

The Roentgen Satellite *ROSAT* resulted from a Germany-US-UK collaboration. It was launched on June 1, 1990 and operated for almost 9 years. Its was equiped with an X-ray telescope used in conjunction with a Position Sensitive Proportional Counter (PSPC) or a High Resolution Imager (HRI), both operating between 0.1 and 2.5 keV.

We used archive *ROSAT* data throughout this dissertation. A large amount of X-ray sources were indeed observed with this observatory and all data are now available to the scientific community. We analyzed archive data for the O-stars within IC 1805 (see Chapter 2), for the non-thermal radio emitters in NGC 6604 (see Chapter 4) and for Cyg OB2 #8A (see Chapter 5). These data were reduced using the XSELECT software.

ASCA

The Advanced Satellite for Cosmology and Astrophysics (*ASCA*) was a Japanese mission launched on February 20, 1993, and was used for scientific observations during 7 and a half years. It was equiped with four Wolter Type I X-ray telescopes working in conjunction with two Gas Imaging Spectrometers (GIS) and two Solid-state Imaging Spectrometers (SIS). Both pairs of instruments were operating between about 0.4 and 10.0 keV.

We retrieved archive *ASCA* data of Cyg OB2 #8A obtained in April 1993 during the performance verification phase, and we reduced them using the XSELECT software. The results of this analysis are described in De Becker et al. (2005b) inserted in Chapter 5.

A.4 γ-ray observations

In this dissertation, we reported on observations of the Cyg OB2 region obtained with the European *INTEGRAL* satellite. The International Gamma-Ray Astrophysics Laboratory of the European Space Agency was launched on October 17, 2002. Its payload consists mainly of two γ-ray instruments, i.e. the SPI spectrometer working between 20 keV and 8 MeV (Vedrenne et al. 2003) and the IBIS imager operating between 20 keV and 10 MeV (Ubertini et al. 2003). The latter instrument consists of a two-layered detector: the upper layer (ISGRI) operating between 20 keV and 1 MeV and the lower layer (PICsIT) operating between 175 keV and 10 MeV. The satellite is also equiped with two Joint European X-ray Cameras (JEM-X 1 and 2) working between 3 and 60 keV (Lund et al. 2003). In addition, there is an Optical Monitoring Camera (OMC) operating between 500 and 850 nm (Mas-Hesse et al. 2003).

We obtained observations with *INTEGRAL* in AO1 (about 80 ks), and we applied for additional observing time in AO2. This additional time was granted (PI: G. Rauw) and our observing programme was amalgamated with a larger programme. Consequently, we otained about 2000 ks of *INTEGRAL* observation with the IBIS imager. The data were reduced and analyzed with various successive releases of the Off-line Science Analysis (OSA) software. Our results are described in Chapter 5.

A.5 Radio observations

In this work, we also discussed several results provided by data obtained and analyzed by R. Blomme in the radio domain, mainly with the Very Large Array (VLA). Even though the observations in the radio domain did not represent the main aspect of this dissertation, the results of the collaboration with the Royal Observatory of Belgium were crucial in several aspects of the discussion of the non-thermal emission from massive stars (see Chapter 6). This is the reason why some of these results are mentioned and used in this work (see Chapters 4 and 5), although the author of this thesis did not contribute to their analysis.

Appendix B

Line profile variability study of massive stars

B.1 General techniques

In different parts of the thesis, we made use of a few techniques to investigate the profile variability of spectral lines in the optical domain. In this section, we briefly describe the tools we used in chapters 2 and 5. Mainly, here we will talk about *Temporal Variance Spectrum* (TVS) analysis, *Fourier analysis*, and *prewhitening*.

Temporal Variance Spectrum analysis

This technique was developed by Fullerton et al. (1996) to search for variations in the profile of aborption lines. It was first applied to O-type stars even though its application should not be considered to be limited to that category of stars.

Let us consider a time series of N consistently normalized spectra arranged in a matrix S where the element S_{ij} represents the jth wavelength pixel of the ith spectrum. If the column average, i.e. the mean value of pixel j in the time series, is

$$\overline{s_j} = \frac{1}{N}\sum_{i=1}^{N} S_{ij},$$

then the deviations at each wavelength can be expressed by a matrix of residuals

$$d_{ij} = S_{ij} - \overline{s_j}.$$

It is assumed that the d_{ij} follow a Gaussian distribution of mean zero with a standard deviation σ_{ij}. This assumption can be justified by the fact that, to a good approximation, the combination of photon and read-out noises is Gaussian for modern detectors.

By definition, the *Temporal Variance Spectrum* (TVS) at wavelength j, i.e. column j of the matrix S_{ij}, is

$$TVS_j = \frac{1}{N}\sum_{i=1}^{N} d_{ij}^2.$$

The statistical distribution of TVS$_j$ is governed by a reduced χ^2 distribution with $N-1$ degrees of freedom and a variance σ^2. In practice, the TVS is computed at each wavelength step for the complete time series. As (TVS)$^{1/2}$ scales linearly with the amplitude of the residuals, (TVS)$^{1/2}$ is generally plotted instead of TVS itself.

The null hypothesis, i.e. no variability, can be rejected if the $(\mathrm{TVS})^{1/2}$ exceeds a threshold corresponding to a sufficiently unlikely value. For a time series of N spectra, this threshold, or significance level (SL), is given by the following relation

$$SL = \sigma_0 \sqrt{\frac{\chi^2}{N-1}}$$

Provided the noise from the continuum pixels in each spectrum, i.e. σ_{ic}, has been determined, σ_0 is obtained from

$$\sigma_0 = \left[\frac{1}{N} \sum_{i=1}^{N} \sigma_{ic}^{-2} \right]^{-1},$$

and χ^2 for $N-1$ degrees of freedom can be evaluated for instance at the 95 % or 99 % confidence level in χ^2 distribution tables.

In this approach, weighting factors $w_i = (\sigma_0/\sigma_{ic})^2$ are introduced to suppress the contribution from lower quality spectra and enhance that of higher quality spectra.

If a significant variability is detected for a given spectral line, one could wonder whether the variations are periodic or not. In order to answer this question, a time series analysis is needed. In the context of this work, we analysed our time series with the Fourier technique that is briefly discussed below.

Fourier analysis

In time series analyses, the Fourier technique has been extensively used and proved its capability to provide excellent results for many applications. However, in its classical approach, a constraining requirement is that the time series have to be equally spaced in time. This can be achieved most of the time in laboratories where the experimental conditions are tightly controlled. But in the case of astronomical measurements, these ideal conditions are not fulfilled. For instance, the sampling of astronomical phenomena is strongly affected by weather conditions, or even by technical problems. And more generally, in the optical domain, observations from ground-based observatories can only be performed at night, and must be interrupted during the day. These constraints render the sampling heterogeneous and the data points are therefore not equally spaced in time. For this reason, the Fourier analysis technique had to be adapted to the more general case of unequally spaced data.

In all our time series analyses, we used the generalized Fourier technique described by Heck et al. (1985) and revised by Gosset et al. (2001). In the particular case of spectral time series, the Fourier analysis is performed at each wavelength step. A two-dimensional periodogram – or power spectrum – is then obtained. Mean periodograms can also be computed to obtain an overview of the power as a function of frequency for the whole wavelength interval considered in the temporal analysis. For instance, such an analysis can be carried out in a spectral domain containing a given spectral line. This is typically what is described in Chapter 2 and in De Becker & Rauw (2004).

A useful tool that has also been used in our time series analysis is the Deeming spectral window. The observed Fourier transform is the result of the convolution of the true Fourier transform with a spectral window. This spectral window is calculated from the data spacing alone and does not depend directly on the data themselves: *the pathology of the data distribution is all contained in the spectral window* (Deeming 1975). The spectral window is defined to have a unit intensity at frequency zero, and may present additional peaks at other frequencies. Typically, because of the peculiarities of the data spacing, subsidiary peaks with significant relative intensities (so-called aliases) will indeed appear in addition to main peaks of the periodogram calculated from the data. In order to interpret the periodograms more efficiently, the relative position of the subsidiary peaks due to the sampling can be checked in the spectral window. This might be helpful to sort out the peaks of periodograms and decide whether they are due to a periodic signal or to the sampling. Once the periodogram has been investigated, the strongest peaks are considered in order to check whether they might correspond to recurrence time-scales related to any physical processes.

Prewhitening

This technique is used to check for the presence of a periodic signal with a recurrence time-scale corresponding to main peaks identified in periodograms obtained with the generalized Fourier technique discussed above.

Let us consider that a peak with a strong intensity has been identified in the periodogram at a frequency ν. As a first step, a periodic mathematical function is fitted to the time series at every wavelength step (or radial velocity step v). The expression used is

$$F(v,t) \;=\; c_0(v) + a_1(v)\,\sin\left(2\,\pi\,\nu\,[t-t_0]\right) + b_1(v)\,\cos\left(2\,\pi\,\nu\,[t-t_0]\right)$$

Then, the sinusoidal variation of frequency ν is subtracted from the data and the Fourier technique is applied again on the resulting time series. The prewhitening can successively be applied to the time series to identify multi-periodic variations likely to produce several peaks in the periodogram of the initial data. If the periodogram obtained after prewhitening is devoid of significant peaks, one may consider that the frequency ν corresponds to a periodic variation with a recurrence time-scale $T = 1/\nu$.

B.2 Application to the study of a sample of Oef stars

As an extensive illustration of the techniques briefly presented above, we propose to discuss the study of a sample of Oef stars by De Becker & Rauw (2004). Oef stars are O-stars displaying a double peaked He II λ 4686 line. The peculiar shape of the latter is tentatively attributed to the fast rotation of the stars of this category. The projected rotational velocities of the Oef stars can indeed reach values up to 450 km s^{-1}, leading to significant departures from the spherical symmetry of their winds, with density enhancements close to the equatorial plane (Conti & Leep 1974). Only six stars are currently known to belong to this category: ζ Pup (O4ef), λ Cep (O6ef), BD +60° 2522 (O6.5ef), HD 192281 (O5(ef)), HD 14442 (O5.5ef) and HD 14434 (O6.5(ef)). As the particular shape of their He II λ 4686 profile is believed to be due to the rotation, any significant variability reported for this line may possibly be related to stellar rotation. These stars offer therefore the interesting possibility to display a variable behaviour ruled by a well-defined time-scale worth investigating with the various techniques presented above.

Our campaign devoted to Oef stars included the study of the four last members of the series enumerated above. The investigation of BD +60° 2522 revealed a puzzling behaviour with strong variations on a yet undetermined time-scale (probably of the order of a few days), that seems to change from one year to the next (Rauw et al. 2003b). The study of HD 192281, HD 14442 and HD 14434 is described with more details in De Becker & Rauw

(2004, included in this appendix), but we summarize below the main results of the study of this sample of Oef stars.

Our campaign on Oef stars was spread over several observing runs between September 1998 and October 2003. We obtained series of spectra in the blue domain with the Aurélie spectrograph mounted on the 1.52 m telescope at OHP. We calculated the TVS for time series from each observing run and it revealed a significant variability mainly of the He II λ 4686 and H β lines. As a first approach, we investigated wavelength intervals 20 or 30 Å wide, therefore allowing us to check which part of the line was undergoing the strongest variability. In most cases, as illustrated by the figures included in the paper inserted below, the wavelength interval could be split in two or three domains that we investigated separately. As a second step, for each line and each data set, we calculated two-dimensional power spectra through the generalized Fourier technique discussed above. When the TVS and the 2D periodogram suggested that at least two different parts of the line were undergoing distinct behaviours, we calculated additional power spectra in each narrow domain to investigate more specifically each part of the line. This approach allowed us to isolate a list of possible recurrent time-scales that were then investigated more carefully by prewhitening our periodograms with the candidate frequencies. At the end of this rather long and systematic procedure, we were able to fill in the Table 9 of De Becker & Rauw (2004, inserted hereafter). The careful inspection of this census of candidate frequencies led us to the discovery of recurrence time-scales of about 1.5 and 1.6 days respectively for HD 192281 and HD 14442 that are compatible with the rotation periods of these fast rotators. However, although a rather stable time-scale has been found for these two stars, we observed a switch of the modulations back and forth between the blue and the red wings even though they never leave the central absorption component of the line. Moreover, the variability level itself changes also depending on the data set. In the case of HD 14434, the variability seems to be even more complex and we failed to determine a stable recurrence time-scale. In addition, on the basis of a time series of about 10 spectra of the latter target obtained during the same night, we did not detect any significant variability on a time-scale of a few hours attributable to non-radial pulsations.

Even though the scenario responsible for the variability investigated in this study remains an open question, the various tools described above in this appendix proved their capability to provide a complete diagnosis of the behaviour of spectral lines provided the quality of the data is satisfactory. For details on the investigation of the puzzling behaviour of Oef stars, see Rauw et al. (2003b) and De Becker & Rauw (2004, inserted in this appendix).

A&A 427, 995–1008 (2004)
DOI: 10.1051/0004-6361:20040548

Astronomy & Astrophysics

Line profile variability in the spectra of Oef stars

II. HD 192281, HD 14442 and HD 14434*

M. De Becker and G. Rauw**

Institut d'Astrophysique et de Géophysique, Université de Liège, 17, Allée du 6 Août, Bât. B5c, 4000 Sart Tilman, Belgium
e-mail: `debecker@astro.ulg.ac.be`

Received 29 March 2004 / Accepted 6 August 2004

Abstract. We present the very first analysis of the spectroscopic variability of the three rapidly rotating Oef stars HD 192281 (O5(ef)), HD 14442 (O5.5ef) and HD 14434 (O6.5(ef)). Radial velocities of the He II λ 4541 line reveal no evidence of binarity on time scales of a few days, or from one year to the next, for any of the targets. The He II λ 4686 double-peaked emission and, to some extent, the Hβ absorption line display significant profile variability in the spectra of all three stars. Data gathered during different observing runs spread over six years reveal a rather stable time scale for HD 192281 and HD 14442, whereas the variability pattern changes significantly from one year to the other. The case of HD 14434 is less clear as no obvious time scale emerges from our analysis. In a tentative way to interpret this variability, stellar rotation remains a possible clock for HD 192281 and HD 14442. However, currently available models addressing stellar rotation fail to explain some crucial aspects of the observed variability behaviour, which appear to be even more complex in the case of HD 14434.

Key words. stars: early-type – stars: individual: HD 192281 – stars: individual: HD 14442 – stars: individual: HD 14434 – stars: variables: general – stars: winds, outflows

1. Introduction

Monitoring of the spectroscopic variability has been used extensively to study the structure of the stellar winds of hot luminous stars (e.g. Fullerton et al. 1996; Massa et al. 1995; Kaper et al. 1997, 1999). Some objects were found to display cyclical variations in their stellar wind lines on time scales of a few days, possibly related to the rotational period of the underlying star. Large scale co-rotating structures in the stellar winds due to photospheric features (magnetic fields, non-radial pulsations, ...) could possibly account for this variability (e.g. Kaper et al. 1999; Rauw et al. 2001). In order to quantify the importance of different processes that could contribute to this variability, more stars should be investigated. The objects of the scarce category of so-called Oef stars (Conti & Leep 1974) appear a priori as promising targets for such an investigation since the double peaked morphology of the He II λ 4686 emission line has been attributed to the effect of fast rotation.

The best studied Oef stars are ζ Pup (O4ef) and λ Cep (O6ef). The two stars display strong spectral variability partly attributed to the effect of rotation (Moffat & Michaud 1981; Howarth et al. 1995; Kaper et al. 1999). In the case of ζ Pup, Eversberg et al. (1998) further reported stochastic modulations of the He II λ 4686 line explained by clumps distributed across the wind. These authors also confirmed the existence of spectral modulations on a time scale compatible with the rotation period, near the core of the He II λ 4686 line.

Recently, Rauw et al. (2003, Paper I) analysed the complex behaviour of the He II λ 4686 line in the spectrum of BD +60° 2522 (O6.5ef). They suggested that rotation was not the only clock ruling this variability, and that possibly non-radial pulsations were responsible for some short term variability. In this paper, we report the results of an intensive study of three other members of the small group of Oef stars, i.e. HD 192281, HD 14442 and HD 14434.

HD 192281 (V = 7.6) is an O5(ef) star of the Cyg OB8 association. On the basis of its large radial velocity quoted in the literature, this star was considered as a runaway candidate by Gies & Bolton (1986), but the results of their study did not confirm this status. The radial velocity of HD 192281 was also studied by Barannikov (1993) who argued that it was a binary with a 5.48 day orbital period, but this result has, so far, never been confirmed.

HD 14442 (V = 9.2) and HD 14434 (V = 8.5) are respectively O5.5ef and O6.5(ef) stars which were believed to belong to the Per OB1 association. On the one hand, HD 14442 has been classified as nitrogen enriched (ON) by Bisiacchi et al. (1982). On the other hand, HD 14434 may have a normal nitrogen spectrum (Schild & Berthet 1986). Both stars have been reported as blue straggler candidates by Kendall et al. (1995) who considered they could have followed a quasi-homogeneous

---

[*] Based on observations collected at the Observatoire de Haute-Provence, France.

[**] Research Associate FNRS (Belgium).

Table 1. Summary of some properties of HD 192281, HD 14442 and HD 14434. References are the following: (1) Conti & Leep (1974), (2) Walborn (1972), (3) Walborn (1973), (4) this study, (5) Bieging et al. (1989), (6) Conti & Burnichon (1975), (7) Leitherer (1988), (8) Kendall et al. (1995), (9) Gies & Bolton (1986), (10) Humphreys (1978), (11) Conti & Ebbets (1977).

	HD 192281	HD 14442	HD 14434
Sp.T.	O5.5(ef)^1	O6ef^1	O6.5(ef)^{1,4}
	O5Vn((f))^2	O5n(f)p^3	O5.5Vn((f))p^2
	O5(ef)^4	O5.5ef^4	
log ($T_{\rm eff}$)	4.67^5	4.62^6	4.60^6
M_* ($M_\odot$)	70^7	44–54^{8,a}	44–52^{8,a}
	93^5		
R ($R_\odot$)	15^7	7.8–16.6^{8,b}	10.0–12.6^{8,b}
	19^5		
d (kpc)	1.78^9	2.88^8	3.00^8
Association	Cyg OB8^{10}	Per OB1^{10,c}	Per OB1^{10,c}
$V_{\rm rot}$ sin i (km s^{-1})	270^{11}	273^{11}	400^{11}

[a] The two values quoted are respectively the spectroscopic and the evolutionary masses.

[b] The first value of the radius is calculated for an assumed value of the distance modulus, and the second one is derived from the spectral type.

[c] The membership to this association is uncertain (see Kendall et al. 1996).

evolutionary track. However, in a subsequent study, Kendall et al. (1996) found no CNO abundance anomalies in the spectrum of HD 14442 and HD 14434. These authors therefore rejected the blue straggler status of these stars and questioned their membership in Per OB1, suggesting that their distance could be larger than that of this association.

The three stars have a large projected rotational velocity: Conti & Ebbets (1977) reported $V_{\rm rot}$ sin i values of 270, 273 and 400 km s^{-1} for HD 192281, HD 14442 and HD 14434 respectively. Very few studies have been performed on these three stars. In Table 1, we summarize the information regarding their fundamental parameters that we have gathered from the literature. Different spectral types have been assigned to these stars and some of them are given in Table 1 for information. We shall briefly return to this point in Sect. 3.

This paper is the second (and last) one of a series devoted to the line profile variability of Oef stars. It describes the first line profile variability study performed on HD 192281, HD 14442 and HD 14434. In Sect. 2, we present the observations and the data reduction. Section 3 discusses the mean spectrum and the spectral type of our three target stars. Radial velocities and equivalent widths are discussed in Sect. 4. Section 5 describes the results of our line profile variability analysis, and Sect. 6 consists in a discussion of our results and in an attempt of a consistent interpretation. The conclusions and prospects for future work are finally given in Sect. 7.

2. Observations and data reduction

Spectroscopic observations of our three targets were collected during seven observing campaigns between September 1998 and October 2003 at the Observatoire de Haute-Provence (OHP). All observations were carried out with the Aurélie spectrograph fed by the 1.52 m telescope (Gillet et al. 1994). For the 1998 and 1999 missions, Aurélie was equipped with a Thomson TH7832 linear array with a pixel size of 13 μm. From 2000 on, the detector was replaced by a 2048 × 1024 CCD EEV 42–20#3, with a pixel size of 13.5 μm squared.

An overview of the different campaigns is displayed in Table 2. Data reduction followed the same approach as described in Paper I. Table 2 also specifies for each campaign which star was observed, as well as the spectral range covered during the run. In the following, we will merge the data collected during the two 1999 campaigns (July and August) into one single set which will be called Summer 1999, because of the small number of spectra taken during these two individual runs.

3. Mean spectrum

3.1. HD 192281

The mean blue spectrum of HD 192281 is shown in Fig. 1. The data of this spectrum are from the 2001 mission (see Table 2). This part of the spectrum is dominated by absorptions of He I λ 4471, He II $\lambda\lambda$ 4541, 4686 and by the strong Hβ line. Mg II λ 4481 is clearly present, partially blended with He I λ 4471. In emission, the most striking feature is due to N III $\lambda\lambda$ 4634-41 and, to some extent, to C III λ 4650 and probably C IV λ 4662. The two emission lines at $\lambda\lambda$ 4487, 4506, identified as S IV lines (Werner & Rauch 2001), are also weakly present. We emphasize the probable presence of N V absorption lines at 4605 and 4620 Å. The presence of these lines in an O5 star is somewhat surprising. Indeed, these lines are commonly found in the spectra of very early (O3) stars (Walborn & Fitzpatrick 2000). However, the lines are observed in the spectrum of HD 14947 (O5If) as reported by Underhill et al. (1989), but not in the spectrum of HD 15629 (O5V) discussed by the same authors. Some Si IV emission lines at 4631 Å and 4654 Å are also present.

The double-peaked structure of the He II λ 4686 emission justifies the spectral type given by Conti & Leep (1974). Such a line shape is supposed to result from a rotating wind (see e.g. Petrenz & Puls 1996). Using the ratio of the equivalent widths (*EW*s) of the He I λ 4471 and He II λ 4541 lines ($\log W' = -0.47 \pm 0.03$) we assign an O5 spectral type, according to the classification criterion given by Mathys (1988). In the following, we will adopt an O5(ef) spectral type for this star, where (ef) expresses the prominence of the central absorption component in the He II λ 4686 line.

3.2. HD 14442

Spectra of HD 14442 have been taken during observing runs in July 1999, August 1999, September 2000, September 2001, September 2002 and October 2003. The middle spectrum in

Table 2. Observing campaigns for the study of HD 192281, HD 14442 and HD 14434. The last three columns specify the number of spectra obtained for each star during a specific observing run.

Campaign	Detector	Spectral range (Å)	Recipr. disp. (Å mm^{-1})	Res. power	HD 192281	HD 14442	HD 14434
September 1998	TH7832	4455–4890	16	8000	6	0	0
July 1999	TH7832	4100–4950	33	4000	7	5	0
August 1999	TH7832	4100–4950	33	4000	4	7	0
September 2000	CCD	4455–4905	16	8000	0	9	0
September 2001	CCD	4455–4905	16	8000	16	12	0
September 2002	CCD	4455–4905	16	8000	10	9	11
October 2003	CCD	4455–4905	16	8000	7	6	19

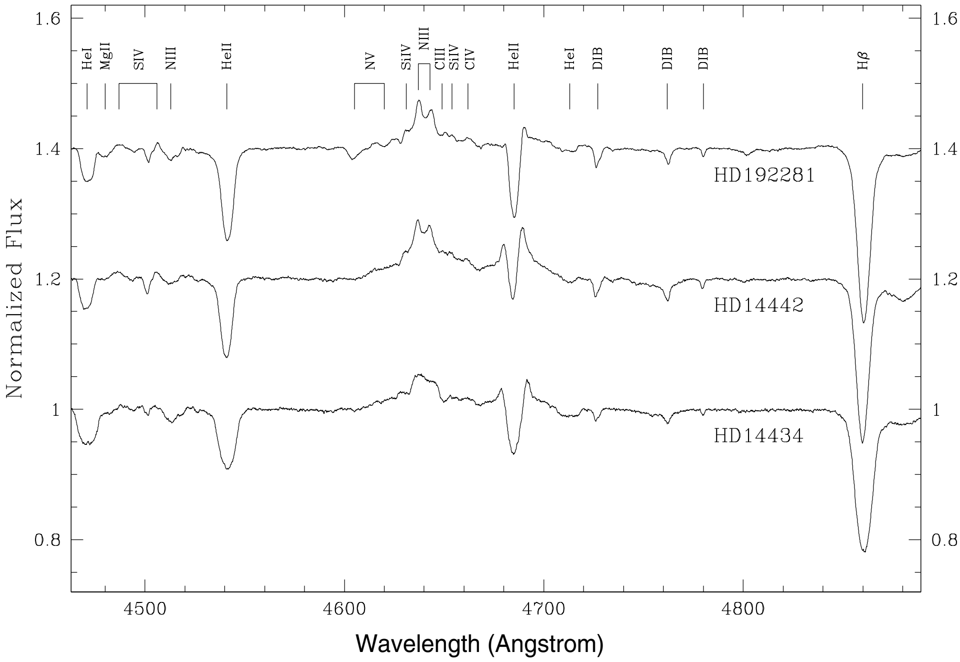

Fig. 1. Mean spectra of our program stars between 4465 Å and 4890 Å. From top to bottom: HD 192281: calculated from spectra of the September 2001 mission, between HJD 2 452 163.43 and HJD 2 452 170.41; HD 14442: calculated from the spectra of the September 2002 mission, between HJD 2 452 518.54 and HJD 2 452 533.48; HD 14434: calculated from the spectra of the October 2003 mission, between HJD 2 452 916.49 and HJD 2 452 934.38.

Fig. 1 shows the same general features as HD 192281 except for the N V lines. The central absorption of the He II λ 4686 line appears less pronounced than in the case of HD 192281. The strong emission wings observed for HD 14442 confirm the Oef classification assigned by Conti & Leep (1974).

The equivalent width determined for the He I λ 4471 and He II λ 4541 lines allowed us to apply the log (W′) criterion as defined by Mathys (1988). The result (−0.41 ± 0.03) implies an O5.5 spectral type. In the following of this paper, HD 14442 will be considered as an O5.5ef star.

3.3. HD 14434

This star was observed during the September 2002 and October 2003 observing runs. The bottom spectrum of Fig. 1 displays the same general features as the spectrum of HD 14442, but the lines are even further broadened by the fast stellar rotation. The fact that the N III λλ 4634-41 emission lines appear also significantly broader could imply that these lines are in fact formed at the level of the photosphere (rather than inside the stellar wind, see e.g. Mihalas 1973). We further note that the fact that N III λλ 4634-41 lines appear in emission is not in agreement with the results of Kendall et al. (1996) who reported the former weakly in absorption, as well as the absence of the latter. The double-peaked structure of the He II λ 4686 line dominated by the central absorption, typical of O(ef), stars is obvious.

From the equivalent width of the He I λ 4471 and He II λ 4541 lines, we infer log (W′) = −0.19 ± 0.04, corresponding to an O6.5 type. In the following of this study, we will thus adopt the O6.5(ef) spectral type for HD 14434, in excellent agreement with the spectral type given by Conti & Leep (1974).

4. Radial velocities and equivalent widths

4.1. HD 192281

As a first step, we have measured the radial velocity (*RV*) of the strongest absorption lines in the blue range. The lines of interest here are He II λ 4541 and Hβ. Since the He II λ 4541 line forms probably deep inside the photosphere, it is likely to provide the most reliable indicator of the actual stellar *RV*. As shown in Fig. 2, the dispersion in radial velocity reaches a maximum of about 10 km s^{-1}, whereas the typical error[1] in the determination of *RV*s with our Gaussian fitting method is about 8 km s^{-1}. For all our data sets, we find a mean radial velocity of −23.1 km s^{-1}. This leads to a value of about 5.0 km s^{-1} for the peculiar velocity (after application of the LSR and Galactic rotation corrections). This value strongly argues against a runaway status for this star. Indeed, according to the criteria of Stone (1991), the peculiar velocity threshold for a star to be a runaway is about 40 km s^{-1}. It has been suggested by Gies & Bolton (1986) that the runaway status was erroneously attributed to stars such as HD 192281 because of their huge wind velocity that yield a large negative *RV* for those spectral lines that are at least partly formed in the wind. The choice of the line for *RV* estimation is thus particularly crucial.

Gies & Bolton (1986) measured also the *RV* of the He II λ 4686 and hydrogen lines for this star. After correction for the velocity component due to the solar motion in the LSR frame, they found a mean of −26.8 km s^{-1} for the He II λ 4686 line, and a mean of −44.7 km s^{-1} for hydrogen lines. For comparison, we find LSR-corrected *RV* means of −33.3 and −46.1 km s^{-1} respectively for He II λ 4686 and Hβ. The reasonable agreement between our values and those of Gies & Bolton suggests that there are no large long-term variations of the *RV*s. The difference of about 18 km s^{-1} between the mean *RV* of these two lines (about 13 km s^{-1} in our case) is again explained by a difference in the depth of the line formation region within the expanding atmosphere. Indeed, the He II λ 4686 line is most probably formed deeper in the wind, where the temperature is higher, and the wind velocity is lower.

Because of its profile variability, which will be discussed hereafter, the He II λ 4686 line yields less reliable *RV*s. Indeed, the radial velocities spread over more than 35 km s^{-1}. We did however not find any systematic trend for this variability in radial velocities.

Barannikov (1993) performed a *RV* variability analysis, the only known, for this star. He claimed to find *RV* variation with a semi-amplitude of 16.1 ± 2.4 km s^{-1} on a 5.48 days period, compatible with the existence of a low mass companion. We have folded our *RV* data with Barannikov's 5.48 days period but no systematic trend appeared. A Fourier analysis was also performed on our *RV* measurements of the He II λ 4541 line. The resulting periodogram does not show any peak with an amplitude larger than 2.4 km s^{-1}. The highest peak appears at a frequency of 0.105 d^{-1}, corresponding to a 9.57 d period. This value is quite close to the period (9.59 d) obtained by Barannikov (1993) for his photometric data. In fact, Barannikov reported also apparently periodic light variations with a peak to peak amplitude of about 0.04 mag. This coincidence is somewhat puzzling. Although this could be regarded as evidence for binarity, we do not consider this to be a plausible scenario. In fact, the amplitude of the *RV* variation (~2.5 km s^{-1}) at the 9.57 d "period" is of the order of the uncertainty on individual data points. Moreover, it seems extremely difficult to account simultaneously for a light curve of amplitude ~ 0.04 mag (peak to peak) and a *RV* variation inferior to about 5 km s^{-1} (peak to peak) within a binary scenario. Assuming that the light variations are due to total eclipses of a companion, we could be dealing with a secondary of spectral type ~ B3V and such an object would produce a *RV* curve with a peak to peak amplitude of ≥80 km s^{-1} (assuming $i \geq 60°$). On the other hand, to account for the amplitude of the *RV* curve, we would need a companion of mass inferior to about 1 $M_\odot$ and such a star would be far too faint to produce a variation of 0.04 mag in the light curve, even if it were still on a pre-main sequence track.

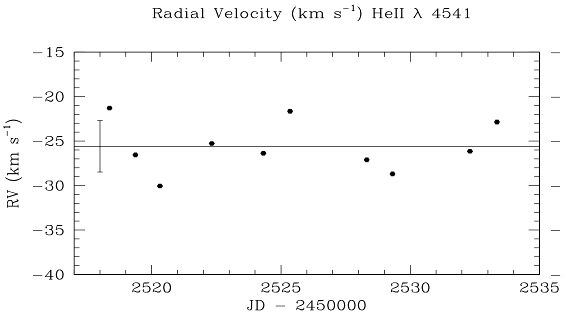

Fig. 2. Radial velocities of HD 192281 determined from the He II λ 4541 line for the September 2002 observing run. The central wavelength was determined by fitting a Gaussian to the line. The error bar gives an idea of the standard deviation obtained for the *RV* data set.

The equivalent width was measured for the He I λ 4471, He II λ 4541 and Hβ lines. The results, as well as the *RV*s, are collected in Table 3. Mean values are given for each observing run with an estimate of the standard deviation. We see that no significant variability appears from one run to the other. Moreover, no significant variability was found during individual observing campaigns.

4.2. HD 14442

Gaussians were fitted to the He II λ 4541 line to determine the radial velocity. The results are illustrated in Fig. 3 which shows the *RV* versus heliocentric Julian day for the September 2002 observing run. We find, for this line, a mean *RV* of about −32.1 km s^{-1} for the whole data set, which is somewhat different from the values reported by other authors such as Conti et al. (1977) who give −42.1 km s^{-1} or

---

[1] The error on the radial velocity estimate corresponds to the standard deviation determined for the radial velocity of a Diffuse Interstellar Band (DIB) at about 4762 Å.

Table 3. Radial velocities and equivalent widths of the strongest absorption lines in the spectrum of HD 192281. The *RV* of the He I λ 4471 line is not quoted because its shape deviates significantly from a Gaussian, leading to a poor estimate of its central position. The complex shape of the He II λ 4686 line, and its strong variability, prevented us to derive any useful *EW* for this line. The error bars represent the $\pm 1\sigma$ standard deviation. An estimate of the mean signal-to-noise ratio of an individual spectrum is given in the last column.

Mission	He I λ 4471	He II λ 4541		He II λ 4686	Hβ		S/N
	EW	*RV*	*EW*	*RV*	*RV*	*EW*	
	(Å)	(km s^{-1})	(Å)	(km s^{-1})	(km s^{-1})	(Å)	
September 1998	0.31 ± 0.04	–22.4 ± 3.0	0.84 ± 0.04	–48.9 ± 7.4	–	–	380
Summer 1999	0.28 ± 0.01	–21.5 ± 2.4	0.81 ± 0.02	–43.7 ± 9.2	–62.8 ± 3.5	1.97 ± 0.03	290
September 2001	0.31 ± 0.01	–22.9 ± 2.8	0.92 ± 0.01	–44.3 ± 5.0	–56.5 ± 2.4	2.05 ± 0.03	450
September 2002	0.30 ± 0.01	–25.6 ± 2.9	0.94 ± 0.01	–48.6 ± 6.0	–58.1 ± 3.9	2.05 ± 0.02	440
October 2003	0.31 ± 0.01	–13.8 ± 5.2	0.88 ± 0.02	–41.8 ± 12.8	–58.1 ± 3.2	2.06 ± 0.04	380

Table 4. Same as Table 3, but for HD 14442.

Mission	He I λ 4471	He II λ 4541		He II λ 4686	Hβ		S/N
	EW	*RV*	*EW*	*RV*	*RV*	*EW*	
	(Å)	(km s^{-1})	(Å)	(km s^{-1})	(km s^{-1})	(Å)	
Summer 1999	0.33 ± 0.02	–30.3 ± 8.2	0.84 ± 0.02	–51.5 ± 18.4	–67.7 ± 3.7	1.84 ± 0.04	160
September 2000	0.32 ± 0.02	–32.2 ± 6.7	0.84 ± 0.02	–59.7 ± 14.9	–66.6 ± 5.1	1.91 ± 0.03	340
September 2001	0.34 ± 0.01	–31.8 ± 5.6	0.84 ± 0.01	–57.1 ± 23.7	–64.5 ± 3.8	1.86 ± 0.03	300
September 2002	0.32 ± 0.01	–34.3 ± 2.9	0.83 ± 0.02	–66.5 ± 16.2	–65.7 ± 4.3	1.84 ± 0.05	430
October 2003	0.32 ± 0.01	–32.0 ± 10.7	0.80 ± 0.01	–57.4 ± 19.6	–64.5 ± 14.5	1.84 ± 0.05	330

Table 5. Same as Table 3, but for HD 14434.

Mission	He I λ 4471	He II λ 4541		He II λ 4686	Hβ		S/N
	EW	*RV*	*EW*	*RV*	*RV*	*EW*	
	(Å)	(km s^{-1})	(Å)	(km s^{-1})	(km s^{-1})	(Å)	
September 2002	0.54 ± 0.03	–15.3 ± 5.7	0.81 ± 0.03	–40.2 ± 18.2	–39.4 ± 3.5	2.09 ± 0.03	530
October 2003	0.52 ± 0.02	–3.9 ± 12.0	0.84 ± 0.03	–28.4 ± 13.4	–35.3 ± 5.3	2.10 ± 0.05	320

Underhill & Gilroy (1990) who published a value of -40.6 km s^{-1}, for averages of several line measurements. As for the differences in *RV*s found for different lines, the discrepancy between our results and those of the authors cited hereabove can probably be explained by the velocity gradient in the stellar wind. The maximum difference in *RV* over the five data sets is only about 30 km s^{-1}. A Fourier analysis was performed on these *RV* data but no peak with an amplitude larger than 4.4 km s^{-1} emerged from the periodogram.

*RV*s were also determined for the He II λ 4686 and Hβ lines. For the first one, *RV* values vary around a mean of -57.0 km s^{-1}, whilst for Hβ, this mean is about -66.3 km s^{-1}. As for HD 192281, the mean *RV* is more negative in the case of the hydrogen line.

The equivalent width was determined for the same lines as for HD 192281. Once again, no significant variability is found during the runs, or from one observing run to the other.

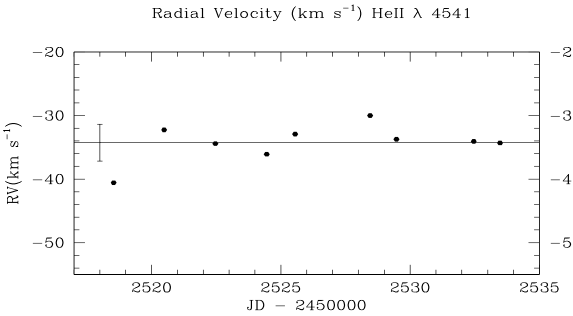

Fig. 3. Same as Fig. 2, but for HD 14442.

4.3. HD 14434

Radial velocities measured on the same lines as for HD 192281 and HD 14442 are given in Table 5. We emphasize that these values are subject to larger uncertainties due the difficulty to fit Gaussians to the very broad absorption of this star: the actual line profiles are not Gaussian and undergo variations which are discussed in more details in Sect. 5.3. The rather large values of the standard deviations given in Table 5 reflect these difficulties. The largest error bars are obtained for the He II λ 4686 line, and are undoubtedly due to the strong variability of this line.

Figure 4 shows the radial velocities measured on the He II λ 4541 line during the September 2002 observing run as a function of time. The dispersion is rather large, but no

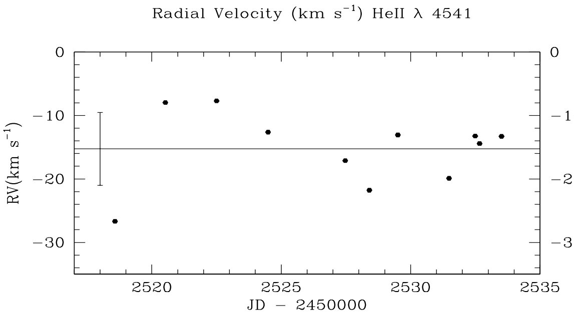

Fig. 4. Same as Fig. 2, but for HD 14434.

systematic trend can be detected. Mean radial velocities for the September 2002 and October 2003 campaigns overlap within their large error bars. The radial velocity reported by Conti et al. (1977), i.e. −11.7 km s^{-1}, is compatible with the value obtained for the He II λ 4541 line. No indication of binarity on time scales of several days, or from one year to the next, has thus been revealed by our time series.

Equivalent width are also quoted in Table 5. These *EW*s are stable on the time scales investigated in our study.

5. Line profile variability

The first step of our line variability analysis (see also Rauw et al. 2003) is the identification of the lines which vary significantly with time. For this purpose, we used the time variance spectrum (TVS) as developed by Fullerton et al. (1996). We evaluated the signal-to-noise ratio of individual spectra over a line free region between 4560 Å and 4590 Å. This estimate is necessary for the determination of the 99% significance level of the variability found with the TVS.

The procedure was applied to each dataset. The lines that show significant (at the 99% confidence level) variability are essentially He II λ 4686 and Hβ. The detailed line profile variability of these two lines is described hereafter.

In order to quantify the variability of the various spectral lines, we performed a 2D Fourier analysis using the technique described by Rauw et al. (2001): at each wavelength step, the detection of candidate frequencies is performed by an unequally spaced data Fourier analysis as described by Heck et al. (1985). The main peaks (ν) and their aliases (essentially $1-\nu$) are identified and are considered for further analysis. As a next step we "prewhite" the data for the variations at frequency ν following a method already described by Rauw et al. (2001) and used in Paper I. The frequencies which give the best results, i.e. a periodogram devoid of significant peaks after prewhitening, are considered as good candidates. Ideally, a physically significant frequency should meet the following criteria:

1. a stable clock ruling the variability should be found in the data of a given line from more than one observing campaign;
2. the frequency should not be found in the periodogram of a constant line (typically an interstellar feature), otherwise such a frequency probably reflects an artificial variability affecting the entire spectrum, and should not be associated with a physical process;
3. the frequency should appear, within the error bars, in the periodograms of more than one variable line if more than one line varies significantly with time.

These criteria concern in fact only the most ideal cases and have to be relaxed in more complex situations (like the case of BD +60° 2522, Paper I). Their strict application would probably lead to the rejection of potentially meaningful frequencies. The last criterion, in particular, is certainly not mandatory because we cannot state that a given variability mechanism will affect all lines in a same manner.

Table 6. Observing runs used for the line profile variability study of HD 192281. The first column gives the name of the campaign as used in the text, the second column yields the amount of spectra taken during each run, the third specifies which line was studied with the corresponding data set, the fourth one gives the time elapsed between the first and the last spectrum of the run, and finally the last column provides the natural width of a peak of the power spectrum taken as $1/\Delta T$.

Mission	Number of spectra	Line	ΔT (d)	$\Delta\nu_{\rm nat}$ (d^{-1})
Sept. 1998	6	He II λ 4686	7.977	0.125
Sum. 1999	11	He II λ 4686 Hβ	33.140	0.030
Sept. 2001	16	He II λ 4686 Hβ	6.979	0.143
Sept. 2002	10	He II λ 4686 Hβ	14.984	0.067
Oct. 2003	7	He II λ 4686 Hβ	15.910	0.063

5.1. HD 192281

An overview of the observing runs is given in Table 6. Generally, one spectrum was obtained during each night the star was observed, except for the 2001 run where at least 2 spectra were taken each night with a mean time separation of about 0.025 d.

He II λ 4686. As shown in Table 6, five data sets were available for the study of this line. TVS and Fourier analyses were performed on the five time series, as well as on a combination of all our data sets. For a better visualization of the behaviour of this line, Fig. 5 shows the mean spectrum and the TVS, as well as the 2D power spectrum as a grey scale representation for the September 2001 observing run, and in the case of the combined data set. The periodogram of the combined data set displays some kind of fine structure due to the strong irregularity of the sampling. The TVS calculated for all our individual data sets reveals that the level of the variability changes from one observing run to the other. The variability affects essentially two separate parts of the line, respectively the violet and the red wings.

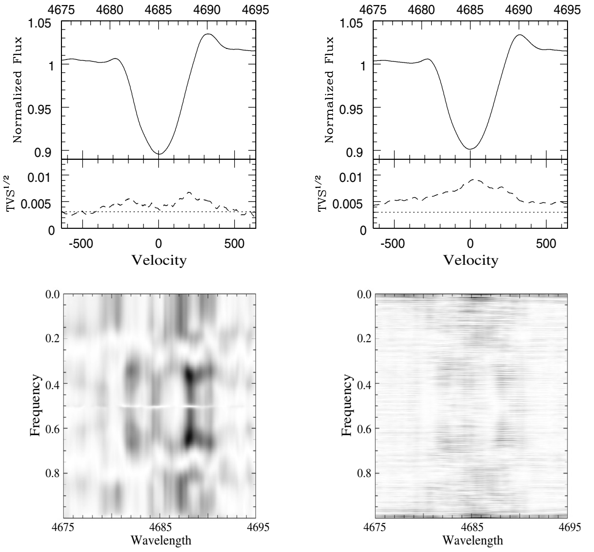

Fig. 5. *Upper panels*: mean spectrum and square root of the time variance spectrum of the He II λ 4686 line of HD 192281 between 4675 Å and 4695 Å respectively for the September 2001 observing run and for the combined data set. The 99% significance level of the TVS$^{1/2}$ is indicated by the horizontal dotted line. Velocities are expressed in km s^{-1}. *Lower panels*: the corresponding two-dimensional power spectra. The darkest regions stand for the highest peak intensities of the periodogram. Frequencies and wavelengths are expressed respectively in d^{-1} and in Å.

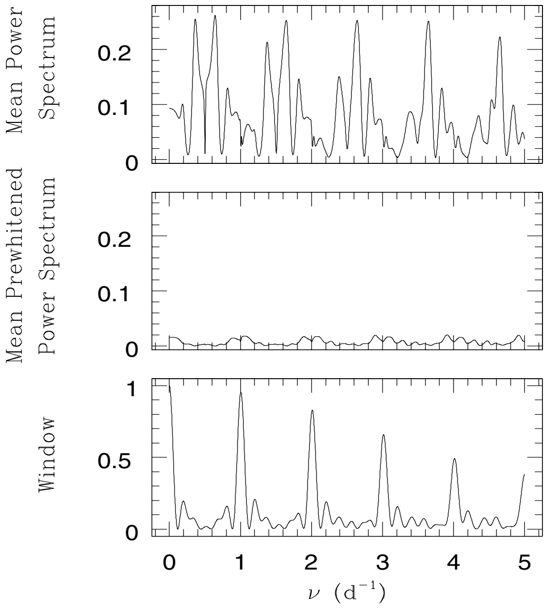

Fig. 6. *Upper panel*: mean power spectrum obtained for the He II λ 4686 line of HD 192281 between 4687.5 Å and 4688.5 Å for the September 2001 observing run, up to 5.0 d^{-1}. *Middle panel*: residual power spectrum obtained after prewhitening with a frequency of 0.64 d^{-1}. *Bottom panel*: power spectral window showing secondary peaks which explain the asymmetrical shape of the peaks of the power spectrum.

The most striking and recurrent feature in these periodograms is the presence of aliases at frequencies of about 0.35 and 0.65 d^{-1}, corresponding respectively to periods of about 2.86 and 1.54 d. Figure 6 shows the mean periodogram obtained for the 2001 run between 0.0 and 5.0 d^{-1}, along with the residual periodogram obtained after prewhitening for a frequency of 0.64 d^{-1} between 4687.5 and 4688.5 Å. The spectral window is displayed in the bottom panel. We emphasize that the time analysis performed on such a narrow wavelength band does not provide any result representative of the behaviour of the whole line, but it allows a clear identification of the time scale of the variability observed in the part of the line where the TVS reaches its highest level. Prewhitening shows that most of the power of the periodogram can be accounted for by aliasing of this 0.64 d^{-1} frequency (or its 1–ν alias).

The periodogram of a Diffuse Interstellar Band (DIB) at 4762 Å has been calculated for each data set, and only the September 1998 campaign gives peaks situated near these candidate frequencies, but with much lower intensities.

The variability pattern of the He II λ 4686 line changes with epoch. Indeed, the strongest variability and hence the ν_1 and $1-\nu_1$ peaks appear essentially in the red and the violet (with lower intensity) wings in the September 1998 and September 2001 periodograms, but appear only in the violet wing in Summer 1999. The width of the wavelength range displaying a significant variability with frequency ν_1 or $1-\nu_1$ changes also from one epoch to the other. A summary of all the frequencies is given in Table 9 (Sect. 6).

Hβ. The same approach as for the He II λ 4686 line was adopted for Hβ. Our data allow us to perform this line profile variability analysis only for the 1999, 2001, 2002 and 2003 campaigns. In this case, the TVS and the 2D power spectra reveal that the variability is concentrated in the core of the line. The Summer 1999 data set analysis leads once again to frequencies of about 0.33 or 0.67 d^{-1}. This observation raises thus the degree of confidence concerning these frequencies already noted for the He II λ 4686 line. However, the situation is less clear for the September 2001 periodogram. Indeed, the peak frequencies found in this case are near 0.14 and 0.46 d^{-1}. For the September 2002 campaign, the variability appears shifted to the red wing of the line, and we are not able to definitely distinguish the peaks from those which appear in the DIB periodogram.

He I λ 4713. Even if no variability is seen for this line until 2001, the September 2002 observing campaign reveals a significant TVS signal in the red wing. The existence of this variability turns out to be robust in the sense that it remains if we omit individual spectra one at the time and repeat the analysis on the remaining data set. Although the periodogram is dominated by a peak at ~0.3 d^{-1}, prewhitening at this frequency yields no satisfactory result.

Table 7. Same as Table 6, but for the observing runs used for the line profile variability study of HD 14442.

Mission	Number of spectra	Line	ΔT (d)	$\Delta\nu_{\rm nat}$ (d^{-1})
Sum. 1999	11	He II λ 4686	34.039	0.029
		Hβ		
Sept. 2000	9	He II λ 4686	10.967	0.091
		Hβ		
Sept. 2001	12	He II λ 4686	7.030	0.142
		Hβ		
Sept. 2002	9	He II λ 4686	14.942	0.067
		Hβ		
Oct. 2003	6	He II λ 4686	17.957	0.056
		Hβ		

5.2. HD 14442

Table 7 gives some information about the observing runs. During the September 2001 mission, two spectra were taken each night with a mean separation between the two spectra of about 0.025 d.

He II λ 4686. In Fig. 8, we show the results obtained for the September 2001 campaign, as well as for the combined data set. The analysis of the individual data sets reveals that the TVS obtained for the September 2002 campaign shows a more complex structure, with an additional varying component in the blue emission peak. To check the robustness of this feature, we have removed each individual spectrum one at the time from our September 2002 time series and performed the variability analysis on the remaining data. This additional component in the TVS appears to be stable. The situation is even more complex in the case of the October 2003 data set, where we can distinguish four distinct varying parts in the line, but it could be due to a rather poor sampling. Due to the poor weather conditions we obtained indeed only 6 spectra during that campaign.

All our data sets (except perhaps in Summer 1999 where the variability is much less significant) yield a relatively stable frequency between 0.35 and 0.40 d^{-1} (or 0.65 and 0.60 d^{-1} for their respective aliases) near the line core. These frequencies give very good prewhitening results and are not the same as those of the main peaks appearing for the DIB at 4762 Å.

Figure 7 shows the mean power spectrum obtained for the September 2001 mission between 4682 Å and 4684 Å. The middle panel of this figure illustrates the residual periodogram obtained after prewhitening with a frequency of 0.60 d^{-1}. It appears that the aliasing of this frequency is sufficient to account for all the peaks of the power spectrum. A similar result is achieved if the prewhitening is performed with a 0.40 d^{-1} frequency.

Other peaks appear also in our periodograms. For example, a frequency of 0.11 d^{-1} (and its aliases) is clearly identified in the red wing for the Summer 1999 campaign. Table 9 in Sect. 6 gives a more complete overview of the frequencies emerging from the analysis of all our time series.

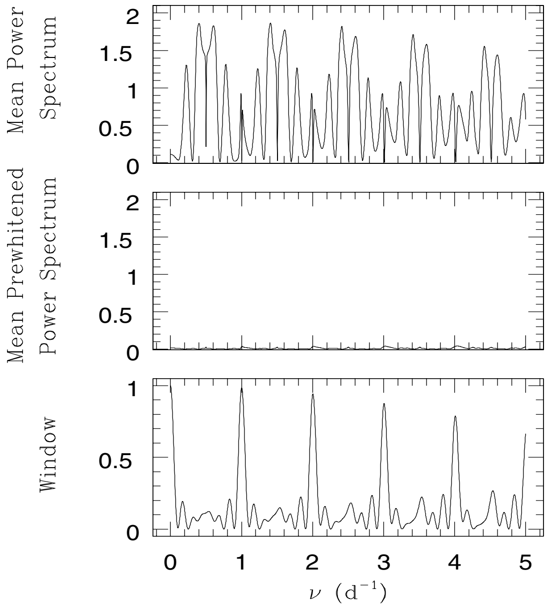

Fig. 7. *Upper panel*: mean power spectrum obtained for the He II λ 4686 line of HD 14442 between 4682 Å and 4684 Å for the September 2001 observing run, up to 5.0 d^{-1}. *Middle panel*: residual power spectrum obtained after prewhitening with a frequency of 0.60 d^{-1}. *Bottom panel*: power spectral window showing secondary peaks which explain the asymetrical shape of the peaks of the power spectrum.

Hβ. No significant variability was found for this line in the Summer 1999 data. Remember that this data set has the poorer signal-to-noise ratio, and also the poorer sampling due to the spread of our observation over 34 days. However, significant variations were found for the other observing runs, especially for the September 2002 and the October 2003 campaigns where it reaches its highest level. The two-dimensional periodograms in Fig. 9 show variability patterns which are very similar to those obtained for the He II λ 4686 line. The simplest case appears for the 2001 data set, where the main feature is completely reproduced by a 0.39 d^{-1} (or 0.60 d^{-1}) frequency. This is very interesting if we remember that it corresponds quite well to the frequencies obtained for the He II λ 4686 line. The situation is more complex in the case of the 2000 and 2002 campaigns. After analysis, it appears that the periodograms are partly explained by some complex long term behaviour probably due to the sampling or normalization irregularities. Nevertheless, frequencies of about 0.35 d^{-1} (or 0.65 d^{-1}) obviously contribute to the power spectra obtained in both cases. The October 2003 periodogram is mainly dominated by peaks at about 0.41 d^{-1} (0.59 d^{-1}).

He II λ 4541. In the 2002 campaign, the good quality of the data allowed us to find a significant (albeit weak) line profile variability in the case of the He II λ 4541 line, especially near the core of the line with some weak contributions in the red wing. The analysis of the periodogram revealed that frequencies between 0.36 and 0.4 d^{-1} (or their 1−ν aliases) contribute

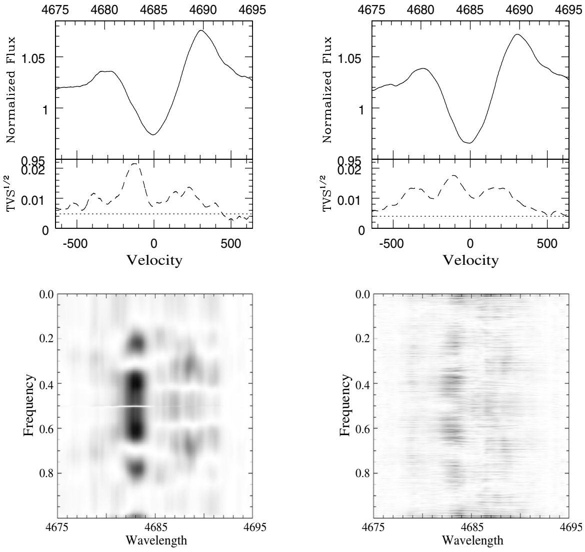

Fig. 8. Same as Fig. 5 but for HD 14442.

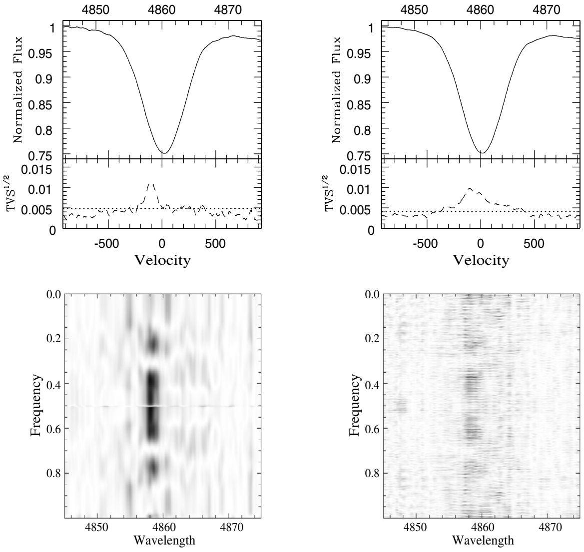

Fig. 9. Same as Fig. 8 but for the Hβ line between 4845 Å and 4875 Å.

Table 8. Observing runs used for the line profile variability study of HD 14434.

Mission	Number of spectra	Line	ΔT (d)	$\Delta\nu_{\rm nat}$ (d^{-1})
Sept. 2002	11	He II λ 4686 Hβ	14.936	0.067
Oct. 2003	19	He II λ 4686 Hβ	17.891	0.056

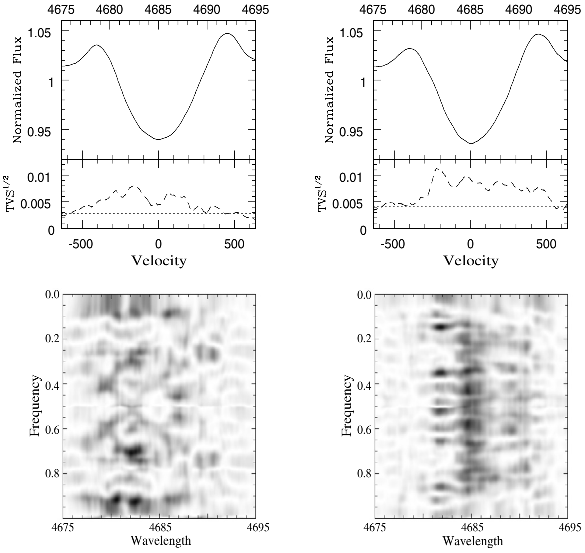

Fig. 10. *Upper panels*: mean spectrum and square root of the time variance spectrum of the He II λ 4686 line of HD 14434 between 4675 Å and 4695 Å respectively for the September 2002 and the October 2003 observing runs. The 99% significance level of the TVS$^{1/2}$ is indicated by the horizontal dotted line. The differences in significance levels are due to differences in signal-to-noise ratios (see Table 5). Velocities are expressed in km s^{-1}. *Lower panels*: the corresponding two-dimensional power spectrum. The darkest regions stand for the highest peak intensities of the periodogram. Frequencies and wavelengths are expressed respectively in d^{-1} and in Å.

significantly to the variability of this line. This range of frequencies matches very well the frequencies obtained for the He II λ 4686 and the Hβ lines discussed hereabove. This result reinforces our trust in the physical origin of the frequencies found for the variations in the spectrum of HD 14442.

5.3. HD 14434

HD 14434 was observed during only two observing runs (see Table 8). In order to search for rapid variations, the star was intensively observed during the night from October 16 to 17, 2003: ten spectra spanning 6 h were obtained. The TVS for this specific night computed over the whole spectrum did not reveal any significant variability. Consequently, we conclude that HD 14434 does not display a variable behaviour on short time scales (a few hours) in the spectral range we investigated.

However, over time scales of several days, a significant variability is detected essentially for the He II λ 4686 line in both data sets, and for Hβ in October 2003. The behaviour of these two lines was investigated and the results are described hereafter. The high quality of our September 2002 data also allowed us to detect some variability for the He I λ 4471 line, but with a level which is too low for a Fourier analysis.

He II λ 4686. In Fig. 10, the TVS shows that a significant variability is detected for the He II λ 4686 line in both data sets. The variability level seems higher in October 2003 than in September 2002. The variations are not restricted to a given part of the line, but extend over a rather broad domain. Lower panels of the same figure display the two-dimensional power spectra obtained through Fourier analysis. The behaviour of the line is rather complex, and the periodograms reveal that different parts of the line apparently display different variability trends. A more detailed analysis, i.e. by focusing on individual parts of the line, yields different time scales.

The September 2002 power spectrum reveals that the dominant frequency is about 0.91–0.92 d^{-1}. This value corresponds to the darkest spots of the lower left panel of Fig. 10. We note that the validity of the corresponding periods (close to one day) can not be totally warranted by our sampling. Other peaks contribute also to the power but the prewhitening failed to reveal unambigously which ones were to be selected to identify the related variability time scales. In October 2003, the situation is also rather complex though the prewhitening indicates that frequencies at about 0.35–0.4 d^{-1} dominate the power spectrum. We note also that the same analysis performed on the DIBs did not reveal significant variability due to normalization errors that could disturb our variability analysis.

Hβ. This line displays also a variable behaviour, but only at a rather low level. The detection of this variability is most significant for the October 2003 data set, even though data of better quality were obtained during the September 2002 campaign. In October 2003, the variable part of the line could be divided into a red and a blue side. The red part seems to be ruled by a combination of frequencies of about 0.14 and 0.35 d^{-1} (or their 1–ν aliases), or by a frequency of about 0.44 d^{-1}. In the blue part, the possible frequencies are close to 0.3 or 0.35 d^{-1} (or their 1–ν aliases). Even though the frequencies of about 0.35 d^{-1} appearing for the He II λ 4686 and Hβ lines could be related to a common physical process, we did not obtain sufficiently consistent results to give a detailed description of the variable behaviour of these lines.

6. Discussion

At this stage, it is interesting to recall the different time scales which emerged from our line profile analyses for the three stars. Table 9 provides the frequencies found (as well as the corresponding periods) for the different lines, and for each data set. Because of the ambiguity between aliases (ν and $1-\nu$), they are both given in most cases, with the one of lowest frequency in brackets.

It appears from Table 9 that some variability time scales are found in different data sets of a same star. This is obvious for HD 192281 and HD 14442. This recurrence in some frequencies suggests that a rather stable process is at work in the variability we observe. However, the case of HD 14434 is much less conclusive. Indeed, our data sets did not reveal any obvious time scale which could be responsible for a large part of the variability detected for the He II λ 4686 line, and to some extent for Hβ. This points to a more complex situation than for HD 192281 and HD 14442. Nevertheless, probably the most important result arising from our line profile analysis of HD 14434 is the absence of variations on time scales of several hours. This is especially important in the framework of scenarios where non-radial pulsations may play a role (see Sect. 6.2). The non-detection of short time scale variations suggests that pulsations do not have a major impact in this Oef star, contrary to what was put forward by the study of BD +60° 2522 (Paper I), ζ Pup (Reid & Howarth 1996) and λ Cep (de Jong et al. 1999).

In addition, there are several points that have to be considered in a model for the variability discussed in this study. First, the stars are rapid rotators and display a double peaked He II λ 4686 emission line. Second, the "periodic" variability observed during a specific observing run affects only part of the line profile. Third, the variability pattern changes from one epoch to the other and more specifically, the wavelength range displaying the periodic behaviour can shift from one wing of the line to the other. Finally, the variability level changes as well from one oberving run to the next.

6.1. Rotational modulation

Since Oef stars are fast rotators, a straightforward question is whether a stable variability time scale as observed in the case of HD 192281 and HD 14442 could be linked to stellar rotation. To address this issue, we must first derive some constraints on the rotational period of these stars. An upper limit on the rotational period can be obtained from the observed projected rotational velocity.

$$P_{\rm max} = \frac{2\,\pi\,R_{\rm eq}}{V_{\rm rot}\ \sin i} \tag{1}$$

where $R_{\rm eq}$ is the stellar radius at the equator (see Table 1).

A lower limit can be evaluated as the inverse of the critical rotational frequency, beyond which the centrifugal acceleration overwhelms the effective gravity acceleration. This condition yields the relation (2)

$$P_{\rm min} = \frac{2\,\pi\,R_*^{3/2}}{(G\,M_*\,(1-\Gamma))^{1/2}} \tag{2}$$

where G is the gravitational constant, M_* the mass of the star, and Γ the ratio of the luminosity of the star to the Eddington luminosity. This parameter was evaluated with the following relation given by Lamers & Leitherer (1993)

$$\Gamma = 7.66 \times 10^{-5}\,\sigma_{\rm e}\left(\frac{L_*}{L_\odot}\right)\left(\frac{M_\odot}{M_*}\right) \tag{3}$$

where all parameters have their usual meaning, with the electron scattering coefficient $\sigma_{\rm e}$ taking the value 0.34 cm^2 g^{-1}.

6.1.1. HD 192281 and HD 14442

Let us first consider the case of HD 192281. We adopt $V_{\rm rot}\ \sin i$ = 270 km s^{-1} as obtained by Conti & Ebbets (1977). With the values taken from Leitherer (1988) for the radius (15 $R_\odot$), the luminosity ($10^{5.94}$ $L_\odot$) and the stellar mass (70 $M_\odot$), we find that the rotation period should be in the range from 0.98 to 2.81 d. Those boundaries correspond respectively to frequencies of 1.02 and 0.36 d^{-1}.

Table 9. Summary of the frequencies emerging from our line profile analyses of HD 192281, HD 14442 and HD 14434. The frequencies are given with their $1-\nu$ aliases in brackets. When two frequencies are quoted the aliases are not specified. When more than one value is provided for a line of an observing run, it indicates the results obtained for different wavelength regions of the same line, from the blue to the red. ND means that "no data" were available for that specific line and NV stands for "no significant variability".

		HD 192281		HD 14442		HD 14434	
Observing run	Line	ν (d^{-1})	P (d)	ν (d^{-1})	P (d)	ν (d^{-1})	P (d)
September 1998	He II λ 4686	0.63 (0.37)	1.59 (2.70)	ND	ND	ND	ND
Summer 1999	He II λ 4686	0.70 (0.33)	1.42 (3.03)	0.66 (0.33)	1.52 (3.03)	ND	ND
				0.59 (0.41)	1.69 (2.44)		
	Hβ	0.67 (0.33)	1.49 (3.03)	NV	NV	ND	ND
September 2000	He II λ 4686	ND	ND	0.62 (0.38)	1.61 (2.63)	ND	ND
				0.69 (0.31)	1.45 (3.23)		
				0.76 (0.24)	1.32 (4.17)		
	Hβ	ND	ND	0.65 (0.35)	1.54 (2.86)	ND	ND
September 2001	He II λ 4686	0.66 (0.35)	1.52 (2.86)	0.61 (0.40)	1.64 (2.50)	ND	ND
		0.64 (0.36)	1.56 (2.78)				
	Hβ	0.14 & 0.46	7.14 & 2.17	0.61 (0.39)	1.64 (2.56)	ND	ND
September 2002	He II λ 4541	NV	NV	0.75 (0.26)	1.33 (3.85)	NV	NV
				0.63 (0.37)	1.59 (2.70)		
	He II λ 4686	0.64 (0.36)	1.57 (2.78)	0.63 (0.37)	1.59 (2.70)	0.91	1.10
		0.65 (0.36)	1.54 (2.78)	0.66 (0.34)	1.52 (2.94)	0.92	1.09
		0.67 (0.33)	1.49 (3.03)	0.77 (0.23)	1.30 (4.35)	0.70 & 0.91	1.43 & 1.10
				0.61 (0.39)	1.64 (2.56)		
	Hβ	NV	NV	0.65 (0.35)	1.54 (2.86)	NV	NV
				0.77 (0.23)	1.30 (4.35)		
				0.64 (0.36)	1.56 (2.78)		
October 2003	He II λ 4686	0.67 (0.33)	1.49 (3.03)	0.61 (0.39)	1.64 (2.56)	0.15 & 0.60	6.67 & 1.67
		0.59 (0.41)	1.69 (2.44)			0.65 & 0.82	1.54 & 1.22
						0.66 & 0.83	1.52 & 1.20
	Hβ	0.13 & 0.26	7.69 & 3.85	0.57 (0.41)	1.75 (2.43)	0.44	2.27
						0.14 & 0.74	7.14 & 1.35
						0.34 & 0.74	2.94 & 1.35

We see in Table 9 that most of the periods range between 1.40 and 1.59 d (with aliases between 2.70 and 3.44 d). It is noticeable that most of the peaks of our periodograms lie so close to each other, and that the results are similar for several epochs. From the limits discussed hereabove, we find that most probably only the group of periods near 1.5 d could possibly be related to the rotational period.

The case of HD 14442 is even more interesting. By the use of Eqs. (1) to (3), we calculated the constraints on the rotational period. We adopted a luminosity of $\log(L/L_\odot) = 5.62$ intermediate between the two values given by Kendall et al. (1995). For the radius, we chose the value 12.4 $R_\odot$ corresponding to the luminosity given hereabove, and the $T_{\rm eff}$ from Table 1. Kendall et al. (1995) estimated the mass of HD 14442 by combining the stellar radius with atmospheric parameters, and by plotting its bolometric magnitude versus $T_{\rm eff}$ on a HR-diagram and interpolating with theoretical evolutionary tracks. They found two values of respectively about 44 $M_\odot$ and 54 $M_\odot$. We use an intermediate value of 49 $M_\odot$. We find limits on the rotational period of $P_{\rm min}$ = 0.82 d and $P_{\rm max}$ = 2.29 d. These periods correspond to frequencies of $\nu_{\rm max}$ = 1.22 d^{-1} and $\nu_{\rm min}$ = 0.44 d^{-1}.

As shown in Table 9, the results are quite consistent from one line to the other (He II λ 4686 and Hβ), and from one epoch to the other. The first group of periods lies between 1.52 and 1.69 d, and the second one between 2.44 and 3.03 d. Since the rotational period of HD 14442 should range between 0.82 and 2.29 d, only the first group of periods could possibly be related to a rotational modulation.

Therefore, assuming that the line profile variability discussed here is indeed related to rotation, we tentatively infer rotational periods of about 1.5 and 1.6 d for HD 192281 and HD 14442 respectively. The uncertainties on these periods would be of the order of 0.1 d. From the projected rotational velocities and the stellar radii (see Table 1 and Sect. 3), we can infer inclination angles of 30–35° and 41–47° for the rotational axis of HD 192281 and HD 14442 respectively.

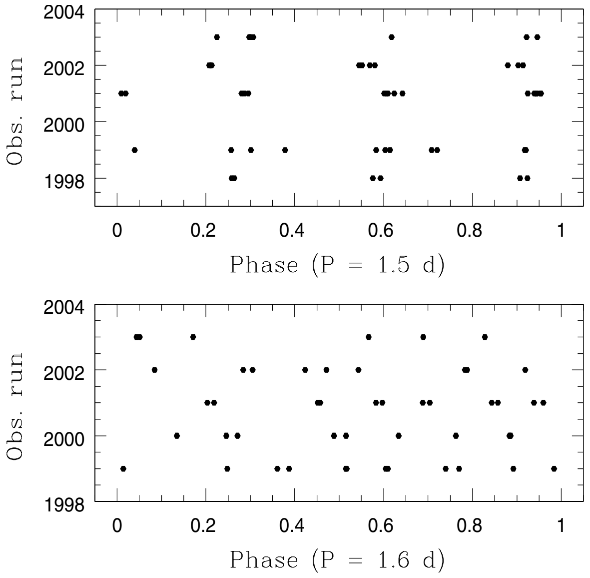

Fig. 11. Phase coverage of our data sets considering the proposed periods of 1.5 and 1.6 d respectively for the variability of HD 192281 (*upper panel*) and HD 14442 (*lower panel*). The zero time for phase calculation is arbitrarily chosen at HJD 2 450 000 for both stars. Each horizontal series of points corresponds to an observing run whose date is indicated on the vertical axis labelled in years.

An important issue to address is whether our data sets provide a sufficient sampling of the periods that apparently rule the line variability in these two stars. Figure 11 shows the phase coverage of all the data sets used for this study. These plots were obtained assuming periods of 1.5 and 1.6 d respectively for HD 192281 and HD 14442. In the case of HD 192281, we see that most points cluster around three phases. This is due to the fact that a period of 1.5 d cannot be fully sampled from a single observatory on the ground, whatever the number of spectra obtained. However, as stated in the previous paragraph, the confidence interval for this period ranges from 1.4 to 1.6 d. Except around the central value of this domain, the phase coverage appears to be satisfactory. The case of HD 14442 is less problematic. With a period of about 1.6 d, we are not confronted to the same difficulty as with HD 192281. For each mission, the phase coverage is satisfactory, except for values close to the lower boundary of the confidence interval. For both stars, the phase coverage for the selected periods becomes satisfactory when all our data sets are combined.

Fast rotation had been suggested to produce so-called wind compressed zones (Bjorkman & Cassinelli 1993) near the stellar equator. However, more recent models suggest that non radial radiative forces prevent the formation of such an equatorial compressed wind (Owocki et al. 1996) and tend rather to focus the wind towards the poles. The non-spherical shape of a rapidly rotating star will also lead to enhanced mass loss at the pole through gravity darkening (Maeder 1999). Still, an equatorially confined wind could be produced by the effect of a stellar magnetic field.

The rotational broadening of absorption lines in the spectra of O stars renders a direct measurement of their magnetic field extremely difficult. Nevertheless, dipolar magnetic fields of 360 G and 1100 G have been measured for β Cep and θ^1 Ori C respectively using spectropolarimetric techniques (Donati et al. 2001, 2002). These magnetic field strengths are sufficient to confine the stellar winds into the region of the magnetic equator. Theoretical models for such confined corotating structures have been developed by Babel & Montmerle (1997) and very recently by ud-Doula (2002). The latter author considered the case of aligned magnetic and rotational axes. He found that a corotating wind structure forms if the rotational velocity reaches a significant fraction of the critical velocity. According to ud-Doula (2002), the corotating structure in the wind consists in a density enhancement of the plasma with a lower outflow velocity. This density enhancement tends to increase as the rotational velocity approaches the critical value, and increases also as the magnetic field strength increases. In our case, the rotational velocities reach several tenths of the critical velocities and a magnetic field of a few hundred Gauss could be sufficient to trigger a corotating wind structure. Such a corotating structure might explain the double-peaked morphology of the He II λ 4686 emission in Oef stars. Moreover, if the magnetic field is tilted with respect to the rotational axis, we expect the corotating confined wind to produce a rotational modulation of the spectral lines formed in the wind. Such an "oblique magnetic rotator" model was put forward e.g. by Moffat & Michaud (1981), Stahl et al. (1996) and Rauw et al. (2001) to explain the line profile variations of ζ Pup, θ^1 Ori C and HD 192639 respectively.

The inclination of an oblique corotating wind structure with respect to our line of sight is expected to vary with a period equal to the rotational period. This general scenario could lead to a large number of variability patterns depending on the inclination angle of the rotation axis on the one hand, and the tilt angle between the magnetic and the rotational axes on the other hand. The larger the tilt angle, the larger the contrast between the observed configuration of the confined corotating wind structure at different phases. The radial extent of the corotating wind would depend on the wind velocity and the magnetic field strength. Therefore, lines formed over a large radius would be less affected by the rotational modulation than those formed in the innermost part of the wind where the effect would be most pronounced.

The oblique magnetic rotator model might account for the recurrence of a stable clock in the line profile variability. However, as pointed out above, the variability with this time scale only occurs over a limited range of wavelength and shifts from the red wing to the blue wing (and vice versa) from one year to the next. If our data provide a good sampling of the phenomenon, this fact cannot easily be explained by the simple tilted magnetic rotator model described hereabove.

6.1.2. HD 14434

In the case of HD 14434, stellar rotation does not appear a priori as a good candidate to interpret the line profile variations that we observed. Our data did not allow us to clearly identify frequencies responsible for the variable behaviour investigated in Sect. 5.3. However, we should notice that the search for a reccurent variability time scale requires more observations of this star.

6.2. Other scenarios

Beside the rotational modulation discussed above, other factors are likely to influence the variability of the objects studied in this paper. Indeed, although the main time scales of the variability of HD 192281 and HD 14442 are broadly compatible with the rotation period, some aspects do not fit this interpretation. This is even more true for the cases of HD 14434 and BD +60° 2522 (Paper I).

First, in the framework of the simulations of ud-Doula (2002), it is shown that for large wind confinement parameters, i.e. large magnetic field strengths, the density structure near the surface becomes quite complex and undergoes a complicated variability behaviour. The occurence of this phenomenon at distances from the star corresponding to the formation region of the He II line could have a strong effect on its shape.

Second, we know that the best studied Oef stars (ζ Pup and λ Cep) undergo non-radial pulsations (see Reid & Howarth 1996; de Jong et al. 1999). Cranmer (1996) considered the propagation of non-radial pulsations (NRPs) into accelerated stellar winds, and showed how this could lead to large scale structures likely able to generate significant line profile modulations. The study of NRPs in rotating early-type stars is also considered by Townsend (1997). According to the latter author, rotation compresses pulsational activity towards the equator. NRPs and probably multimodal pulsations are believed to trigger mass loss enhancements (or depletions) possibly responsible of the apparition of structures in the stellar wind. Moreover, the combined effects of rotation and strong magnetic fields on NRPs is not well understood and can lead to complex cases like the so called "off-axis modes" encountered for Ap stars for which the axis of pulsation does not coincide with the rotation axis (Townsend 1997). These considerations could provide the ingredients for an alternative scenario. The interplay between NRPs, rotation and the stellar wind were proposed to influence the variability behaviour of BD +60° 2522 (Paper I), because of the lack of stability in the variability pattern in that case. However, at least in the case of HD 14434, a series of spectra obtained with about 30 min separation over more than 6 h in October 2003 did not reveal significant short-term variability for any of the spectral lines in our wavelength domain. This result argues against a major role of pulsations at least for HD 14434, but high signal-to-noise ratio and high spectral resolution data, as well as a better sampling, are required to confirm this result.

Third, some variability should also be expected due to outmoving clumps in the wind of O stars. In the case of ζ Pup, spectral substructures similar to those observed in WR spectra are probably the consequence of excess emission from clumps (Eversberg et al. 1998). The variation across the line can reach an amplitude of about 5% of the total line intensity. However, the substructures in ζ Pup vary on time scales of a few hours only, which is too short to suit the variability time scales revealed by the study of our sample of Oef stars and is again at odds with the results of our intense monitoring of HD 14434.

Finally, we should also consider the possibility of the propagation of a clump (as discussed in the previous paragraph) across a putative confined structure within the wind (as discussed in the previous section) or a density wave. Such a scenario could lead to modulations in the profiles of the lines formed within the confined wind. The interaction of such perturbations with a corotating structure should be considered in future theoretical developments, in order to establish its impact on line profiles.

7. Conclusions and future work

We have performed a spectral analysis of the Oef stars HD 192281, HD 14442 and HD 14434. The double peaked structure of the emission component of the He II λ 4686 line of these three objects is obvious, and points to a possible corotating structure covering a significant fraction of the emitting region of this line in the stellar wind (Conti & Leep 1974). We determined spectral types (respectively O5(ef), O5.5ef and O6(ef) for the three stars) in agreement with former classifications. Our radial velocity measurements did not reveal any evidence of binarity on time scales of several days, or from one year to the next. The peculiar velocity of HD 192281 does not support a putative runaway status for this star.

A detailed line profile variability analysis was performed on the strongest lines in the blue spectra of these stars. We have shown that the He II λ 4686 line of HD 192281 and HD 14442 displays the most significant variability, with time scales which are consistently found from one epoch to the other for both stars. We find however that the structure of the profile variability changes with time. The "periodic" modulations of the profile, which are confined in a narrow wavelength domain, switch forth and back between the blue and the red wings, but never leave the central absorption component of the line[2]. The variability level itself changes also depending on the data set. Assuming that the periodicity of this variability is ruled by the rotation of the star, we propose rotational periods of 1.5 ± 0.1 and 1.6 ± 0.1 d for HD 192281 and HD 14442 respectively. HD 14434 displays the most complex behaviour on a yet undefined time scale. However, this star does not display any variations on time scales of a few hours, arguing against a pulsational origin for the observed line profile variations. The Hβ line displays lower level variations. In the case of HD 14442, the variations of Hβ are correlated with those observed in He II λ 4686.

In the framework of the most recent theoretical results concerning the magnetohydrodynamics of magnetic field-aligned rotating winds (ud-Doula 2002), we tentatively propose a scenario to explain some aspects of the observed line profile variability of HD 192281 and HD 14442. In this scenario,

---

[2] Spectral modulations on a time scale compatible with the rotation period, and located in the central region of the He II λ 4686 line, were also observed in the case of ζ Pup (Eversberg et al. 1998).

the interaction of the magnetic field with the wind plasma leads to the confinement of a significant part of the stellar wind in the vicinity of the magnetic equator plane. While several aspects of the observed variability behaviour could be explained by a corotating structure resulting from this interaction, we note that this scenario cannot explain the wavelength confinement of the variability pattern nor the shift of this pattern from the blue to the red from one year to the next, if our sampling is adequate. The wavelength confinement of the variability around zero velocity we describe in this study suggests that the structures embedded in the stellar wind have a limited spatial extent, and the change in the part of the line which suffers this variability points to the fact that these structures are not static. Moreover, like in the case of BD +60° 2522 (Paper I), the variations suffered by the line profiles of HD 14434 can not be explained by this scenario.

The description of the variability of Oef stars constitutes a challenge for theoretical modelizations. Further magnetohydrodynamical models including the interplay between NRPs, magnetic fields and rotation need to be developed in order to clarify the complex behaviour of the lines in the spectra of Oef stars. On the other hand, from the observational point of view, a similar study of ζ Pup and λ Cep should be envisaged to check whether the variability time scales and the variation patterns reported in the literature are stable over longer time scales. We note also that the study of these stars should benefit strongly from the use of a wide-band spectrograph, as well as a denser time sampling.

Acknowledgements. We wish to express our thanks to Dr. Jean Manfroid for taking some of the spectra of the September 2000 campaign. We are greatly indebted to the Fonds National de la Recherche Scientifique (Belgium) for multiple assistance including the financial support for the rent of the OHP telescope in 1999, 2000 and 2002 through contract 1.5.051.00 "Crédit aux chercheurs" FNRS. The travels to OHP for the observing runs were supported by the Ministère de l'Enseignement Supérieur et de la Recherche de la Communauté Française. This research is also supported in part by contracts P4/05 and P5/36 "Pôle d'Attraction Interuniversitaire" (Belgian Federal Science Policy Office) and through the PRODEX XMM-OM Project. We would like to thank the staff of the Observatoire de Haute Provence for their technical support during the various observing runs. The SIMBAD database has been consulted for the bibliography.

References

Babel, J., & Montmerle, T. 1997, A&A, 323, 121
Barannikov, A. A. 1993, Astron. Lett., 19, 420
Bieging, J. H., Abbott, D. C., & Churchwell, E. B. 1989, ApJ, 340, 518
Bisiacchi, G. F., Lopez, J. A., & Firmani, C. 1982, A&A, 107, 252
Bjorkman, J. E., & Cassinelli, J. P. 1993, ApJ, 409, 429
Conti, P. S., & Burnichon, M.-L. 1975, A&A, 38, 467
Conti, P. S., & Ebbets, D. 1977, ApJ, 213, 438
Conti, P. S., & Leep, E. M. 1974, ApJ, 193, 113
Conti, P. S., Leep, E. M., & Lorre, J. J. 1977, ApJ, 214, 759
Cranmer, S. R. 1996, Ph.D. Thesis, University of Delaware
Cranmer, S. R., & Owocki, S. P. 1995, ApJ, 440, 308
de Jong, J. A., Henrichs, H. F., Schrijvers, C., et al. 1999, A&A, 345, 172
Donati, J.-F., Wade, G. A., Babel, J., et al. 2001, MNRAS, 326, 1265
Donati, J.-F., Babel, J., Harries, T. J., et al. 2002, MNRAS, 333, 55
Eversberg, T. E., Lépine, S., & Moffat, A. F. 1998, ApJ, 494, 799
Fullerton, A. W., Gies, D. R., & Bolton, C. T. 1996, ApJS, 103, 475
Gies, D. R., & Bolton, C. T. 1986, ApJS, 61, 419
Gillet, D., Burnage, R., Kohler, D., et al. 1994, A&AS, 108, 181
Heck, A., Manfroid, J., & Mersch, G. 1985, A&AS, 59, 63
Howarth, I. D., Prinja, R. K., & Massa, D. 1995, ApJ, 452, L65
Humphreys, R. M. 1978, ApJ, 38, 309
Kaper, L., Henrichs, H. F., Fullerton, A. W., et al. 1997, A&A, 327, 281
Kaper, L., Henrichs, H. F., Nichols, J. S., & Telting, J. H. 1999, A&A, 344, 231
Kendall, T. R., Lennon, D. J., Brown, P. J. F., & Dufton, P. L. 1995, A&A, 298, 489
Kendall, T. R., Dufton, P. L., & Lennon, D. J. 1996, A&A, 310, 564
Lamers, H. J. G. L. M., & Leitherer, C. 1993, ApJ, 412, 771
Leitherer, C. 1988, ApJ, 326, 356
Maeder, A. 1999, A&A, 347, 185
Massa, D., Fullerton, A. W., Nichols, J. S., et al. 1995, ApJ, 452, L53
Mathys, G. 1988, A&AS, 76, 427
Mihalas, D. 1973, PASP, 85, 593
Moffat, A. F. J., & Michaud, G. 1981, ApJ, 343, 902
Owocki, S. P., Cranmer, S. R., & Gayley, K. G. 1996, ApJ, 472, L115
Petrenz, P., & Puls, J. 1996, A&A, 312, 195
Rauw, G., Morrison, N. D., Vreux, J.-M., Gosset, E., & Mulliss, C. L. 2001, A&A, 366, 585
Rauw, G., De Becker, M., & Vreux, J.-M. 2003, A&A, 399, 287 (Paper I)
Reid, A. H. N., & Howarth, I. D. 1996, A&A, 311, 616
Schild, H., & Berthet, S. 1986, A&A, 162, 369
Stahl, O., Kaufer, A., Rivinius, T., et al. 1996, A&A, 312, 539
Stone, R. C. 1991, AJ, 102, 333
Townsend, R. H. D. 1997, MNRAS, 284, 839
ud-Doula, A. 2002, Ph.D. Thesis, University of Delaware
Underhill, A. B., & Gilroy, K. K. 1990, ApJ, 364, 626
Underhill, A. B., Gilroy, K. K., & Hill, G. M. 1989, AJ, 98, 1063
Walborn, N. R. 1972, AJ, 77, 312
Walborn, N. R. 1973, AJ, 78, 1067
Walborn, N. R., & Fitzpatrick, E. L. 2000, PASP, 112, 50
Werner, K., & Rauch, T. 2001, Eta Carinae and Other Mysterious Stars, ed. T. Gull, S. Johansson, & K. Davidson, ASP Conf. Ser., 242, 229
White, R. L. 1985, ApJ, 289, 698

Appendix C

Overview of the INTEGRAL data around Cyg OB2

In Sect. 5.3, we mentioned that the reconstructed images of a large number of Science Windows present artificial features likely to affect the efficiency of the source detection procedure. Many of these features are undoubtedly related to the presence of the very bright source Cyg X-1. In Table C.1, we present a complete census of the Science Windows used for the analysis of the FCFOV around the expected position of the unidentified EGRET source 3EG J2033+4118. In this table, the column 'ScW ID' provides the identifier of each Science Window according to the conventions established by the Integral Science Data Center (ISDC): the first four digits give the revolution of the satellite, the four next digits specify the Science Window number in a given revolution, and the last four digits consist of a code allowing to distinguish between Science Windows and slews. As mentioned in Sect. 5.3, the slews were not included in our analysis. The column 'Flag' specifies whether the sky image of a given Science Window was strongly ('s'), moderately ('m'), weakly ('w') or almost not ('–') affected by artefacts. A 'NO' means that, for unknown reasons, no image was obtained for this particular Science Window. We note that the level at which the individual images are affected was only estimated by eye, in order to filter the data and try to identify the origin of the large scale structures appearing in the mosaic image presented in Fig. 5.13.

Table C.1: List of Science Windows used for the analysis of the FCFOV around 3EG J2033+4118.

#	ScW ID	Flag	#	ScW ID	Flag
1	008000470010	–	2	008000480010	–
3	008000490010	–	4	008000490020	–
5	008000510010	–	6	008000520010	–
7	008000530010	–	8	008000540010	–
9	008000550010	–	10	008000560010	–
11	008000570010	–	12	008000580010	–
13	008000590010	–	14	008000600010	–
15	008000610010	–	16	008000620010	–
17	008000630010	–	18	008000640010	–
19	008000650010	w	20	008000680010	–
21	019100720010	–	22	019100730010	m
23	019100740010	–	24	019100760010	–
25	019100770010	w	26	019100780010	–
27	019100790010	w	28	019100800010	s
29	019100810010	m	30	019100820010	–
31	019100830010	–	32	019100840010	–
33	019100850010	–	34	019100860010	–
35	021000160010	s	36	021000170010	–
37	021000180010	–	38	021000200010	–
39	021000210010	–	40	021000220010	–
41	021000230010	w	42	021000240010	s
43	021000250010	m	44	021000260010	m
45	021000270010	–	46	021000280010	m
47	021000290010	–	48	021000300010	–
49	021000310010	–	50	021000320010	w
51	021000330010	m	52	021000340010	–
53	021000360010	w	54	021000370010	s
55	021000380010	m	56	021000400010	w
57	021000400020	m	58	021100050010	–
59	021100070010	s	60	021100080010	m
61	021100090010	m	62	021100100010	m
63	021100110010	w	64	021100120010	w
65	021100130010	s	66	021100140010	s
67	021100150010	w	68	021100160010	s
69	021100170010	m	70	021100180010	w
71	021100190010	w	72	021100200010	w
73	021100210010	w	74	021100230010	w
75	021100240010	w	76	021100250010	s
77	021100270010	m	78	021100280010	w
79	021100290010	w	80	021100310010	w
81	021100320010	–	82	021100330010	s
83	021100340010	s	84	021100350010	s
85	021100360010	s	86	021100370010	m
87	021100380010	w	88	021100390010	m

#	ScW ID	Flag	#	ScW ID	Flag
89	021100400010	–	90	021100410010	m
91	021100420010	m	92	021100430010	w
93	021100440010	s	94	021100450010	s
95	021100470010	s	96	021100480010	s
97	021100490010	w	98	021100510010	s
99	021100520010	s	100	021100530010	s
101	021100550010	s	102	021100560010	m
103	021100570010	–	104	021100580010	s
105	021100590010	w	106	021100600010	–
107	021100610010	m	108	021100620010	–
109	021100630010	w	110	021200010010	s
111	021200020010	s	112	021200030010	w
113	021200040010	–	114	021200050010	–
115	021200060010	–	116	021200080010	w
117	021200090010	w	118	021200100010	–
119	021200120010	–	120	021200130010	–
121	021200140010	s	122	021200160010	w
123	021200170010	w	124	021200180010	w
125	021200190010	w	126	021200200010	s
127	021200210010	w	128	021200220010	w
129	021200230010	s	130	021200240010	s
131	021200250010	m	132	021200260010	w
133	021200270010	s	134	021200280010	–
135	021200290010	w	136	021200300010	s
137	021200320010	m	138	021200330010	s
139	021200340010	w	140	021200360010	w
141	021200370010	–	142	021200380010	–
143	021200400010	s	144	021200410010	s
145	021200420010	–	146	021200430010	–
147	021200440010	s	148	021200450010	–
149	021200460010	m	150	021200470010	m
151	021200480010	s	152	021200490010	s
153	021200500010	s	154	021200510010	m
155	021200520010	w	156	021200530010	w
157	021200540010	w	158	021200560010	w
159	021200570010	s	160	021200600010	m
161	021300210010	–	162	021300220010	–
163	021300240010	–	164	021300250010	–
165	021300260010	w	166	021300270010	w
167	021300280010	–	168	021300290010	m
169	021300300010	–	170	021300310010	s
171	021300320010	w	172	021300330010	w
173	021300340010	w	174	021300350010	s
175	021300360010	m	176	021300370010	w
177	021300380010	s	178	021300400010	w
179	021300410010	–	180	021300420010	s

#	ScW ID	Flag	#	ScW ID	Flag
181	021300440010	m	182	021300450010	m
183	021300460010	–	184	021300480010	s
185	021300490010	w	186	021300500010	w
187	021300510010	w	188	021300520010	w
189	021300530010	w	190	021300540010	m
191	021300550010	w	192	021300560010	s
193	021300570010	w	194	021300580010	s
195	021300590010	w	196	021300600010	w
197	021300610010	w	198	021300620010	w
199	021300640010	NO	200	021300650010	–
201	021300660010	w	202	021400010010	w
203	021400020010	w	204	021400030010	w
205	021400050010	w	206	021400060010	–
207	021400070010	w	208	021400080010	w
209	021400090010	–	210	021400100010	w
211	021400110010	m	212	021400120010	–
213	021400130010	w	214	021400140010	w
215	021400150010	w	216	021400160010	w
217	021400170010	w	218	021400180010	m
219	021400190010	s	220	021400210010	s
221	021400220010	w	222	021400230010	m
223	021400250010	w	224	021400260010	w
225	021400270010	w	226	021400290010	s
227	021400300010	w	228	021400310010	–
229	021400320010	w	230	021400330010	–
231	021400340010	–	232	021400350010	w
233	021400360010	m	234	021400370010	s
235	021400380010	s	236	021400390010	–
237	021400410010	–	238	021400420010	–
239	021400430010	–	240	021400450010	w
241	021400460010	s	242	021400470010	–
243	021400490010	m	244	021400500010	s
245	021400510010	–	246	021400530010	w
247	021400540010	w	248	021400550010	s
249	021400560010	w	250	021400560020	w
251	021500020010	m	252	021500030010	m
253	021500040010	s	254	021500050010	w
255	021500060010	w	256	021500070010	w
257	021500080010	m	258	021500090010	w
259	021500100010	s	260	021500110010	w
261	021500120010	s	262	021500140010	s
263	021500150010	w	264	021500160010	w
265	021500180010	w	266	021500190010	m
267	021500200010	m	268	021500220010	s
269	021500230010	w	270	021500240010	w
271	021500250010	m	272	021500260010	w

#	ScW ID	Flag	#	ScW ID	Flag
273	021500270010	w	274	021500280010	–
275	021500290010	m	276	021500300010	w
277	021500310010	m	278	021500330010	–
279	021500340010	s	280	021500350010	–
281	021500360010	w	282	021500380010	w
283	021500390010	w	284	021500400010	w
285	021500420010	s	286	021500430010	s
287	021500440010	w	288	021500470010	w
289	021500480010	w	290	021500490010	w
291	021500500010	w	292	021500510010	w
293	021500520010	w	294	021500530010	w
295	021500540010	–	296	021500550010	w
297	021500560010	m	298	021500570010	–
299	021500580010	w	300	021500590010	w
301	021500600010	w	302	021600010010	m
303	021600020010	–	304	021600030010	–
305	021600050010	–	306	021600060010	w
307	021600070010	w	308	021600090010	w
309	021600100010	–	310	021600110010	m
311	021600120010	s	312	021600130010	m
313	021600140010	w	314	021600150010	–
315	021600160010	–	316	021600170010	–
317	021600180010	–	318	021600190010	–
319	021600200010	m	320	021600210010	s
321	021600220010	–	322	021600230010	m
323	021600250010	–	324	021600260010	w
325	021600270010	–	326	021600290010	s
327	021600300010	w	328	021600310010	w
329	021600330010	w	330	021600340010	w
331	021600350010	w	332	021600360010	w
333	021600370010	w	334	021600380010	m
335	021600390010	–	336	021600400010	w
337	021600410010	w	338	021600420010	w
339	021600430010	s	340	021600440010	w
341	021600450010	–	342	021600460010	w
343	021600470010	m	344	021600490010	m
345	021600500010	w	346	021600510010	w
347	021600530010	s	348	021600540010	–
349	021600550010	w	350	021600570010	w
351	021600580010	w	352	021600590010	m
353	021600600010	w	354	021800220010	w
355	021800230010	m	356	021800240010	w
357	021800250010	–	358	021800260010	w
359	021800270010	w	360	021800280010	–
361	021800290010	w	362	021800300010	w
363	021800310010	–	364	021800330010	w

#	ScW ID	Flag	#	ScW ID	Flag
365	021800340010	NO	366	021800350010	–
367	021800370010	–	368	021800380010	–
369	021800390010	m	370	021800410010	w
371	021800420010	w	372	021800430010	–
373	021800440010	w	374	021800450010	–
375	021800460010	w	376	021800470010	s
377	021800470010	s	378	021800490010	w
379	021800500010	–	380	021800510010	w
381	021800520010	w	382	021800530010	s
383	021800540010	s	384	021800550010	w
385	021800570010	s	386	021800580010	m
387	021800590010	m	388	021800610010	w
389	021800620010	w	390	021800630010	s
391	021800650010	w	392	021800660010	m
393	021800670010	m	394	021800680010	s
395	021800690010	s	396	025100590010	w
397	025100600010	w	398	025100610010	s
399	025100630010	w	400	025100640010	w
401	025100650010	–	402	025100660010	–
403	025100670010	w	404	025100680010	s
405	025100690010	–	406	025100700010	–
407	025100710010	w	408	025100720010	–
409	025100730010	m	410	025100740010	m
411	025100750010	m	412	025100760010	m
413	025100770010	w	414	025100790010	–
415	025100800010	w	416	025100810010	m
417	025100830010	m	418	025100850010	m
419	025100850010	m	420	025100860010	m
421	025200010010	s	422	025200020010	w
423	025200030010	m	424	025200040010	–
425	025200050010	–	426	025200060010	w
427	025200070010	–	428	025200080010	–
429	025200090010	w	430	025200110010	–
431	025200120010	w	432	025200130010	w
433	025200140010	–	434	025200170010	w
435	025200250010	–	436	025200260010	–
437	025200270010	–	438	025200280010	s
439	025200310010	s	440	025200320010	w
441	025200330010	w	442	025200340010	w
443	025200350010	w	444	025200360010	s
445	025200370010	s	446	025200380010	w
447	025200410010	s	448	025200420010	w
449	025200430010	–	450	025200440010	w
451	025200450010	w	452	025200460010	–
453	025200470010	w	454	025200480010	s

#	ScW ID	Flag	#	ScW ID	Flag
455	025200510010	m	456	025200520010	–
457	025200530010	s	458	025200540010	w
459	025200550010	–	460	025200560010	w
461	025200570010	–	462	025200580010	s
463	025200610010	–	464	025300230010	w
465	025300300010	–	466	025300310010	–
467	025300320010	w	468	025300330010	–
469	025300360010	w	470	025300370010	–
471	025300380010	–	472	025300990010	–
473	025300400010	s	474	025300410010	s
475	025300420010	s	476	025300430010	w
477	025300440010	–	478	025300460010	–
479	025300470010	–	480	025300480010	w
481	025300490010	m	482	025300510010	w
483	025300520010	–	484	025500600010	–
485	025500610010	m	486	025500630010	–
487	025500640010	–			

Appendix D

List of the publications related to this work

Publications with a peer review

An *XMM-Newton* observation of the massive binary HD 159176,

De Becker, M., Rauw, G., Pittard, J.M., Antokhin, I.I., Stevens, I.R., Gosset, E., & Owocki, S.P. 2004

A&A, **416**, 221–233 (see p. 79 in this dissertation)

Quasi-simultaneous XMM-Newton and VLA observation of the non-thermal radio emitter HD 168112 (O5.5III(f$^+$)),

De Becker, M., Rauw, G., Blomme, R., Waldron, W. L., Sana, H., Pittard, J. M., Eenens, P., Stevens, I. R., Runacres, M. C., Van Loo, S., & Pollock, A. M. T. 2004

A&A, **420**, 1061–1077 (see p. 96 in this dissertation)

Early-type stars in the young open cluster IC 1805. I. The SB2 system BD +60°497 and the probably single stars BD +60°501 and BD +60°513,

Rauw, G., & De Becker, M. 2004

A&A, **421**, 693–702 (see p. 25 in this dissertation)

A spectroscopic study of the non-thermal radio emitter Cyg OB2 #8A: Discovery of a new binary system,

De Becker, M., Rauw, G., & Manfroid, J. 2004

A&A, **424**, L39–L42 (see p. 137 in this dissertation)

Line profile variability in the spectra of Oef stars. II. HD 192281, HD 14442 and HD 14434,

De Becker, M., & Rauw, G. 2004

A&A, **427**, 995–1008 (see p. 215 in this dissertation)

An XMM-Newton observation of the multiple system HD 167971 (O5-8V + O5-8V + (O8I)) and the young open cluster NGC 6604,

De Becker, M., Rauw, G., Blomme, R., Pittard, J. M., Stevens, I. R., Runacres, M. C. 2005

A&A, **437**, 1029–1046 (see p. 116 in this dissertation)

XMM-Newton observations of the massive colliding wind binary and non-thermal radio emitter Cyg OB2 #8A (O6If + O5.5III(f)),
De Becker, M., Rauw, G., Sana, H., Pollock, A.M.T., Pittard, J. M., Blomme, R., Stevens, I. R., Van Loo, S. 2006
MNRAS, in preparation (see p. 161 in this dissertation)

Publications without a peer review

On the Multiplicity of the O-Star Cyg OB2 #8a and its Contribution to the gamma-ray Source 3EG J2033+4118,
De Becker, M., Rauw, G., & Swings, J.-P. 2005
in *The Multi-wavelength Approach to Unidentified Gamma-Ray Sources* (Hong-Kong, China), eds. K.S. Cheng & G. Romero, Ap&SS, **297**, 291

New colliding wind binaries,
De Becker, M., & Rauw, G. 2004
in *Massive Stars in Interacting Binaries* (Sacacomie, Canada), eds. A.F.J. Moffat & N. St-Louis, ASP Conf. Ser., in press

A spectroscopic investigation of O-type stars in the young open cluster IC 1805,
De Becker, M., & Rauw, G. 2005
in *JENAM 2005: Massive Stars and High-Energy emission in OB Associations* (Liège, Belgium), in press

Evidence for phase-locked X-ray variations from the massive colliding wind binary Cyg OB2 #8A,
De Becker, M., & Rauw, G. 2005
in *JENAM 2005: Massive Stars and High-Energy emission in OB Associations* (Liège, Belgium), in press

On the multiplicity of the non-thermal radio emitters 9 Sgr and HD 168112,
Rauw, G., Sana, H., Gosset, E., De Becker, M., Arias, J., Morrell, N., Eenens, P., & Stickland, D. 2005
in *JENAM 2005: Massive Stars and High-Energy emission in OB Associations* (Liège, Belgium), in press

XMM-Newton observations of the Cyg OB2 association,
Rauw, G., De Becker, M., Linder, N. 2005
in *JENAM 2005: Massive Stars and High-Energy emission in OB Associations* (Liège, Belgium), in press

Bibliography

Abbott, D. C., Bieging, J. H., & Churchwell, E. 1984, ApJ, 280, 671 1

Abbott, D. C. & Lucy, L. B. 1985, ApJ, 288, 679 5

Aharonian, F., Akhperjanian, A., Beilicke, M., et al. 2005, A&A, 431, 197 182

Alfvén, H. 1950, Cosmical Electrodynamics (Oxford University Press) 17

Antokhin, I. I., Owocki, S. P., & Brown, J. C. 2004, ApJ, 611, 434 78

Aznar Cuadrado, R., Jordan, S., Napiwotzki, R., et al. 2004, A&A, 423, 1081 12

Baranne, A., Queloz, D., Mayor, M., et al. 1996, A&AS, 119, 373 207

Barbon, R., Carraro, G., Munari, U., Zwitter, T., & Tomasella, L. 2000, A&AS, 144, 451 93

Baring, M. G., Ellison, D. C., Reynolds, S. P., Grenier, I. A., & Goret, P. 1999, ApJ, 513, 311 152

Baykal, A., Stark, M. J., & Swank, J. 2000, ApJ, 544, L129 181

Bazzano, A., Bird, A. J., Capitanio, F., et al. 2003, A&A, 411, L389 180

Bell, A. R. 1978a, MNRAS, 182, 147 8, 17

Bell, A. R. 1978b, MNRAS, 182, 443 8

Benaglia, P., Cappa, C. E., & Koribalski, B. S. 2001a, A&A, 372, 952 3

Benaglia, P. & Koribalski, B. 2004, A&A, 416, 171 3

Benaglia, P., Romero, G. E., Koribalski, B., & Pollock, A. M. T. 2005, A&A, 440, 743 2

Benaglia, P., Romero, G. E., Stevens, I. R., & Torres, D. F. 2001b, A&A, 366, 605 135, 146, 149, 151, 152

Berghoefer, T. W., Schmitt, J. H. M. M., Danner, R., & Cassinelli, J. P. 1997, A&A, 322, 167 7, 78, 113

Bieging, J. H., Abbott, D. C., & Churchwell, E. B. 1989, ApJ, 340, 518 3, 113, 154, 155, 197

Blandford, R. D. & Ostriker, J. P. 1978, ApJ, 221, L29 8

Blomme, R. 2005, in Massive Stars and High Energy Emission in OB Associations, JENAM 2005, held in Liège, Belgium 196, 204

Blomme, R., van Loo, S., De Becker, M., et al. 2005, A&A, 436, 1033 94, 95, 199

Bolton, C. T. 1974, ApJ, 192, L7+ 197

Bonnell, I. A. & Bate, M. R. 2002, MNRAS, 336, 659 23

Borordin, K., Gilfanov, M., Sunyaev, R., et al. 1990, Pis ma Astronomicheskii Zhurnal, 16, 804 181

Brown, J. C., Richardson, L. L., Antokhin, I., et al. 1995, A&A, 295, 725 5

Bykov, A. M., Krassilchtchikov, A. M., Uvarov, Y. A., et al. 2004, A&A, 427, L21 182

Camero Arranz, A., Wilson, C. A., Connell, P., et al. 2005, A&A, 441, 261 181

Campbell, C. G. 1997, Magnetohydrodynamics in Binary Stars (Kluwer Academic) 10, 11

Cappa, C., Goss, W. M., & van der Hucht, K. A. 2004, AJ, 127, 2885 2

Castor, J. I., Abbott, D. C., & Klein, R. I. 1975, ApJ, 195, 157 5

Chapman, J. M., Leitherer, C., Koribalski, B., Bouter, R., & Storey, M. 1999, ApJ, 518, 890 2

Charbonneau, P. & MacGregor, K. B. 2001, ApJ, 559, 1094 14, 15

Cheng, K. S. & Romero, G. E. 2004, Cosmic Gamma-Ray Sources (Kluwer Academic Publishers, Dordrecht) 20, 21

Conti, P. S. & Leep, E. M. 1974, ApJ, 193, 113 213

Contreras, M. E., Rodriguez, L. F., Tapia, M., et al. 1997, ApJ, 488, L153+ 3, 135, 196

Courvoisier, T. J.-L., Walter, R., Beckmann, V., et al. 2003, A&A, 411, L53 180

Cowley, A. P., Crampton, D., & Hutchings, J. B. 1979, ApJ, 231, 539 180

Cowling, T. G. 1945, MNRAS, 105, 166 11, 13

De Becker, M. 2001, Master's thesis, University of Liège 5, 158, 191

De Becker, M. & Rauw, G. 2004, A&A, 427, 995 212, 213, 214

De Becker, M. & Rauw, G. 2005a, in Massive Stars and High Energy Emission in OB Associations, JENAM 2005, held in Liège, Belgium 35

De Becker, M. & Rauw, G. 2005b, in Massive Stars and High Energy Emission in OB Associations, JENAM 2005, held in Liège, Belgium 159

De Becker, M. & Rauw, G. 2005c, in Massive Stars in Interacting Binaries, held in Sacacomie, Canada 141

De Becker, M., Rauw, G., Blomme, R., et al. 2005a, A&A, 437, 1029 93, 113, 115

De Becker, M., Rauw, G., Blomme, R., et al. 2004a, A&A, 420, 1061 3, 93, 94, 95, 115

De Becker, M., Rauw, G., & Manfroid, J. 2004b, A&A, 424, L39 3, 136, 141, 154, 159

De Becker, M., Rauw, G., Pittard, J. M., et al. 2004c, A&A, 416, 221 77, 78, 115, 209

De Becker, M., Rauw, G., Sana, H., et al. 2005b, MNRAS, in preparation 158, 159, 178, 204, 210

De Becker, M., Rauw, G., & Swings, J. 2005c, Ap&SS, 297, 291 22, 146

Deeming, T. J. 1975, Ap&SS, 36, 137 212

den Herder, J. W., Brinkman, A. C., Kahn, S. M., et al. 2001, A&A, 365, L7 209

Donati, J.-F., Babel, J., Harries, T. J., et al. 2002, MNRAS, 333, 55 18, 19

Donati, J.-F., Semel, M., Carter, B. D., Rees, D. E., & Collier Cameron, A. 1997, MNRAS, 291, 658 18

Donati, J.-F., Wade, G. A., Babel, J., et al. 2001, MNRAS, 326, 1265 18, 19

Dougherty, S. M., Pittard, J. M., Kasian, L., et al. 2003, A&A, 409, 217 21, 152

Dougherty, S. M. & Williams, P. M. 2000, MNRAS, 319, 1005 2

Drake, S. A. 1990, AJ, 100, 572 3, 197

Eichler, D. & Usov, V. 1993, ApJ, 402, 271 135, 149, 151, 152, 155

Eversberg, T., Lepine, S., & Moffat, A. F. J. 1996, in Wolf-Rayet Stars in the Framework of Stellar Evolution, 33rd Liège International Astrophysical Colloquium, held in Liège, Belgium, 225–230 5

Eversberg, T., Lepine, S., & Moffat, A. F. J. 1998, ApJ, 494, 799 5

Feinstein, A., Vazquez, R. A., & Benvenuto, O. G. 1986, A&A, 159, 223 23

Feldmeier, A. 1995, A&A, 299, 523 5

Feldmeier, A., Puls, J., & Pauldrach, A. W. A. 1997, A&A, 322, 878 6

Fermi, E. 1949, Physical Review, 75, 1169 8

Ferrando, P., Arnaud, M., Cordier, B., et al. 2004, in Optics for EUV, X-Ray, and Gamma-Ray Astronomy. Edited by Citterio, Oberto; O'Dell, Stephen L. Proceedings of the SPIE, Volume 5168, pp. 65-76 (2004)., 65–76 203

Ferrario, L. & Wickramasinghe, D. T. 2005, MNRAS, 356, 615 12

Fullerton, A. W., Gies, D. R., & Bolton, C. T. 1996, ApJS, 103, 475 211

Galloway, D. K., Morgan, E. H., & Levine, A. M. 2004, ApJ, 613, 1164 181

García, B. & Mermilliod, J. C. 2001, A&A, 368, 122 23

Garmany, C. D. & Massey, P. 1981, PASP, 93, 500 3, 54

Gies, D. R. 1987, ApJS, 64, 545 3, 198

Gies, D. R., Mason, B. D., Hartkopf, W. I., et al. 1993, AJ, 106, 2072 3

Gillet, D., Burnage, R., Kohler, D., et al. 1994, A&AS, 108, 181 207

Goldoni, P., Bonnet-Bidaud, J. M., Falanga, M., & Goldwurm, A. 2003, A&A, 411, L399 181

González, J. & Levato, H. 2005, A&A, in press 54

Gosset, E. 2005, private communication 3, 198

Gosset, E., Royer, P., Rauw, G., Manfroid, J., & Vreux, J.-M. 2001, MNRAS, 327, 435 212

Grenier, I. A. 2004, in ASSL Vol. 304: Cosmic Gamma-Ray Sources, 47–67 24

Harnden, F. R., Branduardi, G., Gorenstein, P., et al. 1979, ApJ, 234, L51 135

Hartkopf, W. I., Mason, B. D., & McAlister, H. A. 1996, AJ, 111, 370 197

Hartman, R. C., Bertsch, D. L., Bloom, S. D., et al. 1999, ApJS, 123, 79 23

Harvin, J. A., Gies, D. R., Bagnuolo, W. G., Penny, L. R., & Thaller, M. L. 2002, ApJ, 565, 1216 3, 197

Heck, A., Manfroid, J., & Mersch, G. 1985, A&AS, 59, 63 212

Herrero, A., Puls, J., & Najarro, F. 2002, A&A, 396, 949 146

Howarth, I. D. & Prinja, R. K. 1989, ApJS, 69, 527 154

Hubrig, S., Szeifert, T., Schöller, M., Mathys, G., & Kurtz, D. W. 2004, A&A, 415, 685 12

Hulleman, F., in 't Zand, J. J. M., & Heise, J. 1998, A&A, 337, L25 181

Jansen, F., Lumb, D., Altieri, B., et al. 2001, A&A, 365, L1 209

Kaufer, A., Stahl, O., Tubbesing, S., et al. 1999, The Messenger, 95, 8 208

Kitamoto, S. & Mukai, K. 1996, PASJ, 48, 813 158

Kitchatinov, L. L., Jardine, M., & Donati, J.-F. 2000, MNRAS, 318, 1171 11

Knödlseder, J. 2000, A&A, 360, 539 135

Kudritzki, R. P. 1996, in Wolf-Rayet Stars in the Framework of Stellar Evolution, 33rd Liège International Astrophysical Colloquium, held in Liège, Belgium, 467–489 5

Kuznetsov, S., Falanga, M., Blay, P., et al. 2003, A&A, 411, L437 181

Lamers, H. J. G. L. M., Snow, T. P., & Lindholm, D. M. 1995, ApJ, 455, 269 154

Leitherer, C., Chapman, J. M., & Koribalski, B. 1995, ApJ, 450, 289 3, 150

Leitherer, C., Forbes, D., Gilmore, A. C., et al. 1987, A&A, 185, 121 3, 113

Lommen, D., Yungelson, L., van den Heuvel, E., Nelemans, G., & Portegies Zwart, S. 2005, A&A, 443, 231 180

Longair, M. S. 1992, High energy astrophysics (Cambridge University Press, 2nd ed.) 8, 17

Lucy, L. B. & Solomon, P. M. 1970, ApJ, 159, 879 5

Lucy, L. B. & White, R. L. 1980, ApJ, 241, 300 5

Lund, N., Budtz-Jørgensen, C., Westergaard, N. J., et al. 2003, A&A, 411, L231 210

MacDonald, J. & Mullan, D. J. 2004, MNRAS, 348, 702 16

MacGregor, K. B. & Cassinelli, J. P. 2003, ApJ, 586, 480 15

Maeder, A. & Meynet, G. 2003, A&A, 411, 543 16

Maeder, A. & Meynet, G. 2004, A&A, 422, 225 16

Manchanda, R. K., Polcaro, V. F., Norci, L., et al. 1996, A&A, 305, 457 21

Manfroid, J., Sterken, C., Bruch, A., et al. 1991, A&AS, 87, 481 208

Mas-Hesse, J. M., Giménez, A., Culhane, J. L., et al. 2003, A&A, 411, L261 210

Masetti, N., Palazzi, E., Bassani, L., Malizia, A., & Stephen, J. B. 2004, A&A, 426, L41 181

Mason, K. O., Breeveld, A., Much, R., et al. 2001, A&A, 365, L36 209

Massey, P., Johnson, K. E., & Degioia-Eastwood, K. 1995, ApJ, 454, 151 23, 180

McEnery, J. E., Moskalenko, I. V., & Ormes, J. F. 2004, in ASSL Vol. 304: Cosmic Gamma-Ray Sources, 361–395 203

Michaud, G., Charland, Y., & Megessier, C. 1981, A&A, 103, 244 12

Mirabel, I. F. & Rodrigues, I. 2003, Science, 300, 1119 180

Moffat, A. F. J., Lepine, S., Henriksen, R. N., & Robert, C. 1994, Ap&SS, 216, 55 5

Monnier, J. D., Greenhill, L. J., Tuthill, P. G., & Danchi, W. C. 2002, in ASP Conf. Ser. 260: Interacting Winds from Massive Stars, 331 2

Moss, D. 2003, A&A, 403, 693 12

Natalucci, L., Del Santo, M., Ubertini, P., et al. 2003, A&A, 411, L395 180

Negueruela, I., Israel, G. L., Marco, A., Norton, A. J., & Speziali, R. 2003, A&A, 397, 739 181

Neiner, C., Geers, V. C., Henrichs, H. F., et al. 2003, A&A, 406, 1019 18, 19

Nelan, E. P., Walborn, N. R., Wallace, D. J., et al. 2004, AJ, 128, 323 3, 198

Niemela, V. S. & Gamen, R. C. 2005, MNRAS, 356, 974 198

Orosz, J. A. & Kuulkers, E. 1999, MNRAS, 305, 132 180

Owocki, S. P., Castor, J. I., & Rybicki, G. B. 1988, ApJ, 335, 914 5

Owocki, S. P. & Rybicki, G. B. 1985, ApJ, 299, 265 5

Panagia, N. & Felli, M. 1975, A&A, 39, 1 1, 150, 194

Parker, E. N. 1955, ApJ, 122, 293 13

Pauldrach, A., Puls, J., & Kudritzki, R. P. 1986, A&A, 164, 86 5

Pauldrach, A. W. A., Kudritzki, R. P., Puls, J., Butler, K., & Hunsinger, J. 1994, A&A, 283, 525 5

Pittard, J. M., Dougherty, S. M., Coker, O'Connor, E., & Bolingbroke, N. 2006, A&A, submitted 8, 21, 150, 152, 196, 204

Pittard, J. M., Dougherty, S. M., Coker, R. F., & Corcoran, M. F. 2005, in X-Ray and Radio Connections (eds. L.O. Sjouwerman and K.K Dyer), held in Santa Fe, New Mexico, USA. Published electronically by NRAO, http://www.aoc.nrao.edu/events/xraydio 21, 204

Pittard, J. M. & Stevens, I. R. 1997, MNRAS, 292, 298 6

Pollock, A. M. T. 1987, A&A, 171, 135 21

Rauw, G. 2004, in ASSL Vol. 304: Cosmic Gamma-Ray Sources, 105–125 2

Rauw, G., Blomme, R., Waldron, W. L., et al. 2002, A&A, 394, 993 113, 115, 190, 191, 197

Rauw, G. & De Becker, M. 2004, A&A, 421, 693 24

Rauw, G., De Becker, M., Gosset, E., Pittard, J. M., & Stevens, I. R. 2003a, A&A, 407, 925 77, 209

Rauw, G., De Becker, M., & Linder, N. 2005a, in Massive Stars and High Energy Emission in OB Associations, JENAM 2005, held in Liège, Belgium 178, 190, 196

Rauw, G., De Becker, M., & Vreux, J.-M. 2003b, A&A, 399, 287 213, 214

Rauw, G., Sana, H., Gosset, E., et al. 2005b, in Massive Stars and High Energy Emission in OB Associations, JENAM 2005, held in Liège, Belgium 3, 95, 197

Rauw, G., Vreux, J.-M., Antokhin, I., et al. 2003c, in New Visions of the X-ray Universe in the XMM-Newton and Chandra Era (eds. F. Jansen) 3, 198

Rauw, G., Vreux, J.-M., & Bohannan, B. 1999, ApJ, 517, 416 3, 135

Reig, P., Negueruela, I., Fabregat, J., et al. 2004, A&A, 421, 673 181

Reimer, A., Pohl, M., & Reimer, O. 2006, ApJ, submitted. Available at http://arXiv.org/abs/astro-ph/0510701 9, 204

Ribo, M., Combi, J. A., & Mirabel, I. F. 2004, The Astronomer's Telegram, 235, 1 181

Romero, G. E., Benaglia, P., & Torres, D. F. 1999, A&A, 348, 868 24

Rybicki, G. B. & Lightman, A. P. 1979, Radiative processes in astrophysics (New York, Wiley-Interscience) 152

Sana, H., Rauw, G., Nazé, Y., Gosset, E., & Vreux, J.-M. 2005, MNRAS, in press 7

Sanz-Forcada, J., Franciosini, E., & Pallavicini, R. 2004, A&A, 421, 715 197

Schmidt, G. D., Harris, H. C., Liebert, J., et al. 2003, ApJ, 595, 1101 12

Setia Gunawan, D. Y. A., de Bruyn, A. G., van der Hucht, K. A., & Williams, P. M. 2003, ApJS, 149, 123 3

Shi, H. M. & Hu, J. Y. 1999, A&AS, 136, 313 23

Sidoli, L., Mereghetti, S., Larsson, S., et al. 2005, A&A, 440, 1033 181

Skinner, S. L., Zhekov, S. A., Palla, F., & Barbosa, C. L. D. R. 2005, MNRAS, 361, 191 199

Spruit, H. C. 1999, A&A, 349, 189 16

Spruit, H. C. 2002, A&A, 381, 923 16

Sterken, C., Manfroid, J., Anton, K., et al. 1993, A&AS, 102, 79 208

Stevens, I. R., Blondin, J. M., & Pollock, A. M. T. 1992, ApJ, 386, 265 6, 148

Strüder, L., Briel, U., Dennerl, K., et al. 2001, A&A, 365, L18 209

Takahashi, T., Awaki, A., Dotani, T., et al. 2004, in Proceedings of the SPIE, Volume 5488, pp. 549-560 (2004)., 549–560 203

Tassoul, J.-L. 1976, Theory of rotating stars (Princeton University Press) 10, 11, 14, 149

Torres, D. F. 2004, in ASSL Vol. 304: Cosmic Gamma-Ray Sources, 69–103 24

Torres-Dodgen, A. V., Tapia, M., & Carroll, M. 1991, MNRAS, 249, 1 154, 176

Tout, C. A., Wickramasinghe, D. T., & Ferrario, L. 2004, MNRAS, 355, L13 12

Turner, M. J. L., Abbey, A., Arnaud, M., et al. 2001, A&A, 365, L27 209

Ubertini, P., Lebrun, F., Di Cocco, G., et al. 2003, A&A, 411, L131 210

Usov, V. V. & Melrose, D. B. 1992, ApJ, 395, 575 148, 149

Van Loo, S. 2005, PhD thesis, University of Leuven 20, 178, 189, 197

Vasilevskis, S., Sanders, W. L., & van Altena, W. F. 1965, AJ, 70, 806 23

Vedrenne, G., Roques, J.-P., Schönfelder, V., et al. 2003, A&A, 411, L63 210

Vink, J. S., de Koter, A., & Lamers, H. J. G. L. M. 2000, A&A, 362, 295 5, 154

Walborn, N. 2001, in ASP Conf. Ser. 242: Eta Carinae and Other Mysterious Stars: The Hidden Opportunities of Emission Spectroscopy, 217–228 141, 176

Walborn, N. R. 1971, ApJS, 23, 257 141, 142

Walborn, N. R. & Howarth, I. D. 2000, PASP, 112, 1446 141, 176

Waldron, W. L., Cassinelli, J. P., Miller, N. A., MacFarlane, J. J., & Reiter, J. C. 2004, ApJ, 616, 542 158

Waldron, W. L., Corcoran, M. F., Drake, S. A., & Smale, A. P. 1998, ApJS, 118, 217 158

Walter, R., Bodaghee, A., Barlow, E. J., et al. 2004, The Astronomer's Telegram, 229, 1 181

White, R. L. 1985, ApJ, 289, 698 2, 20

White, R. L. & Becker, R. H. 1983, ApJ, 272, L19 1

White, R. L. & Chen, W. 1995, in IAU Symposium, 438–449 151

Williams, P. M. 1996, in ASP Conf. Ser. 93: Radio Emission from the Stars and the Sun, 15–22 113

Wilson, C. A., Finger, M. H., Coe, M. J., Laycock, S., & Fabregat, J. 2002, ApJ, 570, 287 181

Wright, A. E. & Barlow, M. J. 1975, MNRAS, 170, 41 1, 150, 194

Ziółkowski, J. 2005, MNRAS, 358, 851 180